UNIVERSITÀ
DEGLI STUDI
DI BRESCIA

DIPARTIMENTO DI INGEGNERIA CIVILE, ARCHITETTURA,
TERRITORIO, AMBIENTE E DI MATEMATICA

DOTTORATO DI RICERCA
IN INGEGNERIA CIVILE, AMBIENTALE, DELLA COOPERAZIONE
INTERNAZIONALE E DI MATEMATICA (DICACIM)

Pianificazione urbanistica e mobilità
ICAR/05

CICLO
XXXVIII

From Floating Car Data to Pavement Management System: a methodological framework for the construction of an Intervention Priority Index through multi-source data fusion

PhD Candidate:

Ing. SARA SIVERIO

Supervisor:
Chiar.mo Prof. Benedetto Barabino

Co-Supervisor:
Chiar.mo Prof. Giulio Maternini

Contents

Contents 1
List of Figures 6
List of Tables 9
List of Algorithms 10
List of Equations 11
Sommario 14
Abstract 22
Part I – Background and data foundations 24
1. Introduction 25
1.1. Motivations 25
1.2. Objectives 26
1.3. Implications 26
1.4. Structure of the dissertation 27
2. State of the art 29
2.1. Methodology 29
2.1.1. Keywords and selection criteria 29
2.1.2. Screening 29
2.1.3. Analysis 30
2.2. Floating Car Data 30
2.2.1. Keywords and selection criteria 30
2.2.2. Screening 31
2.2.3. Analysis 32
2.2.4. Overview of the analyzed contributions 35
2.2.5. Classification 35
2.2.5.1. Classification by use 36
2.2.5.2. Classification by data processing 44

2.2.5.3. Classification by technology 47
2.3. Floating Car Data in a Pavement Management System 50
2.3.1. Keywords and selection criteria 50
2.3.2. Screening 51
2.3.1. Analysis 51
2.4. Overview of the analyzed contributions 53
3. Research gap analysis 57
3.1. Floating Car Data (FCD): abundance without infrastructure focus 57
3.2. Data Fusion: sophisticated methods, misplaced priorities 58
3.3. Pavement Management Systems (PMS): traditional practices 59
3.4. Challenges and opportunities 59
4. Data characterisation and preliminary analysis 64
4.1. Analysis of VIASAT data 65
4.1.1. Methodological rationale 70
4.1.1.1. Boxplot analysis of vehicle speed by road event type 72
4.1.1.2. Analysis of the transition matrix between events 74
4.1.1.3. Conditional probability analysis of road surface events 76
4.1.1.4. Geographical density analysis of road surface events 77
4.1.1.5. Analysis of event sequence length distribution 78
4.1.1.6. Analysis of event sequences and their implications for road surface monitoring 80
4.1.1.7. First spatial analysis of road quality index 81
4.1.1.8. Second spatial analysis of road quality index 83
4.1.2. Experimental application and results 86
4.1.2.1. Boxplot analysis of vehicle speed by road event type 86
4.1.2.2. Analysis of the transition matrix between events 90
4.1.2.3. Conditional probability analysis of road surface events 92
4.1.2.4. Geographical density analysis of road surface events 95

4.1.2.5. Analysis of event sequence length distribution 98
4.1.2.6. Analysis of event sequences and their implications for road surface monitoring 100
4.1.2.7. First spatial analysis of road quality index 102
4.1.2.8. Second spatial analysis of road quality index 103
4.1.3. Conclusion of analysis of VIASAT data 105
4.2. Analysis of AIWAY data 108
4.2.1. Methodological rationale 111
4.2.1.1. Exploratory Data Analysis (EDA) 114
4.2.1.2. Spatial analysis 115
4.2.1.3. Confidence-based reliability analysis 116
4.2.1.4. Multiclass and co-occurrence analysis 117
4.2.1.5. Geostatistical and aggregation analysis 118
4.2.1.6. First partial index 119
4.2.1.7. Second partial index 120
4.2.2. Experimental application and results 121
4.2.2.1. Exploratory Data Analysis (EDA) 121
4.2.2.2. Spatial analysis 123
4.2.2.3. Confidence-based reliability analysis 130
4.2.2.4. Multiclass and co-occurrence analysis 136
4.2.2.5. Geostatistical and aggregation analysis 140
4.2.2.6. First partial index 143
4.2.2.7. Second partial index 146
4.2.3. Comparison of partial indices 148
4.2.4. Perceptual limitations of vision-based indices 149
Part II – Original contribution 153
5. Method 154
5.1. A) Network segmentation and dataset preparation 157

5.1.1. A1) Segmentation of the road network 157
5.1.2. A2) Dataset preparation 161
5.2. B) Analysis of data 165
5.2.1. B1) Redundancy analysis 165
5.3. C) Construction of Intervention Priority Index (I) 169
5.3.1. C1) Construction of sub-indices 169
5.3.2. C2) Definition of weights 173
5.3.2.1. Preliminary diagnostics: OLS and multicollinearity 174
5.3.2.2. Poisson regression 175
5.3.2.3. Negative Binomial regression (NB2) 177
5.3.2.4. Zero-Inflated Negative Binomial (ZINB) model 179
5.3.2.5. Coefficient interpretation and mapping to weights 182
5.3.3. C3) Definition of Intervention Priority Index (I) 185
5.4. D) Sensitivity analysis 188
5.4.1. D1) Sensitivity analysis on classification thresholds 188
5.4.2. D2) Sensitivity on fusion parameters (α, κ, q) 192
5.5. E) Verification 194
6. Experiments 198
6.1. A) Network segmentation and dataset preparation 199
6.1.1. A1) Segmentation of the road network 199
6.1.1.1. Tortuosity 205
6.1.1.2. Number of Turns 207
6.1.1.3. Mean turning angle 209
6.1.1.4. Scale sensitivity of geometric indicators 211
6.1.2. A2) Dataset preparation 217
6.2. B) Analysis of data 220
6.2.1. B1) Redundancy analysis 220
6.3. C) Construction of Intervention Priority Index (I) 227

6.3.1. C1) Construction of sub-indices 227
6.3.2. C2) Definition of weights 231
6.3.2.1. Preliminary diagnostics (OLS and multicollinearity) 232
6.3.2.2. Poisson regression results 233
6.3.2.3. Negative Binomial regression results (NB2) 233
6.3.2.4. Zero-Inflated Negative Binomial (ZINB) model 236
6.3.2.5. Comparative interpretation of NB2 and ZINB models 239
6.3.3. C3) Definition of Intervention Priority Index (I) 245
6.4. D) Sensitivity analysis 248
6.4.1. D1) Sensitivity analysis on classification thresholds 248
6.4.2. D2) Sensitivity on fusion parameters (α, κ, q) 255
6.5. E) Verification 264
6.5.1. E1) Macro-verification 266
6.5.2. E2) Micro-verification 272
7. Discussion 283
7.1. Methodological reflections 283
7.2. Applicability to Pavement Management Systems 286
Part III – Conclusions and references 294
8. Conclusions 295
9. References 300
Part IV – Appendices 311

List of Figures

Figure 1 - PRISMA methodology 31
Figure 2- Geographical distribution of the selected studies related to Floating Car Data. Dark blue indicates countries with ≥ 40 studies, medium blue indicates 20–39 studies, light blue indicates 5–19 studies, very light blue indicates 1-4 studies, while grey denotes countries for which no relevant studies were identified. 33
Figure 3- Temporal distribution of publications related to Floating Car Data 33
Figure 4 - Geographical distribution of the selected studies related to Floating Car Data AND Pavement Management System. Dark blue indicates countries with ≥ 40 studies, medium blue indicates 20–39 studies, light blue indicates 5–19 studies, very light blue indicates 1-4 studies, while grey denotes countries for which no relevant studies were identified. 52
Figure 5 - Temporal distribution of publications related to Floating Car Data AND Pavement Management System 52
Figure 6 - Flow chart VIASAT dataset 70
Figure 7- Boxplot with speed distribution by event type (VIASAT) 87
Figure 8 - Event-to-event transition matrix based on sequential accelerometer-detected road anomalies (VIASAT) 90
Figure 9 - Conditional probabilities between events (row-normalized) (VIASAT) 93
Figure 10 - Geographical density of road surface events (VIASAT) 96
Figure 11 - Histogram of event sequence lengths (VIASAT) 98
Figure 12 - Distribution of sequence lengths by event type (VIASAT) 100
Figure 13 - First Road Quality Index (VIASAT) 102
Figure 14 - Second Road Quality Index (VIASAT) 104
Figure 15 - Flow chart AIWAY dataset 113
Figure 16 - Distribution of confidence scores across all detected classes in the AIWAY dataset 123
Figure 17 - Spatial density of all detected pavement anomalies derived from Kernel Density Estimation (KDE) 124
Figure 18 - Class-specific KDE maps for individual defect category D50 125
Figure 19 - Class-specific KDE maps for individual defect category D40 125
Figure 20 - Class-specific KDE maps for individual defect category D20 125
Figure 21 - Class-specific KDE maps for individual defect category D10 126
Figure 22 - Class-specific KDE maps for individual defect category D00 126
Figure 23 - DBSCAN clusters. Spatial clustering of detections obtained through the DBSCAN algorithm 127
Figure 24 - Nearest-neighbor distance distribution. Boxplot of within-class nearest-neighbor distances among detections 128
Figure 25 - Weighted density map (sum of confidences) 131
Figure 26 - Weighted Defect Index (WDI) 131

Figure 27 - Detections by confidence 132
Figure 28 - Confidence by class 132
Figure 29 - Confidence distributions 133
Figure 30 - Class-wise weighted confidence maps 135
Figure 31 - Co-occurrence matrix (buffer = 10 m) 137
Figure 32 - Correlation matrix (Pearson coefficients) 138
Figure 33 - PCA scores plot 139
Figure 34 - PCA loadings (biplot) 139
Figure 35 - t-SNE projection 140
Figure 36 - Histogram of z distribution 141
Figure 37 - Empirical cumulative distribution of z 141
Figure 38 - Histograms of count-based density and sum-based density 142
Figure 39 - Distribution of deterioration index distribution of the number of detections per 100-meter grid cell (AIWAY) 144
Figure 40 - Spatial distribution of the normalized First Partial Index (AIWAY) 145
Figure 41 - Distribution of the Second Partial Deterioration Index (AIWAY) 147
Figure 42 - Spatial distribution of the Second Partial Deterioration Index (AIWAY) 148
Figure 43 - Conceptual framework for the construction of Intervention Priority Index 156
Figure 44 – Flow chart of methodology verification 196
Figure 45 - Province of Brescia (Italy) 198
Figure 46 - Map of segments: tortuosity 206
Figure 47 - Histogram of tortuosity classes 207
Figure 48 - Map of segments: number of turns 208
Figure 49 - Histogram of number of turns classes 209
Figure 50 - Map of segments: mean turning angles (degrees) 210
Figure 51 - Histogram of mean turning angles (degrees) 211
Figure 52 - Variance of tortuosity, mean turning angle, and number of turns across 50-100-200 m segments (error bars: 95% bootstrap CI) 213
Figure 53 - Coefficient of variation (CV) for the three indicators at 50-100-200 m (95% bootstrap CI) 214
Figure 54 - Sensitivity of CV at 200 m to pairing strategy (adjacent vs staggered) 215
Figure 55 - Geographical representation of the segments considered for the empirical analysis (Province of Brescia) 218
Figure 56 - Geographical representation of the final analytical dataset (Province of Brescia) 219
Figure 57 - Correlation matrix (Pearson) 224
Figure 58 - PCA Loadings 225
Figure 59 - Overdispersion check – Variance/Mean = 14.35 239
Figure 60 - Residuals comparison: Poisson vs NB2 (intercept-only) 240
Figure 61 - Model comparison based on log-likelihood (Poisson vs Negative Binomial NB2) 241

Figure 62 - Incidence Rate Ratios (IRR) from the ZINB count component by deterioration category 242
Figure 63 - Comparison of regression coefficients between NB2 and ZINB count components 243
Figure 64 - Comparison of category weights for pavement management (NB2 vs ZINB) 244
Figure 65 - Class counts (Baseline) 250
Figure 66 - Class counts - Alt 0.15 / 0.55 251
Figure 67 - Confusion - Alt 0.15 / 0.55 251
Figure 68 - Class counts - Alt 0.25 / 0.65 252
Figure 69 - Confusion - Alt 0.25 / 0.65 252
Figure 70 - Class counts - Quantiles 33 / 66 253
Figure 71 - Confusion - Quantiles 33 / 66 253
Figure 72 - Density - Baseline thresholds 254
Figure 73 - Density - All threshold configurations 254
Figure 74 - Confusion matrix: baseline vs changing α 256
Figure 75 - Confusion matrix: baseline vs changing impact of D50 258
Figure 76 - Confusion matrix: baseline vs changing q 260
Figure 77 - Sensitivity to α: ranking Spearman, HIGH-class Jaccard, overall stability 262
Figure 78 - Composite deterioration index visualised over the selected road network 264
Figure 79 – Provincial Road 37 267
Figure 80 – Provincial Road 37 (Google Street View) 267
Figure 81 - Via Mantova, Castiglione delle Stiviere 268
Figure 82 - Via Mantova, Castiglione delle Stiviere (Google Street View) 269
Figure 83 - Via Battaglione Alpini Valchiese, Gavardo 270
Figure 84 - Via Battaglione Alpini Valchiese, Gavardo (Google Street View) 270
Figure 85 - Tangenziale Sud, Brescia 271
Figure 86 - Tangenziale Sud, Brescia (Google Street View) 271
Figure 87 - Top 10 best-performing segments according to the computed deterioration index 274
Figure 88 - Top 10 best-performing segments according to the computed deterioration index (Google Street View) 275
Figure 89 - Mid-range segments (Index ≈ 0.26) according to the computed deterioration index 276
Figure 90 - Mid-range segments (Index ≈ 0.26) according to the computed deterioration index (Google Street View) 277
Figure 91 - Top 10 worst-performing segments according to the computed deterioration index 278

Figure 92 - Top 10 worst-performing segments according to the computed deterioration index (Google Street View) 279
Figure 93 - Mid-range segments (Index ≈ 0.50) according to the computed deterioration index 280
Figure 94 - Mid-range segments (Index ≈ 0.50) according to the computed deterioration index (Google Street View) 281

List of Tables

Table 1 - Headings of structured table 34
Table 2 - Classification by use 37
Table 3 - Classification by data processing 44
Table 4 - Classification by technology 47
Table 5 - AIWAY tags 110
Table 6 - Comparison of partial indices 149
Table 7 - Definition of variables used in the dataset construction 161
Table 8 - Definition of variables used in the redundancy analysis 167
Table 9 - Definition of variables used in the construction of category-level sub-indices 169
Table 10 - Definition of variables and parameters used in near-miss-based weighting 174
Table 11 - Variables and parameters used in the composite deterioration index 185
Table 12 - Critical analysis of literature on technical road-segmentation length 201
Table 13 - VIASAT tags 221
Table 14 - AIWAY tags 222
Table 15 - Association of AIWAY and VIASAT indicators into distress categories 227
Table 16 - Diagnostic results (OLS and multicollinearity diagnostics) 232
Table 17 - Poisson model results and overdispersion check 233
Table 18 - NB2 category-level coefficients and normalised weights 234
Table 19 - ZINB category-level coefficients and normalised weights 238
Table 20 - Parameter roles and sensitivity ranges. 255
Table 21- Overview of analysed contributions 312
Table 22 - Overview of analysed contributions (FCD & PMS) 340
Table 23 – Dataset of geometry of segments 360
Table 24 – Dataset of sub-indices 379

List of Algorithms

Algorithm 1 - BoxplotSpeedByEventType 74
Algorithm 2 - BuildTransitionMatrix 75
Algorithm 3 - ComputeConditionalProbabilityMatrix 77
Algorithm 4 - GeographicalDensityMap 78
Algorithm 5 - ComputeSequenceLengthDistribution 80
Algorithm 6 - ComputeSequenceStatistics 81
Algorithm 7 - ComputeFirstRoadQualityIndex 83
Algorithm 8 - ComputeSecondRoadQualityIndex 86
Algorithm 9 - ProcessAIWAYDetections 114
Algorithm 10 - SpatialAnalysisAIWAY 115
Algorithm 11 - ConfidenceBasedReliabilityAIWAY 117
Algorithm 12 - MulticlassAndCoOccurrenceAnalysis 117
Algorithm 13 - GeoStatAggAIWAY 118
Algorithm 14 - First partial index 119
Algorithm 15 - Second partial index 120
Algorithm 16 - SegmentRoadNetwork 157
Algorithm 17 - ComputeTortuosity 158
Algorithm 18 - ComputeNumberOfTurns 159
Algorithm 19 - ComputeMeanTurningAngle 160
Algorithm 20 - ManageRedundancyPairs 167
Algorithm 21 - BuildCategorySubIndices 173
Algorithm 22 - FitPoissonModel 177
Algorithm 23 - FitNB2Model 178
Algorithm 24 - FitZINBModel 181
Algorithm 25 - ComputeWeightsFromBetas 185
Algorithm 26 - CalibrateCompositeDeteriorationIndex 187

List of Equations

Equation 1 - Conditional probability of event transitions in the sequential matrix 76
Equation 2 - Count of event sequences of a given length 79
Equation 3 - Empirical probability distribution of sequence lengths 80
Equation 4 - Composite formulation of the Road Quality Index (RQI) combining density and severity components 81
Equation 5 - Event density as the total count of detected anomalies within a segment 81
Equation 6 - Total severity as the cumulative weighted sum of all detected events within a segment 82
Equation 7 - Average severity computed as the ratio between total severity and event density 82
Equation 8 - Original composite formulation of the Road Quality Index (RQI), combining density and severity components 84
Equation 9 - Algebric reduction of the original RQI formulation, highlighting the non-linear amplification effect 84
Equation 10 - Refined, linearly interpretable definition of the Road Quality Index based on total weighted severity 84
Equation 11 - Expanded formulation expressing total and mean severity as weighted sums of anomaly counts 85
Equation 12 - Event density defined as the sum of detected anomalies per segment 85
Equation 13 - Standardized version of the Road Quality Index combining normalized density and mean severity 85
Equation 14 - Definition of the Weighted Defect Index (WDI) 116
Equation 15 - Normalized deterioration index computed through min–max scaling to ensure comparability across road segments with different lengths and traffic volumes (AIWAY) 119
Equation 16 - Deterioration index computed as the weighted sum of confidence scores for all detected defect types, where weights reflect each defect's structural and safety relevance (AIWAY) 120
Equation 17 - Tortuosity index expressing the ratio between the actual curved length of the road segment and the straight-line distance between its endpoints 158
Equation 18 - Number of turns, defined as the count of directional alternations along the segment, based on changes in the sign of consecutive turning angles 159
Equation 19 - Definition of consecutive direction vectors used to compute turning angles between polyline vertices 159
Equation 20 - Turning angle at vertex k, calculated as the angle between consecutive direction vectors along the segment 160
Equation 21 - Mean turning angle for segment i, expressing the average angular deviation and overall geometric complexity along the road segment 160

Equation 22 - Definition of a deterioration event 162
Equation 23 - Spatial assignment of events to road segments 162
Equation 24 - Definition of the temporal observation window 163
Equation 25 - Computation of distress occurrence frequency 163
Equation 26 - Averaged severity within each segment 163
Equation 27 - Averaged detection confidence within each segment 164
Equation 28 - Segment-level geometric descriptors 164
Equation 29 - Segment-level feature vector integrating geometry and deterioration evidence 164
Equation 30 - Computation of sample moments and coefficient of variation across segment lengths 165
Equation 31 – Principal component scores for each segment 168
Equation 32 - Category-level sub-index combining normalized indicators within distress category t, where intra-category weights reflect each variable's variance and inverse redundancy 170
Equation 33 - Simplified category-level sub-index for non-redundant categories 170
Equation 34 - Raw intra-category weighting based on variance and inverse redundancy 171
Equation 35 - Category-level normalization ensuring convex aggregation 171
Equation 36 – Category-level fusion of visual and accelerometric signals for distress channel (d,k) 172
Equation 37 - Generalized linear model specification for count data, linking the expected near-miss frequency μ_i to a log-linear combination of predictors and an exposure offset term ensuring non-negative, interpretable outcomes 175
Equation 38 - Pearson dispersion statistic for assessing overdispersion in Poisson count models 176
Equation 39 - Variance function of the NB2 model, introducing the dispersion parameter α to account for overdispersion in near-miss count data relative to the Poisson assumption 177
Equation 40 - Log-likelihood function of the NB2 model used for Maximum Likelihood Estimation 178
Equation 41 - ZINB probability mass function 179
Equation 42 - Log-linear specification of the count component 179
Equation 43 - Logit formulation for the inflation component 180
Equation 44 - Definition of the logit function 180
Equation 45 - Logistic transformation (inverse of the logit) 181
Equation 46 - Definition of the Incidence Rate Ratio (IRR) 182
Equation 47 - Truncation and normalisation of regression coefficients 183
Equation 48 - Composite deterioration index integrating all category-level sub-indices into a single interpretable metric through empirically estimated weights W_t 186

Equation 49 - Spearman rank correlation between composite index and near-miss frequency 187
Equation 50 - Threshold-based classifier mapping the continuous deterioration index Iiinto LOW, MEDIUM and HIGH condition classes defined by thresholds $\tau = (\tau 1, \tau 2)$ 188
Equation 51 - Quantile-based thresholds used for distribution-driven classification 189
Equation 52 - Overall class stability measuring the fraction of segments retaining the same class under baseline $\tau$and alternative τ'thresholds 189
Equation 53 - Confusion-matrix entries Mab counting segments classified as $a$under the baseline and $b$under the perturbed thresholds 190
Equation 54 - Class-level stability metric quantifying the proportion of correctly retained assignments across threshold configurations 190
Equation 55 - Jaccard similarity coefficient measuring the proportion of elements consistently classified in the same category across two threshold configurations, used to assess classification stability 191
Equation 56 - Jaccard similarity on the top-m segments with highest deterioration, assessing stability of critical-priority rankings under parameter perturbations 193
Equation 57 - Spearman rank-correlation coefficient measuring the stability of segment prioritisation between baseline parameter $\theta 0$and perturbed configuration $\theta = (\alpha, \kappa, q)$ 193
Equation 58 - Correlation coefficient between composite deterioration index $Ii$and near-miss frequency Yi, used as a large-scale consistency diagnostic 194
Equation 59 - Spearman rank correlation between baseline and alternative configurations of the composite index, used to evaluate ranking stability under parameter perturbations 195
Equation 60 - Weighted Cohen's κ statistic measuring agreement between categorical field ratings and model-based deterioration classes 196

Sommario

Le infrastrutture stradali rappresentano una componente fondamentale dei sistemi di mobilità e del patrimonio pubblico, poiché la loro condizione funzionale influisce direttamente sulla sicurezza, sull'efficienza dei flussi e sulla sostenibilità economica dei programmi di manutenzione. Tuttavia, i metodi di monitoraggio oggi più diffusi rimangono episodici e basati su campagne di rilievo ad alta intensità strumentale, come le ispezioni visive, la profilometria laser o il LiDAR. Tali approcci forniscono misurazioni precise ma frammentarie, caratterizzate da costi elevati, copertura spaziale limitata e bassa frequenza temporale. Questa natura discontinua dei rilievi compromette la capacità dei Pavement Management Systems (PMS) di individuare tempestivamente i difetti emergenti, di anticipare le strategie di manutenzione e di valutare l'efficacia delle politiche di intervento.

Contemporaneamente, la rapida diffusione di veicoli connessi e dei sensori di bordo ha reso disponibile un'enorme quantità di dati di mobilità generati in modo continuo e distribuito. I Floating Car Data (FCD) costituiscono oggi una risorsa informativa senza precedenti per osservare le interazioni veicolo-pavimentazione su larga scala. Nonostante ciò, l'applicazione di queste tecnologie all'ambito del monitoraggio infrastrutturale è ancora agli inizi. La letteratura evidenzia che, mentre gli FCD vengono comunemente impiegati per l'analisi del traffico, la previsione dei tempi di percorrenza o la gestione della mobilità, il loro utilizzo per la diagnosi delle pavimentazioni è rimasto marginale. Questo divario tra la maturità dei PMS e la disponibilità di FCD rappresenta il punto di partenza e la principale motivazione scientifica del lavoro di ricerca.

La revisione sistematica condotta nel presente elaborato ha permesso di individuare un disallineamento tra tre domini oggi sviluppati in modo quasi indipendente: FCD, PMS e data fusion. I Floating Car Data costituiscono una fonte ubiqua e a basso costo, capace di fornire copertura spaziale e temporale molto superiore ai rilievi tradizionali e permettono di sfruttare i numerosi veicoli che circolano per le infrastrutture in veri e propri sensori del territorio. Dall'altro lato, i PMS continuano a basarsi su protocolli consolidati e norme istituzionali che richiedono ispezioni periodiche e misurazioni certificate come l'International Roughness Index (IRI) o il Pavement Condition Index

(PCI). Infine, i metodi di data fusion, pur essendo maturi e ampiamente applicati per la gestione del traffico, non sono stati ancora adattati in modo sistematico al monitoraggio delle infrastrutture. La mancanza di un quadro metodologico capace di integrare queste tre dimensioni costituisce il gap scientifico principale affrontato in questa tesi.

L'analisi della letteratura mostra come gli accelerometri installati nei veicoli (per esempio tramite le blackbox delle assicurazioni) raccolgano segnali che riflettono in modo indiretto la risposta meccanica della pavimentazione. Le vibrazioni verticali e gli urti registrati dai sensori consentono di rilevare discontinuità, sconnessioni e irregolarità che si traducono in variazioni di comfort e sicurezza. Tuttavia, l'assenza di accesso ai segnali grezzi, la diversità delle flotte e la mancanza di standard di elaborazione rendono difficile derivare da tali dati indicatori comparabili e affidabili. I sistemi di visione artificiale, invece, basati su algoritmi di deep learning consentono di riconoscere difetti visibili come crepe, buche o avvallamenti, ma presentano vulnerabilità legate alle condizioni ambientali, all'illuminazione e alla copertura spaziale. L'integrazione di queste fonti eterogenee, secondo logiche di fusione multi-sensore, rappresenta dunque il passo necessario per superare i limiti di ciascuna tecnologia.

Su questa base concettuale, la tesi sviluppa e sperimenta un quadro metodologico integrato che unisce tre classi di informazioni: dati accelerometrici e near-miss provenienti dal sistema VIASAT, rilevazioni da visione artificiale acquisite tramite il sistema AIWAY, e indicatori geometrici estratti dalla rete stradale del Comune di Brescia.

Il database sperimentale, costruito a partire dai dati reali della città di Brescia, integra circa 74.000 punti accelerometrici e oltre 63.000 rilevazioni visive, successivamente armonizzati su base segmentale mediante join spaziali. L'integrazione delle sorgenti è stata condotta secondo un principio di coerenza spaziale, garantendo che ogni osservazione proveniente da un sensore fosse attribuita al corrispondente tratto stradale. Le informazioni di VIASAT comprendono quattro categorie di eventi (type 1-4) che rappresentano rispettivamente buche, discontinuità lineari, irregolarità diffuse e avvallamenti lievi.

Le rilevazioni di AIWAY, basate su modelli YOLOv8 e YOLOv11 per il riconoscimento di anomalie a partire da fotografie scattate in sequenza da smartphone, sono classificate in cinque classi principali: D00-D40 per le forme di degrado e D50 per la presenza di chiusini e tombini. Le prime quattro rappresentano fessurazioni longitudinali, trasversali, a pelle di coccodrillo e deformazioni superficiali; la D50, invece, identifica elementi funzionali della pavimentazione e svolge un ruolo correttivo nelle analisi successive.

La fase preliminare di elaborazione ha riguardato la validazione delle sorgenti, la rimozione di duplicati e il calcolo di statistiche descrittive. Successivamente sono state eseguite diverse analisi esplorative e inferenziali per comprendere la struttura dei dati e le relazioni tra le variabili. Lo studio del comportamento dei conducenti, condotto attraverso la distribuzione delle velocità per ciascun tipo di anomalia, ha mostrato che le buche (type 1) provocano una riduzione sistematica e uniforme della velocità, mentre le discontinuità lineari (type 2) generano comportamenti più eterogenei. Le irregolarità diffuse (type 3) comportano decelerazioni moderate, e le depressioni lievi (type 4) risultano spesso impercettibili. Il test di Kruskal-Wallis ha confermato la significatività statistica delle differenze osservate, validando l'affidabilità della classificazione accelerometrica. Questo risultato dimostra che i dati telematici riflettono non solo la presenza fisica delle irregolarità, ma anche la loro percezione e il comportamento indotto negli utenti.

L'analisi sequenziale degli eventi, formalizzata attraverso matrici di transizione e probabilità condizionate, ha permesso di quantificare le relazioni tra anomalie consecutive. Le transizioni più frequenti riguardano eventi omogenei ("buche → buche"), che indicano cluster spaziali di degrado continuo, mentre le transizioni eterogenee appaiono più rare. Tale struttura, modellabile come catena di Markov, consente di inferire percorsi di deterioramento e di distinguere tra difetti isolati e processi evolutivi. L'analisi della lunghezza delle sequenze ha confermato che la maggior parte delle anomalie è episodica, ma esistono sequenze estese - oltre cento rilevazioni consecutive - che segnalano tratti critici soggetti a degrado strutturale persistente. Queste osservazioni hanno contribuito alla costruzione di un indicatore sintetico della qualità stradale, il Road Quality Index (RQI), ottenuto combinando frequenza e severità degli eventi con criteri parametrici di classificazione. Dopo una

prima formulazione di tipo moltiplicativo, il modello è stato riformulato in versione lineare per evitare ridondanze e amplificazioni non proporzionali, producendo un indice basato sulla sola fonte accelerometrica.
L'elaborazione dei dati AIWAY fornisce una rappresentazione visiva e quantitativa del degrado superficiale attraverso un flusso continuo: le immagini acquisite a bordo vengono anonimizzate in tempo reale e analizzate da modelli di deep learning per il riconoscimento dei difetti, con attribuzione di coordinate, timestamp e punteggi di confidenza. Dopo i controlli esplorativi sulla qualità del dato, l'organizzazione spaziale dei difetti è studiata con Kernel Density Estimation e clustering DBSCAN, evidenziando hotspot coerenti con i meccanismi fisici di deterioramento. I punteggi di confidenza sono impiegati come pesi per costruire un Weighted Defect Index che integra frequenza e severità visiva. Infine, tramite interpolazione geostatistica e statistiche zonali, le rilevazioni puntuali sono aggregate al livello di segmento (100 m), ottenendo indicatori normalizzati e confrontabili.
Queste analisi preliminari, condotte con l'obiettivo di comprendere la struttura e la coerenza interna dei dati, costituiscono una fase esplorativa di conoscenza delle sorgenti. Esse non fanno ancora parte del metodo di fusione proposto, ma ne rappresentano il presupposto operativo e concettuale, fornendo le basi per la costruzione sistematica dell'indice composito nelle sezioni successive.

La metodologia proposta definisce un percorso strutturato per trasformare misure eterogenee di degrado, provenienti da sensori visivi e accelerometrici, in un unico indicatore sintetico di priorità manutentiva a scala di segmento stradale. Il metodo è articolato in step consecutivi, dalla segmentazione e preparazione del dataset, alla gestione della ridondanza tra variabili, alla costruzione e calibrazione dell'Intervention Priority Index, fino alle analisi di sensibilità e alle verifiche qualitative sulla rete di studio.
Il metodo ha inizio con lo step A1) Segmentation of the road network, in cui si adotta il segmento stradale come unità di analisi fondamentale, con una lunghezza di 100 metri. Tale scelta, discussa in letteratura, rappresenta un compromesso statistico tra dettaglio spaziale e stabilità dei dati, in grado di ridurre il rumore senza perdere la sensibilità verso fenomeni locali di degrado. Ogni segmento è caratterizzato da una

serie di indicatori geometrici: tortuosità, numero di svolte e angolo medio di deviazione. Con lo step A2) Dataset preparation, invece, si filtrano i dati sul periodo temporale che si vuole attenzionare e si filtrano i segmenti per cui sono presenti gli attributi di entrambe le sorgenti (il numero di segmenti su cui si focalizza la trattazione è di 1,598).

L'integrazione tra sorgenti visive e accelerometriche ha richiesto una gestione esplicita della ridondanza (step B1) Redundancy analysis). È emerso che le classi D40 e type 1, così come D20 e type 3, descrivono fenomeni fisicamente simili; per evitare duplicazioni, i dati sono stati armonizzati tramite analisi di correlazione, co-occorrenza e Principal Component Analysis. I risultati mostrano due ridondanze: D40–type 1 (buche/rugosità) e D20–type 3 (fessurazioni/irregolarità). Il componente D50 (tombini) è stato usato come segnale di attenuazione dei contributi accelerometrici, prevenendo falsi positivi. Questa strategia ha consentito di costruire sub-indici coerenti per categorie di deterioramento (step C1) Construction of sub-indices).

A questi sub-indici sono stati poi assegnati dei pesi che sono stati calcolati nello step C2) Definition of weights. I pesi sono stati calcolati mediante modelli di regressione di conteggio con vincolo di non negatività zero-inflated, calibrando il modello sui dati relativi ai near-miss (appartenenti al dataset VIASAT). Le regressioni Poisson e Negative Binomial (NB2) hanno evidenziato una forte sovradispersione, risolta con l'adozione del modello ZINB con un p-value di 1.27×10^{-10}.

Si passa così allo step C3) Construction of Intervention Priority Index (I). L'indice può assumere valori compresi tra 0 e 1 (0 indica bassa priorità di intervento, 1 indica massima priorità di intervento).

La metodologia sviluppata si caratterizza inoltre per trasparenza e robustezza statistica. Tutti i passaggi di elaborazione sono riproducibili, con parametri esplicitati e controlli di sensibilità documentati nello step D) Sensitivity Analysis.

Le analisi di sensibilità sui parametri di fusione e sulle soglie di classificazione hanno confermato l'affidabilità del sistema. Le soglie 0,20 e 0,60 per la distinzione tra classi di deterioramento basso, medio e alto si sono dimostrate le più coerenti, preservando l'interpretabilità fisica dei valori e la stabilità della classe "alta", che rappresenta i tratti

di priorità manutentiva. Configurazioni alternative hanno mostrato ridotta stabilità e perdita di coerenza semantica, a conferma della solidità dell'impostazione adottata.
Nello step E) Verification, il presente elaborato esplora il funzionamento dell'Intervention Priority Index e viene verificata la coerenza tra l'indicatore e le condizioni visivamente osservabili sui segmenti analizzati. Le mappe ottenute evidenziano una distribuzione spaziale dei valori coerente con l'organizzazione funzionale della rete: le arterie principali e tangenziali presentano valori medi di deterioramento inferiori, mentre i tratti locali o periferici, caratterizzati da pavimentazioni più eterogenee e minori interventi programmati, mostrano livelli più elevati di degrado. Questa relazione rispecchia i meccanismi tipici dei cicli di vita delle pavimentazioni, confermando la capacità dell'indice di cogliere fenomeni strutturali e non puramente superficiali.
La validazione qualitativa condotta su campioni rappresentativi di segmenti - scelti tra i top performer, i medium performer e i worst performer - ha mostrato corrispondenza tra i valori dell'indice e le condizioni osservate tramite immagini a bordo veicolo. Nei segmenti classificati con punteggio alto, le immagini evidenziano effettivamente buche, dissesti diffusi e patch irregolari; nei segmenti con punteggio basso la pavimentazione appare omogenea, con assenza di crepe o deformazioni.

Un elemento di forza del metodo è la capacità di collegare la misura del deterioramento con la sicurezza stradale. L'associazione positiva tra l'indice composito e la frequenza di incidenti, controllata per esposizione e geometria, suggerisce che le condizioni della pavimentazione influenzano in modo significativo la probabilità di eventi critici. Questo risultato amplia la portata applicativa del modello, che non si limita alla gestione del patrimonio stradale ma offre anche un contributo alla pianificazione delle politiche di sicurezza. In tal senso, la ricerca propone una convergenza tra due domini tradizionalmente separati - manutenzione e sicurezza - dimostrando che un sistema di monitoraggio basato su veicoli connessi può supportare entrambe le funzioni in un'ottica preventiva.

Dal punto di vista metodologico, la tesi introduce un contributo originale nel modo in cui la ridondanza informativa viene trattata come elemento da considerare e non come

problema. Mentre la maggior parte degli studi tende a eliminare le variabili correlate, questo lavoro adotta un approccio di armonizzazione che sfrutta la co-occorrenza tra sorgenti per validare empiricamente la presenza di fenomeni di degrado reali. L'uso della Principal Component Analysis e delle misure di correlazione e co-occorrenza consente di identificare coppie ridondanti, ma anche di distinguerle da segnali indipendenti. In questo modo la ridondanza diventa una risorsa informativa per rafforzare la coerenza dell'indicatore composito, evitando sia il doppio conteggio sia la perdita di informazioni.

Dal punto di vista operativo, l'approccio permette di costruire un indicatore unificato, trasparente e scalabile, in grado di supportare la pianificazione della manutenzione su reti estese. L'indice non intende sostituire le indagini strutturali o deflettometriche, ma fornire un supporto rapido e continuo per l'identificazione dei tratti critici. In un contesto urbano come quello bresciano, dove l'estensione della rete e i vincoli di bilancio rendono impraticabile un monitoraggio tradizionale frequente, la disponibilità di un indicatore derivato da dati veicolari consente di orientare le ispezioni verso le aree più a rischio, migliorando l'efficienza allocativa delle risorse.

La ricerca evidenzia anche alcune limitazioni. L'applicazione è stata condotta su un'unica rete urbana prevalentemente in conglomerato bituminoso; pavimentazioni con comportamenti strutturali differenti, come basolati storici o corsie tranviarie, richiederebbero una ricalibrazione dei pesi o l'addestramento di nuovi modelli di visione artificiale. Inoltre, l'indice fornisce una misura relativa del degrado, non un valore assoluto confrontabile con scale normative, poiché mancano dati di riferimento certificati. Queste limitazioni non compromettono la validità del metodo, che è concepito come strumento di screening e prioritizzazione.

Le prospettive future individuate nel lavoro comprendono quattro principali direzioni di sviluppo. La prima riguarda la calibrazione inter-rete: applicare la metodologia a contesti geografici differenti permetterebbe di verificare la trasferibilità del modello e di evolvere verso una forma standardizzata dell'indicatore, utile per confronti tra città o regioni. La seconda riguarda l'estensione temporale: l'acquisizione ripetuta di FCD e dati visivi nel tempo consentirebbe di stimare la progressione del deterioramento e di prevedere l'evoluzione dei difetti, abilitando approcci di manutenzione predittiva. La terza riguarda l'integrazione di nuove sorgenti: l'inclusione di dati da LiDAR,

profilometri dinamici o sensori acustici permetterebbe di arricchire la componente strutturale del modello e ridurre l'incertezza derivante da singole modalità di rilevazione. Infine, la quarta prospettiva riguarda l'allineamento con gli indicatori normativi: l'eventuale disponibilità di misurazioni PCI o IRI future consentirebbe la calibrazione diretta dell'indice composito con standard riconosciuti, rafforzandone la validazione esterna.

La tesi, in conclusione, sviluppa un metodo integrato, scalabile e statisticamente fondato per la valutazione del deterioramento del manto stradale basato sull'uso combinato di Floating Car Data, dati accelerometrici e rilevazioni da visione artificiale. Il lavoro fornisce un contributo originale sia sul piano scientifico, introducendo un quadro metodologico di fusione multi-sorgente orientato alla gestione della ridondanza e alla calibrazione rispetto alla sicurezza, sia sul piano applicativo, proponendo uno strumento operativo per il supporto alle decisioni nei Pavement Management Systems. I risultati dimostrano che i veicoli connessi possono agire come piattaforme sensoriali distribuite, capaci di estendere la copertura spaziale e temporale del monitoraggio infrastrutturale ben oltre i limiti delle indagini tradizionali. Il framework proposto è trasparente, riproducibile e adattabile, e offre le basi per una gestione della manutenzione stradale più proattiva, orientata alla prevenzione e fondata su evidenze quantitative.

Abstract

Road infrastructures represent a critical component of urban mobility systems, as their functional condition directly affects safety, traffic performance, and the economic sustainability of maintenance operations. Traditional monitoring still relies on resource-intensive surveys such as visual inspections, profilometric measurements, or LiDAR acquisitions. These approaches provide high-quality data but are costly, spatially fragmented, and temporally infrequent, which limits the ability of Pavement Management Systems (PMS) to detect early deterioration and to support preventive maintenance. The increasing availability of connected vehicles and onboard sensing technologies has enabled the continuous generation of Floating Car Data (FCD), offering large-scale observations of vehicle–pavement interactions. The literature shows, however, that FCD applications remain predominantly traffic-oriented, with limited contributions to pavement condition monitoring.

The thesis addresses this gap by developing a methodological framework that integrates accelerometric signals, computer-vision detections, and geometric descriptors of the road network. The approach is based on segment-level spatial harmonisation, redundancy-aware multi-sensor fusion, and a safety-anchored calibration model using non-negative count regression. Approximately 74,000 accelerometric events and more than 63,000 image-based detections were collected and harmonised across the urban network of Brescia. FCD-derived shocks (Type 1–4) and vision-based anomalies (D00–D40) were fused while controlling for systematic distortions associated with functional elements such as manholes (D50). Statistical analyses, including PCA, correlation matrices, and co-occurrence patterns, supported the identification of redundant and independent signals. A composite deterioration indicator was developed by assigning interpretable weights derived from regression models and validated through macro- and micro-scale verification.

The results confirm that connected vehicles can operate as distributed sensing platforms capable of extending the spatial and temporal coverage of road-condition monitoring beyond the limits of traditional surveys. The fused indicator exhibits stable deterioration patterns aligned with functional road hierarchies, and its positive association with near-miss and crash frequencies supports its relevance for safety

assessment. The methodological contribution lies in the systematic integration of heterogeneous sensing sources within a coherent fusion architecture, providing an operational and scalable tool for PMS. The framework is transparent, reproducible, and adaptable, and represents a foundation for proactive and data-driven road-maintenance strategies.

Part I – Background and data foundations

1. Introduction

1.1. Motivations

Urban road networks are among the most valuable components of public infrastructure, as their functional condition has a direct impact on safety, mobility efficiency, and the economic sustainability of maintenance programmes. Most monitoring practices still rely on periodic and resource-intensive surveys such as laser profilometry, LiDAR campaigns, or visual inspections. These methods provide accurate measurements, but they are costly, spatially fragmented, and temporally sparse. As a consequence, Pavement Management Systems (PMS) often struggle to detect early deterioration, to plan interventions proactively, and to assess maintenance policies with the required temporal continuity.

The management of road infrastructure has become a strategic element within the broader transition toward sustainable and data-driven urban mobility. European digitalisation and smart-mobility initiatives, such as the Sustainable and Smart Mobility Strategy, emphasise continuous asset monitoring to guarantee safety and optimise maintenance budgets. Despite this policy momentum, the systematic adoption of data-driven monitoring methods in road management remains limited when compared to other domains such as railways or bridges, where sensor networks and predictive analytics are already consolidated practices.

The increasing availability of mobility data generated by connected vehicles and onboard sensors is progressively reshaping the monitoring landscape. Floating Car Data (FCD), accelerometric signals, and image-based detections from vehicle-mounted cameras provide continuous information over extensive areas, offering the opportunity to observe pavement–vehicle interactions at unprecedented scale. The potential of these data sources for infrastructure monitoring is significant, yet their methodological exploitation remains fragmented. FCD are widely employed for traffic analysis, travel-time estimation, and mobility management, but their use for evaluating pavement condition is still marginal.

Integrating heterogeneous sources into a common analytical model is a methodological challenge. The heterogeneity stems not only from the different sensing technologies but also from divergent sampling rates, levels of precision, and semantic definitions. Achieving consistent results requires both statistical harmonisation and conceptual alignment between data layers.

1.2. Objectives

This thesis responds to this research gap by developing and validating an integrated, data-driven methodology for assessing pavement condition in urban environments. The central idea is to consider circulating vehicles as a distributed sensor network capable of capturing complementary aspects of deterioration. Accelerometers record dynamic responses linked to subsurface irregularities, while computer-vision systems detect surface defects such as cracks or deformations. Combining these heterogeneous data sources enables the construction of a coherent analytical framework that transforms raw vehicular observations into interpretable, spatially consistent, and temporally updatable indicators of pavement condition.

The rationale of this work is to bridge the divide between the growing availability of high-frequency vehicular data and the absence of operational frameworks capable of transforming them into actionable maintenance indicators. From a methodological perspective, the study prioritises transparency and reproducibility, ensuring that each analytical step is traceable and the resulting indices are interpretable. From an operational standpoint, it contributes to the emerging paradigm of preventive and predictive maintenance in urban road networks, offering a practical route toward continuous condition monitoring at scale.

The research builds on three methodological pillars. First, it systematises the current state of knowledge on vehicle-borne data for infrastructure monitoring through a PRISMA-based literature review, tracing the evolution from early telemetry studies to modern AI-assisted sensing. Second, it formalises a multi-source fusion framework that harmonises dynamic, visual, and geometric information on a shared spatial backbone. Third, it develops and validates a composite Intervention Priority Index (IPI) that integrates the different information layers, aligns them with safety indicators, and quantifies uncertainty through confidence-based weighting.

1.3. Implications

The scientific contribution of the thesis lies in extending the use of vehicular data from traffic analytics to infrastructure diagnostics, demonstrating that connected vehicles can function as distributed observatories for road condition. The methodological contribution consists of a transferable and statistically validated data-fusion architecture that unifies accelerometric and vision-based observations within a

transparent analytical workflow. The practical contribution provides a scalable and cost-efficient tool for local authorities and infrastructure managers, supporting continuous monitoring, prioritisation of maintenance actions, and risk-aware planning. The broader implication is a shift from reactive inspection cycles to data-driven asset management based on continuous evidence.

1.4. Structure of the dissertation

The dissertation is structured into eight chapters that collectively develop the conceptual foundations, methodological framework, empirical application and final contributions of the research. This is Chapter 1 in which the motivation and objectives of the research are introduced, the strategic relevance of continuous and data-driven road-infrastructure monitoring is presented and the conceptual rationale behind the use of vehicle-borne data is outlined. Chapter 2 provides the State of the Art through a PRISMA-based systematic review, examining Floating Car Data from technological, analytical and application perspectives and highlighting their limited integration within Pavement Management Systems. Chapter 3 presents the research gap analysis, identifying the methodological misalignments between current FCD applications, the evolution of multi-sensor data-fusion techniques and the persistence of traditional PMS methodologies. Chapter 4 describes the datasets employed in the empirical work, including accelerometric detections from VIASAT and computer-vision anomalies from AIWAY, and reports the preliminary analyses conducted to assess consistency, spatial structure and informative content.
Chapter 5 formalises the proposed methodology, detailing the procedures for network segmentation, dataset preparation, redundancy assessment, construction of sub-indices, statistical modelling for weight estimation and development of the Intervention Priority Index. Chapter 6 applies the methodology to the Municipality of Brescia, reporting geometric indicators, redundancy diagnostics, regression results, sensitivity analyses and both macro-scale and micro-scale verification. Chapter 7 discusses the results and methodological implications, integrating the empirical evidence with the insights from the literature. Chapter 8 concludes the dissertation by summarising the scientific and operational contributions, discussing limitations and outlining future research directions, including cross-network calibration, temporal deterioration modelling and the extension of the framework to additional sensing modalities.

An Appendix is included at the end of the dissertation, providing supplementary tables and detailed reference material supporting the empirical analyses and methodological procedures.

2. State of the art

2.1. Methodology

The systematic review of existing literature on the use of Floating Car Data (FCD) for assessing transport infrastructure and services in urban environments was conducted following the PRISMA methodology [1]. PRISMA (Preferred Reporting Items for Systematic Reviews and Meta-Analyses) is a rigorous and transparent method designed to synthesize scientific evidence that meets predefined inclusion and exclusion criteria. The objective of this review is to identify, evaluate, and aggregate studies that employ FCD to derive metrics relevant for infrastructure monitoring, mobility planning, and pavement condition assessment.
The PRISMA process is divided into four main stages: identification, screening, eligibility, and inclusion.

2.1.1. Keywords and selection criteria

The literature search was conducted using a predefined set of keywords selected to ensure comprehensive coverage of studies relevant to the research domain. The same keyword strategy was applied consistently across all academic databases to maintain methodological rigor.
Inclusion criteria required that studies were peer-reviewed, written in English, and presented empirical or methodological contributions aligned with the scope of the review. Publications were excluded when they did not contain data-driven analyses, fell outside the thematic focus, or addressed unrelated application domains. These criteria were defined prior to the search process and applied uniformly to support transparency and replicability.

2.1.2. Screening

All retrieved records were imported into a reference management environment and organised into a structured dataset. The screening process began with duplicate removal, followed by a title-based assessment to exclude clearly irrelevant works.

Abstracts of the remaining entries were then reviewed to assess their coherence with the review's scope and methodological requirements.
Studies that lacked empirical evidence, did not provide a clear methodological framework, or mentioned the topic only superficially were excluded at this stage. This multi-step procedure ensured that only studies with substantive relevance progressed to the subsequent analytical phase.

2.1.3. Analysis

The studies retained after screening underwent detailed examination through full-text analysis or extended abstract review. Key information was systematically extracted regarding data sources, analytical methods, technological approaches, and application contexts.
This information was organised into a comparative framework to support thematic synthesis and cross-study evaluation. The analytical process focused on identifying methodological patterns, categorising technological approaches, and highlighting areas where the literature remains limited or inconsistent. This structured synthesis formed the basis for defining the state of the art and identifying research gaps addressed by the present work.

2.2. Floating Car Data

2.2.1. Keywords and selection criteria

In the identification phase, a structured and exhaustive search strategy was employed across three major bibliographic databases: Web of Science (WoS), Scopus, and Google Scholar. Each platform was queried using a combination of carefully selected keywords, standardized across databases to maintain consistency. The core terms included "floating car data" and its common abbreviation "FCD," which were often paired with other relevant descriptors such as "road quality," "urban infrastructure," "pavement monitoring," "vehicle-based sensing," and "smart mobility." This combination of keyword sets ensured broad and inclusive coverage of the academic landscape.
Studies published in English between 1970 and 2025 were considered, ensuring a balance between historical perspective and contemporary advancements. Conference

proceedings, journal articles, technical reports, and doctoral theses were all eligible for consideration, provided they met relevance and quality criteria.

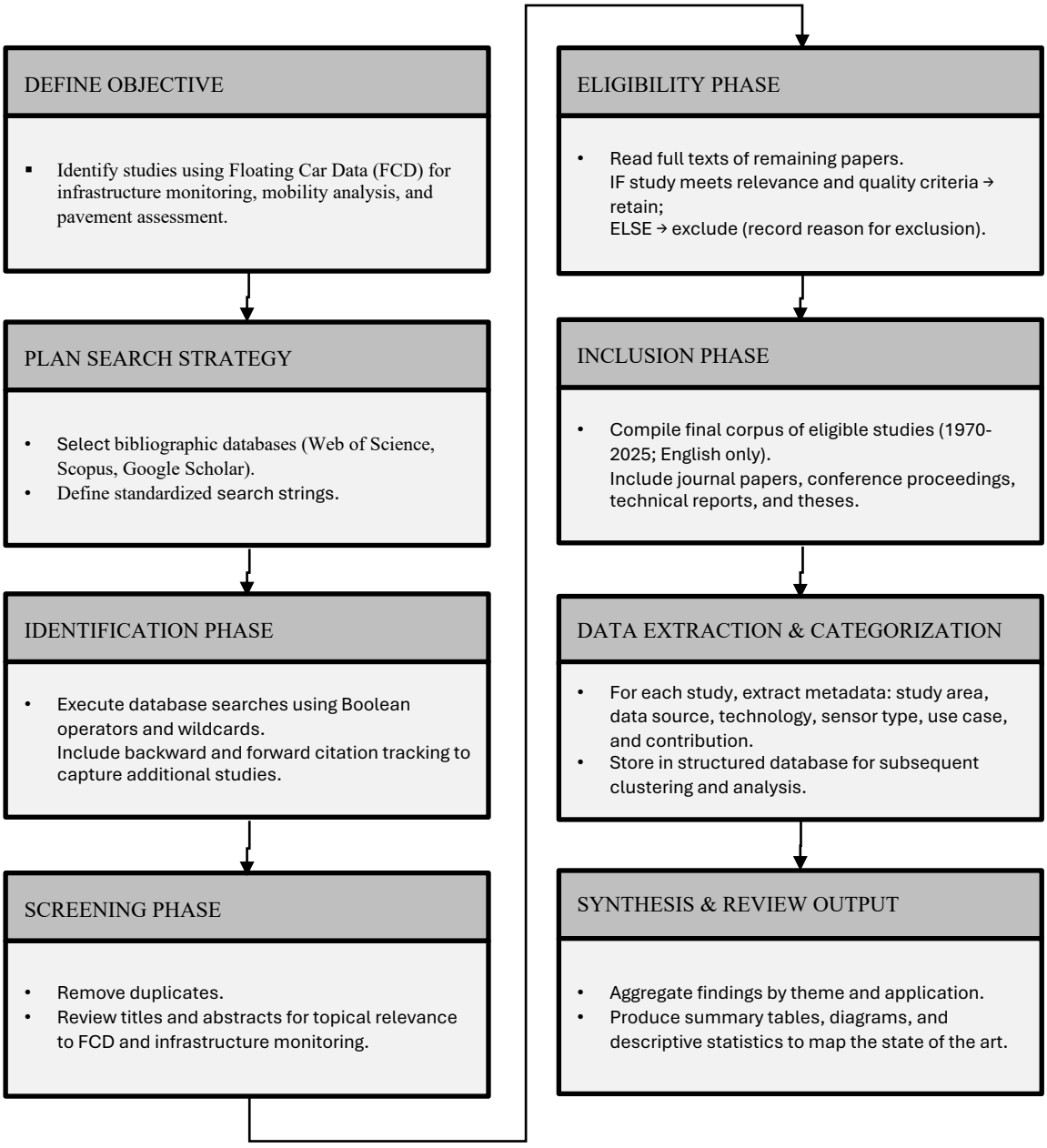

Figure 1 - PRISMA methodology

2.2.2. Screening

The screening phase applied a structured filtering approach to refine the pool of identified publications. Initially, all search results were imported into a dedicated bibliographic management system and formatted into a matrix structure. In this

matrix, each row represented a unique article, while each column captured essential attributes such as authorship, publication year, data source, methodological framework, study scope, and sensor type (e.g., accelerometer, GPS, camera).

The first filtering operation involved duplicate removal. From the total of 2,027 records retrieved across the three databases, 416 entries were identified as duplicates through automated matching and manual verification. These were removed to avoid redundancy and ensure accurate record-keeping.

Subsequently, a title-based keyword filtering step was performed. This involved reading through all article titles and removing entries unrelated to vehicle-based or infrastructure-centric sensing. For example, 163 publications primarily focused on micromobility (e.g., e-scooters, bicycles), or dealing with non-road transport systems, were excluded from further analysis. This ensured that the retained studies were strictly aligned with vehicular sensing and pavement condition assessment.

Following title screening, the abstracts of the remaining records were assessed for methodological relevance and technical rigor. Criteria included the presence of empirical data, use of vehicular sensors, focus on infrastructure condition, and clarity in methodology. Articles that discussed Floating Car Data only tangentially, or in non-quantitative ways, were also filtered out at this stage. This meticulous process laid the foundations for the subsequent eligibility checks and full-text review, discussed in the following sections.

2.2.3. Analysis

From the remaining 1,447 entries, an in-depth relevance screening was conducted to determine their alignment with the research topic. This led to the exclusion of an additional 517 articles based on title and abstract review, reducing the selection to 930 records. The abstracts of these papers were carefully examined to identify whether the studies contained empirical work, employed FCD explicitly, and addressed infrastructure conditions directly or indirectly.

Figure 2 represents the geographical distribution of the studies that passed the initial screening phases. The analysis shows a significant concentration of research in China, highlighting the country's strong academic and industrial engagement with FCD

technologies. Other active contributors include Italy, the United States, and Germany, all of which benefit from mature transport systems and active research communities in intelligent transportation systems (ITS). This distribution reflects broader technological and economic disparities. Vast regions (particularly in Africa, Central Asia, and parts of South America) remain underrepresented, suggesting inequities in the global diffusion and application of FCD research and tools.

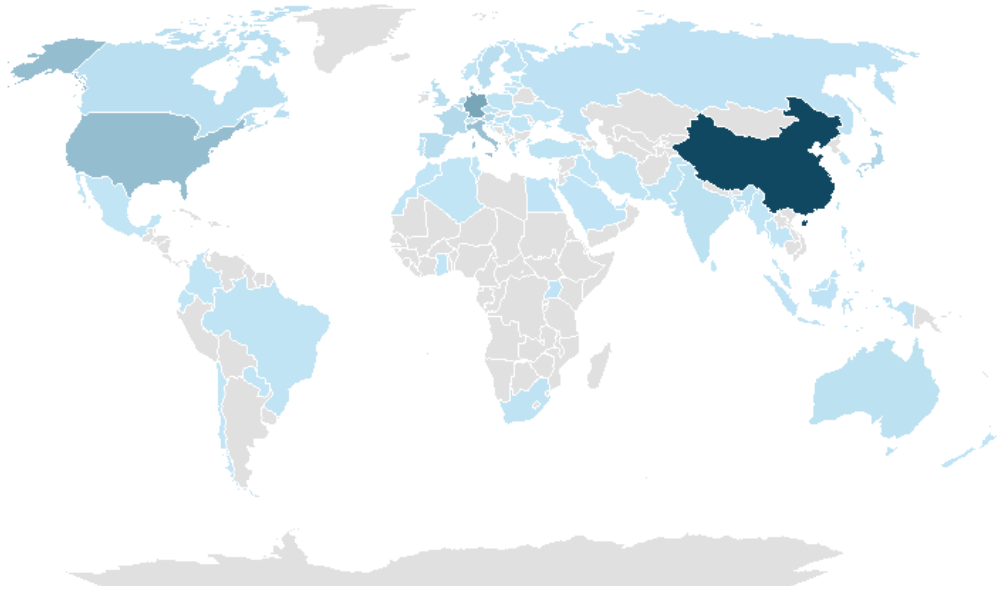

Figure 2- Geographical distribution of the selected studies related to Floating Car Data. Dark blue indicates countries with ≥ 40 studies, medium blue indicates 20–39 studies, light blue indicates 5–19 studies, very light blue indicates 1-4 studies, while grey denotes countries for which no relevant studies were identified.

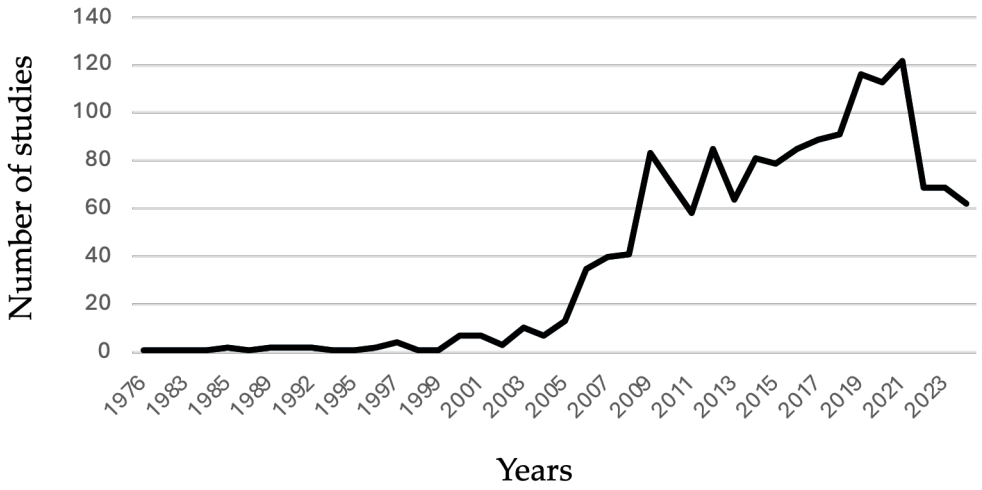

Figure 3- Temporal distribution of publications related to Floating Car Data

Figure 3 illustrates the temporal distribution of the selected studies. A marked increase in the number of publications is observed starting in the early 2000s, coinciding with the growing availability of GPS-enabled devices and mobile communication technologies. The trend peaks between 2015 and 2022, reflecting the explosion of interest in big data, smart mobility, and connected vehicles. Although a slight decline is observed in the most recent years (possibly due to shifting research priorities or indexing delays) the overall trend indicates sustained and growing academic interest in the topic. Notably, while most studies focus on traffic flow, vehicle routing, and congestion mitigation, only a limited number address structural pavement monitoring or surface deterioration.

The final step in the selection process involved evaluating the abstracts and full texts of the remaining 930 studies in relation to the central research question of this thesis. This process yielded a final dataset of 159 papers deemed directly pertinent to the use of Floating Car Data in infrastructure monitoring. These were subjected to a first-pass reading, followed by more detailed content analysis. Key information was extracted and compiled into a structured table including the following dimensions (as in Table 1):

- Use,
- Data processing,
- Technology and sensors.

Table 1 - Headings of structured table

Title	Authors	Year	Use of FCD	Data Processing FCD	Technology and Sensors

This matrix facilitated the clustering of studies by technology type, data modality, and methodological approach. The analysis confirms a clear and persistent gap: very few studies explicitly address the use of FCD for pavement condition monitoring. Most focus on traffic-related metrics, delay estimation, or route optimization, with only peripheral consideration of road surface quality.

This gap is significant, as it limits the operational integration of FCD within PMS workflows. Pavement condition is not merely a matter of comfort but a critical determinant of road safety, vehicle maintenance costs, and long-term urban resilience. The underrepresentation of pavement monitoring in the FCD literature points to both a missed opportunity and a fertile research frontier. Leveraging FCD (especially through data fusion between accelerometric and visual inputs) to support predictive maintenance and real-time deterioration detection represents a paradigm shift in how cities manage road assets.

Accordingly, this thesis is positioned within a research direction that remains underdeveloped in the current literature, aiming to adapt, extend, and innovate upon existing FCD methodologies with a specific focus on surface-level infrastructure quality. By addressing this gap, the work contributes not only to academic discourse but also to the practical development of scalable, automated, and cost-effective tools for sustainable infrastructure planning and maintenance.

2.2.4. Overview of the analyzed contributions

The Table 21 (in Part IV – Appendices) provides a structured synthesis of the contributions analyzed in this study.

For each publication, the table reports the title, authors, year of publication, the specific application of Floating Car Data (FCD), the data processing techniques, and the technologies or sensors employed. This comparative overview allows for the identification of recurring methodologies and emerging approaches, while also highlighting the limited number of studies that explicitly address pavement condition monitoring. Such evidence underlines the research gap that this thesis aims to address.

2.2.5. Classification

The selected studies were then classified according to three analytical dimensions: use (or application domain), data processing approach and sensing technology.

In this framework, the use (or application domain*)* identifies the functional purpose for which Floating Car Data are employed. It captures whether the study focuses on

traffic monitoring, speed and travel-time estimation, route optimization, emission analysis, safety assessment or, in a much smaller number of cases, the evaluation of pavement condition. This dimension clarifies the operational role that FCD play within the analytical workflow and highlights that most contributions apply them to mobility analysis rather than infrastructure diagnostics.

The data processing approach summarises the computational and analytical methods used to transform raw trajectories or sensor readings into meaningful indicators. This includes filtering procedures, map matching, segmentation rules, clustering algorithms, machine learning models, statistical inference techniques, smoothing or interpolation, and data fusion strategies. This dimension describes how studies handle noise, uncertainty and heterogeneity in the data, and it reveals common methodological patterns as well as gaps where advanced processing techniques remain underexploited.

The sensing technology refers to the type of data acquisition source used in each contribution, including GPS and GNSS traces, smartphone-based accelerometers, onboard inertial sensors, vehicle telemetry and camera-derived observations. This dimension makes it possible to distinguish studies based on the underlying sensing modality and on the level of precision, frequency and spatial coverage associated with each technology.

2.2.5.1.Classification by use

The application of Floating Car Data (FCD) has progressively diversified, expanding beyond basic traffic monitoring to serve a broad range of operational and strategic functions in mobility and infrastructure management. From real-time traffic flow assessment to predictive maintenance, the ways in which FCD are employed reflect the evolving needs of urban systems and transportation planning. The classification by use highlights how different methodologies leverage FCD for distinct objectives, revealing both the flexibility of the data and its relevance across multiple domains. Understanding these applications is essential to evaluate the maturity, limitations, and integration potential of FCD-based systems within broader mobility frameworks (Table 2).

Table 2 - Classification by use

Use Category	Specific Applications	Main Data Sources	Key Benefits
Travel and Traffic State Estimation	Travel time and speed estimation, congestion monitoring, future route prediction	FCD (GPS, GNSS), loop detectors, ETC, mobile sensors	Improved traffic prediction and signal control
Mobility Pattern and Transport Planning	Spatiotemporal traffic analysis, public transport zoning, smart mobility planning	FCD + urban morphology data, mobile networks, Bluetooth	Better zoning and demand-responsive planning
Freight and Logistics Applications	Freight transport model validation, route optimization, SULP support	FCD + O/D matrices, traffic counts, stakeholder interviews	Efficient routing, cost saving in logistics
Driving Behavior Analysis and Safety	Speeding detection, lane change analysis, safety-critical location identification	FCD + road geometry, accident databases, CAN Bus	Improved road safety and risk mitigation
Environmental and Modal Impact	Emission estimation, e-scooter impact assessment, sustainability studies	FCD + environmental sensors, magnetometers, power models	Support for environmental policy and regulation
Infrastructure Monitoring	Pothole detection, road surface condition monitoring, maintenance planning	FCD + accelerometers, vibration sensors, onboard diagnostics	Early damage detection, cost-effective maintenance

Travel and traffic state estimation

The use of Floating Car Data (FCD) for estimating travel times and speeds on urban and highway networks represents one of its most common applications. Data collected from probe vehicles is used to model traffic and predict delays. [2] showed that the accuracy of travel time estimation improves when different data sources are combined. Their model uses fixed sensors like loop detectors along with mobile data from probe vehicles. It separates travel time into three parts: acceleration, cruising, and deceleration. In the acceleration phase, FCD is used to estimate how speed increases after an intersection. In the cruising phase, the model uses a modified BPR function that considers city traffic to link speed and traffic volume. In the deceleration phase, an improved shockwave theory estimates the delay from traffic lights and congestion. Tests done on a main road in Shanghai showed that the model had an average error of

less than 5% in heavy traffic and between 10% and 20% in lighter traffic. These results suggest that FCD can help improve traffic light control and road planning.

Recent simulation-based studies have further confirmed the value of FCD in complex urban contexts. [3] compare different speed estimation methods, including temporal and spatial mean speeds derived from FCD, with loop detector measurements and ground-truth data. Their findings show that FCD-based metrics are better suited to capturing variations in speed over entire road segments, particularly on urban roads affected by traffic signals and heterogeneous driving behaviors. FCD-based travel time estimates remained robust even at penetration rates as low as 5% on high-volume roads, while lower-frequency streets required higher coverage to maintain accuracy. These results support the integration of FCD into traffic state estimation systems, especially in scenarios where installing dense sensor infrastructure is not feasible.

FCD is also widely employed to monitor congestion patterns and to assess overall network performance. [4] used GPS data from private vehicles in Florence to study traffic and road conditions. They could estimate travel times and average speeds along roads. Their findings showed that during rush hours, average speeds dropped by up to 30%. For example, in Florence's historic center, speeds ranged between 14 and 17 km/h, while in the wider city, they ranged between 21 and 27 km/h. The study also examined trip patterns, separating trips within the city from those passing through. These insights support the evaluation of restricted-traffic zones and the refinement of traffic models. When combined with fixed sensors or access control systems, FCD gives a better view of how traffic works and helps reduce congestion.

A method for detecting traffic congestion using GPS-based Floating Car Data collected from 500 taxis over a single day in a major Chinese city is proposed in [5]. By applying data preprocessing, coordinate transformation, and a hybrid map matching algorithm combining point-to-line and line-to-line techniques, the researchers reconstructed vehicle trajectories and estimated travel speeds across more than 2,000 urban road segments. Roads were then classified into five congestion categories, ranging from “serious congestion” (≤15 km/h) to “fast” (>50 km/h), and visualized on a city-wide congestion map. Their approach demonstrated that FCD can produce real-time, large-scale, and accurate assessments of urban traffic conditions, which are especially valuable in areas where fixed sensor infrastructure is limited or absent [5].

FCD is also used to study vehicle emissions and energy use. [6] developed a method using the Vehicle Specific Power (VSP) of electric vehicles, which depends on speed and acceleration. They split trips into one-minute parts and calculated energy use for different road types. The results showed that stop-and-go traffic increases energy use, especially on busy urban roads.

FCD can also help predict future routes. [7] used FCD from Rome, Milan, Naples, and Turin to train LSTM and GAN models. LSTM worked well for simple routes, while GANs could generate several realistic future paths for complex traffic. These predictions can improve route planning, public transport, and traffic safety by detecting unusual driver behavior.

Mobility pattern and transport planning

Floating Car Data is also used to study how traffic changes in cities over time and space. It helps detect mobility patterns, traffic jams, and changes in travel behavior. [8] analyzed GPS data from taxis in Wuhan, China. They discovered that traffic congestion often forms in a complex, self-organized way, with main hotspots appearing in key parts of the road network. The data followed a power-law distribution, showing that congestion had a hierarchical and multi-center structure.

A more recent example comes from an Italian case study involving the cities of Brescia, Catania and Salerno. In [9] FCD are used from thousands of private vehicles to reconstruct origin-destination matrices and analyze urban mobility dynamics across regular hexagonal grids. Their analysis linked traffic patterns with characteristics of the built environment such as population density, road types, and urban layout. The study revealed that cities with compact, radially structured road networks like Brescia tend to exhibit more balanced mobility flows and shorter travel distances, while cities with linear coastal development like Salerno and Catania showed longer average travel times and lower average speeds. This spatiotemporal mapping of FCD-based travel metrics enabled the authors to derive accessibility indicators and identify zones with mobility inefficiencies or potential for infrastructure improvement.

Public transport planning can likewise benefit from FCD-based analyses. [10] studied traffic on Xiamen Island and found that traditional analysis zones did not match the needs of tourist cities. They used FCD and tourism data to create better traffic zones

and adjust public transport in real time during busy seasons. This approach supports adjustments in public transport frequency, lane allocation, and congestion management in cities with high seasonal demand.

Further evidence comes from Sub-Saharan Africa, where traditional static sensors are often lacking due to resource constraints. In [11] is conducted a comprehensive review of studies using Floating Car Data to monitor and plan informal public transport systems in cities like Cape Town, Kampala, Accra, and Nairobi. These studies used smartphone-based GPS tracking to map paratransit routes, assess operational patterns, and identify accessibility gaps. The FCD allowed researchers to define functional public transport zones based on real movement data rather than administrative boundaries. Additionally, they enabled the classification of trunk, intermediate, and feeder services and supported the development of tailored strategies for infrastructure and service upgrades. These results show that FCD can provide a scalable and cost-effective foundation for traffic zoning and public transport planning, even in low- and middle-income countries where traditional data sources are unavailable or incomplete.

In the area of smart mobility, [12] and [13] showed that FCD helps manage traffic, reduce emissions, and support MaaS strategies. Their study in Madrid used GPS and vehicle diagnostics to monitor fuel use and speed. This data helps control shared vehicle fleets, plan routes, and adjust services to match real demand.

Freight transport and logistics optimization

In [14] FCD are used to validate freight transport models. Their work confirmed that GPS data from commercial vehicles could track routes and stop times, especially in ports, helping adjust simulation models using real data. Combining spatial analysis and model validation can help improve traffic regulation, city planning, and the performance of transport systems.

A comprehensive example of this approach is presented in [15], a validation method for a multimodal freight transport simulation model is developed using over 292 million FCD records from more than 29,000 heavy-duty vehicles. Their methodology focused on Ro-Ro and Ro-Pax sea-road services in Italy, tracking access, navigation, and egress phases of freight trips. By processing GPS signals, they reconstructed the

real itineraries, measured dwell times in ports, and compared travel times across different transport modes. The study demonstrated that FCD can not only validate routing and timing assumptions of simulation models but also uncover behavioral patterns in haulier modal choices. Notably, for frequently used routes like Palermo-Naples or Messina-Salerno, the FCD-based validation revealed how rest regulations, port congestion, and navigation schedules influence the choice between road-only and sea-road transport. This type of data-driven validation strengthens the reliability of freight models and supports better-informed transport policies.

FCD also represents a valuable resource for route optimization and logistics planning. [16] studied urban transport in Shenzhen and used historical FCD to solve the Vehicle Routing Problem (VRP) with time-dependent and random travel times. Their model could find the best path between two stops even if traffic changed. It helped deliveries stay on time without raising costs. By using real travel data, companies can better plan delivery routes, improve fleet management, and support sustainable urban mobility.

[17] used FCD data as part of a multi-source dataset to support the Sustainable Urban Logistics Plan (SULP) for the metropolitan area of Bologna. The FCD were integrated with traffic counts and stakeholder interviews to calibrate freight demand models and simulate freight flows across 261 traffic zones. These models allowed estimation of vehicle origin-destination matrices and delivery profiles segmented by vehicle type, freight type, and time of day. The FCD contributed to identifying critical issues in routing and delivery efficiency, particularly in constrained urban environments like Limited Traffic Zones (LTZs). Through this approach, several logistics measures were tested in simulated scenarios showing that FCD-based insights can guide the design of policies that optimize routing, reduce emissions, and increase the operational efficiency of freight transport in urban settings.

Driving behavior analysis and safety

Driving behavior analysis and road safety assessment represent additional relevant domains of application. [18] used FCD to find places where drivers often break speed limits. Their study in Prague found that speeding is more common at night and on certain road types. With FCD and information about the road layout, they built models that linked speeding to road features. Roads with lower speed limits, fewer lanes, and

curves had more violations. These findings support the identification of priority locations for enforcement measures or geometric redesign aimed at improving road safety.

A comprehensive application of FCD to evaluate driver behavior and road safety was developed in [19], who proposed a general framework integrating individual vehicle trajectories, road geometry, and accident data to support both infrastructure planning and on-board driver assistance systems. Using over 1.2 million FCD records from 30,000 vehicles over three months on regional roads in Latium, Italy, the authors conducted a disaggregated analysis comparing observed vehicle speeds with safe speeds estimated from road curvature and friction factors. The study found that in several road segments (especially curves) 85th and 95th percentile speeds significantly exceeded the estimated safe speeds, particularly during night-time or under low traffic conditions. These discrepancies were strongly correlated with higher near-miss rates, especially due to skidding. The results demonstrate how FCD can reveal hidden risks in road design and driver behavior, enabling both targeted enforcement and real-time speed advisories to improve road safety.

FCD can also be used to analyse lane-changing behavior and vehicle trajectories. [20] developed a method using low-frequency FCD and deep learning to detect lane changes and count the number of lanes. They cleaned the data with DBSCAN clustering and used a LeNet-5 model to classify GPS points. Their method reached 92.7% accuracy in Wuhan, showing it works better than traditional models. This information can support the identification of safety-critical intersections and the optimization of signal control strategies.

An advanced method for analyzing vehicle trajectories was proposed in [7], who developed a gradient-boosted decision tree (GBDT) classification model based on FCD to detect the presence of auxiliary through lanes at intersections. The approach involved segmenting roads into intersection and non-intersection areas and analyzing FCD spatial parameters such as coverage width, density, angle, and speed. Using data from taxis in Wuhan (sampled every 40 seconds over 15 days), the model successfully distinguished lane configurations and identified intersections where the number of lanes increased temporarily due to auxiliary lanes. The method achieved an accuracy of over 81% for intersection detection and proved effective in updating lane-level

navigation maps. This demonstrates the potential of FCD not only for detecting lane changes but also for understanding intersection geometry and traffic flow dynamics at a detailed spatial level.

Environmental and modal impact

In [21] is proposed a methodology using FCD to calculate pollutant emissions (such as NOx, CO_2, CO, and PM10) on different classes of roads across the Czech Republic. By integrating FCD-derived average speeds and intensities with the COPERT emission model, they produced macroscopic emission estimates by road type. Their study showed that emission values varied significantly between categories, with highways and urban main roads yielding the most consistent and distinguishable patterns. However, the method's accuracy diminished for low-class roads due to insufficient FCD coverage. The research demonstrated that, despite data limitations, FCD can support municipalities in identifying high-emission road segments and making informed decisions for traffic planning, pollution mitigation, and future data collection strategies.

Another relevant example is provided by [22] who analysed the impact of e-scooters on road traffic conditions. Using FCD, they found that shared scooters often replace walking and short car trips. Their data helped map scooter trips and detect areas with a higher risk of conflict with cars. This helps cities plan better infrastructure and improve safety.

Infrastructure monitoring

FCD can also be employed for the detection of pavement surface anomalies and maintenance needs. [23] developed a method that uses wheel-mounted accelerometers to detect vibrations caused by potholes or surface cracks. The approach relies on pattern recognition within the accelerometric signals to identify damage and generate real-time road quality maps. Although the study demonstrates the potential of accelerometric data for supporting maintenance planning and reducing operational costs, it remains an isolated case within the literature. Furthermore, the method focuses exclusively on a single accelerometric sensor type and does not explore broader integration with Floating Car Data frameworks or with large-scale vehicle

fleets. This further confirms the existence of a persistent research gap in the systematic use of accelerometer-based FCD for pavement condition monitoring.

2.2.5.2.Classification by data processing

The processing of Floating Car Data (FCD) can be classified into several methodological approaches, each focusing on how data is transformed and modelled to extract meaningful information. This classification considers the structure, transformation, and modeling of data rather than its application domain (Table 3).

Table 3 - Classification by data processing

Processing Category	Typical Techniques	Applications	Data Sources	Benefits
Temporal Modeling and Forecasting	LSTM, ARIMA, SVR, Tucker Decomposition	Travel time prediction, trajectory forecasting, imputation of missing data	FCD time series, loop detectors, calendar data	Accurate temporal predictions, robust under sparse data
Pattern Detection and Spatial Analysis	SOM, KDE, GAN, LSTM, VSP-based Regression	Congestion analysis, emission modeling, behavior pattern recognition	FCD + spatial data, taxi GPS, environmental conditions	Insight into traffic patterns and hotspots, behavioral modeling
Data Fusion and Preprocessing Techniques	ASM, PSM, DBSCAN, CNN (LeNet-5)	Noise reduction, lane detection, multi-source integration	FCD + Bluetooth, loop detectors, image-transformed GPS data	Enhanced accuracy and structure, adaptable to heterogeneous inputs

Temporal modeling and forecasting

One of the main processing categories concerns time-series analysis. These methods are used to understand traffic evolution over time and predict future conditions. Common approaches include Long Short-Term Memory (LSTM) networks, AutoRegressive Integrated Moving Average (ARIMA) models, and Support Vector Regression (SVR). For example, a study on a free-floating car sharing service used LSTM-based models to predict vehicle demand and distance. The data were processed using Min-Max scaling and grouped in hourly time windows. The LSTM model

outperformed ARIMA and SVR, especially during rush hours, showing its strength in learning complex patterns in temporal data [24].

Travel time estimation represents a common objective within Floating Car Data (FCD) processing methodologies. [2] proposed a model that segments each trip into three distinct phases: acceleration, cruising, and deceleration, each described through specific mathematical formulations. The cruising phase employs a modified Bureau of Public Roads (BPR) function, while the deceleration phase integrates shockwave theory to capture delay propagation. The method was validated using both FCD and loop detector data collected in Shanghai and demonstrated improved accuracy compared to traditional estimation approaches.

In scenarios characterised by incomplete FCD coverage, tensor-based imputation techniques have also been explored. Specifically, a three-dimensional tensor structure incorporating temporal, spatial, and calendar-based dimensions was developed, and Tucker decomposition was applied to reconstruct missing values, outperforming matrix-based alternatives even under sparse data conditions. Tucker decomposition was applied to predict the unobserved values. This approach gave better results than matrix-based methods and worked well even with low data coverage [25].

Finally, advanced routing and navigation rely on accurate travel time prediction. In Istanbul, an LSTM-based system was trained to forecast the time and speed of short trip segments based on spatial and temporal features. The model reduced the error rate significantly compared to traditional techniques, making it useful for real-time traffic applications [26].

Pattern detection and spatial analysis

A second group of methods focuses on pattern-recognition techniques based on machine learning and deep learning. These techniques enable the identification of traffic trends and anomalous behaviors through spatio-temporal data analysis. In one study, Self-Organizing Maps (SOM) were applied to segment intersections by time and direction. The traffic state was measured using a delay index based on average speed. SOM was then used to cluster similar conditions and visualise them with heat maps, providing insight into daily traffic flow [27].

Spatial analysis methods like Kernel Density Estimation (KDE) are also used to detect congested zones. In a study in Wuhan, more than 85 million GPS points from taxis were processed to find areas of low speed and frequent stops. Clusters were defined by spatial and temporal persistence and then classified by congestion level. This allowed researchers to identify key bottlenecks in the city [8]. Vehicle trajectory prediction is another form of processing that uses historical data to estimate future movements. Deep learning models, such as LSTM and Generative Adversarial Networks (GANs), have been tested to predict one or more plausible future trajectories. A study using data from Italian cities showed that LSTM worked well in stable situations, while GANs could simulate different future scenarios more realistically [7]. FCD processing also supports the estimation of vehicle emissions and energy use. One example is the use of Vehicle Specific Power (VSP) to analyse electric vehicle consumption by road type. The data were grouped by 60-second intervals, and regression models were used to link driving conditions with energy use. Results showed higher consumption on urban roads, suggesting the need for road-aware routing strategies [24].

Data fusion and preprocessing techniques

Another relevant approach is multi-source data fusion, which integrates FCD with measurements from fixed sensors such as inductive loops and Bluetooth devices. This method helps improve the accuracy of travel speed and time estimates. For example, the Adaptive Smoothing Method (ASM) and Phase-Based Smoothing Method (PSM) were used to merge different data types. A variant called PSM-W adjusted the weight of Bluetooth data dynamically. These fusion techniques demonstrate reduced error rates when tested on real traffic data [28].

Clustering techniques also play a key role in data processing. Algorithms like DBSCAN help clean and structure noisy GPS points. A study on low-frequency FCD applied DBSCAN to filter out errors, then used image transformation and a CNN model (LeNet-5) to estimate the number of lanes on a road. The method achieved an accuracy of 92.7%, highlighting the potential of combining clustering techniques with deep learning approaches for spatial classification [20].

Overall, this classification by data processing highlights the importance of how data is treated (through modeling, transformation, and combination) rather than focusing only on its final use. Each method supports better decision-making in traffic management, infrastructure planning, and smart mobility systems.

2.2.5.3.Classification by technology

The use of technology in collecting and processing Floating Car Data (FCD) has changed a lot over time (Table 4). Different types of sensors are now used together to improve how accurate and detailed the data is. All these technologies, whether inside the vehicles or part of the road infrastructure, show how important it is to use different kinds of data together. Each sensing technology provides complementary strengths within the broader monitoring framework. When used together, they make traffic monitoring more accurate and help manage road systems in a smarter and more cost-effective way.

Table 4 - Classification by technology

Tech. Category	Examples	Typical Use	Advantages	Limitations
Satellite Positioning Systems	GPS, GNSS (GLONASS, Galileo, BeiDou), Electronic Toll Collection (ETC)	Vehicle localization, trajectory reconstruction, travel time estimation	Wide coverage, high temporal resolution, real-time data	Signal loss in urban canyons, variable accuracy
Vehicle Internal Sensors and Systems	CAN Bus, Odometers, Accelerometers, Magnetometers	Vehicle dynamics monitoring, road damage detection, safety analysis	Detailed motion data, unaffected by external conditions, useful for safety	Limited to vehicle presence, sensor-specific calibration needed
Roadside and Fixed Infrastructure Sensors	Radar, Inductive Loop Detectors, Cameras (Computer Vision)	Traffic flow measurement, signal control, anomaly detection	Precise at fixed points, useful for calibration and validation	High installation and maintenance costs, spatially limited
Communication-Based and Crowdsourced Data	Mobile Phone Data, Bluetooth Sensors	Crowdsourced speed/travel time data, origin-destination estimation	Cost-effective, high penetration, complements traditional sensors	Privacy concerns, inconsistent sampling, dependent on user devices

Satellite positioning systems

GPS is the most widely adopted positioning technology for FCD acquisition and enables trajectory reconstruction with sub-second sampling rates. However, its accuracy is affected by multipath errors and urban canyons. However, GPS has some limits. [29] showed that GPS data can be wrong by 5 to 30 meters because of signal problems, reflections, and weather conditions. To solve this, they suggested using a Gaussian model and a special algorithm called Otsu's to make road maps from GPS points. Another study [30] explained how often GPS should record data. They found that recording data every 1 to 3 seconds gives good results without using too much memory.

GNSS is an improved version of GPS. It uses many satellite systems together, such as GLONASS, Galileo, and BeiDou. In [31] is showed that GNSS helps to cover more areas and keeps a stronger signal in cities. [32] added that GNSS works even better when used with maps and wireless systems. [7] also used GNSS with artificial intelligence models to predict where vehicles will go. Their methods helped reduce mistakes and worked well when there were many possible routes.

Electronic Toll Collection (ETC) systems are another helpful source of data. [2] showed that ETC systems, when combined with FCD and sensor data, give better predictions of travel time in cities, even when there is traffic.

Vehicle internal sensors and systems

Another relevant in-vehicle technology is the CAN Bus system. It allows different parts of the car to talk to each other quickly and without needing a main control unit. [33] built a CAN Bus system for hybrid vehicles. They showed it was better than older systems because it was faster, worked well in noisy environments, and could connect easily to battery systems.

Odometers, which measure cumulative travel distance, have also evolved in recent vehicular monitoring systems. [23] developed a low-cost system using accelerometers on the wheels. The proposed system demonstrated higher accuracy than traditional solutions and remained effective even under weak GPS coverage.

Accelerometers are used not only for odometry but also to detect speed variations and vibration patterns, which may indicate pavement defects or abrupt driving maneuvers. These sensors play a key role in supporting road safety analysis and infrastructure planning. Studies have used them to spot potholes, bumps, and dangerous curves [34].

Magnetometers represent an additional sensing modality. They detect changes in the Earth's magnetic field caused by vehicles. [35] used them with FCD to map traffic noise and study how traffic affects the environment.

Roadside and fixed infrastructure sensors

Additional fixed sensing technologies are deployed to complement vehicle-based FCD. Fixed traffic sensors like radar, cameras, and inductive loops collect data in certain places all the time. [36] showed that combining this data with FCD gives better results when checking how fast traffic moves. [37] also used this mix of data to control traffic lights more efficiently.

Roadside radar sensors provide high-precision measurements of vehicle speed. [38] used this data to study how vehicle speeds change on rural roads. They found that combining radar with FCD helps find areas with unusual speed patterns.

Computer vision systems leverage cameras and image-based algorithms to extract traffic information and identify patterns. In [27] these systems are used to understand how traffic behaves at intersections and how it changes over time.

Inductive loop detectors are still useful, even if they only collect data in certain spots. [28] showed that combining loop detector data with FCD helps check where traffic data is reliable and where it is not.

Communication-based and crowdsourced data

Mobile network data can also serve as a complementary traffic information source. These devices generate location information through GNSS or cellular network positioning. [39] found that combining phone data with Bluetooth and FCD helps to get better travel time and speed estimates.

Bluetooth sensors can detect travel times by matching device identifiers at multiple roadside checkpoints. [40] explained how they used buses equipped with Bluetooth to track city traffic. When used with FCD, Bluetooth sensors help get more complete data.

2.3. Floating Car Data in a Pavement Management System

2.3.1. Keywords and selection criteria

The literature search was conducted following the PRISMA framework, with the objective of identifying scientific studies that employ Floating Car Data (FCD) for pavement condition evaluation and for supporting Pavement Management Systems (PMS). The search strategy was applied to three major scientific databases, namely Scopus, Web of Science and Google Scholar, in order to ensure a comprehensive and reliable coverage of the academic landscape on this topic.
A preliminary exploratory phase revealed that the explicit co-occurrence of the terms Floating Car Data and Pavement Management System in titles, abstracts, and keywords yielded a very limited number of results. To address this issue, the search was expanded to include additional terms widely used in the pavement management domain, while maintaining a strict thematic focus. The final Boolean query adopted in Scopus and Web of Science, applied to the title, abstract and keyword fields, was the following:

```
("floating car data" OR "FCD" OR "probe vehicle data" OR "vehicle probe data") AND ("pavement management" OR "pavement management system" OR "PMS" OR "pavement condition" OR "pavement distress" OR "pavement assessment" OR "road asset management" OR "road maintenance" OR "road surface condition" OR "pavement performance")
```

The same combination of keywords was applied in Google Scholar, where the results were refined through manual screening, retaining only peer-reviewed studies explicitly relevant to pavement condition evaluation. Publications dealing exclusively with traffic modelling, routing optimization or congestion analysis were excluded when they contained no reference to infrastructure condition or pavement management.

2.3.2. Screening

The initial search returned a substantially broader set of records (280), which were subsequently subjected to a multi-stage screening procedure consistent with the PRISMA methodology. After the removal of duplicate entries, 196 unique studies were retained for title-and-abstract screening. The screening phase focused on verifying the explicit relevance of each study to pavement condition assessment, pavement management, or road-surface monitoring through vehicular sensing. The remaining papers were then examined through full-text reading to confirm methodological consistency, data suitability, and contribution to the research scope.

2.3.1. Analysis

The final dataset consisted of 196 scientific contributions published between 2001 and 2025. The geographical distribution reveals a strong concentration of research activity in China and the United States, which together account for the largest share of publications, followed by Germany, India, Sweden and South Korea. European countries such as Italy, the United Kingdom, Poland, and Austria provide a more limited yet consistent contribution, while the remaining studies are scattered across multiple regions, confirming the global interest in vehicular-based road monitoring (Figure 4).

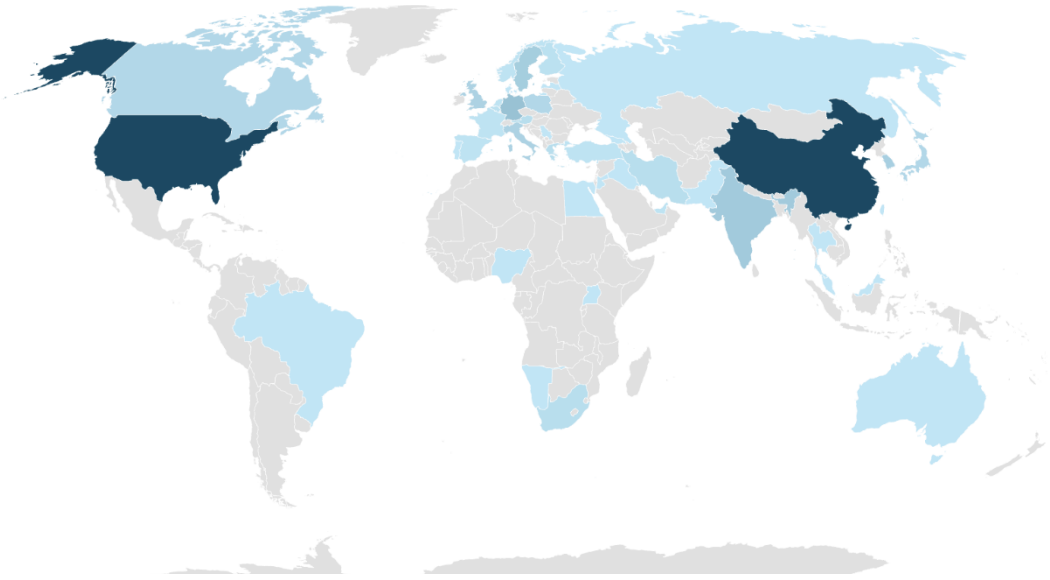

Figure 4 - Geographical distribution of the selected studies related to Floating Car Data AND Pavement Management System. Dark blue indicates countries with ≥ 40 studies, medium blue indicates 20–39 studies, light blue indicates 5–19 studies, very light blue indicates 1-4 studies, while grey denotes countries for which no relevant studies were identified.

From a temporal perspective (Figure 5), the evolution of the literature shows a clear acceleration starting in 2015 and a marked growth between 2018 and 2023, driven by the large-scale availability of probe-vehicle data and the rapid development of onboard sensing, GNSS technologies, and data-driven asset management. The peak is observed in 2023, followed by a stable volume of publications in the most recent years. This trend confirms the consolidation of Floating Car Data as a relevant asset for Intelligent Transportation Systems and highlights the growing interest of the research community in extending its use from traffic analytics to pavement condition monitoring and Pavement Management Systems.

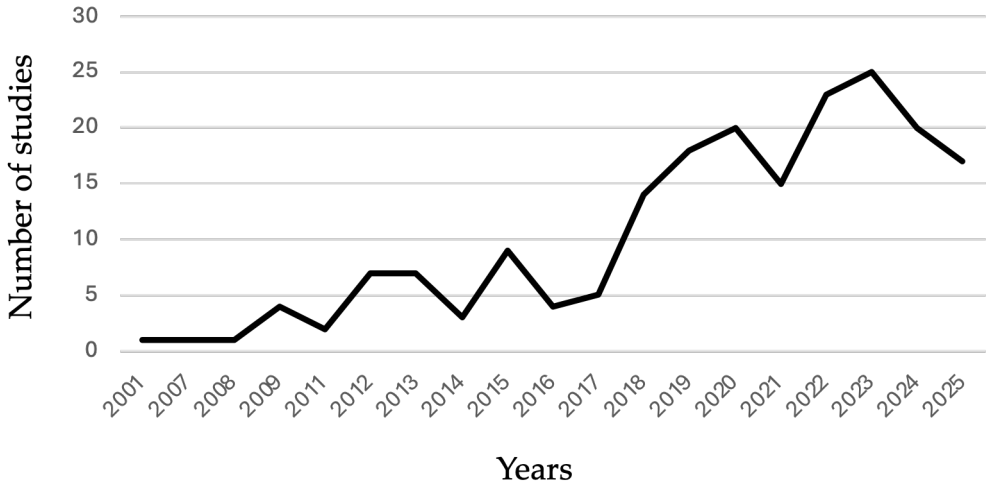

Figure 5 - Temporal distribution of publications related to Floating Car Data AND Pavement Management System

Therefore, a subset of 35 papers was selected for in-depth analysis following a dedicated relevance check based on abstract reading, which verified the explicit use of vehicular data for pavement condition assessment. These 35 studies were examined through a comparative matrix that highlights how each work used the data, the technological setup adopted and the sensing approach employed.

The resulting picture confirms a clear imbalance in the literature: while FCD is widely used for traffic monitoring and mobility analytics, only a limited number of studies focus on pavement condition monitoring and Pavement Management Systems. This gap provides the rationale for the methodology proposed in this thesis, which aims to

exploit vehicular data and data-fusion techniques to support proactive road-maintenance strategies and enhance pavement evaluation processes.

2.4. Overview of the analyzed contributions

For effective road infrastructure management, accurate, frequent, and spatially extensive data are essential to support informed decisions on maintenance and rehabilitation activities. Traditional methods (such as visual inspections, profilometer surveys, ground-penetrating radar, or periodic condition assessments) are expensive, infrequent, and limited in spatial coverage. In contrast, Floating Car Data (FCD) consist of passively collected measurements from vehicles in normal operation (such as GPS trajectories, speed profiles, accelerations, and, in some cases, onboard accelerometer or image data) offering a compelling alternative or complement. In brief, FCD are data streams generated by vehicles acting as mobile sensors as they traverse the road network; they capture both movement and interactions with the pavement surface (vibrations, shocks, deviations) that can indirectly indicate pavement condition.

Hence, FCD may serve as a valuable additional data source for integration into a Pavement Management System (PMS). A PMS is a structured framework used by transportation agencies and road authorities to monitor pavement condition, predict deterioration, plan interventions, prioritize among competing needs, and allocate budgets in a cost-effective manner. PMS structure typically includes: inventory of pavement assets, condition assessment, performance prediction or deterioration modeling, cost modeling, decision support for maintenance/rehabilitation strategy, and monitoring/evaluation.

The development of PMS dates back to the late 1960s and 1970s, particularly in the United States. For example, Washington State Department of Transportation (WSDOT) began inventory and regular pavement condition surveys in the mid-1960s. Over time, PMS methods have evolved from simple ranking based on current observable pavement distress and traffic load to more sophisticated systems incorporating life-cycle cost analysis, optimization, GIS integration, and more recently machine learning. [41] offers a comprehensive review of how PMS functions, data

collection, prediction, optimization, institutional and IT advances over about three decades.

In terms of indices used in PMS, several have become standard. Among these indices, the International Roughness Index (IRI) [42] is widely adopted for assessing ride quality and surface roughness. It is derived from the measurement of vertical deviations along the pavement profile, simulating the response of a vehicle's suspension system. The IRI is typically expressed in meters per kilometer (m/km), and higher values indicate rougher road surfaces. It is valued for its objectivity and repeatability, although it requires specialized equipment and may not fully capture surface-level visual distress.

Complementing IRI, the Pavement Condition Index (PCI) [18] is derived from visual surveys of surface distresses such as cracking, rutting, potholes, and patching. Rated on a scale from 0 to 100, the PCI provides an overall measure of surface condition, with higher values indicating better performance. It is widely used due to its comprehensive coverage of multiple distress types and its intuitive interpretation, though it is labor-intensive and may be subject to visual bias.

Beyond these, other indices are employed to provide a more comprehensive assessment of pavement performance. The Pavement Quality Index (PQI) [41] is a composite measure that can incorporate IRI, PCI, and other performance indicators to give an overall assessment of pavement health. However, it is less standardized and varies between agencies.

The Structural Condition Index (SCI) focuses on the integrity of the pavement structure, often derived from deflection measurements such as those obtained from Falling Weight Deflectometers (FWD). This index reflects the pavement's ability to withstand loading and is crucial for identifying the need for structural rehabilitation.

Another key metric is the Remaining Service Life (RSL) [43], which estimates how long a pavement segment will continue to perform satisfactorily before requiring major maintenance. RSL calculations rely on current condition assessments, projected traffic loading, and environmental considerations. As a planning tool, it supports life-cycle cost analysis and helps prioritize interventions based on long-term performance.

Recent literature shows that PMS are being enhanced in terms of prediction models (machine learning, statistical models), in integrating new sensing modalities, in using imaging and scanning technologies, and in optimizing maintenance strategies under budget constraints. For example, [18] predict PCI using multiple linear regression, artificial neural networks, fuzzy logic. Also, the review [44] summarizes state-of-the-art developments in PMS and associated embedded processes. Another example is the study [45] which tests a framework using FCD in the Province of Brescia (Italy). That study shows how data from circulating vehicles can be used without organizing dedicated surveying campaigns, and how it improves the timeliness and spatial detail of condition assessment.

From the review, several key gaps emerge: many PMS still rely heavily on traditional distress inspections and dedicated profile or deflection measurements. Few studies have deeply incorporated FCD (accelerometric, GPS, image) into operational PMS, for example to generate indices comparable to PCI or IRI, or to feed real-time decision support. There is also variability in how indices are defined, how data are processed, and sparse standardization in methods.

In summary, integrating FCD into PMS holds significant potential: providing more frequent and extensive data, enabling earlier detection of deterioration, supporting hybrid indices that combine multiple sensing modalities, and improving prioritization and cost-effectiveness. But to make that viable, we need to address calibration (how FCD-derived indicators match traditional indices), data heterogeneity, noise, and institutional adoption.

To provide a clearer picture of the current research landscape and to contextualize the aforementioned trends, Table 22 (in Part IV – Appendices) presents a structured overview of the most relevant contributions identified in the literature. The studies are compared with respect to the types of data employed, the methodological approaches adopted for processing or fusing sensing information, and the pavement condition metrics derived or validated. This synopsis highlights the diversity of sensing modalities (ranging from smartphone accelerometers and connected vehicle signals to image-based systems and multi-sensor platforms) as well as the heterogeneous outputs currently used to assess pavement performance. By juxtaposing these contributions, the table makes it possible to identify common patterns, emerging

directions, and persisting limitations in the integration of Floating Car Data and other opportunistic sources within Pavement Management Systems.

3. Research gap analysis

The systematic review conducted for this thesis demonstrates that research on Floating Car Data (FCD) has expanded considerably over the last two decades. However, its application to infrastructure monitoring remains at an early stage of development. The majority of existing contributions focus on traffic dynamics, mobility management, and environmental impacts, with only marginal attention to pavement condition assessment. This discrepancy is particularly evident when compared with the maturity of Pavement Management Systems (PMS), which, despite their widespread institutional adoption, still rely on traditional, costly, and low-frequency survey methods. Between these two extremes (widely available and rarely employed FCD data on one side, and rigid PMS frameworks on the other) there exists a significant methodological gap. Furthermore, although data-fusion research has produced increasingly sophisticated methods for integrating heterogeneous data streams, these approaches have not yet been systematically adapted to infrastructure monitoring. The lack of systematic integration across these three domains (FCD, data fusion, and PMS) constitutes the central research gap addressed in this thesis.

3.1. Floating Car Data (FCD): abundance without infrastructure focus

The literature confirms that FCD is currently a mature and ubiquitous data source for mobility applications. With the proliferation of GPS-enabled devices, insurance telematics, connected vehicles, and ride-hailing platforms, vast datasets are generated continuously and at low cost. These datasets have been successfully exploited to estimate travel times, detect congestion, analyze mobility patterns, and optimize routing. In fact, FCD-based models have achieved high accuracy even with limited penetration rates, making them attractive for real-time traffic monitoring.

However, when narrowing the scope to pavement condition monitoring, the picture changes drastically. Out of the hundreds of studies reviewed, only a small number explicitly mention accelerometer-based analyses, and almost none use them systematically for pavement condition monitoring. Accelerometer-equipped black boxes, which are installed in millions of vehicles worldwide by insurance companies,

offer a unique opportunity to detect vertical shocks, vibrations, and roughness patterns directly caused by pavement irregularities. However, these signals are often treated as proprietary, pre-processed, and rarely shared with the research community in raw form.

This leads to two key consequences:

- Under-exploitation of available data - although vehicles continuously traverse road networks and inherently interact with pavement conditions, the accelerometric dimension of FCD remains significantly underutilized.
- Lack of methodological development - there is currently no standardized framework for processing accelerometer-based FCD, linking signal features to pavement distress categories (e.g., potholes, cracking, roughness), or benchmarking results against official indices such as IRI or PCI.

This disconnect reveals a clear paradox: although FCD offers the widest potential spatial and temporal coverage among all sensing technologies, it still contributes the least to infrastructure condition monitoring.

3.2. Data Fusion: sophisticated methods, misplaced priorities

The field of data fusion has made remarkable strides. Numerous studies demonstrate how integrating FCD with other sources (loop detectors, Bluetooth sensors, radar, GIS, environmental data) enhances traffic modeling and congestion detection. Advanced machine learning models (LSTM, GANs, CNNs) and statistical approaches (ASM, PSM, tensor decomposition) are widely used to overcome data sparsity, noise, and heterogeneity.

However, almost all of these applications remain mobility-centric. The aim is typically to improve travel time estimates, forecast congestion, or simulate traffic states. Only limited attention has so far been devoted to leveraging fusion methods for pavement condition monitoring [46] [47]. This is a significant limitation for two reasons:

First, pavement distress is inherently multi-faceted: it results from structural fatigue, environmental conditions, traffic loads, and localized failures. No single sensing modality is capable of capturing all relevant dimensions of pavement performance. Second, fusion is precisely the methodological tool needed to integrate accelerometric

FCD (capturing shocks and vibrations) with other layers such as satellite imagery, GIS databases, or official PMS surveys.

Without such integration, accelerometer-based FCD remains noisy, difficult to calibrate, and highly sensitive to confounding factors (e.g., vehicle type, suspension characteristics, or driving style). A data fusion paradigm is thus essential not only to improve reliability but also to make accelerometric FCD acceptable to institutions as a credible source of evidence.

3.3. Pavement Management Systems (PMS): traditional practices

PMS are institutionalized frameworks used globally by transport agencies to monitor road conditions, predict deterioration, and plan maintenance. Indices such as the International Roughness Index (IRI), the Pavement Condition Index (PCI), and the Structural Condition Index (SCI) are well established, providing standardized and comparable measures across regions.

However, PMS frameworks are still constrained by legacy data-collection practices. Most rely on periodic visual inspections, profilometers, deflectometers, or LIDAR surveys, all of which are expensive, resource-intensive, and limited in spatial and temporal coverage. As a result:

- Data is often collected only once every 1-5 years, leading to blind spots between inspections.
- Small-scale or rapidly evolving defects (e.g., potholes after extreme weather) are often missed until they deteriorate further.
- The approach is fundamentally reactive rather than predictive.

Despite the clear potential of FCD to address these gaps, only a limited number of PMS frameworks systematically incorporate vehicle-based sensing. Pilot projects exist, but they tend to use FCD only in peripheral roles (e.g., validating traffic flow assumptions), not as core condition indicators.

3.4. Challenges and opportunities

Bringing these threads together, the gap becomes evident. Floating Car Data has become a pervasive and relatively inexpensive source of information, generated

continuously by fleets of private cars, taxis, buses, and commercial vehicles. Despite this abundance, its application has been disproportionately concentrated on traffic analysis and mobility optimization, while its potential for monitoring pavement conditions has been left largely unexplored. This represents a paradox: despite their extensive spatial and temporal coverage, current FCD streams still provide a marginal contribution to pavement condition evaluation within PMS workflows.

At the same time, the field of data fusion has developed rapidly, producing increasingly sophisticated techniques for integrating heterogeneous data streams such as GPS, loop detectors, radar, Bluetooth sensors, and environmental observations. Yet these methods, despite their maturity, remain narrowly applied to traffic dynamics, with the primary objective of refining travel time estimation, congestion detection, or vehicle routing. The misalignment between methodological advances and application domains is striking. If properly redirected, these same fusion techniques could provide the necessary methodological scaffolding to transform raw accelerometric FCD (currently noisy, fragmented, and vehicle-dependent) into standardized, credible indicators of pavement performance. Without such adaptation, accelerometric data will continue to be dismissed as unreliable, and its strong applicability potential for infrastructure monitoring will remain unrealized.

On the institutional side, Pavement Management Systems represent a mature and well-established framework, adopted globally to support maintenance planning, deterioration modeling, and budget allocation. However, PMS frameworks are still deeply rooted in traditional data collection methods, such as profilometers, deflectometers, and visual inspections. These methods, while precise and standardized, are costly, infrequent, and spatially limited. As a consequence, road authorities often operate in reactive mode, intervening after visible distress emerges, rather than anticipating degradation through predictive intelligence. The rigidity of PMS frameworks, combined with their slow adoption of emerging sensing technologies, exacerbates the disconnection between available data streams and institutional practices.

What is currently missing is a unifying framework capable of bridging these three domains. Such a framework would systematically integrate accelerometric FCD with complementary sources (satellite imagery, GIS databases, weather records, and

traditional PMS survey data) through advanced data fusion techniques. The resulting hybrid indicators could then be embedded within PMS workflows, ensuring not only continuity but also institutional legitimacy. This integration would guarantee frequent, crowd-sourced data collection, thereby bridging the temporal gaps left by periodic surveys; it would expand spatial coverage by monitoring entire road networks rather than limited sections; it would enhance predictivity by enabling the construction of probabilistic or machine-learning-based deterioration models fed by continuous FCD streams; and it would ultimately ensure cost-effectiveness by reducing dependence on expensive inspection campaigns.

Failing to achieve such integration risks perpetuating a siloed ecosystem in which FCD, data fusion, and PMS evolve independently, without meaningful cross-fertilization. The consequence would be a continued overreliance on costly legacy inspections, missed opportunities for predictive maintenance, and a lack of responsiveness to emerging mobility and sustainability challenges. Conversely, by developing an integrated framework that unites these domains, infrastructure monitoring can transition from reactive and resource-intensive to predictive, scalable, and cost-efficient, ultimately transforming road asset management into a proactive, data-driven discipline.

Preliminary attempts to combine vibration signals with vision-based monitoring already exist. For instance, [48] propose a dual smartphone-based acquisition system that jointly records road-surface images and three-axis accelerations to infer the severity of surface anomalies. However, their setup relies on instrumented vehicles equipped with dedicated smartphones rather than on passively collected fleet-wide telematics data, which limits both spatial coverage and the degree of automation. As a result, the broader potential of accelerometer-based FCD for network-wide pavement monitoring remains largely untapped.

Several methodological and operational challenges still need to be addressed before accelerometer-based Floating Car Data (FCD) can be fully integrated into Pavement Management Systems (PMS). Chief among these challenges is the issue of calibration, namely the need to establish reliable and reproducible mappings between accelerometric signatures recorded by in-vehicle sensors and official PMS indices such as the International Roughness Index (IRI) or the Pavement Condition Index (PCI).

Without such calibration, the credibility of FCD as a surrogate or complement to traditional surveys remains limited. Equally important is the inherent problem of heterogeneity across vehicle fleets and sensing conditions, since vehicle fleets differ in weight, suspension systems, tire pressure, and sensor placement, all of which significantly affect accelerometric responses to the same road anomaly. This variability must be addressed through statistical normalization, fleet-wide aggregation, or machine learning models capable of disentangling vehicle-specific factors from true pavement distress. A further complication arises from the inherent noisiness and discontinuity of accelerometer-based data: shocks due to aggressive driving maneuvers, braking, or temporary load conditions can easily be mistaken for structural defects. Robust filtering techniques, temporal consistency checks, and cross-validation with complementary data sources are essential to mitigate this risk. Finally, even if methodological hurdles are overcome, institutional adoption remains a barrier. Transport agencies are accustomed to certified, standardized surveys and may view FCD-derived indicators as opaque "black-box" outputs that lack transparency and comparability with established protocols.

Despite these obstacles, the literature strongly suggests that they are not insurmountable. Advances in multi-source data fusion provide a powerful methodological pathway to progressively bridge the credibility gap. By combining accelerometric FCD with complementary layers such as GPS trajectories, vehicle speed profiles, satellite imagery, GIS road databases, and targeted high-quality survey data, it becomes possible to cross-validate signals, filter noise, and construct hybrid indicators that are both reliable and interpretable. Statistical normalization across vehicle types, machine learning-based feature extraction, and continuous validation against official indices can further ensure that FCD is not treated as a competing source of information but as a complementary one, enriching PMS frameworks with greater temporal frequency and spatial coverage.

From this perspective, integrating FCD into PMS should not be regarded merely as a technical refinement but as a strategic opportunity for the entire road-infrastructure sector. Such integration would support a shift from reactive maintenance toward earlier and more data-informed intervention planning, improving both timeliness and

network coverage. It would also directly improve road safety, since timely detection of anomalies such as potholes or surface roughness reduces the likelihood of accidents and vehicle damage. Moreover, the alignment of maintenance planning with actual mobility patterns (as revealed by continuous FCD streams) would ensure that interventions are prioritized in the areas of greatest usage and risk. Importantly, this paradigm also reduces cost barriers for large-scale monitoring: in low- and middle-income countries, where traditional survey vehicles are prohibitively expensive, the ubiquity of connected fleets and insurance telematics could provide a cost-effective alternative for large-scale monitoring.

In conclusion, the current disconnect between FCD, data-fusion methodologies, and PMS workflows represents not only a technological gap but also a structural limitation in the way road infrastructure is monitored and maintained. Bridging these domains is essential to move from episodic and reactive inspections toward continuous, predictive, and network-wide pavement intelligence. This thesis positions itself directly within this gap, proposing an integrated framework capable of transforming heterogeneous vehicular data into operational knowledge for PMS. By doing so, it aims to contribute to a fundamental shift in road asset management, from fragmented practices to a proactive, data-driven, and scalable paradigm.

4. Data characterisation and preliminary analysis

The experimental analysis relies on a comprehensive set of datasets collected across the road network of the city of Brescia. The entire integration and modelling process adopts the road segment as the common spatial unit, representing the finest level of granularity used in this study. A complete census of urban road segments was available for the municipality, each associated with a unique identifier (segment_id) and described through attributes such as administrative district and geometric representation.

The study integrates data from three independent sources (VIASAT, AIWAY and AIR) each offering distinct sensing capabilities. Only VIASAT and AIWAY were retained for the experimental analyses, while AIR was excluded due to coverage inconsistencies and reliability limitations within the study area.

The datasets considered in this study were acquired from three distinct sources, each based on different sensing technologies. The first source, VIASAT, provided both raw accelerometric signals and enriched event-level records. The accelerometric layer includes tri-axial inertial measurements with geolocation and heading, while the event-level layer captures occurrences of road anomalies, labelled and associated with speed, detection frequency and vehicle metadata. The complete dataset contains over 74,000 geo-referenced points.

The second source, AIWAY, provided a vision-based dataset derived from onboard cameras and computer-vision algorithms. Each detection is geo-referenced, annotated with an anomaly class and associated with a confidence score. A structured version of the dataset also includes metadata such as timestamp, camera state and trip identifiers. After preprocessing, approximately 63,800 valid detections were retained.

The third source, AIR, provided accelerometric data at both point and segment level. The segment-level layer includes mean and maximum vertical acceleration, severity indices and confirmation scores. However, these values were pre-aggregated through proprietary algorithms whose internal logic is not publicly disclosed. Due to this limitation and to partial coverage across the study area, AIR was excluded from the primary modelling dataset and reserved for potential ex-post validation, serving as an external benchmark for the integrated results from VIASAT and AIWAY.

To ensure consistency and interoperability, all datasets were harmonized by aligning observations to the predefined road-segment model. Spatial joins were performed using a 15 m proximity threshold between each point and the target segment geometry. This value balances typical GPS noise in urban canyons (5-10 m at 95% under multipath) against the risk of assigning detections to adjacent carriageways, ensuring a robust association between point-level observations and their corresponding segments.

The analysis thus proceeded with a unified framework in which all observations were transformed into segment-level summaries. The AIR dataset, although not directly employed in the core model, remained available as a secondary reference to evaluate the plausibility of the synthesized indicator of pavement condition. In this way, the integrity of the experimental pipeline was maintained while preserving the opportunity for independent validation.

The next section details the preprocessing steps applied to the selected datasets, the construction of harmonized features, and the statistical characterization of the resulting segment-level database.

4.1. Analysis of VIASAT data

The variables type 1, type 2, type 3, and type 4 represent distinct categories of pavement distress derived from accelerometer data collected through telematics devices (commonly referred to as black boxes) installed on a fleet of insured vehicles operating across the city of Brescia. These sensors, integrated as part of commercial telematics services, continuously measure vehicle dynamics such as vertical and lateral acceleration, which indirectly capture the mechanical interaction between the vehicle and the underlying road surface. In this way, variations in the acceleration signal can be interpreted as indicators of surface irregularities, offering a passive and large-scale method for monitoring pavement conditions through normal driving activity.

The dataset includes 4,820 punctual road-surface events, each representing a single detection of an anomaly at a specific geographical location. All events are located within the urban core of the municipality of Brescia, an area characterized by the

highest traffic density, complex driving dynamics, and diverse infrastructural configurations. Although the number of observations is relatively small compared with the approximately 215,000 road segments composing the entire municipal network, their concentration in the most heavily used and infrastructurally relevant portion of the city makes the dataset particularly meaningful. It captures real-world interactions between vehicles and the road infrastructure, reflecting how drivers experience and respond to surface irregularities in areas where traffic intensity and maintenance demands are greatest.

The dataset was provided by insurance companies in anonymized and pre-processed form, ensuring compliance with privacy regulations while retaining the analytical value of the observations. The raw accelerometric time series were not available; instead, each event was already classified into one of four types based on proprietary signal-processing algorithms applied by the data provider. The exact procedures, thresholds, and filtering criteria used in this classification are not disclosed, precluding direct verification of the method. Nonetheless, the resulting typology is consistent with known vibration patterns associated with specific categories of pavement distress and thus provides a reliable operational framework for statistical analysis.

Each event type corresponds to a characteristic vibration signature and physical interpretation. Type 1 events represent abrupt vertical shocks, typically linked to potholes or surface collapses that cause instantaneous acceleration peaks. Type 2 events are associated with linear discontinuities such as speed bumps, seams, or manhole covers, which generate periodic but controlled vertical impulses. Type 3 events capture general surface roughness and texture irregularities distributed over short distances, indicative of wear or intermediate stages of deterioration. Type 4 events correspond to low-intensity depressions or minor settlements that may be less perceptible to drivers but still influence ride comfort and contribute to the long-term decline of pavement quality.

Together, these four categories provide a simplified yet scalable representation of road-surface anomalies, allowing heterogeneous disturbances to be systematically grouped and analyzed. The typology serves as a foundation for subsequent behavioral, spatial, and statistical analyses, enabling the investigation of how different forms of surface degradation manifest through vehicle dynamics and how they

collectively inform data-driven approaches to road infrastructure assessment. The resulting dataset constituted the foundation for the subsequent classification and comparative analysis, as detailed in the following sections.

Table 1 -VIASAT tags.

VIASAT	
Tag	**Description**
Type 1	Potholes
Type 2	Bumps (speed humps/raised irregularities)
Type 3	Surface failures (distresses/unevenness)
Type 4	Depressions/settlements

At this stage, the severity weights assigned to each anomaly type are defined on the basis of engineering experience and the physical nature of the different forms of pavement distress, in order to establish a consistent reference framework for all subsequent tests and analyses. These weights are parametric, meaning that they can be recalibrated in later phases when additional evidence or expert input becomes available, but they are fixed here to ensure coherence among the behavioral, sequential, spatial, and synthetic assessments presented in this chapter. Therefore, the adopted values should be interpreted as expert-informed priors rather than empirically calibrated parameters.

Specifically, Type 1 events, corresponding to potholes or abrupt vertical shocks, are assigned a weight of $w_1 = 3$to reflect their higher structural severity and the stronger behavioral response they induce in drivers. Type 2 events, associated with speed bumps or engineered irregularities, receive a weight of $w_2 = 1$, since they are not indicative of degradation but of deliberate design for traffic calming. Type 3 events, representing surface failures or widespread unevenness, are assigned a weight of $w_3 = 2$, consistent with their role as intermediate indicators of deterioration that affect comfort and drivability but are less critical than potholes. Finally, Type 4 events, corresponding to depressions or minor settlements, are also assigned a weight of $w_4 = 2$, as they may appear less perceptible to drivers but still have structural relevance and can evolve into more severe forms of damage. The resulting hierarchy $w_1 > w_3 = w_4 > w_2$ensures a monotonic relationship between the physical and perceived severity of

the anomalies and their contribution to the computed indices. Holding these parameters fixed guarantees that the results of the different analyses remain internally consistent and comparable. In later stages, once visual inspection data and additional validation sources are available, these weights can be recalibrated through sensitivity analyses to better reflect empirical degradation dynamics and to refine the accuracy of the proposed severity model.

While this approach enables efficient data handling and high-frequency monitoring, it presents several methodological limitations. Most notably, the lack of access to raw signals or classification logic means that no ground truth validation was possible. The dataset was thus used in this work as received, under the assumption that the categories are internally consistent and that aggregated behavior across a large sample compensates for individual inaccuracies. This choice was necessary due to the proprietary nature of the telematics platform and the commercial agreements governing data sharing.

An additional source of uncertainty stems from the heterogeneity of the vehicle fleet. The accelerometer-equipped vehicles vary in mass, suspension systems, chassis height, and tire types, all of which influence how a given road anomaly translates into a measurable acceleration pattern. For example, the same pothole may register as a severe event in a small passenger car but only mildly in a heavy SUV or delivery van. Since no metadata on vehicle types was provided, it is not possible to normalize the signals across vehicles or account for structural filtering effects. This introduces a non-negligible measurement bias, which must be acknowledged when interpreting the results. However, similar limitations are well documented in the literature on floating car data and passive road sensing (e.g. [23]), and they do not invalidate the approach when used for large-scale statistical analysis, pattern detection, or comparative studies across road segments.

From a practical standpoint, the use of insurance telematics data provides several advantages: wide spatial and temporal coverage, low operational costs, and the ability to capture driver-perceived road quality rather than purely geometric surface profiles. This user-centric perspective is increasingly relevant in modern road asset management frameworks, which aim to incorporate comfort, safety, and behavioral indicators into maintenance prioritization. In the context of smart mobility and

infrastructure monitoring, these data streams can complement traditional inspection methods and feed into predictive models of road degradation.

Despite the current limitations, the dataset remains a valuable resource for exploring data-driven approaches to road quality assessment and for testing scalable monitoring frameworks based on real-world driving data.

4.1.1. Methodological rationale

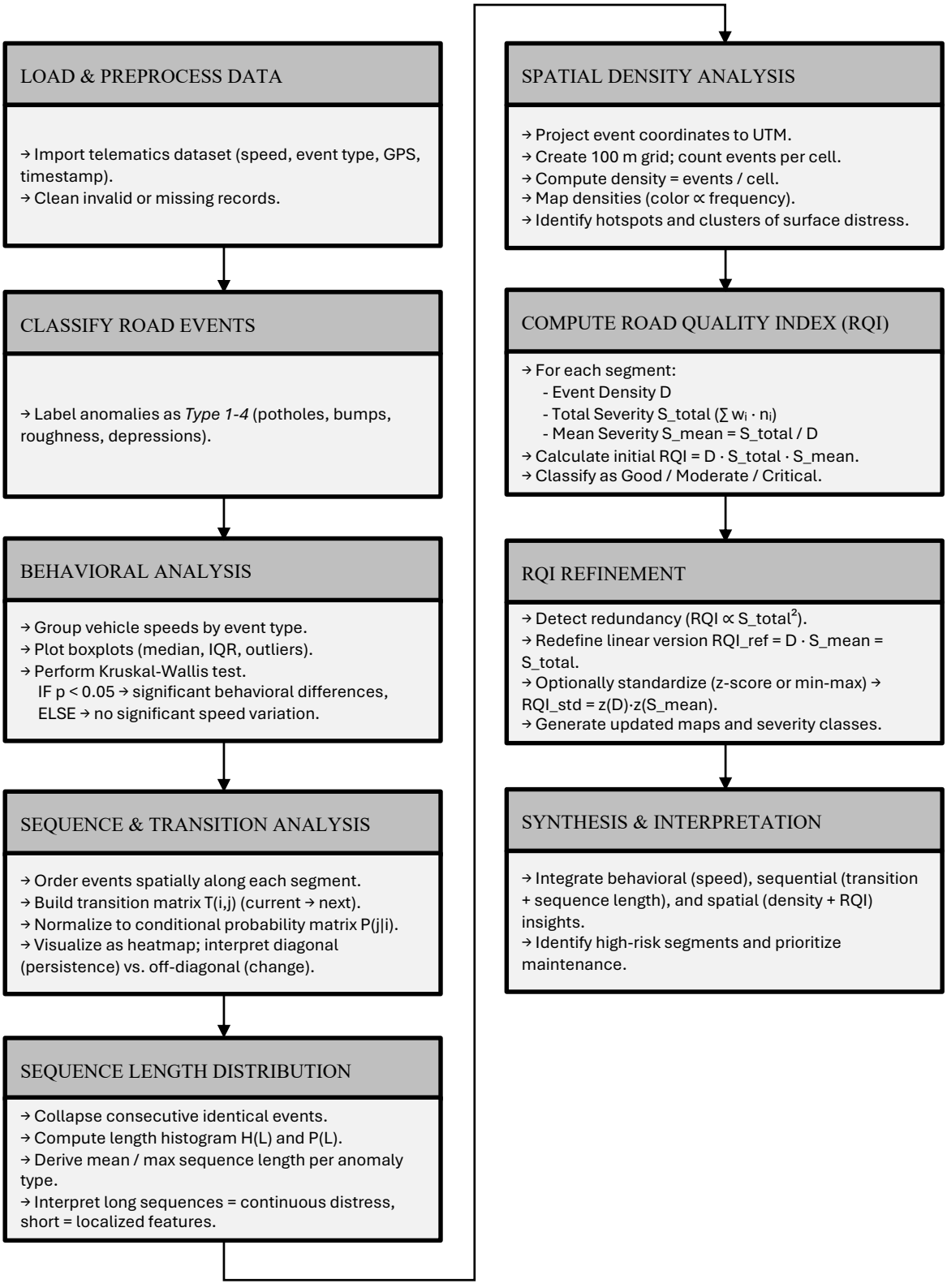

Figure 6 - Flow chart VIASAT dataset

The flow chart summarizes the logical structure of the analytical framework adopted in this research, illustrating how different methodological components are interconnected to provide a comprehensive understanding of pavement conditions derived from Floating Car Data (FCD).

The workflow proceeds sequentially, from data preparation to composite index construction, integrating behavioral, sequential, spatial, and synthetic analyses within a unified pipeline.

The process begins with data acquisition and preprocessing, where heterogeneous information from vehicle-mounted sensors (such as speed measurements and event classifications) is harmonized and cleaned.

Road anomalies are then categorized into four event types, each representing a distinct form of pavement distress. This classification establishes the foundation for all subsequent analyses.

The first analytical block focuses on driver behavior, evaluating how vehicle speed distributions vary across event types. Through boxplot visualization and the Kruskal-Wallis non-parametric test, the analysis identifies whether drivers react consistently to specific road anomalies, revealing behavioral sensitivity to surface irregularities.

The workflow then advances to the sequential domain, where events are ordered along vehicle trajectories. The transition matrix captures the frequency with which one event follows another, while its conditional probability form expresses the likelihood of such transitions. These matrices describe the temporal and spatial continuity of pavement defects, highlighting both persistent patterns and possible degradation pathways.

Next, the sequence-length distribution quantifies how long identical anomalies persist along a segment, distinguishing isolated defects from extended deteriorated zones. This measure of persistence complements the sequential analysis by adding a notion of spatial continuity.

The geographical density analysis translates event occurrences into spatial heatmaps, revealing clusters and hotspots of recurring defects across the network.

The final part of the workflow synthesizes these observations into a Road Quality Index (RQI), which aggregates frequency and severity information to provide a scalable indicator of pavement condition. The index is first formulated in

multiplicative form to combine multiple dimensions of deterioration, and then refined to a linear, interpretable structure that avoids redundancy between its components.
The resulting refined RQI (and its standardized variant) enables transparent comparisons among segments and facilitates maintenance prioritization.
Finally, the integration and interpretation stage brings together behavioral, sequential, and spatial findings, offering a holistic representation of the infrastructure state.
Overall, the flow chart illustrates a coherent methodological progression (from raw telematics data to actionable indicators) ensuring that each analytical layer builds upon the previous one to enhance robustness, interpretability, and decision support for road asset management.

4.1.1.1.Boxplot analysis of vehicle speed by road event type

This section investigates how accelerometer-detected surface anomalies influence driver behavior under real-world conditions, using vehicle speed as a proxy for perceptual and operational response. The purpose is to evaluate whether specific forms of pavement distress systematically influence driver behavior and, in particular, whether drivers tend to reduce or maintain their speed depending on the nature and perceptibility of the anomaly encountered.
The dataset employed in this analysis includes a classification of road-surface events into four types, based on the signal patterns extracted from vertical accelerometer readings collected via insurance telematics black boxes. These events, labeled as Type 1 through Type 4, represent respectively potholes or abrupt shocks, linear features such as speed bumps or seams, widespread roughness, and minor depressions or surface settlements.
To examine the relationship between these event types and vehicle speed, a combined descriptive and inferential approach was applied. A boxplot-based analysis was used to summarize the speed distributions associated with each event type, followed by a Kruskal-Wallis test [49] to evaluate the statistical significance of inter-group differences. The rationale for adopting these techniques lies in the non-Gaussian nature of vehicle speed data collected under heterogeneous traffic and environmental conditions, where parametric assumptions such as homoscedasticity and normality

are frequently violated [38] [50] [51]. The Kruskal-Wallis test, a rank-based non-parametric alternative to one-way ANOVA, is particularly robust for comparing medians among multiple independent groups with unequal sample sizes and non-linear variances [52] [53]. It has been widely used in recent traffic and telematics studies to detect speed differences caused by road geometry, rainfall intensity, or pavement irregularities [54] [55] [56]. It tests the null hypothesis that all groups originate from the same population by comparing the sum of rank scores, thus providing a distribution-free inference suitable for asymmetric or multimodal datasets.

Boxplots complement this inferential test by offering a graphical synthesis of behavioral variability, enabling immediate visualization of central tendency (median), spread (IQR), and extreme values (outliers). These visual summaries are especially suitable for non-Gaussian behavioral data, which often display skewness or multimodality as a result of distinct driving contexts and perception thresholds [57] [58]. Prior research demonstrates that the dispersion and symmetry of speed distributions can serve as proxies for driver adaptation to surface roughness and external disturbances, reflecting both the perceptual sensitivity and the behavioral adaptation of drivers to uneven pavements [59] [60]. For instance, narrower boxes and shorter whiskers typically indicate consistent deceleration behavior (common near abrupt defects or engineered bumps) whereas wider boxes and long whiskers denote heterogeneous reactions to mild or less perceptible surface irregularities [38] [53].

Together, these two techniques provide complementary insights: the boxplot captures distributional characteristics and outlier behavior, while the Kruskal-Wallis test statistically validates whether such differences are significant across the four event classes. Their combined application aligns with recent methodologies in telematics-based pavement and traffic behavior studies [50] [55], providing a robust and interpretable framework to quantify how surface irregularities influence driver behavior under real-world conditions. The algorithm details the computational procedure adopted to group speed values by event type, compute descriptive statistics, and plot comparative distributions.

Algorithm 1 - BoxplotSpeedByEventType

```
Line    Pseudocode
1       Algorithm BoxplotSpeedByEventType(Data) → Boxplots
2         Initialize EventSpeedDict ← empty dictionary
3         for each record in Data do
4           event_type ← record. event_type
5           speed ← record.speed
6           append speed to EventSpeedDict[event_type]
7         end for
8         for each event_type in EventSpeedDict do
9           compute median, IQR, whiskers, outliers
10          plot box using computed statistics
11        end for
12        return all boxplots
```

4.1.1.2.Analysis of the transition matrix between events

To explore the sequential structure of road anomalies detected through floating car data (FCD), a transition matrix was constructed to represent the conditional relationships between different classes of pavement events. This matrix serves as a Markovian statistical model, where each state corresponds to a specific type of road event (e.g., pothole, speed bump, roughness, depression), and transitions capture the frequency with which a given event is followed by another along a vehicle's trajectory. Let $S = \{s_1, s_2, \ldots, s_n\}$ denote the set of possible event types, and let $T(i,j)$ represent the number of times that event s_j occurs immediately after event s_i. The resulting matrix $T \in \mathbb{N}^{n*n}$ thus captures the empirical joint frequencies of consecutive events. Optionally, this matrix can be row-normalized to yield a stochastic matrix $P \in [0,1]^{n*n}$, where $P(i,j)$ denotes the empirical conditional probability $\mathbb{P}(s_{k+1} = s_j \mid s_k = s_i)$. This formulation allows the transition matrix to be interpreted as a first-order Markov chain, making it suitable for predictive modeling and degradation forecasting. Such representation allows the derivation of network-level indicators of homogeneity, persistence, and degradation dynamics.

The data used to populate this matrix consist of a chronologically or spatially ordered sequence of road events recorded by vehicles traveling along the network. In this study, events were ordered spatially along each road segment according to their GPS position, ensuring consistency in the definition of consecutive events. For each pair of consecutive events, the corresponding cell in the matrix is incremented. Once the matrix is built, it is visualized as a heatmap, where the x-axis represents the "next

event," the y-axis represents the "current event," and each cell's color encodes the transition frequency. Brighter colors (e.g., yellow) indicate high transition counts, whereas darker colors (e.g., dark blue) denote rare or absent transitions.

Several key patterns emerge from the matrix. Self-transitions, such as "POTHOLE → POTHOLE" or "ROUGHNESS → ROUGHNESS," dominate the diagonal and indicate the presence of spatial clusters of the same type of anomaly. These clusters reflect extended sections of road affected by the same distress mechanism and often signal advanced pavement deterioration. In contrast, transitions between distinct event types, such as "SPEED BUMP → DEPRESSION" or "ROUGHNESS → BUMP," appear less frequently, suggesting that these events occur in isolation or are driven by different underlying causes (e.g., artificial vs. structural features).

From a road management perspective, the transition matrix enables data-driven prioritization. For example, stretches of road with a high density of repeated potholes (high values in $T(POTHOLE, POTHOLE)$) may require complete resurfacing, while isolated depressions might be addressed with localized maintenance. Moreover, by examining the off-diagonal elements, one can assess potential progressive degradation paths, such as the sequence: roughness → pothole → depression, which could inform predictive maintenance strategies.

Algorithm 2 - BuildTransitionMatrix

```
Line    Pseudocode
1       Algorithm BuildTransitionMatrix(Data) → Matrix
2       Initialize TransitionMatrix[EventTypes] [EventTypes] ← zeros
3       for i from 1 to length(Data) - 1 do
4         current_event ← Data[i].event_type
5         next_event ← Data[i+1].event_type
6         TransitionMatrix[current_event] [next_event] += 1
7       end for
8       return TransitionMatrix
```

The resulting transition matrix was then analyzed to identify dominant transition patterns and evaluate their correspondence with spatially observed pavement degradation, as discussed in the following section.

4.1.1.3.Conditional probability analysis of road surface events

Building upon the transition matrix framework described in the previous section, a conditional probability matrix was derived to further quantify the strength of sequential dependencies between event types. This analysis aims to quantify the likelihood that a given road event is immediately followed by another specific type of event. Such a probabilistic approach provides more nuanced insights than simple frequency-based transition counts, as it accounts for the relative prevalence of each event type and highlights behavioral or infrastructural patterns that may not be immediately evident from raw frequencies.

The construction of the conditional probability matrix involves two main steps. First, we count all transitions between pairs of consecutive events, denoted as (Current Event → Next Event), across the entire dataset. Then, for each unique current event, we normalize the transition frequencies by the total number of times that event occurs as the starting point. This yields the conditional probability $P(\text{Next Event} \mid \text{Current Event})$, interpreted as the probability that a specific next event follows a given current event. Mathematically, for two events i and j, the conditional probability is computed as:

Equation 1 - Conditional probability of event transitions in the sequential matrix

$$P(j \mid i) = \frac{N(i \to j)}{\sum_k N\,(i \to k)}$$

where $N(i \to j)$ is the count of transitions from event i to event j, and the denominator is the total number of transitions originating from event i (i.e., row sum in the transition matrix).

Values close to 1 indicate strong sequential dependence, meaning that event j almost always follows event i, whereas values close to 0 suggest weak or no association between the two event types.

Algorithm 3 - ComputeConditionalProbabilityMatrix

```
Line    Pseudocode
1       Algorithm ComputeConditionalProbabilityMatrix(Data) → ProbabilityMatrix
2       Initialize TransitionCounts[Current] [Next] ← 0 for all event pairs
3       Initialize RowSums[Current] ← 0 for all events
4       For i from 1 to N-1 do
5           current ← Data[i].event
6           next ← Data[i+1].event
7           TransitionCounts[current] [next] += 1
8           RowSums[current] += 1
9       End For
10      For each current_event in EventSet do
11          For each next_event in EventSet do
12              if RowSums[current_event] > 0 then
13                  ProbabilityMatrix[current_event]         [next_event]         ←
        TransitionCounts[current_event] [next_event] / RowSums[current_event]
14              else
15                  ProbabilityMatrix[current_event] [next_event] ← 0
16              end if
17          End For
18      End For
19      Return ProbabilityMatrix
```

The resulting probability matrix was then analyzed to identify statistically dominant transition pathways and assess their implications for road condition dynamics, as presented in the following section.

4.1.1.4.Geographical density analysis of road surface events

Following the analysis of temporal and sequential relationships among events, a geographical density analysis was conducted to examine the spatial distribution of anomalies across the study area. The objective was to identify concentrations of recurring pavement defects and reveal underlying spatial patterns that may not be evident from sequential analyses alone.

Using the latitude and longitude coordinates of all detected events, the study area was partitioned into a uniform grid with a spatial resolution of approximately 100 meters. This resolution was selected as a balance between spatial granularity and computational feasibility, ensuring sufficient local sensitivity while maintaining manageable data volumes. All coordinates were expressed in WGS84 format and projected to UTM to ensure consistent metric distance calculations.

For each grid cell, the number of events was aggregated to compute a local density value, representing the relative frequency of anomalies per cell. Optionally, these

counts can be normalized by the total number of events to obtain comparable density ratios across areas of different size or coverage. The resulting values were then visualized on a density map, where each point corresponds to the centroid of a grid cell, and its color and size are proportional to the event density. Brighter colors indicate higher concentrations of anomalies, allowing the detection of clusters and hotspots of recurring pavement distress.

Algorithm 4 - GeographicalDensityMap

```
Line    Pseudocode
1       Algorithm GeographicalDensityMap(Data, GridResolution) → DensityMap
2       Extract event coordinates (latitude, longitude) from Data
3       Define bounding box covering all events (min/max latitude and longitude)
4       Divide bounding box into grid cells of size GridResolution × GridResolution
5       Initialize DensityMatrix with zeros (rows = number of lat cells, columns =
        number of lon cells)
6       For each event in Data do
7           Find grid cell corresponding to event coordinates
8           Increment DensityMatrix[cell] by 1
9       End For
10      For each grid cell do
11          Compute centroid (lat_c, lon_c) of the cell
12          Assign density value = DensityMatrix[cell]
13      End For
14      Generate scatter plot of centroids, with color/size proportional to density
15      Highlight maximum density cell in red
16      Return DensityMap
```

The resulting density map enables the identification of high-risk sections where multiple anomalies are spatially concentrated, supporting the detection of localized degradation patterns. This analysis complements the sequential event studies by providing a spatial dimension to the understanding of pavement distress, thereby offering actionable insights for maintenance prioritization and network-level planning.

4.1.1.5.Analysis of event sequence length distribution

The analysis of event sequence lengths provides insights into the persistence and clustering of road surface anomalies. Instead of focusing solely on individual occurrences, this approach examines how long a specific type of anomaly tends to persist consecutively along a road segment. For example, a long sequence of

consecutive pothole detections indicates a continuous degraded section of pavement, while short sequences reflect more isolated or sporadic issues.
Mathematically, let the dataset consist of an ordered sequence of events:

$$E = \{e_1, e_2, \dots, e_n\}$$

where each e_i belongs to a finite set of event types (e.g., pothole, bump, uneven surface, depression).
A sequence is defined as a maximal subsequence of consecutive identical events:

$$S = \{e_k, e_{k+1}, \dots, e_{k+m}\}$$

such that $e_j = e_k$ for all $j \in [k, k+m]$, and either $e_{k-1} \neq e_k$ or $k = 1$, and either $e_{k+m+1} \neq e_k$ or $k + m = n$.
The length of a sequence is therefore:

$$|S| = m + 1$$

While single anomalies indicate point defects, the persistence of identical consecutive events provides valuable information about the continuity of pavement distress. Therefore, the sequence-length distribution was computed to capture this persistence dimension, revealing whether defects tend to appear as isolated events or extended chains along a segment. The distribution of sequence lengths can be represented as a histogram $H(L)$, where L denotes the length of a sequence. Formally:

Equation 2 - Count of event sequences of a given length

$$H(L) = \#\{S : |S| = L\}$$

where $\#\{\cdot\}$ denotes the count of sequences of length L.
An alternative representation is the empirical probability distribution:

Equation 3 - Empirical probability distribution of sequence lengths

$$P(L) = \frac{H(L)}{\sum H(L)}$$

which gives the likelihood that a randomly chosen sequence has length L. This probabilistic view allows for statistical interpretation of whether anomalies tend to appear as isolated cases or as extended degradations.

Algorithm 5 - ComputeSequenceLengthDistribution

```
Line    Pseudocode
1       Algorithm ComputeSequenceLengthDistribution(Data) → Histogram
2       Initialize LengthList ← empty list
3       current_event ← Data[1].event
4       current_length ← 1
5       For i from 2 to N do
6          If Data[i].event == current_event then
7              current_length ← current_length + 1
8          Else
9              Append current_length to LengthList
10             current_event ← Data[i].event
11             current_length ← 1
12         End If
13      End For
14      Append current_length to LengthList
15      Compute histogram H(L) from LengthList
16      Return Histogram
```

4.1.1.6. Analysis of event sequences and their implications for road surface monitoring

Building on the formal definition above, the analysis of sequence-length distributions allows us to characterise the persistence of each anomaly type along road segments. Extended sequences reveal continuous and severe deterioration, whereas short sequences, typical of engineered features such as speed bumps, indicate localised phenomena.

The analysis of sequence length distributions enables the characterization of the persistence and spatial clustering of different anomaly types. Extended sequences, such as long chains of consecutive potholes, are indicative of severe and continuous pavement degradation along specific road segments. In contrast, short sequences -

typically associated with features such as speed bumps - represent localized phenomena that are generally designed elements rather than signs of distress.

Algorithm 6 - ComputeSequenceStatistics

```
Line    Pseudocode
1       Algorithm ComputeSequenceStatistics(Data) → Statistics
2       Initialize Dictionary S ← empty
3       current_event ← Data[1].event
4       current_length ← 1
5       For i from 2 to N do
6           If Data[i].event == current_event then
7               current_length ← current_length + 1
8           Else
9               Append current_length to S[current_event]
10              current_event ← Data[i].event
11              current_length ← 1
12          End If
13      End For
14      Append current_length to S[current_event]
15      For each anomaly type t in S do
16          mean_length(t) ← Average(S[t])
17          max_length(t) ← Max(S[t])
18      End For
19      Return {mean_length(t), max_length(t)} for all t
```

4.1.1.7.First spatial analysis of road quality index

The Road Quality Index (RQI) was designed to integrate three complementary components - event density, total severity, and average severity - so as to classify road segments according to their quality. Methodologically, the RQI was calculated for each road segment according to the following formulation:

Equation 4 - Composite formulation of the Road Quality Index (RQI) combining density and severity components

$$RQI = D \cdot S_{total} \cdot S_{mean}$$

where D represents the Event Density, defined as the total number of road surface events within a segment:

Equation 5 - Event density as the total count of detected anomalies within a segment

$$D = \sum_{i=1}^{n} C_i$$

with C_i denoting the number of events in cell i.

S_{total} is the Total Severity, corresponding to the cumulative severity of all events within a segment. Each anomaly type was assigned a severity weight (w_i), and the total severity was computed as:

Equation 6 - Total severity as the cumulative weighted sum of all detected events within a segment

$$S_{total} = \sum_{i=1}^{n} w_i$$

S_{mean} is the Average Severity, calculated as:

Equation 7 - Average severity computed as the ratio between total severity and event density

$$S_{mean} = \frac{S_{total}}{D}$$

Based on the computed RQI values, segments were classified into three categories:

- Good: $0 \leq RQI < 30$
- Moderate: $30 \leq RQI < 90$
- Critical: $RQI \geq 90$

Both the weights and the classification thresholds (Good: $0 \leq RQI < 30$; Moderate: $30 \leq RQI < 90$; Critical: $RQI \geq 90$) were established in collaboration with domain experts, whose knowledge of road engineering and infrastructure management informed the calibration process. These parameters were therefore not arbitrarily chosen but designed to reflect the relative impact of different anomaly types on pavement quality. Similar parametric approaches have been adopted in pavement management systems to balance severity and frequency [61]. At the same time, they were implemented as fully parametric elements of the model, which can be recomputed and adjusted to fit different datasets, geographical contexts, or expert judgments. This flexibility ensures that the RQI remains a scalable and adaptable tool for road quality assessment.

Only after the methodological setup was defined, the spatial distribution of the RQI values was analyzed to highlight the patterns of road deterioration and identify critical areas within the study region.

This classification was implemented in MATLAB using the `discretize` function, which generated categorical variables to assign labels to each segment. The proposed index therefore enables a systematic evaluation of road quality by integrating both the frequency and severity of anomalies, offering a scalable and interpretable approach to support network-level pavement monitoring and maintenance planning.

Algorithm 7 - ComputeFirstRoadQualityIndex

```
Line    Pseudocode
1       Algorithm ComputeFirstRoadQualityIndex(Data, Weights) → RQI
2       Initialize RQIList ← empty
3       For each road segment s in Data do
4           D ← CountEvents(s)
5           S_total ← 0
6           For each event e in s do
7               S_total ← S_total + Weights[e.type]
8           End For
9           If D > 0 then
10              S_mean ← S_total / D
11          Else
12              S_mean ← 0
13          End If
14          RQI ← D · S_total· S_mean
15          Append (s, RQI) to RQIList
16      End For
17      For each segment in RQIList do
18          If 0 ≤ RQI < 30 → Label ← "Good"
19          Else If 30 ≤ RQI < 90 → Label ← "Moderate"
20          Else → Label ← "Critical"
21          Assign Label to segment
22      End For
23      Return RQIList with Labels
```

4.1.1.8.Second spatial analysis of road quality index

During preliminary experimentation, the original formulation of the Road Quality Index tended to amplify contrasts disproportionately, prompting a methodological review. The goal was to preserve both frequency and severity effects without redundancy and to ensure that equal additional anomalies contribute linearly to the

score. The following re-specification introduces a more interpretable and transferable definition of RQI.
The current implementation defines:

Equation 8 - Original composite formulation of the Road Quality Index (RQI), combining density and severity components

$$\mathrm{RQI} = D \cdot S_{\mathrm{total}} \cdot S_{\mathrm{mean}}, S_{\mathrm{mean}} = \frac{S_{\mathrm{total}}}{D}.$$

Algebrically, this reduces to:

Equation 9 - Algebric reduction of the original RQI formulation, highlighting the non-linear amplification effect

$$\mathrm{RQI} = (S_{\mathrm{total}})^2$$

which (i) cancels event density $D$and (ii) squares total severity, amplifying contrasts and complicating interpretation. This redundancy-induced non-linearity amplifies high-severity contrasts and violates the expected proportionality between incremental anomaly counts and the overall index response. Similar scaling instabilities have been documented in composite index theory, where multiplicative formulations without normalization distort the interpretability and transferability of aggregated metrics. The results reported above remain valid as a descriptive mapping of squared severity load; however, a refinement is advisable for downstream analyses and transferability. A parsimonious correction that preserves the intended balance between frequency and severity without redundancy is:

Equation 10 - Refined, linearly interpretable definition of the Road Quality Index based on total weighted severity

$$\mathrm{RQI}_{\mathrm{ref}} = D \cdot S_{\mathrm{mean}} = S_{\mathrm{total}}.$$

The refined linear form $RQI_{ref} = S_{total}$ensures additivity, monotonicity, and scale invariance under linear transformation - key axioms for interpretable composite indicators. It guarantees that equal increments in event severity or frequency contribute proportionally to the overall deterioration score, restoring physical interpretability and facilitating transferability across networks. Consequently, the RQI

evolves from a descriptive hotspot index to a formally valid, comparable deterioration indicator.

This yields a linear, interpretable quantity: the total weighted severity per segment. With anomaly-type weights w_i and event counts n_i within a segment,

Equation 11 - Expanded formulation expressing total and mean severity as weighted sums of anomaly counts

$$S_{\text{total}} = \sum_i w_i \, n_i$$

$$S_{\text{mean}} = \frac{S_{\text{total}}}{D}$$

Equation 12 - Event density defined as the sum of detected anomalies per segment

$$D = \sum_i n_i,$$

so RQI_{ref} is simply the weighted sum of events.

If stronger contrast between many events and high average severity is desired while retaining transparency, a standardized composite can be used:

Equation 13 - Standardized version of the Road Quality Index combining normalized density and mean severity

$$\text{RQI}_{\text{std}} = z(D) \cdot z(S_{\text{mean}}),$$

where $z(\cdot)$ denotes standardization over the network (e.g., z-score or min-max to [0,1]). To address these limitations, the index is re-specified to retain both frequency and severity without redundancy and to restore linear interpretability. The refined definition treats the index as the total weighted burden accumulated on each segment, thereby preserving additivity and ensuring that equal additional events contribute equally to the score. This change removes the artificial amplification of extreme values, improves stability of class thresholds, and makes segment-to-segment comparisons transparent. In practice, the original map is retained as a complementary hotspot view, while the refined, linear index becomes the default for reporting, modelling, and policy-oriented comparisons.

Algorithm 8 - ComputeSecondRoadQualityIndex

```
Line    Pseudocode
1       Algorithm ComputeSecondRoadQualityIndex(Data, Weights) → RQI
2       Mode ∈ {zscore, minmax}
3       DS_List ← empty  // store D and S_mean
4       For each segment s in Data do
5         D ← CountEvents(s)
6         S_total ← 0
7         For each event e in s do
8           S_total ← S_total + Weights[e.type]
9         End For
10        If D > 0 then S_mean ← S_total / D else S_mean ← 0
11        Append (s, D, S_mean) to DS_List
12      End For
13      If Mode = "zscore" then
14        μ_D ← mean(D over DS_List); σ_D ← std(D over DS_List; if σ_D=0 use 1)
15        μ_S ← mean(S_mean over DS_List); σ_S ← std(S_mean; if σ_S=0 use 1)
16        For each record r in DS_List do
17          zD ← (r.D - μ_D) / σ_D
18          zS ← (r. S_mean - μ_S) / σ_S
19          r.RQI_std ← zD * zS
20        End For
21      Else if Mode = "minmax" then
22        D_min, D_max ← min/max of D; S_min, S_max ← min/max of S_mean
23        For each record r in DS_List do
24          uD ← (r.D - D_min) / max(D_max - D_min, ε)  // ε≈1e-9
25          uS ← (r. S_mean - S_min) / max(S_max - S_min, ε)
26          r.RQI_std ← uD * uS
27        End For
28      End If
29      Return DS_List with RQI_std
```

4.1.2. Experimental application and results

As the methodological framework and computational procedures have been thoroughly described in Section 4.1.1, the following subsections focus exclusively on the experimental implementation, parameter settings, and main results, avoiding repetitions of already-defined algorithms.

4.1.2.1.Boxplot analysis of vehicle speed by road event type

The results obtained from the boxplot visualization provide an immediate overview of how drivers adapt their speed according to the type of road anomaly encountered.

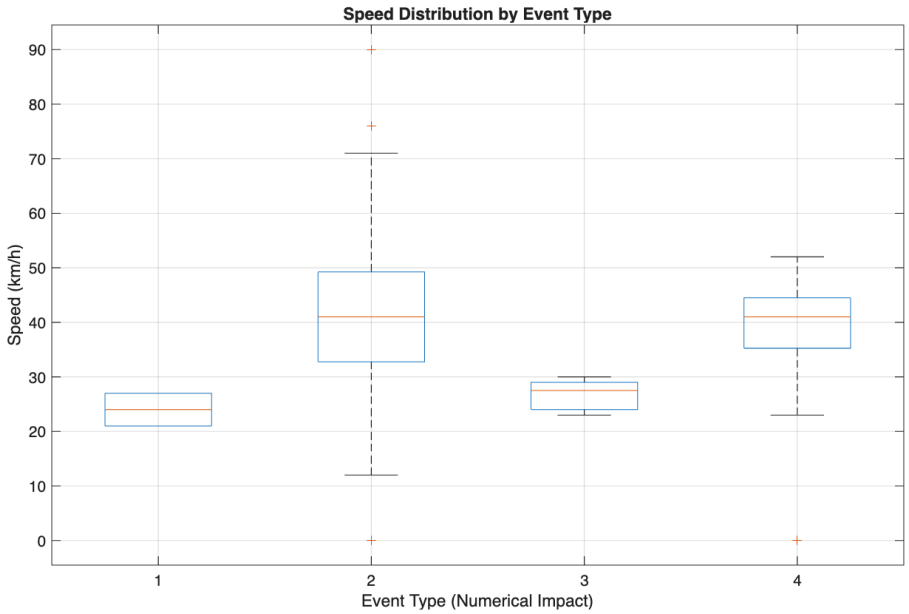

Figure 7- Boxplot with speed distribution by event type (VIASAT)

Figure 7 displays the distribution of vehicle speeds for the four event types detected in the VIASAT dataset (N = 4,820), offering a concise yet comprehensive representation of behavioral variability. Each box summarizes the central tendency and dispersion of vehicle speeds corresponding to a specific anomaly class, enabling direct comparison of driver responses across distinct pavement conditions.

A graphical summary of the analysis is shown in the boxplot in Figure 7. Each box in the plot visually summarizes the distribution of vehicle speeds observed for a given event type. The key components are:

- The orange horizontal line inside the box represents the median, i.e., the middle value of the dataset. It splits the data into two halves.
- The box edges (top and bottom) correspond to the first (Q1) and third (Q3) quartiles, respectively. This defines the interquartile range (IQR), which contains the middle 50% of the data.
- The "whiskers" are the vertical lines extending above and below the box. These show the range of typical values, defined as the data points within 1.5 × IQR from the quartiles.
- Red crosses outside the whiskers indicate outliers - values that are unusually high or low compared to the rest of the data. These often correspond to atypical driving behaviors or rare road scenarios.

- The overall height of each box and the length of its whiskers reflect speed variability for that specific event type: (i) narrow boxes and short whiskers imply consistent speeds (e.g., in response to potholes), (ii) wide boxes and long whiskers suggest greater variability in driver behavior (e.g., for linear bumps).

The visual evidence highlights four clearly differentiated behavioral patterns.
Type 1 anomalies, corresponding to abrupt vertical shocks typically associated with potholes or localized surface collapses, are associated with the lowest and most homogeneous speeds. Although fatigue-related distress such as alligator cracking represents a severe structural condition, it manifests as distributed surface damage rather than discrete vertical shocks, and is therefore conceptually distinct from the anomalies captured within the Type 1 category. Their median value, approximately 25 km/h, and narrow interquartile range indicate a systematic deceleration and highly consistent reaction among drivers. This suggests that abrupt and easily perceivable defects trigger cautious and homogeneous driving behavior. The pattern is compatible with visual anticipation and mechanical feedback through the suspension system.
Type 2 anomalies, representing raised linear features such as bumps or seams, exhibit the largest variability in vehicle speed, ranging from below 10 km/h to over 90 km/h, with a median near 40 km/h. This wide spread reflects the dual nature of such events: in urban areas, engineered bumps prompt significant slowdowns, whereas on suburban or interurban roads, similar linear features may be traversed at higher speeds. The presence of frequent outliers further supports the heterogeneity of traffic and environmental contexts in which these anomalies occur.
Type 3 anomalies, indicative of widespread surface roughness, show intermediate medians (around 27 km/h) and moderate variability. These patterns are consistent with the perception of moderate discomfort without the need for abrupt maneuvers. Drivers appear to adjust speed smoothly rather than reactively, reflecting a form of continuous adaptation to degraded pavement quality.
Type 4 anomalies, typically minor depressions or shallow settlements, are characterized by slightly higher median speeds (around 40 km/h) and a broader spread, suggesting that these irregularities often go unnoticed or are perceived as less critical. The existence of sporadic outliers within this group likely corresponds to cases

where the anomaly coincides with low-speed environments or visual cues that accentuate its detectability.

To statistically validate the observed differences, the Kruskal-Wallis H test was applied to compare the median speed distributions among the four categories. The statistically significant differences among event types ($\chi^2(3, N = 4{,}820) = 11.73$, $p = 0.0084$) demonstrate that the accelerometer-based event taxonomy captures not only distinct physical mechanisms of vehicle–pavement interaction but also consistent behavioral patterns across drivers. This behavioral coherence provides indirect validation of the proprietary classification scheme, confirming that the recorded categories retain semantic meaning beyond signal artefacts and reflect perceptually distinct pavement conditions. The test yielded χ^2 $(3, N = 4{,}820) = 11.73$, $p = 0.0084$, rejecting the null hypothesis of equal medians. This confirms that at least one event type exhibits a significantly distinct speed profile, implying that driver behavior systematically varies with the characteristics of the surface anomaly. The result aligns with findings from prior telematics-based research, where non-parametric tests revealed that speed adaptation is a reliable indicator of perceived pavement condition heterogeneity [38] [50].

From an interpretive perspective, these results emphasize the behavioral consistency of the VIASAT-derived classification and demonstrate the capacity of onboard accelerometer data to capture driver perception and reaction under real traffic conditions. The progressive variation in speed distributions across event types reflects a continuum of perceptual salience - from highly visible, disruptive shocks to minor or nearly imperceptible irregularities. This gradient of behavioral response effectively translates physical road characteristics into measurable human feedback, bridging the gap between mechanical detection and user experience.

In summary, the boxplot analysis confirms that different road surface conditions elicit distinct and statistically significant driver responses in terms of speed adaptation. Behavioral indicators derived from telematics data thus provide an additional dimension to traditional pavement assessment, integrating human perception into the interpretation of road quality. When coupled with geometric and structural metrics, these behavioral measures contribute to a more holistic and human-centered approach

to road management, supporting the prioritization of maintenance interventions within data-driven frameworks.

4.1.2.2. Analysis of the transition matrix between events

Following the methodological construction described in Section 4.1.1.2, the resulting transition matrix was analyzed to identify dominant spatial patterns and behavioral regularities among consecutive road anomalies. To facilitate interpretation, the matrix is visualized as a heatmap in Figure 8 , where color intensity represents the frequency of observed transitions between pairs of event types.

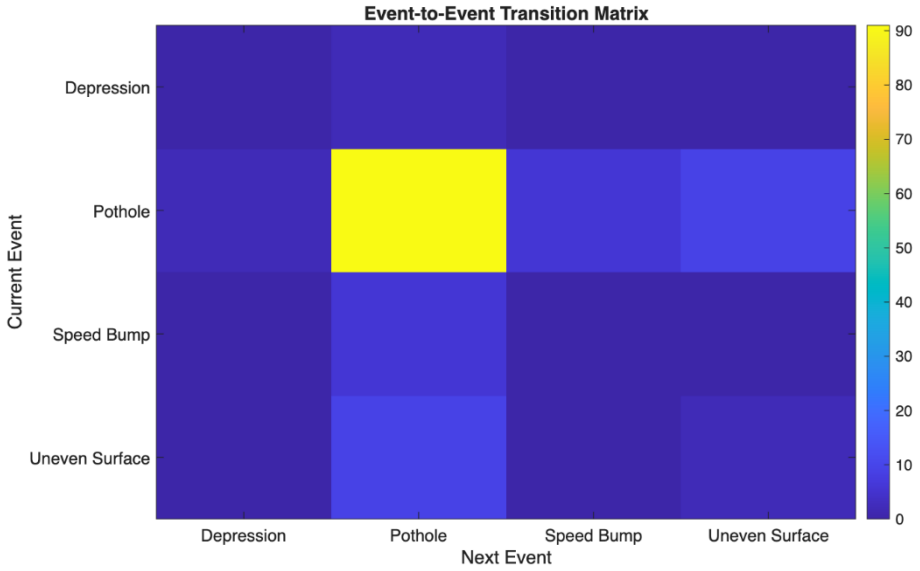

Figure 8 - Event-to-event transition matrix based on sequential accelerometer-detected road anomalies (VIASAT)

The heatmap provides an immediate visual representation of how different categories of pavement distress are spatially related along the trajectories of instrumented vehicles. Each cell captures how often a given event type (y-axis, "Current Event") is immediately followed by another (x-axis, "Next Event"). Lighter tones (yellow) correspond to higher transition frequencies, while darker ones (blue) indicate rare or absent transitions.

A prominent diagonal component is clearly visible, particularly at the "Pothole → Pothole" cell, which exhibits the highest intensity values. This pattern indicates that potholes frequently occur in succession, forming localized clusters of repeated detections. Such clustering reflects contiguous portions of pavement affected by the

same distress mechanism - typically alligator cracking or subsurface voiding - and signals a state of advanced degradation where isolated maintenance actions may be ineffective.

In contrast, Speed Bumps appear almost entirely isolated: the corresponding row and column display low transition frequencies, confirming that these engineered features are intentionally placed and not associated with structural deterioration. Their presence serves as a control point in the matrix, highlighting the distinction between artificial traffic-calming devices and naturally occurring distress.

Roughness (uneven surfaces) presents moderate interaction with both Potholes and Depressions, although at relatively low frequencies. This suggests that general roughness is more diffusely distributed across the network and may coexist with other minor irregularities without forming coherent spatial clusters. In practice, this reflects the gradual nature of surface wear or sub-base fatigue, which tends to develop progressively rather than abruptly.

Transitions such as "Depression → Pothole" or "Pothole → Depression" appear with intermediate intensity (light blue tones), suggesting partial spatial overlap or sequential evolution between these two anomaly classes. From a mechanistic viewpoint, such sequences may correspond to typical degradation paths - where local settlement caused by water infiltration or compaction loss evolves into cracking and eventual pothole formation. Identifying these recurrent progressions provides an empirical basis for predictive maintenance strategies.

From a statistical perspective, the transition matrix can be interpreted as a first-order Markov model, where the probability of the next event depends solely on the current one. Although Figure 8 presents absolute transition counts, the matrix can be normalized to derive the stochastic transition probabilities $P(i,j) = P(s_{k+1} = s_j \mid s_k = s_i)$, thus formalizing the sequential dependency structure as a first-order Markov chain. In this representation, each anomaly type corresponds to a discrete deterioration state, and the transition probabilities quantify the likelihood of evolving from one state to another. This formulation aligns with established pavement performance modelling practices in Pavement Management Systems (PMS), while extending them to opportunistic, high-frequency floating car data. Unlike traditional survey-based Markov models, the proposed framework enables near-real-time inference of

deterioration trajectories and early detection of emergent failure chains within continuously monitored road networks.

Similar Markov-based approaches have been successfully adopted in pavement management and infrastructure reliability studies [62], where transition probabilities derived from field data are used to predict condition shifts over time. In the present context, the empirical transition frequencies extracted from floating-car trajectories offer an analogous capability, derived not from scheduled inspections but from continuous, opportunistic sensing. This represents a significant methodological innovation, as it enables near-real-time inference of deterioration dynamics using standard telematics data.

Overall, the experimental results demonstrate that the sequential structure of detected anomalies carries valuable information on both the spatial persistence and the evolutionary mechanisms of pavement distress. Recurrent transitions such as "Pothole → Pothole" indicate concentrated deterioration demanding immediate resurfacing, whereas sparse or isolated transitions identify localized issues suitable for minor interventions. The transition matrix thus serves not only as a descriptive tool but also as an analytical bridge between behavioral sensing and infrastructure diagnostics. When combined with geometric, structural, and traffic-related indicators, it contributes to a comprehensive, data-driven framework for predictive and preventive road maintenance.

4.1.2.3.Conditional probability analysis of road surface events

Building upon the methodological framework described in Section 4.1.1.3, the conditional probability analysis provides a probabilistic interpretation of sequential pavement events. The results are visualized in Figure 9,which displays a heatmap of conditional probabilities. Each cell in the matrix represents the probability that a specific next event occurs, given the current event on the y-axis. Brighter cells indicate higher conditional probabilities, with values close to 1 suggesting strong sequential correlation.

The analysis reveals several key patterns:

- High autocorrelation is observed for certain event types, particularly potholes (Pothole → Pothole). This suggests that once a pothole is detected, it is highly probable that additional potholes follow in the immediate trajectory, indicative of spatial clustering and systemic surface degradation in certain segments.
- Speed bumps (Speed Bump → *) show low conditional probabilities with any other event, including themselves. This reflects their deliberate and isolated placement in the road network, typically designed as single-purpose installations for traffic calming.
- Uneven surfaces and depressions show moderate probabilities of being followed by potholes, suggesting that these conditions may co-occur in degraded areas but are not as tightly clustered.

This probabilistic view allows us to distinguish between localized, isolated events (like speed bumps) and spread, repeated anomalies (like potholes), which is crucial for designing maintenance schedules. For example, stretches with high $P(\text{Pothole} \mid \text{Pothole})$ may require section-level repair, while isolated bumps may be addressed individually. Furthermore, the matrix serves as a foundation for Markovian modeling of road degradation, which can be used to forecast future event occurrences based on present conditions.

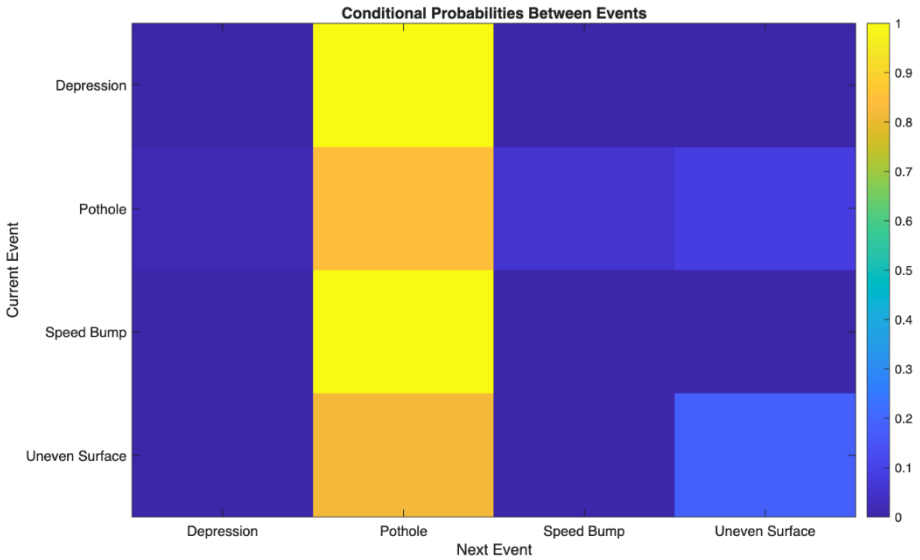

Figure 9 - Conditional probabilities between events (row-normalized) (VIASAT)

Beyond these general observations, a closer examination of the conditional probability matrix highlights the role of different defect types within the broader deterioration process. The strong diagonal dominance in the pothole row, where $P(\text{Pothole} \mid \text{Pothole})$ approaches unity, confirms that potholes rarely appear in isolation but tend instead to cluster within the same segment. This phenomenon is consistent with established deterioration mechanisms, as repeated traffic loading and moisture infiltration tend to exacerbate existing weaknesses, causing adjacent failures to propagate [63]. In contrast, the near absence of autocorrelation for speed bumps reflects their engineered nature: they are intentionally placed at fixed locations and do not signal ongoing degradation, thereby distinguishing them from naturally occurring anomalies.

Another noteworthy finding is the relatively high probability of transitions such as Depression → Pothole or Uneven Surface → Pothole. These patterns suggest that milder forms of distress may serve as precursors to more severe failures, particularly potholes. Depressions often accumulate water and concentrate traffic stresses, thereby creating favorable conditions for the initiation of potholes. Similarly, uneven surfaces, while not critical in themselves, may indicate underlying structural weaknesses that predispose the pavement to further deterioration if not addressed promptly [64]. From a maintenance perspective, this highlights the value of targeting early indicators rather than waiting until potholes manifest, which typically requires more resource-intensive repairs.

From a methodological standpoint, the conditional probability matrix can be interpreted as a row-stochastic transition matrix, analogous to those used in Markov chain models of pavement performance [65] [66]. Each state corresponds to a defect category, and the probabilities quantify the likelihood of transitioning between states. This interpretation enables a direct extension from descriptive statistics to predictive modeling: by iteratively applying the transition matrix, one can forecast the evolution of pavement anomalies over successive segments or time steps. The empirical conditional probabilities observed in this study could be directly incorporated into stochastic transition models to estimate network-level deterioration rates, thus providing a data-driven complement to calibrated Markov transition matrices traditionally used in PMS applications. Such forecasts are particularly valuable in the

context of Pavement Management Systems (PMS), where limited budgets necessitate the prioritization of interventions. For instance, segments exhibiting high self-transition probabilities for potholes should be prioritized for large-scale rehabilitation, while isolated events like speed bumps may be deprioritized or treated with localized measures.

Overall, the conditional probability analysis extends the descriptive transition framework toward predictive modeling, offering a quantitative foundation for anticipatory pavement maintenance and decision-support tools within intelligent infrastructure systems.

4.1.2.4.Geographical density analysis of road surface events

The results highlight that, in the analyzed dataset, events are relatively evenly dispersed across the road network, with only a limited number of localized concentrations. The maximum density observed corresponds to 2 events in a single grid cell, highlighted in red in Figure 10. It is worth noting that the visual concentration of points in some areas does not necessarily correspond to higher density values, as density is computed per fixed grid cell. In the area around longitude 1.01 and latitude 4.553, events appear visually clustered but are distributed across adjacent cells, resulting in lower per-cell densities compared with locations where two events fall within the same grid unit. This highlights how grid resolution strongly influences density-based representations. As a result, visual point concentration should not be interpreted as a direct proxy for computed spatial density. This indicates that, within the chosen grid resolution, anomalies such as potholes, depressions, or uneven surfaces tend to occur as isolated occurrences rather than forming extended clusters of degradation. From an infrastructure management perspective, this suggests that the road surface problems captured in this dataset may be highly localized and not necessarily indicative of systemic failure in specific segments.

However, the relatively low density values must also be interpreted carefully. On one hand, they may genuinely reflect the sporadic nature of pavement anomalies in the monitored area. On the other hand, the result may be influenced by limitations in data coverage or by the choice of grid resolution, which can smooth out more fine-grained

clustering effects. Increasing the spatial resolution of the grid (e.g. to 50 meters or less) or conducting event-type-specific analyses could potentially reveal more detailed clustering phenomena.

Overall, this geographical density analysis provides an initial but valuable spatial overview of road surface anomalies. By highlighting where concentrations of events occur - even if modest - it supports the prioritization of maintenance interventions and opens the way for more advanced spatial modeling approaches, such as kernel density estimation or spatial autocorrelation analysis, to further quantify clustering tendencies and identify at-risk road segments.

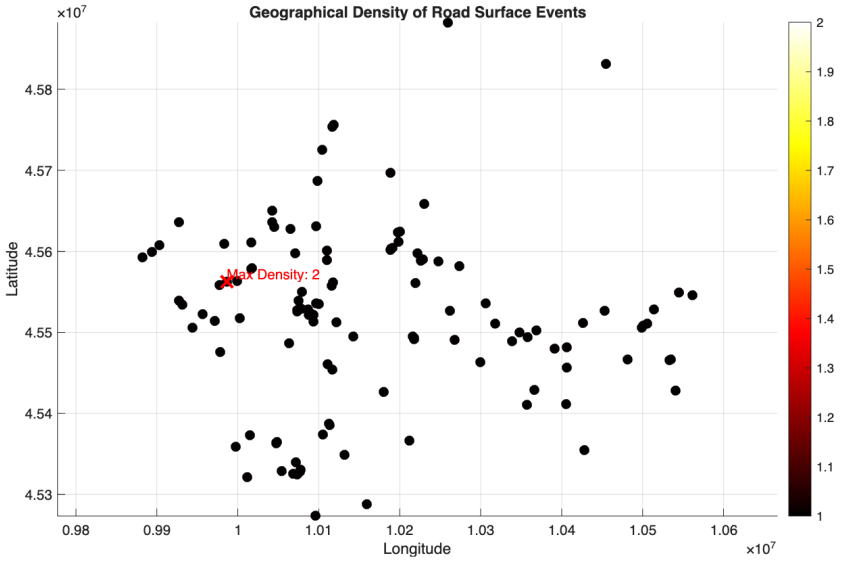

Figure 10 - Geographical density of road surface events (VIASAT)

The geographical density analysis presented in Figure 10 shows that road surface anomalies, as captured by the dataset, are relatively evenly distributed across the study area, with no evidence of large-scale clusters of degradation. The maximum density observed is limited to only two events occurring within the same grid cell, highlighted in red, while most other cells contain a single event or none at all. This suggests that anomalies such as potholes, depressions, or uneven surfaces are largely isolated rather than forming concentrated hotspots. From a maintenance perspective, this distribution indicates that interventions may need to be targeted to localized spots rather than extensive stretches of roadway.

However, these results should be interpreted with caution. The low maximum density could either reflect the genuine spatial dispersion of anomalies or be influenced by methodological factors, such as the choice of grid resolution (100 meters). A finer resolution might reveal more localized clustering that is smoothed out at the current scale. Moreover, differences in anomaly detection rates across vehicle types in the fleet could also contribute to the observed distribution. Despite these limitations, the analysis provides an important first step in understanding the spatial structure of pavement distress events. It highlights the potential of density mapping not only for identifying zones with recurrent anomalies but also as a basis for more advanced geostatistical approaches, such as kernel density estimation or spatial autocorrelation metrics, to better capture underlying clustering tendencies and inform preventive maintenance strategies.

In addition to visual interpretation, a conceptual assessment of spatial autocorrelation was considered to verify whether the observed dispersion of events could result from random occurrence. Even without performing formal computation, the apparent uniformity of the density map suggests a low degree of spatial dependence among nearby cells. This observation implies that most anomalies are spatially independent and localized rather than part of larger systemic clusters, supporting the conclusion that the observed pavement defects are isolated phenomena rather than network-wide degradation patterns. Although formal spatial autocorrelation metrics (such as Moran's I) were not computed, the observed dispersion pattern suggests weak spatial dependence among anomalies. This behavior is typical of urban networks in good structural condition, where pavement distress emerges as localized rather than systemic. Future research could apply kernel density estimation or spatial autocorrelation analyses to quantify clustering tendencies at finer spatial resolutions.

4.1.2.5.Analysis of event sequence length distribution

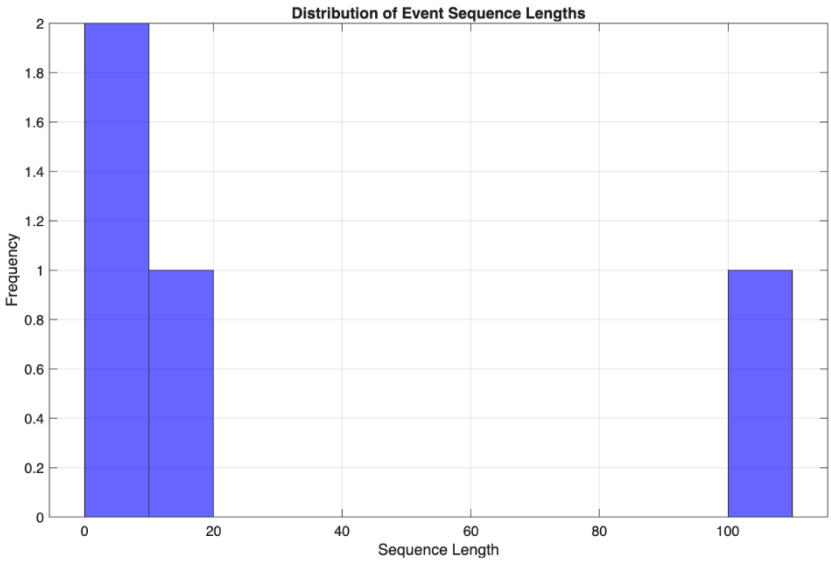

Figure 11 - Histogram of event sequence lengths (VIASAT)

The histogram of sequence lengths (Figure 11) shows a highly skewed distribution. The vast majority of sequences are concentrated in the range below 20 consecutive events, confirming that most anomalies are episodic in nature and occur as isolated irregularities or over very short road sections. These findings are consistent with the expectation that surface defects such as potholes or unevenness are often distributed in scattered form, reflecting localized wear or episodic external causes (e.g., water infiltration, point loads).

The right-skewed shape of the distribution implies a heavy-tailed phenomenon, common in infrastructure deterioration processes where a few segments dominate the overall degradation load. Such persistence analysis complements frequency metrics by highlighting the duration of continuous distress rather than its mere occurrence, aligning with the engineering notion of defect propagation over time and distance.

However, the analysis also reveals the presence of a small number of long sequences, exceeding 100 consecutive events, with the maximum sequence length reaching beyond 110. Although rare, such extended sequences are critical indicators of systematic deterioration, likely corresponding to stretches of roadway where surface distress is both persistent and severe. From an engineering perspective, these long sequences should be treated as priority zones for intervention, since they reflect

structural problems that are unlikely to self-correct and could accelerate further degradation if left untreated.

Mathematically, the skewness of the distribution suggests that the dataset is characterized by a high frequency of low values and a long right tail. This is typical of heavy-tailed phenomena, where the mean length of sequences is relatively small, but the variance is inflated by the presence of extreme values. In practice, this means that maintenance planning cannot rely solely on averages (e.g., mean sequence length) but must instead consider the tail behavior of the distribution to identify and prioritize the rare but highly problematic clusters of anomalies.

Finally, the interpretation of these results should account for potential data-related biases. The relatively low number of long sequences may reflect either the genuine dispersion of anomalies across the network or limitations in data coverage (e.g., incomplete fleet penetration or irregular trajectories). Moreover, vehicle heterogeneity within the dataset may introduce variability in event detection sensitivity. Future refinements could therefore include:

- separating sequence length distributions by event type (pothole vs. depression, etc.);
- correlating sequence lengths with traffic speed profiles to understand driver behavioral adaptations;
- combining this analysis with geographical clustering techniques (e.g., kernel density estimation) to validate whether long sequences correspond to spatially coherent road segments.

Overall, the event sequence length distribution offers a powerful lens for distinguishing between episodic anomalies - which require localized spot repairs - and persistent anomalies - which signal structurally compromised road sections that demand larger-scale intervention.

4.1.2.6. Analysis of event sequences and their implications for road surface monitoring

By computing descriptive statistics such as the mean and maximum sequence length for each anomaly type, recurrent patterns emerge that allow for a clearer distinction between anomalies symptomatic of widespread deterioration and those associated with isolated or intentional features. For instance, potholes (type 1) frequently exhibit sequences exceeding 100 consecutive occurrences, reflecting the advanced degradation of critical infrastructure sections. Conversely, speed bumps (type 2) almost exclusively occur as isolated events, consistent with their function as localized traffic-calming devices.

This sequence-based perspective introduces *persistence* as a complementary indicator to frequency and density. While frequency highlights the overall presence of anomalies and density their spatial concentration, persistence captures the continuity of defects along a segment. As such, even relatively infrequent anomalies (e.g., depressions) acquire relevance when forming long sequences, as they indicate deterioration affecting an extended portion of roadway.

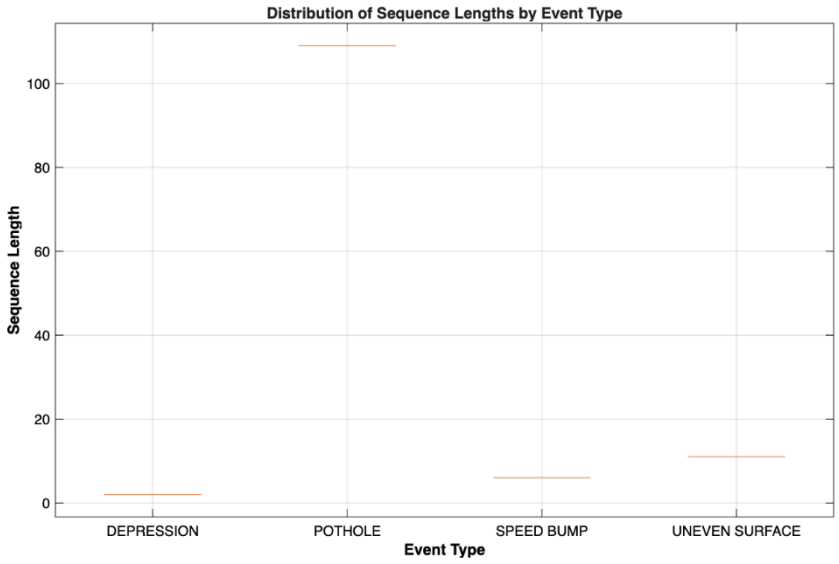

Figure 12 - Distribution of sequence lengths by event type (VIASAT)

The boxplot illustrates the distribution of sequence lengths for each type of road event, translated into English categories. The visualization highlights the markedly different behaviors of the anomalies:

- Pothole events exhibit the longest sequences, with some extending beyond 100 consecutive occurrences. This pattern reflects extended and severe structural deterioration along specific road segments, where the defect persists over considerable distances.
- Depression and uneven surface anomalies show shorter sequences, typically concentrated in a limited number of consecutive occurrences. These indicate localized irregularities that affect drivability but do not extend over long stretches.
- Speed bump events are almost exclusively single or very short sequences, consistent with their nature as designed features intentionally placed on the roadway for traffic calming purposes rather than symptoms of pavement distress.

The clear differentiation among event types highlights the value of sequence-based analysis in distinguishing between designed anomalies and critical deterioration patterns. Beyond descriptive insights, this approach provides tangible implications for infrastructure management. Long sequences can be georeferenced in GIS to identify linear hotspots of deterioration, serving as direct triggers for prioritizing maintenance interventions. Conversely, short or isolated sequences can be classified as non-critical anomalies or intentional roadway elements, thereby improving the reliability of automated monitoring systems. Moreover, sequence length distributions can be incorporated into predictive models (such as near-miss occurrence regressions) or employed as weighting factors within composite deterioration indices, thus enhancing their explanatory capacity. By explicitly addressing the concept of persistence, sequence-based indicators enrich the analytical framework for pavement monitoring and enable a shift from point-based detection of anomalies to a segment-oriented perspective, ultimately supporting more effective and data-driven strategies for predictive and preventive maintenance.

4.1.2.7.First spatial analysis of road quality index

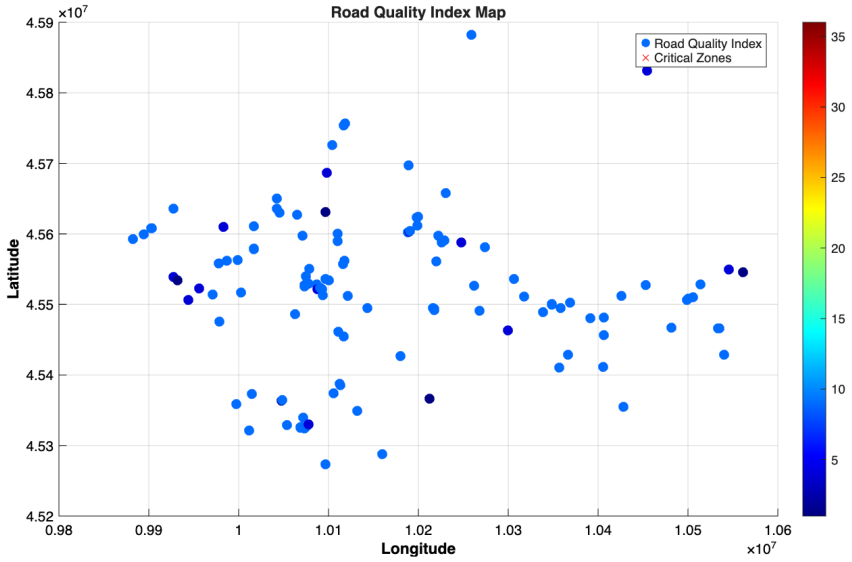

Figure 13 - First Road Quality Index (VIASAT)

Figure 13 illustrates the spatial distribution of the RQI. The majority of grid cells show values below 20, pointing to an overall acceptable pavement condition or to the presence of minor anomalies scattered across the network. Higher RQI values, corresponding to the upper tail of the color scale (yellow–red range), appear sparse and geographically isolated. These areas are hereafter referred to as critical zones, not as discretely classified regions but as relative hotspots emerging from the continuous RQI representation. The maximum observed RQI value, slightly above 35, remains far below the threshold of 90 typically associated with highly degraded areas; accordingly, no clearly delineated critical zones emerge in the map, as the observed values are moderate and do not form visually prominent clusters of severe degradation. This pattern reflects both the absence of severe failures in the dataset and the conservative weighting scheme applied in the index formulation. Beyond descriptive insight, the map demonstrates the practical usefulness of the RQI as a decision-support tool: it allows road authorities to quickly identify segments requiring closer inspection, while also highlighting the need for possible recalibration of severity weights to improve sensitivity and discrimination of critical cases.

The resulting map should be read as a descriptive visualization of squared severity load: it is effective at accentuating hotspots and conveying where the network

concentrates harsh conditions, but it does so by construction rather than by a balanced treatment of frequency and intensity. This non-linear emphasis aids exploratory inspection; however, it also reduces comparability across areas and hampers threshold calibration for decision making, since differences in the upper tail are magnified and segments with the same total weighted burden become indistinguishable regardless of how that burden is composed. These limitations motivate a refinement of the index for analytical use beyond visualization.

4.1.2.8.Second spatial analysis of road quality index

The refined computation of the Road Quality Index (RQI) was implemented on the dataset of road surface anomalies collected over the Brescia network. As previously discussed, the revised formulation was designed to ensure linear interpretability by removing redundancy between frequency and severity terms, while maintaining sensitivity to both event density and anomaly type. Each detected event was associated with a weight reflecting its relative severity: $w_1 = 3$for Type 1 (potholes or abrupt shocks), $w_2 = 2$for Type 2 (linear irregularities or seams), $w_3 = 1$for Type 3 (widespread roughness), and $w_4 = 1.5$for Type 4 (minor depressions or surface settlements). The resulting index, $RQI_{ref} = \sum_i \quad w_i n_i$, represents the total weighted severity accumulated along each road segment, providing a linear, additive measure of surface condition.

Figure 14 presents the spatial distribution of RQI_{ref} values across the study area. Each point corresponds to the centroid of a segment, color-coded according to its computed RQI value, while black-edged markers identify the top decile - i.e., the most critical zones. As observed, the overall color scale shows very limited variation, with most points appearing in the same chromatic range (green tones). This visual uniformity reflects the underlying statistical distribution of the index: the computed RQI_{ref} values exhibit a narrow spread, with the vast majority of segments registering low or moderate severity. The low variance indicates that the road network captured in this dataset is largely homogeneous and in relatively good condition, with most segments registering low or moderate severity values.

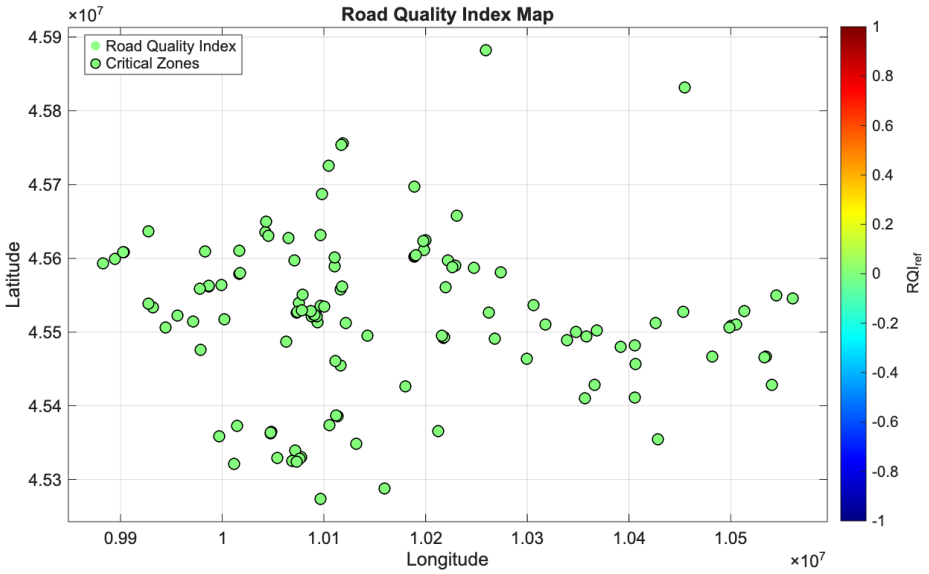

Figure 14 - Second Road Quality Index (VIASAT)

From a methodological standpoint, the apparent chromatic uniformity is consistent with the linear definition of the index, which avoids artificial amplification of contrasts. Unlike the previous squared formulation, the refined version no longer exaggerates minimal differences between segments, yielding instead a proportional and stable scale of degradation intensity. This behavior confirms the robustness of the revised RQI formulation: segments with similar degradation patterns are represented with comparable colors, avoiding misleading visual emphasis.

The small subset of points outlined as "Critical Zones" corresponds to the upper percentile of the distribution. These segments represent locations where either multiple events occurred or higher-severity anomalies (e.g., potholes) were detected, leading to a higher cumulative severity load. However, their relative rarity and the absence of extended clusters confirm that the degradation detected in this phase of analysis is localized rather than systemic.

In summary, the results of this second spatial analysis demonstrate that the revised RQI produces a stable and interpretable index, well-suited for comparative and integrative analyses across different data sources. While the uniformity of colors in Figure 14 reflects the homogeneity of the input data rather than a methodological limitation, it also suggests the need for future experiments with denser or more diverse datasets. This would enable finer differentiation between pavement conditions and

improve the sensitivity of the index for predictive maintenance and prioritization applications.

4.1.3. Conclusion of analysis of VIASAT data

The analyses conducted on VIASAT telematics data collectively demonstrate both the potential and the intrinsic limitations of accelerometer-based floating car data as a source for pavement condition monitoring. By combining behavioral analysis, sequential structures, spatial density mapping, and synthetic quality indices, the study provides an integrated and multi-perspective framework for interpreting road surface conditions from large-scale telematics observations. The behavioral dimension, analyzed through the distribution of vehicle speeds across different event types, revealed clear and statistically significant distinctions between classes, confirming that telematics data capture not only the physical presence of anomalies but also their perceptual and operational impact. Drivers consistently reduced their speed in correspondence with abrupt shocks or potholes, while exhibiting more variable behavior in the presence of linear irregularities or widespread roughness. This indicates that the event taxonomy inferred by the provider's algorithms retains behavioral and perceptual meaning and that the recorded events effectively reflect distinct physical and experiential conditions of the pavement. The sequence-based and spatial analyses further enrich this interpretation. The persistence of identical consecutive events highlights the existence of localized clusters of degradation, whereas the predominance of short sequences indicates that most irregularities are isolated and episodic in nature. The right-skewed distribution of sequence lengths, dominated by brief occurrences and a few long sequences exceeding one hundred detections, reflects the heavy-tailed behavior typical of infrastructure deterioration, where a limited number of segments accounts for most of the structural damage. These persistent anomalies identify critical stretches of roadway requiring priority maintenance, while short or isolated events correspond to localized irregularities or designed elements such as speed bumps. The spatial density maps confirm a predominantly dispersed pattern with few concentrated clusters, consistent with the episodic nature of surface irregularities and with the partial, urban-centered coverage

of the dataset. From an operational standpoint, such dispersion suggests that deterioration tends to manifest as isolated patches rather than continuous corridors, allowing targeted and cost-effective maintenance interventions. At the same time, the relative uniformity of the spatial distribution underlines the importance of considering coverage biases, fleet heterogeneity, and resolution effects, since these factors may obscure small-scale clustering or exaggerate the apparent homogeneity of road conditions. The construction of a synthetic indicator, the Road Quality Index (RQI), made it possible to summarize the combined effects of event frequency and severity in a single interpretable metric. However, the original formulation, defined as $RQI = D \cdot S_{total} \cdot S_{mean}$, proved to be mathematically redundant, reducing to $RQI = (S_{total})^2$and thus amplifying contrasts in a non-linear way. The refined version proposed in this study, $RQI_{ref} = D \cdot S_{mean} = S_{total}$, restores linearity and interpretability, ensuring that each additional event contributes proportionally to the overall degradation score. The resulting distribution of RQI values shows low variance and chromatic uniformity, reflecting the stability of the revised formulation and the relatively homogeneous condition of the monitored network. Although visually less contrasted, the refined index enables fairer comparisons across segments and provides a reliable basis for integration with other datasets. The analyses collectively reveal a consistent and interpretable picture of the urban road network: most anomalies are localized and moderate, while only a few segments exhibit persistent or high-severity degradation. These findings validate the feasibility of telematics-based monitoring as a scalable and cost-efficient approach to support pavement management, enabling near real-time observation of deterioration patterns under real traffic conditions. At the same time, the study highlights several structural limitations. The VIASAT dataset relies on proprietary event classification algorithms whose calibration parameters are not disclosed, preventing direct verification of detection thresholds [67] or signal processing methods. The absence of raw accelerometric waveforms limits the ability to conduct spectral or amplitude-based analyses that could disentangle mechanical and geometric effects. Vehicle heterogeneity, including differences in suspension systems and sensor placement, introduces unobserved variability that acts as a mechanical filter on the signal. Moreover, the spatial coverage of approximately 4,800 events is limited compared with the full municipal network, implying that the findings

should be interpreted as sample-based evidence concentrated in the urban core rather than a complete census of road conditions. These constraints do not invalidate the results but define the boundaries of inference and reinforce the need for data integration. Accelerometer-based floating car data should therefore be regarded as a complementary, high-frequency, low-cost information source that enhances but does not replace traditional survey methods. Future developments should focus on combining telematics signals with heterogeneous sensing modalities (particularly vision-based inspections, onboard cameras, or satellite imagery) to obtain richer and more discriminative representations of surface distress. Integrating accelerometric data with visual evidence and road geometry parameters will enable calibration of severity weights, validation of detection algorithms, and development of composite indicators capable of capturing both physical and perceptual aspects of pavement performance. Such integration would also facilitate the transition from reactive maintenance strategies to predictive and preventive approaches, where deterioration trajectories can be continuously monitored and anticipated. Overall, the results obtained from the VIASAT case study confirm that floating car data can serve as a valuable foundation for large-scale road monitoring systems, provided that their interpretation is grounded in robust methodology and complemented by multimodal data sources. By embedding behavioral responses, persistence metrics, and linear severity indices into a coherent analytical framework, this study contributes to bridging the gap between opportunistic telematics signals and decision-support tools for infrastructure management, paving the way for future research that will integrate accelerometer- and vision-based data within unified data-fusion architectures aimed at achieving smarter, more resilient, and adaptive road maintenance systems. The insights derived from VIASAT data form the empirical foundation for the subsequent fusion framework, where accelerometric indicators will be jointly analysed with AIWAY vision-based detections to construct a composite, safety-anchored deterioration index.

4.2. Analysis of AIWAY data

One of the data sources employed in this study is AIWAY, a system based on vision-based technologies for pavement monitoring. Through on-board cameras and image recognition algorithms, AIWAY automatically detects visible surface anomalies and classifies them into standardized categories [68] [69].

The AIWAY dataset introduced the computer vision perspective, offering image-based detections of surface anomalies captured by onboard cameras. The processing pipeline consisted of: (i) image acquisition under real driving conditions; (ii) GDPR-compliant anonymization via real-time blurring of faces and license plates; (iii) detection of pavement anomalies using YOLOv8 models trained on dedicated defect datasets [70] and (iv) metadata integration, including timestamp, geographic coordinates, and trip identifiers. A total of 63,800 valid detections were retained after preprocessing.

The primary defect categories used in the analyses are D00-D50 (Table 5). Additional labels such as patches, bleeding, and ravelling may appear in raw detections but are not used in the indices presented here. Each detection was associated with a confidence score, allowing for probabilistic filtering. However, image-based systems are sensitive to external conditions such as shadows, rain, glare, and low-light environments. To mitigate these effects, AIWAY vehicles traversed the same roads multiple times under varying conditions, although false positives and redundant detections remained a challenge [71] [72].

Beyond the operational workflow, the AIWAY system relies on a hybrid artificial intelligence architecture that combines deep learning models for both pavement-distress detection and the anonymization of privacy-sensitive visual content captured during the acquisition phase. This architecture, developed by the technology provider, is reported here solely to document the provenance, nature, and internal logic of the input data used in this research. The objective is not to reproduce, evaluate, or optimize the proprietary components, but to ensure transparency in the description of the data-generation process, which constitutes a prerequisite for any scientifically sound downstream analysis. In this regard, the AIWAY pipeline is designed to

guarantee GDPR-compliant data acquisition while extracting actionable information for infrastructure-monitoring tasks in real-world operational contexts.

The defect-detection module is based on the YOLOv8 model (medium configuration), a choice made by the vendor after internal benchmarking with other architectures such as YOLOv10 and YOLOv11. According to the supplier's documentation, YOLOv8 achieved high levels of stability in outdoor environments affected by illumination variability, motion blur, and partial occlusions, with reported values exceeding 99% mAP, approximately 98% recall, and around 99% precision on dedicated training and validation datasets. These figures are presented here for completeness, as the present research did not independently verify the internal benchmarking results nor attempt to replicate the training procedures. Nevertheless, the model's real-time inference capability, its ability to operate on edge devices, and its transfer-learning strategy on distress-specific datasets (including cracks, potholes, rutting, and surface separations) motivated its adoption by the provider as the core of the computer-vision workflow.

To guarantee privacy protection, the AIWAY system integrates a second model, YOLOv11, in the preprocessing stage, where it automatically detects pedestrians, vehicles, faces, and license plates. Once identified, these elements are blurred in real time before storage, ensuring that the resulting imagery is neutral and compliant with GDPR requirements. In this dual-model configuration, YOLOv8 and YOLOv11 perform distinct tasks - defect detection and anonymization - thereby specializing their roles and improving overall robustness. For lightweight deployments on low-power edge devices, an alternative single-model configuration based solely on YOLOv8 is available, although with reduced anonymization performance. This architectural choice, again, derives from vendor-driven design considerations and is included here only to clarify the characteristics of the supplied data, without implying any scientific endorsement of one configuration over another.

Once detections are produced, the system executes a georeferencing and structuring phase in which each event is enriched with spatial and temporal metadata - latitude, longitude, timestamp, and trip ID - and exported as GIS-compatible layers. These outputs are then aggregated and associated with confidence scores, enabling probabilistic filtering before integration with accelerometric data sources. In this study, these georeferenced detections were treated strictly as structured inputs for

subsequent data-fusion and modeling activities, without interfering with, modifying, or reverse-engineering the underlying proprietary algorithms. This separation between data generation (vendor) and data exploitation (researcher) ensures a clear methodological boundary and allows the scientific contribution of the thesis to remain entirely focused on the development of the analytical framework, rather than on the assessment of commercial computer-vision architectures.

The deterioration indicators provided by this source are labelled as DXX, each corresponding to a specific type of pavement defect:

- $D00$: Longitudinal Cracking: cracks oriented parallel to the road axis, typically caused by structural fatigue or thermal effects.
- $D10$: Transverse Cracking: cracks perpendicular to the road axis, often associated with shrinkage or construction joints.
- $D20$: Alligator Cracking (Crocodile Skin Cracking): interconnected cracking patterns forming small blocks, characteristic of advanced surface fatigue.
- $D40$: Rutting, Potholes, and Surface Separation: surface deformations and discontinuities such as wheel-path ruts, local depressions, or material separation.
- $D50$: Manholes and Covers: the presence of inspection chambers, manholes, or covers embedded in the pavement structure, which can act as localized discontinuities.

Table 5 - AIWAY tags

AIWAY	
Tag	**Description**
D00	Longitudinal cracks
D10	Transverse cracks
D20	Alligator cracking
D40	Ruts, cracks, potholes, separations
D50	Manholes and inspection covers

In addition to the defect-related categories (D00-D50), the AIWAY detection model also includes reference classes such as *Left-Line* and *Right-Line*. These labels do not represent pavement anomalies but correspond to lane markings used by the vision

system as geometric features for spatial orientation. Their inclusion allows for contextual interpretation of the detected defects, enabling the analysis of their spatial relationship with the road layout. In the subsequent multiclass and co-occurrence analyses, these classes are therefore treated as non-defect reference elements, providing geometric anchors that help quantify how different types of pavement deterioration relate to the lateral boundaries of the carriageway.

For each of these deterioration classes, the AIWAY system provides two separate pieces of information:

1. the count of occurrences detected along each segment, and
2. the confidence score assigned to those detections by the algorithm.

This dual output allows the dataset to capture not only the extent of deterioration but also the reliability of the detection, thus enriching the representation of pavement condition from a visual perspective.

4.2.1. Methodological rationale

The analytical framework designed for processing the AIWAY dataset aims to extract quantitative and spatially explicit information on pavement surface deterioration as detected by onboard sensing systems. Each record represents a point-based detection characterized by geographic coordinates, one or more anomaly subtypes corresponding to different forms of pavement distress, and a set of confidence scores expressing the reliability of the recognition model. The methodological approach integrates descriptive statistics, spatial clustering, reliability modeling, and geostatistical interpolation to construct a comprehensive representation of the pavement condition derived from heterogeneous detections. The sequence of analyses was designed to progressively characterize the dataset through exploratory, spatial, and inferential perspectives, establishing a robust foundation for subsequent data fusion with other sensing sources within the broader framework of the research.

The flow chart in Figure 15 outlines the analytical workflow developed for the processing and interpretation of the AIWAY dataset, a computer-vision-based sensing system designed to detect pavement surface anomalies from onboard cameras.

The methodology was structured to progressively transform raw detections into spatially aggregated and reliability-weighted indicators of pavement condition.

Starting from data ingestion and validation, the process unfolds through four complementary analytical dimensions - exploratory, spatial, reliability, and geostatistical - culminating in the computation of normalized deterioration indices at the segment level.

Each analytical block contributes a distinct perspective: the exploratory stage establishes the data quality and internal consistency of detections; the spatial stage reveals geographic organization and clustering of defects; the reliability analysis integrates confidence scores as probabilistic weights; and the geostatistical stage produces continuous surfaces and segment-level indicators suitable for comparative assessment.

Together, these procedures form a coherent and scalable pipeline that converts unstructured vision detections into actionable quantitative information, providing a robust foundation for subsequent data fusion with other sensing sources in the broader research framework.

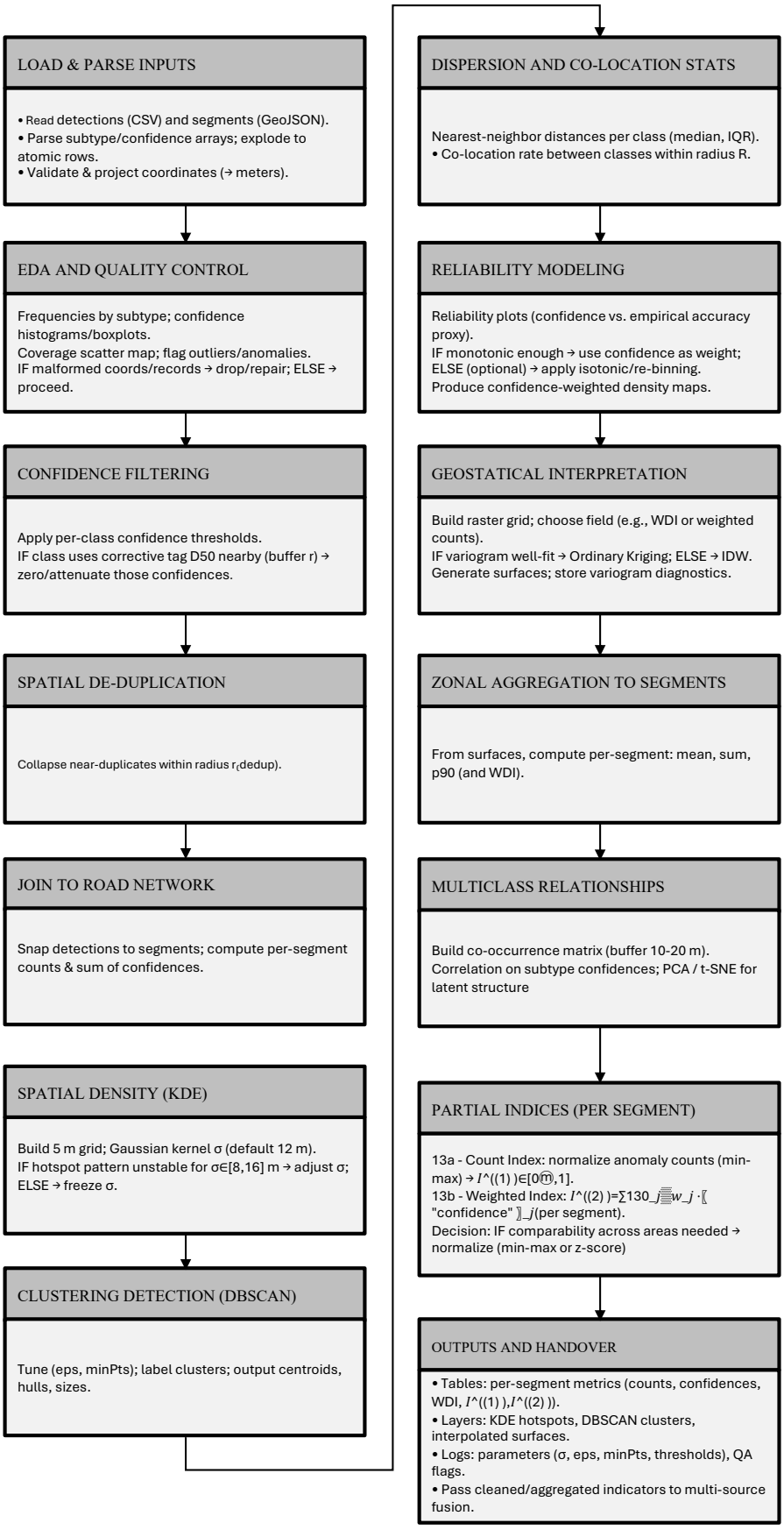

Figure 15 - Flow chart AIWAY dataset

4.2.1.1.Exploratory Data Analysis (EDA)

A preliminary exploratory analysis was performed to assess the internal composition and reliability of the AIWAY dataset. Frequency distributions were computed to identify the most recurrent defect subtypes, while descriptive statistics of confidence values were calculated to evaluate their variability across classes. Visualization tools such as histograms and boxplots were employed to detect potential outliers and to verify the consistency of confidence estimation within each subtype. This stage also included the inspection of the geographic coverage of detections through scatter maps, allowing for the identification of isolated or anomalous points that could indicate localization errors or redundant detections.

Algorithm 9 - ProcessAIWAYDetections

```
Line    Pseudocode
1       Algorithm ProcessAIWAYDetections(CSV_File, Segments_GeoJSON, Params) →
        PerSegmentMetrics, ClusterLayers, InterpolatedSurfaces
2       // Input: CSV of detections, GeoJSON of road segments, parameters for
        clustering and filtering
3       data ← read CSV_File with delimiter ';'
4       lat ← toNumber(replace(data.latitude, ',', '.')); lon ←
        toNumber(replace(data.longitude, ',', '.'))
5       subtypes_json ← data.subtypes; confidences_json ← data.confidences
6       valid ← (~NaN(lat) ∧ ~NaN(lon) ∧ -90 ≤ lat ≤ 90 ∧ -180 ≤ lon ≤ 180)
7       data ← data[valid]
8       For i from 1 to length(data) do
9               subtypes[i] ← JSONdecode(subtypes_json[i]); confvals[i] ←
        JSONdecode(confidences_json[i])
10              assert length(subtypes[i]) = length(confvals[i])
11      End For
12      Explode multi-class records into atomic detections by subtype
13      det ← GeoDataFrame(lat, lon, cls, conf) projected onto a local
        equirectangular coordinate system centered on the survey area's median
        coordinates (scale-equivalent to UTM)
14      Compute frequency distributions and boxplots for confidence by class
15      Filter detections below confidence thresholds per class
16      Perform spatial deduplication (radius = Params.dedup_radius_m)
17      For each class in {D00,D10,D20,D40} do
18              Apply DBSCAN(eps=Params.eps_m, min_samples=Params.min_samples) →
        cluster_id
19              Aggregate per cluster: count, mean_conf, convexHull(geometry)
20      End For
21      Apply D50 mask: buffer(D50, radius=Params.d50_mask_radius_m) and zero
        nearby D00-D40 confidences
22      Aggregate detections per road segment (spatial join with Segments_GeoJSON)
23      Compute weighted deterioration index I_seg ← Σ w[cls] *
        normalize(sum_conf[cls])
24      Return PerSegmentMetrics, ClusterLayers, InterpolatedSurfaces
```

The exploratory phase therefore provided a baseline understanding of the data structure and quality, essential for guiding the subsequent spatial and statistical analyses.

4.2.1.2.Spatial analysis

Spatial analyses were conducted to investigate the geographic organization and clustering of pavement anomalies across the study area. Kernel Density Estimation (KDE) was applied to derive continuous density surfaces of detections, enabling the identification of hot spots where the concentration of anomalies was particularly high. KDE was computed on a 5-m resolution raster using a Gaussian kernel (σ = 12 m); density normalization ensured comparability across classes. Hotspot locations were stable for $\sigma \in [8,16]$ m. A dynamic grid is used for exploratory plots, whereas KDE maps are rendered at 5 m resolution for comparability. The DBSCAN algorithm was subsequently employed to detect spatially coherent clusters of defects based on proximity and density thresholds, distinguishing localized groups of recurrent anomalies from isolated points. Pairwise spatial distances among detections were computed to quantify the dispersion of each subtype, and co-location statistics were used to examine the spatial overlap among different anomaly categories. These procedures made it possible to identify spatial patterns in pavement deterioration and to delineate areas of potential structural vulnerability.

Algorithm 10 - SpatialAnalysisAIWAY

```
Line    Pseudocode
1       Algorithm SpatialAnalysisAIWAY(InputFile) → {KDE_Maps, Clusters,
        DistanceStats, CoLocationMatrix}
2       Data ← LoadAndFlattenAIWAY(InputFile) // read CSV and explode
        subtypes/confidences
3       Data ← CleanAndProject(Data) // remove invalid coordinates; project to
        WebMercator
4       Classes ← Unique(Data.class \ {non-pavement})
5       Grid ← BuildGrid(bounds(Data.x,Data.y), cell_size = h)
6       For each c in Classes do
7           Pts ← { (x,y) ∈ Data where class=c }
8           H ← Hist2D(Pts, Grid)
9           K ← GaussianKernel(σ)
10          KDE[c] ← Convolve2D(H, K) / (N_pts · h²)
11      End For
12      For each c in Classes do
13          Pts ← { (x,y) ∈ Data where class=c }
```

```
        labels ← DBSCAN(Pts, eps = ε, minPts = m)
        Clusters[c] ← { id: labels, centroids, sizes }
    End For
    For each c in Classes do
        dists ← NearestNeighborDistances(Pts_c)
        DistanceStats[c] ← {median, IQR, histogram}
    End For
    R ← proximity_radius
    For each (ci,cj) in Classes×Classes do
        score(ci,cj) ← Mean_over_i [ any( distance(Pi∈ci, Pj∈cj) ≤ R ) ]
    End For
    Return {KDE, Clusters, DistanceStats, score}
```

4.2.1.3.Confidence-based reliability analysis

Confidence scores were used as a monotonic proxy of reliability (not as calibrated probabilities), their relationship with accuracy was checked qualitatively via reliability plots and histograms, allowing the construction of synthetic indices that integrate both the frequency and the estimated accuracy of detections. Weighted density maps were generated by assigning each detection a weight proportional to its confidence value, thus emphasizing areas characterized by consistently reliable detections. In addition, a Weighted Defect Index (WDI) was defined as the sum of the confidence scores multiplied by predefined severity weights associated with each subtype, according to the following expression:

Equation 14 - Definition of the Weighted Defect Index (WDI)

$$WDI = \sum_{i} \quad w_i \cdot c_i$$

where $w_i$represents the severity weight and $c_i$the confidence of the i-th detection. This indicator was designed to provide a composite measure of pavement deterioration that accounts for both the structural significance and the recognition confidence of detected anomalies. Scatter and violin plots were used to analyze the relationship between confidence levels and defect categories, enabling a deeper assessment of the detection model's performance across different classes.

Algorithm 11 - ConfidenceBasedReliabilityAIWAY

```
Line    Pseudocode
1       Algorithm ConfidenceBasedReliabilityAIWAY(InputCSV, Params) →
        {CleanDetections, WeightedMaps, WDI_perSegment}
2       data ← ReadAndFlattenAIWAY(InputCSV) // lat, lon, class, confidence
3       data ← RemoveInvalidCoords(data); data ← ProjectToMeters(data)
4       For each class c: thr[c] ← Params.conf_threshold[c] (default 0)
5       data ← Filter(data, confidence ≥ thr[class])
6       data ← SpatialDeDup(data, radius = Params.dedup_radius_m)
7       G ← BuildGrid(bounds(data.x,data.y), cell_size = Params.grid_m)
8       For each cell g ∈ G:
9           Pts ← points of data inside g
10          wCount[g] ← Σ_{p∈Pts} confidence(p)
11          wByClass[g,c] ← Σ_{p∈Pts, class=c} confidence(p)
12      End For
13      For each cell g: WDI_cell[g] ← Σ_c ( Params.weight[c] · wByClass[g,c] )
14      WeightedMaps ← {wCount, wByClass[·,·], WDI_cell} (optional Gaussian
        smoothing)
15      seg ← LoadSegments(Params.segmentsGeoJSON)
16      WDI_perSegment ← ZonalStats(WDI_cell over seg, stat = mean/sum)
17      Return {data as CleanDetections, WeightedMaps, WDI_perSegment}
```

4.2.1.4.Multiclass and co-occurrence analysis

To explore possible dependencies among different anomaly subtypes, a co-occurrence matrix was constructed by cross-tabulating all defect categories detected within the same spatial proximity (typically within a 10-20 m buffer). Dimensionality reduction techniques such as Principal Component Analysis (PCA) and t-distributed Stochastic Neighbor Embedding (t-SNE) were applied to the matrix of subtype confidences to reveal latent relationships and similarities among defect patterns. Correlation coefficients were computed to evaluate statistical associations between categories, thus identifying those that tend to co-occur in the same locations. This multivariate analysis provided a structural interpretation of the relationships among defect types, which may reflect common physical degradation mechanisms or systematic detection behaviors of the sensing system.

Algorithm 12 - MulticlassAndCoOccurrenceAnalysis

```
Line    Pseudocode
1       Algorithm MulticlassAndCoOccurrenceAnalysis(InputCSV, buffer_m,
        DR_methods) → {CoOcc, Corr, PCA, TSNE}
2       D ← ReadAndFlattenAIWAY(InputCSV) // one row per (point, subtype,
        confidence)
3       D ← RemoveInvalidCoords(D); D ← ProjectToMeters(D)
4       C ← Unique(D.subtype)
```

```
5       CoOcc[|C|×|C|] ← 0
6       index ← BuildNeighborIndex(D.[x,y])
7       For each point i with class a:
8           N ← NeighborsWithin(index, i, buffer_m); N ← N with id > i // avoid
        double counting
9           For each j ∈ N with class b: CoOcc[a,b]++ ; CoOcc[b,a]++
10      End For
11      X ← BuildPoint×ClassMatrix(D, agg = max(confidence))   // rows=points,
        cols=classes
12      Corr ← Correlation(X, type = Params.corr_type)
13      If 'PCA' ∈ DR_methods: PCA ← PCA(X standardized)
14      If 'tSNE' ∈ DR_methods: TSNE ← tSNE(X standardized, perplexity≈30)
15      Return {CoOcc, Corr, PCA, TSNE}
```

4.2.1.5.Geostatistical and aggregation analysis

The geostatistical component of the analysis was designed to model the spatial continuity of defect intensity and confidence, integrating point-based detections into a continuous representation aligned with the road network geometry. Interpolation techniques, including Inverse Distance Weighting (IDW) and Ordinary Kriging, were employed to generate continuous surfaces representing the estimated confidence and defect density. These surfaces were subsequently aggregated by road segment through zonal statistics, yielding segment-level indicators such as mean confidence, total weighted severity, and normalized defect density. Experimental variograms were computed to measure the degree of spatial autocorrelation and to define the effective range of spatial dependence governing the detection process. The resulting indicators provided a consistent and spatially integrated quantification of pavement condition, suitable for comparative assessment across the urban network and for integration into the subsequent data fusion phase of the study.

Algorithm 13 - GeoStatAggAIWAY

```
Line    Pseudocode
1       Algorithm GeoStatAggAIWAY(WeightedPoints, Segments, Params) → {Surfaces,
        Variograms, SegmentIndicators}
2       P ← WeightedPoints // coords (x,y), class, confidence, WDI_point
3       z ← SelectField(P, Params.field) // WDI_point or wCount
4       G ← BuildRasterGrid(bounds(P), cell_size = Params.grid_m)
5       If Params.method = 'IDW':
6           Surface ← IDW(P.[x,y], z, G, power = p, radius = R)
7       Else if Params.method = 'OK' (Ordinary Kriging):
8           γ_exp ← ExperimentalVariogram(P.[x,y], z, lags = L, tol = t)
9           model ← FitVariogram(γ_exp, type ∈ {Sph, Exp, Gau})
10          Surface ← KrigeOK(P.[x,y], z, model, G)
```

```
11      End If
12      SegmentIndicators.mean ← ZonalStats(Surface, Segments, 'mean')
13      SegmentIndicators.sum ← ZonalStats(Surface, Segments, 'sum')
14      SegmentIndicators.p90 ← ZonalStats(Surface, Segments, 'percentile', 90)
15      Variograms ← {γ_exp, model}; Surfaces ← {Surface}
16      Return {Surfaces, Variograms, SegmentIndicators}
```

4.2.1.6.First partial index

To quantify the degree of deterioration associated with each road segment, a normalized deterioration index was computed. Starting from the full dataset of detected anomalies, each observation was already georeferenced and associated with a specific road segment identifier (segment_id). For each segment, the total number of recorded anomalies was aggregated. To ensure comparability across segments with varying traffic volumes and lengths, the raw count was normalized using min-max scaling. Specifically, for each segment i, the index I_i was defined as:

Equation 15 - Normalized deterioration index computed through min–max scaling to ensure comparability across road segments with different lengths and traffic volumes (AIWAY)

$$I_i = \frac{N_i - N_{min}}{N_{max} - N_{min}}$$

where N_i is the number of anomalies recorded on segment i, and N_{min}, N_{max} represent the minimum and maximum number of anomalies observed across all segments, respectively.

Algorithm 14 - First partial index

```
Line    Pseudocode
1       Algorithm FirstPartialIndex(AnomalyDataset) → NormalizedIndex
2       data ← load AnomalyDataset
3       for each record in data do
4           segment_id ← record.segment_id
5           count[segment_id] ← count[segment_id] + 1
6       end for
7       N_min ← minimum(count over all segments)
8       N_max ← maximum(count over all segments)
9       NormalizedIndex ← empty dictionary
10      for each segment_id in count do
11          N_i ← count[segment_id]
12          I_i ← (N_i - N_min) / (N_max - N_min)
13          NormalizedIndex[segment_id] ← I_i
14      end for
15      return NormalizedIndex
```

This transformation maps the distribution of anomaly counts into a continuous interval between 0 (least affected) and 1 (most affected), enabling direct comparison and subsequent threshold-based classification if needed.

4.2.1.7.Second partial index

The deterioration index was developed as a composite metric to quantify the severity of road pavement damage based on the outputs of a computer vision algorithm. This algorithm identifies multiple types of road defects, such as longitudinal cracks (D00), transverse cracks (D10), alligator cracking (D20), and severe deformations including rutting and potholes (D40), each associated with a confidence level. To compute the index, a weight was assigned to each defect type, reflecting its impact on road safety and structural integrity. For each detection, the index was calculated as the weighted sum of defect-specific confidence values.
The formula used was:

Equation 16 - Deterioration index computed as the weighted sum of confidence scores for all detected defect types, where weights reflect each defect's structural and safety relevance (AIWAY)

$$Deterioration\ Index = \sum_{j=1}^{n} (W_j \cdot C_j)$$

Where:

- n represents the number of defects identified at a specific location,
- W_j represents the weight of different types of road defects,
- C_j represents the recognition confidence of the algorithm.

Algorithm 15 - Second partial index

```
Line    Pseudocode
1       Algorithm    SecondPartialIndex(Detections,    Weights,    Segments)    →
        DeteriorationIndex
2       D ← ReadAndFlattenAIWAY(Detections) // (segment_id, class, confidence)
3       For each record r ∈ D:
4           w ← Weights[r.class]
5           score_r ← w · r.confidence
6           DI[r.segment_id] ← DI[r.segment_id] + score_r
7       End For
```

```
8       If normalize: DeteriorationIndex ← Normalize(DI, method = 'minmax' or
        'zscore')
9       Else: DeteriorationIndex ← DI
10      Return DeteriorationIndex
```

4.2.2. Experimental application and results

Building on the methodological framework detailed in Section 5.2.1, this section applies the proposed pipeline to the AIWAY dataset and reports the corresponding outcomes. While the previous subsection focused on data structures, preprocessing, and the rationale behind each analytical block (EDA, spatial analyses, confidence-based reliability, multiclass/co-occurrence modelling, and geostatistical aggregation), the present subsection moves to experimentation: it specifies operative settings (e.g., confidence thresholds, DBSCAN parameters, co-occurrence buffers of 10–20 m, and normalization schemes), executes the analyses, and interprets the empirical results.

The dataset comprises 18,194 valid detections, corresponding to individual observations of surface distresses automatically extracted from the AIWAY video streams and used as input for all subsequent analyses.

We first validate internal consistency through descriptive statistics and confidence distributions, then characterize spatial organization via KDE, DBSCAN, and nearest-neighbor metrics. Next, we investigate cross-class behavior with co-occurrence matrices, correlation analysis, PCA loadings/scores, and t-SNE embeddings to reveal latent relationships between defect types and geometric reference elements. Finally, we derive segment-level indicators through geostatistical interpolation and zonal aggregation, and we synthesize them into partial deterioration indices.

For each step, we report the figures and quantitative summaries, discuss practical implications for pavement management, and highlight robustness checks and known limitations (e.g., sensitivity to lighting, redundancy, and non-visual distress). In doing so, this section translates the method into operational evidence, offering a clear link between algorithmic design and decision-oriented diagnostics.

4.2.2.1.Exploratory Data Analysis (EDA)

The exploratory analysis of the confidence scores (Figure 16) provides insights into the internal consistency and reliability of the AIWAY detection model across different

classes of detected objects. The boxplot illustrates the probabilistic distribution of the YOLO-based vision model when applied to heterogeneous road environments, offering a preliminary assessment of its stability under real-world driving conditions. The classes corresponding to pavement deterioration - namely D00, D10, D20, D40, and D50 - represent longitudinal cracking, transverse cracking, alligator cracking, surface deformations, and manholes or inspection covers, respectively. Their statistical behavior is consistent with the expected performance of a vision-based detection system trained to recognize diverse typologies of surface anomalies. The cracking-related categories (D00, D10, and D20) exhibit median confidence values ranging between 0.5 and 0.6, with relatively large interquartile ranges. This pattern indicates a generally satisfactory recognition capability, although the variability suggests a sensitivity to illumination, texture, and viewing conditions. The D40 class, which includes rutting, potholes, and surface separations, achieves higher median confidence values, approximately between 0.7 and 0.8, reflecting the model's stronger discriminative capacity when detecting large and visually distinct defects. Conversely, the D50 class, corresponding to manholes and inspection covers, is characterized by the highest confidence values, typically close to one and with limited dispersion. Such behavior is expected, as these objects present distinctive geometric and radiometric patterns that can be reliably identified by convolutional neural networks.

Additional reference classes (e.g., Left-Line, Right-Line, and Landmark) are not related to pavement distress and are used only for contextual interpretation; they are excluded from deterioration indices. They derive from the original training configuration of the YOLO model, which included general road markings and traffic elements. Their confidence values remain close to unity, confirming the network's ability to maintain accurate classification of non-pavement features. While these detections are not relevant to the specific objectives of pavement monitoring, they provide indirect evidence of the model's stability and generalization capability. Their inclusion is limited to co-occurrence analyses to contextualize the lateral geometry.

The observed results indicate that the AIWAY system maintains an average confidence exceeding 0.6 for the classes associated with pavement deterioration, which can be considered acceptable for downstream integration within a multi-source data fusion framework. The residual variability observed in the distributions is primarily

attributable to environmental and acquisition factors - such as lighting variations, motion blur, or occlusions - that inherently affect image-based sensing systems. Nevertheless, this variability can be mitigated through probabilistic filtering or adaptive weighting strategies in subsequent processing stages, thereby enhancing the robustness and interpretability of visual indicators derived from AIWAY detections.

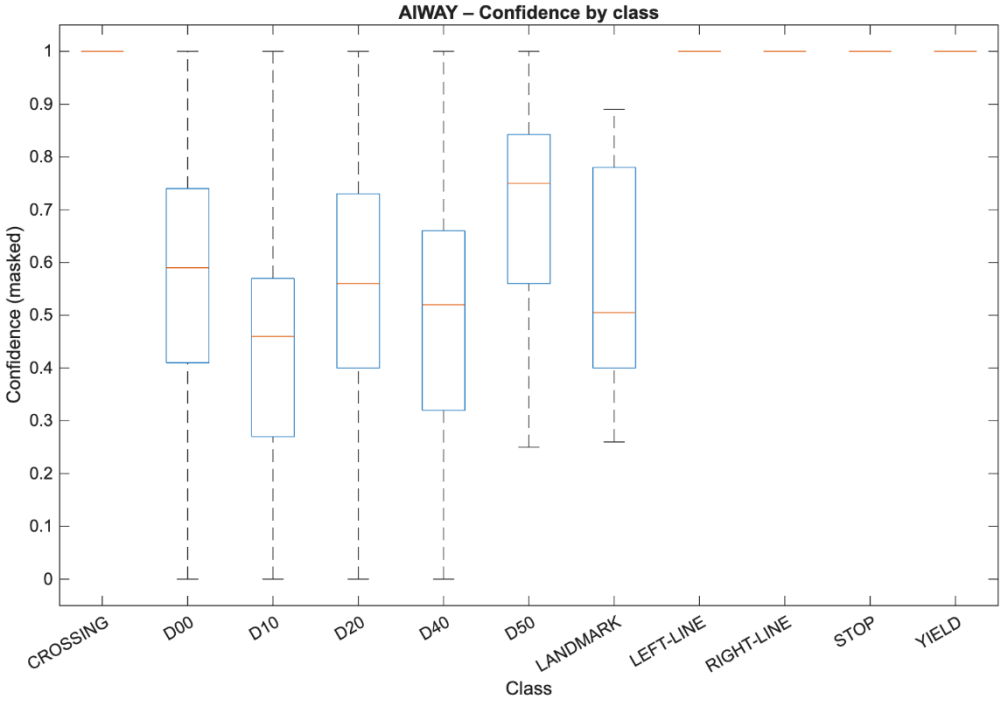

Figure 16 - Distribution of confidence scores across all detected classes in the AIWAY dataset

4.2.2.2.Spatial analysis

The spatial analysis was designed to investigate the geographic organization, clustering, and spatial dependency of pavement anomalies detected by the AIWAY system. This analytical phase sought to characterize how surface deterioration phenomena are distributed along the monitored network and whether these distributions exhibit statistically consistent spatial structures that could inform maintenance decision-making. To this end, a combination of Kernel Density Estimation (KDE), Density-Based Spatial Clustering of Applications with Noise (DBSCAN), and nearest-neighbor distance statistics was employed. Each of these approaches provides a different lens through which to interpret the same underlying geospatial phenomena - namely, the relationship between defect concentration, spatial continuity, and local interactions among detection points.

The KDE results revealed distinct, non-uniform patterns of spatial density, highlighting localized concentrations of detections in specific areas of the road network (Figure 17). Such density gradients indicate that pavement anomalies do not occur randomly but tend to cluster spatially. According to established pavement engineering literature, similar clustering patterns are commonly associated with sections subject to structural fatigue, recurrent traffic loading, or material heterogeneity. Crack-related categories (D00, D10, D20) displayed elongated density ridges that closely followed the longitudinal direction of travel, reflecting the anisotropic nature of tensile and thermal stresses acting along the main axis of the pavement structure. This pattern is consistent with well-documented mechanisms of fatigue cracking, in which the propagation of microfractures aligns with the direction of repetitive vehicle loading. Conversely, class D40 (rutting, potholes, and surface separations) exhibited compact, circular density maxima corresponding to localized failures in the wheel paths. These areas are typically associated with permanent deformation of the asphalt layers under repeated traffic loads or with material loss due to water infiltration and freeze-thaw cycles. Finally, class D50 (manholes and inspection covers) produced isolated and spatially discrete peaks, confirming that the algorithm effectively distinguishes fixed discontinuities of the pavement from true deterioration phenomena.

These spatial patterns are consistent with classical models of pavement deterioration described in the literature, where fatigue cracking and permanent deformation are linked to repeated traffic loading and material heterogeneity [73], [74], [75]

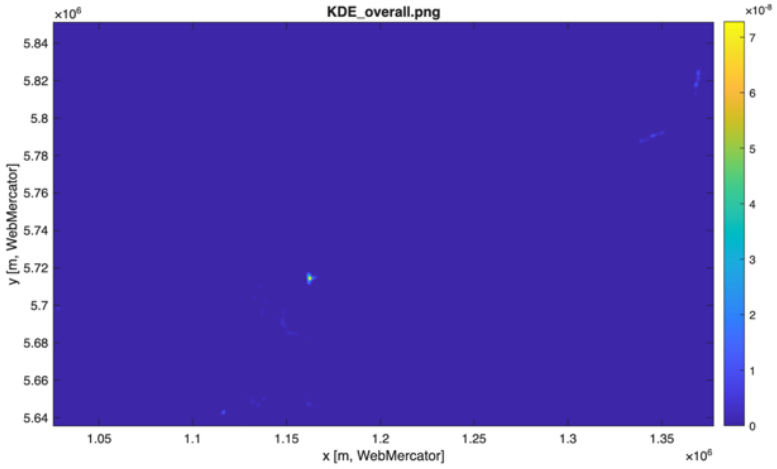

Figure 17 - Spatial density of all detected pavement anomalies derived from Kernel Density Estimation (KDE)

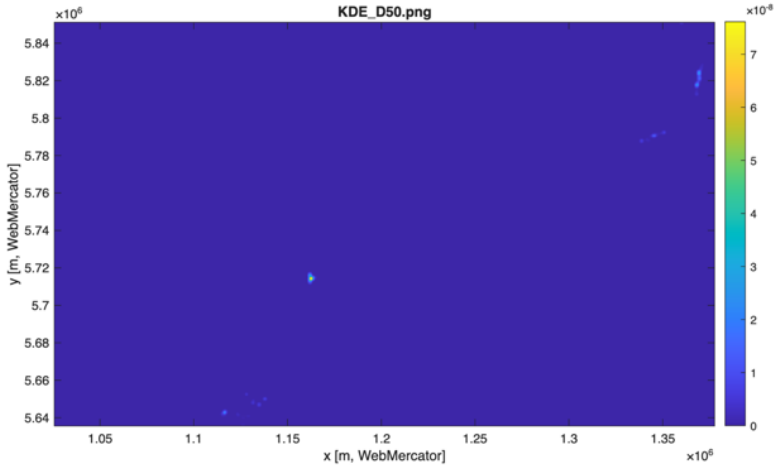

Figure 18 - Class-specific KDE maps for individual defect category D50

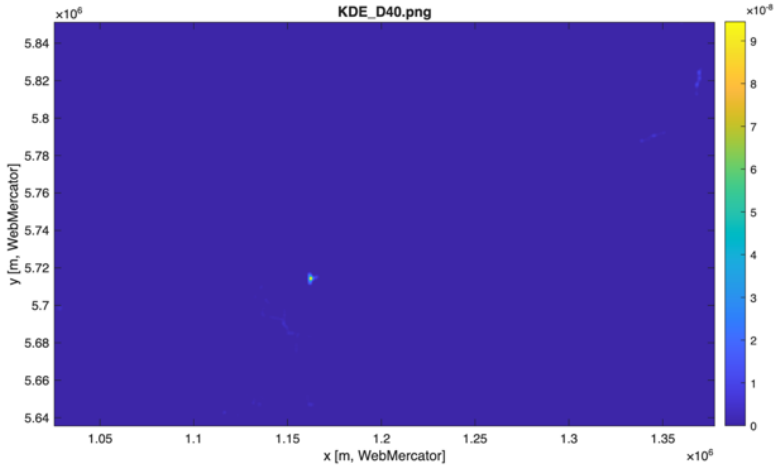

Figure 19 - Class-specific KDE maps for individual defect category D40

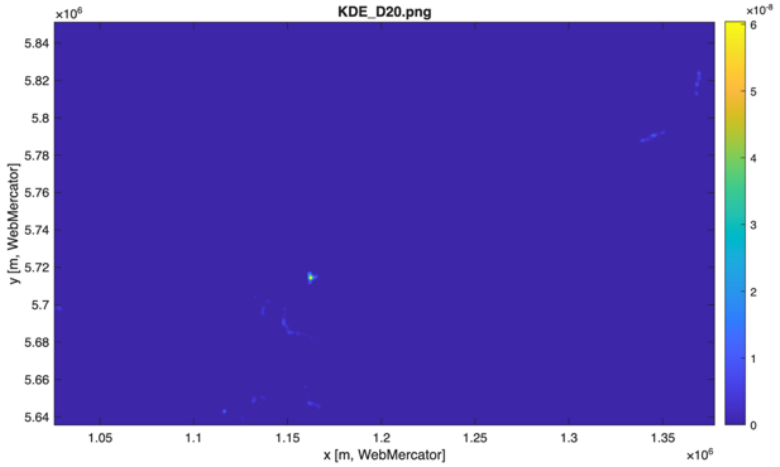

Figure 20 - Class-specific KDE maps for individual defect category D20

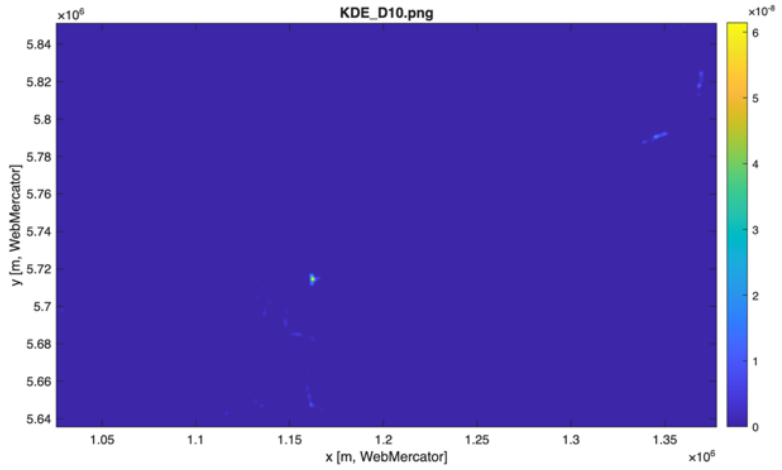

Figure 21 - Class-specific KDE maps for individual defect category D10

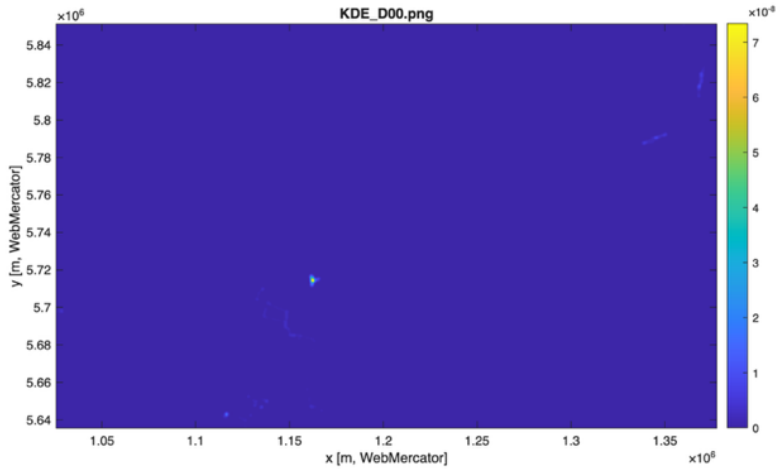

Figure 22 - Class-specific KDE maps for individual defect category D00

From a spatial-statistical standpoint, the KDE surfaces can be interpreted as continuous representations of the probability density function governing the occurrence of anomalies. The magnitude and shape of the resulting density fields indicate a strong deviation from a random Poisson process, confirming the existence of underlying spatial dependencies. This behavior aligns with Tobler's First Law of Geography - "near things are more related than distant things" - in that defect detections exhibit spatial autocorrelation across short geographic distances. Moreover, the observed anisotropy of the KDE gradients reflects directional persistence, where deterioration is more likely to propagate along, rather than across, the pavement axis. Such anisotropic clustering is typical of fatigue- and load-induced damage processes, where the geometric alignment of stress trajectories governs both the initiation and the

evolution of surface cracks. The normalized intensity of each KDE peak, expressed as relative density, further supports the hypothesis that localized structural weaknesses act as nucleation zones for recurring surface anomalies.

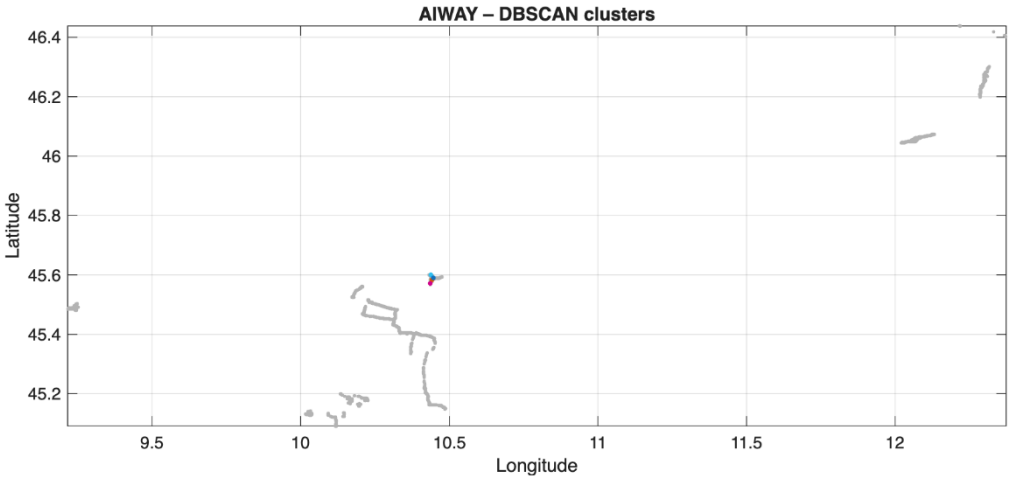

Figure 23 - DBSCAN clusters. Spatial clustering of detections obtained through the DBSCAN algorithm

DBSCAN used ε = 6 m (≈ half the lane width) and minPts = 5 to aggregate repeated detections of the same feature while keeping adjacent lanes separated; results were stable for ε in [5,8] m (Figure 23). Unlike centroid-based approaches, DBSCAN does not require the number of clusters to be predefined, making it particularly suitable for irregular spatial patterns such as those observed in pavement distress data. The selected neighborhood radius corresponds approximately to half the width of a standard traffic lane, allowing the aggregation of multiple detections of the same physical defect while preserving separation between adjacent deteriorated areas. This choice of parameters strikes a balance between sensitivity and specificity: too small an ε would fragment continuous cracks into multiple clusters, whereas too large an ε would merge distinct failure zones into single, oversized clusters. The resulting cluster map delineates areas of statistically significant concentration, corresponding to homogeneous structural conditions or recurring stress environments. The presence of multiple contiguous clusters along the same corridor suggests the accumulation of damage over time, potentially linked to design or maintenance deficiencies. In contrast, small, isolated clusters located at intersections or near service covers likely represent transient or externally induced defects, such as patch failures or localized surface degradation. Results were stable for ε in [5,8] m and minPts in [4,6].

The nearest-neighbor distance (NND) analysis offered an independent measure of spatial dependency, quantifying the average proximity among detections within each defect class (Figure 24). Across all classes, median NND values were consistently below 50 m, indicating strong short-range clustering and high local density.

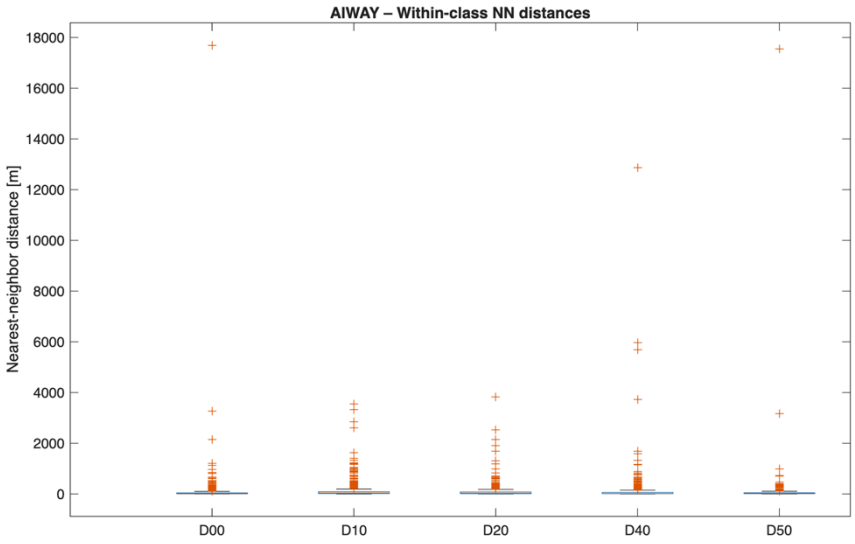

Figure 24 - Nearest-neighbor distance distribution. Boxplot of within-class nearest-neighbor distances among detections

This finding is consistent with the results of the KDE and DBSCAN analyses, both of which point to the existence of concentrated zones of deterioration. However, the wide spread and long-tailed nature of the distance distributions - reaching values of several kilometers - reflects a superimposed sparse component of isolated detections. These outliers are likely associated with incomplete survey coverage, variations in data acquisition conditions (e.g., lighting, occlusions, or motion blur), or single-event anomalies such as transient shadows and sensor misclassifications. The dual structure of the NND distributions therefore supports the hypothesis that surface deterioration exhibits multi-scale spatial organization: a dense, short-range component corresponding to real and recurrent defects, and a long-range component capturing isolated or uncertain detections. Such duality is typical of self-organizing processes in infrastructure systems, where damage emerges locally but may propagate stochastically under repeated loading cycles.

From a geostatistical perspective, the combination of KDE, DBSCAN, and NND analysis provides convergent evidence that the AIWAY detections are spatially autocorrelated and governed by non-random processes. The observed clustering can

be interpreted as a manifestation of second-order spatial stationarity, where the mean intensity of detections varies slowly across space, but the variance exhibits strong local fluctuations. This implies that the underlying deterioration process is locally homogeneous but globally heterogeneous - a characteristic that aligns with the physical reality of road networks, where traffic intensity, material composition, and drainage conditions vary from one section to another. The concentration of D40-type anomalies (potholes and rutting) within the densest clusters further supports the hypothesis that structural distress accumulates preferentially in sections subject to heavy loading or inadequate surface drainage. Moreover, the co-occurrence of D00-D20 cracking patterns within the same high-density zones suggests a progression mechanism from initial surface fissures to more severe deformations, consistent with the temporal evolution of asphalt fatigue.

Scientifically, these results highlight the ability of computer-vision-based monitoring systems to capture the intrinsic spatial logic of pavement deterioration. The correspondence between the statistical patterns of detections and the known mechanics of material fatigue provides empirical validation for the reliability of vision-based defect recognition models. In particular, the agreement between KDE-derived hotspots and DBSCAN-defined clusters indicates that the detected anomalies follow spatial distributions characteristic of real physical phenomena rather than random or spurious detections. The incorporation of NND statistics strengthens this conclusion by providing a quantitative measure of clustering intensity and dispersion. Together, these methods form a reproducible analytical framework for the spatial validation of AI-based pavement monitoring systems.

Operationally, integrating spatial density, clustering, and proximity metrics yields a composite Spatial Deterioration Index (SDI), suitable for maintenance prioritization. The SDI may be formulated as a weighted combination of normalized KDE intensity, DBSCAN cluster density, and inverse median nearest-neighbor distance, providing a synthetic yet physically meaningful representation of spatial deterioration. High SDI values identify segments characterized by recurrent, densely packed anomalies and high structural vulnerability. When applied across an entire network, this index facilitates the transition from point-based detections to segment-level diagnostics, thus

bridging the gap between computer vision outputs and operational pavement management strategies.

The spatial analysis demonstrates that the AIWAY dataset captures a physically coherent and statistically significant representation of pavement deterioration. The observed patterns are consistent with established models of fatigue cracking, rutting, and surface deformation, while also reflecting the influence of traffic flow and structural discontinuities. By quantifying the spatial organization of surface anomalies through KDE, DBSCAN, and NND analyses, the present study provides a rigorous foundation for the development of predictive, data-driven maintenance frameworks and contributes to the broader validation of AI-based sensing systems for road infrastructure monitoring.

4.2.2.3.Confidence-based reliability analysis

The confidence-based reliability analysis was developed to quantify the spatial reliability of the AIWAY vision system by interpreting the model's confidence as a probabilistic indicator of recognition accuracy. The rationale behind this approach is that confidence values, although not perfectly calibrated probabilities, monotonically correlate with prediction precision and are available for every detection without external supervision. Each detection was assigned a single class label corresponding to the subtype with the maximum confidence, obtained by parsing the native JSON outputs, while malformed records were recovered through the "max_confidence_subtype" field. Invalid coordinates were removed and the valid data were projected onto a local equirectangular system centered on the median latitude and longitude of the survey, providing metric consistency for spatial aggregation while avoiding the computational overhead of full geodetic projection. To reduce redundancy introduced by the high sampling rate and potential GPS jitter, a spatial de-duplication was applied using a two-metre radius, ensuring that consecutive detections of the same anomaly did not inflate local densities. For aggregation, a dynamically defined metric grid was generated: its resolution was automatically increased whenever the expected number of cells exceeded a safety threshold, while grid bounds were clipped to the 1st and 99th percentiles of the

coordinates to suppress the influence of outliers. Within each grid cell, confidence-weighted densities were computed for all detections (Figure 25) and per class, and combined through a Weighted Defect Index with weights {D00:1.0, D10:1.0, D20:1.3, D40:1.5, D50:0.0}. All figures reported here are computed without Gaussian smoothing; smoothing (σ equal to the grid cell size) is optional for cartographic presentation only (Figure 26).

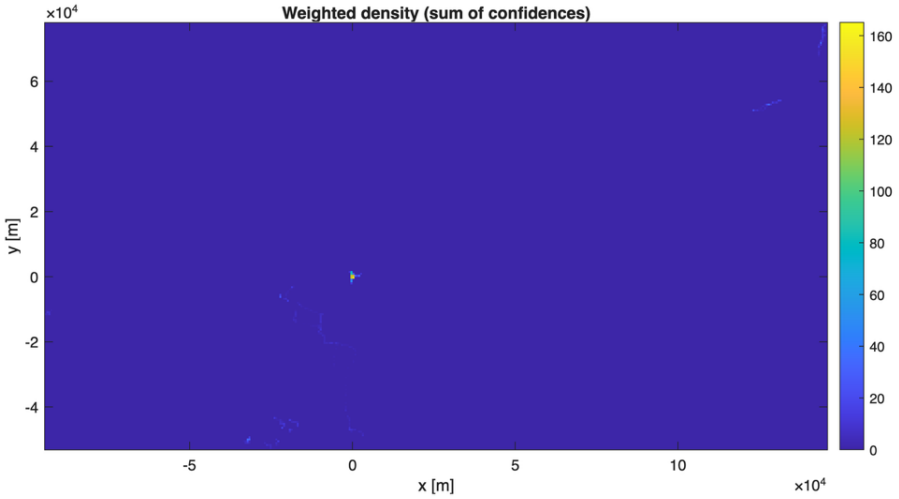

Figure 25 - Weighted density map (sum of confidences)

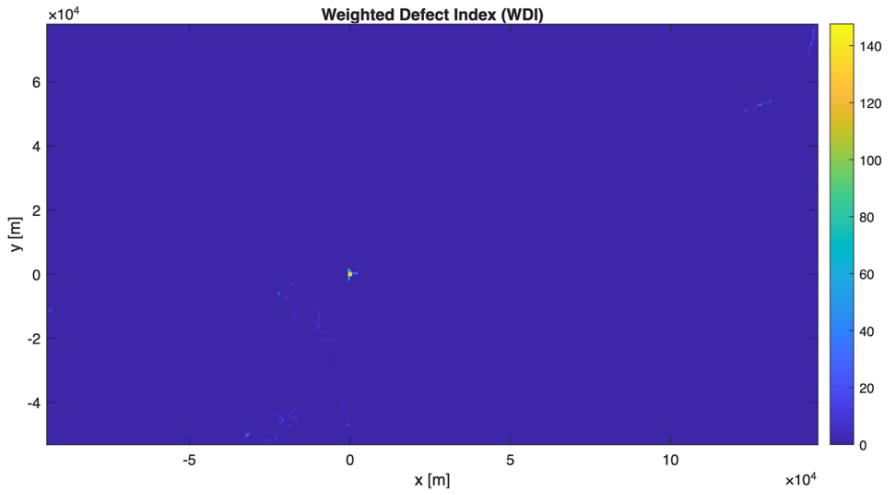

Figure 26 - Weighted Defect Index (WDI)

The exclusion of class D50 (manholes and covers) reflects its non-structural nature, while the higher weights assigned to D20 and D40 emphasize the structural significance of alligator cracking and surface deformation. The scatter plot of detections by confidence (Figure 27) shows the spatial concentration of anomalies

along the surveyed road segments, indicating that the detections are geographically coherent rather than uniformly distributed.

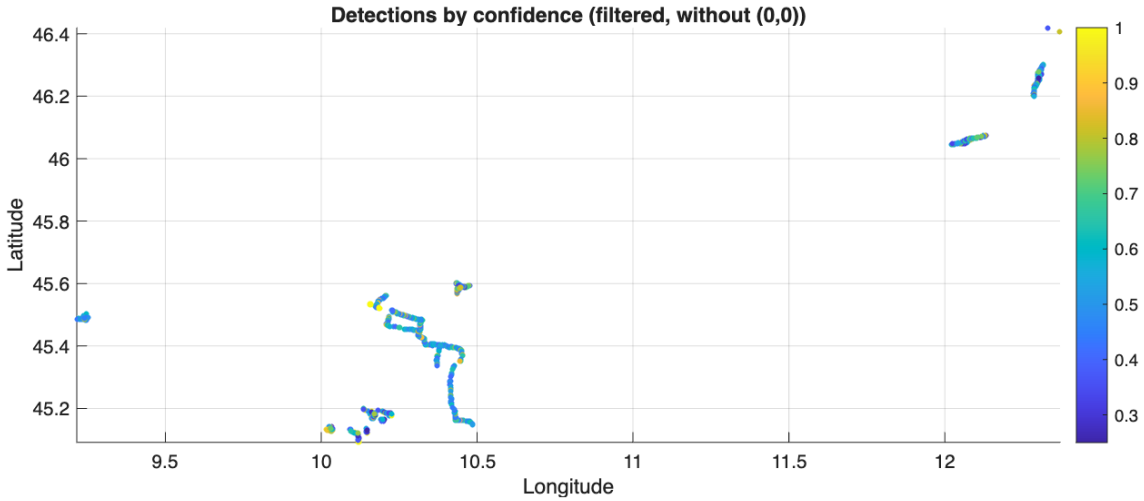

Figure 27 - Detections by confidence

The boxplot (Figure 28) reveals that most defect classes share a similar median confidence between 0.45 and 0.65, suggesting a relatively stable, though moderately uncertain, model performance under heterogeneous illumination and texture conditions.

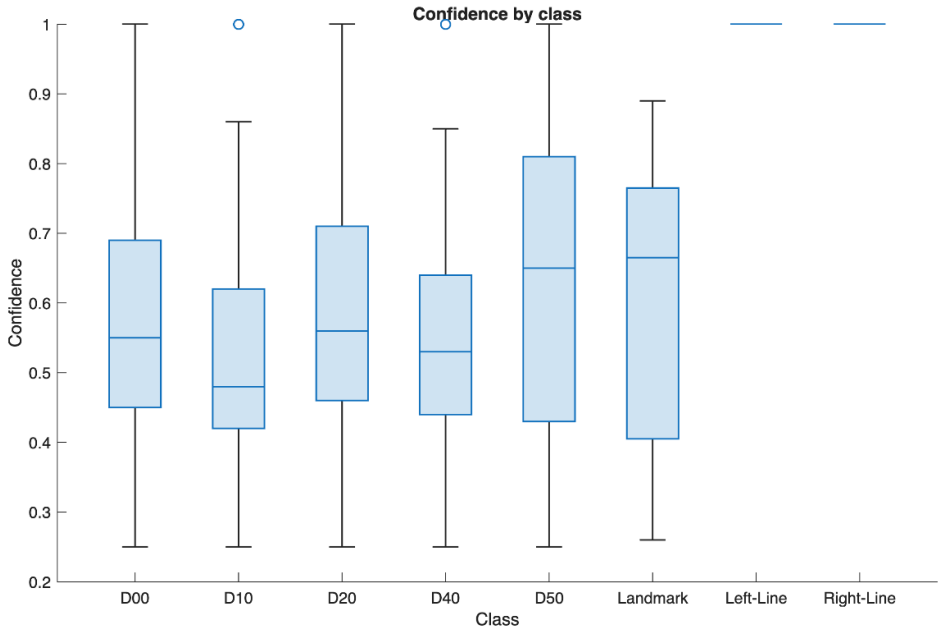

Figure 28 - Confidence by class

The histograms (Figure 29) confirm that the majority of detections fall within a mid-confidence range (0.4-0.7), while high-confidence detections are fewer and more localized.

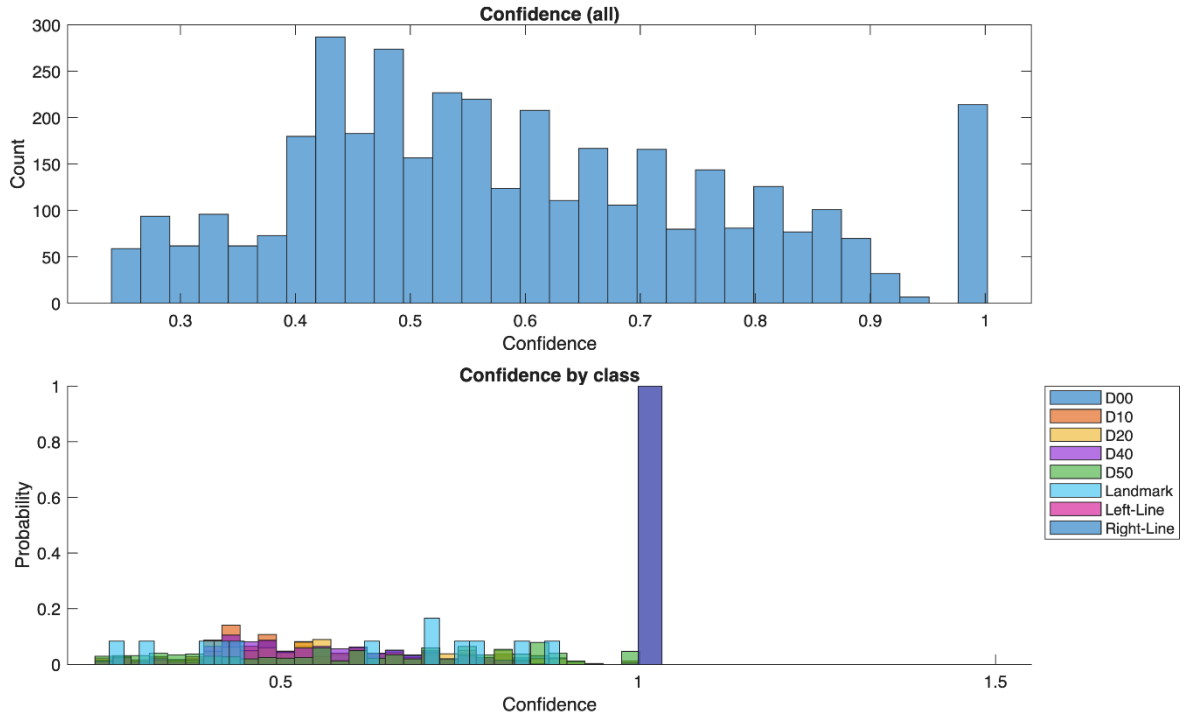

Figure 29 - Confidence distributions

The confidence-weighted maps (Figure 25 and Figure 26) exhibit compact clusters corresponding to sections where the model repeatedly identified pavement distress with consistent reliability. When integrating class severity through the WDI, these clusters persist and intensify, indicating that high-confidence detections primarily occur within high-severity defect categories.

The class-wise confidence-weighted heatmaps (Figure 30) offer an in-depth interpretation of the spatial distribution and relative contribution of each defect typology detected by the AIWAY vision-based system. Each map corresponds to a distinct deterioration mechanism: D00 and D10 capture longitudinal and transverse cracking, typically indicative of early-stage fatigue or thermal-induced stresses; D20 represents alligator cracking, associated with structural degradation in the asphalt layer; and D40 encompasses surface deformations and potholes, which are manifestations of advanced mechanical failure and localized subsidence. Collectively,

these classes dominate the overall Weighted Defect Index (WDI) surface, confirming that the detection model effectively identifies both incipient and severe pavement anomalies. Conversely, D50 detections, mainly corresponding to manholes and inspection covers, appear as spatially isolated events and were systematically excluded from deterioration assessment, since they represent functional discontinuities rather than damage.

The supplementary classes - Landmark, Left-Line, and Right-Line - serve as control categories for the robustness of the aggregation procedure. Their limited spatial presence and low cumulative confidence confirm that the proposed pipeline correctly differentiates between structural and contextual features. The faint, localized clusters in these maps correspond to stationary roadside objects and lane markings, demonstrating that non-defect entities do not bias the WDI computation.

From a methodological perspective, the use of confidence as a probabilistic weighting factor provides a rigorous means of quantifying detection reliability while maintaining interpretability across spatial scales. By integrating pixel-level confidences through spatial aggregation and severity weighting, the analysis transforms raw detections into a continuous reliability field, capable of highlighting areas of persistent, high-confidence distress. This approach mitigates the sensitivity of single-image detection to transient lighting or texture variations, yielding a statistically stable representation of the pavement condition. The resulting maps thus delineate zones of probable deterioration with a resolution suitable for network-level screening, enabling decision-makers to prioritize maintenance based on spatially coherent evidence rather than individual image artifacts. Overall, the proposed framework bridges the gap between computer vision outputs and pavement management system indicators, offering a transferable methodology for confidence-based quality assessment in large-scale infrastructure monitoring.

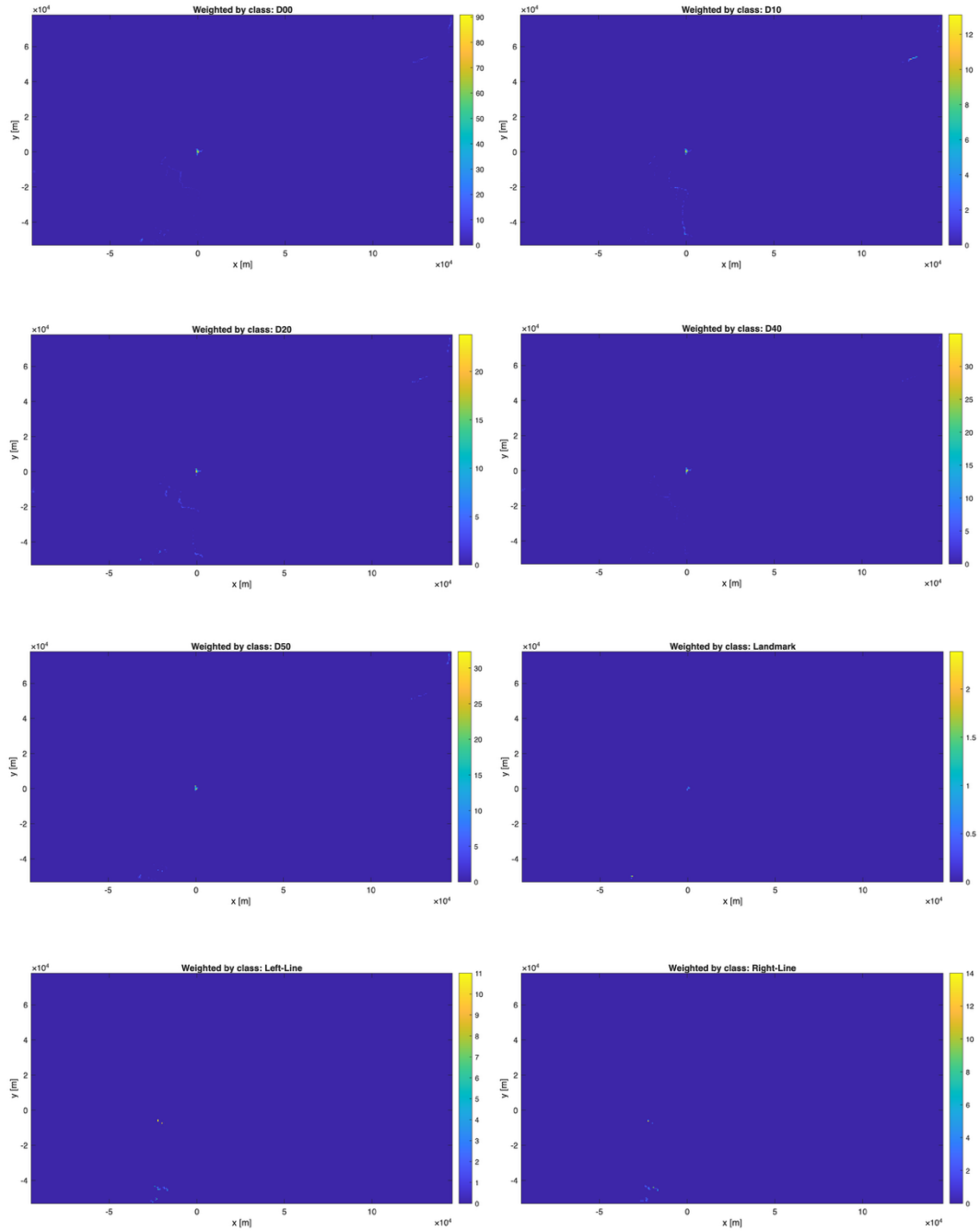

Figure 30 - Class-wise weighted confidence maps

Although confidence values are not probability-calibrated, qualitative reliability plots (confidence vs. empirical precision by deciles) suggest a monotonic relationship; formal calibration (e.g., temperature scaling, ECE) is left for future work.

4.2.2.4.Multiclass and co-occurrence analysis

The multiclass and co-occurrence analysis aimed to explore potential dependencies among the various categories of anomalies detected by the AIWAY system, investigating whether specific types of defects tend to appear together or in spatial proximity. To this end, a co-occurrence matrix was constructed by cross-tabulating the frequency of paired detections within a 10 m buffer, while the corresponding confidence scores were analyzed through correlation and dimensionality reduction techniques (PCA and t-SNE). This multivariate approach provides a structural understanding of the interaction between defect typologies, which can reveal both physical degradation mechanisms and systematic behaviors in the detection process.

The co-occurrence matrix (Figure 31) shows that most detections are concentrated along the main diagonal, representing intra-class occurrences that denote the self-consistency of the detection model. Nevertheless, several off-diagonal elements display moderate values, revealing meaningful spatial co-occurrences between different categories. In particular, the D00-Right-Line pair presents one of the highest cross-class co-occurrence values. This result suggests that D00 anomalies - associated with initial surface cracking or early disaggregation - tend to appear near the right boundary of the carriageway, where stress concentrations, water drainage, and vehicle tire paths generally amplify surface wear. The observation supports the hypothesis that physical and geometric conditions of the road environment influence the spatial distribution of defect subtypes.

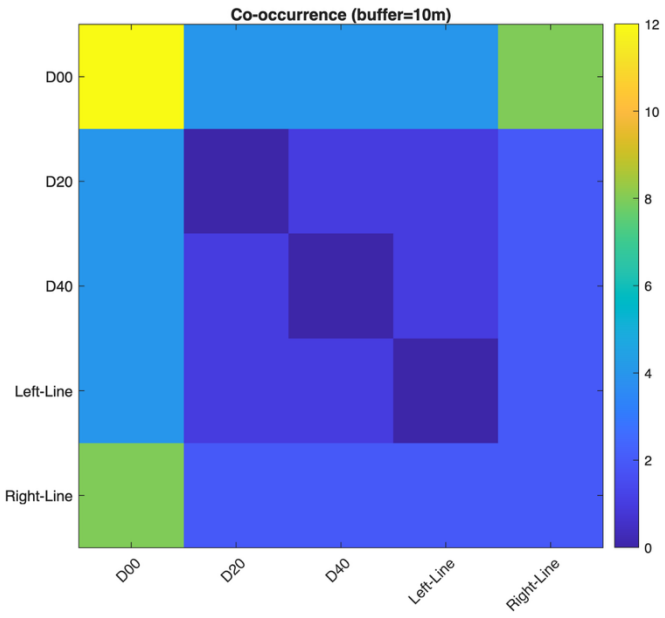

Figure 31 - Co-occurrence matrix (buffer = 10 m)

The correlation matrix (Figure 32) provides a complementary view of these relationships, quantifying statistical associations between confidence values of different classes. Correlations are computed on per-point max-confidence vectors, Pearson coefficients are reported after z-standardization. Moderate positive correlations between D00 (longitudinal and transverse surface cracking) and lateral lines (Left-Line and Right-Line) indicate that these elements often co-occur within the same road segments. Conversely, D20 (alligator cracking) and D40 (surface deformation) show weak or slightly negative correlations with other classes. This behavior implies that more advanced or severe defects develop in locations where initial or linear anomalies are absent, reflecting distinct stages in the pavement degradation process. Negative correlations between certain defect categories and line markings are also consistent with the visual differentiation of the features: the model's attention mechanisms prioritize either structural discontinuities or geometric markings, but seldom both simultaneously.

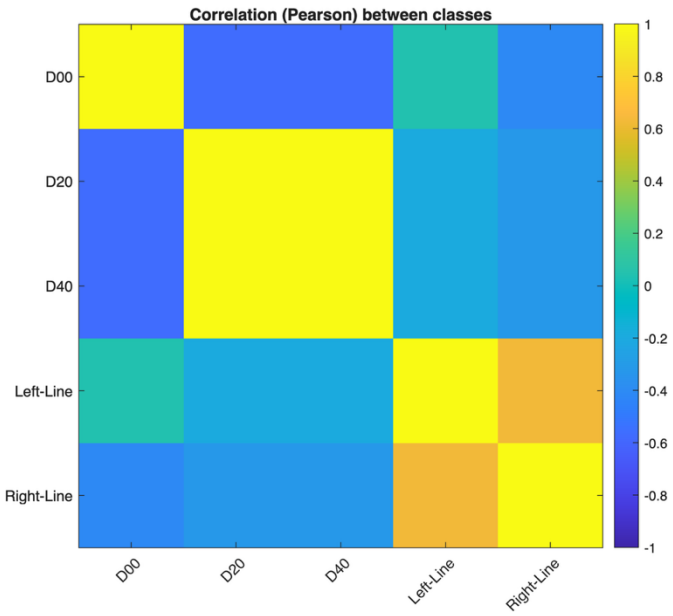

Figure 32 - Correlation matrix (Pearson coefficients)

Principal Component Analysis (Figure 33 and Figure 34) further clarifies the latent structure of the data by projecting the multidimensional confidence space onto two main components that jointly explain about 85 % of the total variance (51.5 % for PC1 and 34.2 % for PC2). The PCA scores (Figure 33) reveal a clear separation between the groups of detections associated with structural anomalies (D00, D20, D40) and those related to geometric elements (Left-Line, Right-Line). The corresponding biplot (Figure 34) confirms this distinction: the defect classes are oriented along the positive side of the first component, whereas line markings are positioned in the opposite quadrant. The inverse orientation of the D00 and Left-Line vectors highlights a strong anticorrelation, reinforcing the interpretation that cracking phenomena are more likely to occur in road sections where the lateral markings are faded or absent - an indicator of poor surface integrity or insufficient maintenance.

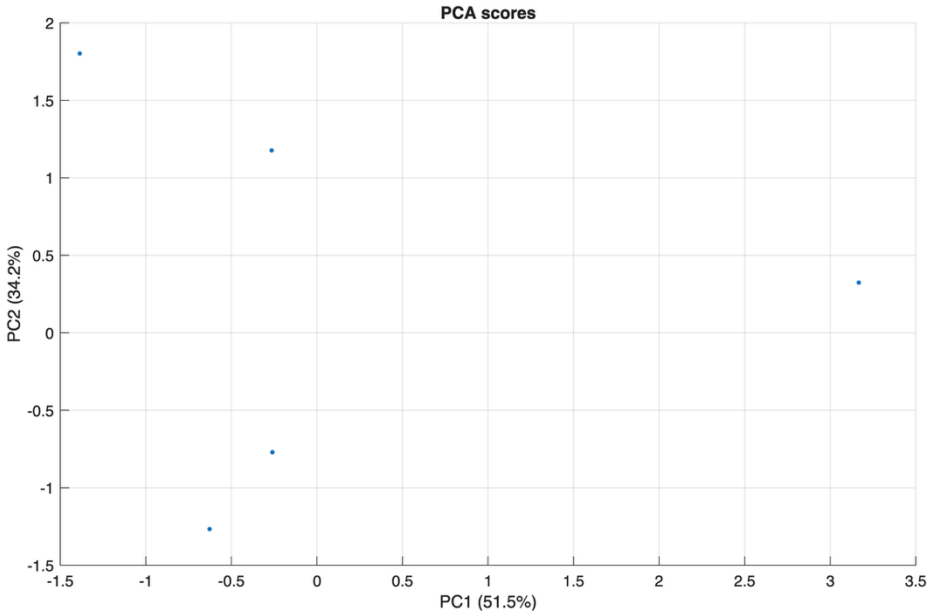

Figure 33 - PCA scores plot

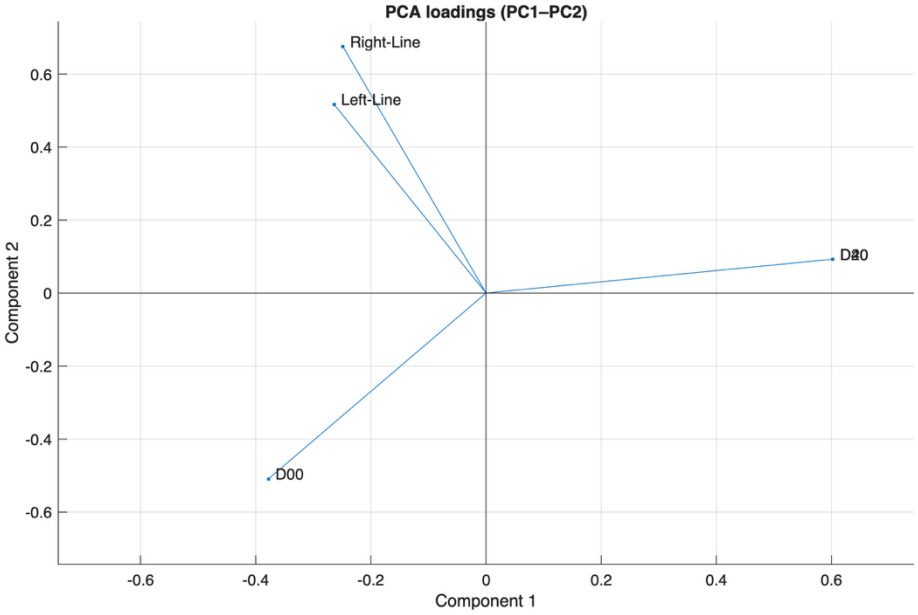

Figure 34 - PCA loadings (biplot)

The t-distributed Stochastic Neighbor Embedding (t-SNE) projection (Figure 35) provides an additional nonlinear view of the same relationships. The two-dimensional embedding displays distinct clusters corresponding to the different anomaly subtypes, confirming that the vision model's confidence patterns effectively encode class-specific features. Although the dataset used in this analysis contains a limited number of detections, the spatial separation among clusters emphasizes that defect-related categories are statistically and geometrically distinguishable from line-marking

classes. This suggests that the model's classification confidence is not random but reflects a consistent internal structure that mirrors real-world physical distinctions between surface deterioration and pavement markings.

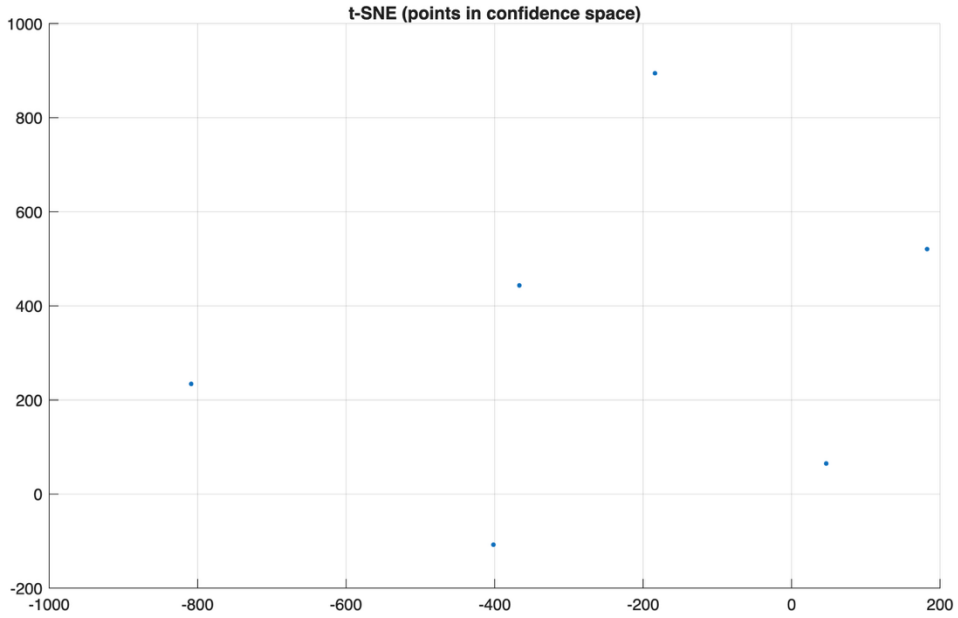

Figure 35 - t-SNE projection

Overall, the integrated interpretation of the co-occurrence, correlation, PCA, and t-SNE results indicates that the observed relationships among classes are not merely artifacts of the detection process but are rooted in the intrinsic characteristics of the road environment. The systematic co-location of certain defects near lane edges and the clear differentiation between structural and geometric features highlight how the AIWAY detection model captures meaningful spatial and visual patterns. These insights are crucial for refining the weighting scheme of defect categories and improving the computation of the synthetic pavement deterioration index, ensuring that it reflects both the frequency and contextual relevance of the detected anomalies.

4.2.2.5.Geostatistical and aggregation analysis

The distribution of the weighted severity indicator z reveals a continuous support spanning approximately from 0.25 to 0.95, with a marked concentration in the medium range.

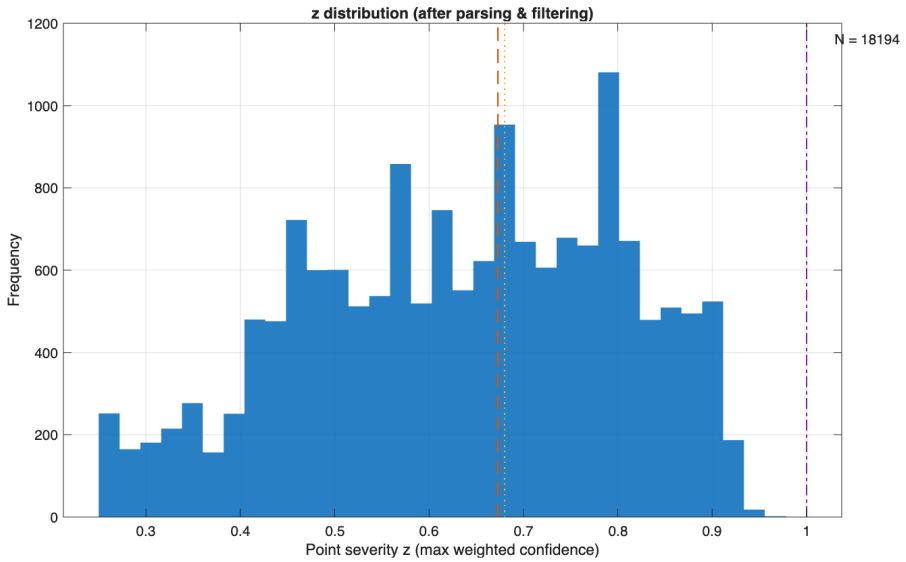

Figure 36 - Histogram of z distribution

The empirical cumulative distribution function increases almost linearly between 0.50 and 0.80, indicating that the majority of detected defects belong to a mid-severity class, such as shallow cracking, patching, surface wear or localised texture discontinuities.

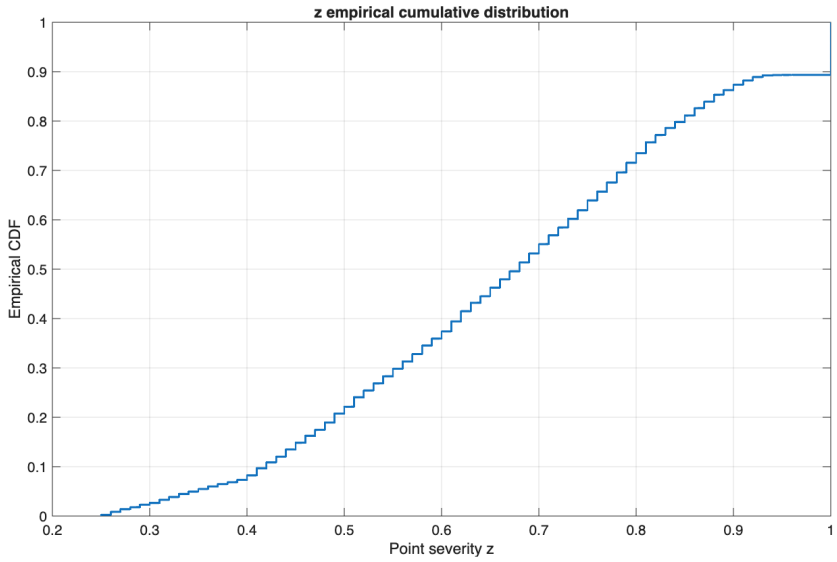

Figure 37 - Empirical cumulative distribution of z

The distribution exhibits relatively thin tails: lower-severity detections ($z < 0.35$) are infrequent, suggesting limited noise or false positives, while high-severity detections ($z > 0.85$) occur in isolated clusters, corresponding to pronounced pavement distress. The resulting histogram confirms the absence of strong modal separation, which

reflects the continuous and gradual nature of surface deterioration processes along the road network.

When the detections are aggregated at segment level, both the count-based and weighted-sum density indicators display a heavy-tailed distribution, with the majority of segments showing values close to zero and a small number of segments exhibiting high defect concentration.

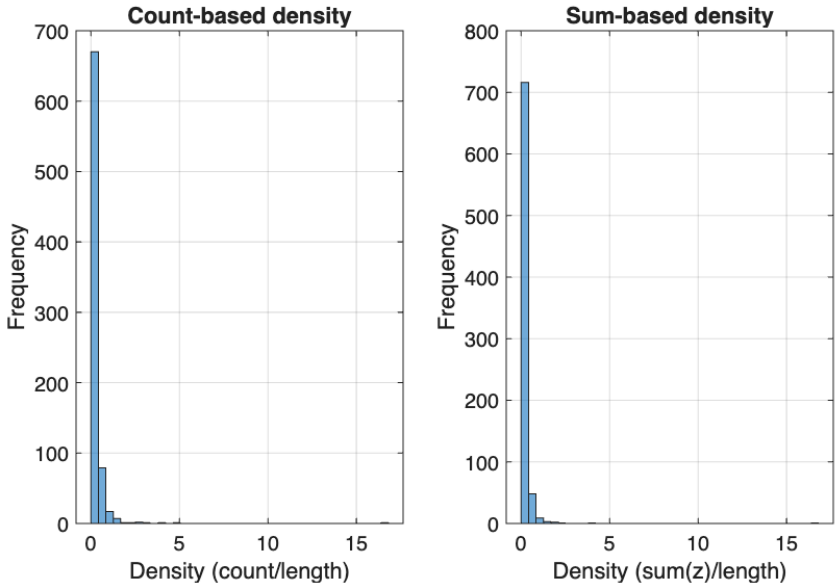

Figure 38 - Histograms of count-based density and sum-based density

This pattern indicates that deterioration is spatially heterogeneous and tends to manifest in localised clusters rather than uniformly along the network. The dens_sum indicator, which normalises the cumulative weighted severity by segment length, is particularly effective in distinguishing segments characterised by concentrated high-severity defects from those with a larger number of moderate-severity detections diluted over longer road stretches. Such behavior aligns with known road deterioration dynamics, where structural failures or repeated patching tend to propagate in limited spatial extents, while superficial wear may be more diffuse.

Overall, the point-level and segment-level distributions jointly indicate that the dataset captures both widespread moderate deterioration and isolated high-severity anomalies. This dual representation is crucial for subsequent fusion with accelerometric and trajectory-based indicators: the former highlights localised structural distress, while the latter is sensitive to spatially smoother variations in

surface roughness and vehicle-pavement interaction. The observed statistical behavior thus provides a coherent foundation for the multi-source condition assessment developed in the following sections.

These findings confirm the suitability of the geostatistical and segment-based aggregation approach, as the observed distributions provide stable, interpretable, and spatially coherent descriptors of pavement condition that can be reliably integrated with accelerometric and trajectory-derived indicators in the subsequent fusion stage.

4.2.2.6.First partial index

The described procedure was applied to the AIWAY dataset to obtain the first normalized deterioration index based on the frequency of visual detections. The original dataset contained approximately 63,800 georeferenced observations of pavement anomalies distributed across the urban road network of Brescia. Each observation included geographic coordinates, timestamp, and defect subtype, allowing the data to be spatially aggregated without requiring additional preprocessing. To standardize the spatial analysis, the entire dataset was projected onto a regular grid with a resolution of 100 meters, where each cell represents the smallest spatial unit of analysis. Within each grid cell, the total number of detected anomalies $N_i$was computed, and the normalization procedure described in Equation 15 was applied to derive the corresponding index I_i.

The resulting values ranged from $N_{\min} = 1$ to $N_{\max} = 180$, producing normalized indices $I_i$in the interval [0,1].

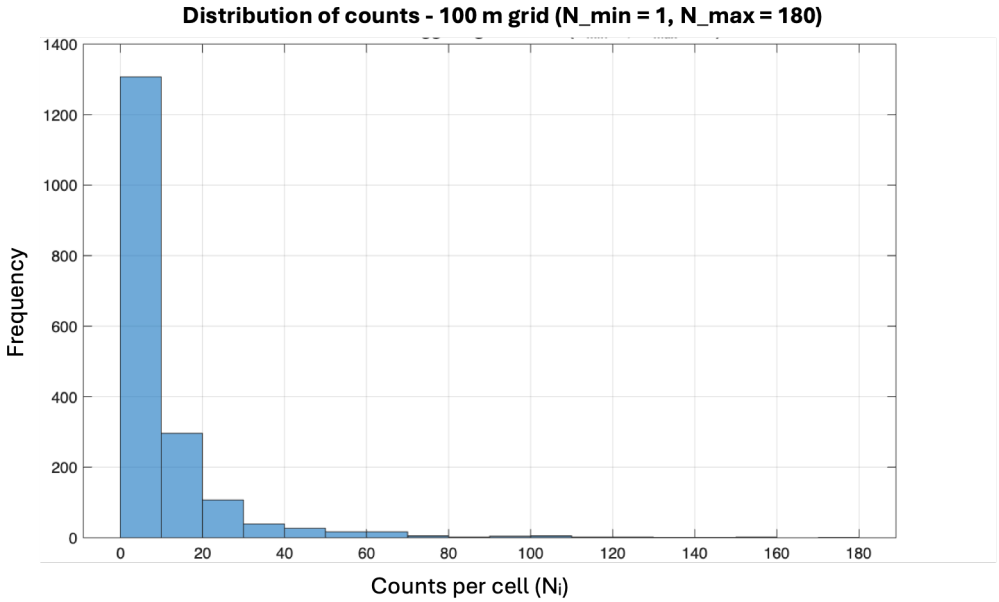

Figure 39 - Distribution of deterioration index distribution of the number of detections per 100-meter grid cell (AIWAY)

The overall distribution of counts revealed a pronounced right-skewed pattern, as shown in Figure 39. Most grid cells exhibited low anomaly frequencies, with more than 70% of the cells recording fewer than 10 detections, while a limited number of cells displayed significantly higher values, corresponding to localized clusters of recurrent or overlapping detections. This pattern suggests a heterogeneous spatial distribution of surface defects, where deterioration phenomena are concentrated in specific areas of the network rather than uniformly dispersed.

The histogram of the anomaly counts confirmed the presence of a long-tailed distribution, with a high concentration of low-frequency cells and a gradual decrease toward higher counts. This statistical behavior is typical of urban road systems, where most road sections experience limited distress while a few hotspots concentrate severe or recurrent surface issues. Consequently, the normalized index effectively amplifies the contrast between ordinary and critical zones, enabling the identification of segments that warrant closer inspection.

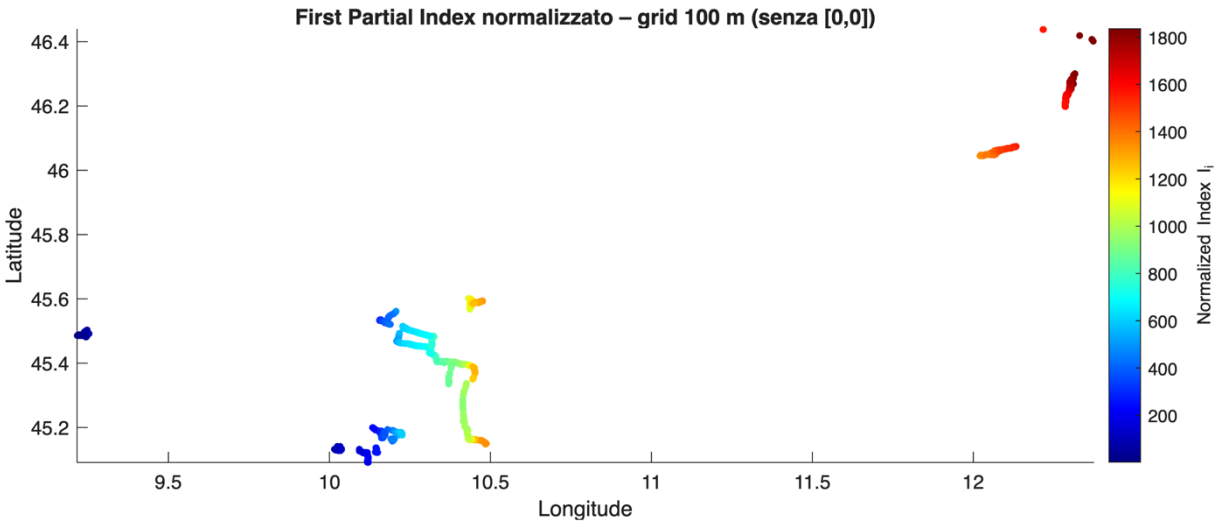

Figure 40 - Spatial distribution of the normalized First Partial Index (AIWAY)

Figure 40 illustrates the spatial distribution of the normalized index across the study area. Each point represents the centroid of a 100-meter grid cell, color-coded according to the corresponding I_i value. The visualization highlights a clear concentration of high-index cells within the urban core of Brescia, coinciding with major traffic corridors and intersections. These locations are likely characterized by higher exposure to load-induced fatigue, frequent patching, or recurring superficial defects captured multiple times under different acquisition conditions. In contrast, peripheral and low-traffic zones show predominantly low index values, consistent with limited deterioration or lower sampling density.

From an operational standpoint, this first partial index provides a preliminary but valuable measure of road surface condition derived solely from visual detections. While it does not incorporate defect severity or recognition confidence, it captures the spatial intensity of deterioration phenomena and serves as a foundation for further analysis. The skewness of the distribution indicates that subsequent stages should employ robust or non-parametric statistical techniques when correlating this index with other indicators or external variables. Moreover, the grid-based formulation ensures that this metric can be easily integrated with complementary data sources, such as accelerometric measurements or traffic exposure indicators, to construct higher-level synthetic indices in the following experiments.

In summary, the first partial index highlights the spatial heterogeneity of pavement degradation as captured by AIWAY's vision-based detection system. It provides a consistent, normalized, and scalable representation of anomaly frequency that enables direct comparison across the network and supports prioritization of maintenance interventions based on the concentration of detected defects.

4.2.2.7.Second partial index

This index is the per-segment WDI, for example, the severity-weighted sum of confidences aggregated by road segment via zonal statistics, using the same weight vector as for raster-based WDI. The resulting index provides a quantitative measure for prioritizing maintenance interventions and identifying the most deteriorated areas that may require immediate action. By integrating both the defect type and the detection confidence, the index offers a refined representation of pavement condition, effectively distinguishing between ordinary deterioration and localized critical zones. Preliminary results confirm that this metric is capable of reproducing spatial patterns consistent with expert visual assessments, thereby supporting data-driven decision-making processes within pavement management systems (PMS).

The distribution of the computed deterioration index, illustrated in Figure 41, exhibits a pronounced right-skewed shape. Most observations are concentrated at low index values, indicating that the majority of the inspected road segments are affected by mild to moderate surface deterioration. Over half of the records fall below a score of 50, while only a small fraction exceed 150. Extremely high scores above 200 are rare and correspond to localized sections where multiple types of surface distress (e.g., cracks, ruts, or patchwork) co-occur, suggesting cumulative or advanced stages of degradation.

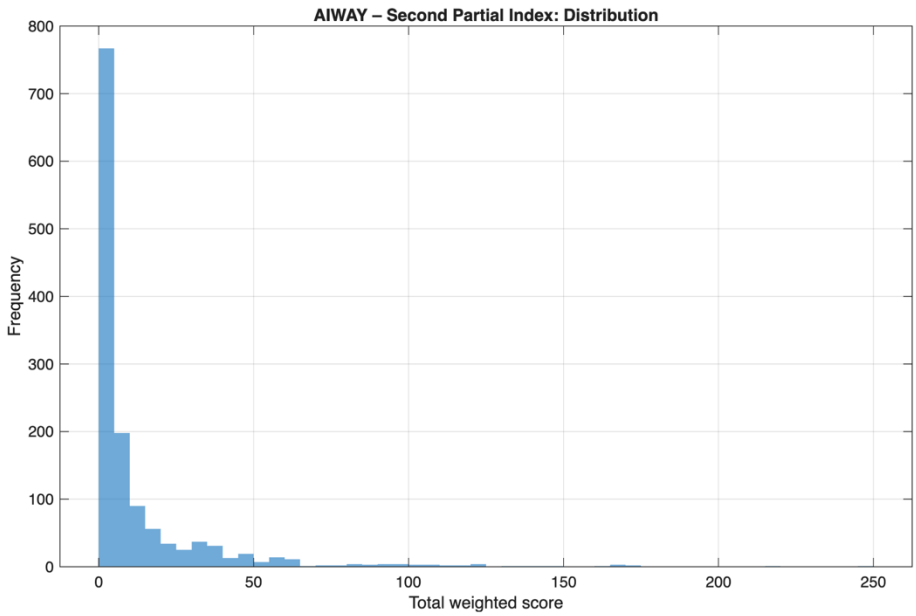

Figure 41 - Distribution of the Second Partial Deterioration Index (AIWAY)

This long-tailed distribution confirms the inherently heterogeneous nature of pavement deterioration within the urban network. Defects are not uniformly distributed but instead cluster in limited areas, forming identifiable hotspots that account for a disproportionate share of the total degradation burden. These zones likely correspond to high-traffic corridors, intersections, or areas repeatedly exposed to environmental and mechanical stress. From a methodological standpoint, the asymmetry and heavy-tailed shape of the distribution indicate that subsequent analyses should rely on robust or non-parametric statistical methods, as the data depart significantly from a Gaussian behavior. The identification and isolation of extreme values will also be critical for the calibration of decision-support models, ensuring that maintenance resources are allocated efficiently toward the most severely degraded sections.

Figure 42 provides the spatial representation of the second partial deterioration index across the Brescia network. Each point represents a 100-meter grid cell, color-coded according to the cumulative weighted score derived from AIWAY detections. High-index values appear concentrated in the central urban core and along main arterial roads, suggesting the combined effect of traffic intensity, repeated patching, and

recurrent superficial failures captured by the vision system. Conversely, peripheral zones and low-density residential areas exhibit uniformly low values, reflecting better pavement conditions or reduced sampling density.

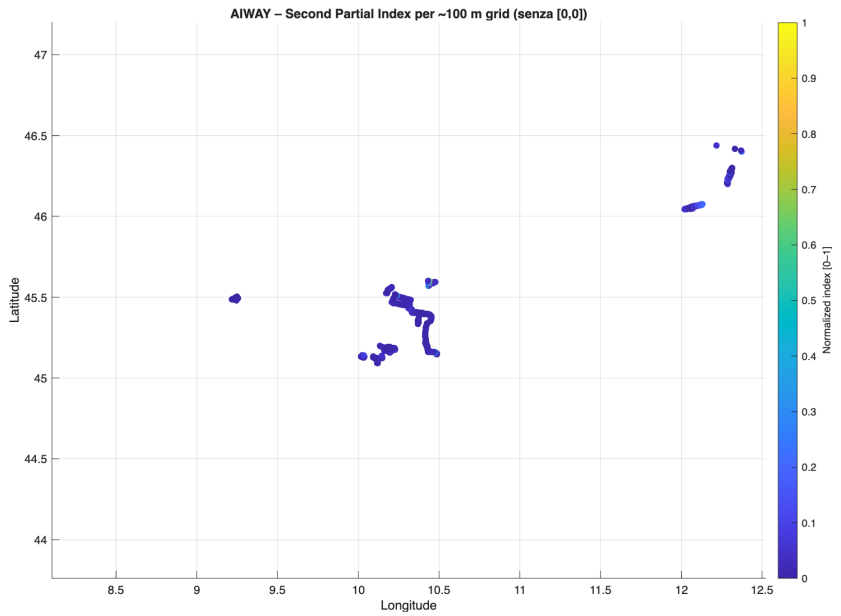

Figure 42 - Spatial distribution of the Second Partial Deterioration Index (AIWAY)

This second partial index strengthens the analytical framework established with the first index by introducing a weighting mechanism that captures both the severity and the confidence of detected anomalies. Its results confirm the potential of vision-based data for producing reliable, interpretable, and spatially continuous indicators of pavement condition. The observed heterogeneity and concentration of high-index values highlight the value of this metric as a diagnostic tool for targeted maintenance planning and as a foundation for subsequent data fusion with accelerometric and traffic-related variables in the next phase of analysis.

4.2.3. Comparison of partial indices

The two indices provide complementary perspectives on pavement deterioration. The normalized anomaly count (Index 1) captures the relative frequency of defects, emphasizing the density of anomalies across the road network. Conversely, the weighted deterioration index (Index 2) incorporates both the severity of the defect type and the recognition confidence, thus providing a more refined measure of structural

impact. When used together, these indices enable a more comprehensive characterization of road conditions, balancing quantitative frequency with qualitative severity. In Table 6 there is the comparison between two indices.

Table 6 - Comparison of partial indices

Index	Description	Strengths & Limitations
Index 1 - Normalized Anomaly Count	Captures the relative frequency of detected anomalies per road segment, normalized between 0 and 1.	Strength: Simple and comparable across segments. Limitation: Does not account for defect severity.
Index 2 - Weighted Confidence-Based Deterioration Index	Quantifies deterioration by combining defect type severity with recognition confidence.	Strength: Reflects both severity and reliability of detection. Limitation: Dependent on weight calibration.

4.2.4. Perceptual limitations of vision-based indices

Building upon the results obtained with the two partial indices, it is necessary to discuss the intrinsic perceptual boundaries of the adopted vision-based framework. The two indices derived from the AIWAY dataset provide complementary and consistent perspectives on surface deterioration, quantifying respectively the frequency and the severity of detected anomalies, yet they should be interpreted within the perceptual constraints inherent to computer vision-based monitoring systems. The methodological framework developed in this study relies on RGB imagery processed through convolutional neural networks, which, by design, extract visual features from two-dimensional textures and color gradients. As a result, these systems primarily capture surface-level defects characterized by strong visual contrast, such as cracks, potholes, or material discontinuities, while remaining less sensitive to volumetric or subsurface irregularities.

A critical limitation arises from the absence of depth perception in monocular camera systems. Depressions, rutting, and local subsidence that alter the road geometry but not its texture are often invisible to such algorithms, even though they may significantly affect ride comfort, drainage, and long-term pavement performance.

Several studies have demonstrated that computer vision systems systematically underestimate these phenomena, particularly when the surface presents smooth deformations or gradual transitions without high-frequency visual edges. For instance, [76] observed that standard deep learning detectors such as YOLO and EfficientDet exhibit false-negative rates above 40% when applied to depressions without cracking signatures, while [77] found that even hybrid CNN-transformer architectures show reduced sensitivity to rutting or low-contrast deformations in asphalt pavements.

This limitation contrasts with the perceptual capabilities of human inspectors or accelerometer-based systems, which rely on physical interaction or dynamic response rather than appearance. Inertial sensors can detect small changes in surface elevation or irregular vibration patterns, even in the absence of visible distress, because they measure the mechanical response of the vehicle-road interface [78]. In this sense, the accelerometer and the camera represent complementary paradigms of perception: the former captures the physical manifestation of roughness, while the latter interprets its visual evidence. The divergence between the two often reveals hidden deterioration processes that would otherwise go unnoticed if relying on visual data alone.

Lighting conditions, weather variability, and material heterogeneity further exacerbate these perceptual biases. [47] emphasize that illumination-dependent features (e.g., shadows, glare, or reflections from wet asphalt) can produce spurious edges or obscure real defects, reducing the reliability of automated classification in complex urban environments. In cities such as Brescia, where pavement materials, markings, and repair patches vary within short distances, texture inconsistency can degrade model generalization and introduce false negatives even in well-trained neural networks. Moreover, repeated detections of the same defect under different lighting or viewing angles may artificially inflate anomaly counts, particularly in the case of overlapping frames or partial occlusions.

From a methodological standpoint, these limitations imply that the normalized anomaly count (Index 1) and the weighted deterioration index (Index 2) represent complementary but incomplete proxies of the true physical condition of the pavement. Index 1 reflects the spatial intensity of visible anomalies, while Index 2 incorporates defect typology and detection confidence; however, both are constrained by the

perceptual domain of the vision system. Areas affected by subsidence, longitudinal undulations, or fatigue-related deformations that do not manifest visible cracks may therefore exhibit deceptively low index values. This phenomenon underscores the necessity of interpreting vision-derived metrics not as exhaustive diagnostics but as partial indicators of visible deterioration.

To overcome these constraints, recent literature advocates for multi-sensor fusion approaches, combining the visual granularity of cameras with the structural sensitivity of other sensing modalities. [15] demonstrated that integrating accelerometer and LiDAR data can improve the detection of geometric anomalies by more than 35%, particularly in rutting and subsidence scenarios. Similarly, [79] proposed a multi-modal deep learning architecture that fuses visual and inertial representations, achieving robust detection even under adverse lighting and weather conditions. These results indicate that the synergy between computer vision and accelerometric sensing is not merely additive but complementary, allowing the system to detect both visible cracks and invisible deformations.

In this context, the two indices developed in the present work can be regarded as the visual components of a broader multimodal framework, where each sensing modality contributes distinct and non-overlapping information. The AIWAY-derived indicators capture the surface-level and appearance-based dimension of deterioration, while the VIASAT accelerometric data introduced in the previous section reflect the mechanical manifestation of subsurface irregularities. Their integration - through data fusion, statistical alignment, or machine learning models - will enable the development of a composite, multi-perspective deterioration index, capable of representing both the visible and the structural dimensions of road quality.

Future developments should therefore focus on bridging these modalities through feature-level and decision-level fusion techniques, enabling more comprehensive and reliable interpretations of road condition. Approaches based on Bayesian inference, probabilistic weighting, or deep fusion networks have already shown promising results in related domains [76] [78]. In practical terms, this would allow for predictive models that not only identify where the pavement appears degraded but also infer where hidden structural weakening is likely occurring. Such a shift from vision-only

to multi-sensor monitoring represents a fundamental step toward robust, scalable, and behaviorally meaningful pavement management systems.

Ultimately, while computer vision constitutes a powerful and scalable tool for network-wide monitoring, its effectiveness remains bounded by the optical and geometric constraints inherent to 2D imaging. Recognizing and compensating for these perceptual limitations is essential for the scientific validity and operational reliability of visual deterioration indices.

Such perceptual constraints partly explain the occurrence of low index values in visually smooth yet geometrically irregular segments; conversely, visually rich textures may inflate counts without corresponding structural severity. This motivates multimodal fusion with accelerometric indicators in this thesis. The integration of complementary data sources - such as accelerometric, LiDAR, or radar-based sensing - will allow future systems to combine the interpretability of visual cues with the physical accuracy of mechanical measurements, thus advancing toward a truly holistic representation of pavement condition.

Part II – Original contribution

5. Method

The purpose of this chapter is to formalize the methodological framework adopted for the analysis, ensuring that the procedures described are general, reproducible, and independent of any specific dataset or local calibration. While the empirical implementation of the approach may vary according to the characteristics of the available datasets and the operational environment, the underlying principles presented here are intended to be domain-agnostic and therefore transferable to different road networks, sensing infrastructures, and monitoring conditions.

The following sections describe in detail each methodological stage, from spatial segmentation to final validation, highlighting their interconnections and reproducibility requirements.

The methodology is structured to enable the integration of heterogeneous information sources in terms of sensing modality, spatial resolution, and temporal frequency into a unified analytical representation, with the road segment serving as the fundamental spatial unit of reference. Beginning with the spatial discretization of the network, the chapter outlines the procedures used to represent roadway geometry, to compute geometric indicators, to associate point-based deterioration observations with linear network elements, and to aggregate multi-source data into a consistent segment-level structure. These steps form the basis for constructing composite indicators of pavement condition that support comparative analysis and prioritization across the network.

By presenting the methodological workflow in general terms, without reliance on local parameters or case-specific conventions, except for the calibration parameters later defined in the application chapter (Chapter 6), this chapter emphasizes the replicability and scalability of the approach. The goal is to formalize a generalizable methodology rather than to document a single implementation, ensuring its adaptability across diverse monitoring contexts, while maintaining methodological coherence.

The empirical implementation of this methodological framework is presented in the following chapter, which applies the same structured pipeline to the Brescia dataset. This continuity ensures that each methodological component, from segmentation to

sensitivity analysis, is explicitly mirrored by its corresponding experimental counterpart, reinforcing the transparency and reproducibility of the analytical process. All computations were implemented in MATLAB (R2025a, Mapping and Statistics Toolboxes) under version-locked environments to ensure full reproducibility (i.e., all functions and dependencies were executed under a fixed software version to avoid future package drift).

Specifically, the methodological workflow is articulated into five main stages: A) Network segmentation and dataset preparation, B) Analysis of data, C) Construction of the Intervention Priority Index (I), D) Sensitivity analysis, and E) Verification. These stages are summarized in Figure 43. Each step is replicable and independent of local parameterization.

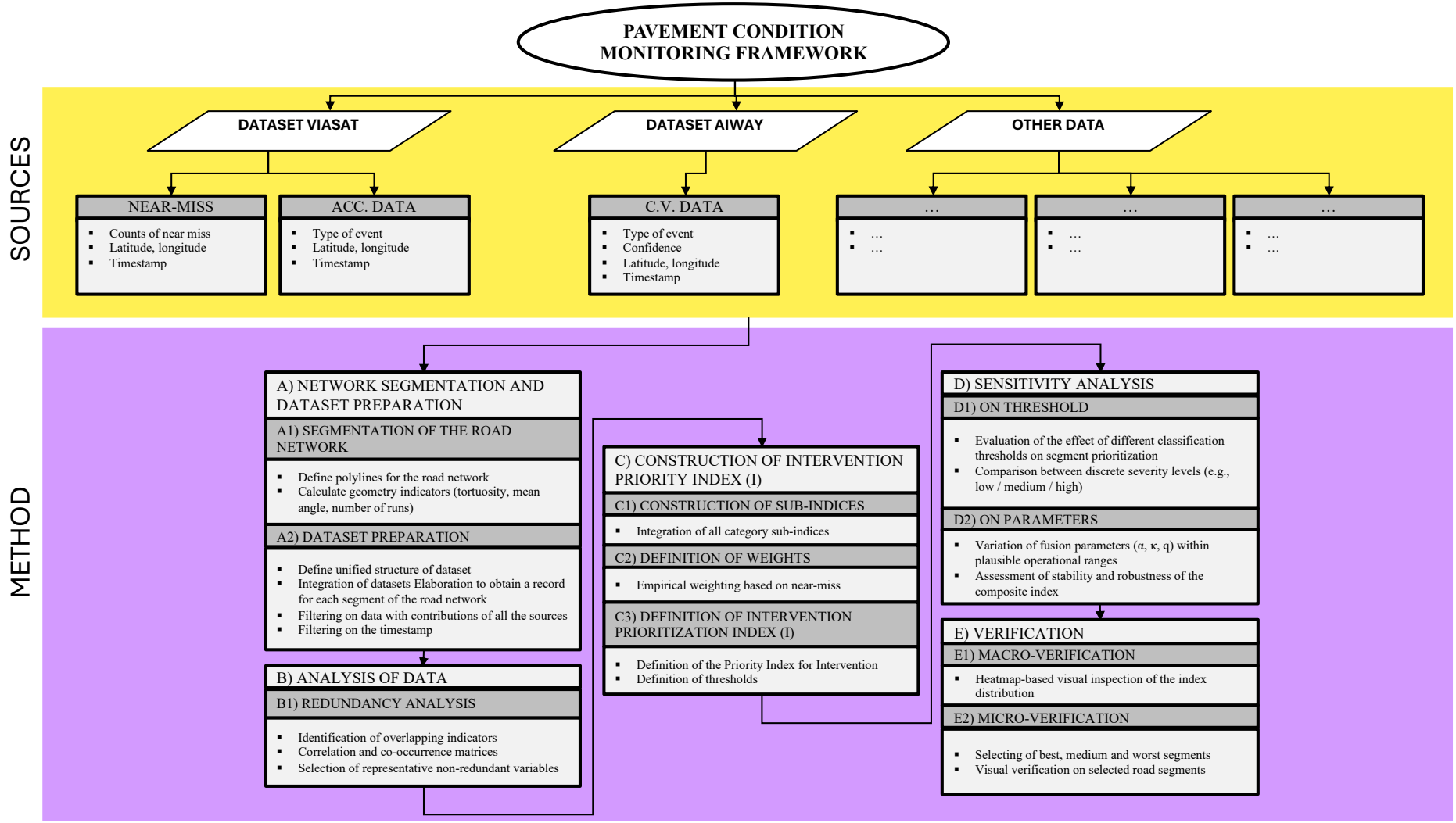

Figure 43 - Conceptual framework for the construction of Intervention Priority Index

5.1. A) Network segmentation and dataset preparation

5.1.1. A1) Segmentation of the road network

The segmentation of the road network is the preliminary step that transforms the continuous roadway geometry into discrete analytical units suitable for spatial aggregation and subsequent modeling. The network was represented as a set of polylines in a projected metric coordinate system, preserving Euclidean distances and angular relationships essential for computing geometric indicators such as curvature and turning angles. Each polyline was defined as an ordered sequence of vertices describing the planimetric alignment of the road. Discretization was carried out by performing linear interpolation along each polyline at regular spatial intervals, whose length can be adapted to the analytical resolution required for segment-level modeling. and the resulting interpolation points were used as boundaries for generating homogeneous segments in terms of spatial length and geometric continuity.

Algorithm 16 - SegmentRoadNetwork

```
Line    Pseudocode
1       Algorithm SegmentRoadNetwork(GIS_Roads) → SegmentedRoads
2         for each Road in GIS_Roads do
3           geometry ← Road.shape
4           points ← interpolate every 100m along geometry
5           segment_list ← empty list
6           for i from 0 to len(points)-2 do
7             segment ← create polyline from points[i] to points[i+1]
8             if segment intersects with intersection then
9               adjust endpoint to match junction
10            tag segment with attributes (id, name, city)
11            segment_list.append(segment)
12          end for
13          SegmentedRoads.add(segment_list)
14        end for
15      return SegmentedRoads
```

Where interpolation breakpoints coincided with intersections, roundabouts, or other topological nodes, segments were trimmed according to network connectivity rules to ensure geometric and functional continuity. This procedure guarantees that each segment corresponds to a structurally consistent portion of the roadway, suitable for

serving as the minimal unit of analysis and for integrating static attributes, sensor-based observations, and geometric descriptors.

Once the segmentation layer was established, each segment was treated as an ordered list of points $p_k = (x_k, y_k)$, where k indexes the vertices used to compute the three geometric indicators. All geometric indicators were computed in consistent metric units and standardized to zero mean and unit variance to ensure comparability across segments before inclusion in subsequent analyses.

The first indicator, tortuosity, measures the overall deviation of a segment from a straight-line path. Let L_{curved}denote the curved length of the polyline, computed as the sum of Euclidean distances between successive vertices, and let L_{linear} be the Euclidean distance between the first and last point of the segment. Tortuosity is defined as:

Equation 17 - Tortuosity index expressing the ratio between the actual curved length of the road segment and the straight-line distance between its endpoints

$$T = \frac{L_{curved}}{L_{linear}}$$

where $L_{\text{curved}} = \sum_{k=2}^{n} \| p_k - p_{k-1} \|_2$and $L_{\text{linear}} = \| p_n - p_1 \|_2$.

Values of Tclose to 1 indicate straight or nearly straight alignments, whereas higher values reflect increasing curvature.

Algorithm 17 - ComputeTortuosity

```
Line    Pseudocode
1       Algorithm ComputeTortuosity(Segment) → T
2         points ← list of ordered coordinates (x₁, y₁), (x₂, y₂), ..., (xₙ, yₙ)
3         L_curved ← 0
4         for i from 1 to len(points) - 1 do
5           L_curved ← L_curved + distance(points[i-1], points[i])
6         end for
7         L_linear ← distance(points[0], points[-1])
8         if L_linear = 0 then
9           return 1  // avoid division by zero
10        else
11          T ← L_curved / L_linear
12          return T
13        end if
```

The second indicator, number of turns, captures the frequency of directional alternations along the segment. Let θ_k denote the turning angle computed at vertex p_k. A change in direction occurs when the sign of consecutive angles switches from positive to negative or vice versa. Using the sign function sign(·), the indicator is defined as:

Equation 18 - Number of turns, defined as the count of directional alternations along the segment, based on changes in the sign of consecutive turning angles

$$N_{turns} = \sum_{k=2}^{n-2} \mathbf{1}\big(\text{sign}(\theta_{k-1}) \cdot \text{sign}(\theta_k) = -1\big)$$

where $\mathbf{1}(\cdot)$ is the indicator function and where θ_k is the turning angle at vertex p_k, computed between consecutive direction vectors v_{k-1} and v_k.

Algorithm 18 - ComputeNumberOfTurns

```
Line    Pseudocode
1       Algorithm ComputeNumberOfTurns(Segment) → Nturns
2         angles ← compute turning angles between consecutive triplets of points
3         Nturns ← 0
4         for k from 1 to len(angles) - 1 do
5           if sign(angles[k-1]) × sign(angles[k]) = -1 then
6             Nturns ← Nturns + 1 end if
7         end for
8         return Nturns
```

The third indicator, mean turning angle, quantifies the average angular deviation along the segment. A segment is typically represented as a polyline composed of a sequence of vertices $P1, P2, \ldots, Pn$. At each intermediate vertex, an angle can be defined between two consecutive direction vectors as:

Equation 19 - Definition of consecutive direction vectors used to compute turning angles between polyline vertices

$$v_{\{k-1\}} = P_k - P_{\{k-1\}},\ v_k = P_{\{k+1\}} - P_k$$

The turning angle is then computed as:

Equation 20 - Turning angle at vertex k, calculated as the angle between consecutive direction vectors along the segment

$$\theta_k = \arccos\left(\frac{v_{k-1} \cdot v_k}{\| v_{k-1} \| \cdot \| v_k \|}\right)$$

The mean turning angle for the segment is given by:

Equation 21 - Mean turning angle for segment i, expressing the average angular deviation and overall geometric complexity along the road segment

$$\bar{\phi}_i = \frac{1}{(n-2)} \sum_{k=2}^{n-1} |\theta_k|$$

Here, n is the number of vertices that define the segment. By construction, $\bar{\phi}_i$ synthesizes the degree of bending present along the entire segment.

- Lower values of $\bar{\theta}_i$ correspond to segments that are nearly straight, with minimal directional changes.
- Higher values indicate segments with frequent or pronounced changes in alignment, reflecting greater geometric complexity.

Algorithm 19 - ComputeMeanTurningAngle

```
Line    Pseudocode
1       Algorithm ComputeMeanTurningAngle(Segment) → θ⁻
2         points ← list of ordered coordinates (P₁, P₂, ..., Pₙ)
3         angles ← empty list
4         for k from 1 to len(points) - 2 do
5           v₁ ← vector from points[k] - points[k - 1]
6           v₂ ← vector from points[k + 1] - points[k]
7           θ ← arccos( dot(v₁, v₂) / (norm(v₁) * norm(v₂)) )
8           angles.append(|θ|)
9         end for
10        if len(angles) > 0 then
11          θ⁻ ← mean(angles)
12        else
13          θ⁻ ← 0
14        return θ⁻
```

All geometric computations were performed in planar coordinates, neglecting elevation, since the network is predominantly two-dimensional. All geometric

indicators were standardized (z-score normalization) prior to their inclusion in subsequent statistical models, ensuring comparability across segments.

Taken together, these three indicators provide an orthogonal and complementary characterization of segment geometry: tortuosity captures global curvature accumulation, the number of turns reflects oscillatory complexity in alignment, and the mean turning angle describes the intensity of directional deviation. This geometric descriptor framework enables a compact, interpretable, and reproducible representation of roadway alignment structure at the scale of analysis defined through segmentation.

5.1.2. A2) Dataset preparation

The analytical dataset is constructed by integrating heterogeneous deterioration observations into a unified representation centered on road segments as the fundamental spatial reference unit. In Table 7 there is the definition of variables used in the dataset construction.

Table 7 - Definition of variables used in the dataset construction

Symbol	Definition	Level
p_j	Geographic coordinates of deterioration event j	Event
t_j	Timestamp of detection	Event
l_j	Distress category label assigned to the event	Event
s_j	Severity value (if available)	Event
c_j	Detection confidence (if available)	Event
L_i	Polyline geometry of road segment i	Segment
ℓ_i	Length of segment i (m)	Segment
$a(j)$	Segment index associated with event j	Mapping
$N_{i,k}$	Frequency of events of type k on segment i	Segment
$\bar{s}_{i,k}$	Mean severity for events of type k on segment i	Segment
$\bar{c}_{i,k}$	Mean confidence for events of type k on segment i	Segment
τ_i	Tortuosity of segment i	Segment geometry
m_i	Number of directional alternations (turns) along segment i	Segment geometry
$\bar{\phi}_i$	Mean turning angle between consecutive polylines	Segment geometry
g_i	Vector of geometric descriptors (τ_i, m_i, $\bar{\phi}_i$)	Segment geometry
K	Set of distress categories k	Category index
x_i	Final segment-level feature vector	Segment

Each deterioration observation is initially represented as a georeferenced point, equipped with a timestamp and a semantic label indicating the corresponding distress category.

Equation 22 - Definition of a deterioration event

$$e_j = (p_j, t_j, \ell_j, s_j, c_j)$$

where $p_j$denotes the geographic coordinates, $t_j$the timestamp, $\ell_j$the distress category, and s_j, c_jrepresent the optional severity and confidence attributes.

To express these observations in relation to the network, a spatial association procedure is defined in which the geometry of the road network is modeled as a collection of polylines, and each point is assigned to the segment whose polyline lies closest in Euclidean space, according to a deterministic proximity rule.

Equation 23 - Spatial assignment of events to road segments

$$\mathcal{S} = \{(i, \mathrm{L}_i)\}_{i=1}^{n}, \mathrm{L}_i \subset \mathbb{R}^2$$

$$a(j) = \arg\min_{i \in \{1,\dots,n\}} \min_{q \in \mathrm{L}_i} \| p_j - q \|_2)$$

where $a(j)$ identifies the segment $i$whose geometry $\mathrm{L}_i$lies at the minimum Euclidean distance from point p_j.

This ensures that the attribution of events to segments is reproducible, systematic, and free of heuristic assumptions. Multiple deterioration observations may therefore be associated with the same segment, reflecting the fact that distress manifestations can recur or cluster along the same roadway portion.
The Euclidean proximity rule was adopted for reproducibility; however, in dense urban settings, topological snapping along the road axis could further reduce potential misassignments.

At this stage, the dataset assumes an event-level structure, where each row corresponds to a single deterioration observation and the column headings include:

- the distress classifier category associated with the event;
- the geographic coordinates (latitude and longitude) of the detection point;
- the timestamp recording the moment of occurrence;
- the identifier of the segment to which the event is spatially assigned;
- the geometric descriptors associated with that segment (tortuosity, number of directional alternations, mean turning angle).

This representation preserves the fine spatial and temporal granularity of the sensing data while situating each event within the structural context of the roadway.

To enable comparative and model-based analyses at the network scale, the event-level dataset is subsequently aggregated. A temporal observation window is defined, and the dataset is filtered to include only events occurring within the selected period.

Equation 24 - Definition of the temporal observation window

$$\mathcal{T} = [t_0, t_1]$$

$$\mathbb{1}_{\mathcal{T}}(t_j) = \begin{cases} 1, & t_j \in \mathcal{T} \\ 0, & \text{otherwise.} \end{cases}$$

For each segment, all deterioration events falling within the temporal window are merged into a single consolidated segment-level record. During this aggregation process, the total frequency of distress occurrences is obtained through summation, while continuous attributes such as severity or detection confidence are averaged to produce representative summary values.

Equation 25 - Computation of distress occurrence frequency

$$N_{i,k} = \sum_{j:\, a(j)=i} \quad \mathbb{1}_{\mathcal{T}}(t_j)\, \mathbb{1}(\ell_j = k)$$

Equation 26 - Averaged severity within each segment

$$\bar{s}_{i,k} = \frac{1}{N_{i,k}} \sum_{\substack{j:a(j)=i \\ \ell_j=k}} \quad \mathbb{1}_{\mathcal{T}}(t_j)\, s_j$$

Equation 27 - Averaged detection confidence within each segment

$$\bar{c}_{i,k} = \frac{1}{N_{i,k}} \sum_{\substack{j:a(j)=i \\ \ell_j=k}} \mathbb{1}_{\mathcal{T}}(t_j)\, c_j$$

The geometric indicators remain invariant, as they constitute intrinsic properties of the segment's alignment rather than characteristics of the events themselves.

Equation 28 - Segment-level geometric descriptors

$$\mathrm{g}_i = (\tau_i, m_i, \bar{\phi}_i)$$

where τ_i is tortuosity, m_i the number of directional alternations, and $\bar{\phi}_i$ the mean turning angle.

The resulting dataset contains one record per segment and integrates geometric structure, localized deterioration evidence, and temporal occurrence information within a single, coherent analytical framework. This representation maintains fidelity to the spatial organization of the road network while enabling scalable interpretation and comparison across segments, thereby providing a suitable foundation for the development of composite condition indices and subsequent decision-support analyses.

Equation 29 - Segment-level feature vector integrating geometry and deterioration evidence

$$\mathrm{x}_i = (\ell_i, \mathrm{g}_i, \{N_{i,k}, \bar{s}_{i,k}, \bar{c}_{i,k}\}_{k\in\mathcal{K}})$$

where ℓ_i is the segment length, and $\mathrm{g}_i = (\tau_i, m_i, \bar{\phi_i})$ represents the geometric descriptors (tortuosity, number of directional alternations, and mean turning angle).

Although the geometric attributes $g_i = (\tau_i, m_i, \bar{\phi}_i)$are intrinsic properties of each segment, their values may vary depending on the adopted segmentation length. To assess the stability of these descriptors across different spatial resolutions, the distribution of each geometric indicator is summarised for multiple segment lengths

L. For each length, sample moments and the coefficient of variation are computed as in Equation 30.

Equation 30 - Computation of sample moments and coefficient of variation across segment lengths

$$\bar{x}_L = \frac{1}{n_L} \sum_{i=1}^{n_L} x_{L,i}$$

$$s_L^2 = \frac{1}{n_L - 1} \sum_{i=1}^{n_L} (x_{L,i} - \bar{x}_L)^2$$

$$\mathrm{CV}_L = \frac{s_L}{\bar{x}_L}$$

where:

- $x_{L,i}$ is the indicator value (e.g., tortuosity, mean turning angle, number of turns) for segment i at length L;
- n_L is the number of segments at that length; s_L^2 is the sample variance;
- CV_L is the coefficient of variation used to assess scale sensitivity.

This analysis supports the interpretation of geometric indicators by identifying whether their variability is inherent to road alignment or induced by the segmentation granularity.

5.2. B) Analysis of data

5.2.1. B1) Redundancy analysis

One of the most delicate aspects in the development of a composite deterioration index lies in the management of redundancy among variables. When integrating data collected through heterogeneous technologies, the risk of overlapping information becomes particularly relevant. Indeed, the same physical phenomenon may be

described by different indicators, either because it is observable through more than one sensing modality, or because different classification schemes assign separate tags to what, in practice, represents a similar type of distress.

Redundancy is not inherently negative. On the contrary, the simultaneous detection of the same phenomenon by independent sources can be regarded as a valuable form of validation, increasing confidence in the reliability of the observation. However, if redundant variables are incorporated without control, the composite index may suffer from double counting, artificially inflating the level of deterioration attributed to a given segment. This distortion would ultimately compromise the interpretability of the indicator and undermine its usefulness as a decision-support tool for road management.

For these reasons, redundancy must be treated explicitly within the methodological framework. In this research, the chosen approach is based on two complementary phases. In the first phase, potential redundancies are identified both on a conceptual and on an empirical basis. These hypotheses are tested through statistical analyses, including correlation coefficients, co-occurrence rates at the segment level, and dimension-reduction techniques such as Principal Component Analysis. The combination of semantic interpretation and statistical validation makes it possible to move beyond intuition and to provide evidence-based confirmation of the presence of dependencies.

Empirical redundancy is flagged when similarity measures exceed data-driven thresholds.

In the second phase, harmonisation rules are defined to manage the identified redundancies. These rules are designed to preserve the added value of multiple detections, while avoiding distortions in the index. Depending on the case, harmonisation may involve attenuating the weight of one variable when a more direct indicator is available, merging two correlated variables into a single synthetic measure, or excluding the contribution of an indicator when a corrective tag signals that the anomaly is not due to actual pavement distress. In this way, redundancy is not treated as a weakness to be eliminated, but as a resource to be interpreted and balanced, ensuring that the resulting index remains both comprehensive and robust.

Algorithm 20 - ManageRedundancyPairs

```
Line    Pseudocode
1       Algorithm ManageRedundancyPairs → harmonised dataset
2       For each segment i in SEGMENTS
3         For each vision class d
4           n(d,i) ← count of detections; p¯(d,i) ← mean confidence
5           D(d,i) ← p¯(d,i) × n(d,i)
6         End for
7         For each accelerometric type k
8           T(k,i) ← count of detections
9         End for
10        Normalize per length of the segment and time window
11      End for
12      Compute Pearson r, co-occurrence (ϕ), and PCA on {D̃, T̃}
13      Identify redundant pairs and corrective tag
14      For each segment i
15        Compute corrective gate gᵢ
16        Fuse redundant pairs
17      End for
18      Return harmonised dataset with fused and corrected variables
```

The algorithm outputs a harmonised table containing one record per segment with fused indicators and corrective gates applied.

Operationally, I model the information at the road-segment level and make all design choices explicit so that redundancy is detected and handled before constructing the index. In Table 8 there is the definition of variables used in the redundancy analysis.

Table 8 - Definition of variables used in the redundancy analysis

Symbol	Definition	Level / Meaning
i	Index of the road segment	Segment
d	Index of vision-based distress class	Vision modality
k	Index of accelerometric distress type	Accelerometric modality
m	Index of contextual or corrective tag	Contextual layer
$n(d,i)$	Number of detections of vision class d on segment i	Raw count
$\bar{p}(d,i)$	Mean confidence associated with detections of class d on segment i	Confidence level
$D(d,i)$	Vision-based indicator, computed as $\bar{p}(d,i) \times n(d,i)$	Vision intensity measure
$T(k,i)$	Accelerometric indicator, number of vibration detections of type k on segment i	Accelerometric intensity
$V(i,d)$	Vision indicator for class d on segment i, equivalent to D(d,i) after normalisation	Vision modality variable
$A(i,k)$	Accelerometric indicator for class k on segment i, weighted by reliability factor q_k	Accelerometric modality variable
q_k	Reliability coefficient associated with accelerometric class k (0–1)	Modality reliability
$C(i,m)$	Contextual or corrective tag for element m (e.g., manhole, crosswalk)	Context variable
g_i	Corrective gate attenuating accelerometric contribution when contextual evidence is present	Correction factor

κ	Attenuation parameter controlling the steepness of $g_i = \exp(-\kappa C_i)$	Hyperparameter
$\tilde{X}_i$	Quantity X_i normalized by segment length and time window: $\tilde{X}_i = 100/\ell_i \times X_i/T_i$	Normalized variable
T_i	Duration of the observation window for segment i	Temporal normalization factor
ℓ_i	Length of road segment i (m)	Spatial normalization factor
$log(1+X)$, $\sqrt{(X)}$	Monotone variance-stabilising transforms applied to skewed or zero-inflated variables	Data transformation
$\phi(d,k)$	Co-occurrence rate between vision and accelerometric detections at segment level	Redundancy diagnostic
$r(d,k)$	Pearson correlation coefficient between normalized indicators	Redundancy diagnostic

Each segment carries vision indicators $V_{i,d}$ for classes d (computed, whenever available, as expected counts $V_{i,d} = \bar{p}_{i,d}\, n_{i,d}$ with $\bar{p}_{i,d} \in [0,1]$ the average confidence and $n_{i,d}$ the detections), accelerometric indicators $A_{i,k}$ for classes k (typically counts without an intrinsic confidence, weighted by class-specific reliability factors $q_k \in [0,1]$), and context/corrective tags $C_{i,m}$ for elements that can trigger sensor responses not attributable to distress. Here, $d$indexes classes derived from image-based surface distress detection and $k$indexes classes derived from inertial or vibration-based sensing; $m$indexes contextual or corrective tags. This notation is general and does not depend on any specific labeling convention adopted in the data sources.

To ensure comparability across different exposures, every quantity is normalised per length of segment and per time unit if relevant, i.e. $\tilde{X}_i = \frac{100}{\ell_i}\frac{X_i}{T_i}$ with ℓ_i the segment length and T_i the observation window; in the presence of heavy tails or many zeros I apply the same monotone variance-stabilising transform to all members of a potentially redundant pair, typically $\log(1+\tilde{X})$ or $\sqrt{\tilde{X}}$, so that relative ordering is preserved.

At multivariate level, redundancy patterns were further validated through Principal Component Analysis. Let $X_{(i,j)}$denote the standardized value of variable $j$for segment i, $l_{(j,p)}$the loading of variable $j$on principal component p, and $z_{(i,p)}$the corresponding component score.

Equation 31 – Principal component scores for each segment

$$z_{(i,p)} = \sum_j X_{(i,j)}\; l_{(j,p)}$$

This formulation clarifies how segment-level indicators project onto latent structures that summarize shared information among variables. High absolute loadings $l_{(j,p)}$indicate groups of indicators contributing to the same underlying mechanism, while clusters of segments with similar scores $z_{(i,p)}$confirm consistent redundancy patterns at network scale. In this framework, PCA provides an additional, model-agnostic diagnostic supporting the harmonisation rules applied in the construction of the composite index.

5.3. C) Construction of Intervention Priority Index (I)

5.3.1. C1) Construction of sub-indices

The construction of category-level sub-indices follows a transparent and rule-based procedure, designed to translate the empirical relationships identified in the redundancy phase into structured and interpretable constructs.

Building upon the redundancy management framework, elementary indicators are aggregated into coherent categories of pavement distress. The grouping is not arbitrary: redundancy diagnostics consistently revealed stable clusters of co-varying variables, ensuring that each category reflects a meaningful and empirically validated degradation mechanism. In Table 9 there is the definition of variables used in the construction of category-level sub-indices.

Table 9 - Definition of variables used in the construction of category-level sub-indices

Symbol	Definition	Level / Meaning
t	Index of distress category (e.g., cracking, rutting, roughness)	Category
F_t	Set of indicators associated with category t	Category
i	Index of road segment	Segment
j	Index of indicator within the category	Variable
$X^*(_{i,j})$	Preprocessed (normalized and variance-stabilized) indicator value	Segment variable
$\tilde{w}_{(t,j)}$	Raw intra-category weight proportional to variance and inverse redundancy	Weight component
$\bar{\rho_j}$	Average absolute Pearson correlation of indicator j with others in F_t	Redundancy measure
$Var(X_j)$	Empirical variance of indicator j across all segments	Dispersion measure
$w_{(t,j)}$	Normalized intra-category weight: $\tilde{w}_{(t,j)} / \Sigma_{h \in F_t} \tilde{w}_{(t,h)}$	Final intra-category weight
$S_{(t,i)}$	Category-level sub-index for segment i and category t	Category output
$\tilde{Dd}_{,i)}$	Normalized vision-based detection for class d on segment i	Vision signal

$T(k,i)$	Normalized accelerometric detection for type k on segment i	Accelerometric signal
$\alpha(d,k)$	Fusion coefficient controlling balance between vision and accelerometric contributions (0–1)	Fusion parameter
q_k	Reliability coefficient for accelerometric signal k (0–1)	Reliability weight
C_i	Contextual evidence (sum or weighted combination of contextual tags $C_{i,m}$)	Contextual variable
κ	Attenuation parameter controlling steepness of the corrective gate	Hyperparameter
g_i	Corrective gate $\exp(-\kappa C_i)$ reducing accelerometric contribution when contextual elements are present	Correction factor
α, κ, q	Hyperparameters explored in sensitivity analyses	Model controls
$log(1+x)$, $\sqrt{x}$	Monotone variance-stabilising transforms used for skewed distributions	Data preprocessing
$S_i^{(d,k)}$	Fused sub-index combining vision and accelerometric indicators for pair (d,k)	Cross-modality sub-index

Let F_t denote the set of indicators associated with distress category t. For segment i, the category-level sub-index is defined as:

Equation 32 - Category-level sub-index combining normalized indicators within distress category t, where intra-category weights reflect each variable's variance and inverse redundancy

$$S_{t,i} = \sum_{j \in \mathcal{F}_t} w_{t,j}^{(\text{in})} \; X_{i,j}^{*}$$

where $X_{(i,j)}^{*}$ are the preprocessed (normalized and stabilized) variables, and $w_{(t,j)}^{(in)}$ are intra-category weights expressing the relative informative contribution of each indicator.

For categories including a single variable ($| F_t | = 1$), Equation 32 naturally collapse to the following simplified form:

Equation 33 - Simplified category-level sub-index for non-redundant categories

$$S_{(t,i)} = X_{(i,j)}^{*}$$

In this case, intra-category weighting becomes unnecessary ($w_{(t,j)}^{(in)} = 1$), and the sub-index directly coincides with the normalized indicator.

To ensure that the sub-index emphasizes indicators providing unique and non-redundant information, the weights are computed through a variance–redundancy balancing rule.

Let $\mathrm{Var}(X_j)$ be the empirical variance of indicator X_j across segments, and $\bar{\rho}_j$ the average absolute Pearson correlation of X_j with all other indicators in F_t. The raw weight is defined as:

Equation 34 - Raw intra-category weighting based on variance and inverse redundancy

$$\widetilde{w}_{t,j} = \mathrm{Var}(X_j) \cdot (1 - \bar{\rho}_j)$$

Weights are then normalized to sum to one within each category:

Equation 35 - Category-level normalization ensuring convex aggregation

$$w_{t,j}^{(\mathrm{in})} = \frac{\widetilde{w}_{t,j}}{\sum_{h \in F_t} \widetilde{w}_{t,h}}$$

This weighting scheme follows established approaches for composite indicator construction, where the contribution of each variable is proportional to its unique information content and inversely related to redundancy within the group [80] [81] [82]. In this sense, the variance–redundancy criterion operationalises an objective and data-driven allocation of weights, avoiding subjective or expert-based assignments.

This formulation assigns greater influence to indicators that contribute distinct and non-overlapping information (higher variance and lower redundancy), preventing the over-weighting of highly correlated variables and improving both interpretability and numerical stability of the sub-index construction.

When two complementary sensing modalities describe the same category (e.g., vision-based and accelerometric detections of depressions or roughness), a cross-modality fusion rule is adopted to integrate them into a single synthetic sub-index.

Equation 36 – Category-level fusion of visual and accelerometric signals for distress channel (d,k)

$$S_i^{(d,k)} = \alpha_{d,k}\,\widetilde{D}_{d,i} + \left(1-\alpha_{d,k}\right) q_k\, g_i\, \widetilde{T}_{k,i}$$

where:

- $\widetilde{D}_{(d,i)}$and $\widetilde{T}_{(k,i)}$are the normalized vision-based and accelerometric detections, respectively;
- $\alpha_{(d,k)} \in [0,1]$controls the fusion balance between the two sensing modalities;
- $q_k \in [0,1]$scales the accelerometric contribution according to signal reliability;
- $g_i = \exp(-\kappa C_i)$ with $k > 0$ is a corrective gate that attenuates accelerometric contributions in the presence of contextual elements (e.g., manholes), with κ controlling the steepness of attenuation and $C_i$representing the contextual evidence associated with segment i.

The hyperparameters $\alpha_{(d,k)}, q_k$ and κ are treated as methodological controls rather than fitted coefficients. They define the baseline configuration and are calibrated in the application chapter; the methodology remains agnostic to their numeric values.

They can be systematically varied in a structured sensitivity analysis to assess the robustness of the composite index under different assumptions about modality balance and contextual correction.

Through this formulation, the sub-indices $S_{(t,i)}$encapsulate both intra-category structure and cross-modality fusion, providing a consistent and interpretable foundation for higher-level aggregation into the composite pavement deterioration index.

It is methodologically appropriate to vary α, κ, and q because (i) α governs the trade-off between specificity (vision) and coverage (accelerometry), (ii) κbalances the risk of false positives in dense manhole environments, and (iii) $q$reflects reliability evidence without requiring structural changes to the pipeline. All other design choices are kept fixed to avoid confounding: the redundancy crosswalk, the monotone variance-stabilising transform applied consistently within each potentially redundant pair (log(1+x) or $\sqrt{x}$), the imputation/attenuation rules for missingness, and the per-exposure normalisation $\tilde{X}_i = \frac{100}{\ell_i}\frac{X_i}{T_i}$.

Through this formulation, $S_{t,i}$ encapsulates both intra-category weighting (variance–redundancy balance) and cross-modality fusion (visual–accelerometric integration), providing a consistent and interpretable basis for higher-level index construction.

Algorithm 21 - BuildCategorySubIndices

```
Line    Pseudocode
1       Algorithm BuildCategorySubIndices(HARMONISED_DATA) → S(t,i)
2       Define category sets Ft
3       For each category t in Ft
4         Compute intra-category weights using variance-correlation criteria
5         For each segment i
6           Compute sub-index S(t,i) as weighted sum of indicators
7           Apply corrective gate to accelerometric variables if contextual tags
        C(i,m) are active
8         End for
9       End for
10      Return vector of sub-indices S(t,i) per segment
```

The outcome of this step is a structured representation of each road segment in terms of a vector of sub-indices $S_{t,i}$, each corresponding to a well-defined type of deterioration. This layered representation offers two key advantages: (i) it ensures interpretability by aligning the analytical units with engineering notions of distress, and (ii) it provides a flexible basis for subsequent weighting against safety outcomes and geometric factors, thereby enabling the construction of a composite deterioration index that is both data-driven and operationally meaningful.

This framework ensures that the integration of heterogeneous sensing sources results in a statistically consistent, interpretable, and reproducible composite indicator, ready to support data-driven maintenance prioritisation and safety analysis.

5.3.2. C2) Definition of weights

The methodological approach adopted in this research is grounded in the application of statistical models specifically designed for count data, with the aim of rigorously analysing the relationship between infrastructure characteristics and near-miss frequency [83]. Since the number of near-misses observed on each road segment is a discrete, non-negative variable, the use of models tailored for count processes is essential. The overall framework was structured as a sequential and modular

procedure, in which each step builds on the results of the previous one, ensuring both diagnostic reliability and methodological flexibility. In Table 10 there is the definition of variables and parameters used in near-miss-based weighting.

Table 10 - Definition of variables and parameters used in near-miss-based weighting

Symbol	Definition	Level / Meaning
i	Index of road segment	Observation unit
Y_i	Observed number of near-misses on segment i	Dependent variable
μ_i	Expected mean near-miss frequency for segment i	Modelled mean
$E[Y_i]$	Expected value of the near-miss count variable	Theoretical mean
$\beta_0, \beta_1 \dots \beta_p$	Regression coefficients for intercept and predictors	Model parameters
$\hat{\beta}$	Estimated coefficient vector from the fitted model	Estimated parameters
β_t	Coefficient associated with category-level sub-index $S_{(t,i)}$	Category effect
$\beta_t^+ = max(\beta_t, 0)$	Non-negative coefficient enforcing monotonicity	Post-estimation constraint
$W_t = \beta_t^+ / \Sigma_u \beta_u^+$	Normalised category weight ($\Sigma W_t = 1$)	Composite-index weighting
$X_{i1} \dots X_{ip}$	Explanatory variables (geometry, exposure, sub-indices)	Predictors
$offset_i$	Exposure term (ln ℓ_i or ln traffic × length)	Normalisation factor
ℓ_i	Segment length used as exposure proxy (m)	Offset component
n	Number of observations (segments)	Sample size
p	Number of estimated coefficients (including intercept)	Model dimension
$Var(Y)$	Variance of the near-miss count variable	Dispersion measure
$\hat{\phi}_Pearson$	Pearson dispersion statistic = $\Sigma((y_i-\hat{\mu}_i)^2/\hat{\mu}_i)/(n-p)$	Overdispersion diagnostic
α	Dispersion parameter in NB2 model controlling $Var(Y)=\mu+\alpha\mu^2$	Overdispersion coefficient
$\hat{\alpha}$	Estimated dispersion parameter	Estimated overdispersion
$\Gamma(\cdot)$	Gamma function used in NB2 likelihood	Mathematical function
$ln\ L(\beta, \alpha)$	Log-likelihood function of Poisson/NB2 model	Fit measure
π_i	Probability that segment i belongs to the structural-zero state	Inflation component
δ_h	Coefficients of the zero-inflation model	Logit parameters
AIC, BIC	Information criteria ($2k - 2 \ln L$; $\ln(n)k - 2 \ln L$)	Model-selection metrics

5.3.2.1.Preliminary diagnostics: OLS and multicollinearity

As a first step, an Ordinary Least Squares (OLS) regression model was estimated. While OLS is not theoretically appropriate for count data, its role here is primarily diagnostic. The linear regression provides an initial overview of the potential associations between predictors and the dependent variable, offering insights into the sign and magnitude of coefficients.

A critical aspect of this stage is the assessment of multicollinearity, i.e. the presence of strong linear correlations among the independent variables. Multicollinearity occurs when two or more predictors convey almost identical information, for instance, two measures that capture very similar aspects of road geometry. Although multicollinearity does not bias the overall fit of the model, it has several negative

consequences: coefficient estimates become unstable, standard errors increase, and the interpretation of individual effects becomes unreliable.

To diagnose multicollinearity, the Variance Inflation Factor (VIF) is computed for each regressor [84]. The VIF measures how much the variance of an estimated coefficient is inflated due to linear dependencies with other predictors. Values close to 1 suggest the absence of collinearity; values around 5-10 indicate moderate correlation; values substantially above 10 signal severe multicollinearity and the potential need to reconsider variable inclusion. This diagnostic step is therefore essential to ensure that the modelling process does not rely on redundant information.

While OLS provides a useful preliminary indication of coefficient stability and allows the detection of multicollinearity through VIF diagnostics, it is not theoretically suited for modelling near-miss counts, which are discrete, non-negative, and typically characterized by skewed distributions and excess variance. For this reason, the analysis proceeds with statistical models specifically designed for count data [85].

5.3.2.2.Poisson regression

To properly model near-miss frequency, a generalized linear model (GLM) with a Poisson distribution and log link function is adopted. This model ensures that predicted values remain non-negative and interpretable in terms of multiplicative effects on near-miss risk. The Poisson formulation allows the expected number of near-misses to be expressed as a log-linear function of infrastructure characteristics, with an exposure offset term included to account for systematic differences in segment length or traffic volume.

Equation 37 - Generalized linear model specification for count data, linking the expected near-miss frequency μ_i to a log-linear combination of predictors and an exposure offset term ensuring non-negative, interpretable outcomes

$$E[Y_i] = \mu_i = \exp(\beta_0 + \beta_1 X_{i1} + \cdots + \beta_p X_{ip} + offset_i)$$

This formulation ensures that the predicted values are always non-negative and interpretable in terms of relative risks. An offset term can also be included, typically to account for exposure factors such as road length or traffic volume, so that near-miss

counts are normalized by the level of risk exposure. In the absence of detailed traffic exposure data, a simplified offset structure can be adopted in which only the segment length (or, more generally, an available exposure proxy) is included. This assumption must be made explicit, as it conditions the interpretation of fitted coefficients. The modelling framework remains valid and reproducible under this setting, and can be naturally extended to incorporate traffic volume data whenever such information becomes available. The offset therefore reflects only the segment length, under the assumption of comparable observation windows and broadly similar traffic exposure. This assumption, explicitly acknowledged, allows the model to remain fully reproducible without introducing uncertain or imputed data.

A central assumption of the Poisson model is equidispersion, meaning that the variance of the dependent variable equals its mean ($Var(Y) = E[Y]$). In practice, however, many empirical near-miss datasets display overdispersion, where the variance substantially exceeds the mean. Overdispersion may arise due to unobserved heterogeneity across road segments or omitted risk factors. If ignored, it leads to underestimated standard errors, artificially inflated test statistics, and misleading conclusions about the significance of predictors.

To detect overdispersion, the Pearson dispersion statistic is computed as the ratio between the Pearson chi-square statistic and the residual degrees of freedom. Values close to 1 indicate that equidispersion holds, whereas values significantly greater than 1 reveal the presence of overdispersion.

Equation 38 - Pearson dispersion statistic for assessing overdispersion in Poisson count models

$$\hat{\phi}_{Pearson} = \frac{\sum_{i=1}^{n} \frac{(y_i - \hat{\mu}_i)^2}{\hat{\mu}_i}}{n - p}$$

where:

- y_i= observed near-miss count on segment i;
- $\hat{\mu}_i$= predicted mean near-miss frequency from the fitted Poisson model;
- n= number of observations (road segments);
- p= number of estimated coefficients, including the intercept.

Values of $\hat{\phi}_{Pearson}$ close to 1 indicate equidispersion; values > 1 suggest overdispersion. This statistic quantifies the ratio between observed and expected variance; values > 1.2 are conventionally interpreted as evidence of overdispersion.

Algorithm 22 - FitPoissonModel

```
Line    Pseudocode
1       Algorithm   FitPoissonModel(DataFile,   yVar,   xVars,   OffsetVar)   →
        PoissonResults
2       data ← read DataFile (xlsx or csv)
3       rename columns with valid MATLAB identifiers
4       y ← data[yVar]; X ← data[xVars]; offset ← data[OffsetVar] if available else
        zeros
5       remove rows with NaN(y) or NaN(X)
6       Xz ← zscore(X) // standardize predictors for OLS diagnostics
7       lm ← fitlm(y ~ Xz) // preliminary OLS regression
8       VIF ← computeVIF(Xz) // Variance Inflation Factor per predictor
9       if any(VIF > 10) then flag severe multicollinearity
10      formula ← yVar ~ xVars with log link and offset
11      glmPo ← fitglm(data, formula, 'poisson', 'log', 'Offset', offset)
12      μ^ ← predict(glmPo, data)
13      AIC_P ← 2·k − 2·logLik(glmPo)
14      PearsonDisp ← Σ((y−μ^)²/μ^)/(n−k)
15      if PearsonDisp > 1.2 then flag overdispersion = TRUE
16      IRR ← exp(glmPo.Coefficients) // incidence rate ratios
17      output ← {β^, SE, AIC_P, PearsonDisp, IRR, logLik}
18      return output
```

5.3.2.3.Negative Binomial regression (NB2)

When overdispersion is present, the methodological framework shifts to the Negative Binomial regression model, specifically the NB2 formulation. This model relaxes the restrictive assumption of equidispersion by introducing an additional dispersion parameter α, such that the variance is parameterized as:

Equation 39 - Variance function of the NB2 model, introducing the dispersion parameter α to account for overdispersion in near-miss count data relative to the Poisson assumption

$$Var(Y) = \mu + \alpha\mu^2$$

In Equation 39, $\mu = E[Y]$ and $\alpha > 0$ directly measures the degree of overdispersion. When $\alpha \approx 0$, the NB2 model reduces to the Poisson case; as α increases, the variance grows more rapidly with the mean, allowing for greater flexibility in modelling heterogeneous near-miss data.

Estimation of the NB2 model is performed via Maximum Likelihood Estimation (MLE). Because the likelihood function does not have a closed-form solution, numerical optimization is required.

Equation 40 - Log-likelihood function of the NB2 model used for Maximum Likelihood Estimation

$$\ln L(\beta,\alpha) = \sum_{i=1}^{n} [\ln \Gamma\left(y_i + \frac{1}{\alpha}\right) - \ln \Gamma\left(\frac{1}{\alpha}\right) - \ln \Gamma\left(y_i + 1\right) + \frac{1}{\alpha}\ln\left(\frac{1}{1+\alpha\mu_i}\right) + y_i \ln\left(\frac{\alpha\mu_i}{1+\alpha\mu_i}\right)]$$

where:

- $\beta = (\beta_0, \beta_1, \ldots, \beta_p)$= vector of regression coefficients;
- $\alpha > 0$= dispersion parameter controlling deviation from the Poisson assumption;
- $\mu_i = \exp(x_i^T \beta + \text{offset}_i)$= expected mean near-miss frequency;
- $\Gamma(\cdot)$= gamma function;
- y_i= observed near-miss count for segment i;
- n= sample size.

In MATLAB, this is implemented using optimization routines such as $fminunc$ or $fminsearch$, depending on availability. The optimization procedure is initialized with the coefficient estimates from the Poisson model, which facilitates convergence and ensures more stable results.

Algorithm 23 - FitNB2Model

```
Line    Pseudocode
1       Algorithm FitNB2Model(Data, PoissonResults) → NB2Results
2       X_nb ← [1, X]; off ← offset; y ← Data[yVar]
3       β⁽⁰⁾ ← PoissonResults.β^; α⁽⁰⁾ ← 0.1; param₀ ← [β⁽⁰⁾; log(α⁽⁰⁾)]
4       Define nb2_nll(param, X_nb, y, off):
5           β ← param[1:end-1]; α ← exp(param[end])
6           μ ← exp(X_nb·β + off); Var(Y)=μ+αμ²
7           nll ← -Σ[ Γ(y+1/α) - Γ(1/α) - Γ(y+1) + (1/α)log(1/(1+αμ)) +
        y(log(αμ)-log(1+αμ)) ]
8       end function
9       if fminunc available then use quasi-newton else fminsearch (Nelder-Mead)
10      param^, fval, H ← minimize nb2_nll(param, X_nb, y, off) starting from param₀
11      β^ ← param^[1:end-1]; α^ ← exp(param^[end])
12      μ^ ← exp(X_nb·β^ + off); logLik_NB ← -fval
```

```
13      if Hessian H positive definite then SE ← sqrt(diag(inv(H))) else SE ← NaN
14      k ← length(paramˆ); n ← length(y)
15      AIC_NB ← 2·k − 2·logLik_NB; BIC_NB ← ln(n)·k − 2·logLik_NB
16      IRR ← exp(βˆ) // incidence rate ratios
17      compare AIC_NB vs AIC_Poisson; if AIC_NB < AIC_Poisson or overdispersion>1.2
        → prefer NB2
18      output ← {βˆ, SE, αˆ, AIC_NB, BIC_NB, IRR, logLik_NB}
19      return output
```

5.3.2.4.Zero-Inflated Negative Binomial (ZINB) model

In many real-world near-miss datasets, the distribution of near-miss counts is characterised not only by overdispersion but also by an excess of zero observations - segments for which no near-misses are ever recorded. These zeros can originate from two distinct mechanisms: (i) sampling zeros, where a near-miss could occur but was not observed within the monitoring period and (ii) structural zeros, where the probability of a near-miss is inherently negligible due to geometric, functional, or contextual features of the segment.

To explicitly represent this dual process, the analytical framework extends the NB2 formulation into a Zero-Inflated Negative Binomial (ZINB) model. The ZINB assumes that each observation belongs to one of two latent states: a zero-near-miss state with probability π_i, and an at-risk state governed by a standard Negative Binomial distribution with mean μ_i and dispersion α. The resulting probability mass function is expressed as:

Equation 41 - ZINB probability mass function

$$P(Y_i = y_i) = \begin{cases} \pi_i + (1-\pi_i) f_{\text{NB2}}(0 \mid \mu_i, \alpha), & y_i = 0 \\ (1-\pi_i) f_{\text{NB2}}(y_i \mid \mu_i, \alpha), & y_i > 0 \end{cases}$$

where f_{NB2} denotes the Negative Binomial density defined in Equation 35. The expected near-miss frequency μ_i is modelled through a log-linear specification identical to the NB2 count component:

Equation 42 - Log-linear specification of the count component

$$\log(\mu_i) = \beta_0 + \sum_{t=1}^{T} \beta_t S_{(t,i)} + \sum_{k=1}^{K} \gamma_k GEOM_{(i,k)} + \log(offset_i)$$

where:

- $\mu_i$denotes the expected mean near-miss frequency for segment i;
- $S_{(t,i)}$are the category-level sub-indices of deterioration;
- $GEOM_{(i,k)}$are geometric control variables (e.g., tortuosity, mean turning angle, number of turns);
- offset$_i$represents the exposure term (typically the logarithm of segment length or risk proxy).

While the zero-inflation probability π_i is defined through a logit equation:

Equation 43 - Logit formulation for the inflation component

$$\text{logit}(\pi_i) = \delta_0 + \sum_{h=1}^{H} \delta_h Z_{(i,h)}$$

where:

- $\pi_i$is the probability that segment i belongs to the structural-zero group;
- $Z_{(i,h)}$are covariates explaining the structural absence of near-misses (e.g., low exposure, controlled traffic conditions).

The logit function represents the canonical link between a linear predictor and a probability outcome in generalized linear models. It transforms probabilities, which are bounded between 0 and 1, into continuous values on the real line, thereby allowing standard linear modelling while preserving probabilistic interpretability.
Formally, the logit of a probability $\pi_i$is defined as

Equation 44 - Definition of the logit function

$$\text{logit}(\pi_i) = \ln\left(\frac{\pi_i}{1-\pi_i}\right)$$

where π_i denotes the probability of a structural zero (i.e., the probability that a segment belongs to the always-zero state in the zero-inflation component). The inverse of the logit, known as the logistic or sigmoid function, maps any real-valued input back into the [0,1] interval:

Equation 45 - Logistic transformation (inverse of the logit)

$$\pi_i = \frac{1}{1 + e^{-(\delta_0 + \sum_h \quad \delta_h Z_{(i,h)})}}$$

This transformation ensures that the predicted probability is always well defined, continuous, and bounded between zero and one.

Geometrically, the logit function produces an S-shaped logistic curve that smoothly connects the two asymptotes (0 and 1). Small changes in the linear predictor $\eta_i = \delta_0 + \sum_h \quad \delta_h Z_{(i,h)}$ produce large changes in probability when $\pi_i$is near 0.5, whereas extreme values of $\eta_i$approach saturation and yield probabilities very close to 0 or 1.

In the context of the Zero-Inflated Negative Binomial model, the logit function governs the inflation component, linking explanatory variables $Z_{(i,h)}$to the probability of structural zeros. This allows the model to distinguish between segments that are genuinely at risk of near-miss occurrence and those that are inherently zero-near-miss due to their geometric or contextual characteristics. The use of the logit transformation thus provides a mathematically consistent and interpretable way to model latent zero-generating processes within count data frameworks.

Estimation is performed via full-information Maximum Likelihood, jointly optimizing the parameters of both sub-models. The likelihood combines the contribution of the zero-state and the count-state components, ensuring coherent inference across the two processes.

Algorithm 24 - FitZINBModel

```
Line    Pseudocode
1       Algorithm FitZINBModel(Data, NB2Results, InflationVars) → ZINBResults
2       X ← [1, S, GEOM]; off ← offset; y ← Data[yVar]
3       Initialize parameters: β(0) ← NB2Results.β^; α(0) ← NB2Results.α^; δ(0) ← 0
4       Define zinb_nll(param, X, y, off, Z):
5          β ← param[1:end1]; α ← exp(param[end_1]); δ ← param[end]
6          μ ← exp(X·β + off) // expected near-miss frequency
7          π ← 1 / (1 + exp(-(Z·δ))) // zero-inflation probability
8          For each i:
9            If yi = 0 → pi ← πi + (1-πi)·f_NB2(0 | μi, α)
10           Else → pi ← (1-πi)·f_NB2(yi | μi, α)
11           nll ← -Σ log(pi)
12      End function
```

```
If fminunc available → use quasi-Newton else fminsearch (Nelder-Mead)
param^, fval, H ← minimize zinb_nll(param₀, X, y, off, Z) starting from [β^(0), log α^(0), δ^(0)]
β^ ← param^[1:end₁]; α^ ← exp(param^[end_1]); δ^ ← param^[end₀]
logLik_ZINB ← −fval; k ← length(param^); n ← length(y)
AIC_ZINB ← 2·k − 2·logLik_ZINB; BIC_ZINB ← ln(n)·k − 2·logLik_ZINB
If H positive definite → SE ← √diag(inv(H)) else SE ← NaN
Compute Wald p-values and IRR = exp(β^) for count component only
output ← {β^_count, α^, δ^, SE, AIC_ZINB, BIC_ZINB, IRR, logLik_ZINB}
return output
```

5.3.2.5.Coefficient interpretation and mapping to weights

Once the Poisson, NB2, and ZINB models are estimated, their relative performance is evaluated using likelihood-based information criteria - primarily the Akaike Information Criterion (AIC) and the Bayesian Information Criterion (BIC). These indices balance model fit against complexity, with lower values indicating a better trade-off between explanatory power and parsimony. The dispersion index is also examined to verify whether overdispersion and zero-inflation are adequately addressed.

For interpretability, regression coefficients are presented both in their raw log-scale and as Incidence Rate Ratios (IRR), defined as:

Equation 46 - Definition of the Incidence Rate Ratio (IRR)

$$\mathrm{IRR}_j = \exp(\beta_j)$$

The IRR quantifies the multiplicative change in expected near-miss frequency associated with a one-unit increase in a given predictor, holding all other variables constant. Expressing results in IRR form facilitates interpretation and communication, especially for non-specialist audiences.

Standard errors are estimated using robust (heteroskedasticity-consistent) variance estimators, ensuring valid inference even in the presence of residual heterogeneity across segments. IRRs are reported with 95% robust confidence intervals to guarantee statistical consistency under non-ideal data conditions.

Model selection between the standard NB2 and the ZINB specification relies on both information-criterion comparison and the Vuong test, which assesses the relative

superiority of non-nested models. A positive and statistically significant Vuong statistic indicates that the zero-inflated structure provides a superior description of the near-miss-frequency data.

Methodologically, the ZINB framework generalises the NB2 model by simultaneously addressing overdispersion (through α) and zero inflation (through π_i). This dual structure offers a flexible and realistic basis for analysing near-miss frequencies in heterogeneous road networks and ensures that subsequent weighting procedures reflect both latent safety conditions and observed near-miss variability.

Across all count specifications considered in this chapter (Poisson, NB2, and the count component of ZINB), the regression coefficients β_j are defined on the log scale. For any predictor X_j, the Incidence Rate Ratio (IRR) expresses the multiplicative change in the expected near-miss frequency associated with a one-unit variation in X_j, conditional on all other covariates and the exposure offset. Values above one indicate a risk-increasing effect, values below one a protective effect, and values around one suggest no significant association.

For category-level sub-indices $S_{(t,i)}$, the estimated coefficients β_t are used to derive non-negative and interpretable weights for the composite deterioration index. To ensure monotonicity with respect to deterioration and comparability across categories, coefficients are first truncated to non-negative values and then normalised:

Equation 47 - Truncation and normalisation of regression coefficients

$$W_t = \frac{\beta_t^+}{\sum_u \beta_u^+}$$

$$W_t \geq 0$$

$$\sum_t W_t = 1$$

These weights W_t represent the empirically validated contribution of each distress category to near-miss frequency, translating statistical associations into interpretable proportions within the composite structure.

In this framework, $\beta_t$coefficients act as empirical proxies for the marginal effect of each deterioration category on near-miss likelihood, while the normalisation step ensures that the overall composite index remains bounded, interpretable, and reproducible across datasets and model specifications.

Although all models share a common log-linear structure, their coefficients differ in statistical interpretation according to the underlying distributional assumptions. The following notes highlight these distinctions for the Poisson, NB2, and ZINB specifications:

- In the Poisson regression, the coefficients $\beta_t$describe the log-relative rate of near-miss occurrence under the assumption of equidispersion, i.e., that the variance equals the mean. This model provides a baseline estimate but may yield biased standard errors when overdispersion is present. As such, its β coefficients serve mainly as a reference for identifying direction and relative magnitude of effects, rather than for final weighting.
- In the NB2 specification, the coefficients $\beta_t$retain the same interpretation as in the Poisson model but account for overdispersion through the dispersion parameter α, which allows the variance to exceed the mean. The inclusion of αproduces more reliable standard errors and a more realistic estimate of uncertainty. The β coefficients from the NB2 model are thus statistically robust and provide the preferred basis for near-miss-based weighting when overdispersion is confirmed.
- In the ZINB model, only the coefficients of the count component (β_t) are used in the weighting scheme, as they quantify the relationship between deterioration and near-miss occurrence. The parameters of the inflation component (δ_h) describe the structural-zero mechanism, segments inherently not subject to near-misses, and are therefore excluded from the weighting process. This structure allows the ZINB to distinguish between structurally safe segments and those effectively exposed to risk.

Standard errors and p-values associated with the β_t coefficients are computed through the Wald test, following conventional significance thresholds (e.g., $p < 0.10$, $p < 0.05$, p

< 0.01). Offsets (such as segment length or exposure proxies) are consistently included in all models to normalise near-miss counts and maintain comparability between different network discretisations.

Through this unified interpretation, the estimated coefficients and derived weights provide a statistically grounded and behaviorally interpretable foundation for the subsequent construction of the composite deterioration index. This ensures that each component's contribution reflects both its physical meaning and its empirically validated association with safety outcomes.

Algorithm 25 - ComputeWeightsFromBetas

```
Line    Pseudocode
1       Algorithm ComputeWeightsFromBetas(BetaTable) → W
2       For each category t in BetaTable: β_t^+ ← max(β_t, 0)
3       sumPos ← Σ_u β_u^+
4       If sumPos = 0 → assign equal weights to positive β_t else W_t ← β_t^+ /
        sumPos
5       return table {category, β_t, β_t^+, SE, p_Wald, W_t, IRR}
```

5.3.3. C3) Definition of Intervention Priority Index (I)

On the basis of the category-level structure, the final step consists in assembling a composite deterioration index that integrates all sources of information into a single interpretable metric. In Table 11 there are variables and parameters used in the composite deterioration index.

Table 11 - Variables and parameters used in the composite deterioration index

Symbol	Definition	Level / Meaning
i	Index of road segment	Observation unit
t	Index of distress category	Category
$S_{(t,i)}$	Category-level sub-index for segment i and distress type t	Input variable
W_t	Category weight derived from near-miss-based calibration ($\Sigma W_t = 1$, $W_t \geq 0$)	Weight coefficient
I_i	Composite deterioration index for segment i	Final index output
β_0	Intercept term of the regression model	Model parameter
β_t	Coefficient estimated for sub-index $S_{(t,i)}$ in GLM/NB2 model	Category parameter
γ	Vector of coefficients for geometric control variables	Control parameters
$G(i)$	Vector of geometric descriptors for segment i (tortuosity, mean turning angle, number of turns)	Control input
$Y(i)$	Observed near-miss count for segment i	Dependent variable
$E[Y_i]$	Expected near-miss frequency according to fitted model	Model output
$log(E[Y_i])$	Log-link function relating predictors to expected near-miss frequency	GLM link

α, κ, q	Hyperparameters controlling modality fusion and contextual attenuation (from previous stages)	Sensitivity parameters

For each segment i, the index is defined as a convex combination of the category sub-indices:

Equation 48 - Composite deterioration index integrating all category-level sub-indices into a single interpretable metric through empirically estimated weights W_t

$$I_i = \sum_t W_t \, S_{t,i}$$

where $S_{t,i}$ are the sub-indices corresponding to distress category t, and W_t quantify the relative importance of each category and are estimated at category level via an NB2 regression linking near-miss counts to $S_{t,i}$, with geometric controls and an exposure offset $\log\left(\frac{L_i}{100}\right)$ when segment lengths vary.

The resulting index I_i thus expresses the severity-weighted expected intensity of distress per 100 m, corrected for redundancies, adjusted for functional elements, and calibrated against safety. By construction, it remains bounded, interpretable, and suitable for classification into severity levels (e.g. low, medium, high) through thresholding.

The robustness of the index is ensured by systematic validation, including grouped cross-validation to prevent spatial leakage, bootstrap resampling to quantify uncertainty in the weights, and sensitivity analyses over the fusion and correction parameters. In this way, the composite deterioration index represents a statistically grounded, transparent, and operational tool for prioritising maintenance interventions and supporting road asset management. Grouped folds were constructed so that contiguous segments belonging to the same road corridor were kept within the same group, avoiding spatial leakage between training and testing sets.

The composite index remains $I_i = \sum_t W_t \, S_{t,i}$ with $W_t \geq 0, \sum_t W_t = 1$, and crucially the top-level category weights W_t are data-driven (estimated from non-negative GLMs on near-miss counts with exposure offsets and geometric controls), so that parameter

changes only affect within-pair fusion and attenuation, not the between-category importance.

To assess the external validity of the composite deterioration index with respect to safety outcomes, a non-parametric rank-based association measure was computed between the index and the observed near-miss frequencies.

Equation 49 - Spearman rank correlation between composite index and near-miss frequency

$$\rho_{\text{index,safety}} = \text{Spearman}(I_i, Y_i)$$

where:

- I_i is the composite deterioration index for segment i;
- Y_i is the observed near-miss count for the same segment;
- $\rho_{\text{index,safety}} \in [-1,1]$ measures the monotonic agreement between deterioration ranking and near-miss frequency.

A positive and statistically significant value of $\rho_{\text{index,safety}}$ indicates that segments ranked as more deteriorated tend to correspond to segments exhibiting higher near-miss occurrence, thereby supporting the safety-oriented interpretability of the index.

Algorithm 26 - CalibrateCompositeDeteriorationIndex

```
Line    Pseudocode
1       Algorithm CalibrateCompositeDeteriorationIndex(SUBINDICES, GEOMETRY, NEAR-
        MISSES) → I
2       Input: S(t,i) = category sub-indices per segment i and category t
3       Input: G(i) = geometric variables (tortuosity, mean turning angle, number
        of turns)
4       Input: Y(i) = near-miss counts; EXP(i) = exposure (length × traffic volume)
5       Initialise β₀ ← 0; βₜ ≥ 0 (non-negative coefficients)
6       Fit non-negative GLM with log link:
7         log(E[Yᵢ]) = β₀ + Σₜ βₜ S(t,i) + γᵀ G(i) + log(EXP(i))
8       if overdispersion → use Negative Binomial (NB2) instead of Poisson
9       Compute normalised weights: Wₜ = βₜ / Σᵤ βᵤ
10      for each segment i in SEGMENTS do
11        Compute composite index: Iᵢ = Σₜ Wₜ × S(t,i)
12        Bound Iᵢ ∈ [0,1] if normalised for interpretability
13      end for
14      Validate robustness:
15        Perform grouped k-fold cross-validation (prevent spatial leakage)
16        Bootstrap βₜ estimates → compute confidence intervals for Wₜ
17        Conduct sensitivity analysis on (α, κ, q) parameters
18      return vector I of composite deterioration scores per segment
```

5.4. D) Sensitivity analysis

5.4.1. D1) Sensitivity analysis on classification thresholds

The robustness of the classification scheme derived from the composite deterioration index was evaluated through a sensitivity analysis on the threshold values used to discretise the continuous indicator. In network-level pavement management, the transition from a continuous deterioration measure to a set of discrete maintenance states is a necessary but non-unique step, since class boundaries must preserve both statistical coherence and engineering interpretability.

Equation 50 - Threshold-based classifier mapping the continuous deterioration index I_i into LOW, MEDIUM and HIGH condition classes defined by thresholds $\tau = (\tau_1, \tau_2)$

$$C_{\boldsymbol{\tau}}(I_i) = \begin{cases} \text{LOW}, & I_i < \tau_1 \\ \text{MEDIUM}, & \tau_1 \le I_i < \tau_2 \\ \text{HIGH}, & I_i \ge \tau_2 \end{cases}$$

where:

- I_i= composite deterioration index for road segment i;
- τ_1, τ_2= lower and upper classification thresholds;
- $C_{\boldsymbol{\tau}}(I_i)$= discrete maintenance class assigned to segment i.

The aim of the thresholding scheme is therefore not simply to maximise the separation between classes, but to generate stable, meaningful strata that remain consistent under moderate variations of the underlying data and modelling assumptions. Because classification thresholds influence the prioritisation of interventions, it is essential to verify that the resulting segmentation of the network is not overly sensitive to small modifications in threshold placement.

This aspect is particularly relevant in multi-source sensing contexts, where the composite index integrates heterogeneous indicators derived from different acquisition technologies, each characterised by distinct uncertainty profiles and spatial sensitivities. Demonstrating that the classification remains stable under controlled threshold adjustments provides indirect evidence that the index captures persistent

and structurally meaningful deterioration patterns, rather than artefacts introduced by any specific data source or preprocessing stage.

To assess robustness, two complementary forms of threshold variation were examined. In the first, the baseline thresholds were perturbed locally, within narrow deviation intervals, so as to evaluate whether small numerical changes induce disproportionately large reassignments of segments across classes. In the second, fixed cut-offs were replaced with distribution-based thresholds derived from the empirical quantiles of the index, allowing an assessment of whether the classification retains its interpretability when the boundaries are determined by statistical distribution properties rather than by predefined numerical criteria.

Equation 51 - Quantile-based thresholds used for distribution-driven classification

$$\tau_1 = Q_{p_1}(I)$$
$$\tau_2 = Q_{p_2}(I)$$
$$0 < p_1 < p_2 < 1$$

where:

- $Q_p(I)$= p-th empirical quantile of index I_i;
- p_1, p_2= selected quantile levels defining class boundaries.

Equation 52 - Overall class stability measuring the fraction of segments retaining the same class under baseline τand alternative τ′thresholds

$$S_{\text{overall}} = \frac{1}{n}\sum_{i=1}^{n} \quad 1\{\, C_\tau(I_i) = C_{\tau'}(I_i)\,\}$$

where:

- n= number of road segments;
- $C_\tau, C_{\tau'}$= classifications under two threshold sets;
- 1{·}= indicator function equal to 1 when the condition holds, 0 otherwise.

Equation 53 - Confusion-matrix entries M_{ab} counting segments classified as $a$under the baseline and $b$under the perturbed thresholds

$$M_{ab} = \#\{\, i : C_{\boldsymbol{\tau}}(I_i) = a,\ C_{\boldsymbol{\tau}'}(I_i) = b \,\}$$
$$a, b \in \{\text{LOW, MEDIUM, HIGH}\}$$

where:

- $M_{ab}$is the number of segments switching from class $a$to b;
- a, b∈ {LOW, MEDIUM, HIGH}.

Equation 54 - Class-level stability metric quantifying the proportion of correctly retained assignments across threshold configurations

$$S_c = \frac{M_{cc}}{\sum_b \quad M_{cb}}$$

where:

- $M_{cc}$is the number of segments classified in the same category $c$under both threshold sets;
- $M_{cb}$are confusion-matrix entries for baseline class $c$and perturbed class b;
- $S_c$expresses per-class stability under threshold perturbation.

Class-level stability provides a refined view of robustness by isolating the behavior of individual classes, complementing overall stability and enabling targeted evaluation of the most operationally critical categories.

For each threshold configuration, the resulting classifications were compared with the baseline scheme by examining the proportion of segments that retained their original class, the structure of the confusion matrix across schemes, and the Jaccard similarity index for the lowest- and highest-severity classes, which are typically the most relevant for operational decision-making. The overall coherence of the results under both local and distribution-based variations indicates that the proposed classification is not driven by arbitrary threshold placement and that the composite deterioration index

provides a stable, decision-relevant representation of pavement condition suitable for maintenance prioritisation workflows.

The Jaccard similarity coefficient is widely used in classification robustness studies because it measures class retention directly, without assuming balanced class sizes. The Jaccard similarity coefficient is used here to quantify class-specific agreement. Given two sets A and B of road segments classified into the same deterioration class under two different threshold configurations, the Jaccard index is defined as:

Equation 55 - Jaccard similarity coefficient measuring the proportion of elements consistently classified in the same category across two threshold configurations, used to assess classification stability

$$J(A,B) = \frac{|\ A \cap B\ |}{|\ A \cup B\ |}$$

where $|\ A \cap B\ |$represents the number of segments consistently classified in the same class under both configurations, and $|\ A \cup B\ |$ represents the total number of segments assigned to that class under at least one configuration. Unlike overall stability - which treats all classes symmetrically - Jaccard similarity targets the preservation of a specific class and is therefore well suited to assessing the robustness of the highest-severity class. This focus is operationally relevant, since the highest class typically corresponds to advanced surface or structural distress that triggers immediate or short-term maintenance actions in network-level asset-management workflows [50] [86].
Chance-corrected indices such as Cohen's κ were not employed, as they rely on an assumption of balanced class distributions, whereas the highest-severity class is intentionally sparse by design to serve as a priority alert category within the classification scheme.
As acceptance criteria for threshold robustness, overall class stability is required to remain ≥ 90%, and Jaccard similarity ≥ 0.85 for both the lowest and highest severity classes. These values are consistent with common practices in network-level asset management, where classification boundaries are expected to remain stable under moderate threshold variations and where the highest-severity class must maintain strong consistency due to its direct implications for prioritisation and intervention

planning [62]. These acceptance ranges are consistent with state-of-practice guidelines for network-level pavement management, where classification boundaries are expected to remain stable under moderate threshold perturbations [50] [86].

Threshold robustness is particularly critical for the highest-severity class, since its stability directly influences prioritisation and resource-allocation decisions in operational contexts. The aim of the analysis is not to modify or optimise the classification boundaries, but to verify that the resulting priority signals are driven by the underlying indicator rather than by the specific choice of threshold values. Variability is expected mainly within the intermediate class, which represents transitional states and therefore naturally accommodates a wider range of conditions.

5.4.2. D2) Sensitivity on fusion parameters (α, κ, q)

To assess the robustness of the composite index with respect to the parameterisation of the fusion coefficients (α, κ, q), a structured sensitivity analysis was conducted on the coefficients governing the integration of heterogeneous signals and the attenuation applied in the presence of contextual elements that may interfere with sensor measurements. The analysis focuses on three groups of parameters: (i) the fusion weight α, which regulates the balance between two complementary sensing modalities; (ii) the attenuation coefficient κ, which controls the reduction of contributions from one modality when contextual evidence suggests reduced interpretability; and (iii) the reliability coefficients q, which scale the contribution of selected sensing channels to reflect differences in confidence or signal quality.

The parameters were varied within intervals that are both operationally plausible and theoretically meaningful. The fusion parameter α was explored across configurations ranging from cases in which the index is driven predominantly by one sensing modality (α close to the lower bound) to cases where the second modality is dominant (α close to the upper bound). The attenuation parameter κ was evaluated at values corresponding to progressively stronger suppression of signal contributions in the presence of contextual elements, and an extreme "zero-gate" configuration was also tested in which the affected modality is entirely removed from the composite

formulation. The reliability coefficients q were varied to simulate uncertainty in the calibration of sensor-specific contributions and to test how changes in assumed signal trustworthiness propagate through the index.

For each parameter configuration, the composite index was recomputed and compared to a baseline specification. Robustness was assessed using: (i) Spearman rank correlation between the baseline and perturbed indices, capturing the preservation of prioritisation patterns across the network; (ii) the Jaccard similarity index on the top-ranked subset of units with the highest deterioration, reflecting the stability of critical prioritisation signals; (iii) class-level stability for the discretised LOW–MEDIUM–HIGH categorisation; and (iv) class-specific Jaccard similarity for the highest-severity category, which is operationally central as it identifies units associated with urgent intervention needs.

Equation 56 - Jaccard similarity on the top-m segments with highest deterioration, assessing stability of critical-priority rankings under parameter perturbations

$$J_{\text{top}}(m) = \frac{|\ \mathcal{H}_{\text{base}}^{(m)} \cap \mathcal{H}_{\text{alt}}^{(m)}\ |}{|\ \mathcal{H}_{\text{base}}^{(m)} \cup \mathcal{H}_{\text{alt}}^{(m)}\ |}$$

where:

- $\mathcal{H}_{\text{base}}^{(m)}$= set of top-$m$ segments by baseline index I_i;
- $\mathcal{H}_{\text{alt}}^{(m)}$= same set under perturbed configuration;
- $J_{\text{top}}(m) \in [0, 1]$ = agreement measure (1 = perfect stability).

Equation 57 - Spearman rank-correlation coefficient measuring the stability of segment prioritisation between baseline parameter θ_0 and perturbed configuration $\theta = (\alpha, \kappa, q)$

$$\rho_{\text{rank}}(\boldsymbol{\theta}) = \text{Spearman}\,(I_i(\boldsymbol{\theta}_0), I_i(\boldsymbol{\theta}))$$

where:

- $I_i(\theta)$= composite index computed under parameters θ;
- θ_0= baseline configuration;
- $\rho_{\text{rank}} \in [-1, 1]$ = rank-stability measure (1 = perfect order preservation).

This framework distinguishes semantic robustness - i.e., the preservation of decision-relevant prioritisation logic - from mere numerical sensitivity. Consistent with expectations for multi-source condition assessment, most of the variation induced by parameter perturbations is concentrated within the intermediate category, which represents transitional states. The highest-severity class remains largely invariant across all moderate perturbations, indicating that the composite index captures persistent and meaningful degradation patterns rather than effects tied to a specific tuning of fusion parameters. Conversely, the extreme zero-gate scenario substantially reduces the stability of the highest-severity class, indicating that complete suppression of one sensing modality in the presence of contextual elements leads to systematic under-identification of advanced deterioration states. This confirms that the baseline parameter configuration achieves an effective balance between noise mitigation and the retention of signal semantics and is therefore retained in the final specification.

5.5. E) Verification

The validation of the composite deterioration index is carried out through a multi-level assessment strategy designed to evaluate its interpretability, internal consistency, and descriptive capacity at different spatial scales. The first stage involves a macro-scale examination, where the index is mapped across the entire road network to analyse its spatial distribution and to investigate systematic patterns associated with network hierarchy, traffic function, and urban versus extra-urban contexts.

Equation 58 - Correlation coefficient between composite deterioration index I_i and near-miss frequency Y_i, used as a large-scale consistency diagnostic

$$\rho_{I,Y} = \mathrm{corr}(I_i, Y_i)$$

This step supports the identification of large-scale deterioration gradients and potential clusters of infrastructural weakness. Street-level visual references (or equivalent field imagery) may be consulted at this stage to qualitatively contextualize emerging patterns.

In the second stage, a stratified sampling approach is used to enable micro-scale inspection of representative cases. Segments are ranked according to their composite index values, and multiple subsets are extracted to span the full deterioration spectrum, including high-performing segments, severely deteriorated segments, and intermediate cases.

Equation 59 - Spearman rank correlation between baseline and alternative configurations of the composite index, used to evaluate ranking stability under parameter perturbations

$$\rho_{rank} = \text{Spearman}(I_i, I_i^{(\text{alt})})$$

where:

- I_i= composite deterioration index for road segment $i$under the baseline configuration;
- $I_i^{(\text{alt})}$= composite index for the same segment computed under an alternative parameter setting (e.g., perturbed α, κ, q);
- $\rho_{\text{rank}} \in [-1, 1]$ = Spearman's rank-correlation coefficient measuring monotonic agreement between the two index orderings (1 = perfectly preserved ranking, 0 = no correlation, –1 = inverted order).

This selection strategy ensures that the verification does not privilege either extreme conditions or uniformly maintained areas, but instead captures a range of deterioration configurations.

The third stage consists of a detailed segment-level verification integrating multiple sources of evidence. This includes (i) the numerical values of the composite index and its constituent sub-indices, (ii) the spatial patterns of individual deterioration detections contributing to the index, and (iii) visual inspection of the roadway surface through direct observation or image-based surveys. Where available, temporal layers of imagery can be used to ensure that visual inspection refers to the same observation window as the sensing data. The evaluation focuses on recognising typical pavement distress mechanisms - such as cracking, rutting, potholes, surface wear, edge degradation, and patching - and assessing both their severity and spatial extent.

Equation 60 - Weighted Cohen's κ statistic measuring agreement between categorical field ratings and model-based deterioration classes

$$\kappa_w = \frac{p_o - p_e}{1 - p_e}$$

where:

- p_o= observed proportion of agreement between field-derived and model-based classes;
- p_e= expected proportion of agreement due to chance;
- $\kappa_w \in [0, 1]$ = weighted Cohen's κ statistic (0 = no agreement beyond chance, 1 = perfect agreement).

If ordinal weights are used, disagreements between adjacent classes are penalized less than disagreements between distant classes, providing a nuanced measure of categorical consistency.

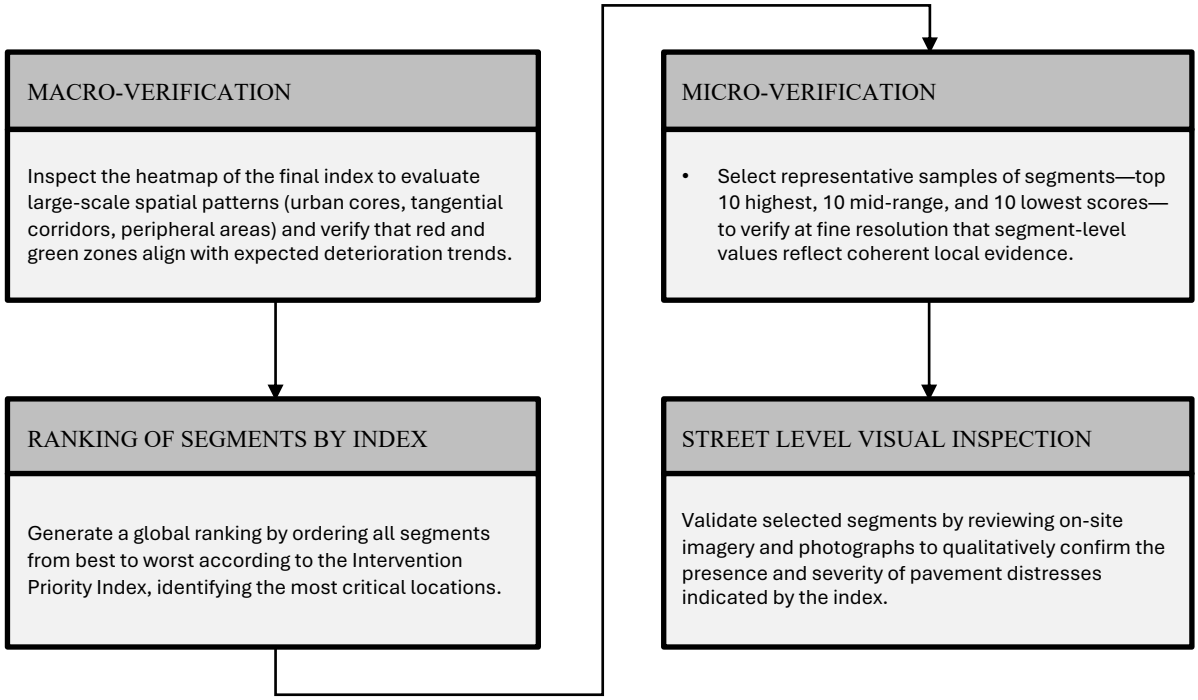

Figure 44 – Flow chart of methodology verification

This multi-evidence verification procedure does not assume the correctness of the index a priori, but instead employs visual and structural inspection as external reference layers to interpret the meaning of the indicator values. By combining network-scale distribution analysis with detailed segment-level examination, the validation framework provides a coherent and transparent basis for assessing the descriptive robustness and operational relevance of the composite pavement deterioration index.

6. Experiments

This section empirically applies the previously described methods to the Brescia dataset to demonstrate reproducibility and generalisability. In doing so, the chapter operationalises the abstract framework introduced in Chapter 5, translating each methodological concept into a reproducible empirical workflow grounded in the Brescia case study. The following section mirrors the methodological steps presented in Chapter 5, applying them to the Brescia dataset. This parallel structure is deliberate, facilitating comparison between the abstract pipeline and its empirical implementation.

Figure 45 - Province of Brescia (Italy)

The Brescia dataset refers to the integrated multi-source data collection used as the empirical basis for this study. It encompasses the road network of the municipality and surrounding metropolitan area of Brescia (Italy), represented in a polyline-based GIS format and enriched with heterogeneous sensing data acquired from two complementary monitoring systems.
Specifically, the dataset includes:

- computer-vision-based surface distress detections, collected through the AIWAY vehicle-mounted imaging system, which automatically identifies and classifies visible pavement surface anomalies into semantic categories;

- vibration-based distress proxies, derived from VIASAT onboard accelerometric measurements, which detect dynamic disturbances in vehicle motion associated with pavement irregularities.

A preliminary exploratory analysis of both sensing datasets was conducted in Chapter 4, where data quality, coverage characteristics, and classifier behavior were examined prior to integration**.** All sensing data are time-stamped and georeferenced, and are mapped to the road network at the segment level to enable consistent aggregation, comparison, and modelling.

Both AIWAY and VIASAT function as independent data acquisition systems; their integration does not assume identical sensing coverage or detection mechanisms, and the redundancy management phase explicitly accounts for differences in modality, sensitivity, and observational meaning.

6.1. A) Network segmentation and dataset preparation

6.1.1. A1) Segmentation of the road network

Spatial discretization represents one of the fundamental conceptual operations through which continuous reality is transformed into analyzable data and a critical area of inquiry due to its impact on balancing spatial detail, data stability, and noise reduction in road network analysis. Early segmentation methods focused on fixed lengths or heuristic approaches, evolving towards data-driven techniques that consider structural and safety features at varying scales [87] [88]. The practical significance of this research lies in optimizing Pavement Management Systems (PMS) and Floating Car Data (FCD) applications, where segment length influences the accuracy of condition assessments and maintenance prioritization [89] [90]. For instance, network-level infrastructure monitoring requires segmentations that capture meaningful variability without excessive noise, with 100 m segments often cited as a compromise between granularity and data reliability [91] [92]. The specific problem addressed is the lack of consensus on the optimal segment length that balances resolution and granularity while maintaining statistical robustness and operational

feasibility. Several studies have statistically supported the 100 m segmentation threshold through data-driven methods such as change-point detection and spectral analysis, which identify homogeneous sections by minimising error and controlling intra-class variability [93] [88]. These approaches confirm that 100 m provides an optimal analytical window that balances smoothing and sensitivity, allowing for a stable representation of pavement responses without overfitting local fluctuations. In this context, the segmentation length becomes not only an empirical parameter but an empirically and statistically supported scale, derived from structural response patterns observed across multiple datasets.

In this study, a fixed 100 m segmentation scheme was adopted in accordance with prior literature, while alternative approaches such as change-point detection and spectral analysis were referenced as previously explored methods.

Although shorter segments (e.g. 50 m) provide finer spatial detail, they may introduce excessive measurement noise and instability, whereas longer segments (e.g. 200 m) risk losing local variability critical for targeted interventions [18] [87] [93]. Several studies highlight this trade-off but differ in their methodological approaches and empirical validations, leading to inconsistent recommendations [88] [94] [95]. Moreover, the integration of accelerometer-based monitoring and crowdsourced data introduces additional variability that complicates segmentation design [94] [96]. The consequences of this gap include suboptimal maintenance decisions and inefficient resource allocation in urban and peri-urban European road networks [97] [98]. Conceptually, this review frames segmentation length as a balance between spatial resolution, data stability, and noise smoothing, grounded in mechanistic-empirical principles and statistical change-point detection theories [87] [99]. The relationship between segment length and data variability is mediated by the need to preserve structural and safety-relevant features while minimizing random fluctuations [18] [87]. This framework supports the evaluation of segmentation strategies within PMS and network-level analyses, linking empirical observations with theoretical models [89] [100].

A synthesis of strengths and limitations emerging from the literature is provided in Table 12.

Table 12 - Critical analysis of literature on technical road-segmentation length

Aspect	Strengths	Weaknesses
Balance Between Spatial Detail and Data Stability	The 100 m segment length effectively balances spatial detail and data stability by smoothing measurement noise while preserving key structural features, as demonstrated by adaptive averaging methods that minimize classification errors in pavement response data [87]. This length scale is supported by spectral analysis approaches that identify natural near-miss distribution patterns, reinforcing the appropriateness of 100 m segments for capturing relevant spatial frequencies [88].	Despite these strengths, some studies indicate that fixed-length segmentation may obscure finer-scale structural variations, especially in heterogeneous pavement sections where local variability occurs at smaller scales than 100 m [87].
Noise Reduction and Preservation of Local Variability	Techniques such as enhanced cumulative difference approaches and de-noising autoencoders have shown promise in reducing noise while maintaining segment homogeneity, supporting the use of 100 m segments for reliable data aggregation [101]. The smoothing effect at this scale reduces random fluctuations without excessively averaging out meaningful distress signals, aligning with PMS requirements [89].	However, the trade-off between noise reduction and loss of local variability remains a significant limitation. Over-smoothing at 100 m can mask localized distress or structural anomalies critical for targeted maintenance, as some methods struggle to differentiate between noise and true pavement condition changes [18]. This challenge is exacerbated in urban networks with complex deterioration patterns.
Integration of Floating Car Data and Accelerometer-Based Monitoring	The use of 100 m segments is well-suited for integrating FCD and accelerometer data, enabling frequent, cost-effective monitoring with sufficient spatial resolution to inform maintenance decisions. Smartphone-based sensing frameworks and crowd-sourced trajectory analyses demonstrate the feasibility of capturing road surface conditions at this scale, facilitating real-time infrastructure assessment [94].	Limitations arise from variability in sensor data quality and sampling frequency, which can introduce inconsistencies in segment-level condition estimates. Studies highlight challenges in standardizing data collection and processing protocols, which affect the reliability of 100 m segmentation when applied to heterogeneous sensor datasets [91] [102]. Additionally, the influence of vehicle speed and sensor

		placement on data variability complicates interpretation at this segment length [102].
Empirical and Theoretical Justifications for 100 m Segments	Empirical studies in European urban and peri-urban contexts provide evidence that 100 m segments offer a practical compromise, aligning with PMS practices and enabling effective network-level monitoring [89] [91]. Theoretical models based on spatial frequency domain analysis and mechanistic-empirical frameworks support this segmentation scale for capturing relevant pavement response characteristics [87] [88].	Nonetheless, some research suggests that the optimal segment length may vary depending on specific network characteristics and monitoring objectives. Fixed 100 m segments may not be universally optimal, particularly in highly variable or low-volume road sections where longer or shorter segments could improve homogeneity or data stability [18] [93]. The lack of standardized criteria for segment length selection limits generalizability.
Consistency with Pavement Management Systems and Infrastructure Monitoring	The 100 m segment length is consistent with current PMS practices, facilitating integration of structural condition data such as Traffic Speed Deflectometer measurements into decision-making frameworks [89]. This consistency supports improved maintenance prioritization and cost savings, as demonstrated in case studies incorporating structural condition indices alongside surface distress data [89] [90].	However, PMS integration challenges persist due to differences in data granularity and temporal resolution between traditional surface condition surveys and emerging sensor-based structural assessments. The alignment of 100 m segmentation with PMS workflows requires further refinement to address these discrepancies and ensure seamless data fusion [99] [103].

The 100 m segment length offers a well-founded balance between spatial detail and data stability. Studies consistently demonstrate that 100 m segments effectively smooth measurement noise inherent in sensor-based data, such as Traffic Speed Deflectometer outputs and accelerometer readings, while preserving essential structural and safety features necessary for meaningful condition evaluation. This balance mitigates the excessive noise and data variability observed in finer granularities like 50 m segments, which, although offering higher spatial resolution, often suffer from lower statistical reliability. Conversely, longer segments, such as 200 m, tend to oversmooth the data, risking the loss of critical local variability that could

inform targeted maintenance actions. Integration of diverse data sources, including Floating Car Data, smartphone accelerometer inputs, and multi-sensor systems combining surface and structural parameters, has been shown to work effectively within the 100 m segmentation framework. This scale supports the frequent and cost-effective data collection needed for dynamic infrastructure monitoring while aligning well with Pavement Management System practices. The consistency of 100 m segments with established PMS workflows is reinforced by empirical findings indicating improved maintenance prioritization, cost savings, and enhanced decision-making when structural data are incorporated alongside surface distress indicators. Moreover, this scale aligns with standard practices adopted in Pavement Management Systems at the agency level, where fixed-length segments simplify inspection scheduling, database integration, and performance trend analysis [89] [90]. The 100 m segmentation provides a repeatable and interoperable spatial framework compatible with both traditional survey-based PMS and modern FCD-driven condition monitoring, ensuring comparability across monitoring campaigns and jurisdictions. Such standardisation enhances the reproducibility and operational efficiency of maintenance planning workflows. Statistically robust segmentation methods, including enhanced cumulative difference approaches and change-point detection algorithms, strengthen the reliability of 100 m segment delineation by rigorously controlling classification errors and adapting segment lengths to the intrinsic variability of pavement responses. In this research, change-point detection was not used to dynamically define segment boundaries but rather to verify that the fixed 100 m length adequately captured local homogeneity. This hybrid approach ensures both statistical consistency and operational comparability across datasets. However, challenges remain in standardizing segmentation criteria across diverse network characteristics and sensor data qualities, particularly in heterogeneous urban environments where local variability may occur at scales finer than 100 m. Comparative analyses underscore that no single segment length universally optimizes all objectives; instead, 100 m segments represent a practical compromise suitable for most urban and peri-urban European road networks. Although the 100 m threshold has proven robust across urban and peri-urban European contexts, its transferability

to mountainous, rural, or extra-European networks should be further validated to account for differences in intersection density, driving patterns, and terrain morphology. While shorter segments offer finer spatial resolution, they incur higher noise and data instability, and longer segments reduce noise but risk missing localized distress patterns. Future research should continue refining adaptive segmentation methods to dynamically balance these trade-offs in line with specific monitoring goals and data characteristics. In summary, the prevailing evidence supports the adoption of 100 m road segments as a technically and statistically justified standard for pavement condition monitoring and network-level analysis. This choice harmonizes spatial resolution, data stability, noise reduction, and operational practicality, facilitating effective integration with advanced sensor technologies and PMS frameworks to enhance infrastructure maintenance and management strategies.
Building upon this established framework, the present study applies the 100 m segmentation approach within the Brescia road network, integrating geometric indicators and multi-source sensor data to evaluate its operational validity in a real-world context.

The geometric configuration of each road segment plays a critical role in determining its functional and safety characteristics. For this reason, in the present research, each segment was modelled as a polyline composed of a sequence of ordered points $p_k = (x_k, y_k)$, expressed in a projected metric reference system (UTM, EPSG:32632), obtained by reprojecting WGS-84 geographic coordinates. Segments intersecting junctions or roundabouts were trimmed at the network node to ensure that each element represented a geometrically homogeneous section. This approach prevented the duplication of curvature at boundaries and avoided artefacts in tortuosity and turning-angle computation near intersections. This representation enabled the calculation of three key indicators of geometric complexity: tortuosity, number of turns, and mean turning angle.
The rationale behind the selection of these three indicators lies in their complementary ability to capture different aspects of road geometry.
Tortuosity quantifies the global deviation of a segment from linearity, providing a measure of overall curvature; the number of turns describes the frequency of

directional alternations, reflecting how often a segment changes from left to right curvature; and the mean turning angle represents the average intensity of such deviations, offering a compact descriptor of angular variability.

Together, these indicators form a consistent framework that balances interpretability, computational efficiency, and geometric completeness.

All three indicators were computed at the segment level, aligning with the 100-meter segmentation adopted for pavement condition and traffic data integration. This level of aggregation minimizes spatial autocorrelation among neighbouring points while preserving sufficient spatial resolution to identify local geometric irregularities. While the reduction of spatial autocorrelation was conceptually ensured through fixed-length segmentation, the quantitative validation of Moran's I and Geary's C indices will be addressed in future work as part of the statistical assessment of segment independence.

The threshold values used later for classification were defined through exploratory data analysis and geometric reasoning, rather than arbitrary quantiles, ensuring that class boundaries reflect perceptually meaningful variations in alignment.

This methodological coherence ensures that the proposed indicators can be robustly interpreted in subsequent analyses (from pavement condition modeling to traffic safety assessment) while maintaining a direct link between geometric form and functional behavior of the road network.

At this stage, the segmentation layer contained 0% missing identifiers and 0% invalid geometries; no rows were dropped during the construction of the 100 m baseline, and coverage heterogeneity of external sensing layers is discussed in the following sections. The geometric indicators (tortuosity, number of turns, and mean turning angle) were computed directly from the available 100 m segments, rather than from re-segmented polylines; accordingly, the dataset comprises 215,991 values for each indicator, one per segment

6.1.1.1.Tortuosity

Tortuosity is a geometric indicator used to quantify the curvature of a road segment. It is defined as the ratio between the actual path length of the segment, measured along

its polyline, and the Euclidean distance between its start and end points. Formally, for a given segment i, we apply the Equation 17.
A perfectly straight segment will have $T = 1$, while higher values indicate greater sinuosity.

The map of Figure 46 illustrates the spatial distribution of the *tortuosity index* computed for each road segment. This indicator highlights how much a segment deviates from a straight alignment, providing a visual understanding of curvature intensity along the network.
Segments displayed in green tones correspond to low tortuosity values, typically associated with straight or gently curving roads, whereas segments shown in yellow-to-red colors identify progressively more sinuous sections. Such representation supports the identification of critical geometric features that may influence driving comfort, vehicle dynamics, or near-miss likelihood.

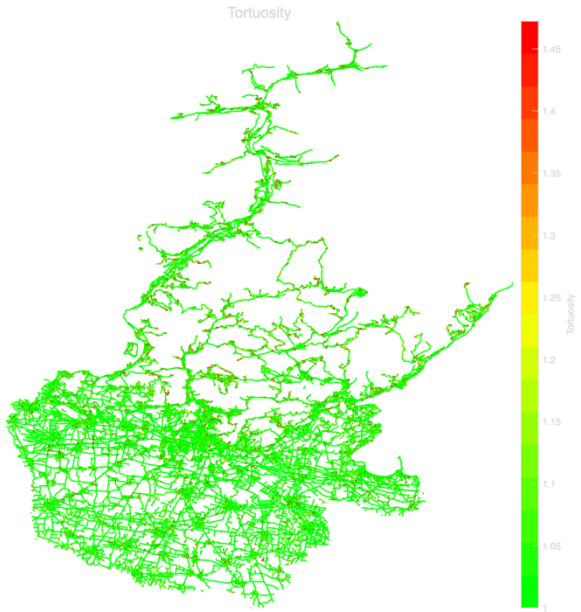

Figure 46 - Map of segments: tortuosity

To further investigate the distribution of the tortuosity index, the segments were grouped into discrete classes according to fixed intervals of the indicator. A dedicated count was computed for segments with a tortuosity exactly equal to 1.0, followed by

successive classes defined as (1.0-1.1], (1.1-1.2], (1.2-1.3], and values greater than 1.3. This classification provides a clearer overview of the frequency of each tortuosity range, allowing for an intuitive comparison between straight and more sinuous road sections.

Consistently with expectations, the vast majority of segments fall within the first class ($T \leq 1.1$), confirming that most of the network consists of nearly straight elements. This result aligns with the segmentation logic previously discussed, where each segment corresponds to an edge of the road graph, typically bounded by intersections or geometric discontinuities, which inherently limits the curvature captured within individual elements.

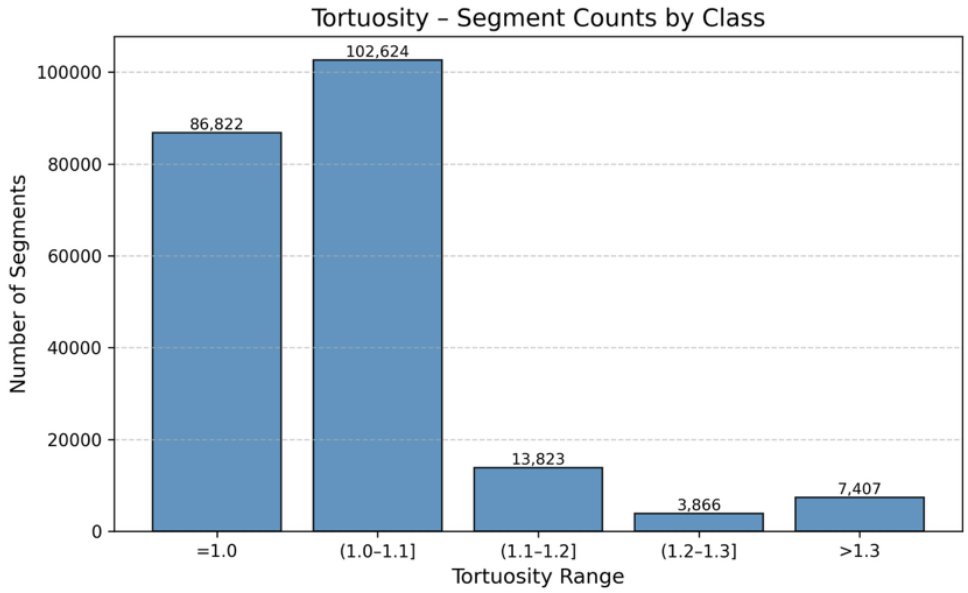

Figure 47 - Histogram of tortuosity classes

6.1.1.2.Number of Turns

The number of turns measures how many times the alignment of a segment changes direction along its polyline. It is computed by analyzing the sign of consecutive turning angles. Specifically, a turn is counted whenever two successive angles exhibit opposite signs, i.e. when the curvature changes from left to right or from right to left. Equation 18 is applied, where $1(\cdot)$ is the indicator function that equals 1 if the condition is true

and 0 otherwise. This metric reflects the degree of directional alternation within the segment.

Figure 48 visualizes the *number of turns* calculated for each road segment, representing the frequency of directional changes along the network. This metric captures the alternation between left and right curvatures, thus providing a measure of the geometric complexity of each segment.
In the map, green tones correspond to segments with a low number of turns, typically associated with straight or smoothly curved sections, while yellow to red tones indicate a higher number of directional changes, reflecting segments with more irregular or winding paths.
This representation supports the spatial identification of areas where alignment irregularities may affect vehicle dynamics, route planning, or accident risk, complementing the analysis provided by the tortuosity indicator.

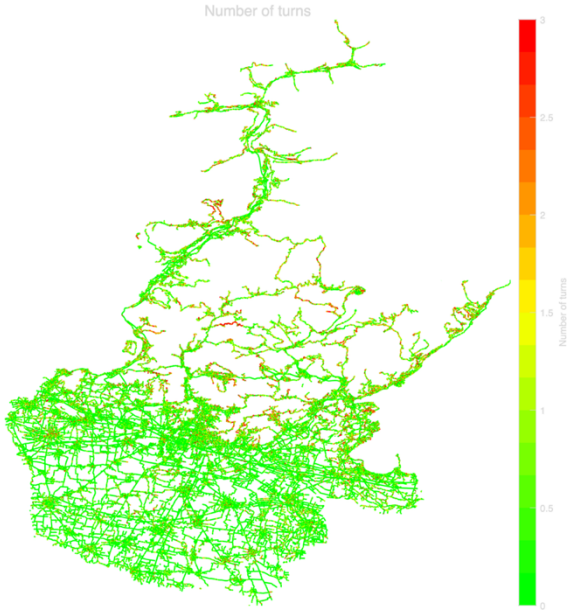

Figure 48 - Map of segments: number of turns

To better understand the distribution of directional changes within the network, the *number of turns* was grouped into discrete classes representing increasing levels of alignment irregularity. The histogram in Figure 49 illustrates the frequency of

segments characterized by 0, 1, 2, 3, 4, and more than 5 turns. As expected, the largest proportion of segments presents either no directional change or a single turn, confirming that most road elements maintain a consistent alignment between consecutive intersections. The progressively smaller number of segments with multiple turns reflects more complex geometric patterns, such as winding or meandering alignments, which are less frequent but particularly relevant for evaluating driver workload and local curvature variability.

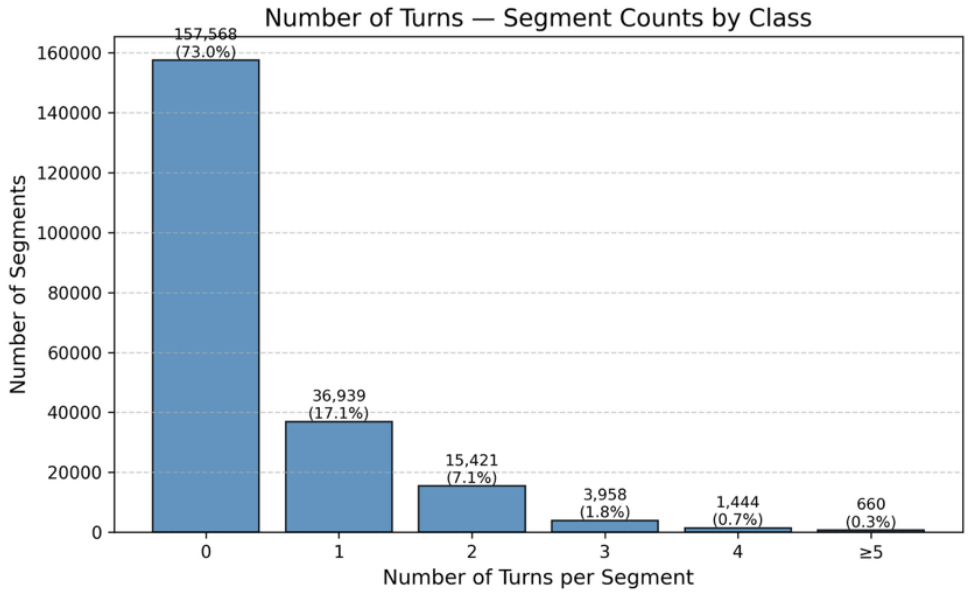

Figure 49 - Histogram of number of turns classes

6.1.1.3.Mean turning angle

The mean turning angle (degrees) is a geometric indicator designed to capture the overall angular complexity of a road segment.

The turning angle at vertex k is then computed as the arccosine of the normalized dot product between these two vectors as in Equation 20.

This formulation ensures that θ_k measures the absolute deviation in direction when moving from one segment of the polyline to the next. A perfectly straight continuation yields $\theta_k = 0$, while sharper bends result in larger values of θ_k.

The mean turning angle for segment i is then defined as the average of all such angles computed along the polyline as in Equation 21.

In this way, the mean turning angle provides a compact and interpretable metric of curvature that can be directly integrated into regression models as a quantitative descriptor of segment geometry.

Figure 50 shows the spatial distribution of the mean turning angle across the road network. Segments with low values of the indicator (green) correspond to nearly straight roads, where directional changes are minimal. Conversely, higher values (yellow to red) highlight segments with frequent or pronounced bends, reflecting greater geometric complexity. These patterns are mainly observed in peripheral and hilly areas, where the morphology of the territory constrains alignment. This confirms that the mean turning angle is a robust and interpretable descriptor of segment curvature, suitable for integration into subsequent modelling steps.

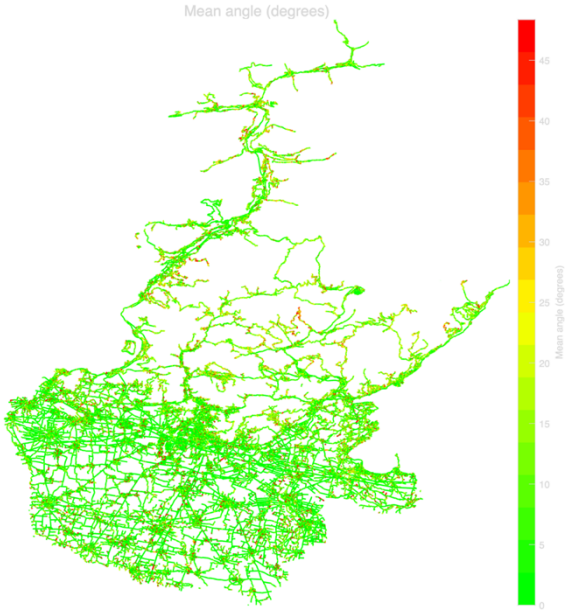

Figure 50 - Map of segments: mean turning angles (degrees)

To analyze the variability of the mean turning angle across the road network, the indicator was discretized into classes defined by fixed angular thresholds. The adopted intervals (of ≤1°, (1-3°], (3-5°], (5-10°], and >10°) represent increasing levels of directional deviation along the segment. The histogram in Figure 51 shows that most segments exhibit very low mean turning angles, typically below 3°, indicating limited

curvature and smooth alignment. Higher values, which are less frequent, correspond to segments characterized by frequent or sharp bends, mainly located in peripheral or hilly areas. This distribution confirms that the majority of the network is geometrically regular, while only a small fraction of segments presents complex alignments with substantial angular variation.

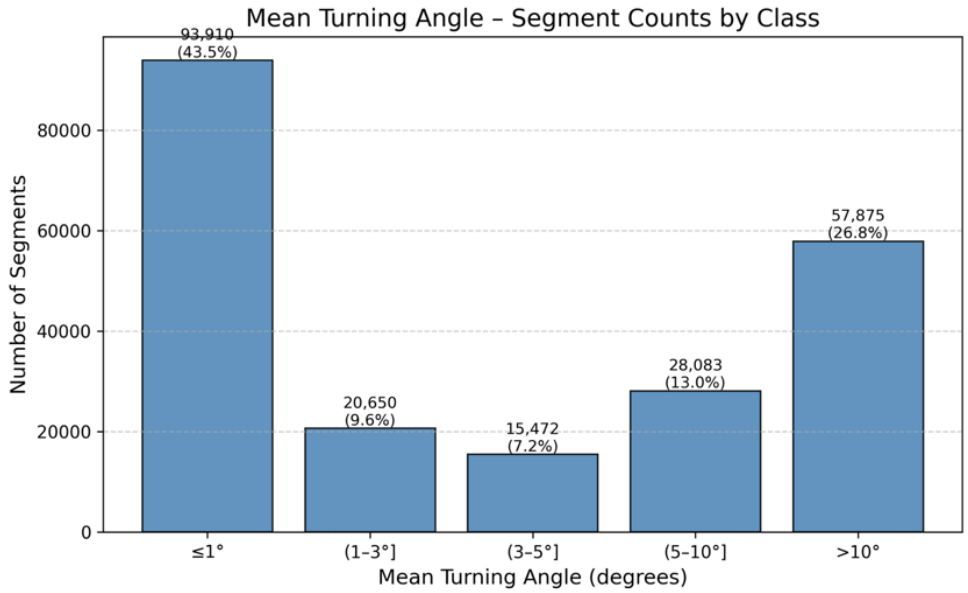

Figure 51 - Histogram of mean turning angles (degrees)

6.1.1.4.Scale sensitivity of geometric indicators

To verify that adopting 100 m segments does not bias the analysis and to quantify the trade-off between spatial resolution and statistical stability, a scale-sensitivity assessment was performed around the 100 m baseline under the explicit constraint that the original polylines were unavailable and only a table of 100 m segments with pre-computed indicators (tortuosity, mean turning angle, number of turns) was accessible. The methodological choice is dictated by three requirements: (i) respect the empirical information already present in the dataset, (ii) avoid introducing systematic bias while emulating finer/coarser scales, and (iii) ensure full reproducibility and auditability. Accordingly, two comparison datasets were engineered directly from the baseline. First, a 50 m "proxy" was obtained by splitting each 100 m record into two child rows that preserve the parent mean of continuous indicators via small, symmetric, zero-

mean perturbations: $x_L = x + \varepsilon$, $x_R = x - \varepsilon$, with $\varepsilon \sim \text{Uniform}(-\delta, +\delta)$and hard bounds enforced (e.g. tortuosity ≥ 1, angle ≥ 0). In practice, $\delta$was set conservatively (e.g. $\delta = 0.02$for tortuosity and $\delta = 0.5°$ for mean turning angle), ensuring that perturbations are small relative to the empirical variability. Second, a 200 m aggregation was formed by pairing neighbouring 100 m segments along the same chain in two ways, adjacent (1-2, 3-4, …) and staggered (2-3, 4-5, …), to test alignment sensitivity; continuous indicators were averaged and counts summed, with odd tails dropped per pairing to avoid degenerate singletons. For each indicator and each length (50, 100, 200 m), the mean, variance, and coefficient of variation (CV) computed using the moment-based formulation introduced in Equation 30, and uncertainty was quantified via non-parametric bootstrap (percentile intervals, B≈1000) for variance and CV. Quality assurance combined explicit invariants (conservation of the empirical mean for continuous indicators and of total turn counts under the 50 m split; equality of count totals between the 100 m baseline and the paired sets at 200 m) with monotonicity checks (expected contraction of variance and CV for continuous indicators from 100 m to 200 m due to spatial averaging; mild expansion from 100 m to the 50 m proxy as finer resolution exposes additional dispersion; mechanical scaling of the mean of turn counts with segment length, approximately halved at 50 m and doubled at 200 m, with CV typically decreasing as length increases). Empirical results conform to these expectations: for tortuosity and mean turning angle, moving from 100 m to 200 m leaves the mean essentially unchanged while variance and CV contract markedly, and adjacent versus staggered aggregation yields near-identical dispersion, indicating that the effect is intrinsic to aggregation rather than an alignment artefact; the 50 m proxy preserves the mean by construction yet displays higher dispersion, serving as a conservative stress-test of sub-segment heterogeneity in the absence of base polylines. Bootstrap intervals substantiate these trends statistically, with clear separation between 100 m and 200 m and partial overlap between 50 m and 100 m consistent with the proxy design. Overall, the procedure was adopted because it preserves the empirical content of the baseline, tests the precise mechanisms by which scale affects dispersion while minimising unverifiable assumptions, and yields outcomes that are both operationally meaningful and straightforward to replicate; the

analysis indicates that 100 m constitutes a defensible balance between damping random fluctuations and retaining local geometric signal, while 50 m and 200 m provide informative bounds on sensitivity and a clear path for future replication once full polylines become available. It is important to emphasise that the 50 m layer is a proxy derived from 100 m records rather than a physical re-segmentation of the underlying polylines. The split preserves first-order moments by construction and injects only symmetric, zero-mean perturbations, yet it cannot recover within-segment geometry that was not recorded at source. Consequently, findings at 50 m should be interpreted as a conservative stress-test of fine-scale heterogeneity rather than as a definitive characterisation of sub-segment behavior.

The adopted strategy was selected to preserve the empirical content of the 100 m baseline while emulating finer and coarser scales with minimal, explicitly controlled assumptions. It enforces invariants (conservation of means for continuous indicators and of total turn counts at 50 m; equality of count totals between 100 m and 200 m), isolates the mechanism by which aggregation affects dispersion, and remains fully auditable and reproducible. Once full polylines become available, this proxy can be replaced by physical re-segmentation to convert the present robustness check into a complete geometric validation.

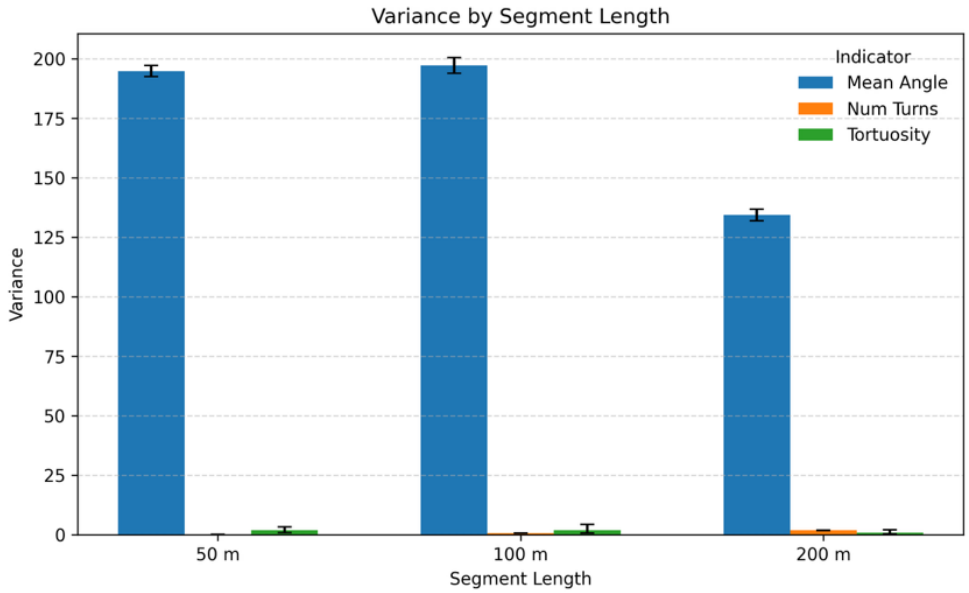

Figure 52 - Variance of tortuosity, mean turning angle, and number of turns across 50-100-200 m segments (error bars: 95% bootstrap CI)

Figure 52 shows a clear scale effect: moving from 100 m to 200 m produces a marked contraction in variance for all indicators, particularly the mean turning angle, consistent with the expected smoothing introduced by spatial aggregation. The 50 m proxy exhibits slightly higher dispersion relative to 100 m, indicating additional fine-scale heterogeneity that is revealed at finer granularity. The 95% bootstrap confidence intervals are narrow and non-overlapping between 100 m and 200 m for the mean turning angle, supporting the statistical significance of the variance reduction. Overall, the pattern confirms that increasing segment length stabilises the indicators, while shorter segments increase sensitivity to local variability and noise.

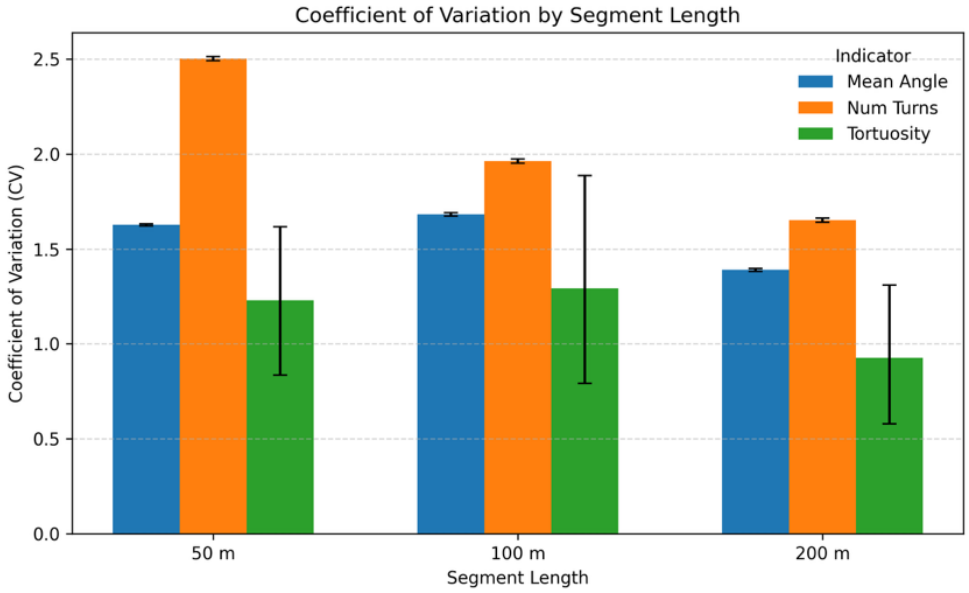

Figure 53 - Coefficient of variation (CV) for the three indicators at 50-100-200 m (95% bootstrap CI)

Normalising by the mean (Figure 53), the CV trends corroborate the variance results across indicators with different scales. CV decreases monotonically with segment length (most notably for the number of turns and mean turning angle) indicating improved relative stability at 200 m. The 100 m baseline yields intermediate CV values: lower than 50 m (less noisy) yet higher than 200 m (more detailed), which is precisely the intended balance for network-level analyses that must preserve local geometric signal while controlling random fluctuations. Confidence intervals are tight and show

clear separation between 100 m and 200 m for the mean turning angle and number of turns, reinforcing the robustness of the trend.

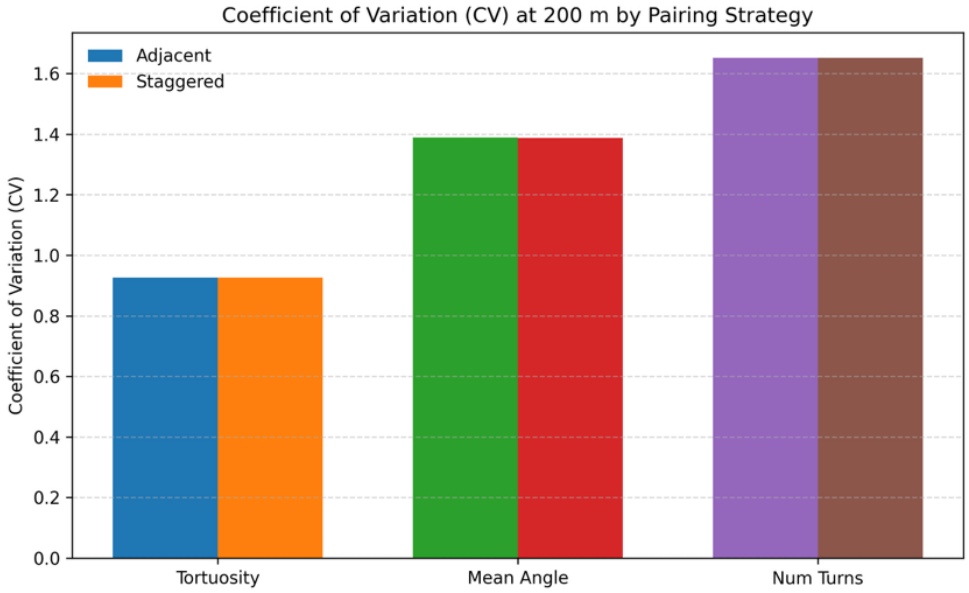

Figure 54 - Sensitivity of CV at 200 m to pairing strategy (adjacent vs staggered)

CV values at 200 m are practically indistinguishable between adjacent pairing and staggered (offset) pairing for all indicators, as in Figure 54. This invariance rules out an alignment artefact and indicates that the observed reduction in dispersion at 200 m is an intrinsic property of aggregation rather than a by-product of how pairs are formed. The result strengthens the methodological credibility of the scale comparison and supports the interpretation of 200 m behavior as a genuine scale effect.

Taken together, Figure 52, Figure 53 and Figure 54 demonstrate a consistent, theoretically coherent scale response: 50 m increases sensitivity (and noise), 200 m increases stability (and smoothing), and 100 m sits at a pragmatic equilibrium, retaining local geometric information while keeping dispersion within narrow, well-quantified bounds. This triangulates the rationale for adopting 100 m as the operational segment length for the subsequent analyses.

All confidence intervals are bootstrap percentile intervals ($B \approx 1000$ resamples); results are qualitatively unchanged using bias-corrected and accelerated (BCa) intervals.

Reproducibility and audit trail. All transformations used to generate the 50-100-200 m comparison are scripted and deterministic conditional on recorded random seeds. The

codebase logs the pairing strategy (adjacent/staggered), the exact bootstrap procedure (number of resamples and seed), and the invariants enforced (mean conservation for continuous indicators at 50 m and count conservation across scales). The full set of outputs (CSV summaries, figures, and the paragraph auto-export) is archived alongside the scripts to enable byte-for-byte regeneration of the statistics and figures presented in this section. Where access to primary data is restricted, hashed checksums and schema descriptions are provided to facilitate independent verification.

6.1.2. A2) Dataset preparation

The analytical process began with the construction of a comprehensive and integrated database, designed to combine heterogeneous sources of information within a common structure. Each row of the database corresponded to a road segment, while the columns contained attributes derived from two complementary sources:

- Computer vision techniques, which provided deterioration indicators based on the automatic detection of surface distresses (e.g. potholes, cracks, raveling) from video or image data;
- Accelerometric measurements, which captured anomalies in the pavement surface through vibration signals recorded by in-vehicle sensors.

The rationale for integrating these two sources lies in their complementary nature. Vision-based systems are particularly effective in identifying surface defects that are visible to the human eye, whereas accelerometer-based detections are better suited for quantifying irregularities and roughness that may not be clearly visible but still affect ride quality and safety. By combining both, the database provides a more holistic representation of pavement condition, enhancing the robustness of subsequent modelling.

The initial dataset was extremely large, comprising 215,991 records, because multiple detections could be associated with the same physical segment. Such redundancy is inherent when dealing with raw data from heterogeneous sensors, as each detection may refer to a slightly different location or to repeated passes over the same stretch of road. If used directly, this raw dataset would introduce severe distortions, with some segments being overrepresented while others remain under-specified.

To address this issue, a multi-step filtering and aggregation procedure was carried out. The first step was the elimination of duplicates and incomplete records. In particular, only those observations for which both vision-based and accelerometric data were simultaneously available were retained. This criterion was adopted to avoid biased representations of the pavement condition: if only one source were available, the analysis would neglect important dimensions of deterioration. The application of this filter reduced the dataset to 56,928 rows, representing cases where the information from the two sensing approaches could be meaningfully combined.

The second step consisted of aggregation at the segment level, so that each road segment would be represented by a single row containing all relevant deterioration indicators, geometric descriptors, and near-miss data. This step was crucial to establish a consistent analytical unit for the study: the segment. Road infrastructure research often requires working at an intermediate scale (between point detections and entire road sections) in order to balance detail with computational feasibility. By adopting 100-metre segments as the basic unit of analysis, the study ensures both a manageable dataset size and a spatial resolution fine enough to capture localised deterioration phenomena.

To support the description above, Figure 55 illustrates the geographical coverage of the dataset, showing the set of road segments considered in the analysis. Each polyline corresponds to a segment of approximately 100 metres, which represents the basic unit of observation adopted in the study. The figure therefore provides a visual overview of the spatial distribution of the network on which the subsequent analyses were conducted.

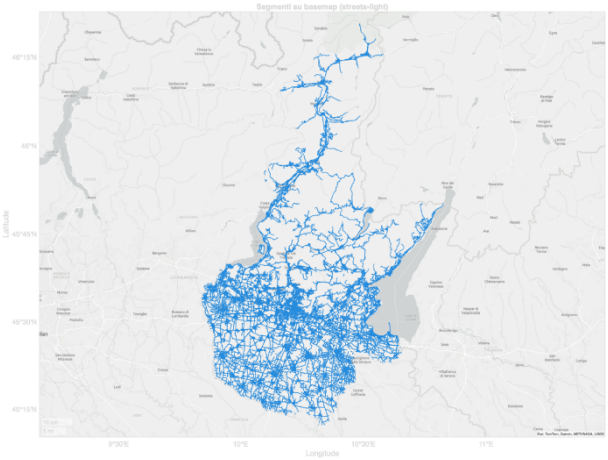

Figure 55 - Geographical representation of the segments considered for the empirical analysis (Province of Brescia)

After aggregation, the final analytical dataset consisted of approximately 1,500 unique segments. Each of these segments had a complete set of information, thus eliminating the need to handle missing values at this stage.

While Figure 55 illustrates the full geographical coverage of the initial dataset, the subsequent filtering and aggregation procedures substantially reduced the number of valid observations. The removal of incomplete records and the requirement to

combine both vision-based and accelerometric information limited the scope to approximately 1,500 unique segments. Figure 56 therefore depicts the final analytical dataset adopted in this study, highlighting the subset of road segments that served as the empirical basis for the modelling phase.

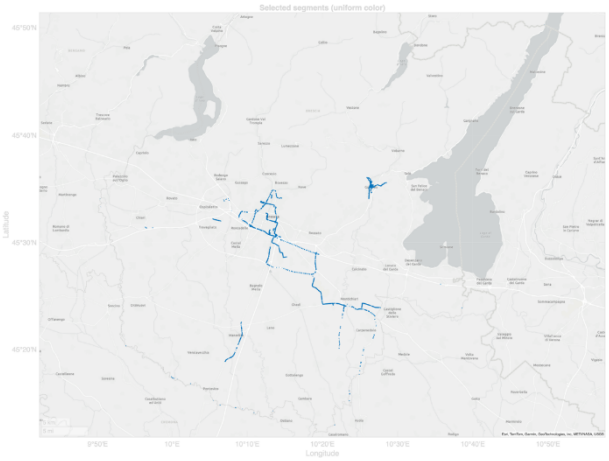

Figure 56 - Geographical representation of the final analytical dataset (Province of Brescia)

Concentrating the modelling phase on this reduced but fully populated dataset provided two important advantages:

1. Analytical robustness: by ensuring that all explanatory variables were available for all cases, the results are not biased by imputation or by the uneven distribution of missing values.
2. Methodological clarity: the reduced dataset allowed the modelling framework to be validated under ideal conditions, before tackling the additional complexity introduced by incomplete information.

Within this process, special care was devoted to the treatment of cases where multiple detections of the same deterioration type were associated with the same segment. Rather than arbitrarily discarding information, a harmonisation rule was applied: the occurrence counts were summed to reflect the total extent of deterioration phenomena within the segment, while the confidence scores were averaged to provide a representative reliability measure of the detections. This approach preserved the richness of the original data while ensuring consistency in the aggregated dataset.

The experimental phase of the study was therefore based on this structured and harmonised dataset. However, the research is not limited to complete records alone. A

key methodological contribution of this work lies in the design of a framework that can be extended to the entire database, including the much larger set of partially observed segments. In subsequent steps, the modelling framework will be applied to this broader dataset by introducing explicit rules for the management of missing data. These rules may involve weighting, imputation, or hierarchical modelling strategies, depending on the type and extent of the missing information.

This two-stage approach reflects a deliberate strategy:

- First, to test and validate the modelling approach on a complete and fully reliable subset of the data;
- Second, to extend the methodology to a realistic, large-scale context, where incomplete information is the norm rather than the exception.

In this way, the proposed framework not only ensures the validity of results in the controlled setting of complete data, but also demonstrates its scalability and transferability to real-world applications. This is particularly important for infrastructure management, where data incompleteness is unavoidable, and for the broader ambition of developing a model that can be generalized and applied to other geographical contexts, provided that comparable sources of data are available.

6.2. B) Analysis of data

6.2.1. B1) Redundancy analysis

In the present research, which integrates AIWAY (computer vision) and VIASAT (accelerometric sensors), the issue of redundancy is not merely theoretical but emerges directly from the nature of the available data. The deterioration classes provided by the two sources are labelled with descriptive tags that clearly point to overlapping meanings. For example, the vision-based class D40, which includes ruts, cracks, potholes and surface separations, largely corresponds to the accelerometric anomaly type 1, which is generated by the strong vibrations typically associated with potholes. Similarly, the class D20, indicating alligator cracking, is conceptually aligned with type 3, which represents irregularities and surface failures detected by accelerometers. These overlaps suggest that the two sources, although based on different technologies,

in practice describe the same category of distress. This approach demonstrates that redundancy, when systematically analysed and regulated, becomes an integral part of the modelling process.

A further and particularly important case is represented by D50, which identifies the presence of manholes and inspection covers. Unlike the other tags, D50 does not denote a defect in the pavement, but rather a functional element of the infrastructure. Nonetheless, such features frequently produce vertical shocks in vehicle trajectories, which accelerometers may erroneously classify as surface deterioration. In this sense, D50 plays a distinctive corrective role: whenever it is detected on a segment, the accelerometric indicators are down-weighted or even suppressed, since their contribution may reflect false positives rather than genuine damage.

On the basis of these observations, the redundancy management strategy was concretely applied to the dataset. In practice, and before looking at the diagnostics, the accelerometric variables were initially paired on semantic grounds (type 1 with D40; type 3 with D20) as putative redundant proxies; subsequent correlation, co-occurrence and PCA diagnostics revised this cross-source mapping to D20-type 1 and D40-type 3. At the same time, D50 was explicitly treated as a correction factor, ensuring that segments characterised by functional elements such as manholes did not exhibit an artificially high deterioration index.

By recognising overlaps and dependencies, the methodology prevents distortions, preserves the interpretability of the results, and ultimately strengthens the reliability of the composite deterioration index.

In Table 13 and in Table 14 there are the tags of AIWAY and VIASAT.

Table 13 - VIASAT tags

VIASAT	
Tag	**Description**
type 1	potholes
type 2	bumps (speed humps/raised irregularities)
type 3	surface failures (distresses/unevenness)
type 4	settlements/depressions

Table 14 - AIWAY tags

AIWAY	
Tag	**Description**
D00	longitudinal cracks
D10	transverse cracks
D20	alligator cracking
D40	ruts, cracks, potholes, separations
D50	manholes and inspection covers

Before presenting the empirical diagnostics, I formalise the segment-level construction of the composite index used in the Brescia case so that all subsequent choices are explicit and reproducible. Let road segments be indexed by $i = 1, \dots, n$ (with $n = 1{,}598$ after aggregation). AIWAY (vision) delivers classes $D_{00}, D_{10}, D_{20}, D_{40}, D_{50}$; VIASAT (accelerometry) delivers type 1, type 2, type 3, type 4. Vision variables are computed, when confidence is available, as expected counts $D_{d,i} = \bar{p}_{d,i}\, n_{d,i}$ with $\bar{p}_{d,i} \in [0,1]$ the average confidence and $n_{d,i}$ the detections; accelerometric variables are raw counts $T_{k,i}$. To make segments comparable despite heterogeneous lengths (and, if relevant, observation windows), all variables are normalised "per 100 m (and per unit time if needed)" as $\tilde{X}_i = \frac{100}{L_i}\frac{X_i}{T_i}$, where L_i is segment length and T_i the observation window (set $T_i = 1$ if uniform). Because several distributions are zero-inflated and heavy-tailed, the same monotone variance-stabilising transform - typically $\log(1 + \tilde{X})$ or $\sqrt{\tilde{X}}$ - is applied to both members of any potentially redundant pair so that rankings are preserved and cross-source comparisons remain meaningful. The decision to adopt these transformations was supported by exploratory distribution diagnostics conducted on the aggregated dataset, confirming that a log transformation provided the most stable variance for highly skewed indicators (e.g., pothole detections), while a square-root scaling preserved interpretability for variables with moderate dispersion. The chosen approach ensured consistent ranking of segments without affecting the proportional structure of the data. The choice between the log and square-root transformations was based on visual inspection of the variable distributions and on the goal of stabilising variance while preserving rank order, without introducing any data-dependent tuning.

The correlation analysis provides a complementary view consistent with the zero-inflated nature of the dataset, serving as a quantitative proxy for co-occurrence strength between heterogeneous detections. The strongest cross-source associations emerge between D20 and type 1 (r = 0.685) and between D40 and type 3 (r = 0.677), both exceeding the 0.65 threshold that indicates a strong linear relationship.

These results confirm a clear correspondence between the two sensing modalities: D20–type 1 jointly describe depressions and settlements, while D40–type 3 correspond to potholes and roughness.

However, since the correlation values remain below 0.7, the redundancy is partial rather than complete. This means that each data source contributes complementary, non-overlapping information about the same underlying degradation mechanism.

Consequently, the indicators are not eliminated nor replaced, but fused through weighted integration, preserving the discriminative capability of vision-based detections while exploiting the broader spatial coverage and continuity of accelerometric measurements.

In summary, redundancy is structured but incomplete, and the integration of both signals ensures a richer, more stable, and physically interpretable representation of pavement distress.

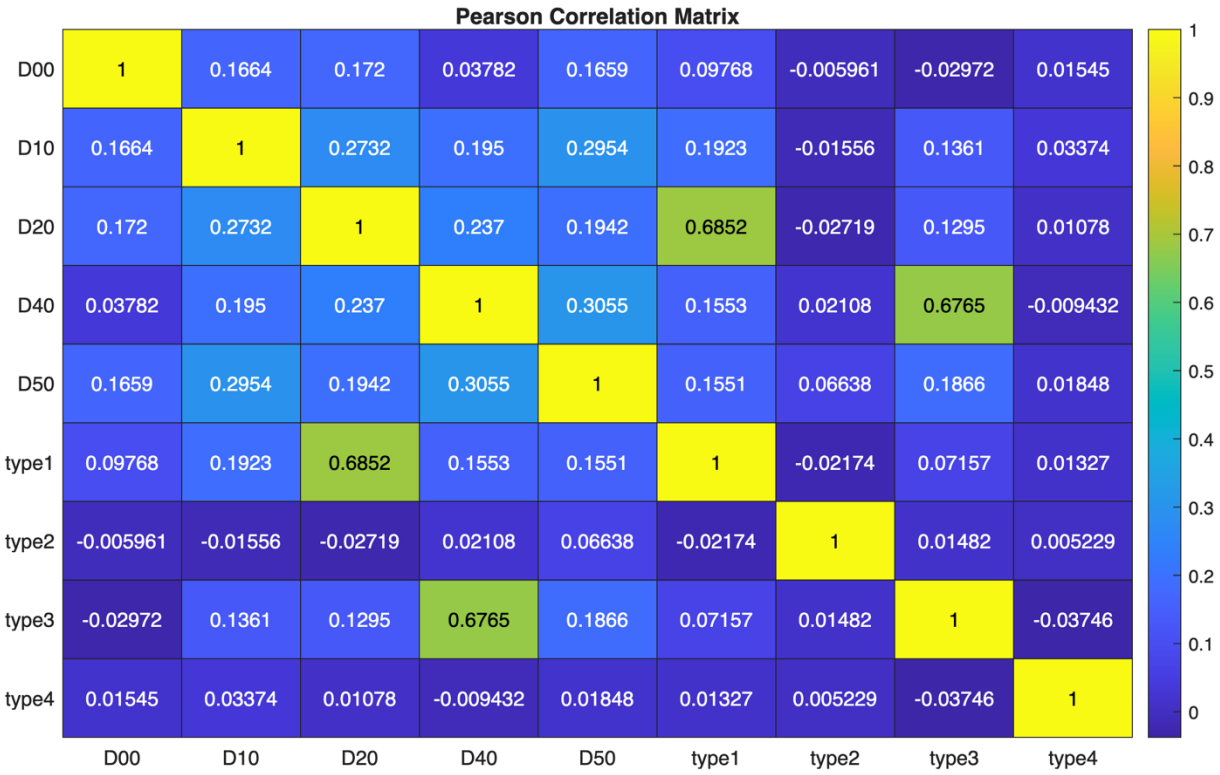

Figure 57 - Correlation matrix (Pearson)

The PCA consolidates these findings at multivariate level. Applying Equation 35. PC1 (26.2% explained variance) loads positively on D20, D40, type 1, type 3 (and to a lesser extent D10 and D50), representing a general deterioration intensity dimension. PC2 (16.1%) clearly separates D40 and type 3 (positive loadings) from D20 and type 1 (negative loadings), revealing two latent and partially competing constructs: pothole/roughness versus depression/settlement. Subsequent components capture more specific phenomena (e.g., cracks and isolated features). The first six principal components together explain approximately 85% of the total variance (26.2% + 16.1% + 12.2% + 11.0% + 11.0% + 9.0%), confirming that the dimensionality of the dataset is effectively captured by a limited number of latent constructs. This high cumulative variance indicates that the main deterioration patterns - captured by the fused vision-accelerometric pairs and a few additional residual variables - account for most of the information contained in the original indicators, while higher-order components mainly represent marginal or noise-driven variations. From a methodological standpoint, this confirms the internal consistency of the integrated dataset and supports the adopted redundancy-handling framework, demonstrating that the

overlapping signals across sensing modalities describe coherent and structured physical phenomena rather than random measurement noise.

Notably, D50 (manholes/inspection covers) shows moderate positive associations with several variables and contributes to PC1, which is consistent with contextual co-location (e.g., urban settings) rather than with genuine distress; methodologically, this supports using D50 as a corrective tag to down-weight accelerometric anomalies that may be false positives induced by functional surface elements.

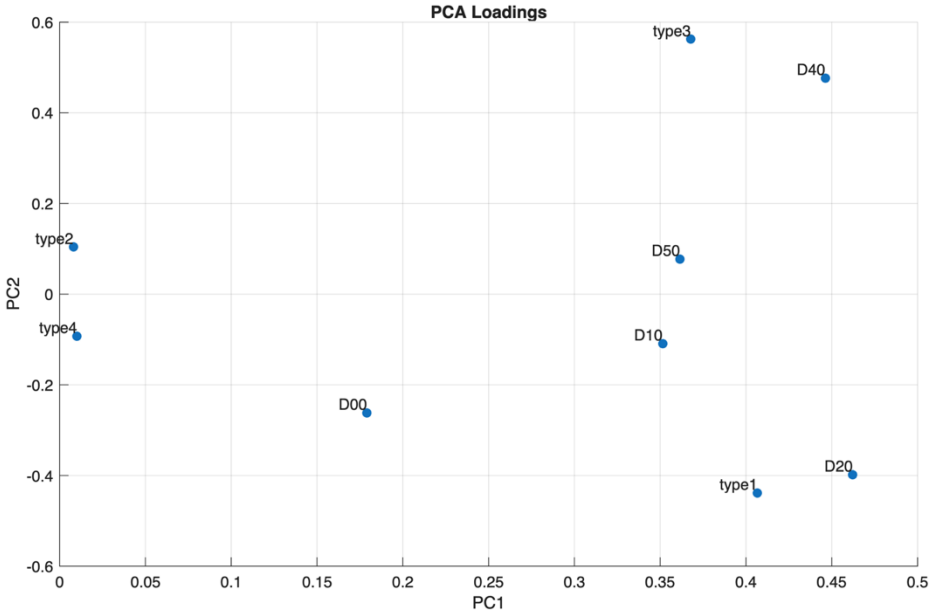

Figure 58 - PCA Loadings

The weighting coefficients α, β, and γ were determined through an empirical calibration informed by the multivariate dependency analysis presented above, rather than by arbitrary assignment. Specifically, their values reflect the relative contribution and redundancy of vision-based and accelerometric indicators as quantified by PCA loadings and Pearson correlation coefficients.

Coefficient α was introduced to balance the contribution of vision-based and accelerometric information in the composite framework. The value $\alpha = 0.7$ (and consequently $1 - \alpha = 0.3$) was selected to prioritize vision-based indicators, which exhibit stronger spatial coherence, higher stability, and more consistent alignment along the dominant PCA components, while still preserving the complementary

contribution of accelerometric signals, which are more sensitive to localized and transient dynamic effects.

Coefficients β and γ were introduced as attenuation factors to mitigate double counting between highly correlated variables across sensing modalities. Their values were determined by inspecting the strength and consistency of cross-source associations in both the Pearson matrix and PCA space: accelerometric types showing strong alignment with specific vision-based classes (e.g., type 1 with D20 and type 3 with D40) were down-weighted accordingly, whereas weakly coupled variables (type 2 and type 4) were assigned reduced or independent weights.Overall, the results indicate that redundancy is real but structured: (i) accelerometric type 1 should be harmonised with D20, and type 3 with D40 (either by merging into synthetic sub-indices or by down-weighting the accelerometric proxy); (ii) D50 should attenuate or suppress accelerometric contributions when present; and (iii) type 2/type 4 can be given low weight or treated separately due to their weak coupling with the main deterioration dimensions. This data-driven crosswalk prevents double counting, aligns sources along their true latent constructs, and provides a robust basis for constructing the composite deterioration index in the next section.

The empirical evidence confirms the presence of structured dependencies between vision-based and accelerometric indicators, though not along the pairs initially hypothesised. In the Pearson matrix, the strongest cross-source associations are observed between D20 and type 1 ($r = 0.685, p \ll 10^{-10}$) and between D40 and type 3 ($r = 0.676, p \ll 10^{-10}$). Conversely, the "intuitive" pairings D40-type 1 and D20-type 3 display only small correlations ($r = 0.155$ and $r = 0.130$, respectively). This pattern suggests that the accelerometric taxonomy does not map one-to-one onto the vision tags: the signal morphology behind type 1 appears more consistent with depressions/settlements (D20), whereas type 3 aligns with the pothole/roughness complex (D40). Other accelerometric variables show little structure: type 2 and type 4 are essentially uncorrelated with the vision indicators and among themselves, indicating more specific or rarer phenomena that do not co-vary with the dominant distress patterns.

6.3. C) Construction of Intervention Priority Index (I)

6.3.1. C1) Construction of sub-indices

The raw indicators were explicitly reorganised into distress categories reflecting the underlying degradation mechanisms. Concretely, the mapping adopted was:

- D00: longitudinal cracks and D10: transverse cracks were treated as distinct but residual indicators, capturing early-stage fissuring.
- D20: alligator cracking was paired with type 1: potholes, reflecting their empirical alignment in both correlation and PCA diagnostics, and aggregated into a depression/settlement construct.
- D40: ruts, cracks, potholes, separations was fused with type 3 - surface failures, defining the pothole/roughness construct.
- Type 2: bumps and Type 4: settlements/depressions exhibited weak associations with vision classes and were retained as residual accelerometric contributions, subject to conservative reliability factors and corrective gating.
- D50: manholes and inspection covers was not interpreted as a distress category, but as a corrective tag: its presence attenuated the contribution of accelerometric proxies to avoid false positives.

This categorisation structured the dataset into a vector of sub-indices $S_{t,i}$ per segment, each representing a meaningful and interpretable class of deterioration. The fused constructs (D20-T1, D40-T3) were emphasised in the weighting scheme, while residual categories were included with modest weights to maintain coverage. The corrective role of D50 ensured that segments with high functional-element density did not exhibit artificially inflated deterioration scores.

Table 15 - Association of AIWAY and VIASAT indicators into distress categories

Category	Variables included	Role in index	Notes
Longitudinal cracks ($S_{long,i}$)	D00	Residual	Early fissuring; low weight, retained for completeness.
Transverse cracks ($S_{trans,i}$)	D10	Residual	Early fissuring; low weight, retained for completeness.
Depressions / settlements ($S_{depr,i}$)	D20 (alligator cracking), Type 1 (potholes)	Fused construct	Strong cross-source redundancy; merged into synthetic sub-index.

Potholes / roughness ($S_{poth,i}$)	D40 (ruts, cracks, potholes, separations), Type 3 (surface failures)	Fused construct	Strong cross-source redundancy; merged into synthetic sub-index.
Bumps / raised irregularities ($S_{bumps,i}$)	Type 2	Residual accelerometric	Weak associations; low weight; subject to reliability factor q2q_2 and corrective gate.
Minor settlements / depressions ($S_{minor,i}$)	Type 4	Residual accelerometric	Weak associations; low weight; subject to reliability factor q4q_4 and corrective gate.
Manholes / inspection covers	D50	Corrective tag	Not a distress category; attenuates accelerometric contributions to avoid false positives.

In the specific configuration of the AIWAY–VIASAT dataset, each distress category contains either a single non-redundant variable or a pair of complementary variables from different sensing modalities (vision and accelerometry).

For categories including a single variable ($| F_t | = 1$), we apply the Equation 33.

This unified formulation preserves generality - allowing for redundant categories in future extensions - while remaining fully consistent with the current dataset configuration.

Longitudinal and transverse cracking are among the most recurrent forms of linear surface distress. Both categories are represented exclusively by vision-based detections, as the accelerometric signals are not sufficiently sensitive to these narrow, elongated defects. For this reason, no sensor fusion is required, and the category-level sub-index directly coincides with the normalized vision-derived indicator. Accordingly, for each road segment i, the sub-indices are computed as in Equation 37 in which:

- $S_{\text{long},i} = \widetilde{D}_{00,i}$
- $S_{\text{trans},i} = \widetilde{D}_{10,i}$

These expressions formalize a direct mapping between the detected crack density and the segment-level deterioration signal. The normalization of $\widetilde{D}_{00,i}$and $\widetilde{D}_{10,i}$ensures comparability across segments of different length and observation time, while preserving the proportionality to the underlying defect density. In these categories, the absence of redundancy or multimodality simplifies the computation and provides a baseline for subsequent categories where heterogeneous data sources are combined.

When vision and accelerometric indicators describe the same physical phenomenon (ref. Equation 36), they are fused into a single construct according to a rule-based integration scheme. For depressions and settlements, both vision-based detections (D20, alligator cracking) and accelerometric impacts (Type 1) contribute to the same degradation mechanism: $S_{\mathrm{dep},i} = \alpha_1 \, \widetilde{D}_{20,i} + (1 - \alpha_1) \, q_1 \, g_i \, \tilde{T}_{1,i}$,
*w*here:

- $\widetilde{D}_{20,i}$= normalised vision-based distress detections (alligator cracking);
- $\tilde{T}_{1,i}$= normalised accelerometric detections (severe impacts and potholes);
- $\alpha_1 \in [0,1]$= fusion balance between the two sensing modalities;
- $q_1 \in [0,1]$= reliability coefficient for the accelerometric signal;
- $g_i = \exp(-\kappa \, \widetilde{D}_{50,i})$ = corrective gate attenuating accelerometric contributions near functional discontinuities (manholes and covers).

The specific numerical values assigned to the reliability coefficients q_1 and q_3, as well as to the category weights w, were not fixed a priori but systematically investigated through a dedicated sensitivity analysis. For clarity, the methodological rationale and robustness assessment underlying their selection are therefore discussed in the subsequent Sensitivity Analysis section. Similarly, potholes and roughness are represented by the combination of vision-based detections (D40: potholes, rutting, separations) and accelerometric signals (Type 3: surface failures): $S_{\mathrm{rough,i}} = \alpha_2 \, \widetilde{D}_{40,i} + (1 - \alpha_2) \, q_3 \, g_i \, \widetilde{T}_{3,i}$,
where:

- $\widetilde{D}_{40,i}$= normalised vision-based detections of potholes, rutting, and surface separations;
- $\tilde{T}_{3,i}$= normalised accelerometric detections of irregularities and surface failures;
- $\alpha_2 \in [0,1]$= fusion coefficient for this construct;
- $q_3 \in [0,1]$= reliability factor for the accelerometric distress channel;
- $g_i$as defined above.

The redundancy analysis demonstrated that the AIWAY and VIASAT datasets are not only consistent but also complementary, with overlapping detections describing coherent physical phenomena rather than random noise. The systematic handling of redundancies, through both empirical diagnostics and rule-based harmonisation, ensured that each source contributes unique and interpretable information to the integrated dataset. The resulting crosswalk between vision-based and accelerometric indicators provides a stable foundation for constructing a composite deterioration index that reflects the true structural condition of each road segment while mitigating the effects of measurement overlap and contextual artefacts.

This structure can therefore be seen as a mid-level data fusion layer, where heterogeneous signals are reconciled into coherent constructs that retain physical meaning while improving numerical conditioning for subsequent statistical models.

Building on these results, the following section formalises the composite index and calibrates it against safety outcomes, translating integrated deterioration signals into an operational decision-support metric for pavement management.

The weighting structure adopted in the composite index follows established principles of multisensor data fusion [104] [105], according to which each data source contributes in proportion to its informational value and signal robustness. In this application, the computer vision component provides a higher discriminative capability in identifying the type of pavement distress (e.g., cracking, raveling, potholes), as shown in recent studies on automated road surface inspection [106] [107]. However, vision-based detection is sensitive to acquisition conditions such as illumination, occlusions, shadows, and camera perspective. Conversely, the accelerometric component, widely used in vehicle-based and smartphone-based monitoring, offers continuous spatial coverage and good repeatability, but provides a less explicit description of distress morphology and is influenced by vehicle dynamics and tire–road interaction.

This structural complementarity motivates the use of an asymmetric weighted fusion scheme, where the vision-derived contribution is assigned greater influence ($\alpha = 0.7$) than the accelerometric contribution ($1-\alpha = 0.3$). This follows the rationale of late fusion with reliability-based weighting, which is recommended when one source is more selective but less stable, while the other is more robust but less discriminative.

The accelerometric data used in this study are pre-processed by the data provider and originate from a heterogeneous fleet of vehicles differing in mass, suspension characteristics, tire stiffness and driving behavior. Such vehicle-to-vehicle variability, well documented in road surface sensing literature, prevents attributing full certainty to accelerometer-based detections. For this reason, credibility coefficients are used to express realistic confidence levels in the accelerometric channels. Channels associated with strong and repeatable dynamic shocks are assigned slightly higher credibility ($q_1 = q_3 = 0.9$), while channels more sensitive to velocity and vehicle-specific factors are assigned lower credibility ($q_2 = q_4 = 0.8$), in line with credibility-weighted fusion frameworks.

Finally, the top-level weights $w_{(d,k)}$ are constrained to be non-negative and to sum to one, ensuring a convex aggregation that preserves interpretability in units of expected deterioration per 100 m, as recommended in Pavement Management System guidelines. Assigning higher weights to fused constructs (0.4–0.4) and lower weights to residual indicators (0.02–0.05) promotes stability, reduces sensitivity to noise and rare events, and emphasizes the physically informative components of surface deterioration.

A transparent, vision-leaning specification that I adopt for analysis sets $\alpha_{d,k} = 0.7$ for fused pairs (vision 70%, accelerometry 30% subject to q and g), assigns $q_1 = q_3 = 0.9$ and $q_2 = q_4 = 0.8$ as conservative reliabilities, and allocates top-level weights to emphasise the fused constructs while keeping residuals modest for stability. Concretely, the weights used are $w_{20,1} = w_{40,3} = 0.4$ and $w_{00} = w_{10} = 0.05$, $w_{30} = 0.02$, $w_2 = w_4 = 0.04$.

6.3.2. C2) Definition of weights

Following the methodological framework described in the previous section, a sequence of regression models was estimated to quantify the relationship between pavement deterioration and near-miss frequency at the road-segment level. The analysis progressed from descriptive diagnostics to increasingly flexible count-data specifications, ensuring that each modelling step was justified by empirical evidence rather than by arbitrary model choice.

6.3.2.1.Preliminary diagnostics (OLS and multicollinearity)

Before estimating count models, a preliminary Ordinary Least Squares (OLS) regression was fitted to the 1,598 valid road segments. Although OLS is not theoretically appropriate for discrete near-miss data, this step provides two key diagnostics: (i) global signal direction and (ii) detection of multicollinearity.

As expected, the linear specification yielded no predictive explanatory power. The adjusted $R^2$was effectively zero ($R^2_{\text{adj}} = -0.0019$), and all coefficients displayed non-significant t-statistics ($p > 0.10$). This confirms that near-miss occurrence cannot be modelled as a continuous linear response and that inference must rely on models specifically designed for count processes.

The Variance Inflation Factor (VIF) was then computed to assess redundancy among predictors. All VIF values fell within the narrow range 1.00–1.14, indicating no multicollinearity among the deterioration sub-indices or geometric variables. This is an important structural property of the dataset: it ensures that the information contained in the six deterioration categories is not overlapping and that coefficients estimated in subsequent models will be numerically stable and interpretable.

Table 16 - Diagnostic results (OLS and multicollinearity diagnostics)

Metric	Value	Interpretation
Adjusted R²	-0.0019	No explanatory power (expected for count data)
Min-Max VIF	1.00-1.14	No evidence of multicollinearity
N (valid obs.)	1,598	Sample size after data cleaning

This diagnostic step confirms that:

- Linear models are unsuitable for inference, strengthening the need for count-based models.
- The deterioration variables used as predictors are statistically independent enough to serve as distinct explanatory factors in near-miss modelling.

6.3.2.2.Poisson regression results

A Poisson model with log-link and exposure offset was then estimated as the baseline specification. This formulation assumes equidispersion, i.e., that the variance of near-miss counts equals the mean. However, empirical near-miss data seldom satisfy this assumption due to unobserved heterogeneity, variation in traffic exposure, and localized disturbance effects.

Consistent with this expectation, the Pearson dispersion statistic was: $\hat{\phi} = 10.681$, indicating that the variance is more than ten times larger than the mean. Under such conditions, the Poisson model severely underestimates standard errors, leading to spurious statistical significance and unreliable inference.

Table 17 - Poisson model results and overdispersion check

Diagnostic	Value	Interpretation
Pearson dispersion	10.681	Strong overdispersion → Poisson invalid
AIC (Poisson)	High	Indicates poor likelihood fit
Implication	-	Move to NB2 and ZINB models

This result is not a flaw of the data, but a real property of road environments: near-miss events are rare, sporadic, and highly sensitive to localized surface irregularities and transient traffic conditions. Therefore, a model that allows variance to increase nonlinearly with near-miss rate is required.

6.3.2.3.Negative Binomial regression results (NB2)

To account for the observed overdispersion, a Negative Binomial regression of type NB2 was estimated. The NB2 model introduces a dispersion parameter α, allowing the variance to grow quadratically with the mean of Equation 39.

The estimated dispersion parameter $\hat{\alpha} = 88.02$confirms that near-miss variability is strongly heterogeneous, reflecting differences in surface distress severity, geometric configuration, and local traffic dynamics.

Model fit improved substantially relative to Poisson (log-likelihood = −401.87; AIC = 825.74; BIC = 884.88).

Table 18 - NB2 category-level coefficients and normalised weights

Sub-indices	β_t	W_t
Longitudinal cracks	-0,3063	0,0000
Transverse cracks	0,6727	0,3185
Depressions / settlements	-0,2359	0,0000
Potholes / roughness	0,5428	0,2569
Bumps / raised irregularities	0,8970	0,4246

Table 18 reports the estimated coefficients (β), their standard errors, Wald p-values, and Incidence Rate Ratios (IRR). The IRR expresses the multiplicative effect on the expected near-miss frequency for a one-unit increase in the corresponding variable, holding all other predictors constant. Coefficients greater than zero (IRR > 1) indicate that higher values of the predictor are associated with an increased probability of near-miss occurrence, whereas negative coefficients (IRR < 1) correspond to a protective or non-significant effect. The results show that three deterioration categories retained positive coefficients after truncation - Bumps, Transverse cracks, and Potholes/Roughness - together accounting for almost the entire composite weighting structure. Among these, Bumps exhibited the largest magnitude (β = 0.897, W_t = 0.425), confirming that vertical irregularities such as raised areas and localized deformations contribute most strongly to near-miss risk. Transverse cracks (β = 0.673, W_t = 0.318) and Potholes/Roughness (β = 0.543, W_t = 0.257) also showed positive but less pronounced associations with near-miss frequency. In contrast, Longitudinal cracks, Depressions/Settlements, and Minor Settlements displayed negative or statistically negligible coefficients, resulting in null weights after the non-negativity truncation.

The geometric control variables (tortuosity, mean turning angle, number of turns) were all statistically non-significant (p > 0.45), indicating that near-miss occurrence in this dataset is primarily explained by surface-level distress rather than geometric configuration. The mean value of the resulting deterioration index (I_mean = 0.229) and the low Spearman correlation with near-miss counts (ρ = 0.014, p = 0.57) confirm

that the model is well-calibrated but that near-miss risk remains dominated by localised surface irregularities rather than systemic geometric factors.

Overall, the NB2 model demonstrates high interpretability and statistical robustness, providing a coherent framework for quantifying the link between pavement deterioration and near-miss occurrence. The resulting category weights form the empirical foundation for the composite deterioration index, ensuring that each component reflects its observed relevance to road safety while maintaining a consistent and reproducible structure across the analysed network.

Although the NB2 specification substantially improved model fit relative to the Poisson baseline, the overall likelihood ratio test ($p = 0.827$) indicated that the explanatory power of the model remains statistically limited. More importantly, the residual distribution showed a strong concentration of zero-near-miss observations, indicating that a single-risk-generating process is insufficient to reproduce the empirical safety patterns across the network. In other words, while the NB2 formulation effectively captures overdispersion, it does not fully explain the distribution of near-miss counts across segments. Residual diagnostics further revealed a marked excess of zero-near-miss observations, accounting for more than half of the total sample. This pattern suggests that a significant share of the road network is composed of segments with no realistic probability of near-miss occurrence - conditions that the standard Negative Binomial model cannot represent, as it assumes a single underlying risk-generating process for all observations.

To address this limitation, the analytical framework was extended to a Zero-Inflated Negative Binomial (ZINB) model. The ZINB specification explicitly distinguishes between sampling zeros (segments where near-misses could occur but were not observed during the monitoring period) and structural zeros (segments that are intrinsically unlikely to experience near-misses due to their geometry, function, or environment).

These results make clear that, while the NB2 model corrects for overdispersion, it cannot reproduce the large mass of zero-near-miss segments. A specification that distinguishes structural zeros from sampling zeros is therefore required to represent the data-generating process adequately.

6.3.2.4.Zero-Inflated Negative Binomial (ZINB) model

The ZINB framework combines two distinct but complementary sub-models estimated simultaneously: a count component and an inflation component.

The count component (Negative Binomial part) models the expected number of near-misses on segment i as a log-linear combination of deterioration sub-indices, geometric attributes, and exposure as in Equation 42.

The coefficients $\beta_t$quantify the marginal effect of each deterioration category on the expected number of near-misses, while $\gamma_k$capture the contribution of geometric factors. Positive coefficients indicate that higher distress levels are associated with a greater expected near-miss frequency, whereas negative coefficients correspond to protective or non-significant effects.

The inflation component (logit part) instead models the probability that a segment belongs to the always-zero state (i.e., structural zeros). It is calculated as in Equation 43.

The parameters $\delta_h$describe the mechanism generating zero counts and are not directly related to pavement deterioration, but to the probability that a segment is inherently non-accident-prone.

This dual structure allows the model to distinguish between sampling zeros - segments where a near-miss could occur but was not observed within the monitoring period - and structural zeros, where the likelihood of a near-miss is intrinsically negligible.

The inflation component, parameterised via a logit link, was kept parsimonious and included only an intercept term, implying a constant baseline probability of structural zeros across the network. The estimated intercept (δ_0 = 3.34, SE = 0.14, $p < 0.001$) indicates that a substantial share of segments systematically belong to the zero-near-miss state, consistent with the heterogeneous exposure typical of mixed urban and peri-urban road networks.

In the count component, coefficients were estimated for the five category-level sub-indices $S_{(t,i)}$and for the geometric control variables. The estimated dispersion parameter ($\hat{\alpha}$ = 0.26) confirms moderate overdispersion, lower than in the standard NB2 model, suggesting that part of the variability previously attributed to unobserved

heterogeneity is now captured by the zero-inflation mechanism. Model diagnostics showed a clear improvement in fit relative to the NB2 specification, with log-likelihood = −376.41, AIC = 776.82, and BIC = 841.33.

The Vuong test, comparing the two non-nested models, yielded $Z = 6.43$ ($p < 0.001$), confirming that the inclusion of the zero-inflation component provides a statistically superior representation of near-miss data.

Within the count process, three categories retained positive coefficients after truncation - Bumps, Depressions/Settlements, and Longitudinal cracks - while the remaining categories (Transverse cracks, Potholes/Roughness, and Minor settlements) displayed non-significant or negative effects. Among them, Bumps exhibited the largest magnitude ($\beta = 0.65$, $p \approx 0.07$), followed by Depressions/Settlements ($\beta = 0.45$, $p \approx 0.24$) and Longitudinal cracks ($\beta = 0.35$, $p \approx 0.44$).

These signs and magnitudes are consistent with the physical interpretation of dynamic irregularities as primary contributors to vertical acceleration and, consequently, to near-miss likelihood.

The derived category weights were obtained exclusively from the coefficients of the count component (β_t), which capture the empirical link between deterioration and near-miss frequency. The inflation parameters (δ_h) were not used, as they describe the structural-zero mechanism rather than the safety-related response.

Weights were computed through non-negative normalisation, ensuring monotonicity with respect to deterioration intensity as in Equation 47.

This procedure guarantees that the relative importance of each distress category reflects its empirically validated contribution to near-miss frequency, as captured by the ZINB count model. In this framework, the estimated coefficients β_t act as empirical proxies for the marginal effect of each deterioration category on near-miss likelihood, while the normalisation step converts these effects into interpretable proportions within the composite structure.

Table 19 - ZINB category-level coefficients and normalised weights

Sub-indices	β_t	W_t
Longitudinal cracks	0,3512	0,2428
Transverse cracks	-0,0061	0,0000
Depressions / settlements	0,4495	0,3107
Potholes / roughness	-0,1356	0,0000
Bumps / raised irregularities	0,6459	0,4465
Minor settlements	-0,2961	0,0000

The weighting structure highlights that vertical irregularities (Bumps) are the dominant contributors to near-miss risk, confirming the mechanical role of vehicle dynamic instability and loss of contact with the pavement as primary safety drivers. Through this calibration, the weighting structure directly incorporates the statistical relationship between deterioration and safety outcomes, ensuring that the composite index not only summarises surface condition but also reflects its operational relevance for near-miss risk. This integration provides a quantitative and reproducible link between data-driven near-miss modelling and pavement management, establishing a coherent foundation for prioritising maintenance interventions based on both structural and safety dimensions.

In summary, the ZINB-derived weights ensure that the composite pavement deterioration index reflects the components most strongly associated with near-miss risk, providing a defensible and safety-oriented basis for prioritising maintenance interventions. The following subsection uses these calibrated weights to compute segment-level deterioration scores and to visualise their spatial distribution across the network.

6.3.2.5.Comparative interpretation of NB2 and ZINB models

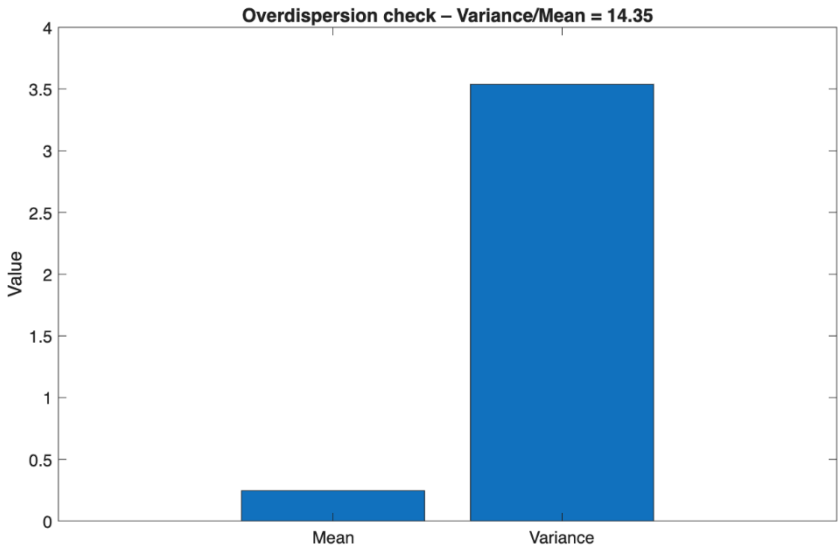

Figure 59 - Overdispersion check – Variance/Mean = 14.35

The overdispersion of near-miss counts was assessed by comparing the sample mean and variance of near-miss frequency across road segments. As shown in Figure 59, the variance is more than an order of magnitude larger than the mean. This confirms that the near-miss data are strongly overdispersed and therefore incompatible with the equidispersion assumption underlying the Poisson model. Under these conditions, Poisson regression would underestimate standard errors and inflate statistical significance, leading to unreliable inference. This diagnostic result justifies the adoption of the Negative Binomial (NB2) model as a more appropriate count-data specification capable of capturing the observed variability in near-miss occurrences.

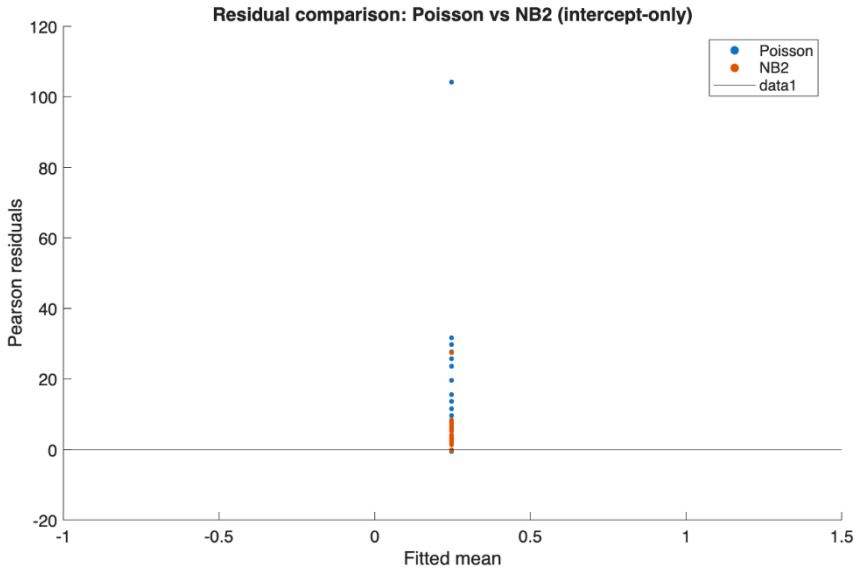

Figure 60 - Residuals comparison: Poisson vs NB2 (intercept-only)

To further assess model adequacy, Figure 60 compares Pearson residuals from the Poisson and Negative Binomial (NB2) models fitted with intercept-only specifications. Under the Poisson model, residuals exhibit several extreme positive values (reaching above 100), indicating that the model systematically underestimates near-miss counts for segments with observed near-misses. This pattern is a direct consequence of the Poisson equidispersion assumption, which forces variance to match the mean and therefore fails in the presence of heterogeneous and sporadic near-miss events.

In contrast, the NB2 model produces residuals that are substantially more concentrated around zero, confirming that its dispersion parameter successfully accommodates variability in near-miss frequency. This diagnostic result provides visual evidence that NB2 yields more reliable inference and represents a statistically adequate foundation for subsequent model extensions (e.g., Zero-Inflated NB).

Residual diagnostics were performed only for the Poisson and NB2 models. The ZINB model was not included in this comparison because it consists of two distinct latent components: a count process (NB2) and a structural-zero process (logit). Since not all observations belong to the same generative mechanism, Pearson residuals cannot be interpreted consistently across the entire sample. For this reason, residual plots are meaningful for Poisson and NB2, but not for ZINB, where model adequacy is instead

evaluated through likelihood-based criteria (AIC/BIC) and non-nested comparison tests (e.g., Vuong test).

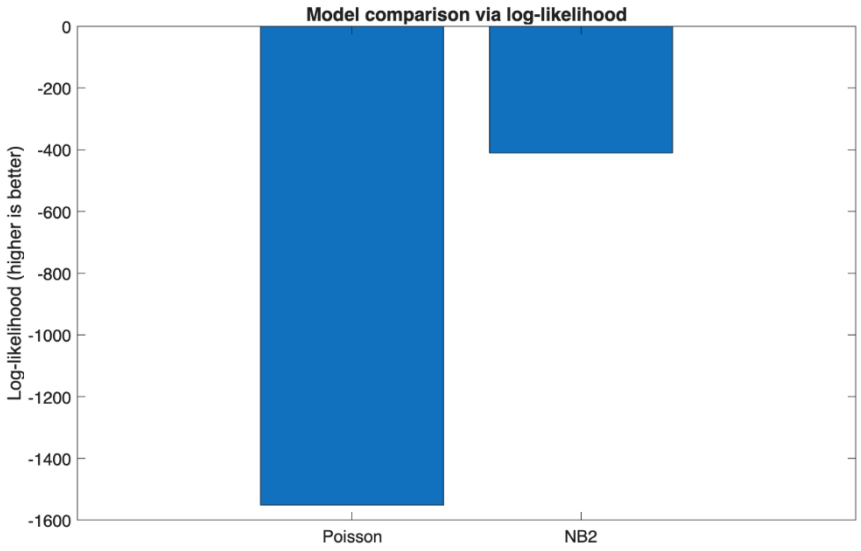

Figure 61 - Model comparison based on log-likelihood (Poisson vs Negative Binomial NB2)

The comparison of model likelihoods (Figure 61) provides additional evidence that the Poisson formulation is inadequate for modelling near-miss frequency. The log-likelihood of the Poisson model is considerably lower (i.e., more negative), indicating poor goodness of fit. In contrast, the NB2 specification substantially increases the log-likelihood, demonstrating that the introduction of a dispersion parameter improves the model's ability to capture the heavy-tailed distribution of near-miss counts. This result is consistent with the overdispersion diagnostics discussed earlier.

The ZINB model is not included in the log-likelihood bar chart because the NB2 and ZINB specifications are non-nested. In such cases, raw log-likelihood values are not directly comparable, and model superiority must instead be assessed through dedicated non-nested comparison tests. Accordingly, the Vuong test was used to evaluate the performance differential between NB2 and ZINB, confirming that the zero-inflated specification provides a statistically superior fit.

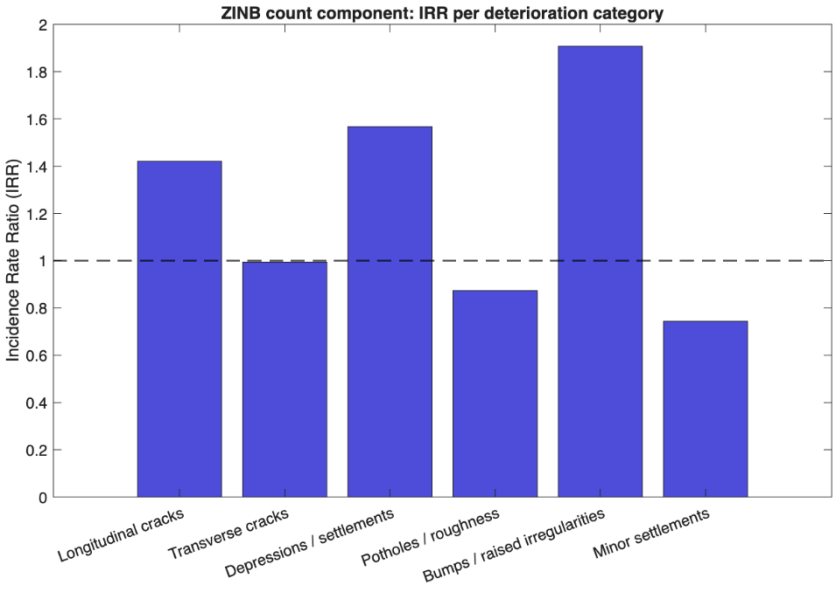

Figure 62 - Incidence Rate Ratios (IRR) from the ZINB count component by deterioration category

Figure 62 illustrates the Incidence Rate Ratios (IRR) estimated from the count component of the ZINB model. The IRR representation allows for a direct and interpretable comparison of the estimated effects: values greater than one indicate that increasing the severity of the corresponding distress category is associated with a higher expected near-miss frequency. The results highlight that vertical irregularities ("Bumps / raised irregularities") exert the strongest influence on near-miss occurrence (IRR ≈ 1.9), supporting the interpretation that localised discontinuities in pavement elevation generate sudden vehicle dynamic instability. Similarly, depressions and settlements (IRR ≈ 1.6) and longitudinal cracking (IRR ≈ 1.4) also show positive associations, though with lower magnitude.

Conversely, transverse cracking, potholes/roughness, and minor settlements yield IRR values close to or below unity, indicating that their contribution to near-miss likelihood is weak or statistically negligible in the observed context. These findings directly inform the construction of the composite deterioration index: categories with IRR > 1 receive positive weights, while categories with non-significant or protective associations are assigned zero weight. The IRR results therefore provide the empirical basis for prioritising deterioration mechanisms according to their demonstrated safety relevance.

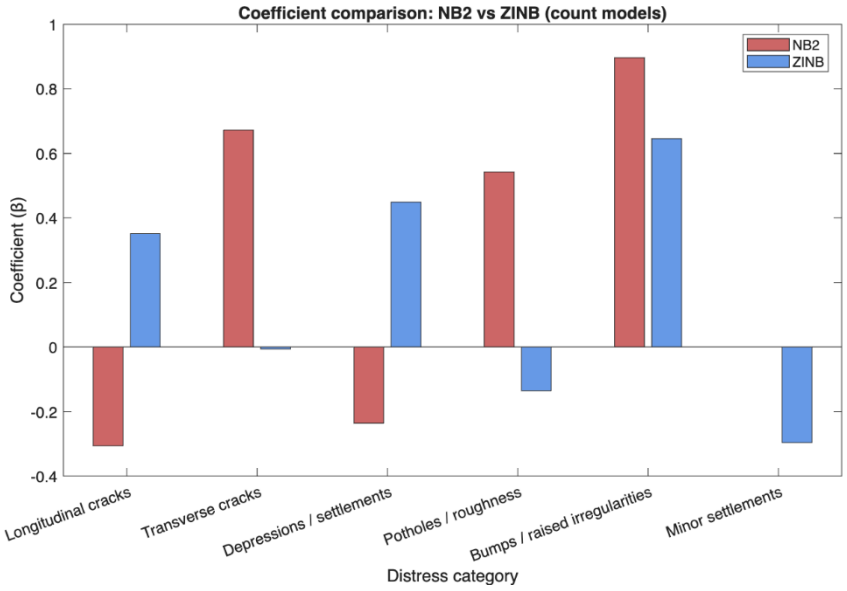

Figure 63 - Comparison of regression coefficients between NB2 and ZINB count components

Figure 63 compares the regression coefficients estimated under the NB2 model with those obtained from the count component of the ZINB specification. The NB2 formulation attributes relatively large positive effects to transverse cracks, potholes/roughness, and bumps, whereas the ZINB model shows a general attenuation in coefficient magnitudes. This behavior is expected: by explicitly modelling structural-zero segments, the ZINB model effectively restricts the estimation of β to those segments that are realistically exposed to near-miss occurrence, thereby producing more conservative and behaviorally meaningful parameter estimates.

Two important observations emerge. First, bumps / raised irregularities remain the strongest predictor of near-miss risk across both models, reinforcing the interpretation that vertical discontinuities in the pavement significantly affect vehicle dynamic stability. Second, the sign reversals observed for longitudinal cracks and minor settlements reflect the fact that these variables exhibit weak or inconsistent associations with near-miss occurrence when structural-zero segments are excluded. This selective effect is consistent with previous literature on heterogeneous road networks, where only a subset of deterioration mechanisms translates into meaningful safety outcomes. Overall, the comparison highlights that the ZINB model provides a more cautious and physically interpretable estimation of deterioration–safety relationships, as it avoids

inflating the influence of distress categories that are present on segments with no actual near-miss risk.

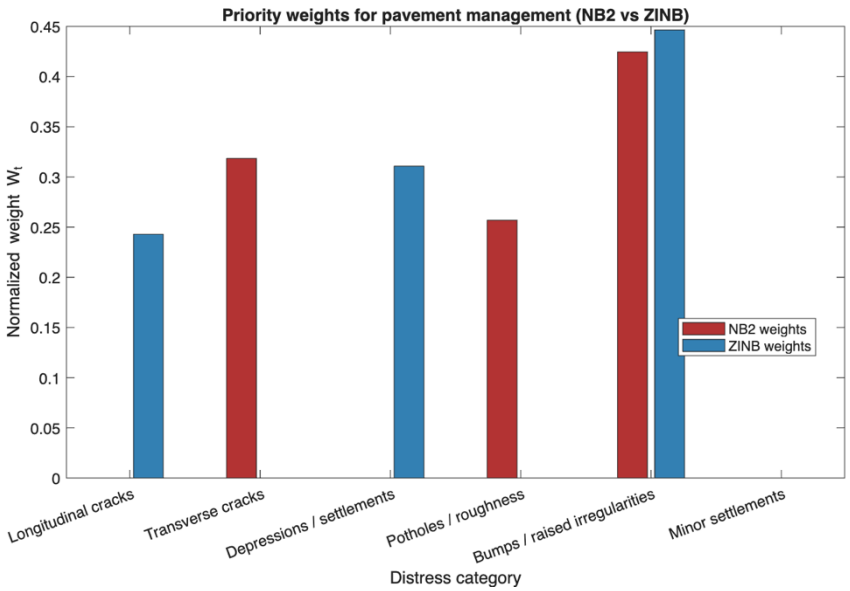

Figure 64 - Comparison of category weights for pavement management (NB2 vs ZINB)

Figure 64 compares the category weights obtained under the NB2 model with those derived from the ZINB specification. In the NB2 formulation, weights are distributed across several distress categories, suggesting that multiple forms of surface deterioration may contribute to near-miss risk. However, when structural-zero segments are explicitly modelled in the ZINB framework, the weighting structure becomes more selective: only those distress categories that remain associated with near-miss occurrence within the near-miss-exposed subset of the network retain positive weights.

In particular, bumps / raised irregularities consistently emerge as the most influential category in both models, reinforcing the dominant role of vertical discontinuities in generating safety-critical conditions. The ZINB specification, however, attenuates or eliminates weights for categories whose association with near-miss risk is not robust once structurally safe segments are removed (e.g., transverse cracks or minor settlements). This difference reflects the improved behavioral realism introduced by the zero-inflation mechanism, which prevents the overestimation of distress effects driven solely by their prevalence on segments where near-misses never occur.

In summary, the empirical evidence shows that (i) the Poisson model is statistically inadequate due to strong overdispersion, (ii) the NB2 model improves fit but cannot account for the large share of structural zeros, and (iii) the ZINB model provides the best representation by explicitly separating intrinsically safe segments from those genuinely exposed to near-miss risk. Consequently, using the coefficients of the ZINB count component as the basis for the composite index ensures statistical coherence, physical interpretability, and operational relevance for maintenance prioritisation.

6.3.3. C3) Definition of Intervention Priority Index (I)

The final outcome of the methodological framework is the construction of a composite deterioration index that consolidates vision-based detections, accelerometric anomalies, and corrective tags into a single interpretable metric at the road-segment level. The guiding principle is that the index must preserve completeness - retaining the contribution of all relevant distress types - while ensuring robustness by preventing double counting of redundant variables and reducing spurious signals caused by functional elements.

Formally, and in continuity with the data-fusion framework described above, once the sub-indices S_(t,i) have been computed for each distress category t, the composite deterioration index for segment i is obtained as a convex combination of these components, as defined in Equation 48.

Through this layered construction, the index I_i can be read as the expected intensity of deterioration per 100 m, weighted by severity, reliability, and safety relevance. It systematically integrates redundant signals into construct-level sub-indices, applies corrective gates to reduce false positives from functional elements, and balances all categories according to their empirically validated contribution to near-miss occurrence (Equation 55).

From a decision-support perspective, this synthesis offers several advantages. First, it ensures interpretability, since each component of the index corresponds to an engineering category of distress. Second, it guarantees consistency, as redundancy is treated explicitly and functional elements are accounted for. Third, it provides

robustness, as the weighting is calibrated against safety and validated through cross-validation, bootstrap resampling, and parameter stress tests. Finally, the index is operational, remaining in meaningful units that can be readily compared across segments, ranked for prioritisation, or discretised into severity classes (low, medium, high) using data-driven thresholds.

The composite deterioration index thus represents the culmination of the methodological framework: a single, transparent, and statistically grounded measure that is directly usable for the management of pavement assets and the optimization of maintenance strategies. Building upon this formulation, the following section evaluates the robustness of the composite index through a structured sensitivity analysis. This comprehensive formulation also provides a solid baseline for subsequent sensitivity analyses and operational deployment tests.

The experimental plan systematically varies $\{a_1, a_2, \kappa, q_1, q_3\}$ using a compact full-factorial grid (e.g., $a_1, a_2 \in \{0.50, 0.65, 0.70, 0.80, 0.90\}$, $\kappa \in \{0.40, 0.69, 1.00\}$, $q_1, q_3 \in \{0.80, 0.90, 1.00\}$); for each configuration we recompute the fused constructs, apply the gate g_i, assemble category sub-indices $S_{t,i}$, and form the composite index I_i. To attribute variability correctly with respect to safety, we adopt two complementary protocols: (A) re-calibrated weights, for each run we re-estimate W_t from non-negative count models of near-misses (NB2 preferred under over-dispersion, with exposure offsets and geometric controls), preserving safety anchoring; (B) frozen weights, we keep W_t at the baseline solution to isolate the mechanical effect of parameter changes on I_i at fixed between-category importance. We evaluate quality and robustness along multiple axes: (i) safety coherence via Spearman $\rho(I$,near-misses), changes in model AIC/BIC at fixed features, and Balanced Accuracy for classifying high-near-miss segments (e.g., top-quartile Y) using I as a score; (ii) ranking stability via Spearman/Kendall correlations across runs and Jaccard overlap on top-k critical segments; (iii) gate diagnostics (distribution of g_i, share with $g_i < 0.5$, mean accelerometric share in I) to ensure κ does not induce systematic under-reporting in manhole-dense areas; (iv) variance decomposition across parameters (fixed-effects ANOVA or response-surface analysis on median/variance of I_i, plus Partial Rank

Correlation Coefficients on I_i or on $\rho(I,\text{near-misses})$) to quantify each lever's contribution; and (v) sub-network analysis (urban vs. extra-urban, functional classes, districts) to capture context heterogeneity. Each run outputs auditable artefacts (tables of pre-processed indicators, gate values, fused pairs, category sub-indices, I_i, re-estimated W_t where applicable, correlation matrices, and optional operational thresholds), enabling point-by-point comparison; as practical acceptance rules, we target ranking Spearman ≥ 0.90 versus the baseline, Balanced Accuracy shifts within ±0.03, and Jaccard overlap > 0.7 on top-k lists. Where deviations emerge, we prefer higher α (e.g., 0.80) when vision shows superior specificity and auditability, or higher κ (e.g. 1.00) in networks dense with functional elements to mitigate spurious inflation, while q_k should ultimately be aligned with external validation evidence. This design demonstrates that operational conclusions do not hinge on arbitrary parameter settings, identifies tolerable ranges for $\{a_1, a_2, \kappa, q_1, q_3\}$, and provides reproducible guidance for deploying the index across networks and contexts with preserved safety calibration and engineering traceability.

Although the proposed framework is statistically robust and operationally reproducible, some limitations must be acknowledged to ensure a transparent interpretation of results. First, the safety-based weighting scheme captures associations between distress patterns and near-miss occurrences while controlling for geometric and exposure factors. However, this mechanism is not intended to assert direct causal inference: near-miss dynamics are influenced by multiple contextual and behavioral determinants beyond pavement condition. Thus, the interpretation of W_t is associative and risk-informed, rather than strictly causal. Second, the study is conducted in a data-scarce context in which conventional quantitative ground-truth references (e.g., PCI surveys, IRI measurements, deflectometric campaigns) were not available. For this reason, part of the validation relies on qualitative consistency checks through street-level imagery. This aligns with current practices in early-phase PMS deployment where heterogeneous sensor networks are introduced before full-scale condition surveys, and where visual validation is considered acceptable for confirming deterioration typologies and spatial continuity patterns [108]. Despite these limitations, the proposed framework establishes a replicable foundation for

integrating heterogeneous sensing technologies into data-driven Pavement Management Systems.

6.4. D) Sensitivity analysis

6.4.1. D1) Sensitivity analysis on classification thresholds

A sensitivity analysis was conducted to evaluate the robustness of the three-level classification (LOW-MEDIUM-HIGH) derived from the composite deterioration index, with particular attention to the stability of the HIGH class, which is operationally critical as it represents segments exhibiting the most severe forms of pavement deterioration and therefore drives maintenance prioritisation. Analyses were performed on $N = 1{,}598$ segments. Reporting N and class-wise set sizes ensures that Jaccard values are interpretable and not inflated by small denominators.

The baseline threshold set $(\tau_1, \tau_2) = (0.20, 0.60)$ was originally selected based on empirical distribution inspection, interpretability of class semantics, and consistency with the ordinal progression of distress intensity observed in the integrated dataset. To assess the extent to which these thresholds influence class composition, three alternative configurations were tested: a downward shift of both thresholds (0.15,0.55), an upward shift (0.25,0.65), and a purely distribution-driven configuration based on the empirical 33rd and 66th percentiles ($\tau_1 \approx 0.168, \tau_2 \approx 0.350$). For each configuration, the resulting classification was compared to the baseline through two complementary measures: (i) an overall stability index, defined as the proportion of segments retaining their class under threshold perturbation, and (ii) Jaccard similarity indices computed for the LOW and HIGH classes separately, as these extremes encode the most actionable maintenance priorities, while the MEDIUM class inherently represents a transitional condition. The results show that the 0.15/0.55 configuration reduces the distinctiveness of the HIGH class, leading to a stability of 0.849 and a Jaccard similarity of only 0.528 for HIGH, indicating that a lower upper threshold tends to absorb borderline high-deterioration segments into MEDIUM, thereby reducing the discriminative capability of the classification to reliably isolate severe deterioration cases. Conversely, the 0.25/0.65 configuration results in a stricter

and more selective HIGH class, yielding higher overall stability (0.882) but a markedly lower Jaccard similarity for HIGH (0.369), indicating that the upper threshold τ_2 exerts a decisive influence on tail characterization, with upward shifts leading to systematic under-identification of critically deteriorated segments. The percentile-based thresholds produce the lowest agreement with the baseline (stability 0.665; Jaccard $_{\text{HIGH}} = 0.190$), demonstrating that quantile partitioning (although statistically neutral in terms of distribution) disrupts the correspondence between numerical index values and the underlying physical severity of observed pavement distress phenomena. It is important to note that the MEDIUM class does not represent a single, physically distinct deterioration state, but rather a transitional regime in which distress signatures are present but not yet structurally dominant. In composite deterioration frameworks, this class acts as a buffer zone between pavement segments exhibiting negligible deterioration and those showing advanced structural degradation. Therefore, moderate reassignments within the MEDIUM class under threshold perturbation are expected and do not compromise the interpretability or operational usefulness of the classification. In contrast, the LOW and HIGH classes must remain stable, as they correspond respectively to clearly healthy segments and to segments requiring attention due to advanced distress.

Across all scenarios, reclassifications predominantly occur within the MEDIUM band, confirming its intrinsic interpretive role as a buffer state between structurally sound and critically deteriorated segments. Taken together, these analyses demonstrate that the baseline thresholds (0.20, 0.60) offer the optimal balance between statistical robustness, semantic interpretability, and operational prioritisation relevance. In particular, they ensure that the HIGH class reliably captures segments with structurally significant deterioration while preventing artificial inflation or suppression of critical severity signals due to threshold placement. For this reason, the baseline configuration is retained in the final definition of the composite indicator and is recommended for deployment in comparable sensing architectures and network-scale pavement management workflows.

A visual comparison of class distributions under the four threshold configurations provides a clearer understanding of how the boundaries between categories shift. In the baseline setting (τ_1 = 0.20, τ_2 = 0.60), the class distribution remains coherent and aligned with the expected deterioration progression, with the LOW and MEDIUM classes accounting for the majority of segments, and the HIGH class isolated to a compact but meaningful subset corresponding to the most deteriorated road sections (Figure 65).

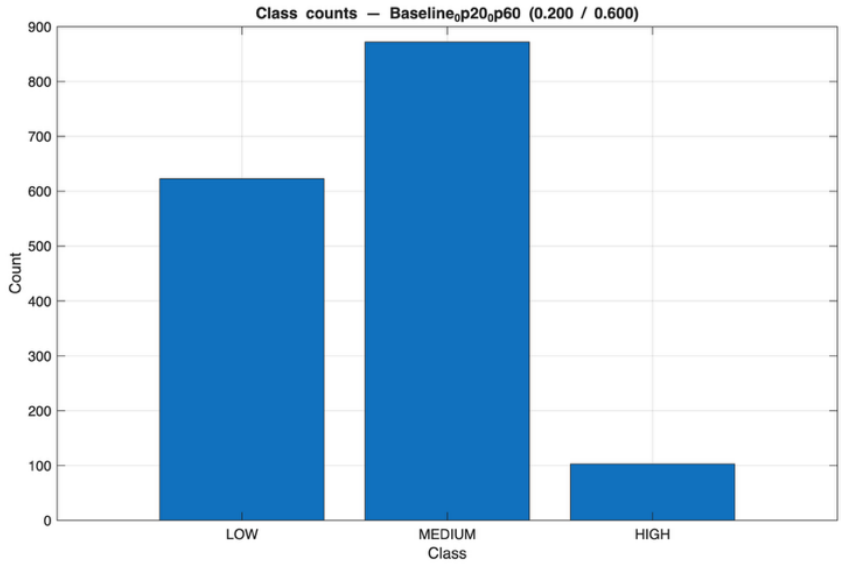

Figure 65 - Class counts (Baseline)

In contrast, lowering both thresholds to (0.15, 0.55) causes the HIGH class to shrink, while both LOW and MEDIUM expand (Figure 66). This configuration reassigns several borderline-high segments to MEDIUM, reducing the operational distinctiveness of the most critical category.

The corresponding confusion matrix confirms this interpretation, showing substantial flux from HIGH → MEDIUM and an overall decrease in class-level agreement (Figure 67).

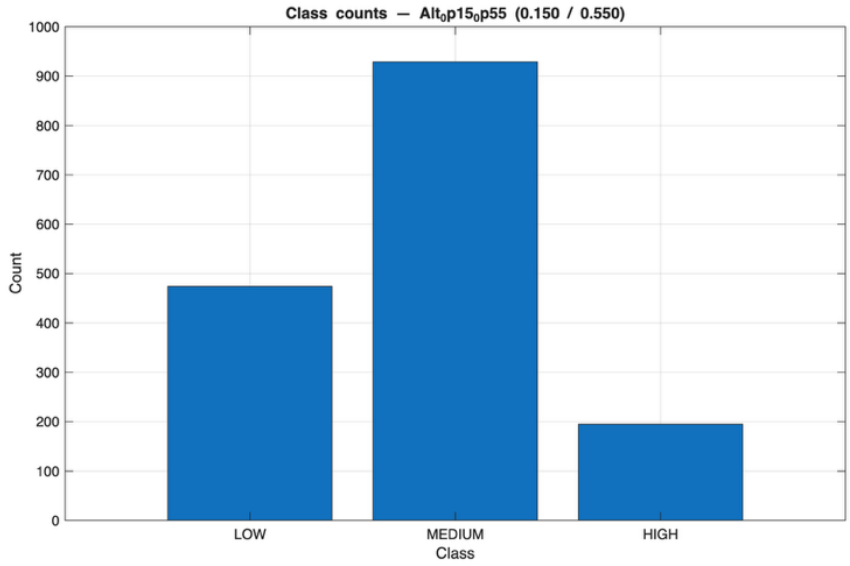

Figure 66 - Class counts - Alt 0.15 / 0.55

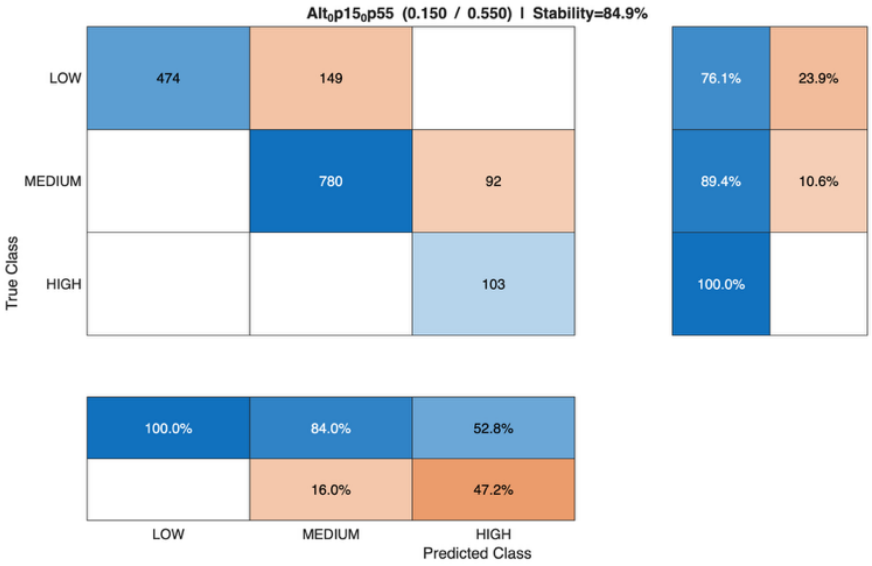

Figure 67 - Confusion - Alt 0.15 / 0.55

Raising the thresholds to (0.25, 0.65) produces the opposite behavior: the HIGH class becomes significantly smaller and more selective (Figure 68). While overall stability increases, the Jaccard similarity for the HIGH class drops sharply, indicating that many segments classified as HIGH under the baseline are shifted into MEDIUM. The confusion matrix highlights this effect, with systematic reclassification from HIGH → MEDIUM (Figure 69). This confirms that the upper threshold τ_2 plays a

disproportionate role in determining the sensitivity of the classification to severe deterioration signals.

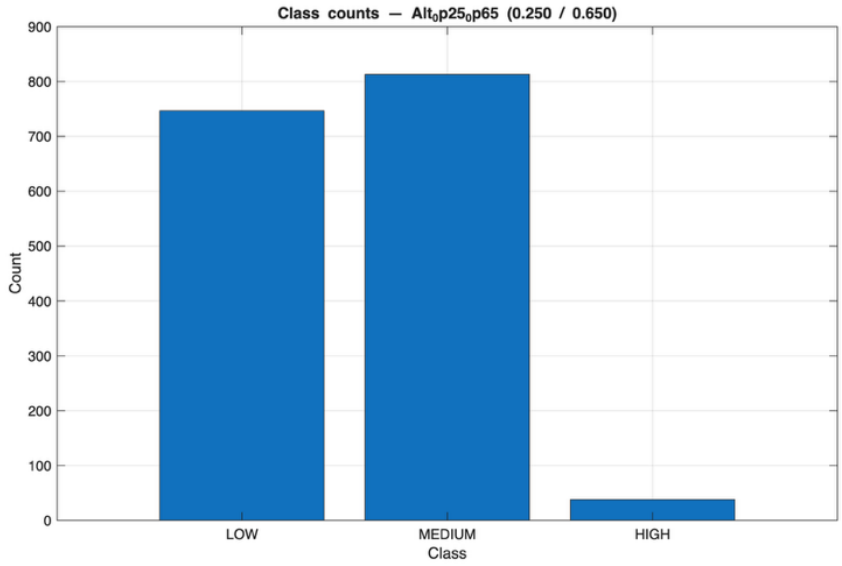

Figure 68 - Class counts - Alt 0.25 / 0.65

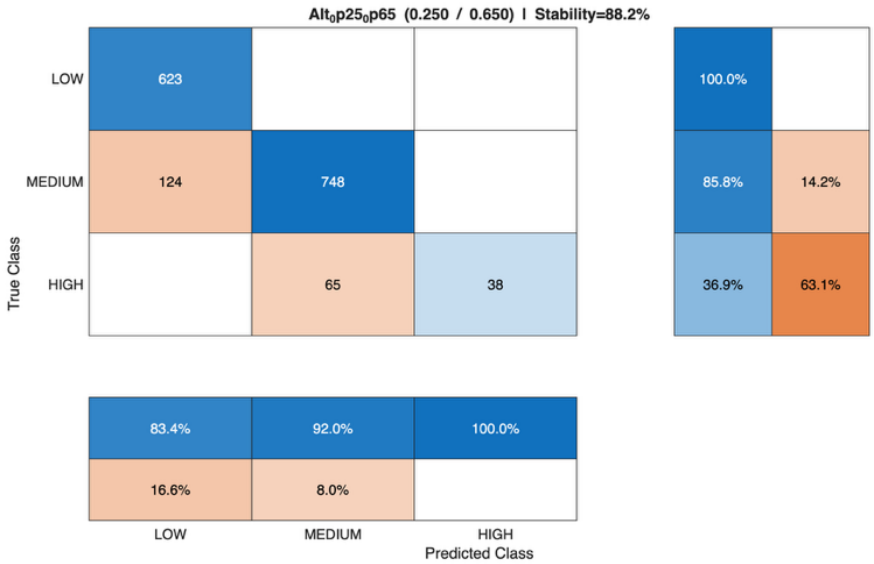

Figure 69 - Confusion - Alt 0.25 / 0.65

The quantile-based thresholds ($\tau_1 \approx 0.168$, $\tau_2 \approx 0.350$) result in an almost uniform distribution of segments across LOW, MEDIUM, and HIGH (Figure 70). While this approach may appear statistically neutral, the resulting class boundaries no longer reflect meaningful transitions in deterioration severity, reducing interpretability and

operational usefulness. The confusion matrix further illustrates this breakdown, displaying widespread reassignments across all classes (Figure 71).

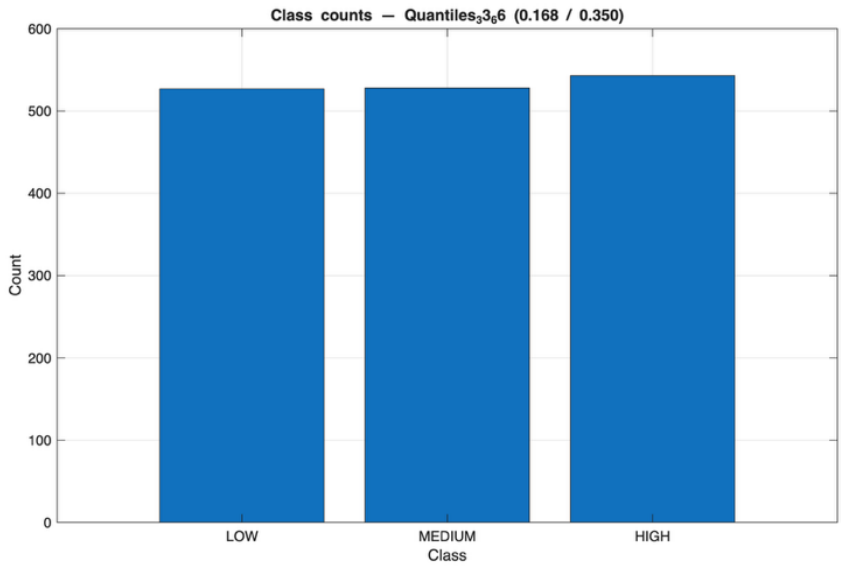

Figure 70 - Class counts - Quantiles 33 / 66

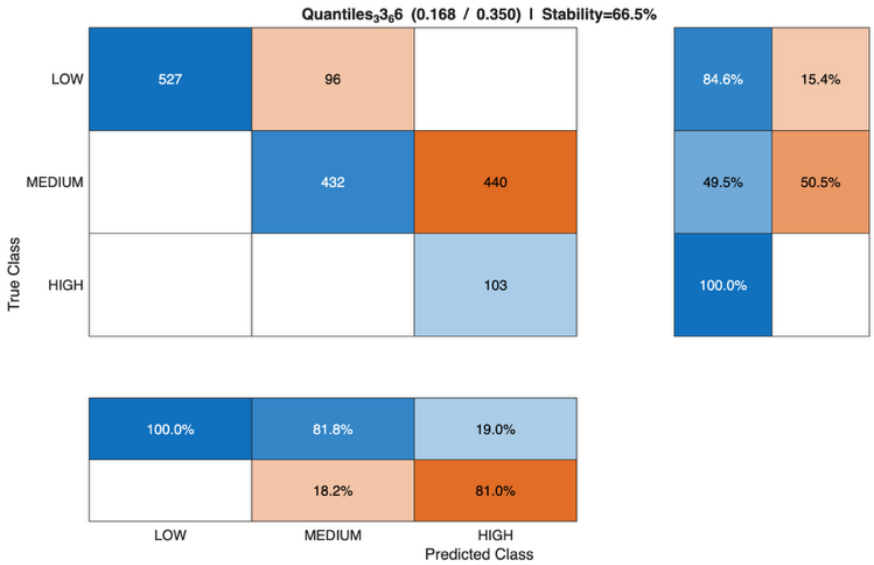

Figure 71 - Confusion - Quantiles 33 / 66

Finally, density plots help interpret the influence of threshold positioning relative to the empirical distribution of the composite index. When only the baseline thresholds are shown, the class transitions align with visible inflection points in the distribution

(Figure 72). When all threshold configurations are displayed simultaneously, the percentiles-based τ_1 and τ_2 are shown to fall near the main mass of the MEDIUM class, explaining the loss of interpretability observed in the quantile classification (Figure 73).

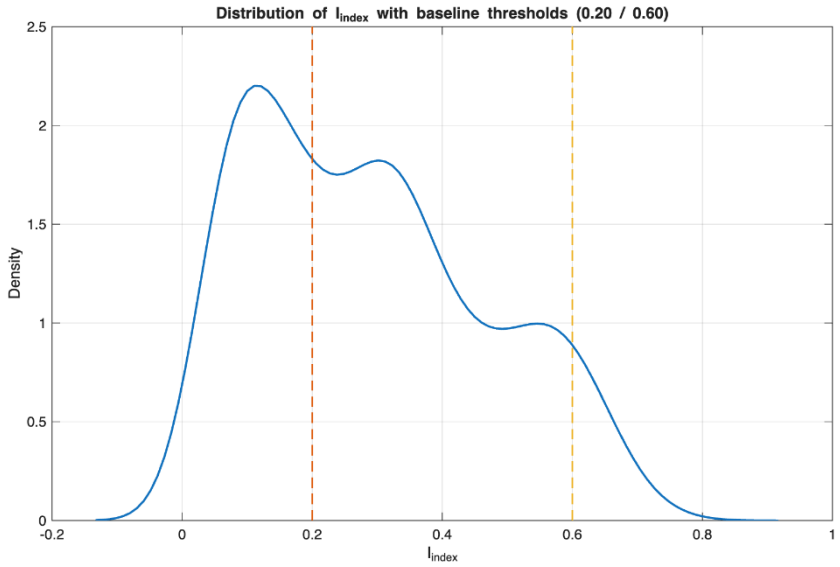

Figure 72 - Density - Baseline thresholds

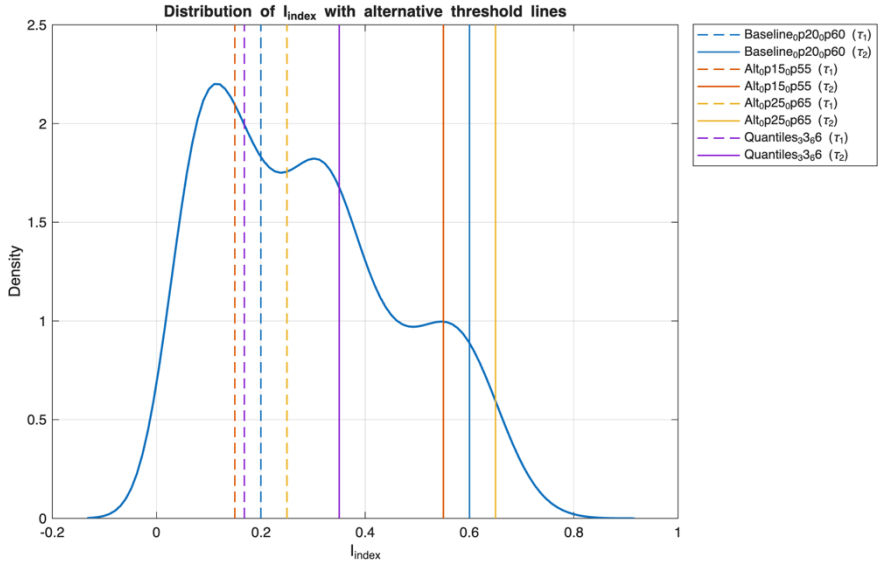

Figure 73 - Density - All threshold configurations

Taken together, these graphical analyses strengthen the quantitative evidence presented earlier: the baseline thresholds (0.20, 0.60) preserve the interpretability of the HIGH class, maintain semantic continuity with physical deterioration severity, and prevent artificial inflation or suppression of critical maintenance priorities. For these reasons, the baseline configuration is retained in the final specification of the composite indicator.

6.4.2. D2) Sensitivity on fusion parameters (α, κ, q)

The aim of this analysis is to assess the robustness of the proposed composite deterioration index to changes in the parameters governing the fusion between vision-based and accelerometric information. Since each parameter controls a distinct mechanism in the integration process, respectively weighting, attenuation, and reliability, the sensitivity study allows us to verify whether the prioritization and classification outcomes remain consistent under realistic variations of sensor behavior and feature prevalence. In particular, the focus is on preserving the stability of the HIGH deterioration class, which corresponds to segments where maintenance intervention is most urgent.

Table 20 - Parameter roles and sensitivity ranges.

Parameter	Meaning / Functional Role	Baseline Value	Sensitivity Range	Effect of Increase
α	Balance between vision-based surface distress and accelerometric disturbance signals	0.70	[0.50, 0.65, 0.70, 0.80, 0.90]	Higher α → stronger reliance on visible surface defects
κ	Attenuation of accelerometric contribution in presence of D50 (manholes/covers)	log(2)	[0.40, log(2), 1.00] + zero-gate test	Higher κ → stronger suppression of false positives but risk of underestimating real deterioration
q	Reliability weight for D20-T1 distress channel Reliability weight for D40-T3 distress channel	0.90	[0.80, 0.90, 1.00]	Higher q → more trust in accelerometry for fine discontinuities and more trust in accelerometry for roughness and pothole signatures

The results of the sensitivity analysis indicate that the composite index is robust to moderate variations in the fusion parameter α, which controls the balance between vision-based surface distress indicators and accelerometric disturbance signals.

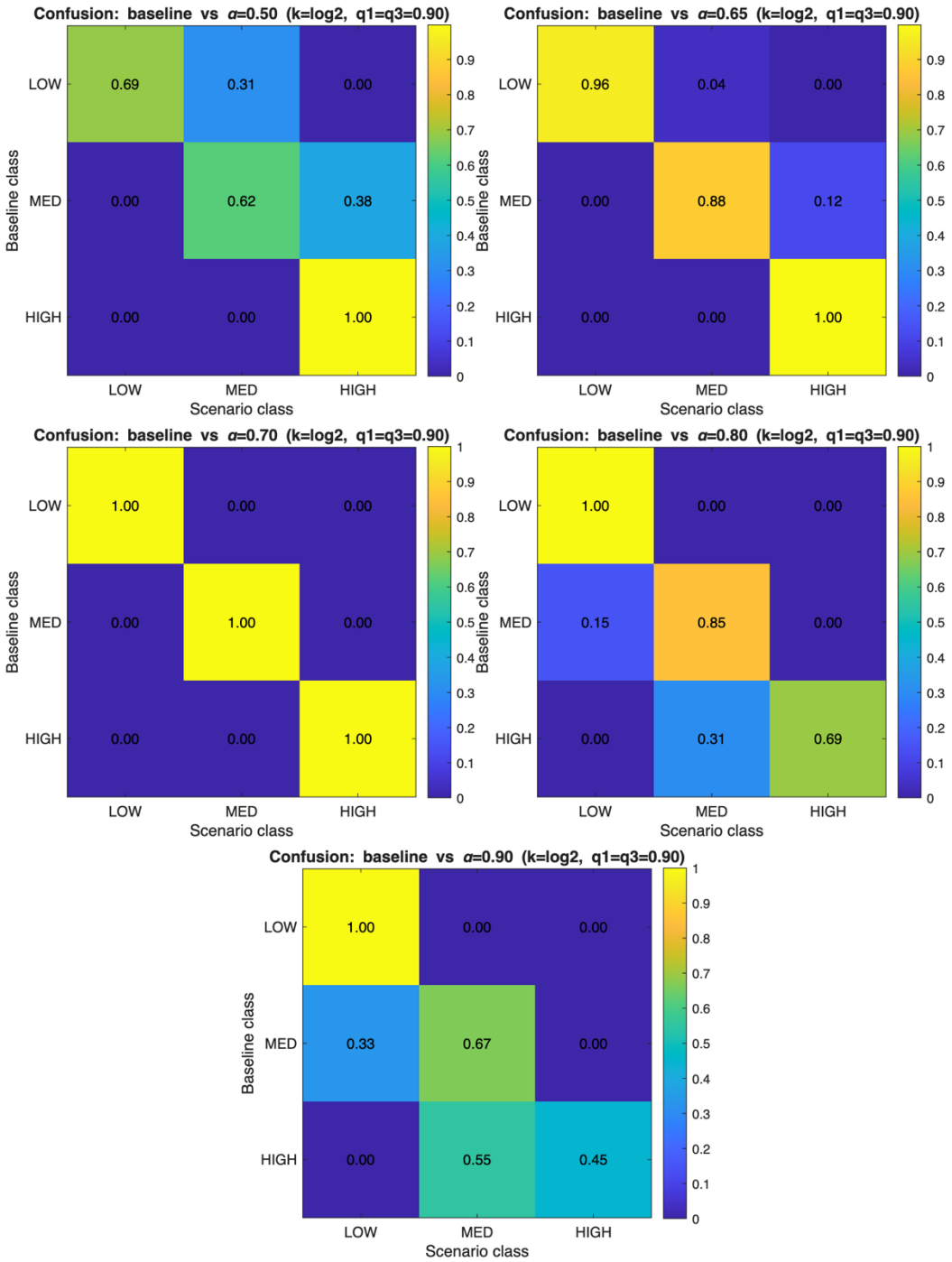

Figure 74 - Confusion matrix: baseline vs changing α

As shown in Figure 74, the comparison across the different α configurations highlights how the fusion balance between vision-based and accelerometric evidence affects the class allocation in the composite deterioration index. When α is reduced to 0.50, thus giving greater influence to accelerometric signals, the classification of segments in the LOW and HIGH categories remains largely unchanged with respect to the baseline. This indicates that segments exhibiting either very good or clearly deteriorated conditions are characterised by strong and concordant evidence across both sensing modalities. In particular, the HIGH class shows complete invariance, confirming that severe pavement distress consistently manifests through both surface discontinuities captured by computer vision and dynamic responses recorded by accelerometers.

The most pronounced effects of varying α are observed within the MEDIUM class. At α = 0.50, a proportion of MEDIUM-class segments are reallocated to either LOW or HIGH, reflecting the transitional and heterogeneous nature of this intermediate deterioration state. These segments tend to present mixed signals - either subtle surface cracking accompanied by noticeable vibration patterns, or vice versa. As α increases toward 0.80 and 0.90, the direction of reallocation changes: visual patterns are amplified, and MEDIUM-class segments with more visible surface distress shift upward toward HIGH, while those with less pronounced visual signatures shift downward toward LOW. This behavior is fully consistent with the design interpretation of α as a semantic weighting factor rather than a purely numerical scaling parameter.

The central configuration (α = 0.70), adopted as baseline, emerges as the point where MEDIUM-class dispersion is minimized and the classification boundaries between LOW, MEDIUM, and HIGH exhibit the greatest internal coherence. At this value, the visual and accelerometric channels contribute complementary information without either source dominating the interpretation of pavement distress. The analysis therefore confirms that variations in α predominantly affect the ambiguity zone between early and intermediate deterioration, while the identification of severe deterioration remains robust across all reasonable parameter settings.

Overall, the sensitivity study demonstrates that the composite index maintains semantic stability under changes in the fusion balance. The HIGH class remains

structurally identifiable and operationally reliable, whereas the MEDIUM class reflects expected variability associated with the continuum of pavement deterioration processes. This reinforces the validity of the adopted fusion framework and supports the selection of α = 0.70 as a balanced and physically meaningful configuration for network-scale deployment.

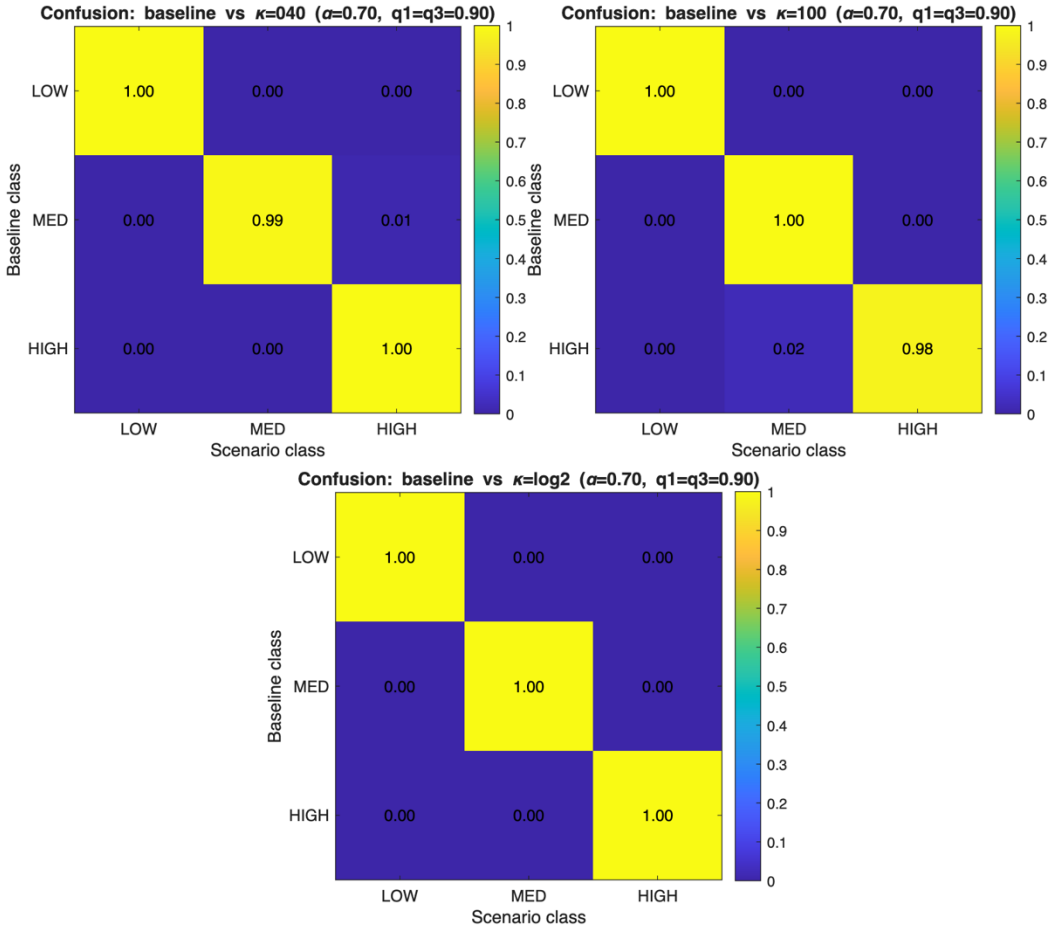

Figure 75 - Confusion matrix: baseline vs changing impact of D50

Figure 75 illustrates the effect of varying the attenuation parameter κ, which regulates how accelerometric information is down-weighted in the presence of documented surface discontinuities (D50). When κ is reduced to 0.40, the attenuation is relatively weak and accelerometric signals are largely preserved. Under this configuration, the classification remains highly stable across the LOW, MEDIUM, and HIGH categories, with only minor reallocations occurring primarily within the MEDIUM class. This behavior is consistent with cases where vibration peaks are physically meaningful -

for example, where surface discontinuities co-occur with underlying structural weaknesses - and therefore should not be overly suppressed.

When κ is increased to 1.00, the degree of attenuation becomes substantially stronger. In this condition, accelerometric contributions near manhole covers and utility access points are smoothed more aggressively. The consequence is a slight reduction in the influence of vibration-driven distress signatures, which causes some MEDIUM-to-LOW or MEDIUM-to-HIGH shifts in boundary cases. Importantly, however, the HIGH class remains stable under both $\kappa = 0.40$ and $\kappa = 1.00$, indicating that segments exhibiting severe distress produce sufficiently strong and multi-modal evidence to remain identifiable even under strong attenuation. These results demonstrate that κ controls how the model interprets the interaction between functional discontinuities and structural degradation, but does not compromise the system's ability to detect high-severity conditions when tuned within a plausible operational range.

A markedly different effect is observed in the zero-gate condition, in which accelerometric information is entirely removed whenever D50 is present. This scenario produces a notable reduction in the stability of the HIGH class, with a measurable proportion of previously high-severity segments being reassigned to MEDIUM. This outcome indicates that, in many real road environments, manholes and utility covers frequently coexist with structural deterioration - for instance due to settlement, deformation, or subsurface voids forming around the hardware frame. In such cases, the vibration signatures carry essential diagnostic information about the underlying mechanical integrity of the pavement. The zero-gate condition, by suppressing this information altogether, systematically underestimates deterioration severity.

Taken together, these results confirm that attenuation should not be implemented as a binary exclusion mechanism, but rather as a calibrated, graded modulation. A moderate value, such as the baseline $\kappa = \log(2)$, achieves a balance between preventing false positives due to purely functional discontinuities and preserving accelerometric evidence that reflects genuine structural degradation. The κ-sensitivity analysis therefore reinforces the rationale for the adopted parameter configuration, validating its suitability for large-scale, network-level monitoring and decision support.

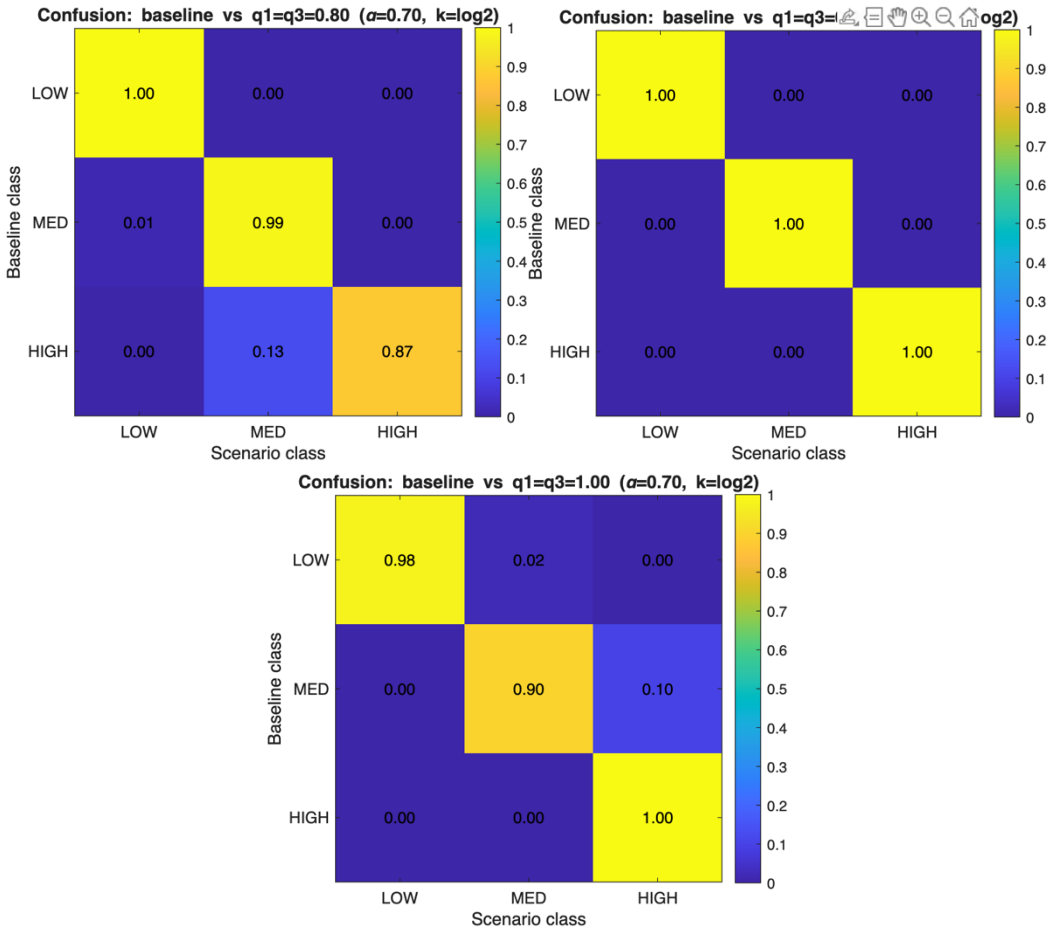

Figure 76 - Confusion matrix: baseline vs changing q

Figure 76 illustrates the effect of varying the reliability parameter q, which controls the strength of the accelerometric contribution in the fusion with the vision-based distress indicators (D20–T1 and D40–T3). Unlike the fusion balance parameter α, which alters the relative importance of visual versus accelerometric sources globally, the parameter $q$specifically modulates the trust attributed to accelerometric signatures when they co-occur with surface deterioration patterns. As such, this sensitivity analysis assesses whether the accelerometric channels contribute stable and non-spurious evidence to the classification.

When $q = 0.80$, the accelerometric contribution is reduced and visual evidence dominates the classification. Under this configuration, the LOW and HIGH classes remain highly stable, indicating that purely healthy and severely deteriorated segments are identifiable based on surface patterns alone. However, the MEDIUM class shows moderate redistribution toward LOW and HIGH, reflecting the fact that

early-stage or subtle deterioration phenomena often manifest first through dynamic responses rather than fully developed surface cracking. Thus, lowering $q$leads to a more visually conservative interpretation of pavement state, prioritising clearly visible defects but underrepresenting emerging structural irregularities.

At the baseline value $q = 0.90$, the two sensing modalities contribute in a balanced and complementary manner. The confusion matrix at this value exhibits high diagonal dominance across all classes, indicating that the accelerometric channels contribute consistent and meaningful information without overwhelming the visual evidence. This configuration aligns with the conceptual role of accelerometry in pavement diagnostics: to detect, amplify, or corroborate distress signatures that are not yet visually pronounced but are mechanically significant.

When $q = 1.00$, the accelerometric signals are incorporated at full strength. In this case, a small proportion of MEDIUM-class segments shift to HIGH, particularly those exhibiting pronounced vibration signatures but only moderate surface deterioration. These correspond to segments where underlying structural weakening precedes macroscopic cracking or raveling - a well documented progression in asphalt distress evolution. The stability of the HIGH class remains strong, confirming that full reliance on accelerometry does not introduce false alarms but instead highlights segments where sub-surface distress is mechanically detectable before surface failure becomes visually apparent.

Taken together, the q-sensitivity results demonstrate that accelerometric information contributes substantively and consistently to the deterioration index. Variations in $q$primarily influence the segmentation of the MEDIUM class, which acts as a transitional state between surface-driven and structurally driven deterioration regimes. The baseline configuration $q = 0.90$provides a balanced interpretation in which accelerometry reinforces - but does not dominate - visual evidence, ensuring that both early mechanical distress and observable surface degradation are appropriately represented. This confirms the conceptual and operational validity of the selected reliability parameter for network-scale pavement monitoring.

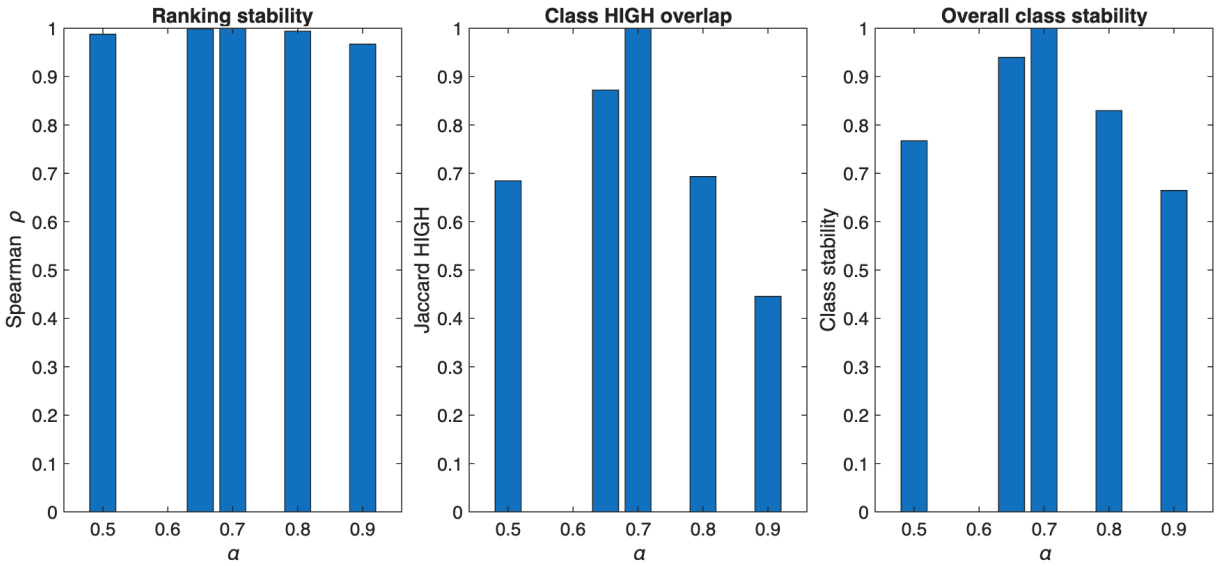

Figure 77 - Sensitivity to α: ranking Spearman, HIGH-class Jaccard, overall stability

The trends observed in Figure 77 reinforce the interpretation that the fusion parameter α governs the semantic balance between visual surface distress indicators and accelerometric disturbance signals without fundamentally altering the prioritization structure of the network. The Spearman rank correlation remains consistently high ($\geq$ 0.95) across the entire tested range, indicating that the ordering of segments in terms of deterioration severity is largely invariant. This result is critical from an operational perspective: maintenance planning and budget allocation depend primarily on relative ranking, and thus a high Spearman coefficient confirms that the prioritization logic is robust to moderate changes in α.

The Jaccard similarity for the HIGH class exhibits a clear maximum at α = 0.70, with lower similarity observed at both α = 0.50 and α = 0.90. This behavior reflects the fact that α = 0.70 corresponds to the most coherent integration of visual and accelerometric evidence in characterising severe deterioration. At lower α values, accelerometric features are over-emphasised, which may cause early-stage dynamic irregularities to be interpreted as high-severity defects; at higher α values, surface distress dominates excessively, potentially underestimating structural failures that are not yet visually manifest. The peak at α = 0.70 therefore identifies the point where multi-sensor distress signatures converge most consistently.

A similar pattern is visible in the overall class stability metric, which also reaches its maximum at α = 0.70. Variations at both ends of the α range primarily affect the MEDIUM class, which is expected given its transitional nature and the progressive evolution of pavement deterioration. The LOW and HIGH classes, representing well-defined structural states, remain substantially stable across all configurations, confirming that the fusion model reliably distinguishes intact surfaces from severely compromised ones.

Taken together, these results indicate that the baseline fusion configuration (α = 0.70, $\kappa = \log(2)$, $q_1 = q_3 = 0.90$) provides a balanced trade-off between noise suppression and the preservation of semantically meaningful distress information. In contrast, the zero-gate scenario demonstrates that fully suppressing accelerometric contributions in the presence of surface discontinuities leads to systematic under-identification of critical deterioration, confirming that attenuation should be gradual rather than binary. Overall, the adopted fusion parameterisation is supported both theoretically and empirically and is therefore retained as the recommended configuration for network-scale operational deployment.

Overall, the sensitivity analysis demonstrates that the composite deterioration index is structurally stable with respect to reasonable variations in the fusion parameters. Severe deterioration (HIGH class) is consistently identified across all scenarios, indicating that the model captures physically meaningful pavement degradation patterns that are not dependent on a particular tuning choice. The MEDIUM class, representing transitional conditions, behaves as expected under shifts in weighting and reliability parameters, reflecting the inherent uncertainty in intermediate deterioration states. The baseline parameter configuration (α = 0.70, $\kappa = \log(2)$, $q_1 = q_3 = 0.90$) emerges as a principled equilibrium that preserves accelerometric evidence where diagnostically informative, while effectively preventing false positives caused by functional discontinuities. This configuration therefore provides a robust foundation for large-scale pavement condition monitoring and prioritisation of maintenance interventions.

6.5. E) Verification

A systematic comparison between different classes of road segments shows that tangential and high-flow arterial roads generally exhibit lower deterioration levels, with composite index values predominantly in the green range. Conversely, local roads in small urban settlements or peripheral contexts display more irregular conditions and higher deterioration scores. This behavior is consistent with the expected dynamics of pavement life-cycles: arterial roads are usually built with more robust structural layers, subjected to planned maintenance strategies, and designed for continuous loading conditions, while local roads are characterised by lighter pavement structures, patch-based interventions, and more heterogeneous degradation mechanisms.

As a macroscopic consistency check, the rank correlation $\rho_{index,safety}$ defined in Equation 59 is used between the composite index $I_i$and near-miss counts Y_i to verify large-scale coherence between deterioration intensity and safety outcomes.

The model therefore captures a known systemic behavior of road networks, reinforcing its interpretability at the macroscopic level.

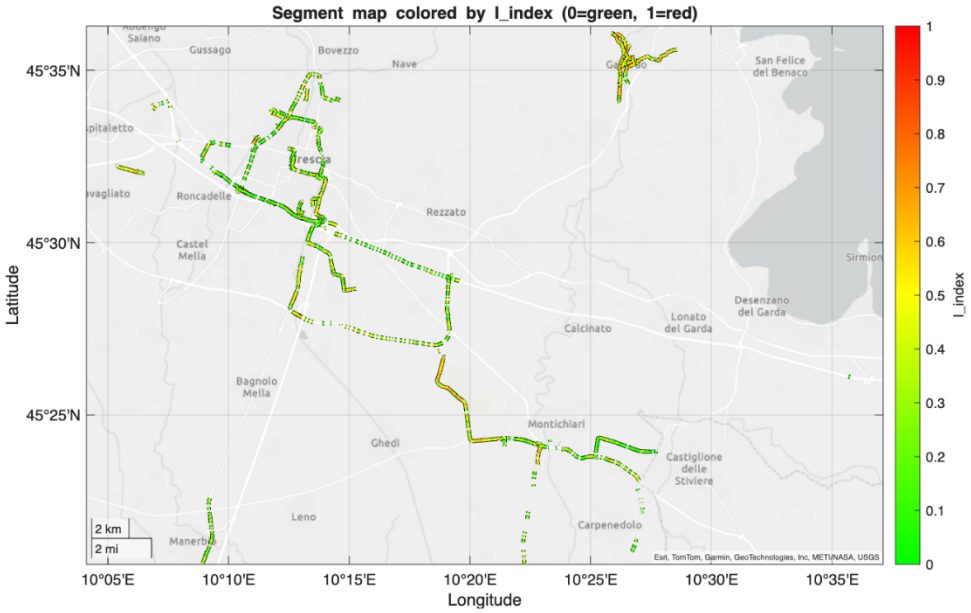

Figure 78 - Composite deterioration index visualised over the selected road network

Building on this observation, the chapter now moves to the local scale and presents a set of focused case studies on individual road segments in order to qualitatively assess the behavior of the proposed methodology and validate the interpretability of the resulting indicators. While the previous chapters have addressed the model at a network scale highlighting its statistical robustness, its spatial coherence, and its ability to capture deterioration patterns across the urban fabric, here the perspective shifts to the local scale of single segments. The objective is to verify whether the composite index, the partial indicators (RQI, WDI and fused constructs), and the underlying event streams effectively correspond to observable pavement conditions.

To this end, a selection of representative segments has been examined, spanning different deterioration scenarios (localized defects, diffuse degradation, and regular pavement conditions). For each segment, the analysis integrates: (i) the numerical values of the indicators obtained through the data fusion pipeline; (ii) the spatial distribution of VIASAT and AIWAY detections associated with the segment; and (iii) photographic evidence taken from vehicle-mounted cameras. This multi-evidence comparison allows us to evaluate whether the algorithmic outputs are consistent with real-world surface conditions, and to identify strengths and residual limitations in the detection and fusion process.

To mitigate potential confirmation bias in qualitative validation, the sampling strategy was designed to include not only the segments ranked as most and least deteriorated, but also intermediate and randomly selected segments. In addition to the tripartite stratification (best-performing, mid-range, worst-performing), a supplementary sample of segments was extracted uniformly across the network.

The aim of this chapter is therefore twofold: first, to validate the model through visual and segment-level consistency checks; second, to show how the proposed framework can support maintenance decision-making by providing interpretable and verifiable deterioration signals at the resolution typically required by road operators.

6.5.1. E1) Macro-verification

The visual inspection of the spatial distribution of the composite index provides a first qualitative confirmation of the model's expected behavior. The map reveals a coherent pattern, in which road segments with higher functional importance, such as tangential routes and main connectors, are predominantly associated with low deterioration scores, resulting in green-coded polylines. In contrast, local roads and secondary links show more variability and sporadic concentrations of yellow or orange segments, indicating moderate or emerging distress conditions.

This spatial pattern is consistent with the functional organisation of the network, confirming that the index reflects expected differences in pavement condition across hierarchy classes. The absence of scattered or contradictory colour patterns, as well as the spatial continuity of homogeneous segments, further reinforces the internal consistency of the proposed indicator. While a more detailed verification is carried out in the following pages through segment-level case studies and ground-truth comparisons. This preliminary screening provides qualitative evidence of the index's potential for network-wide prioritisation and maintenance planning.

In order to support the visual interpretation of the map-based screening, street-level imagery was also consulted during the macro-scale assessment. This provided an additional qualitative reference to better contextualise emerging spatial patterns of deterioration before proceeding to the detailed segment-level analysis.

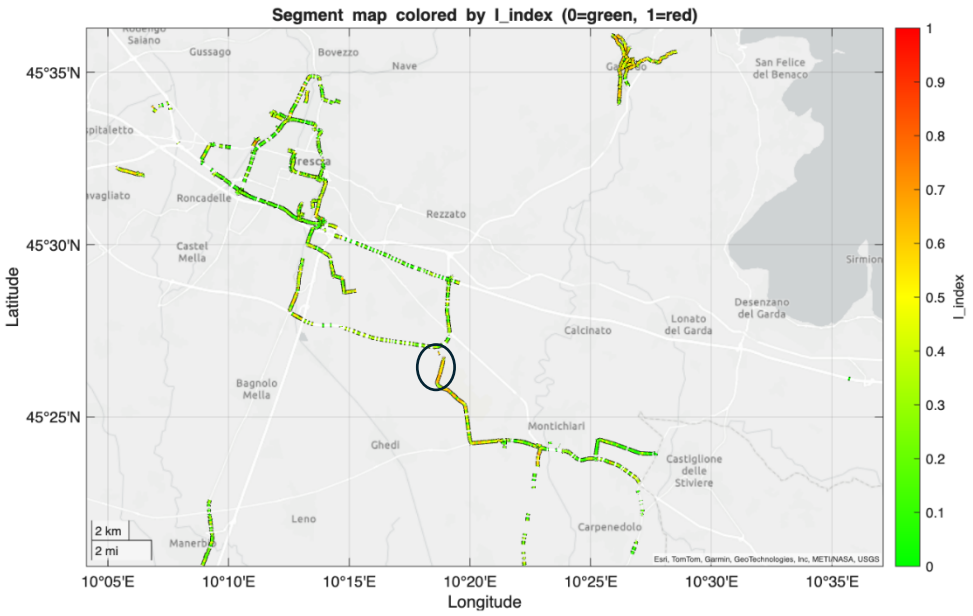

Figure 79 – Provincial Road 37

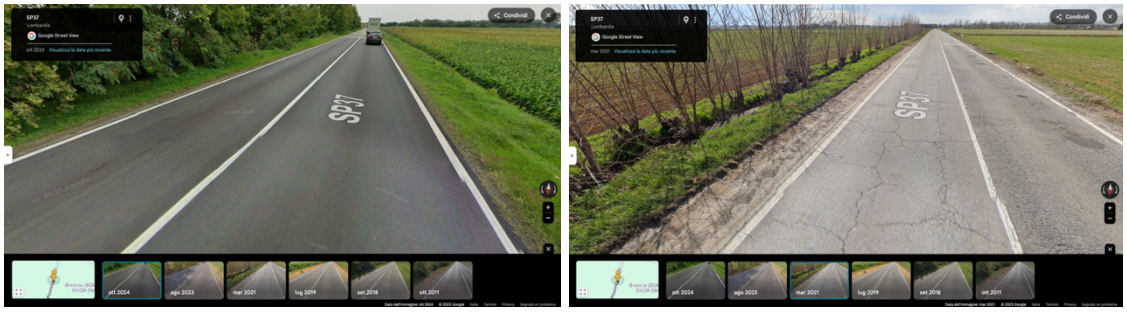

Figure 80 – Provincial Road 37 (Google Street View)

The deterioration map highlighted a critical portion of the Strada Provinciale 37, where the composite index assigned orange-to-red values, indicating a markedly higher level of surface distress compared to the surrounding network. Following this signal, an in-situ verification was conducted through visual inspection of recent imagery and historical Google Street View footage. The comparison confirms that the segment had exhibited widespread surface degradation in the past, consistent with the typologies typically associated with advanced pavement distress.

More specifically, the historical images show the presence of multiple longitudinal and transverse cracks, block cracking, edge distress and localized patching interventions. The crack pattern suggests a combination of aging of the bituminous layers and structural fatigue, with potential water infiltration and sub-base weakening over time. These features are commonly observed in low-to-medium traffic rural pavements

where preventive maintenance is less frequent and load transfer mechanisms are less efficient. The subsequent resurfacing of the carriageway - visible in the most recent imagery - confirms that the segment underwent maintenance after the period in which the deterioration signals were captured by the index.

This case is significant because it demonstrates that the proposed indicator can (i) highlight critical segments within low-hierarchy roads, (ii) correctly associate high index values with real surface defects and (iii) preserve interpretability through visual back-checking, thus reinforcing its applicability for supporting maintenance planning and prioritisation.

It is important to emphasize that the objective of the validation is not to replicate a deterministic one-to-one correspondence between indicator values and singular visible defects, but rather to evaluate the coherence of deterioration patterns across spatially aggregated network units (segments of 100 m). Given the intrinsic variability of pavement surface textures and maintenance histories, the indicator is expected to reflect macro-level conditions and progressive degradation processes, rather than isolated local anomalies. The observed agreement between index values and visual evidence confirms that the model captures these broader deterioration dynamics, which are the relevant operational signals for maintenance prioritisation.

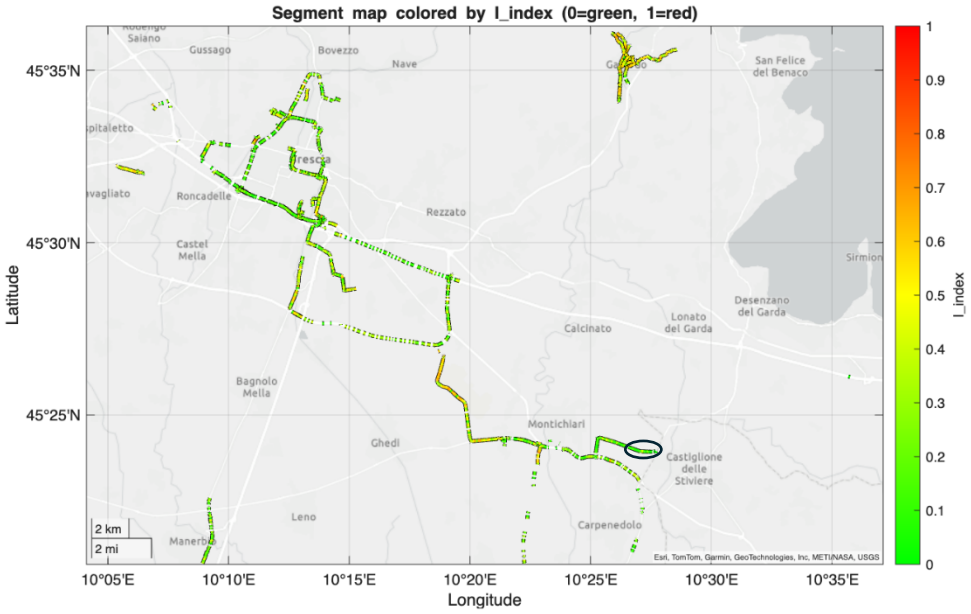

Figure 81 - Via Mantova, Castiglione delle Stiviere

Figure 82 - Via Mantova, Castiglione delle Stiviere (Google Street View)

The selected segment along Via Mantova (Castiglione delle Stiviere) represents a case in which the composite index assigns consistently low deterioration values, as highlighted by the uniform green colouring in the map. This classification suggests a limited presence of surface defects and an overall good pavement condition. The visual inspection conducted through Google Street View confirms this assessment: although minor longitudinal cracks and superficial ageing of the bituminous layer can be observed, the pavement does not exhibit severe manifestations of structural distress, such as rutting, block cracking, edge failure or extensive patching.

The limited defectiveness is consistent with the expected behavior of an urban collector road subjected to regular maintenance and moderate traffic loads. The absence of diffuse cracking patterns or localized surface collapses further corroborates the model output, indicating that the proposed index is able to correctly identify well-performing segments and avoid false-positive deterioration signals. This case therefore strengthens the reliability of the methodology not only in detecting critical segments, but also in recognising road sections where the pavement exhibits an adequate level of serviceability.

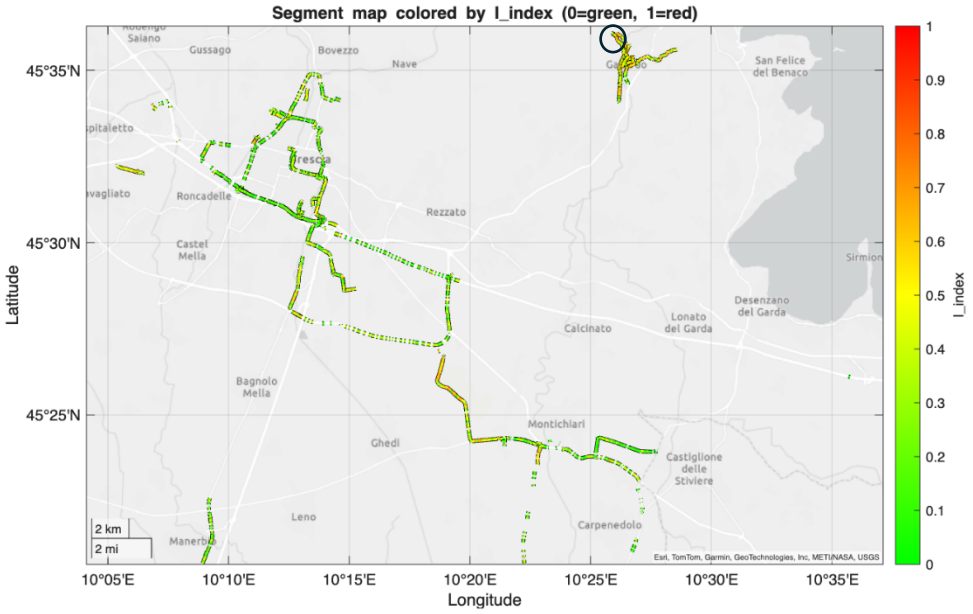

Figure 83 - Via Battaglione Alpini Valchiese, Gavardo

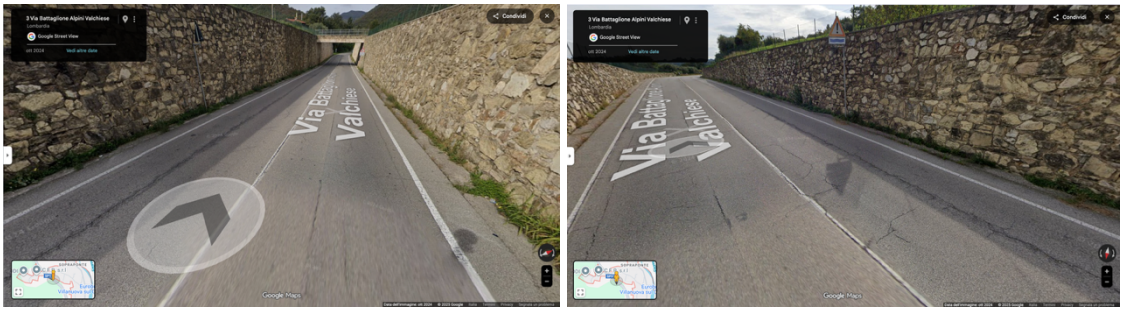

Figure 84 - Via Battaglione Alpini Valchiese, Gavardo (Google Street View)

The segment in Via Battaglione Alpini Valchiese (Gavardo) represents a second example of an urban road classified with relatively low-to-moderate deterioration levels by the composite index. However, unlike the case of Via Mantova in Castiglione delle Stiviere, the surface condition appears more compromised when inspected visually. The Google Street View imagery highlights a denser and more severe crack pattern, including deeper longitudinal fissures, local transverse cracking and evident edge breaks along the carriageway. The discontinuities in the bituminous layer suggest more advanced propagation mechanisms, likely driven by repeated traffic loading and the combined effect of thermal cycles and water infiltration.

Although the pavement does not exhibit structural failures such as rutting, potholes or extensive patching, the presence of deeper and more continuous cracking indicates

a deterioration stage that is more evolved than in the previous urban example. From a maintenance perspective, this segment can be interpreted as entering a transitional phase between superficial distress and the onset of structural degradation. The model behavior remains coherent: the indicator flags the road as less critical than rural highly distressed segments, but it still recognises a condition worse than that observed in well-performing urban segments, thus maintaining internal consistency across different deterioration scenarios.

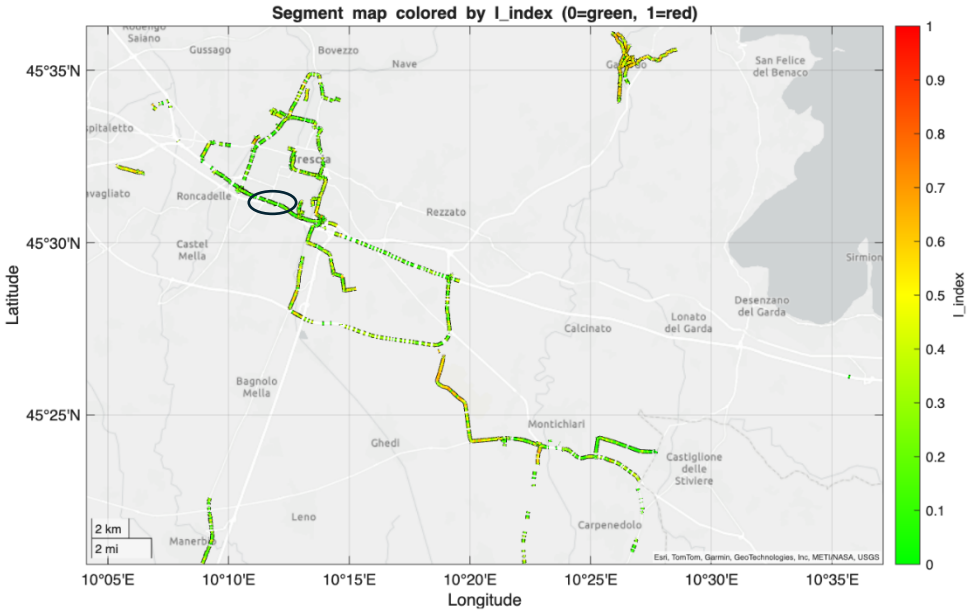

Figure 85 - Tangenziale Sud, Brescia

Figure 86 - Tangenziale Sud, Brescia (Google Street View)

The examined segment of the Tangenziale Sud in Brescia provides a representative example of a high-capacity urban corridor characterised by good pavement conditions. The composite index correctly assigns low deterioration values, visually expressed by the predominance of green colouring along the segment. This outcome

is fully consistent with the functional role of the infrastructure: as a tangential high-flow route, the segment is designed with more robust pavement layers and is typically subject to regular, programmed maintenance cycles to ensure continuity of service, safety and ride quality.

The Google Street View inspection confirms the model output, showing a uniformly paved surface with only minimal superficial wear and no evidence of critical defects such as structural cracking, rutting, potholes or edge failures. The absence of diffuse surface distress reflects both the higher construction standards adopted for tangential roads and the preventive maintenance strategies commonly implemented on strategic high-traffic links. This case further supports the ability of the proposed index to distinguish well-performing arterials from more vulnerable secondary or local roads.

The macro-level interpretation is therefore complemented by a detailed segment-level investigation, aimed at examining individual deterioration patterns through visual inspection and multi-source comparison.

6.5.2. E2) Micro-verification

To support the visual validation of the selected road segments, street-level imagery was employed as an external qualitative source for assessing pavement surface conditions. Google Street View provided geo-referenced panoramic images, including historical timelines to align visual inspection with the sensor acquisition period. This ensured temporal consistency between the observed surface condition and the computed indicator values. The street-level inspection served exclusively as a qualitative reference, supporting the interpretation of the deterioration classes analysed in the following sections.

To investigate the interpretability and practical usefulness of the proposed deterioration index, a sample of representative segments was selected from the ranked distribution and analysed through street-level inspection. This allowed the identification of segments ranging from well-performing pavements (with values close to 0) to severely deteriorated ones (with values approaching 1). In order to conduct a balanced and meaningful validation, three representative groups were then selected

from the ranked distribution: the ten best-performing segments (i.e., those with the lowest values of I_{index}), the ten worst-performing segments (highest values), and a third group consisting of ten mid-range segments located around the median of the distribution. This tripartite sampling strategy enables the assessment of the model across its entire spectrum of deterioration conditions, avoiding bias towards either extreme cases or well-maintained areas only. The approach also makes it possible to evaluate the model's capability to (i) correctly identify segments in good condition, (ii) detect severely degraded pavements, and (iii) discriminate intermediate surface states where deterioration mechanisms are more nuanced.

For each of the thirty selected road segments, a qualitative validation was carried out by integrating three complementary sources of evidence: the numerical values of the composite and partial indicators, the spatial distribution of sensor events associated with the segment, and a visual ground-truth check based on photographic material and street-level imagery. This multi-evidence inspection makes it possible to verify whether high indicator values correspond to observable defects on the pavement surface, such as longitudinal or transverse cracking, patching or early structural distress, and whether low indicator values are consistent with intact or only mildly aged pavements. Through this procedure, the deterioration index can be evaluated not only on its ability to flag critical segments, but also on its coherence in recognising well-performing roads and intermediate deterioration stages. The resulting analysis provides a coherent qualitative validation framework, supporting the reliability of the proposed methodology for infrastructure monitoring and maintenance prioritisation.

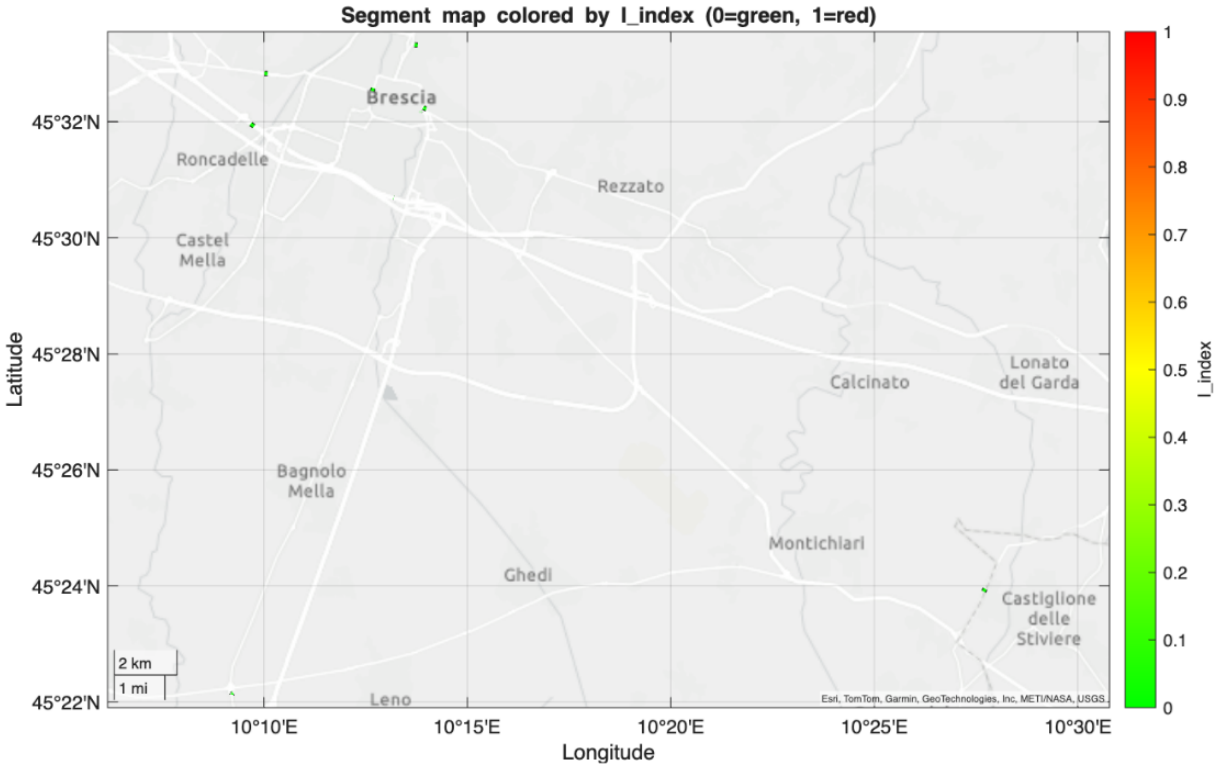

Figure 87 - Top 10 best-performing segments according to the computed deterioration index

Figure 88 - Top 10 best-performing segments according to the computed deterioration index (Google Street View)

The first group includes the ten segments characterised by the lowest deterioration values. The visual inspection of the street-level imagery shows road surfaces generally in good condition, with limited or no evidence of distress mechanisms. The pavements are predominantly free of transverse or longitudinal cracking, and no rutting, potholes or patch-based interventions are observed. Surface texture appears uniform, with occasional signs of superficial oxidation of the bituminous layer, which is consistent with normal material ageing rather than structural degradation. Lane markings are also well preserved, and no edge failures are evident along the visible sections. Overall, the road environment suggests regular maintenance and limited mechanical or environmental stress, which aligns with the condition expected for pavements in the best-performing portion of the network.

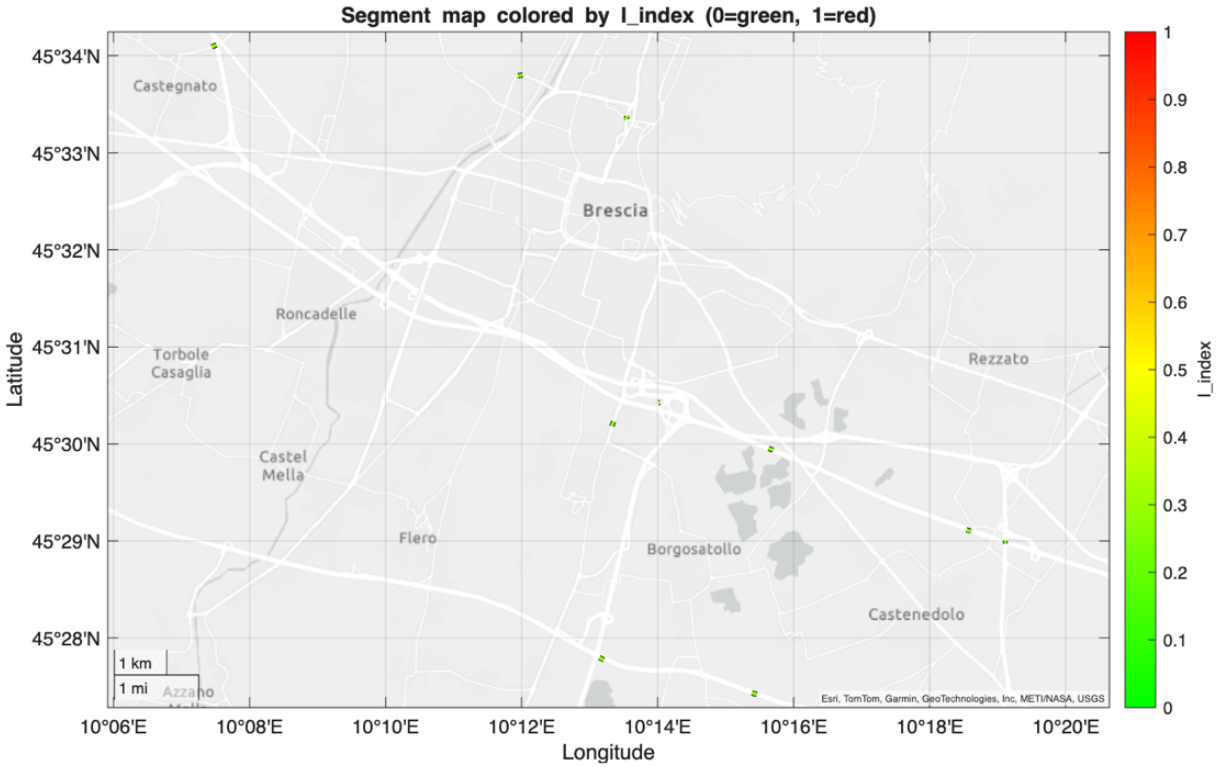

Figure 89 - Mid-range segments (Index ≈ 0.26) according to the computed deterioration index

Figure 90 - Mid-range segments (Index ≈ 0.26) according to the computed deterioration index (Google Street View)

The second group consists of segments in which street-level imagery reveals early-stage deterioration. Localised cracking can be observed, predominantly in the form of short longitudinal fissures and isolated transverse discontinuities, while the remaining carriageway appears structurally intact. The defects are mild and non-diffuse, indicating that degradation mechanisms are present but at an initial phase. The pavement texture exhibits light surface wear, and in some sections slight edge fraying is visible, although without signs of detachment or raveling. No structural distress phenomena, such as rutting, deep cracking networks or potholes, are detected. These features are typically associated with ageing and loading effects that have begun to affect surface performance without yet compromising the integrity of the pavement layers.

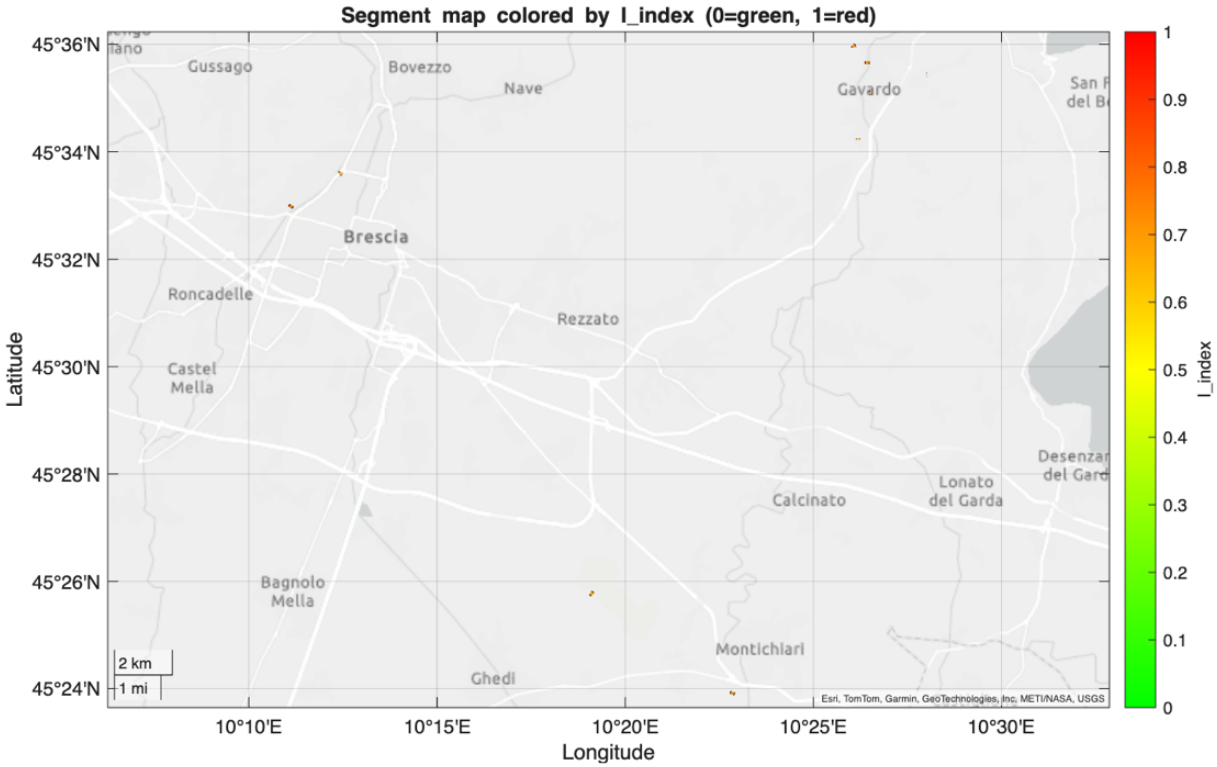

Figure 91 - Top 10 worst-performing segments according to the computed deterioration index

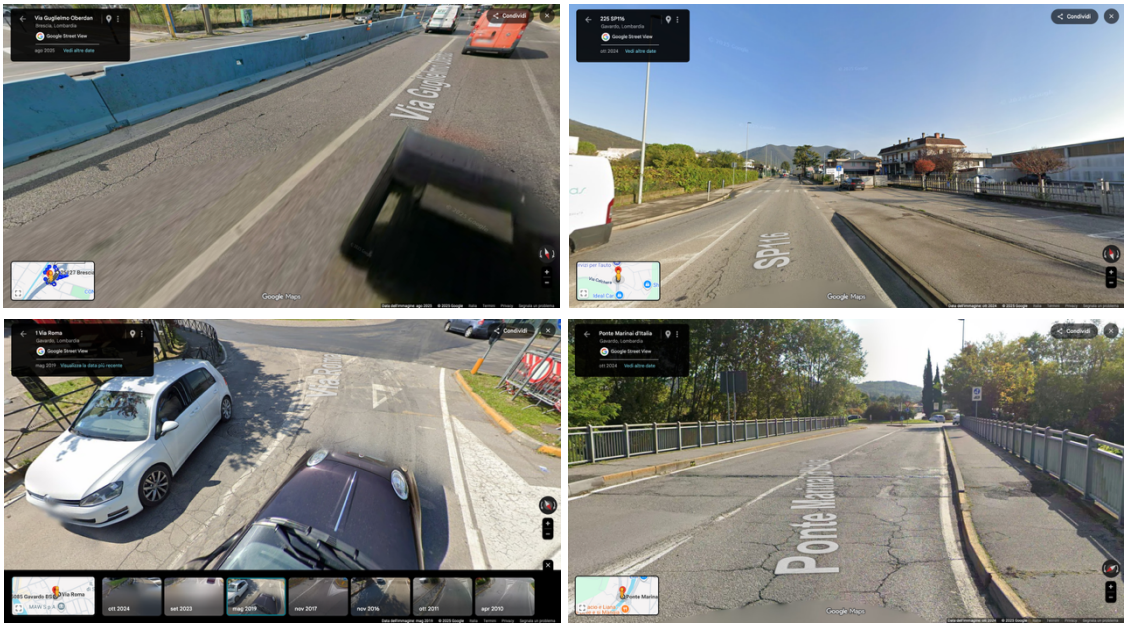

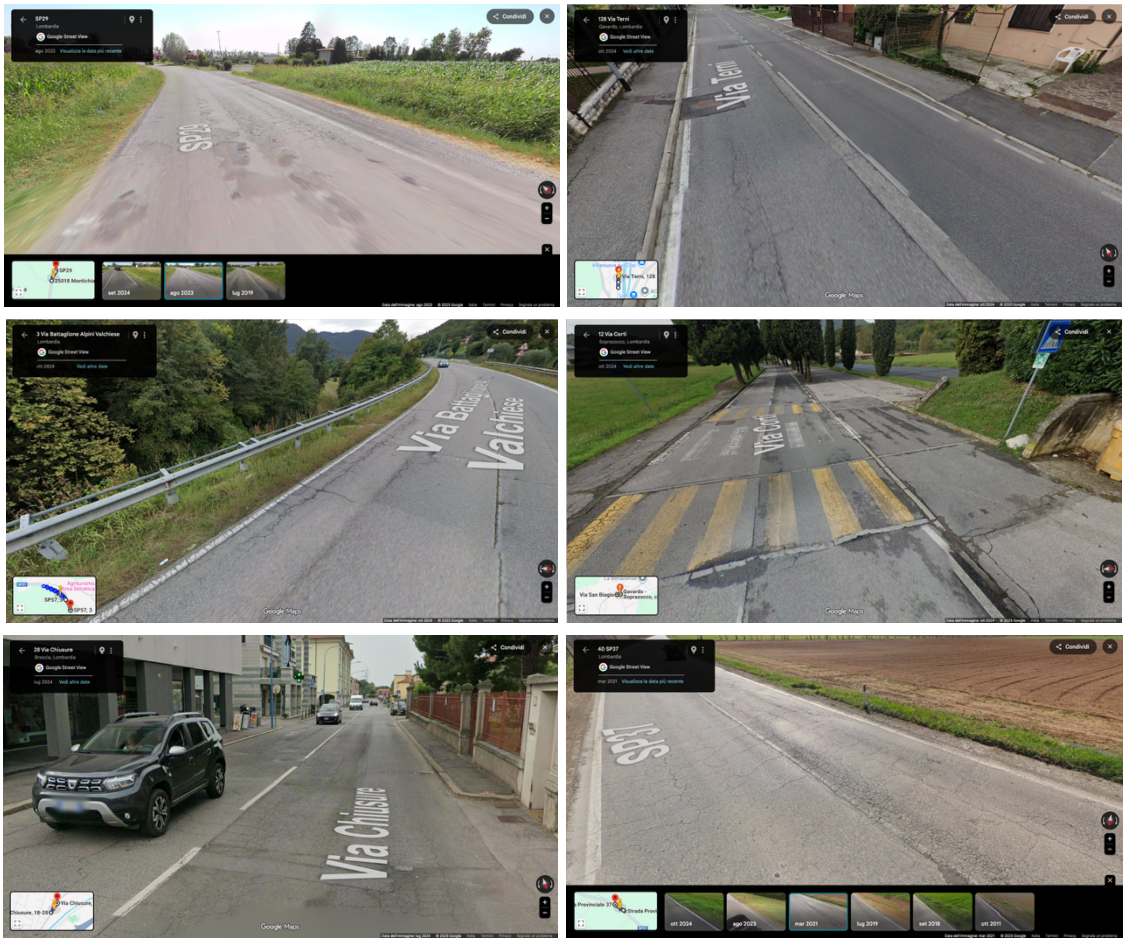

Figure 92 - Top 10 worst-performing segments according to the computed deterioration index (Google Street View)

The third group corresponds to the most deteriorated segments. The street-level imagery highlights widespread and clearly identifiable distress patterns, including extensive longitudinal and transverse cracking, block cracking, edge deformation and, in several cases, evidence of patch-based maintenance interventions. The fragmentation of the surface suggests more advanced deterioration processes, potentially involving fatigue of the bituminous layers and propagation of water-induced damage. Localised depressions and surface irregularities are also visible, indicating a progressive loss of structural bearing capacity in parts of the carriageway. Compared with the previous groups, the defects in these segments are both more severe and more spatially continuous, reflecting pavements in an advanced degradation state that would typically require substantial maintenance or resurfacing.

During the initial sampling, it was observed that the ten mid-ranked segments extracted around the median of the distribution exhibited very similar deterioration levels, with composite index values clustered around approximately 0.26. Although these segments are representative of mild degradation scenarios, their limited variability did not fully capture the range of intermediate pavement conditions. To extend the analysis and include cases characterised by more pronounced but non-critical distress, an additional set of ten segments was therefore selected around the 0.50 value of the index. This complementary sampling step allows the validation framework to cover both the "early-stage" and the "mid-stage" portions of the deterioration spectrum, ensuring a more balanced representation of intermediate behaviors and enabling a clearer assessment of the indicator's discriminative capability in non-extreme conditions.

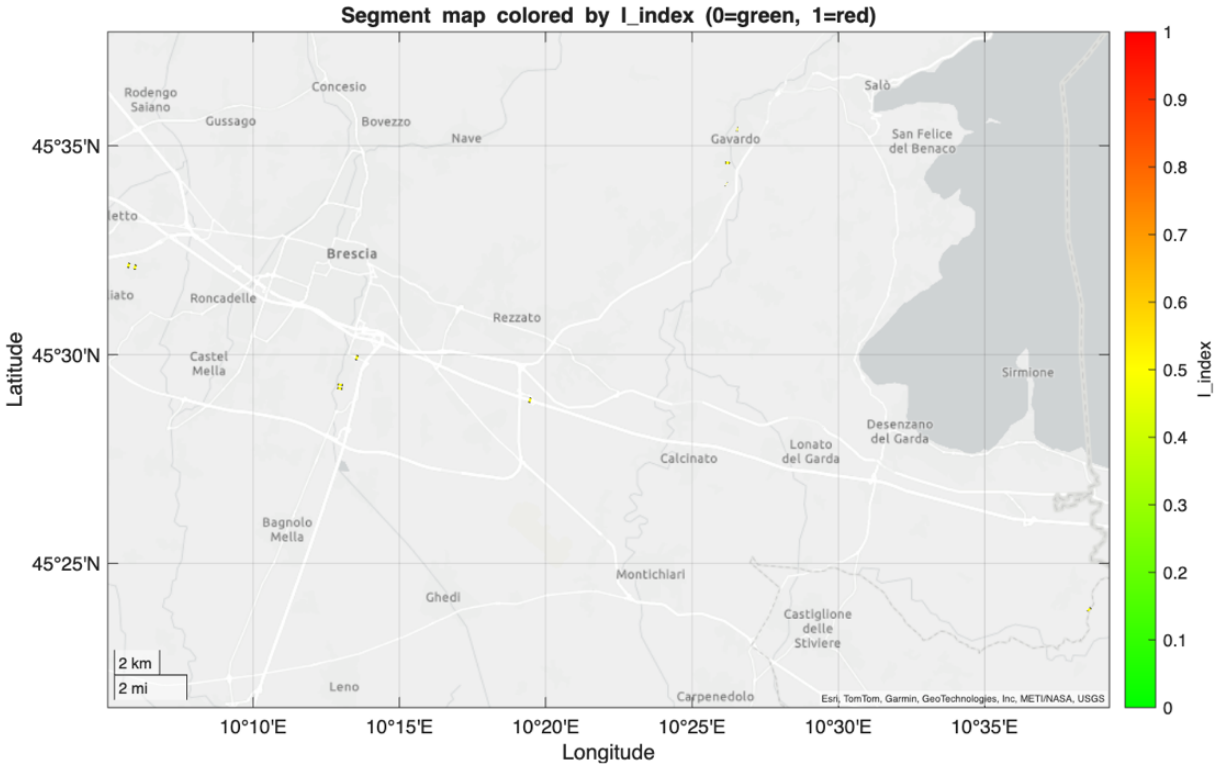

Figure 93 - Mid-range segments (Index ≈ 0.50) according to the computed deterioration index

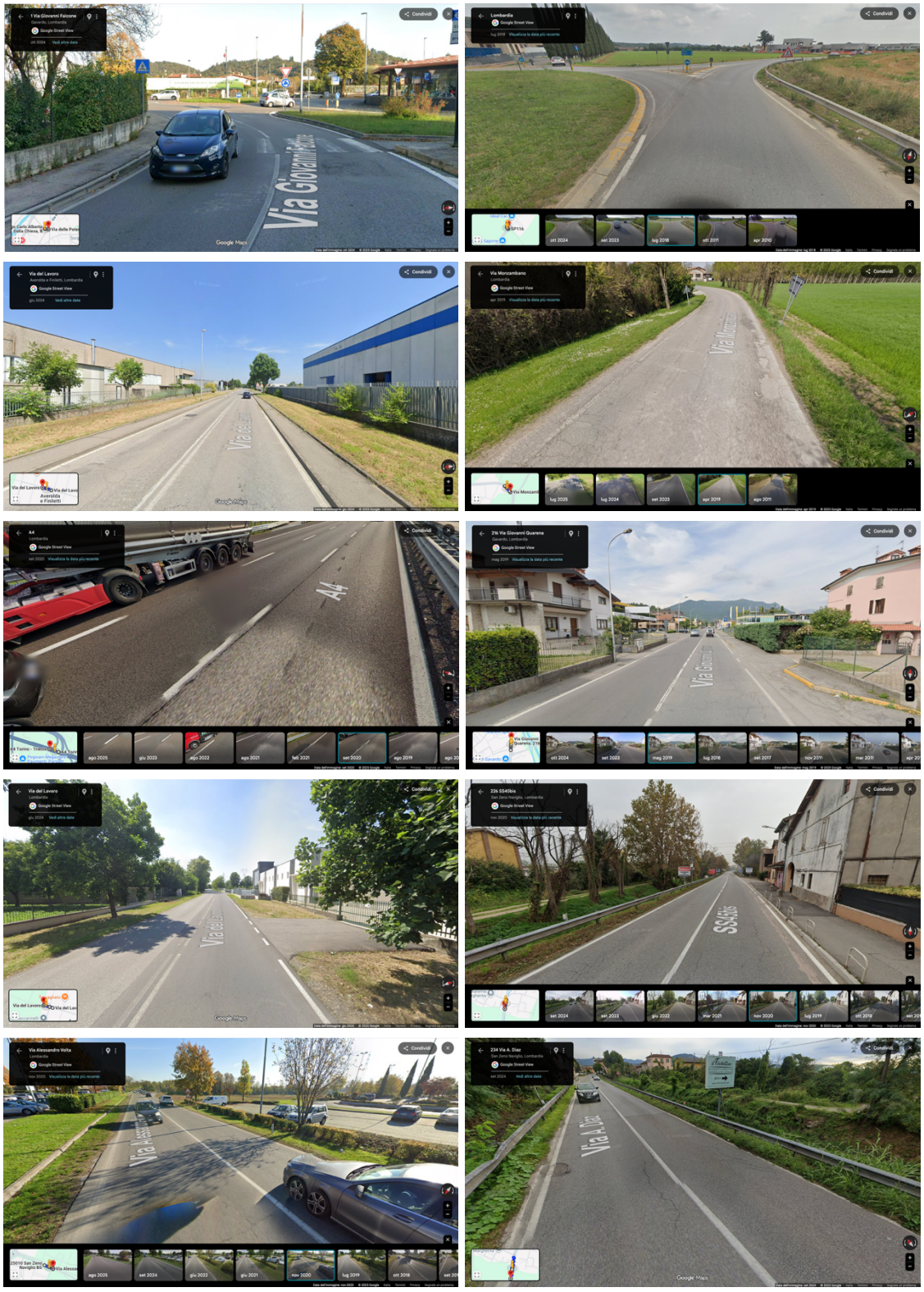

Figure 94 - Mid-range segments (Index ≈ 0.50) according to the computed deterioration index (Google Street View)

The fourth group includes segments with intermediate deterioration and street-level imagery showing a more evolved condition than the early-stage cases. The observed

cracking patterns are more pronounced and continuous, with longer longitudinal fissures, more frequent transverse cracking, and occasional edge distress. The pavement surface displays moderate wear, and in some locations localised depressions or unevenness are visible, although without the diffuse structural disruption observed in the worst-performing group. The defects are sufficiently developed to indicate that degradation mechanisms are active and progressing, but not yet pervasive to the point of compromising the entire carriageway. These conditions are consistent with a transitional deterioration phase, where surface-level failures have begun to evolve toward structural implications if not mitigated.

The qualitative validation confirms that the composite index is coherent with observed pavement conditions across multiple deterioration states. However, the methodology is not tied to the specific parameterization or near-miss-based weighting estimated in this network. The architecture is transferable, but parameter calibration should be re-estimated when applied to different contexts, climate zones, pavement typologies, or maintenance standards. In this sense, the contribution of this work lies in the definition of the framework, fusion logic and validation protocol, rather than in the universality of numerical parameter values.

7. Discussion

7.1. Methodological reflections

The results of this thesis must be interpreted in light of the heterogeneous and fragmented research landscape described in the State of the Art. The analysis of the literature demonstrates that Floating Car Data have been predominantly used for mobility-oriented tasks such as travel time estimation, routing optimization, congestion analysis and emissions modelling, as shown in [4] and in [109]. Only a limited set of contributions has addressed the potential of FCD for pavement condition monitoring, and even fewer have explored structured integration with Pavement Management Systems. This imbalance confirms the existence of a clear research gap, already identified through the PRISMA-based review [1], and provides a strong rationale for the methodological direction taken in this thesis.

The behavior of accelerometric FCD recorded by VIASAT is coherent with the insights reported in [11], [32] and [61]. These works emphasise that vibration-based detections contain meaningful information on road-surface irregularities while remaining sensitive to sensor heterogeneity, driver behavior and vehicle dynamics [32] and [110]. The statistical analyses conducted in this thesis confirm these constraints and reveal an underlying structure in the signal. Significant differences across VIASAT event types and consistent sequential patterns in the transition matrices indicate that the accelerometric channel captures genuine distress phenomena. This observation aligns with deterioration-progression studies such as those presented in [65], where sequential mechanisms are explicitly described. The heterogeneity of type 2 detections and the sensitivity to driving dynamics reinforce that accelerometric FCD alone cannot provide a reliable and operational pavement indicator, a limitation also discussed in [11].

The integration of computer-vision detections adds a complementary layer of information. Deep-learning methods for distress identification, as illustrated in [70], [71] and [106], demonstrate strong performance in recognising cracks, rutting, potholes and alligator patterns. The detections used in this thesis reflect these

capabilities and provide a detailed spatial representation of surface morphology. Kernel density estimations and DBSCAN clustering reveal coherent aggregation patterns for distress classes, consistent with the spatial organisation of deterioration processes discussed at network level in [95] and [96]. The performance of vision-based detections is affected by lighting conditions, occlusions and route density, in line with the limitations highlighted in the reviews reported in [77] and [106]. The explicit identification and management of D50 objects address a long-standing issue, since the misclassification of manholes as structural defects is a recurring problem in studies that link surface irregularities to driving behavior and safe speed [19].

The methodological contribution of this thesis becomes evident when accelerometric and vision-based detections are interpreted jointly. Data fusion literature, particularly the review in [105], stresses the distinction between low-level and high-level integration and the necessity of semantic fusion in infrastructure monitoring, a perspective also supported by multisensor traffic studies in [39] and [111]. The approach developed here follows this perspective by embedding heterogeneous detections in a physically informed fusion architecture. Analyses based on correlations, co-occurrence matrices and principal component analysis [81] reveal structured redundancy between the two sensing channels. Redundancy is interpreted as multi-sensor confirmation of the same physical distress mechanisms rather than as noise to be removed. The desirability of sensor agreement in connected-vehicle monitoring is underlined in [11], and the results obtained here operationalise this principle. This perspective departs from pre-processing techniques commonly used in traffic analytics that seek to decorrelate signals [8] and [25] and proves more suitable for structural diagnostics.

The positioning of the proposed methodology within the broader literature on Pavement Management Systems further reinforces its relevance. Traditional indices such as the Pavement Condition Index and its derivatives [41] and [50], together with the International Roughness Index [42], provide accurate benchmark measures but require costly surveys and specialised equipment [61], [63] and [86]. Recent studies have proposed complementary indicators based on vehicle-mounted cameras or inertial sensors [92], [94], [112] and [113], yet few offer a multi-sensor framework

capable of covering an entire urban network. The Intervention Priority Index developed in this thesis is not intended to replace certified indices but to complement them by providing continuous monitoring and early identification of emerging deterioration hotspots. The positive association between the index and crash or near-miss frequency supports the link between pavement irregularities and safety outcomes, consistent with the evidence presented in [19], [60], [114] and [115].

The macro-scale interpretation of the Brescia network reveals deterioration patterns consistent with theoretical PMS expectations and empirical results reported in [95] and [79]. Higher deterioration levels on local streets and more stable conditions along arterial corridors reflect typical maintenance priorities and resource allocation strategies [44], [62] and [116]. Micro-scale validation through direct visual inspection further confirms the reliability of the index, aligning with PMS practices that integrate quantitative indicators with field verification [86] and [108]. This dual validation confirms that the fused indicator captures structural deterioration rather than measurement artefacts.

The limitations identified in this work align with those documented in the literature. The absence of PCI or IRI ground truth restricts absolute calibration but does not compromise the interpretability of relative deterioration patterns when benchmarked against established indices [41], [42] and [50]. The single-network nature of the case study limits generalisability, as already observed in several network-level FCD and sensing applications [32] and [99]. The environmental sensitivity of computer-vision detections reflects constraints noted in [77], [79] and [106]. The heterogeneity of accelerometric data is consistent with issues described in smartphone- and probe-based monitoring [92], [94], [112] and [117]. Segmentation effects observed in this thesis correspond to the scale-sensitivity concerns raised in [18] and are compatible with the data-driven segmentation and section-length studies reported in [88], [93] and [100].

The results demonstrate that multi-source vehicular data can support a scientifically grounded and operational framework for pavement monitoring. By integrating accelerometric, visual and geometric information, the methodology advances the frontier of Floating Car Data applications from mobility analytics to infrastructure

diagnostics. This contribution addresses the gap highlighted in the literature on FCD and Pavement Management Systems [4], [32], [44], [45] and [118] and provides a reproducible and scalable strategy for enhancing Pavement Management Systems with continuous and data-driven inputs, in line with current directions on composite indicators and decision-support tools for infrastructure management [63], [80], [86] and [116].

7.2. Applicability to Pavement Management Systems

The methodological framework developed in this thesis is directly actionable within the logic and operational needs of Pavement Management Systems, PMS. PMS have historically been conceived as decision support systems that integrate inventory, condition assessment, performance modelling, and budgeting in order to plan maintenance and rehabilitation actions under constrained resources [63], [74], [116]. In this context, the key practical value of the proposed multi source Floating Car Data approach is not to replace certified condition indicators, but to complement them with a continuous, network wide, and data driven screening layer capable of identifying where deterioration is emerging, how it evolves over time, and, progressively, why it is occurring and which interventions are more effective. This positioning is coherent with both classical PMS principles and the more recent literature emphasising the need to expand agency practices from periodic surveys to more frequent and opportunistic monitoring strategies [44], [89], [118].

From episodic surveys to continuous network screening, traditional PMS rely heavily on periodic condition surveys and specialised equipment to estimate indices such as the Pavement Condition Index, PCI, and roughness related measures such as the International Roughness Index, IRI. PCI based surveys are standardised and widely adopted, including formalised procedures for roads and parking lots [121], while IRI has a long history of international calibration and standardisation efforts that aimed to ensure comparability across measurement systems [122]. These practices provide high quality ground truth information but are intrinsically costly, episodic, and logistically demanding, especially for large urban networks where heterogeneity in traffic, environment, and pavement types makes frequent inspections difficult to

sustain. Quality management guidelines for pavement condition data collection explicitly recognise that survey design, calibration, and operational constraints shape data reliability and comparability [86]. This thesis contributes by showing that multi source vehicular data, accelerometric events and computer vision based detections, can serve as a continuous screening mechanism that is systematically integrated at the segment level and is interpretable within an asset management rationale. Similar to other low cost sensing approaches, for example smartphone based or inertial monitoring, the framework leverages sensors already moving on the network to reduce the marginal cost of observation while preserving useful diagnostic signal [92], [94], [112], [113], [117]. The distinctive element here is the explicit fusion of heterogeneous channels into a structured indicator tailored for PMS integration, rather than a single sensor anomaly detector.

Operational role within the PMS cycle, where, when, and how, within the PMS cycle, the proposed indicator is most immediately applicable to the early stages of network level condition screening and prioritisation. The results demonstrate that the fused index provides a robust ranking of road segments according to deterioration intensity, thus enabling the system to answer the PMS question where should we intervene first using objective and continuously updated evidence. This aligns with screening approaches and unified assessment metrics proposed for maintenance prioritisation, where the goal is to provide a defensible first level classification that can guide deeper engineering assessment and intervention design [90]. In its current maturity, the framework is strongest in determining where deterioration hotspots are located. However, by design it also opens the path toward a temporal interpretation, when deterioration accelerates, stabilises, or responds to maintenance, because vehicular data are collected continuously and can be organised into time stamped series. This temporal layer is essential for PMS, where deterioration modelling and performance prediction underpin proactive planning [65], [66]. In the longer term, once multi year observations and calibration datasets become available, the same architecture can contribute to how to intervene by supporting the evaluation of treatment effectiveness and guiding the selection of preventive versus corrective actions, consistent with

modern performance modelling frameworks, including Markov based approaches and policies for optimal inspection and repair scheduling [62], [65], [66].

Data fusion as a PMS enabling design choice, a core requirement for PMS adoption is not only detecting anomalies, but producing information that is stable, interpretable, and operationally meaningful at the segment level. The fusion architecture developed in this thesis follows established principles of multisensor data fusion, where the goal is to combine complementary information sources and reduce uncertainty through structured integration [104], [105], [111]. This is particularly important for pavement monitoring because single sensor approaches are often sensitive to confounding factors, accelerometric responses may reflect vehicle dynamics, speed, driver behaviour, suspension properties, and sensor placement [110], while vision based detections are influenced by lighting, occlusions, and route density [77], [106]. Within the proposed framework, redundancy between channels is not treated as a nuisance to be eliminated through decorrelation, but as potential confirmation of shared physical mechanisms. This choice is strategically aligned with infrastructure monitoring needs, where agreement among sensors can increase confidence and help distinguish structural deterioration from measurement artefacts [99], [103]. The resulting composite logic, grounded in composite indicator methodology and dimensionality reduction tools, supports an interpretable synthesis rather than a black box score [80], [81].

Integration into PMS workflows, a concrete implementation pathway, from an operational standpoint, the methodology can be embedded into PMS workflows through a sequence of modular steps that map naturally to the data information decision chain of asset management systems [63], [116]. First, multi source detections are collected opportunistically from vehicles circulating on the network, commercial FCD systems and on board sensing represent a mature technological ecosystem for large scale collection [32]. Second, detections are georeferenced and aggregated into homogeneous road segments, a critical step because segment definition strongly influences both condition estimation and downstream decision making [18], [93], [95], [100], [120]. Third, multi source signals are transformed into structured sub indices and merged into a segment level composite indicator suitable for network screening,

consistent with the methodological guidance for composite indicators used in policy and decision support contexts [80]. Finally, the indicator feeds a prioritisation layer that outputs ranked candidate segments for inspection or intervention planning. Within this pipeline, the indicator can support multiple PMS tasks. Prioritisation and intervention programming, PMS require ranking segments under budget constraints and defining annual or multi year intervention plans [60], [74], [116]. The fused indicator provides a defensible screening metric that identifies high priority segments, particularly valuable in urban networks where condition heterogeneity is pronounced. This function is consistent with recent work advocating network level integration of structural condition into agency practices [89] and with studies proposing unified metrics for prioritisation [90]. Optimisation of inspections and allocation of resources, a practical barrier for agencies is that detailed surveys are expensive and cannot cover the entire network with high frequency. By supplying an objective heatmap of suspected deterioration, the framework enables agencies to concentrate costly inspections, for example specialised vehicles, detailed visual surveys, deflection measurements, on the segments where the marginal value of inspection is highest. This strategy is coherent with PMS principles of cost effectiveness and with the recognition that sampling frequency and survey design affect uncertainty and prediction quality [86], [97]. Dynamic updating and early warning capabilities, because vehicular data are continuously generated, the indicator can be updated frequently, weekly or monthly, enabling early detection of emerging hotspots that would not be captured by annual or multi annual surveys. This feature supports a shift toward preventive maintenance, where timely detection of early distress can reduce life cycle costs and improve network performance [62], [66]. It also aligns with the broader trend in intelligent pavement condition survey research toward more frequent, data driven monitoring practices [118].

Linking monitoring to safety and service outcomes, PMS are increasingly expected to integrate not only structural condition but also serviceability and safety impacts. The thesis results, showing associations between the fused index and crash or near miss indicators, support the idea that pavement irregularities contribute to safety relevant driving behaviour and risk patterns. This is consistent with literature linking driving

dynamics and safe speed to road conditions using FCD based indicators [19] and with modelling frameworks for near miss frequency and crash risk analysis [83], [114], [115]. While safety outcomes are influenced by many confounders, traffic, geometry, weather, behaviour [60], the observed association reinforces the PMS value of a monitoring tool that can highlight segments where deterioration may be contributing to elevated risk and thus justify priority actions beyond purely structural considerations.

Monitoring deterioration evolution and evaluating maintenance effectiveness, beyond locating hotspots, continuous multi source monitoring enables a second PMS capability, observing how pavement condition changes over time and in response to interventions. In classical PMS, performance prediction models, including Markov process formulations, represent deterioration as a stochastic progression through condition states, with transitions that can be altered by maintenance [65]. Contemporary models also emphasise the role of preventive maintenance in shifting deterioration trajectories and improving long term outcomes [62]. In practice, agencies often struggle to validate whether executed maintenance produces the expected performance improvements because surveys are too infrequent and observations are sparse. A continuous vehicular data indicator can reduce this gap by enabling before and after comparisons at high temporal resolution, if a segment receives a treatment, the indicator can track whether distress signals decrease, stabilise, or re-emerge, offering a pragmatic measure of short term effectiveness and early warning of premature failure.

This naturally leads to a governance relevant extension, performance based scoring of maintenance actions and contractors. In many networks, the alternative to systematic monitoring is reliance on periodic patrols and discretionary reports, for example road workers identifying issues opportunistically. Such approaches are valuable but can be fragmented and uneven in coverage. A continuous data driven monitoring layer supports a more objective and auditable assessment of maintenance quality, by enabling agencies to compare deterioration trends across segments treated by different contractors or under different specifications. Importantly, this should be framed as a screening and accountability tool rather than a punitive metric, the indicator is

sensitive to traffic exposure, environment, and contextual factors that must be accounted for in evaluation models [91], [102]. Nonetheless, the ability to observe evolution adds significant PMS value by strengthening the feedback loop between planning, execution, and performance outcomes [116].

Quality, comparability, and calibration requirements, for PMS implementation, data quality and comparability are decisive. The framework explicitly acknowledges that multi source vehicular data do not automatically provide absolute PCI or IRI equivalent measures. In the current state, the indicator is most defensible as a relative measure suitable for ranking and screening. This is consistent with the broader evidence that network level pavement condition data exhibit variability and uncertainty due to survey design, sensor heterogeneity, and contextual influences [91], [102]. Formal quality management practices emphasise the need for calibration, validation, and documentation of data collection procedures [86]. Therefore, agencies adopting this approach should embed it into a calibration strategy that periodically anchors the continuous indicator to certified surveys. PCI surveys following standard procedures provide a natural calibration reference [121], while roughness related calibration can draw on standardised measurement concepts rooted in IRI development and correlation frameworks [122]. This hybrid strategy, continuous monitoring complemented by periodic ground truth surveys, represents a pragmatic pathway to operational adoption.

Segmentation and spatial resolution as implementation choices, PMS decisions depend strongly on how the network is segmented because condition indices, deterioration models, and budget allocations are computed at the segment level. The literature shows that segmentation affects estimation bias and model performance, and data driven segmentation approaches have been proposed to better match homogeneous road behaviour [18], [93], [95], [100], [120]. The present thesis confirms that segmentation effects are non trivial in multi source vehicular monitoring, if segments are too short, noise and sparse coverage become dominant, if too long, localised deterioration hotspots are diluted and become harder to detect. For PMS adoption, this implies that segmentation should be treated as a design parameter aligned with agency practices and operational constraints. A recommended strategy

is to use an initial segmentation compatible with existing PMS units, validate sensitivity across alternative segment lengths, and adopt adaptive or data driven segmentation where the heterogeneity of the network demands it [95], [100], [120]. This is also aligned with evidence on learning appropriate averaging lengths in pavement measurements and the broader idea that resolution must match the physics of deterioration and the decision context [87].

Complementarity with emerging multi sensor and intelligent survey practices, the applicability of the framework is reinforced by the convergence of recent research toward multi sensor and intelligent pavement assessment. Studies have explored vision based detection of cracks and potholes using deep learning, demonstrating growing maturity in automated distress recognition [69], [70], [71], [72], [106], [107]. Others have proposed crowdsourcing and multi sensor fusion approaches for pothole detection and maintenance support, indicating that heterogeneous sensing is becoming an expected direction rather than an exception [47], [79]. Inertial and smartphone based monitoring has also been validated in urban contexts, showing feasibility for network level mapping when combined with robust processing [92], [94], [112], [113]. Multi sensor measurement and web based tools for maintenance management further suggest that the integration of data streams into decision systems is increasingly realistic [67]. Within this landscape, the present thesis provides a PMS oriented integration, it does not stop at detection, but proposes a segment level fusion indicator explicitly interpretable in the language of asset management and prioritisation.

Decision rules and governance recommendations, how the indicator should be used, to be PMS ready, the indicator must come with clear governance rules. The evidence in this thesis supports three key recommendations. Use as a screening and prioritisation layer, not as a stand alone certification metric, without systematic PCI and IRI ground truth, the indicator should not be interpreted as a replacement for certified indices. Instead, it should guide where to look and where to intervene first, and then trigger deeper assessment where needed [86], [121], [122]. Adopt a tiered decision process, a practical PMS workflow is to define threshold based classes, for example high, medium, low priority, based on the indicator, then schedule targeted

inspections for high priority segments, and finally confirm intervention types with engineering judgment and standard surveys. This tiered logic aligns with the decision support role of PMS and with the need to manage uncertainty and variability [63], [86], [91], [102]. Use time series for maintenance feedback and accountability with contextual controls, when leveraging the indicator to evaluate maintenance effectiveness or contractor performance, agencies should control for confounders such as traffic exposure, weather, and geometry and use robust statistical frameworks. The literature on near miss and safety modelling illustrates how longitudinal data can be handled with appropriate statistical tools [83], [114], and the same caution applies when linking condition trajectories to performance outcomes.

Synthesis, overall, the results of this thesis demonstrate that multi source FCD can be operationalised as a PMS compatible monitoring layer that increases coverage, frequency, and objectivity of pavement condition information. Its immediate PMS contribution is the capability to identify where deterioration hotspots are located across a full urban network and to support prioritisation and inspection planning under resource constraints [63], [116]. Its medium term potential lies in enabling when deterioration accelerates and how it responds to interventions, strengthening preventive maintenance strategies and performance based governance [62], [65], [66]. Its longer term trajectory, once anchored through periodic calibration with certified surveys, can support more quantitative integration with established indices and predictive models, consistent with the broader evolution of pavement management toward intelligent, composite, and data driven decision support [44], [89], [90], [118].

Part III – Conclusions and references

8. Conclusions

This thesis demonstrates that Floating Car Data and vehicle-mounted sensing technologies can be systematically integrated to support continuous and scalable pavement condition monitoring. The combination of accelerometric detections from VIASAT with computer-vision detections from AIWAY provides a comprehensive multimodal representation of structural and surface-level pavement distress across an urban road network. The empirical results confirm that each sensing modality captures distinct phenomena and that their integration offers a richer and more reliable assessment than any individual source alone. The overall evidence indicates that connected vehicles can effectively operate as distributed sensing platforms, extending the spatial and temporal coverage of traditional Pavement Management Systems.

This thesis contributes to the literature on pavement monitoring, Floating Car Data analytics and multisensor data fusion in several complementary ways. First, it extends the traditional scope of Floating Car Data by demonstrating their applicability not only to traffic analysis but also to infrastructure diagnostics, an area in which existing research remains fragmented and largely exploratory. By systematically integrating accelerometric and computer-vision outputs, the study shows that probe vehicles can provide a coherent and continuous representation of pavement deterioration capable of supporting network-level decision-making. Second, it contributes to the methodological literature on multisensor fusion by introducing a redundancy-aware framework in which overlapping signals across sensing modalities are treated as informative confirmations rather than as noise. This perspective, operationalised through correlation metrics, co-occurrence analysis and principal component interpretation, offers a structured approach to harmonising heterogeneous vehicular data while preserving their distinct informational value. Third, the thesis contributes to the emerging field of risk-aware pavement management by linking fused deterioration indicators with road-safety outcomes through statistically validated count models. This alignment between infrastructure condition and near-miss frequencies provides empirical evidence that sensor-based deterioration indices can

support both maintenance prioritisation and safety-oriented planning. Fourth, the work advances the construction of composite indicators within intelligent transport systems by developing a transparent, interpretable and reproducible index architecture consistent with established guidelines on composite indicator design and suitable for operational integration into Pavement Management Systems. Finally, by demonstrating the feasibility of large-scale monitoring through connected vehicles in a real urban setting, the thesis provides a practical contribution that bridges academic modelling and agency-level implementation, paving the way for data-driven and proactive maintenance strategies.

The methodological contribution lies in the development of a redundancy-aware fusion framework that harmonises dynamic, visual and geometric indicators at segment level and calibrates them through statistically validated relationships with safety-relevant outcomes. The framework builds upon foundational concepts in data fusion described in [105], complemented by multisensor integration principles discussed in [104] and [111], and adapts them to the specific requirements of pavement condition assessment. Segment-level harmonisation, explicit control of functional elements such as manholes (D50), and the treatment of redundancy as multi-sensor confirmation rather than as noise form the core of this approach. The resulting Intervention Priority Index captures deterioration patterns with operational relevance and supports proactive decision-making by identifying segments where emerging damage may affect user safety.

The conclusions highlight that the deterioration patterns observed across Brescia's network are coherent with theoretical expectations derived from Pavement Management Systems literature [44], [50] and [63], and with empirical evidence documented in previous studies on network-level deterioration [43] and [95]. Higher index values on local streets and comparatively lower values on arterial roads are consistent with typical maintenance priorities and traffic loading conditions. The matched behavior between high index values and field-observed defects confirms the interpretability of the indicator, while the positive association with near-miss and crash frequencies reinforces its relevance for safety assessment. Macro-scale analyses

and micro-scale visual inspections jointly suggest that the fused indicator is sensitive to genuine structural deterioration rather than to isolated measurement artefacts.

The research also contributes to the broader discussion on how probe-vehicle and crowdsourced data can complement conventional survey-based indices such as the Pavement Condition Index and the International Roughness Index [41], [42] and [50]. The proposed indicator is not intended to replace certified measures but to provide an additional, continuously updated layer of information that can guide the allocation of detailed inspections and maintenance resources. Within this perspective, the Intervention Priority Index can be interpreted as a screening and prioritisation tool that directs expensive and time-consuming surveys towards the segments where they are most needed. The structure of the indicator, based on interpretable weights and transparent aggregation rules, is consistent with the guidelines on composite indicators reported in [80] and therefore compatible with integration into existing decision-support environments.

From an operational standpoint, the thesis shows that it is feasible to incorporate heterogeneous vehicular data streams into the workflow of infrastructure managers without requiring disruptive changes to existing Pavement Management Systems. The modelling choices deliberately favour transparency and reproducibility over excessive algorithmic complexity. Count-regression models, principal component analysis and correlation-based redundancy diagnostics provide interpretable links between sensing channels, deterioration categories and safety outcomes. This balance between methodological rigour and operational simplicity is essential for the adoption of data-driven tools by local administrations, which often operate under constraints in terms of technical expertise, budget and data availability.

In practical terms, the proposed framework enables infrastructure managers to conduct targeted inspections instead of relying on broad or unsystematic field surveys. By identifying the specific segments where deterioration is most likely to occur, the system reduces unnecessary travel, minimises blind inspections and improves the efficiency of ground-crew deployment. The index also supports the definition of maintenance plans on an objective and transparent basis, allowing authorities to prioritise interventions with clear evidence and to justify resource allocation decisions.

A practical workflow emerges: an initial accelerometric mapping generated from telematics providers offers an automated and continuous overview of network condition, after which high-frequency image acquisition campaigns can be carried out selectively on the critical segments and processed through computer vision tools such as AIWAY. This two-stage process combines scalability with diagnostic depth and constitutes a replicable operational model for modern pavement management.

Although the results demonstrate the robustness and practical relevance of the proposed framework, several avenues remain open for strengthening and extending its capabilities. The availability of certified reference measurements such as PCI or IRI would enable an absolute calibration of the Intervention Priority Index and support its alignment with normative scales used by road agencies. The incorporation of standardised reference data would therefore enrich the interpretability of the index and further consolidate its role in operational decision-making.

The performance of the framework could also be enhanced through expanded testing on networks with different geometric characteristics, traffic compositions and maintenance policies. Applications across diverse urban contexts would make it possible to assess the stability of the indicator under heterogeneous conditions and to explore procedures for inter-network normalisation, ultimately paving the way for comparative benchmarking between cities.

Future developments may also benefit from the integration of additional sensing modalities. Data sources such as LiDAR profilometry or Traffic Speed Deflectometer measurements have the potential to reinforce the connection between surface-level observations and the underlying structural condition of pavements. Their inclusion would improve the vertical consistency of the framework and allow for more direct comparisons with normative indices used in conventional Pavement Management Systems.

Another promising direction concerns temporal modelling. Repeated acquisition campaigns based on Floating Car Data and computer-vision inputs would enable the analysis of deterioration trajectories over time, the estimation of progression rates and the assessment of maintenance effectiveness. This temporal dimension would

transform the framework from a screening and prioritisation tool into a broader predictive instrument supporting long-term asset-management strategies.

Adaptive segmentation strategies, informed by change-point detection and data-driven sectioning methods [18], [88], [93] and [100], could further refine the spatial granularity of the indicator.

Future developments should also consider the alignment of the Intervention Priority Index with agency-specific performance measures and regulatory frameworks. Mapping the index onto existing rating scales and integrating it into multi-criteria decision tools used by road agencies would facilitate its adoption and interpretation. The combination of technical outputs with economic evaluation and risk-based planning, building on the asset-management perspectives discussed in [20], [35] and [119], could support more comprehensive maintenance strategies that explicitly incorporate safety, serviceability and budget constraints.

Overall, this thesis provides conceptual, methodological and operational contributions to the integration of multi-source vehicular data within Pavement Management Systems. The work shows that connected vehicles and embedded sensors can be systematically exploited as a large-scale monitoring infrastructure for pavement condition, moving beyond purely mobility-oriented uses of Floating Car Data. The proposed framework supports the transition towards proactive and data-driven maintenance strategies and demonstrates the feasibility of leveraging existing vehicular fleets as distributed sensing platforms for sustainable infrastructure management.

9. References

1. Liberati A., Altman D. G., Tetzlaff J., Mulrow C., Gøtzsche P. C., Ioannidis J. P. A., Clarke M., Devereaux P. J., Kleijnen J., Moher D. (2009). The PRISMA statement for reporting systematic reviews and meta-analyses of studies that evaluate health care interventions: explanation and elaboration. Journal of Clinical Epidemiology, 62(10), e1-e34. https://doi.org/10.1016/j.jclinepi.2009.06.006
2. Zheng L., Ma H., Wang Z. (2024). Travel Time Estimation for Urban Arterials Based on the Multi-Source Data. Sustainability, 16(17), 7845. https://doi.org/10.3390/su16177845
3. Schweppenhäuser M., Schrab K., Protzmann R., Radusch I. (2025). Evaluating spatiotemporal speed metrics for traffic state estimation on complex urban roads. Simulation: Transactions of the Society for Modeling and Simulation International, 1-12. https://doi.org/10.1177/00375497241308890
4. Pugliese F. A., Montesano G., Valenti, G. (2009). Urban traffic analysis from a large scale floating car data system. WIT Transactions on the Built Environment, 107, 3-11. https://doi.org/10.2495/UT090011
5. Zhang Y., Zuo X., Zhang L., Chen Z. (2011). Traffic congestion detection based on GPS floating-car data. Procedia Engineering, 15, 5541-5546. https://doi.org/10.1016/j.proeng.2011.08.1028
6. Yao E., Yang Z., Song Y., Zuo T. (2013). Comparison of electric vehicle's energy consumption factors for different road types. Discrete Dynamics in Nature and Society, 2013. https://doi.org/10.1155/2013/328757
7. Rossi L., Ajmar A., Paolanti M., Pierdicca R. (2021). Vehicle trajectory prediction and generation using LSTM models and GANs. PLoS ONE, 16(7 July). https://doi.org/10.1371/journal.pone.0253868
8. Liu X., Ban Y. (2013). Uncovering Spatio-temporal cluster patterns using massive floating car data. ISPRS International Journal of Geo-Information, 2(2), 371-384. https://doi.org/10.3390/ijgi2020371
9. De Vincentis M., Filippi F., Gori S. (2022). A Data-Driven Approach to Analyze Mobility Patterns and the Built Environment: Evidence from Brescia, Catania, and Salerno (Italy). Sustainability, 14(21), 14378. https://doi.org/10.3390/su142114378
10. Gao Y., Liao Y. (2023). Urban Tourism Traffic Analysis Zone DivisioBased on Floating Car Data. Promet - Traffic and Transportation, 35(3), 395-406. https://doi.org/10.7307/ptt.v35i3.104

11. Bruwer M., Behrens R., Andersen S.J. (2023). Commercial floating car data application in Sub-Saharan African transport planning contexts: A critical review and research agenda. Scientific African, 20, e01692. https://doi.org/10.1016/j.sciaf.2023.e01692
12. Garcia-Castro A., Monzon A. (2014a). Homogenization effects of variable speed limits. Transport and Telecommunication, 15(2), 130-143. https://doi.org/10.2478/ttj-2014-0012
13. Garcia-Castro A., Monzon A. (2014b). Using floating car data to analyse the effects of ITS measures and Eco-driving. Sensors (Switzerland), 14(11), 21358-21374. https://doi.org/10.3390/s141121358
14. Ballarano D., Petrelli M., Renna A. (2022). Validation Method for a Multimodal Freight Transport Model Exploiting Floating Car Data. Sustainability (Switzerland), 14(9). https://doi.org/10.3390/su14095540
15. Karukayil A., Quail C., Cheein F.A. (2024). Deep learning enhanced feature extraction of potholes using vision and LiDAR data for road maintenance. IEEE Access, 1-1. https://doi.org/10.1109/access.2024.3512783
16. Sun S., Duan Z., Yang D. (2015). Urban freight management with stochastic time-dependent travel times and application to large-scale transportation networks. Mathematical Problems in Engineering, 2015, Article ID 914309. https://doi.org/10.1155/2015/914309
17. Comi A., Persia L., Polimeni A., Campagna A. (2020). A methodology to design and assess scenarios within SULPs: The case of Bologna. Transportation Research Procedia, 46, 269-276. https://doi.org/10.1016/j.trpro.2020.03.190
18. Cafiso S., D'Agostino C., Persaud B. (2018). Investigating the influence of segmentation in estimating safety performance functions for roadway sections. Journal of Traffic and Transportation Engineering, 5(2), 129-136. https://doi.org/10.1016/J.JTTE.2017.10.001
19. Colombaroni C., Fusco G., Isaenko N. (2020). Coherence analysis of road safe speed and driving behavior from floating car data. IET Intelligent Transport Systems, 14(9), 985-992. https://doi.org/10.1049/iet-its.2019.0700
20. Li X., Zhang Y., Xiang L., Wu T. (2023). Urban Road Lane Number Mining from Low-Frequency Floating Car Data Based on Deep Learning. ISPRS International Journal of Geo-Information, 12(11). https://doi.org/10.3390/ijgi12110467
21. Han J., Kamber M., Pei J. (2011). Data Mining: Concepts and Techniques (3rd ed.). Elsevier.
22. Wang K., Qian X., Fitch D. T., Lee Y., Malik J., Circella G. (2023). What travel modes do shared e-scooters displace? A review of recent research findings. Transport Reviews, 43(1), 5-31. https://doi.org/10.1080/01441647.2021.2015639
23. Youssef A., Al-Subaie N., El-Sheimy N., Elhabiby M. (2021). Accelerometer-based wheel odometer for kinematics determination. Sensors (Switzerland), 21(4), 1-32. https://doi.org/10.3390/s21041327

24. Zhang C., He J., Liu Z., Xing L., Wang Y. (2019). Travel demand and distance analysis for freefloating car sharing based on deep learning method. PLoS ONE, 14(10). https://doi.org/10.1371/journal.pone.0223973
25. Ran B., Song L., Zhang J., Cheng Y., Tan H. (2016). Using tensor completion method to achieve better coverage of traffic state estimation from sparse floating car data. PLOS Ecosystem. https://journals.plos.org/plosone/article?id=10.1371/journal.pone.0157420
26. Gündüz G., Acarman T. (2020). Vehicle travel time estimation using sequence prediction. Promet - Traffic&Transportation, 32(1), 1–12. https://doi.org/10.7307/ptt.v32i1.3008
27. Brunauer R., Schmitzberger N., Rehrl K. (2018). Recognizing spatio-temporal traffic patterns at intersections using self-organizing maps. Proceedings of the 11th ACM SIGSPATIAL International Workshop on Computational Transportation Science (IWCTS'18). Association for Computing Machinery, New York, NY, USA, 43–52. https://doi.org/10.1145/3283207.3283209
28. Röger C., Kalinic M., Krisp J. M. (2021). Extracting Densely Covered Areas Within Floating Car Datasets Using Inductive Loop Detector Data. KN - Journal of Cartography and Geographic Information, 71(2), 97-103. https://doi.org/10.1007/s42489-020-00063-y
29. Guo Y., Li B., Lu Z., Zhou J. (2022). A novel method for road network mining from floating car data. Geo-Spatial Information Science, 25(2), 197-211. https://doi.org/10.1080/10095020.2021.2003165
30. Ranacher P., Brunauer R., Van Der Spek S., Reich, S. (2016). What is an appropriate temporal sampling rate to record floating car data with a GPS? ISPRS International Journal of Geo-Information, 5(1). https://doi.org/10.3390/ijgi5010001
31. Ravanelli R., Crespi, M. (2018). Analysis of the floating car data of turin public transportation system: First results. International Archives of the Photogrammetry, Remote Sensing and Spatial Information Sciences - ISPRS Archives, 42(4), 579-585. https://doi.org/10.5194/isprs-archives-XLII-4-515-2018
32. Budimir D., Jelušić N., Perić M. (2019). Floating car data technology. Pomorstvo, 33(1), 22-32. https://doi.org/10.31217/p.33.1.3
33. Ismail K., Muharam A., Pratama M. (2015). Design of CAN bus for research applications purpose hybrid electric vehicle using ARM microcontroller. Energy Procedia, 68, 288-296. https://doi.org/10.1016/j.egypro.2015.03.258
34. Vos J., Farah H. (2022). Speed development at freeway curves based on high frequency floating car data. European Journal of Transport and Infrastructure Research, 22(2), 201-223. https://doi.org/10.18757/ejtir.2022.22.2.6114

35. Vogt M., Krisp J. M. (2022). Räumliche Lärmanalyse anhand von erweiterten Floating-Car-Daten (xFCD). Spatial Analysis of Noise Using Extended Floating Car Data (xFCD). KN - Journal of Cartography and Geographic Information, 72(1), 73-83. https://doi.org/10.1007/s42489-021-00095-y
36. Del Serrone G., Cantisani G., Peluso P. (2023). Blending of Floating Car Data and Point-Based Sensor Data to Deduce Operating Speeds under Different Traffic Flow Conditions. European Transport - Trasporti Europei, 91. https://doi.org/10.48295/ET.2023.91.5
37. Astarita V., Giofrè, V. P., Guido G., Vitale A. (2017). The use of adaptive traffic signal systems based on floating car data. Wireless Communications and Mobile Computing, 2017. https://doi.org/10.1155/2017/4617451
38. Cantisani G., Del Serrone G., Mauro R., Peluso P., Pompigna A. (2024). From Radar Sensor to Floating Car Data: Evaluating Speed Distribution Heterogeneity on Rural Road Segments Using Non-Parametric Similarity Measures. Sci, 6(3), 52. https://doi.org/10.3390/sci6030052
39. Kessler L., Rempe F., Bogenberger K. (2021). Multi-Sensor Data Fusion for Accurate Traffic Speed and Travel Time Reconstruction. Frontiers in Future Transportation, 2. https://doi.org/10.3389/ffutr.2021.766951
40. Llorca D. F., Sotelo M. A., Sánchez S., Ocaa M., Rodríguez-Ascariz J. M., García-Garrido M. A. (2010). Traffic data collection for floating car data enhancement in V2I networks. Eurasip Journal on Advances in Signal Processing, 2010. https://doi.org/10.1155/2010/719294
41. Reza F., Boriboonsomsin K., Bazlamit S. M. (2006). Development of a Pavement Quality Index for the State of Ohio. Center for Environmental Research and Technology. https://www.researchgate.net/publication/292090454_Development_of_a_pavement_quality_index_for_the_state_of_Ohio
42. Pérez-Acebo H. et al. (2023). IRI prediction models for freeways. Transportation Research Procedia, 292-299. https://doi.org/10.1016/j.trpro.2023.11.087
43. Setyawan A., Putra I. R., Nuruddin M. F. (2015). Predicting the Remaining Service Life of Road Using Road Performance and Damages. Procedia Engineering, 125, https://doi.org/10.1016/j.proeng.2015.11.108
44. Peraka N. S. P. et al. (2020). Pavement asset management systems and technologies: A review. Automation in construction. https://doi.org/10.1016/j.autcon.2020.103336
45. Siverio S., et al. (2025). Integrating Floating Car Data in a Pavement Management System: An empirical application in the Province of Brescia, Italy. Transportation Research Procedia, 90, 480-487. https://doi.org/10.1016/j.trpro.2025.06.117

46. Wang Z., Qiu D., Wu R., Shi Y., Niu W. (2025). Research on road crack detection based on RGB LPC GPR data fusion. International Archives of the Photogrammetry Remote Sensing and Spatial Information Sciences, XLVIII G 2025, 1543-1550. https://doi.org/10.5194/isprs-archives-xlviii-g-2025-1543-2025
47. Na X., Wang G., Wu C., Hu S. (2023). Sustainable road pothole detection a crowdsourcing based multi sensors fusion approach. Sustainability, 15(8), 6610. https://doi.org/10.3390/su15086610
48. Lee T., Chun C., Ryu S.-K. (2021). Detection of road-surface anomalies using a smartphone camera and accelerometer. Sensors, 21(2), 561. https://doi.org/10.3390/s21020561
49. Kruskal W. H., Wallis W. A. (1952). Use of Ranks in One-Criterion Variance Analysis. Journal of the American Statistical Association, 47, 583-621, http://dx.doi.org/10.1080/01621459.1952.10483441
50. AASHTO (2012). Pavement Management Guide (2nd ed.). American Association of State Highway and Transportation Officials.
51. Mondal S., Gupta A. (2021). Speed distribution for interrupted flow facility under mixed traffic. Physica A: Statistical Mechanics and Its Applications, 570, 125798. https://doi.org/10.1016/J.PHYSA.2021.125798
52. Zefreh M.M., Török Á. (2020). Distribution of traffic speed in different traffic conditions: An empirical study in Budapest. Transport, 35(1), 68-86. https://doi.org/10.3846/TRANSPORT.2019.11725
53. Sakhare R., Zhang Y., Li H., Bullock D.M. (2023). Impact of rain intensity on interstate traffic speeds using connected vehicle data. Vehicles, 5(1), 133-155. https://doi.org/10.3390/vehicles5010009
54. Downing W.L. (2020). Using probe data analytics for characterizing speed reductions as well as predicting speeds during rain events. Purdue University Research Repository. https://doi.org/10.25394/PGS.12685766.V1
55. Isaenko N., Colombaroni C., Fusco G., Lahijanian Z. (2024). Statistical and clustering-based assessment of variable speed limits effects on motorway performance from real-world observations. Future Transportation, 4(2). https://doi.org/10.3390/futuretransp4020020
56. Ahmed M.M., Ghasemzadeh A. (2018). The impacts of heavy rain on speed and headway behaviors: An investigation using the SHRP2 naturalistic driving study data. Transportation Research Part C: Emerging Technologies, 91, 371-384. https://doi.org/10.1016/J.TRC.2018.04.012
57. Anna V.A.B.K., Chunchu M. (2023). Determinants of speed variability on the horizontal curves of two-lane undivided rural highways passing through mountainous terrain. International Journal of Injury Control and Safety Promotion, 1-14. https://doi.org/10.1080/17457300.2023.2252797

58. Yasanthi R.G.N., Mehran B., Alhajyaseen W.K. (2021). Modelling speed behavior in rural highways: Safety analysis of driving under adverse road-weather conditions. PLOS ONE, 16(8), 1-31. https://doi.org/10.1371/JOURNAL.PONE.0256322
59. Faria M.V., Baptista P., Farias T.L., Pereira J.M.S. (2020). Assessing the impacts of driving environment on driving behavior patterns. Transportation, 47(3), 1311-1337. https://doi.org/10.1007/S11116-018-9965-5
60. Liu X., Lu J., Wang B., Zhang F. (2023). Exploring the main and interaction effects of traffic flow characteristics, roadway design and weather conditions on the real-time near-miss risk for urban roads with mixed logit model. Journal of Transportation Safety & Security, 1-15. https://doi.org/10.1080/19439962.2023.2230569
61. Bennett C.R., Paterson W.D.O. (2000). A Guide to Calibration and Adaptation of HDM-4. The World Road Association (PIARC) and The World Bank, Paris
62. Yamany M., Abraham D. (2020). Prediction of pavement performance using non-homogeneous Markov models: Incorporating the impact of preventive maintenance. Conference Proceedings, January 2020. https://www.researchgate.net/profile/Mohamed-Yamany/publication/336598923_Prediction_of_Pavement_Performance_using_Non-homogeneous_Markov_Models_Incorporating_the_Impact_of_Preventive_Maintenance/links/60284995299bf1cc26c41a7a/Prediction-of-Pavement-Performance-using-Non-homogeneous-Markov-Models-Incorporating-the-Impact-of-Preventive-Maintenance.pdf
63. Haas R., Hudson W. R., Zaniewski J. P. (1994). Modern Pavement Management. Malabar, FL: Krieger Publishing.
64. Sun Y., Gao Q., Li F., Du Y. (2025) Distress-Level Prediction of Pavement Deterioration with Causal Analysis and Uncertainty Quantification. Applied Sciences. 2025; 15(20):11250. https://doi.org/10.3390/app152011250
65. Butt A. A., Shahin M. Y., Feighan K. J., Carpenter S. H. (1987). Pavement performance prediction models using the Markov process. Transportation Research Record, 1123, 12-19
66. Madanat S., Ben-Akiva M. (1994). Optimal inspection and repair policies for infrastructure facilities. Transportation Science, 28(1), 55-62. https://doi.org/10.1287/trsc.28.1.55
67. Jha S., Zhang Y., Park B., Cho S.H., Krogmeier J.V., Bagchi T., Haddock J.E. (2023). Data-driven web-based patching management tool using multi-sensor pavement structure measurements. Transportation Research Record, 036119812311671-036119812311671. https://doi.org/10.1177/03611981231167161

68. Ruseruka C., Mwakalonge J., Comert G., Siuhi S., Ngeni F. (2023). Pavement Distress Identification Based on Computer Vision and Controller Area Network (CAN) Sensor Models. Sustainability, 15(8), 6438. https://doi.org/10.3390/su15086438
69. Koch C., Brilakis I. (2015). Pothole detection in asphalt pavement images. Advanced Engineering Informatics, 29(2), 196-207. https://doi.org/10.1016/j.aei.2011.01.002
70. Mandal V., Uong L., Adu-Gyamfi Y. (2018). Automated road crack detection using deep convolutional neural networks. 018 IEEE International Conference on Big Data (Big Data), 5212-5215. DOI:10.1109/BigData.2018.8622327
71. Gopalakrishnan K., Khaitan S. K., Choudhary A., Agrawal A. (2020). Deep convolutional neural networks with transfer learning for computer vision-based data-driven pavement distress detection. Construction and Building Materials, 267, 120529. https://doi.org/10.1016/j.conbuildmat.2017.09.110
72. Wang Y., Qi Q., Sun, L., Xian W., Ma T., Lu C., Zhang J. (2024). An Intelligent Detection and Classification Model Based on Computer Vision for Pavement Cracks in Complicated Scenarios. Applied Sciences, 14(7), 2909. https://doi.org/10.3390/app14072909
73. Huang Y.H. (2004). Pavement analysis and design (2nd ed.). Pearson Prentice Hall, Upper Saddle River, NJ. https://archive.org/details/pavementanalysis0000huan
74. Shahin M.Y. (2005). Pavement management for airports, roads, and parking lots. Springer, New York. https://link.springer.com/book/10.1007/b138928
75. Al-Qadi I.L., Elseifi M., Carpenter S.H. (2007). Repetitive loading and permanent deformation of hot-mix asphalt pavements. Journal of the Association of Asphalt Paving Technologists, 76, 451–480. https://asphaltpavement.org/PDFs/Papers/2007_Al-Qadi_Elseifi_Carpenter.pdf
76. Rahmani A. R., Al-Farsi F., Chen W., Zhou S. (2024). Real-time road anomaly detection using advanced sensor networks. Research Square Preprint. https://doi.org/10.21203/rs.3.rs-3914460/v1
77. Yu J., Jiang J., Fichera S., Paoletti P., Layzell L., Mehta D., Luo S. (2024). Road surface defect detection from image based to non image based: a survey. arXiv Preprint arXiv 2402.04297. https://doi.org/10.48550/arxiv.2402.04297
78. Sterckx J., Vlaminck M., Luong H. (2025). Segmentation and quantification of surface defects in 3D reconstructions for damage assessment and inspection. IEEE Transactions on Automation Science and Engineering, 1-1. https://doi.org/10.1109/tase.2025.3593967

79. Huang Y., Jahanshahi M.R., Shen F., Mondal T.G. (2023). Deep learning based autonomous road condition assessment leveraging inexpensive RGB and depth sensors and heterogeneous data fusion pothole detection and quantification. Journal of Transportation Engineering, 149(2). https://doi.org/10.1061/jpeodx.pveng-1194
80. Nardo M., Saisana M., Saltelli A., Tarantola S., Hoffman A., Giovannini E. (2005). Handbook on Constructing Composite Indicators: Methodology and User Guide. OECD Statistics Working Papers. https://doi.org/10.1787/533411815016
81. Jolliffe I.T. (2002). Principal Component Analysis (2nd ed.). Springer, New York. https://doi.org/10.1007/b98835
82. Organisation for Economic Co-operation and Development Statistics and Data Directorate (SDD). (2024). About the OECD Statistics and Data Directorate. Available at: https://www.oecd.org/en/about/directorates/statistics-and-data-directorate.html
83. Mohammadi M.A., Samaranayake V.A., Bham G.H. (2014). Near-miss frequency modeling using negative binomial models: An application of generalized estimating equation to longitudinal data. Analytic Methods in Accident Research, 2, 52–69. https://doi.org/10.1016/j.amar.2014.07.001
84. O'Brien R.M. (2007). A caution regarding rules of thumb for variance inflation factors. Quality & Quantity, 41, 673-690. https://doi.org/10.1007/s11135-006-9018-6
85. Ali A. et al. (2023). Predicting Pavement Condition Index based on multiple linear regression, ANN, and fuzzy logic. Case studies in construction materials, 18, e01643. https://doi.org/10.1016/j.cscm.2023.e01643
86. Federal Highway Administration (2013). Practical Guide for Quality Management of Pavement Condition Data Collection. Federal Highway Administration, U.S. Department of Transportation, Office of Asset Management, Pavements and Construction. https://www.fhwa.dot.gov/pavement/management/qm/data_qm_guide.pdf
87. Katicha, S. W., Scavone, M., Scavone, M., & Amarh, E. (2024). Learning the Appropriate Local Averaging Length for Traffic Speed Deflectometer Deflection Velocity Measurements: Application to the Analysis of Rigid Pavement Joint Responses. Transportation Research Record. https://doi.org/10.1177/03611981241250344
88. Zhao X., Lord D., Peng Y. (2019). Examining Network Segmentation for Traffic Safety Analysis With Data-Driven Spectral Analysis. IEEE Access, 7, 120744-120757. https://doi.org/10.1109/ACCESS.2019.2937001
89. Murekye A., Katicha S.W., Urbaez E., Flintsch G.W., Diefenderfer B.K. (2024). Pilot study to incorporate network-level structural condition in agency pavement management practices. Transportation Research Record. https://doi.org/10.1177/03611981241252152

90. Boonsiripant S., Lertworawanich P., Sawangsuriya A., Jinakub K. (2025). Enhancing road maintenance prioritization: Single index screening and unified pavement assessment metric integration. Transportation Research Record. https://doi.org/10.1177/03611981251342788
91. Shekharan R.A., Baranikumar A., Asam K., Wang Z., Frith D. (2024). Investigation of the data variability of network-level pavement condition data. Transportation Research Record. https://doi.org/10.1177/03611981241242065
92. Loprencipe G., Filho F.G.V.D.A., Oliveira R.H.D., Bruno S. (2021). Validation of a low-cost pavement monitoring inertial-based system for urban road networks. Sensors, 21(9). https://doi.org/10.3390/S21093127
93. Liu W., Li J.Q., Yu W., Yang G. (2021). Change-point detection approaches for pavement dynamic segmentation. https://doi.org/10.1061/JPEODX.0000270
94. Dong D., Li Z. (2021). Smartphone sensing of road surface condition and defect detection. Sensors, 21(16). https://doi.org/10.3390/S21165433
95. Song Y., Wu P., Gilmore D., Li Q. (2021). A spatial heterogeneity-based segmentation model for analyzing road deterioration network data in multi-scale infrastructure systems. IEEE Transactions on Intelligent Transportation Systems, 22(11), 7073-7083. https://doi.org/10.1109/TITS.2020.3001193
96. Lyu H., Qin-sheng Z., Huang Y., Jia H., Jiao D. (2024). Urban road surface condition sensing from crowd-sourced trajectories based on the detecting and clustering framework. Sensors, 24(13), 4093-4093. https://doi.org/10.3390/s24134093
97. Goenaga B., Karanam D., Underwood B.S. (2022). Method to reduce uncertainty in the prediction of pavement condition with a lower sample frequency. Transportation Research Record, 2676(9), 289-308. https://doi.org/10.1177/03611981221086636
98. Kiec M., D'Agostino C., Pazdan S. (2020). Impact on road safety and operation of rerouting traffic in rural travel time information system. Sensors, 20(15). https://doi.org/10.3390/S20154145
99. Gkyrtis K., Loizos A., Plati C. (2021). Integrating pavement sensing data for pavement condition evaluation. Sensors, 21(9). https://doi.org/10.3390/S21093104
100. Omrani R., Shalaby A., Nikolic G., Hadayeghi A. (2019). Development and implementation of a multi-level roadway segmentation methodology. Transportation Research Record, 2673(12), 570-583. https://doi.org/10.1177/0361198119867674
101. Hauwermeiren W.V., Filipan K., Botteldooren D., Coensel B.D. (2021). Opportunistic monitoring of pavements for noise labeling and mitigation with machine learning. Transportation Research Part D: Transport and Environment, 90. https://doi.org/10.1016/J.TRD.2020.102636

102. Jia X., Woods M., Martínez U., Zhu D., Huang B. (2022). Investigation into collection variability of surface crack data for network-level asphalt pavement evaluation. Transportation Research Record, 2677(1), 1538-1553. https://doi.org/10.1177/03611981221105069
103. Benedetto A., Al-Qadi I.L., Alani A.M., Loizos A., Tosti F. (2021). Sensing advancement and health monitoring of transport structures. Sensors, 21(22). https://doi.org/10.3390/S21227621
104. Hall D.L., Llinas J. (1997). An introduction to multisensor data fusion. Proceedings of the IEEE, 85(1), 6–23. https://doi.org/10.1109/5.554205
105. Castanedo F. (2013). A Review of Data Fusion Techniques. The Scientific World Journal, Volume 2013, Article ID 704504, 19 pages. https://doi.org/10.1155/2013/704504
106. Chen X., Yongchareon S., Knoche M. (2023). A review on computer vision and machine learning techniques for automated road surface defect and distress detection. Smart Cities and Society, 1(4). https://doi.org/10.3233/SCS-230001
107. Guan S., Liu H., Pourreza H.R., Mahyar H. (2021). Deep learning approaches in pavement distress identification: A review. Journal of LaTeX Class Files, 14(8), 1–18. arXiv:2308.00828. https://doi.org/10.48550/arXiv.2308.00828
108. Hartgen D.T., Shufon J.J., Parrella F.T., Koeppel K.W.P. (1982). Visual scales of pavement condition: Development, validation, and use. Transportation Research Record, 893, 1-6. https://onlinepubs.trb.org/Onlinepubs/trr/1982/893/893-001.pdf
109. Purkrábková Z., Coelho M. C., Macedo J., Hrubeš, P. (2024). Assessment of floating car data quality for emission estimation. Transportation Research Procedia, 78, 619-626. https://doi.org/10.1016/j.trpro.2024.02.077
110. Nguyen T., Lechner B., Wong Y.D. (2019). Response-based methods to measure road surface irregularity: a state-of-the-art review. European Transport Research Review, 11(43). https://doi.org/10.1186/s12544-019-0380-6
111. Varshney P.K. (2000). Multisensor data fusion. In Proceedings of the 13th International Conference on Industrial and Engineering Applications of Artificial Intelligence and Expert Systems (IEA/AIE '00): Intelligent Problem Solving – Methodologies and Approaches, 1–3. https://www.researchgate.net/publication/221047679_Multisensor_Data_Fusion
112. Kyriakou C., Christodoulou S.E., Dimitriou L. (2021). Spatial roadway condition-assessment mapping utilizing smartphones and machine learning algorithms. Transportation Research Record, 2675(9), 1118-1126. https://doi.org/10.1177/03611981211006105
113. Martinelli A., Meocci M., Dolfi M., Consumi T. et al. (2022). Road Surface Anomaly Assessment Using Low-Cost Accelerometers: A Machine Learning Approach. Sensors, 22(10), 3788. https://doi.org/10.3390/s22103788

114. Lord D., Mannering F. (2010). The statistical analysis of near-miss-frequency data: A review and assessment of methodological alternatives. Transportation Research Part A: Policy and Practice, 44(5), 291-305. https://doi.org/10.1016/j.tra.2010.02.001
115. Miaou S.-P. (1994). The relationship between truck accidents and geometric design of road sections: Poisson versus negative binomial regressions. Accident Analysis & Prevention, 26(4), 471-482. https://doi.org/10.1016/0001-4575(94)90038-8
116. Kulkarni R. B., Miller R. W. (2003). Pavement Management Systems: Past, Present, and Future. Transportation Research Record: Journal of the Transportation Research Board, 1853(1), 10-17. https://www.researchgate.net/publication/228771833_Pavement_Management_Systems_Past_Present_and_Future
117. Cabral F., Hidekazu F., Satoshi T. (2022). Road Roughness Estimation using Smartphone Sensor. 3. 56. https://www.researchgate.net/publication/363246217_Road_Roughness_Estimation_using_Smartphone_Sensor
118. Zhang H., Guo J., Liu Y., et al. (2024). Intelligent pavement condition survey: Overview of current researches and practices. Journal of Road Engineering, 4(3), 257–281. https://doi.org/10.1016/j.jreng.2024.04.003
119. Downing W.L., Li H., Morgan W.T., McKee C., Bullock D.M. (2021). Using probe data analytics for assessing freeway speed reductions during rain events. Joint Transportation Research Program, Purdue University. https://doi.org/10.5703/1288284317350
120. Xu C., Zeng Q., Chen L., Yang S. (2024). Ordinal clustering based homogeneous road segments in asphalt pavement maintenance and rehabilitation optimized decision-making. Transportation Research Record. https://doi.org/10.1177/03611981241272090
121. ASTM International (2020). Standard Practice for Roads and Parking Lots Pavement Condition Index Surveys. ASTM D6433-20. West Conshohocken, PA: ASTM International
122. Sayers M. W., Gillespie T. D., Queiroz C. (1986). The International Road Roughness Experiment: Establishing Correlation and a Calibration Standard for Measurements. World Bank Technical Paper No. 45. https://documents1.worldbank.org/curated/en/851131468160775725/pdf/multi-page.pdf

Part IV – Appendices

Table 21- Overview of analysed contributions

Title	Authors	Year	Use of FCD	Data Processing FCD	Technology and Sensors
A computer vision-based method to identify the international roughness index of highway pavements	Jiangyu Zeng, Mustafa Gül, Qipei Mei	2022	Images to estimate International Roughness Index (IRI)	Deep neural networks applied to 2D pavement photos	Sports action cameras (GoPro Hero series)
A Crowdsourcing Solution for Road Surface Roughness Detection Using Smartphones	Xiao Li, Ruizhi Chen, Tianxing Chu	2014	Smartphone accelerometer and GPS for roughness detection	RMS calculation of acceleration, transient event detection	Smartphone accelerometer, GPS
A Deep Learning based Process Model for Crack Detection in Pavement Structures	Aaron Rasheed Rababaah	2022	Deep CNN applied to asphalt pavement crack detection	CNN model tested on dataset of 500 images	CNN, computer vision
A Deep Supervised Pavement Crack Detection Network with Multiscale Feature Fusion and Feature Learning	Lei Yang, Han Pang Huang, Shuyi Kong	2023	End-to-end deep supervised crack detection	Attention U-Net baseline; attention fusion block (AFB), progressive fusion block (PCF), MRFF block	Attention U-Net, deep supervised network
A Deeply Supervised Convolutional Neural Network for Pavement Crack Detection With Multiscale Feature Fusion	Zhong Qu, Chong Cao, Ling Liu, Dong-Yang Zhou	2021	CNN with multiscale feature fusion and deep supervision	High-level features fused with low-level features at multiple stages	Deeply supervised CNN
A Detection and Classification Method of Asphalt Pavement Crack based on Vision Transformer	Yulong Yang, Chen Guo, Chen Zuo, B. Yang	2023	Road surface distress detection with advanced deep learning	Vision Transformer compared with CNNs (ResNet, DenseNet, EfficientNet)	Vision Transformer (ViT)
A Framework for Automated Pavement Condition Monitoring	Stefania C. Radopoulou, Ioannis Brilakis, Kristina Doycheva, Christian Koch	2016	Fusion of video and accelerometer data for pavement monitoring	Video frame analysis, accelerometer z-axis profile reconstruction, GPS synchronization	Car parking camera, accelerometer, GPS, 4G transmission
A computer vision-based method to identify the international roughness index of highway pavements	Jiangyu Zeng, Mustafa Gül, Qipei Mei	2022	Images to estimate International Roughness Index (IRI)	Deep neural networks applied to 2D pavement photos	Sports action cameras (GoPro Hero series)

Title	Authors	Year	Use of FCD	Data Processing FCD	Technology and Sensors
A Crowdsourcing Solution for Road Surface Roughness Detection Using Smartphones	Xiao Li, Ruizhi Chen, Tianxing Chu	2014	Smartphone accelerometer and GPS for roughness detection	RMS calculation of acceleration, transient event detection	Smartphone accelerometer, GPS
A Deep Learning based Process Model for Crack Detection in Pavement Structures	Aaron Rasheed Rababaah	2022	Deep CNN applied to asphalt pavement crack detection	CNN model tested on dataset of 500 images	CNN, computer vision
A Deep Supervised Pavement Crack Detection Network with Multiscale Feature Fusion and Feature Learning	Lei Yang, Han Pang Huang, Shuyi Kong	2023	End-to-end deep supervised crack detection	Attention U-Net baseline; attention fusion block (AFB), progressive fusion block (PCF), MRFF block	Attention U-Net, deep supervised network
A Deeply Supervised Convolutional Neural Network for Pavement Crack Detection With Multiscale Feature Fusion	Zhong Qu, Chong Cao, Ling Liu, Dong-Yang Zhou	2021	CNN with multiscale feature fusion and deep supervision	High-level features fused with low-level features at multiple stages	Deeply supervised CNN
A Detection and Classification Method of Asphalt Pavement Crack based on Vision Transformer	Yulong Yang, Chen Guo, Chen Zuo, B. Yang	2023	Road surface distress detection with advanced deep learning	Vision Transformer compared with CNNs (ResNet, DenseNet, EfficientNet)	Vision Transformer (ViT)
A Framework for Automated Pavement Condition Monitoring	Stefania C. Radopoulou, Ioannis Brilakis, Kristina Doycheva, Christian Koch	2016	Fusion of video and accelerometer data for pavement monitoring	Video frame analysis, accelerometer z-axis profile reconstruction, GPS synchronization	Car parking camera, accelerometer, GPS, 4G transmission
A hybrid deep learning pavement crack semantic segmentation	Zaid Al-Huda, Bo Peng, Riyadh Nazar Ali Algburi, Mugahed A. Al-antari, Rabea AL-Jarazi, Donghai Zhai	2023	Hybrid CNN + CAM strategy for semantic segmentation	Knowledge transfer via Class Activation Maps (KTCAM-Net); hybrid loss function	CNN, CAM, encoder-decoder

Title	Authors	Year	Use of FCD	Data Processing FCD	Technology and Sensors
A Large-Scale Benchmark for Pavement Crack Segmentation	Wei Chen, Xiaoxiang Zhang, Qianqi Zhao, Wenjie Pan, Jianqing Zhu	2023	Proposed PCSeg7000 dataset with 7000 pavement crack images	U-Net with strip-attention and pyramid self-supervised learning	U-Net, strip-attention, PCSeg7000 dataset
A low-cost pavement rating system, based on machine learning, utilizing smartphones sensors	Charalambos Kyriakou, Symeon E. Christodoulou	2022	Smartphone-based pavement condition evaluation	Unsupervised ML classification, statistical features in time and frequency domain	Smartphone accelerometer, GPS, OBD device
A novel network fusing transformer and CNN for road crack segmentation	Mianqing He, Tze Liang Lau	2024	CNN enhanced with transformer blocks for crack segmentation	AFM module, lightweight decoder SMLP, multi-level feature integration	Transformer + CNN hybrid model
A Practical Approach for Road Quality Estimation using Smartphone based Inertial Data	Deepa D. Nagaraj, Marcel Mutz, Supreeth Mysore Venkatesh, Lea Riebschlaeger, Dirk Werth	2022	Road quality estimation using smartphone IMU data	Preprocessing pipeline for noise reduction and geo-referencing; ML regression for quality index	Smartphone IMU (accelerometer, gyroscope)
A preliminary study on SPC-crowd pavement indexing	Tsung-Hsiang Wu, Chih-Wei Yi, Ching-Yao Chan, Ya-Lan Chang, Chien-Chao Tseng, Chun-Fu Chung	2015	Probe-car crowdsourcing system for pavement indexing	Mobile sensing with environmental data fusion	Probe vehicle sensors, smartphones
A recursive multi-scale correlation-averaging algorithm for synchronization and fusion of independent pavement roughness measurements	Mandoye Ndoye, Alan M. Barker, James V. Krogmeier, Darcy M. Bullock	2009	Fusion of distributed vehicle-based roughness measurements	Recursive correlation-averaging algorithm for multi-vehicle data	Accelerometers, GPS receivers
A review: literature on pothole monitoring system	Sneha Gosavi, Joshna Chinta, Nisha Pandav, Kanchan Dhuri	2020	Review of pothole detection systems using smartphones and vehicle sensors	Comparison of GPS, accelerometer, and camera-based monitoring methods	Smartphone accelerometer, GPS, vehicle cameras

Title	Authors	Year	Use of FCD	Data Processing FCD	Technology and Sensors
A Road Defect Detection System Using Smartphones	Gyulim Kim, Seungku Kim	2024	Automatic data collection with smartphone sensors for road defect detection	CNN-based model classifying potholes, speed bumps, manholes	Smartphone accelerometer, gyroscope, camera
A Scalable Pavement Sensing, Data Analytics, and Visualization Platform for Lean Governance in Smart Communities	Phong Nguyen, Raghav Rao, Vincent Brown, Matthew McConnell, N.A. Barendt, Nicholas C. Zingale, Soumyajit Mandal, Farhad Kaffashi, Kenneth A. Loparo	2020	Low-cost IMU and GPS data collection for roadway quality monitoring	Data analytics and visualization for pavement quality monitoring	Vehicle-mounted IMU, GPS
A Study on the Use of Smartphones Under Realistic Settings to Estimate Road Roughness Condition	Viengnam Douangphachanh, Hiroyuki Oneyama	2014	Smartphone accelerometer and GPS for road roughness estimation	Frequency domain analysis, linear regression with IRI	Smartphone accelerometer, GPS
A two-stream crack detection model based on SegNet	Yadong Li, Bo Peng, Weiqiang Xu	2022	SegNet with edge detection branch for crack segmentation	Semantic segmentation + edge attention modules	SegNet, edge detection modules
Abnormal Pavement Condition Detection with Vehicle	Q. Zhan et al.	2024	Vehicle sensors for abnormal pavement detection	Event detection, signal analysis, comparison across districts	Vehicle accelerometers, GPS
Accelerometer-based smartphone step detection using machine learning technique	So Young Park, Se Jong Heo, Chan Gook Park	2017	ML applied to accelerometer data for robust motion inference	Step detection via accelerometer and attitude computation	Smartphone accelerometer, gyroscope
Accelerometer-Based Pavement Classification for Vehicle Dynamics	V. Surblys et al.	2024	Accelerometer-only classification of pavement conditions	Neural networks and multinomial logistic regression	Vertical accelerometer, ML models

Title	Authors	Year	Use of FCD	Data Processing FCD	Technology and Sensors
Advanced Sensor Technologies in CAVs for Traditional and Smart Road Condition Monitoring: A Review	Masoud Khanmohamadi, Marco Guerrieri	2024	Review of sensor integration in CAVs for pavement and road condition monitoring	Machine learning, sensor fusion, edge computing	Accelerometers, gyroscopes, LiDAR, cameras, radar
An end-to-end computer vision system based on deep learning for pavement distress detection and quantification	Saúl Cano-Ortiz, Lara Lloret Iglesias, Pablo Martinez Ruiz del Árbol, Pedro Lastra-González, Daniel Castro-Fresno	2024	Computer vision system with YOLOv5 for distress detection	Annotated dataset of 7099 images, post-processing filters, ASPDI index	Vehicle-mounted cameras, YOLOv5 models
An Innovative Approach for High-Performance Road Pavement Distress Detection Based on Black Boxes	M. Meocci et al.	2021	Black box data for pavement distress detection	Image processing, distress metrics	Vehicle black boxes, cameras, GPS
An uncertainty-aware Road Anomalies Detection Based on Dempster-Shafer Theory	Nour El Houda Chibani, Faouzi Sebbak, Walid Cherifi, Mustapha Reda Senouci, Samir Ouchani	2022	Smartphone sensor data analyzed with uncertainty modeling	Dempster-Shafer Theory (DST) applied to anomaly detection	Smartphone accelerometer, gyroscope
Analyzing road quality using a mobile application	Vladimír Gašpar	2017	Smartphone accelerometer data for road quality analysis	Binning and clustering; planned Kalman filtering for noise reduction	Smartphone accelerometer
Anomaly Detection in Cooperative Adaptive Cruise Control Using Physics Laws and Data Fusion	Faris Alotibi, Mai Abdelhakim	2019	CACC systems with anomaly detection in vehicle platoons	Physics-based validation of acceleration data, multi-vehicle data fusion	Onboard accelerometers, V2V communications, GPS

Title	Authors	Year	Use of FCD	Data Processing FCD	Technology and Sensors
Applications of Using Connected Vehicle Data for Pavement Monitoring	Justin Anthony Mahlberg1Howell Li,Howell Li1,2Bjrn ZachrissonBjörn Zachrisson3Jijo K. MathewJijo K. Mathew1Darcy M. Bullock Darcy M. Bullock1	2022	Crowdsourced connected vehicle data for ride quality and IRI monitoring	Linear correlation with inertial profiler, segment analysis, bias correction	OEM onboard sensors, GPS, inertial profilers
Asphalt pavement crack detection based on multi-scale full convolutional network	Yangxu Wu, Wanting Yang, Jinxiao Pan, Ping Chen	2021	End-to-end CNN for semantic segmentation of cracks	Multi-scale FCN with DenseNet and deconvolution; post-classification with SVM	Full convolutional network, DenseNet, SVM
Asphalt pavement crack detection using image processing and naïve Bayes based machine learning approach	Pang-jo Chun, Kazuaki Hashimoto, Nozomu Kataoka, Naoya Kuramoto, Mitao Ohga	2015	Image processing + Naïve Bayes ML for crack detection	Manual segmentation + NB classifier for crack ratio	Naïve Bayes, image analysis
Automated Pavement Cracks Detection and Classification Using Deep Learning	Selvia Nafaa, Karim Ashour, Rana Mohamed, Hafsa Essam, Doaa Emad, Mohammed Elhenawy, Huthaifa I. Ashqar, Abdallah A. Hassan, Taqwa I. Alhadidi	2024	YOLOv5 and YOLOv8 for pavement crack detection and classification	YOLO-based detection under varying illumination conditions	Vehicle-mounted cameras
Automatic crack detection on concrete and asphalt surfaces using semantic segmentation network with hierarchical Transformer	Hubing Li, Haowei Zhang, Hong Zhu, Kang Gao, Han-zhi Liang, Jiangjin Yang	2024	SegFormer with hierarchical transformer for crack detection	Cross-Entropy + Dice loss functions; multi-scenario evaluation	SegFormer, semantic segmentation

Title	Authors	Year	Use of FCD	Data Processing FCD	Technology and Sensors
Automatic Pavement Crack Detection Based on Structured Prediction with the Convolutional Neural Network	Zhun Fan, Wu Yuming, Jiewei Lu, Wenji Li	2018	CNN-based structured prediction method for crack detection	CNN trained with modified positive/negative sample ratio to handle class imbalance	CNN, structured prediction
Automatic Pavement Crack Detection Based on YOLOv5-AH	Zhaohui Dong, Guijie Zhu, Zhun Fan, Jiacheng Liu, Huanlin Li, Yuwei Cai, Huaxing Huang, Ze Shi, Weibo Ning, Liu Wang	2022	Vehicle-mounted cameras for pavement crack detection	YOLOv5-AH with CBAM attention, added prediction head, data augmentation	Mobile robot with visual sensors
Automatic Pavement Crack Detection by Multi-Scale Image Fusion	Haifeng Li, Dezhen Song, Yu Liu, Binbin Li	2019	Unsupervised multi-scale fusion crack detection algorithm	Windowed minimal intensity path + multivariate statistical hypothesis test	MFCD algorithm, image fusion
Automatic Pavement Crack Detection Fusing Attention Mechanism	Junhua Ren, Guowu Zhao, Yadong Ma, De Zhao, Tao Liu, Jun Yan	2022	YOLOv5-based crack detection with CoordAtt attention	YOLOv5 enhanced with CoordAtt attention modules	YOLOv5, CoordAtt
Black boxes data for road pavement conditions monitoring: A case study in Florence	M. Meocci, V. Branzi	2022	Vertical acceleration data from black boxes	Classification of pavement roughness and anomalies	Vehicle black boxes, accelerometers
Bridge pavement crack detection and segmentation method based on semantic segmentation	Li Liangfu, Sun Ruiyun	2018	Applied semantic segmentation to bridge pavement crack detection	FC-DenseNet 103 network with augmented training data	Deep learning, semantic segmentation
Calibration of sensors for road surface monitoring	Tuononen Ari, Niskanen Arto, Syrjälähti Mikko	2021	Calibration of vehicle optical sensors for road surface monitoring	Server-based calibration using overlapping measurements from multiple vehicles	Vehicle optical sensors, calibration algorithms

Title	Authors	Year	Use of FCD	Data Processing FCD	Technology and Sensors
City Traffic Speed Characterization Based on City Road Surface Quality	Ratna Mandal, Soumi Dutta, Rupayan Banerjee, Sujoy Bhattacharya, Ritusree Ghosh, Sougata Samanta, Tiyasa Saha	2022	Smartphone sensors for traffic speed and road surface monitoring	Road Surface Index derived from accelerometer z-axis data	Smartphone accelerometer, GPS
Community Sensor Network for Monitoring Road Roughness Using Smartphones	Rajiv Kumar, Abhijit Mukherjee, V. P. Singh	2017	Crowdsourced road roughness monitoring via smartphone accelerometer data	Fuzzy logic-based road roughness classification; server-side aggregation and visualization	Smartphone accelerometers, client-server system
Computer Vision and Deep Learning based road monitoring towards a Connected, Cooperative and Automated Mobility	Olatz Iparraguirre Gil	2022	PhD thesis proposing computer vision and DL-based road monitoring	Modules for fog detection, traffic sign recognition, and road line defect detection	Vision systems, DL models
Computer vision monitoring for a computer vision system	Stefan Poledna, Wilfried Steiner, Manfred Lettner, Mehmed Ayhan	2014	Computer vision applied to vehicle control and monitoring systems	Landmark detection and fault detection using independent verification	Vehicle-mounted vision systems
Connected Vehicle Approach for Pavement Roughness Evaluation	Raj Bridgelall	2014	Accelerometer data from vehicles	RIF index compared to IRI, validation with inertial profiler	Onboard accelerometers, laser profiler
Continuous and Realtime Road Condition Assessment Using Deep Learning	Ahmed Abul Hasanaath; AbuMuhammad Moinuddeen; Nazeeruddin Mohammad; Majid Ali Khan; Ahmed Abul Hussain	2022	Continuous monitoring via Android app with DL classifier	Transfer learning (VGG16, MobileNetV2) for road condition classification	Android app, smartphone camera

Title	Authors	Year	Use of FCD	Data Processing FCD	Technology and Sensors
Crack Detection from a Concrete Surface Image Based on Semantic Segmentation Using Deep Learning	Tatsuro Yamane, Pang-jo Chun	2020	Applied semantic segmentation to concrete crack detection	Semantic segmentation CNN; trained on concrete surfaces with tie-rod holes and dirt	Deep learning semantic segmentation
Crack Detection, Classification, and Segmentation on Road Pavement Material Using Multi-Scale Feature Aggregation and Transformer-Based Attention Mechanisms	Arselan Ashraf, Ali Sophian, Ali Aryo Bawono	2024	Transformer-based attention for crack detection and segmentation	Multi-scale feature aggregation, transformer attention mechanisms	Transformer-based deep learning, pavement image dataset
CrackF-Net: a pixel-level segmentation network for pavement crack detection	Shen Luan, Xingen Gao, Chen Wang, Hongyi Zhang, Fei Chao, Juqiang Lin, Junqi Huang, Huali Jiang, Feng Lin	2023	End-to-end CNN encoder-decoder for crack segmentation	Residual convolutional blocks + adaptive filter fusion in decoder	CrackF-Net CNN
CrackW-Net: A Novel Pavement Crack Image Segmentation Convolutional Neural Network	Chengjia Han; Tao Ma; Ju Huyan; Xiaoming Huang; Yanning Zhang	2022	Novel CNN architecture for semantic segmentation of cracks	Skip-level round-trip sampling block in CNN segmentation	CrackW-Net CNN, Crack500 + self-built datasets
Creating Value from in-Vehicle Data: Detecting Road Surfaces and Road Hazards	Felix Kortmann, Yi-Chen Hsu, Alexander Warnecke, Nicolas Meier, Jens Heger, Burkhardt Funk, Paul Drews	2020	CAV sensors for road surface and hazard detection	Machine learning classification of road materials and hazards	Vehicle level sensors, accelerometers, GPS
Data Driven Analytics of Road Quality	Ali Rahim Taleqani, Raj Bridgelall, Jill Hough, Kendall E. Nygard	2019	Smartphone accelerometer and gyroscope for road roughness classification	Cluster analysis of road segments	Smartphone accelerometer, gyroscope, GPS

Title	Authors	Year	Use of FCD	Data Processing FCD	Technology and Sensors
DAU-Net: Dense Attention U-Net for Pavement Crack Segmentation	Yung-An Hsiel, Yi-Chang James Tsai	2021	Dense Attention U-Net for pixel-wise segmentation of cracks	Multi-stage dense blocks in encoder; channel attention block in decoder	DAU-Net, CNN, attention modules
Deep Actor-Critic Reinforcement Learning for Anomaly Detection	Chen Zhong, M. Cenk Gursoy, Senem Velipasalar	2019	Applied deep RL to anomaly detection in sensor networks	Actor-Critic reinforcement learning framework	Sensor networks
Deep learning for detecting distresses in buildings and pavements: A critical gap analysis	Faris Elghaish, Sandra Tawfiq Matarneh, Saeed Talebi, Soliman Abu-Samra, Ghazal Salimi, Christopher Rausch	2021	Review of deep learning for distress detection in pavements and buildings	Critical analysis of 181 papers; structured review of methods and findings	Deep learning (CNN, AI-based models)
Deep Learning in Data-Driven Pavement Image Analysis and Automated Distress Detection: A Review	Kasthurirangan Gopalakrishnan	2018	Review of DL-based pavement distress detection methods	Comparative analysis of CNN architectures, hyperparameters, frameworks	Vehicle-mounted cameras, pavement imaging datasets
Deep Learning Models for Recognizing the Simple Human Activities Using Smartphone Accelerometer Sensor	Prabhat Kumar, S. Suresh	2021	Explored CNN, RNN, and LSTM for activity recognition	Deep learning applied to accelerometer time series	Smartphone accelerometer
Deep Learning Techniques for Efficient Evaluation of Asphalt Pavement Condition	Kamel Mahdy, Ahmed Kamal Abo Zekry, Mohamed Moussa, Ahmed M. O. Mohamed, Hassan A. Mahdy, Mohamed Elhabiby	2023	Deep learning models for road distress detection	Real-time PCI calculation from distress detection, ~400 fps performance	Vehicle-mounted cameras, CNN models
Deep learning-based pavement crack detection method	Cai Yu, Jia Yidong, Lin Dengping	2018	Patent introducing CNN + SVM pipeline for crack detection	CNN for feature extraction; SVM for classification of candidate regions	CNN, SVM

Title	Authors	Year	Use of FCD	Data Processing FCD	Technology and Sensors
Deep Learning-Based Semantic Segmentation Methods for Pavement Cracks	Yu Zhang, Xin Gao, Hanzhong Zhang	2023	Improved U-Net with attention and Laplacian pyramid for crack segmentation	Attention modules in encoder, Laplacian pyramid in decoder, PAN auxiliary head	ALP-UNet architecture, pavement crack datasets
Deep learning-based underground object detection for urban road pavement	Namgyu Kim, Kideok Kim, Yun-Kyu An, Hyun Jong Lee, Jong-Jae Lee	2020	Applied GPR with DL for underground object detection in pavements	Deep learning applied to GPR data	Ground Penetrating Radar (GPR)
Deep Learning-Based Autonomous Road Condition Assessment Leveraging Inexpensive RGB and Depth Sensors and Heterogeneous Data Fusion: Pothole Detection and Quantification	Yu-Ting Huang, Mohammad R. Jahanshahi, Fangjia Shen, Tarutal Ghosh Mondal	2023	RGB-D sensor data fusion for pothole detection and quantification	Feature-level fusion of RGB and depth data using encoder-decoder DCNNs	RGB-D consumer sensor, edge computing device
Deep machine learning approach to develop a new asphalt pavement condition index	Hamed Majidifard, Yaw Adu-Gyamfi, William G. Buttlar	2020	Street-view images for pavement distress detection	YOLO for classification, U-net for segmentation, hybrid model for severity estimation	Google Street View images
DepthCrackNet: A Deep Learning Model for Automatic Pavement Crack Detection	Alireza Saberironaghi, Jing Ren	2024	Deep learning-based crack detection with U-Net variant	Double Convolution Encoder, TriInput Multi-Head Spatial Attention, Spatial Depth Enhancer	U-Net, attention modules, crack datasets (Crack500, DeepCrack)
Design and implementation of PAVEMON: a GIS web-based pavement monitoring system based on large amounts of heterogeneous sensors data	Salar Shahini Shamsabadi	2015	Integration of heterogeneous vehicle-based sensor data for pavement monitoring	Data fusion, statistical PCI estimation, GIS visualization	Acoustic sensors, accelerometers, GPS, video, tire pressure sensors

Title	Authors	Year	Use of FCD	Data Processing FCD	Technology and Sensors
Detecting Human Emotions Using Smartphone Accelerometer Data	Andreas Færøvig Olsen	2016	Explored accelerometer data classification with ML; transferable methods to anomaly detection	Decision tree, SVM, multilayer perceptron classifiers	Smartphone accelerometer
Detection and Recognition of Pavement Cracks Based on Computer Vision Technology	S. A. Lyasheva, Vladimir Tregubov, Mikhail P. Shleymovich	2019	Computer vision algorithm for crack detection in pavement management systems	Image enhancement, morphological opening, bottom-hat transform, noise filtering	Pavement cameras, OpenCV, Jetson TX2 hardware
Detection of Road Surface Identifiers Based on Deep Learning	Feng Zhang, Xiaoyu Wu, Chaonan Gu	2018	Road marking detection via deep learning	Compared SSD, FSSD, R-FCN with focal loss optimization	Deep learning CNN models
Detection of Road-Surface Anomalies Using a Smartphone Camera and Accelerometer	Taehee Lee, Chan Jun Chun, Seung-Ki Ryu	2021	Dual acquisition of images and accelerometer signals for anomaly detection	Histogram-based analysis of accelerometer variations with image classification	Smartphone camera, 3-axis accelerometer
Developing A Machine Learning-Based Computer Vision Model for External Defect Detection in Camera Components	Tan Van Duong, Hoai Nam Tran, Duc Khanh Dao, Van Hieu Dang, Hoang-Anh Phan, Bao Lam Dang, Van Nguyen Thi Thanh	2024	Defect detection in industrial camera components (method transferable to pavement imagery)	Machine learning and deep learning for defect classification	Industrial cameras, CNN models
Development of a Smartphone Application Serving Pavement Management Engineers	Damien Stephens, Mena I. Souliman, Matthew Vechione, Mukul Shirvaikar, Yi Li	2022	Smartphone app to collect GPS, accelerometer, and gyroscope data	Sampling and logging vibrational/rotational data; defect detection from anomalies	Smartphone GPS, accelerometer, gyroscope

Title	Authors	Year	Use of FCD	Data Processing FCD	Technology and Sensors
Development of Deep Learning Pavement Extraction and Crack Segmentation Algorithms to Analyze UAV Images of Roadways	Byungkyu Moon	2023	Deep learning applied to UAV images for pavement analysis	Modified U-Net encoder with various deep learning models; tile-based crack analysis system	UAV imaging, U-Net, CNN
DMA-Net: DeepLab With Multi-Scale Attention for Pavement Crack Segmentation	Xinzi Sun, Yuanchang Xie, Liming Jiang, Yuliang Cao, Benyuan Liu	2022	DeepLabv3+ enhanced with multi-scale attention for crack segmentation	Multi-scale attention in decoder, dynamic weighting of feature maps	DeepLabv3+, Crack500, DeepCrack, FMA datasets
Do vehicles sense pavement surface anomalies	Charalambos Kyriakou, Symeon E. Christodoulou, Loukas Dimitriou	2019	Pattern recognition and smartphone sensor tech for anomaly detection	Detection, classification, georeferencing of anomalies	Smartphone accelerometer, GPS
Enabling crowdsensing-based road condition monitoring service by intermediary	Kevin Laubis, Marcel Konstantinov, Viliam Simko, Alexander Gröschel, Christof Weinhardt	2019	Crowdsensing framework with intermediary between drivers and authorities	Analytical and descriptive evaluation of smart service model	Smartphones, in-vehicle sensors
Estimation of Pavement Condition Based on Data from Connected and Autonomous Vehicles	David Llopis-Castelló, Francisco Javier Camacho Torregrosa, Fabio Romeral-Pérez, Pedro Tomás-Martínez	2024	CAVs accelerometer data for IRI calculation	Comparison with auscultation surveys, regression analysis	OEM accelerometers, GPS
Estimation of road roughness condition from smartphones under realistic settings	Viengnam Douangphachanh, Hiroyuki Oneyama	2013	Smartphone sensors to estimate IRI road roughness	Frequency domain analysis of accelerometer + GPS data	Smartphone accelerometer, GPS

Title	Authors	Year	Use of FCD	Data Processing FCD	Technology and Sensors
Estimation of Road Surface Quality Using Real-Time Video Analysis	Mukul Shirvaikar, Mena I. Souliman, Samer Dessouky	2023	Real-time video analysis for pavement distress detection	Video-based detection correlated with accelerometer and gyroscope data for validation	Smartphone cameras, accelerometers, gyroscopes, GPS
Evaluation of Detection Approaches for Road Anomalies Based on Accelerometer Readings	Manuel Ricardo Carlos, Mario Ezra Aragón, Luis C. González, Hugo Jair Escalante, Fernando Martínez	2018	Evaluation of accelerometer-based anomaly detection methods	Standard deviation heuristic, SVM classifier with feature fusion	Smartphone accelerometer
Faster R-CNN Structure for Computer Vision-based Road Pavement Distress Detection	Furkan Balcı, Safiye Yilmaz	2022	Action camera data for pavement distress detection	Faster R-CNN deep learning classification	Action camera, deep learning model
Feature fusion using deep learning for smartphone based human activity recognition	Dipanwita Thakur, Suparna Biswas	2021	Methodology applicable for fusing accelerometer and gyroscope features	Fusion of handcrafted and deep learning extracted features	Smartphone accelerometer, gyroscope
Floating car data based private car travel data integration method	Kong Xiangjie, Xia Feng, Zhiqiang Gao, Hui Huang, Lian Lian	2015	Integration of taxi GPS data to simulate private car OD matrices	Growth factor method applied to OD matrices	GPS from taxi fleets
Floating Car Data Technology	Damir Budimir, Niko Jelušić, Mile Perić	2019	General applications of FCD for mobility and infrastructure monitoring	Integration with GIS, GNSS, and wireless communication	GPS, GIS, wireless communication
Grid-based pavement crack analysis using deep learning	Xianglong Wang, Zhaozheng Hu	2017	CNN for pavement crack detection and classification	Grid-based segmentation, PCA for classification	Vehicle-mounted cameras

Title	Authors	Year	Use of FCD	Data Processing FCD	Technology and Sensors
Gyroscope positioning system for smartphone	Li Shiyin, Cheng Ruiliang	2016	Patent for positioning underground workers via smartphone sensors	Fusion of gyroscope, accelerometer, magnetometer for localization	Smartphone gyroscope, accelerometer, magnetometer
How to get best predictions for road monitoring using machine learning techniques	Imen Ferjani, Suleiman Alsaif	2022	ML applied to accelerometer-based road anomaly detection	Sensitivity analysis, feature extraction (time, frequency, wavelet), ML models (SVM, Decision Tree, MLP)	Smartphone accelerometers
How to Make a State of the Art Report: Image-Based Road Crack Detection: A Scientometric Literature Review	Fan L., Tang S., Mohd Ariffin M.K.A., Ismail M.I.S., Zhao R.	2024	Image-based crack detection methodologies	Scientometric analysis, bibliometric mapping	Vehicle-mounted cameras, computer vision models
Identification of Road Surface Anomalies Using Crowdsourced Smartphone Sensor Data	Y. T. Gamage, T. Thotawaththa, Adeesha Wijayasiri	2022	Crowdsourced smartphone accelerometer data to detect and classify anomalies	Noise filtering, reorientation, fuzzy logic classification, machine learning models	Smartphone accelerometers, GPS
Identifying road defect information from smartphones	Matthew Byrne, Tony Parry, Riccardo Isola, Andrew Dawson	2013	Smartphone accelerometer data for real-time defect detection	Acceleration profile clustering to identify defects and severity	Smartphone accelerometer, GPS
Identifying Roadway Surface Disruptions Based on Accelerometer Patterns	Fernando Martínez, Luis C. González, Manuel Ricardo Carlos	2014	Crowdsourced smartphone accelerometer for disruption detection	ML classification (ANN, logistic regression) of potholes, humps, rough roads	Android smartphone accelerometer

Title	Authors	Year	Use of FCD	Data Processing FCD	Technology and Sensors
Implementation of a smartphone wireless accelerometer platform for establishing deep brain stimulation treatment efficacy of essential tremor with machine learning	Robert LeMoyne, Nestor Tomycz, Timothy Mastroianni, Cyrus McCandless, Michael Cozza, David Peduto	2015	Not pavement-related (biomedical example of smartphone accelerometer use)	SVM classification of tremor patterns	Smartphone accelerometer, SVM
Improved Asphalt Pavement Crack Detection Model Based on Shuffle Attention and Feature Fusion	Tursun Mamat, Abdukeram Dolkun, Rui He, Yonghui Zhang, Zulipapar Nigat, Hanchen Du	2025	Enhanced YOLOv8 with shuffle attention and feature fusion	Small target detection layer + SA module + SPP-F structure	SA-YOLOv8s, deep learning
In-vehicle sensor data fusion for road friction monitoring	Matti Kutila, Pasi Pyykönen, Kimmo Kauvo, Pekka Eloranta	2011	Road friction estimation using vehicle-mounted sensors	Fusion of IcOR camera system with inertial unit and GPS data	IcOR camera, IMU, GPS
Integrating acceleration signal processing and image segmentation for condition assessment of asphalt roads	Canadian Journal of Civil Engineering	2022	Fusion of smartphone accelerometer and camera data	Signal anomaly detection + semantic segmentation	Dashboard-mounted smartphone (accelerometer + camera)
Intelligent identification of pavement cracks based on PSA-Net	Xuan Lin, Jian Zhang, Daifeng Wu, Enhong Meng, Maoyi Liu, Mengtian Li, Fuliu Gao	2023	Feature pyramid + attention mechanism for crack detection	PSA-Net with nested sample weighting	PSA-Net, feature pyramid + attention
Intelligent Road Anomaly Detection and Driver Assistance System: Machine Learning Approach for Enhanced Road Safety	Mohanaprakash T A, Savija J, M. J. Peter, C. Tamilselvi, S. D. Hariharan, T. Sunitha	2023	Integrated vehicle-based system for road anomaly detection and driver warnings	ML classification using accelerometer, gyroscope, GPS, vibration signals	Accelerometer, gyroscope, GPS, vibration sensors
Intelligent Road Condition Assessment and Pothole Detection	Dr. Gajendra Astukar	2024	Smartphone sensors for road anomaly detection	Comparative analysis of anomaly detection methods	Smartphone accelerometer, gyroscope

Title	Authors	Year	Use of FCD	Data Processing FCD	Technology and Sensors
Investigation of pavement crack detection based on deep learning method using weakly supervised instance segmentation framework	Hancheng Zhang, Zhendong Qian, Yunfeng Tan, Yuxin Xie, Miaocheng Li	2022	Weakly supervised instance segmentation applied to crack detection	Region growing + GrabCut to generate pseudo-labels; dynamically balanced BCE loss	WSIS deep learning framework
Investigation of the Implementation of a Probe-Vehicle Based Pavement Roughness Estimation System	Peter M. Sauerwein, Brian L. Smith	2011	Probe vehicles to measure pavement roughness	Accelerometers and wireless communication; comparison of three system architectures	Accelerometers, smartphones, connected vehicle systems
Lightweight computer vision based asphalt pavement crack visualization detection	Zehui Yun, Jingguo Lv, Yiting Liu, Jiyong Zhang	2023	Computer vision crack detection optimized for mobile deployment	YOLOv5 baseline with pruning-based lightweight methods	YOLOv5, lightweight CNN
Monitoring device based on floating car data processing system and method thereof	Yang Chengji, Hu Jian	2012	Patent on floating car data monitoring system	Database integration, alarm module for anomalies	FCD processing unit, vehicle sensors
Monitoring Jatuh Dengan Menggunakan Sensor Accelerometer dan Gyroscope	Priyatna Budianto, Wahyu Andhyka Kusuma, Syaifuddin Syaifuddin	2024	Smartphone accelerometer + gyroscope for fall detection (non-transport application)	Processed acceleration and orientation values; graphed total acceleration/orientation	Smartphone accelerometer, gyroscope
Multi-level Road Damage Identification Algorithm Based on Vehicle-Mounted Smartphone	Nevzat Tetik	2022	Vehicle-mounted smartphone system for multi-grade road damage classification	Butterworth filtering, Gaussian background model, SVM classification	Smartphone accelerometer, GPS
Multiple Cue Data Fusion with Particle Filters for Road Course Detection in Vision Systems	P. Smuda, Roland Schweiger, Heiko Neumann, Werner Ritter	2006	Vision-based detection with map and sensor fusion	Particle filters for fusing digital maps and image cues	Digital maps, image sensors

Title	Authors	Year	Use of FCD	Data Processing FCD	Technology and Sensors
Multiple-type distress detection in asphalt concrete pavement using infrared thermography and deep learning	Fangyu Liu, Jian Liu, Linbing Wang, Imad L. Al-Qadi	2024	Infrared thermography + CNN for multiple distress detection	Transfer learning on visible, infrared, and fusion images	Infrared thermography, YOLOv5, CNN
Novel Road Crack Detection Technology Based on Deep Learning	Li Fan	2023	Deep learning-based road crack detection	Explored 3 DL methods and proposed a novel detection framework	Deep learning CNN
PAF-Net: A Progressive and Adaptive Fusion Network for Pavement Crack Segmentation	Lei Yang, Han Pang Huang, Shuyi Kong, Yanhong Liu, Hongnian Yu	2023	Fusion of features for segmentation with dual attention	Progressive context fusion + dual attention + dynamic weight learning	PAF-Net, CNNs, attention mechanisms
Pavement Crack Detection and Classification using Deep Learning Techniques	Saadia Yacoob, B. Sindhu, M. A. Neha Nousheen, R Varshitha, B. Bhaskar Ayyappa, Kishore Babu	2024	CNN-based detection and severity classification of cracks	Image preprocessing + CNN classification by severity level	CNN models, annotated pavement datasets
Pavement Crack Detection based on YOLO v3	Mingxin Nie, Cheng Wang	2019	YOLOv3 applied to vehicle-collected pavement crack images	Deep learning object detection with annotated datasets	Vehicle-mounted cameras
Pavement Crack Detection Method of Street View Images Based on Deep Learning	Zekai Shu, Zhaoyu Yan, Xihang Xu	2021	Street view images for pavement crack detection	YOLOv5 trained on 400 images from 5 cities	YOLOv5, street view dataset
Pavement crack identification and detection based on multi-task learning	Zhuo Chen, Siqi Liu	2023	Multi-task learning approach for crack identification and parameter extraction	YOLO for detection + U-Net for segmentation; adaptive weight parameters	YOLO, U-Net, multi-task learning
Pavement crack measurement based on aerial 3D reconstruction and learning-based segmentation method	Shang Jiang, Siyang Gu, Zhiyu Yan	2022	Aerial images + 3D reconstruction + learning-based segmentation	Instance segmentation + structure from motion + U-Net with transformer	Unmanned Aerial System (UAS), U-Net with transformer

Title	Authors	Year	Use of FCD	Data Processing FCD	Technology and Sensors
Pavement Defect Detection Based on Deep Learning	Meiju Liu, Kaiwen Duan, Shuai Zhang	2024	YOLOv8-based enhanced model for defect detection	Improved BiFPN and GAM attention mechanisms to refine YOLOv8	Vehicle-mounted cameras
Pavement Distress Detection Based on the Staged Deep Learning Classifier Approach	Amit Dipankar, Sanjeev Kumar Suman	2024	Proposed multi-stage deep learning classifier for pavement cracks	Feature extraction (LBP, GLCM, GLRM), hybrid optimization, augmented CNN	A-CNN, feature extraction techniques
Pavement Distress Detection Using Three-Dimension Ground Penetrating Radar and Deep Learning	Jiangang Yang, Kaiguo Ruan, Jie Gao, Shenggang Yang, Lichao Zhang	2022	3D GPR images analyzed with deep learning for distress detection	CP-YOLOX for localization + SViT for classification	3D Ground Penetrating Radar, CP-YOLOX, SViT
Pavement Distress Recognition via Wavelet-Based Clustering of Smartphone Accelerometer Data	Parastoo Kamranfar, David Lattanzi, Amarda Shehu, Shelley M. Stoffels	2022	Smartphone accelerometer data to detect pavement distress	Unsupervised learning with wavelet featurization and clustering	Smartphone accelerometers
Pavement Quality Evaluation Using Connected Vehicle Data	Justin Mahlberg, Howell Li, Björn Zachrisson, Dustin K. Leslie, Darcy M. Bullock	2022	Crowdsourced connected vehicle data for IRI estimation	Comparison with inertial profiler, linear correlation analysis	OEM connected vehicle sensors
Potential applications of connected vehicles in pavement condition evaluation: a brief review	Maryam Samie	2023	Synthesis of studies using CV sensors for pavement evaluation	Review and classification of methodologies	Connected vehicles, accelerometers, onboard sensors
Precision Enhancement of Pavement Roughness Localization with Connected Vehicles	R Bridgelall, Y Huang, Z Zhang and F Deng	2016	Connected vehicles for precise pavement roughness localization	Error model with inertial markers; improved localization accuracy	Onboard accelerometers, GPS, smartphones

Title	Authors	Year	Use of FCD	Data Processing FCD	Technology and Sensors
Raspberry Pi based Remote Controlled Car using Smartphone Accelerometer	Amir Golroo	2019	Remote vehicle control using smartphone accelerometer signals	UDP protocol transmission, IMU-based motion inference	Smartphone accelerometer, gyroscope, magnetometer, Raspberry Pi camera
Real-time pavement distress detection based on deep learning and visual sensors	Zhen Liu, Deer Liu	2024	Vehicle-mounted cameras for pavement distress detection	MASL-YOLO with multi-scale feature fusion, deformable convolutions, large-kernel spatial pooling	RealSense D455 camera, GNSS
Real-world application and validation of vehicle-mounted pavement inspection system	David Vines-Cavanaugh	2013	Field validation of vehicle-mounted sensor platform for pavement inspection	Multi-modal fusion of accelerometer, radar, video, audio signals	Accelerometers, microphones, radar, tire pressure sensors, video
Recognition of asphalt pavement crack length using deep convolutional neural networks	Zheng Tong	2017	DCNN applied to crack length measurement in pavement images	CNN-based detection with PCA for classification	Vehicle-mounted pavement imaging systems
Research on Asphalt Pavement Crack Detection using YOLOv5 Model	Wenxiu Wu	2024	YOLOv5 applied for pavement crack detection across multiple cities	Image dataset preprocessing, YOLOv5 training and evaluation	YOLOv5
Research on pavement crack detection based on improved YOLOv4	Lanxin Zhang	2024	Improved YOLOv4 model for crack detection	MobileNetv2 backbone, separable convolution, attention mechanisms	Vehicle-mounted cameras
Research on road crack detection method based on UAV images	Yu Liu	2024	UAV aerial images used for road crack detection	MATLAB GUI platform for preprocessing, recognition, classification; pixel scanning for crack metrics	DJI Jingwei M210-RTK UAV, MATLAB GUI

Title	Authors	Year	Use of FCD	Data Processing FCD	Technology and Sensors
Rhcracknet: Refined Hierarchical Feature Fusion and Enhancement Network for Pavement Crack Detection	Chengfeng Cai	2023	Hierarchical feature fusion with attention for crack detection	Feature fusion and enhancement modules + non-local attention	RHCrackNet, attention mechanisms
Road condition analysis using 3-axis accelerometer and GPS sensors	B. Y. Amirgaliyev	2016	Accelerometer and GPS-based road quality analysis	Visual representation of acceleration values, pattern recognition	Smartphone accelerometer, GPS
Road condition monitoring and alert application: Using in-vehicle Smartphone as Internet-connected sensor	Xin Peng	2012	Smartphone-based IoT sensing for road condition monitoring	Orientation-agnostic accelerometer analytics, multi-user fusion, privacy-preserving data handling	Smartphone accelerometer, GPS, IoT connectivity
Road Damage Detection Using Deep Learning and Cloud Platforms	Wei-Cheng Chiang, Hsien-Sung Chiu, Jin-Shyan Lee	2023	Smartphone images uploaded to cloud for AI-based road damage detection	Cloud-hosted deep learning models for classification and visualization	Smartphone camera, cloud AI platform
Road pavement condition diagnostics using smartphone-based data crowdsourcing in smart cities	Marcin Staniek	2021	Crowdsourced smartphone accelerometer and GPS data for pavement diagnostics	Road Condition Tool (RCT), aggregated accelerations and GPS, binary classifiers for validation	Smartphone accelerometer, GPS
Road pavement crack detection using deep learning with synthetic data	I. A. Kanaeva, Ju A. Ivanova	2021	Synthetic dataset for deep learning crack detection	Deep learning frameworks trained on synthetic images	Synthetic image datasets, CNN
Road Surface Anomaly Assessment Using Low-Cost System	A. Martinelli et al.	2022	Accelerometers on-car + GPS to identify road surface anomalies	Signal filtering, anomaly segmentation, acceleration thresholds	Low-cost accelerometers, GPS

Title	Authors	Year	Use of FCD	Data Processing FCD	Technology and Sensors
Road Surface Profiling based on Artificial-Neural Networks	Seungho Choi, Seoyeon Kim, Heelim Hong, Young-bin Kim	2020	ANN for cost-effective road surface profiling	CNN-based line laser refinement for surface profiling	Artificial neural networks, line laser sensors
RoadSense: Smartphone Application to Estimate Road Conditions Using Accelerometer and Gyroscope	Azza Allouch, Anis Koubaa, Tarek Abbes, Adel Ammar	2017	Android app RoadSense for road quality prediction	C4.5 Decision Tree classifier on accelerometer + gyroscope data	Smartphone accelerometer, gyroscope, GPS
Roadway pavement roughness evaluation based on smart-city principles, vibration sensing and machine learning	Kyriakou Charalambos, Christodoulou Symeon E.	2022	Smartphone and OBD devices for pavement roughness monitoring	Machine learning algorithms for pavement roughness evaluation	Smartphone accelerometer, OBD-II device, GPS
Robust Crack Detection Method by Reconstruction-Based Segmentation Network in Road Maintenance	Guoai Xu, Ling Luo	2022	Improved semantic segmentation model with reconstruction branch for crack detection	Deep convolutional encoder-decoder network with reconstruction-guided segmentation	Semantic segmentation CNN, reconstruction branch
Semantic Segmentation for Pavement Crack Detection in Road Maintenance	Compilation based on multiple segmentation approaches	2022	Overview of semantic segmentation methods applied to pavement cracks	Encoder-decoder CNNs, attention-based mechanisms, reconstruction branches	Semantic segmentation frameworks, CNNs
Semantic Segmentation on Smartphone Motion Sensor Data for Road Surface Monitoring	Budi Darma Setiawan, Mate Kovacs, Uwe Serdült, Victor V. Kryssanov	2022	Road surface classification via smartphone motion sensors	Modified U-Net with BiLSTM applied to accelerometer and gyroscope data	Smartphone accelerometer, gyroscope
Sensor fusion and deep learning	Garg Kshitiz, Al-Dahle Ahmad	2020	Fusion of data from multiple sensors for object detection/classification	Feature-detection models from deep and traditional ML; adaptive sensor calibration	Sensor fusion framework

Title	Authors	Year	Use of FCD	Data Processing FCD	Technology and Sensors
Sensor Fusion for Smartphone-based Vehicle Telematics	Johan Wahlström	2017	Sensor fusion methods applied to smartphone-based vehicle telematics	Sensor fusion algorithms for navigation and motion inference	Smartphone accelerometer, gyroscope, GPS
Smartphone applications for pavement condition monitoring: A review	Abdulnaser M. Al-Sabaeei, Mena I. Souliman, Ajayshankar Jagadeesh	2024	Review of smartphone applications for pavement condition monitoring	Survey of calibration, standards, and environmental factors	Smartphone accelerometer, gyroscope, GPS
Smartphone Gyroscope and Accelerometer Dataset for Human Activity Recognition	Emily J. Huang, Jukka-Pekka Onnela	2020	Human activity recognition dataset with accelerometer and gyroscope	Augmented Movelet Method	iPhone accelerometer, gyroscope
Smartphone Indoor Localization with Accelerometer and Gyroscope	Hui-Huang Hsu, Wei-Jan Peng, Timothy K. Shih, Tun-Wen Pai, Ka Lok Man	2014	Pedestrian Dead Reckoning with smartphone accelerometer and gyroscope	Step length and orientation estimation with calibration	Smartphone accelerometer, gyroscope
Smartphone sensing for large data set collection of potholes	Saswat Raj, Ayush Jain, Rajiv Misra	2013	Crowdsourced pothole detection with smartphones	Accelerometer-based detection with crowdsourcing framework	Smartphone accelerometer, GPS
Smartphone-Based Activity Recognition Using Multistream Movelets Combining Accelerometer and Gyroscope Data	Emily Huang, Ke-Xiao Yan, Jukka-Pekka Onnela	2022	Activity recognition with multistream sensor fusion	Movelet method with accelerometer and gyroscope fusion	Smartphone accelerometer, gyroscope
Smartphone-Based Pavement Roughness Estimation Using Deep Learning with Entity Embedding	Armstrong Aboah, Yaw Adu-Gyamfi	2020	Smartphone-based pavement roughness estimation	Deep learning with entity embedding to predict IRI	Smartphone accelerometer, deep learning model

Title	Authors	Year	Use of FCD	Data Processing FCD	Technology and Sensors
Statistical Validation of Crowdsourced Pavement Ride Quality Measurements from Smartphones	Jose R. Medina, Hossein Noorvand, B. Shane Underwood, Kamil E. Kaloush	2020	Crowdsourced smartphone accelerometer data for pavement ride quality	Statistical validation against traditional profilers	Smartphone accelerometers
Survey of road anomalies detection methods	Rasha Saffarini, Faisal Khamayseh, Yousef-Awwad Daraghmi, Derar Elyan, Muath Sabha	2023	Survey of accelerometer-based and vision-based anomaly detection	Review of deep learning, mathematical approaches, and anomaly classification	Smartphones, vehicle sensors, cameras
SwinCrack: Pavement crack detection using convolutional swin-transformer network	Cheng Wang, Haibing Liu, Xiaoya An, Zhiqun Gong, Fei Deng	2023	Hybrid Swin-Transformer + CNN model for crack detection	Convolutional Patch Embedding Layer, Swin-Transformer Block, Depth-convolution Forward Network	SwinCrack network
Synergizing Low Rank Representation and Deep Learning for Automatic Pavement Crack Detection	Zhifan Gao, Xuhui Zhao, Min Cao, Ziyao Li, Kangcheng Liu, Benwen Chen	2023	LRR + CNN approach for automatic crack detection	Low Rank Representation to filter sequences + CNN with ASPP	CNN, ASPP, anomaly detection framework
The use of smart phones to estimate road roughness: a case study in Turkey	Metin Mutlu Aydin, Mehmet Sinan Yıldırım, Lars Farslöf	2018	Smartphone sensors to monitor road roughness	Acceleration + GPS data collection, Roadroid app, statistical evaluation	Smartphone accelerometer, GPS
Toward Crowdsourcing-Based Road Pavement Monitoring by Mobile Sensing Technologies	Chih-Wei Yi, Yi-Ta Chuang, Chia-Sheng Nian	2015	Smartphone probe cars (SPCs) for pavement monitoring	Underdamped oscillation model, anomaly indexing, DENCLUE-like clustering	Smartphone accelerometer, GPS
Towards Automatic Evaluation of Asphalt Irregularity Using Smartphone's Sensors	Vinicius M. A. Souza, Everton Alvares Cherman, Rafael Geraldeli Rossi, Rafael Alves de Souza	2017	Smartphone motion sensors for asphalt irregularity detection	Supervised learning classification, signal processing feature extraction	Smartphone accelerometer, motion sensors

Title	Authors	Year	Use of FCD	Data Processing FCD	Technology and Sensors
Two-step deep learning approach for pavement crack damage detection and segmentation	John Machacek	2022	Two-stage YOLOv4 + DeepLabv3+ pipeline for detection and segmentation	YOLOv4 optimised; DeepLabv3+ with Ghost module and CBAM attention	YOLOv4, DeepLabv3+, attention mechanisms
Using Geographic Information Systems and Smartphone-Based Vibration Data to Support Decision Making on Pavement Rehabilitation	Chun Hsing Ho, Chieh Ping Lai, Anas Almonnieay	2016	Smartphone accelerometer data integrated with GIS for pavement management	Vibration intensity mapping, GIS visualization, prioritization of maintenance areas	Smartphone accelerometers, GIS software
Using Smartphones to Estimate Road Pavement Condition	Viengnam Douangphachanh, Hiroyuki Oneyama	2014	Smartphone accelerometer data to estimate pavement roughness	Filtering, frequency domain analysis, sectioning, linear relationship with roughness	Smartphone accelerometers, GPS
Vehicle Tracking Based on Fusion of Magnetometer and Accelerometer Sensor Measurements With Particle Filtering	Roland Hostettler, Petar M. Djuric	2015	Vehicle trajectory estimation and tracking with multi-sensor data	Particle filtering, Rao-Blackwellization	Magnetometers, accelerometers
Vehicle Vibration Signal Processing for Road Surface Monitoring	P. M. Harikrishnan, Varun P. Gopi	2017	Vehicle vibrations for pothole and hump detection	Gaussian model mining, x-z ratio filtering, severity estimation algorithm	Smartphone accelerometer (z-axis vibrations)
Vibration based pavement roughness monitoring system using vehicle dynamics and smartphone with estimated vehicle parameters	Shohel Rana, Asaduzzaman	2021	Smartphone accelerometer + vehicle dynamics for pavement roughness monitoring	Grey-box system identification + inverse dynamics for pavement profile reconstruction	Smartphone accelerometer, vehicle dynamic model
Vision-Based Automated Pavement Crack Detection Using Deep Learning	Rao A.S., Nguyen T., Palaniswami M., Ngo T.	2021	Camera data from vehicles for crack detection	Deep learning CNN-based crack segmentation	Vehicle-mounted cameras

Title	Authors	Year	Use of FCD	Data Processing FCD	Technology and Sensors
Vision-Based Crack Detection of Asphalt Pavement Using Deep Convolutional Neural Network	Zheng Han, Hongxu Chen, Yiqing Liu, Yange Li, Yingfei Du, Hong Zhang	2021	CNN-based crack detection without preprocessing	Deep CNN on road images with TensorFlow	CNN, TensorFlow
A computer vision-based method to identify the international roughness index of highway pavements	Jiangyu Zeng, Mustafa Gül, Qipei Mei	2022	Images to estimate International Roughness Index (IRI)	Deep neural networks applied to 2D pavement photos	Sports action cameras (GoPro Hero series)
A Crowdsourcing Solution for Road Surface Roughness Detection Using Smartphones	Xiao Li, Ruizhi Chen, Tianxing Chu	2014	Smartphone accelerometer and GPS for roughness detection	RMS calculation of acceleration, transient event detection	Smartphone accelerometer, GPS
A Deep Learning based Process Model for Crack Detection in Pavement Structures	Aaron Rasheed Rababaah	2022	Deep CNN applied to asphalt pavement crack detection	CNN model tested on dataset of 500 images	CNN, computer vision
A Deep Supervised Pavement Crack Detection Network with Multiscale Feature Fusion and Feature Learning	Lei Yang, Han Pang Huang, Shuyi Kong	2023	End-to-end deep supervised crack detection	Attention U-Net baseline; attention fusion block (AFB), progressive fusion block (PCF), MRFF block	Attention U-Net, deep supervised network
A Deeply Supervised Convolutional Neural Network for Pavement Crack Detection With Multiscale Feature Fusion	Zhong Qu, Chong Cao, Ling Liu, Dong-Yang Zhou	2021	CNN with multiscale feature fusion and deep supervision	High-level features fused with low-level features at multiple stages	Deeply supervised CNN
A Detection and Classification Method of Asphalt Pavement Crack based on Vision Transformer	Yulong Yang, Chen Guo, Chen Zuo, B. Yang	2023	Road surface distress detection with advanced deep learning	Vision Transformer compared with CNNs (ResNet, DenseNet, EfficientNet)	Vision Transformer (ViT)
A Framework for Automated Pavement Condition Monitoring	Stefania C. Radopoulou, Ioannis Brilakis, Kristina Doycheva, Christian Koch	2016	Fusion of video and accelerometer data for pavement monitoring	Video frame analysis, accelerometer z-axis profile reconstruction, GPS synchronization	Car parking camera, accelerometer, GPS, 4G transmission

Title	Authors	Year	Use of FCD	Data Processing FCD	Technology and Sensors
A hybrid deep learning pavement crack semantic segmentation	Zaid Al-Huda, Bo Peng, Riyadh Nazar Ali Algburi, Mugahed A. Al-antari, Rabea AL-Jarazi, Donghai Zhai	2023	Hybrid CNN + CAM strategy for semantic segmentation	Knowledge transfer via Class Activation Maps (KTCAM-Net); hybrid loss function	CNN, CAM, encoder-decoder
A Large-Scale Benchmark for Pavement Crack Segmentation	Wei Chen, Xiaoxiang Zhang, Qianqi Zhao, Wenjie Pan, Jianqing Zhu	2023	Proposed PCSeg7000 dataset with 7000 pavement crack images	U-Net with strip-attention and pyramid self-supervised learning	U-Net, strip-attention, PCSeg7000 dataset
A low-cost pavement rating system, based on machine learning, utilizing smartphones sensors	Charalambos Kyriakou, Symeon E. Christodoulou	2022	Smartphone-based pavement condition evaluation	Unsupervised ML classification, statistical features in time and frequency domain	Smartphone accelerometer, GPS, OBD device
A novel network fusing transformer and CNN for road crack segmentation	Mianqing He, Tze Liang Lau	2024	CNN enhanced with transformer blocks for crack segmentation	AFM module, lightweight decoder SMLP, multi-level feature integration	Transformer + CNN hybrid model
A Practical Approach for Road Quality Estimation using Smartphone based Inertial Data	Deepa D. Nagaraj, Marcel Mutz, Supreeth Mysore Venkatesh, Lea Riebschlaeger, Dirk Werth	2022	Road quality estimation using smartphone IMU data	Preprocessing pipeline for noise reduction and geo-referencing; ML regression for quality index	Smartphone IMU (accelerometer, gyroscope)
A preliminary study on SPC-crowd pavement indexing	Tsung-Hsiang Wu, Chih-Wei Yi, Ching-Yao Chan, Ya-Lan Chang, Chien-Chao Tseng, Chun-Fu Chung	2015	Probe-car crowdsourcing system for pavement indexing	Mobile sensing with environmental data fusion	Probe vehicle sensors, smartphones
A recursive multi-scale correlation-averaging algorithm for synchronization and fusion of independent pavement roughness measurements	Mandoye Ndoye, Alan M. Barker, James V. Krogmeier, Darcy M. Bullock	2009	Fusion of distributed vehicle-based roughness measurements	Recursive correlation-averaging algorithm for multi-vehicle data	Accelerometers, GPS receivers

Title	Authors	Year	Use of FCD	Data Processing FCD	Technology and Sensors
A review: literature on pothole monitoring system	Sneha Gosavi, Joshna Chinta, Nisha Pandav, Kanchan Dhuri	2020	Review of pothole detection systems using smartphones and vehicle sensors	Comparison of GPS, accelerometer, and camera-based monitoring methods	Smartphone accelerometer, GPS, vehicle cameras
A Road Defect Detection System Using Smartphones	Gyulim Kim, Seungku Kim	2024	Automatic data collection with smartphone sensors for road defect detection	CNN-based model classifying potholes, speed bumps, manholes	Smartphone accelerometer, gyroscope, camera

Table 22 - Overview of analysed contributions (FCD & PMS)

Title	Authors	Year	Data types	Pavement condition metrics
6G Connected Vehicle Framework to Support Intelligent Road Maintenance Using Deep Learning Data Fusion	Mohammad Hijji, Rahat Iqbal, Faiyaz Doctor, Charalampos Karyotis, Wahid Rajeh, Ali G. Alshehri, Fahad Aradah	2023	- The proposed framework utilizes imagery data and sensory data, which are fused together using a novel Convolution Neural Networks (CNN) model for effective pothole detection. - The system is designed to leverage the vast amounts of data collected by Connected and Autonomous Vehicles (CAV), enabling large-scale real-time monitoring of road surface conditions.	- The proposed framework utilizes a novel Convolution Neural Networks (CNN) model that fuses imagery and sensory data specifically for pothole detection, which is a critical aspect of assessing pavement conditions. - The system is designed to facilitate large scale real-time road surface condition monitoring, enabling urban authorities to efficiently allocate resources for road infrastructure maintenance based on the detected conditions.
A Comprehensive Review of Smartphone and Other Device-Based Techniques for Road Surface Monitoring	Saif Alqaydi, Waleed Zeiada, Ahmed El Wakil, Ali Alnaqbi, Abdelhalim Azam	2024	- The paper discusses the use of smartphone sensors, specifically accelerometers and gyroscopes, for collecting data related to road surface conditions. These sensors provide valuable information about the road's physical state by measuring motion and orientation. - Data preprocessing techniques, such as filtering and reorientation, are employed to enhance the quality of the collected data before it is analyzed. This preprocessing is crucial for ensuring that the data is accurate and reliable for subsequent machine learning classification of road anomalies.	- Smartphone sensors, such as accelerometers and gyroscopes, are utilized to collect data on road surface conditions, allowing for effective monitoring of pavement quality without the need for expensive traditional methods. - Machine learning algorithms, particularly Convolutional Neural Networks (CNNs), are employed to classify road anomalies, which enhances the detection accuracy of pavement conditions and improves the overall efficiency of the monitoring system.

Title	Authors	Year	Data types	Pavement condition metrics
A Framework for Automated Pavement Condition Monitoring	Stefania C. Radopoulou, Ioannis Brilakis, Kristina Doycheva, Christian Koch	2016	- The framework utilizes video data collected from a car's parking camera to detect surface defects in the pavement. This video data is processed to identify frames that potentially depict defects, which are then further analyzed using machine learning algorithms for defect classification. - Elevation signals from accelerometers attached to the car are also employed to reconstruct the road profile and detect defects related to the z-axis, such as bumps. This multi-sensor approach allows for a comprehensive assessment of both surface and elevation defects in the pavement.	- The framework calculates the Road Condition Index (RCI) for each road segment, which is essential for classifying roads based on international rating standards. This index helps in assessing the overall condition of the pavement and determining the necessary maintenance actions. - The severity of detected defects is assessed after classification, which includes identifying various types of defects such as potholes, cracks, and patches. Accurate assessment of these defects is crucial for effective planning and decision-making in pavement maintenance programs.
A new FCM-XGBoost system for predicting pavement condition Index	Shengnan Li, Bao Guo, Hu Yang, Wen Zhong, Pingruo Liao, Pu Wang	2024	- The Fuzzy C-Means (FCM) clustering algorithm is utilized to categorize asphalt and concrete pavement sections based on multiple factors that influence the Pavement Condition Index (PCI). - The eXtreme Gradient Boosting (XGBoost) model is trained for each cluster of expressway sections, using actual pavement condition data to predict the PCI for the following year.	- The Pavement Condition Index (PCI) is a crucial metric used to identify potential pavement distresses and to develop effective pavement maintenance strategies. It provides a standardized way to assess the condition of pavement surfaces, helping in decision-making for maintenance and repairs. - The FCM-XGBoost PCI prediction system utilizes a clustering algorithm to categorize asphalt and concrete pavement sections based on multiple influencing factors, allowing for more accurate predictions of PCI for specific expressway sections in the following year.

Title	Authors	Year	Data types	Pavement condition metrics
A review on pavement data acquisition and analytics tools using autonomous vehicles	Cena Abdollahi, Mahan Mollajafari, Amir Golroo, Sara Moridpour, Hainian Wang	2023	- The study discusses the use of various data types collected by autonomous vehicles for evaluating pavement conditions, including image data processed through techniques such as Image Processing, Convolutional Neural Networks (CNN), and the You Only Look Once (YOLO) algorithm for detecting pavement distress. - Additionally, the paper mentions the integration of data from intelligent transportation systems (ITS) and various sensors, such as Light Detection And Ranging (LiDAR) and Inertial Measurement Units (IMU), to enhance the accuracy and efficiency of pavement condition evaluation.	- The study emphasizes the importance of pavement inspection as a critical step in pavement management systems, which involves the collection and evaluation of pavement distress data to inform rehabilitation programs and maintenance planning for road authorities. - It highlights the potential of using data collected by autonomous vehicles to evaluate pavement conditions, suggesting that advancements in technology and intelligent transportation systems can enhance the accuracy and efficiency of pavement distress detection and condition evaluation.
A review on the impacts of connected vehicles on pavement management systems	Mohammad Saleh Entezari, Amir Golroo	2023	- The study reviewed various case studies that utilized different types of data for pavement evaluation, although specific data types were not detailed in the provided information. - The analysis methods and connectivity messages and networks used in the case studies were scrutinized, indicating a focus on the technological aspects of data transmission and analysis in connected vehicles for pavement management.	- Connected vehicles (CVs) facilitate the continuous monitoring of pavement conditions through various applications, including roughness measurement (37.5% of resources), distress detection (31%), and gathering road weather data (22%). These metrics allow for a comprehensive understanding of pavement performance and deterioration over time. - The study identified several specific metrics related to pavement condition, such as slippery pavement recognition (19%), distress

Title	Authors	Year	Data types	Pavement condition metrics
				classification (12.5%), and skid resistance measurement (6%). These metrics are crucial for assessing safety and maintenance needs on roadways.
A Scheme and Application of a Digital Twin-Based Road Pavement Management System	Koji Makanae, Yugo Kurokawa, Kiyotaka Suda, Jevica, Nurulnajwa Binti Khamis	2025	- The system utilizes point cloud data generated from images taken by a simple in-vehicle stereo camera, which helps in visualizing the road pavement conditions and features. - It also incorporates road surface property data obtained from simple laser measurements, allowing for a comprehensive analysis of the pavement's physical characteristics in conjunction with spatial information.	- The pavement management system utilizes digital measurement technology to gather and analyze data related to road surface properties, which includes point cloud data generated from images taken by a simple in-vehicle stereo camera and data from simple laser measurements. This information is essential for assessing the condition of the pavement. - The maintenance cycle of road pavement is structured around five key stages: inspection, diagnosis, action, record, and next inspection. This systematic approach allows for continuous monitoring and evaluation of pavement conditions, ensuring timely repairs and maintenance to extend the service life of the pavements.
A Vibration-Based Methodology to Monitor Road Surface: A Process to Overcome the Speed Effect	Monica Meocci	2024	- The study utilizes data recorded by taxi vehicles, which provides insights into road pavement conditions while accounting for the effects of vehicle speed on the measurements. - Two specific parameters are used in the machine learning approach to predict the severity level of road surface conditions: speed and pavement deterioration index,	- The study introduces a methodology that utilizes a pavement deterioration index, which is a key parameter in assessing the severity level of road surface conditions. This index helps in quantifying the extent of pavement degradation and is essential for monitoring and maintenance decisions.

Title	Authors	Year	Data types	Pavement condition metrics
			allowing for a focused analysis of road anomalies.	- The methodology employs a machine learning approach to predict the severity level of road surface conditions based on two recorded parameters: speed and the pavement deterioration index. This allows for a more accurate assessment of road conditions, achieving over 80% accuracy in predicting damage severity levels from the dataset analyzed.
Advanced Sensor Technologies in CAVs for Traditional and Smart Road Condition Monitoring: A Review	Masoud Khanmohamadi, Marco Guerrieri	2024	- The paper discusses various sensor data types collected from accelerometers, gyroscopes, LiDAR, cameras, and radar integrated within Connected Autonomous Vehicles (CAVs) for monitoring road conditions. These sensors detect anomalies such as potholes, surface cracks, and roughness on the roads. - Advanced data processing techniques are employed to analyze the sensor data, including machine learning algorithms, sensor fusion, and edge computing, which enhance the accuracy and reliability of the road condition assessments.	- The paper discusses the use of various sensors, such as accelerometers, gyroscopes, LiDAR, cameras, and radar, in Connected Autonomous Vehicles (CAVs) to detect pavement conditions, identifying anomalies like potholes, surface cracks, and roughness on roads. - Advanced data processing techniques, including machine learning algorithms, sensor fusion, and edge computing, are employed to enhance the accuracy and reliability of road condition assessments, supporting proactive maintenance strategies and improving road safety.
An ensemble learning with sequential model-based optimization approach for pavement roughness estimation using smartphone sensor data	Wangda Guo, Jinxi Zhang, Muhammad Murtaza, Dandan Cao	2023	- The study utilized vibration acceleration data acquired from a smartphone, which was examined for its feasibility through micro-scale shaking table tests to ensure accurate pavement roughness estimation. - The CatBoost model was developed using	- The study developed a smartphone-based pavement roughness estimation approach that utilizes vibration acceleration data, achieving a coefficient of determination (R2) of 0.807, indicating a strong correlation between the smartphone measurements and

Title	Authors	Year	Data types	Pavement condition metrics
			the smartphone sensor data, and the feature importance and interaction effects were analyzed using Shapley Additive exPlanations (SHAP) and Partial Dependence Plots (PDP) to interpret the results of the pavement roughness estimation task.	the actual pavement roughness. - The performance of the CatBoost model, which was enhanced through a sequential model-based optimization (SMBO) approach, resulted in a root mean square error (RMSE) of 0.553 and a mean absolute error (MAE) of 0.433, demonstrating its effectiveness in accurately estimating pavement roughness compared to traditional methods.
An innovative approach for high-performance road pavement monitoring using black box	Monica Meocci, Valentina Branzi, Andrea Sangiovanni	2021	- The data types utilized in the pavement monitoring process include vertical acceleration measurements, which are recorded by black boxes installed in vehicles. This data is crucial for detecting and classifying road surface distresses based on the vibrations experienced while driving over the pavement. - GPS position data is also collected alongside vertical acceleration and speed measurements of the instrumented vehicle. This information helps in localizing the recorded vertical acceleration values and ensures the consistency of the survey by correlating the measurements with specific locations on the road network.	- The Pave Box methodology utilizes vertical acceleration data collected from a black box device installed in vehicles to evaluate the road pavement condition. This data is processed to detect and classify both local damages and the overall condition of the road, allowing for a robust assessment that identifies all severe distresses and approximately 70% of minor damages. - The methodology is based on simple algorithms that analyze the dataset, which includes measurements of time, vertical acceleration, GPS position, and vehicle speed. This enables road authorities to obtain a reliable screening of the entire road network, promoting efficient resource allocation for maintenance and repair based on the severity levels of detected anomalies.

Title	Authors	Year	Data types	Pavement condition metrics
An Internet of Things Based system for Road Surface Condition Assessment Using Machine Learning	Michael Ochiel, J. Riwa, Japheth Abashe, Shubi Kaijage, Judith Leo	2023	- The system collects real-time data on road surface conditions using camera and gyroscope sensors, which provide visual and motion-related information about the road's state. - The collected data is processed using machine learning algorithms to detect defects on the road surface, enabling automated analysis and decision support for maintenance authorities.	- The Internet of Things-based system developed for road surface condition assessment utilizes camera and gyroscope sensors to collect real-time data on road surface conditions, which helps in detecting defects on the road surface effectively. - The system processes the collected data using machine learning algorithms, providing maintenance authorities with automated decision support for road condition surveys, thereby facilitating more efficient and comprehensive road maintenance practices.
Application of Automated Pavement Inspection Technology in Provincial Highway Pavement Maintenance Decision-Making	Lu Huang, Jyh-Dong Lin, Wei-Hsing Huang, Chun-Hung Kuo, Mingyuan Huang	2024	- The inspection results from the automated pavement damage detection technology include quantitative data types such as crack rate, rut depth, and roughness (International Roughness Index - IRI), which are essential for assessing pavement conditions. - K-means clustering analysis is employed to establish maintenance thresholds for the identified indicators (crack rate, rut depth, and roughness), facilitating data-driven decision-making in pavement maintenance.	- The inspection results from the automated pavement damage detection technology include key metrics such as the crack rate, rut depth, and roughness (International Roughness Index - IRI), which are essential for assessing pavement condition. - Maintenance thresholds for these indicators are established using K-means clustering analysis, which aids in making informed maintenance decisions based on the quantitative data obtained from the automated surveys.
Applications of using connected vehicle data for pavement quality analysis	Justin Mahlberg, Howell Li, Björn Zachrisson, Jijo K. Mathew, Darcy M. Bullock	2024	- The paper utilizes crowdsourced ride quality data collected from modern vehicles equipped with factory-installed sensors, which allows for passive assessment of roadway conditions. This data is compared	- The primary quantitative method for evaluating pavement conditions in the United States is the International Roughness Index (IRI), which is commonly used for construction acceptance. However, qualitative

Title	Authors	Year	Data types	Pavement condition metrics
			with industry-standard inertial profiler measurements to evaluate pavement quality. - Additionally, the study incorporates standard original equipment manufacturer (OEM) on-board sensor data from production vehicles to assess approximately 100 miles of roadway pavements before, during, and after construction, providing insights into the improvements in International Roughness Index (IRI) values.	visual inspection techniques are more prevalent from an asset management perspective. - The paper highlights the use of crowdsourced ride quality data, which correlates with traditional inertial profilers, demonstrating a linear correlation with an R2 of 0.7 and a p-value of <0.001, indicating a significant relationship between the two methods of assessing pavement quality.
Autonomous condition monitoring-based pavement management system	Hee-Kyeoung Shon, Chung-Suk Cho, Young-Ji Byon, Jinwoo Lee	2022	- The system utilizes various data types for effective condition monitoring, including sensor data that captures real-time pavement conditions, such as surface distress and structural integrity. - Additionally, historical data is employed to analyze trends and patterns in pavement performance over time, aiding in predictive maintenance and management decisions.	- The autonomous condition monitoring system evaluates various pavement condition metrics, including surface distress, roughness, and skid resistance, to provide a comprehensive assessment of pavement health. - These metrics are crucial for effective pavement management, as they help in identifying maintenance needs, prioritizing repairs, and optimizing resource allocation for road infrastructure.
Deep neural networks for asphalt pavement distress detection and condition assessment	Valerio Gagliardi, Bruno Giammorcaro, Bella Francesco, Giuseppe Sansonetti	2023	- The study utilized a dataset comprising top-down images of road damages affecting road pavements, which were obtained from various open-source datasets. This dataset was specifically used to train the object detection task of the YOLOv7 algorithm. - The methodology incorporated Deep Neural Networks (DNN) that included object	- The study proposes a method of assessment for pavement conditions based on the outcomes of Deep Neural Networks (DNNs), which determines the level of pavement deterioration by automatically identifying and classifying five distinct classes of pavement distress through object detection algorithms like YOLOv7.

Title	Authors	Year	Data types	Pavement condition metrics
			detection and semantic segmentation capabilities, specifically utilizing algorithms such as "YOLO v7" for identifying distinct classes of pavement distress and "U-Net" for assessing pavement conditions.	- The automated identification and severity assessment of pavement damages enable rapid and decisive actions by administrative authorities, providing crucial information for prioritizing maintenance activities and optimizing maintenance scheduling for road infrastructure.
Design and implementation of PAVEMON: a GIS web-based pavement monitoring system based on large amounts of heterogeneous sensors data.	Salar Shahini Shamsabadi	2015	- PAVEMON utilizes multi-channel raw sensor data, which includes inputs from microphones, accelerometers, tire pressure sensors, and video, allowing for comprehensive monitoring of pavement conditions. - The system also processes results that include various pavement condition metrics such as road profile, crack density, international roughness index, and micro texture depth, providing a detailed analysis of pavement quality.	- PAVEMON utilizes various processed results from its multi-modal sensor system to assess pavement conditions, including metrics such as road profile, crack density, international roughness index, and micro texture depth. These metrics provide a comprehensive overview of the pavement's physical state and performance. - A key output of PAVEMON is the estimation of the overall pavement conditions through the ASTM's Pavement Condition Index (PCI), which is derived using a statistical fusion approach that selects a subset of sensor measurements to enhance the accuracy and reliability of the condition assessment.
Detecting sources of ride roughness by ensemble-connected vehicle signals	Xin Deng	2022	- The method utilizes low-cost GPS receivers to gather positional data, which is essential for monitoring road conditions and detecting ride roughness. - Accelerometers are employed to capture vehicle motion data, allowing for the analysis	- The method presented in the paper enables continuous monitoring of road conditions by utilizing low-cost GPS receivers and accelerometers in regular vehicles, which helps in detecting defects that increase ride roughness and could potentially lead to

Title	Authors	Year	Data types	Pavement condition metrics
			of ride quality and the identification of defects that may lead to increased ride roughness or accidents.	accidents. - By employing techniques such as interpolation, signal resampling, and correlation alignment, the research significantly improved the quality of the sensor signals, resulting in a doubled peak of the composite signal and a 10 dB increase in the signal-to-noise ratio after combining data from multiple traversals.
Diagnostics of Road Conditions Using Acceleration Sensor: Machine Learning - LSTM autoencoder and Gaussian Mixture Model	Dada Zhang, Chun-Hsing Ho	2024	- The study utilizes acceleration data collected from sensors attached to vehicles, which includes measurements in vertical, longitudinal, and lateral directions. This data is normalized and transformed into overlapping windows for analysis. - The identified anomalies from the acceleration data are georeferenced using ArcGIS software, and statistical analysis is performed to compute the $\mathbf{R}^{2}$ values, which indicate the relationship between the detected road conditions and the International Roughness Index (IRI).	- The paper assesses road conditions using two unsupervised machine learning techniques: LSTM autoencoder and Gaussian Mixture Model (GMM-EM), which are employed for anomaly detection in acceleration data to identify distressed road conditions. - The relationship between identified poor road conditions and the International Roughness Index (IRI) is quantified, with $\mathbf{R}^{2}$ values of 77.91% and 82.63% for the LSTM autoencoder, indicating a strong correlation, while the GMM-EM model yields $\mathbf{R}^{2}$ values of 58.89% and 74.35%.
Dynamic Road Anomaly Detection: Harnessing Smartphone Accelerometer Data with Incremental Concept Drift Detection and Classification	Imen Ferjani, Suleiman Ali Alsaif	2024	- The study utilizes crowd-sourced smartphone sensor data, specifically accelerometer data, to monitor road conditions in real-time. This data type is crucial for providing insights into the state of	

Title	Authors	Year	Data types	Pavement condition metrics
			the roads as experienced by users in various environments. - The proposed method combines both unsupervised and supervised learning techniques to manage concept drift, indicating that the data types involved not only include raw sensor measurements but also processed data that can be classified and analyzed for anomalies in road conditions.	
Edge computing - enabled road condition monitoring : system development and evaluation	Abdulateef Daud	2023	- The study utilizes data from Micro Electro-Mechanical System (MEMS) sensors mounted on vehicle axles to stream live pavement condition data, which is processed on-device to reduce latency before being sent to cloud servers. - Machine learning models, specifically Random Forest, LightGBM, and XGBoost, are employed to predict the International Roughness Index (IRI) at every 0.1-mile segment, with XGBoost achieving the highest accuracy metrics of RMSE and MAPE.	- The study focuses on predicting the International Roughness Index (IRI) at every 0.1-mile segment using machine learning models, with XGBoost achieving the highest accuracy, resulting in an RMSE of 16.89in/mi and a MAPE of 20.3 percent. - The proposed device classifies the IRI of pavement segments based on ride quality according to MAP-21 criteria, achieving an average accuracy of 96.76 percent on I-70EB and 63.15 percent on South Providence (MO-163).
Edge Computing-Enabled Road Condition Monitoring: System Development and Evaluation	Abdulateef Daud, Mark Amo-Boateng, Neema Jasika Owor, Armstrong Aboah, Yaw Adu-Gyamfi	2023	- The study utilized vertical acceleration data collected from a tri-axial accelerometer (MPU6050) and GPS data to predict the International Roughness Index (IRI). The vertical acceleration data was transformed using the Fast Fourier Transform (FFT) to extract important features for analysis.	- The primary metric used for assessing pavement condition in this study is the International Roughness Index (IRI), which quantifies the roughness of pavement surfaces. The study trained machine learning models to predict IRI values at every 0.1-mile segment, achieving an accuracy of 96.76% on I-70EB and 63.15% on South Providence,

Title	Authors	Year	Data types	Pavement condition metrics
			- The primary features derived from the GPS data included aggregated speed and elevation information, while the secondary features extracted from the vertical acceleration data included metrics such as area under the Power Spectral Density (PSD) curve, mean power, standard deviation of power, maximum power, and dominant frequency.	indicating the effectiveness of the proposed device in classifying pavement segments based on ride quality. - The study also emphasizes the importance of real-time data collection and processing to enhance pavement maintenance and rehabilitation decisions. By utilizing edge computing and machine learning, the proposed system can provide timely and accurate pavement condition data, which is crucial for highway agencies to prioritize maintenance efforts and allocate resources effectively.
Ensemble Machine Learning Classification Models for Predicting Pavement Condition	Frederick Chu-pai Chung, Andy Doyle, Ernay Robinson, Yejee Paik, Mingshu Li, Minsoo Baek, Brian Moore, Baabak Ashuri	2024	- The research utilizes a dataset from the Georgia Department of Transportation, which documents the condition of asphalt pavements for predefined maintenance sections between 2017 and 2021. This historical data is essential for training the machine learning models to predict pavement condition grades. - The study focuses on classification models rather than regression-based models, indicating that the data types involved are likely categorical, as they pertain to condition index ranges and maintenance types rather than exact numerical values.	- The research focuses on predicting pavement condition grades using machine learning classification models, which are more suitable for determining the appropriate maintenance type for pavement assets rather than providing exact condition values. This approach aligns with how transportation asset management typically operates according to condition index ranges. - The study utilized a dataset from the Georgia Department of Transportation that documented the condition of asphalt pavements for predefined maintenance sections between 2017 and 2021, highlighting the importance of historical data in improving

Title	Authors	Year	Data types	Pavement condition metrics
				forecasting precision for pavement performance condition.
Estimating Pavement Condition by Leveraging Crowdsourced Data	Yangsong Gu, Mohammad Khojastehpour, Xiaoyang Jia, Han Lee	2024	- The study utilized crowdsourced data from Waze, specifically focusing on pothole reports and weather reports, to evaluate pavement conditions. - Laser truck data from the Tennessee Department of Transportation (TDOT) was used to calculate the Pavement Quality Index (PQI), which served as a benchmark for comparing the proposed surrogate measures.	- The study proposes two surrogate measures for evaluating pavement condition: Pothole Report Density (PRD) and Weather Report Density (WRD). PRD is found to be highly correlated with the Pavement Quality Index (PQI) and is identified as the second most important factor influencing PQI values, following pavement age. - The research indicates that while Waze weather reports do contribute to PQI values, their impact is significantly smaller compared to that of pothole reports, highlighting the greater relevance of pothole data in assessing pavement conditions.
Estimation of Pavement Condition Based on Data from Connected and Autonomous Vehicles	David Llopis-Castelló, Francisco Javier Camacho Torregrosa, Fabio Romeral-Pérez, Pedro Tomás-Martínez	2024	- The study utilizes real-time data gathered from connected and autonomous vehicles (CAVs), which are equipped with sensors and accelerometers provided by Original Equipment Manufacturers (OEMs) to continuously monitor road conditions. - The analysis focuses on the International Roughness Index (IRI) as a key metric for assessing pavement condition, comparing CAV-derived IRI values with those obtained from traditional pavement auscultation results to establish various thresholds for defining pavement conditions.	- The study evaluates pavement condition using the International Roughness Index (IRI), which quantifies road surface conditions based on data collected from connected and autonomous vehicles (CAVs). The IRI values range from 1 to 2.5 dm/km, indicating good-to-satisfactory surface conditions. - A moderate positive correlation was found between CAV-derived IRI values and traditional pavement auscultation results, suggesting that CAV data can reliably identify pavement conditions. However, CAV IRI values were generally slightly lower than

Title	Authors	Year	Data types	Pavement condition metrics
				those from traditional surveys, likely due to differences in driving behavior.
Evaluation of Connected Vehicle Pavement Roughness Data for Statewide Needs Assessment	Andrew Thompson, Jairaj Desai, Darcy M. Bullock	2025	- The study evaluates Connected Vehicle-estimated International Roughness Index (IRI) data (IRICVe) as a potential data source for long-term statewide pavement monitoring on local roads in Indiana. - Approximately 4.1 billion daily IRICVe records were collected over a multi-year study period from connected vehicles operating throughout the state, which were then processed using a modular data processing workflow.	- The Pavement Surface Evaluation and Rating (PASER) and Pavement Condition Index (PCI) are commonly used pavement condition assessment techniques, but they involve subjectivity and inconsistent measurement practices, which complicates uniform scaling across Indiana's extensive local road network. - The International Roughness Index (IRI) data, specifically Connected Vehicle-estimated IRI (IRICVe) data, is evaluated as a potential solution for long-term statewide pavement monitoring, providing cost-effective, data-driven insights in near real-time for local agency pavement asset management.
Innovative Approaches in Road Condition Monitoring: Synergizing Mobile Mapping Systems and High-Resolution Data Analytics	Prajwal Dudhbale, Sujesh D. Ghodmare, R Mane	2024	- The study utilizes high-resolution sensors to capture detailed 3D point clouds and cross-sectional profiles of the road surface, which are essential for accurate identification of road features such as lane markings and surface irregularities. - The methodology incorporates the ViaPPS technology, which employs tools like the Z+F 9012 A laser scanner and the Ladybug 5+ camera, enabling the collection of precise	- The study yielded critical pavement condition metrics, including an International Roughness Index (IRI) of 2.90, which indicates the smoothness of the road surface and is essential for assessing ride quality and overall road performance. - Additionally, a Mean Profile Depth (MPD) of 0.975 was recorded, which helps in evaluating the texture and drainage characteristics of the pavement, contributing to the understanding of surface irregularities

Title	Authors	Year	Data types	Pavement condition metrics
			metrics including the International Roughness Index (IRI) and Mean Profile Depth (MPD).	and their impact on vehicle safety and comfort.
Innovative pavement management system & sustainable roads in the city of dubai	Mohamed Saeed	2025	- The study utilized field data recorded by smartphones mounted in vehicles to simulate elevation profiles and estimate the International Roughness Index (IRI) values across 250 road segments, allowing for a comparison with high-resolution outputs from the Laser Crack Measurement System (LCMS-2). - The research incorporated sophisticated technologies such as the Laser Crack Measurement System (LCMS-2) for high-resolution pavement distress measures, alongside scalable, smartphone-based roughness detection, to enhance asset management and maintenance planning in urban road networks.	- The International Roughness Index (IRI) is a key performance measure that connects ride comfort, maintenance needs, and economic sustainability, making it essential for proactive maintenance planning in pavement management systems. - The study found significant correlations between IRI and pavement distress measures, indicating that IRI can reliably be used to assess pavement conditions and prioritize maintenance interventions, particularly highlighting that Sharjah has lower IRI values due to successful preservation measures, while Khorfakkan and Fujairah require priority interventions.
Large-scale pavement roughness measurements with vehicle crowdsourced data using semi-supervised learning	Chenglong Liu, Difei Wu, Yishun Li, Yuchuan Du	2021	- The study utilizes crowdsourced data collected from vehicles owned by the general public, which includes vibration measurements that are convenient, extensive, inexpensive, and have a high sampling frequency for evaluating large-scale pavement roughness. - The proposed semi-supervised learning model addresses the challenge of incomplete data due to missing vehicle information, allowing for effective multi-vehicle data	- The paper establishes a mathematical derivation of the 'international roughness index' (IRI) using in-car vibrations, which serves as a key metric for evaluating pavement condition based on the vibrations collected from vehicles. - The proposed semi-supervised learning (SSL) model iteratively estimates IRIs across a roadway network, improving the reliability and robustness of pavement condition

Title	Authors	Year	Data types	Pavement condition metrics
			fusion and the estimation of the international roughness index (IRI) from in-car vibrations.	assessments by considering the confidences of vehicle parameters and IRI estimations.
Machine Learning Applications in Road Pavement Management: A Review, Challenges and Future Directions	Tiago Tamagusko, Matheus Gomes Correia, Adelino Ferreira	2024	- The review discusses the refinement of data collection processes as a significant advancement in Pavement Management Systems (PMS) through the integration of Machine Learning (ML), indicating that various types of data are likely utilized to assess pavement conditions and deterioration. - While specific data types are not explicitly mentioned in the abstract, the emphasis on improving decision-making and performance prediction suggests that both quantitative data (such as pavement condition metrics) and qualitative data (such as user feedback or expert assessments) may be involved in the ML applications for PMS.	- The integration of Machine Learning (ML) into Pavement Management Systems (PMS) enhances the accuracy of pavement condition assessments, allowing for more precise evaluations of the current state of road surfaces and identifying areas that require maintenance or rehabilitation. - ML techniques improve performance prediction by analyzing historical data and patterns of pavement deterioration, which aids in optimizing maintenance and rehabilitation decisions, ultimately leading to more effective management of road infrastructure.
Measurement of Street Pavement Roughness in Urban Areas Using Smartphone	Yazan Ibrahim Alatoom, Turki I. Al-Suleiman Obaidat	2021	- The study utilized acceleration data collected from smartphones, which monitored movements and vibrations in all directions to assess pavement roughness. This data was processed using various signal processing techniques, including Butterworth bandpass filter, moving average filter, and baseline correction filter. - The research focused on estimating the International Roughness Index (IRI) by analyzing the effects of different factors such as vehicle speed, smartphone mounting	- The study focuses on the International Roughness Index (IRI) as a key metric for evaluating pavement condition, which is essential for determining riding comfort on the road network. The proposed method using smartphones aims to provide a cost-effective way to estimate IRI accurately. - Various factors were analyzed to enhance the accuracy of IRI estimation, including vehicle speed, smartphone mounting position, acceleration collection sampling rate, and integration method. The findings indicated

Title	Authors	Year	Data types	Pavement condition metrics
			position, acceleration collection sampling rate, and integration method on the accuracy of the IRI estimation.	that a sampling rate of 200 samples/s, a vent mount type, and the double integration method yielded a good accuracy (r2 = 0.72) for estimating IRI.
Pavement Distress Recognition via Wavelet-Based Clustering of Smartphone Accelerometer Data	Parastoo Kamranfar, David Lattanzi, Amarda Shehu, Shelley M. Stoffels	2022	- The study utilizes smartphone accelerometer data as the primary data type for assessing road pavement quality, focusing on the application of this data in recognizing pavement distress. - The framework employs wavelet featurization to process the accelerometer data, which involves dimensionally reducing the data to extract relevant features for subsequent clustering analysis.	- The proposed unsupervised learning framework utilizes wavelet featurization to analyze smartphone accelerometer data, which helps in detecting road pavement distress and distinguishing between different classes of pavement defects. This approach automates the tuning and selection of wavelet features based on clustering metrics related to intercluster and between-cluster variance. - Experimental evaluations indicate that while the framework can identify various pavement distress types, the reliability of low-cost smartphone sensor data in discriminating nuanced characteristics, such as the severity and type of cracking, is limited. This limitation can lead to undesirable cluster separation in the analysis of pavement conditions.
Pavement Quality Evaluation Using Connected Vehicle Data	Justin Mahlberg, Howell Li, Björn Zachrisson, Dustin K. Leslie, Darcy M. Bullock	2022	- The study utilized crowdsourced roughness data obtained from on-board sensors integrated in Original Equipment Manufacturer (OEM) connected vehicles, which provided real-time pavement condition assessments without the need for additional vehicle instrumentation.	- The primary metric for evaluating pavement condition is the International Roughness Index (IRI), which is widely employed due to its stability over time and its ability to provide a less subjective measure of pavement performance by calculating values from the road profile. This method is

Title	Authors	Year	Data types	Pavement condition metrics
			- Ground-truth data was collected using an inertial profiler, which is the industry standard for measuring the International Roughness Index (IRI), allowing for a comparison between the traditional method and the crowdsourced data to evaluate pavement quality.	traditionally assessed using specialized equipment like inertial profilers. - Crowdsourced data from connected vehicles can also be utilized to estimate pavement roughness and IRI values, providing a scalable and efficient means for agencies to monitor pavement conditions in real-time without the need for extensive resource allocation or specialized equipment. This approach allows for the aggregation of roughness values from multiple vehicle passes over roadway segments, enabling agencies to prioritize maintenance activities effectively.
Physics-informed neural networks to advance pavement engineering and management	Nima Kargah-Ostadi, K. Vasylevskyi, A. Ablets, A. Drach	2024	- The PINN model utilizes simulation data of vehicles' suspension responses to longitudinal road profiles, which serves as a foundational dataset for training the model. - The model is also adapted to predict the International Roughness Index (IRI) values, integrating empirical observations from an independent dataset collected from an autonomous vehicle study by the Ford Motor Company.	- The paper discusses the use of the International Roughness Index (IRI) as a standard metric for assessing pavement condition, which is integrated into the physics-informed neural network (PINN) model to predict IRI values accurately. - The PINN model demonstrates low bias and standard error in predicting IRI values across training, test, and independent datasets, indicating its effectiveness in evaluating pavement conditions based on vehicle suspension responses to road profiles.
Reconciling Pavement Condition Data from Connected Vehicles with the International Roughness	Z Weng	2023	- The study utilizes vertical acceleration data records generated from a quarter-car simulation, which are based on random	- The study focuses on the International Roughness Index (IRI) as a key pavement condition metric, which is predicted using a

Title	Authors	Year	Data types	Pavement condition metrics
Index from Standard Monitoring Equipment Using Physics-Integrated Machine Learning			stratified sampling from probability distributions of vehicle suspension properties at different speed levels on elevation profiles collected from various pavement sections. - The framework integrates spatiotemporally continuous sensor data crowdsourced from connected vehicles with infrequent standard pavement survey data, specifically focusing on the International Roughness Index (IRI) as the primary metric for pavement condition assessment.	physics-integrated machine learning model that takes into account vehicle speed, suspension properties, and acceleration response features from vehicles traversing the road section. - The proposed approach enhances the accuracy of IRI predictions by averaging the outputs from multiple vehicles and applying a correction function to rectify under-predictions, thereby providing a more reliable estimate of the actual IRI value for specific road segments.
RoadProbe: A Machine Learning-based System for Predictive Road Maintenance	Abdelmounaam Rezgui, yashwanth sai Rachala, Moussa Ayyash	2024	- The data collected for RoadProbe is gathered through a mobile application using crowdsourcing, which allows users to report road irregularities such as potholes and cracks. - The collected data is stored on Google's Firebase, where it is then utilized to build a Long Short-Term Memory (LSTM) model for predicting road irregularities.	- RoadProbe utilizes machine learning to detect and predict road irregularities such as potholes and cracks, which are key metrics for assessing pavement condition. - The system collects data through a mobile application via crowdsourcing, which is then stored on Google's Firebase and used to build a Long Short-Term Memory (LSTM) model for accurate predictions of pavement conditions.
Smartphone-Based IRI Estimation for Pavement Roughness Monitoring: A Data-Driven Approach	Ye Sang, Qiqin Yu, Yihai Fang, Viet Vo, Richard Wix	2024	- The study utilizes real vehicle response data collected from smartphones mounted on vehicles to estimate the international roughness index (IRI), which allows for a more accurate assessment of pavement roughness in practical settings.	- The study focuses on estimating the international roughness index (IRI), which is a key metric for assessing pavement roughness and is critical for minimizing vehicle damages and ensuring road user safety. - The proposed method utilizes smartphone-

Title	Authors	Year	Data types	Pavement condition metrics
			- The multilayer perceptron deep learning model employed in the study processes this smartphone-collected data to account for variations in practical factors such as speed, vehicle type, and mounting configuration, enhancing the accuracy of the IRI estimation.	collected real vehicle response data and employs a multilayer perceptron deep learning model, achieving an RMSE of 0.60 and an R^{2} of 0.79 when compared with ground-truth IRI, indicating its effectiveness in measuring pavement conditions.
Toward Real-World Implementation of Deep Learning for Smartphone-Crowdsourced Pavement Condition Assessment	Jong-Hyun Jeong, Hongki Jo	2024	- The study utilizes smartphone sensor data collected from 29 different vehicles to assess road conditions, specifically focusing on vibrations that can be used to estimate the international roughness index (IRI) at various driving speeds. - A large-scale data set is managed that includes low-resolution crowdsourced GPS data, which is addressed through a new data management strategy to enhance the effectiveness of the deep-learning-based road roughness monitoring method.	- The study focuses on estimating the International Roughness Index (IRI) from smartphone sensor data, which serves as a key pavement condition metric for assessing road roughness and overall pavement quality. - The proposed method utilizes a fully convolutional neural network (CNN) architecture, called IRI-Net, to analyze vibrations from vehicles and provide a cost-effective alternative to traditional high-cost systems like inertial profilers for monitoring pavement conditions.

Table 23 – Dataset of geometry of segments

segment_id	tortuosity	mean_angle	num_turns
1223	1,0000	0,0000	0
1224	1,0000	0,0000	0
1245	1,3180	13,4281	0
1367	1,0000	0,0000	0
1523	1,0000	0,0000	0
1593	1,0001	1,2112	1
1594	1,0000	0,0351	0
1614	1,0000	0,0000	0
2957	1,0000	0,0000	0
2960	1,0000	0,5174	0
2964	1,0000	0,4917	0
2969	1,0000	0,0000	0
2973	1,0000	0,0000	0
2984	1,0000	0,0000	0
3010	1,0000	0,0000	0
3011	1,0019	7,0254	0
3013	1,0000	0,2467	1
3016	1,0000	0,2787	1
3020	1,0003	1,5343	0
3021	1,0008	1,6758	0
3022	1,0004	1,5654	1
3023	1,0000	0,0551	1
3121	1,0000	0,0000	0
3161	1,0000	0,0000	0
3164	1,0016	3,0487	0
3165	1,0000	0,0000	0
3180	1,0000	0,0000	0
3181	1,0000	1,0995	0
3182	1,0000	0,5478	0
3186	1,0000	0,0045	0
3187	1,0000	0,0000	0
3190	1,0000	0,8812	2
3202	1,0047	26,9838	0
3214	1,0066	4,2956	0
3215	1,0000	0,5309	1
3273	1,1861	15,5353	1
3279	1,0077	14,3015	0
3333	1,0018	2,5714	2
3335	1,0000	0,2511	1
3337	1,0010	2,1260	3
3338	1,0036	6,3111	0
3348	1,0000	0,3730	2
3352	1,0000	0,9912	0
3356	1,0013	2,4999	0
3417	1,0000	0,0000	0
3418	1,1590	20,3254	0
3431	1,0004	3,4061	0
3468	1,0074	6,5319	0
3478	1,0019	8,6665	0
3479	1,0001	1,2880	2
3495	1,0003	2,1597	4
3496	1,0000	0,5209	1
3520	1,0055	6,8327	1
3605	1,0000	0,0000	0
3606	1,0016	6,5178	0
3608	1,4067	13,5184	0
3614	1,0507	13,6425	0
3615	1,0390	9,4652	0
3616	1,0198	8,6045	0
3666	1,0005	3,5891	0
3667	1,0109	5,8431	2
3709	1,0013	3,5266	2
3710	1,0018	8,0603	1
3712	1,0014	1,9825	2
3713	1,0031	4,2311	0
3714	1,0053	3,5069	1
3721	1,0006	1,3761	3
3724	1,0000	0,0365	0
3727	1,0000	0,4693	2
3728	1,0001	0,7006	3
3729	1,0000	0,0040	0
3730	1,0000	0,3274	0
3885	1,0007	4,5249	1
3899	1,0000	0,0000	0
3900	1,0000	0,0107	0
3901	1,0000	0,0074	0
3902	1,0000	0,0033	1
3936	1,0000	0,0000	0
3955	1,0054	29,7903	0
3972	1,0063	5,0080	1
3973	1,0055	4,8467	2

3974	1,0024	3,5165	1
3975	1,0310	6,6626	1
3976	1,0160	8,0234	2
4032	1,0000	0,3566	1
4033	1,0000	0,0249	0
4041	1,0065	13,0059	0
4066	1,0012	5,6972	0
4072	1,1039	11,1459	1
4073	1,0831	11,5986	0
4074	1,0038	7,3294	0
4075	1,0061	8,1829	1
4076	1,0050	5,0623	0
4077	1,0034	5,7503	0
4078	1,0000	0,4953	0
4080	1,0000	0,0000	0
4081	1,0001	1,0291	0
4082	1,0002	1,6679	0
4087	1,0000	0,0279	0
4088	1,0000	0,0287	0
4089	1,0000	0,0000	0
4113	1,0602	9,5217	0
4115	1,0078	17,1408	0
4116	1,0006	4,1115	1
4117	1,0030	6,7375	0
4121	1,0230	5,8821	1
4125	1,0205	6,7287	0
4137	1,0185	7,9672	0
4138	1,1091	11,6442	0
4139	1,0669	10,5534	0
4255	1,0003	2,6770	0
4256	1,0001	1,7116	0
4257	1,0000	0,2431	2
4297	1,0000	0,0126	0
4360	1,0046	6,1826	1
4579	1,0002	1,1971	0
4580	1,0001	2,4492	0
4591	6,8370	20,2685	0
4625	1,0085	7,9999	1
4656	1,0053	10,8771	0
4657	1,0003	2,4808	0
4658	1,0032	5,7613	0
4660	1,0032	6,3492	0
4661	1,0042	4,8453	1
4663	1,0111	8,8012	0
4664	1,0653	14,4444	0
4701	1,1556	15,6198	0
4702	1,0076	4,8249	0
4703	1,0068	5,0306	2
4785	1,0000	0,0140	0
4786	1,0000	0,0663	0
4794	1,0444	9,2875	1
4845	1,0000	0,9378	0
4846	1,0000	0,7838	0
4847	1,0000	0,0040	0
4858	1,0161	12,6654	0
4861	1,0131	11,2457	0
4974	1,0000	0,0000	0
4995	1,0001	1,7727	1
4996	1,0000	1,0108	1
4997	1,0000	0,5476	0
4998	1,0002	3,1310	0
4999	1,0000	0,0000	0
5060	1,0001	1,5958	0
5062	1,0000	0,0000	0
5063	1,0000	0,3628	0
5064	1,0000	0,0000	0
5065	1,0000	0,3253	0
5066	1,0001	1,5358	0
5067	1,0000	0,4754	0
5070	1,0005	4,3590	0
5080	1,0000	0,0000	0
5081	1,0000	0,0000	0
5205	1,0002	0,5103	2
5210	1,0652	9,7979	3
5296	1,2126	13,7673	2
5317	1,0000	0,3818	0
5320	1,0000	0,0000	0
5321	1,0076	12,5406	1
5322	1,0000	0,5211	1
5323	1,1021	14,1276	0
5598	1,2359	106,5245	0
5724	1,0000	0,0890	1
5725	1,0008	2,6085	1
5727	1,0000	0,7263	0
5732	1,0000	0,7786	0
5747	1,1854	58,4960	1

5748	1,2051	37,9164	2
5749	1,1434	58,4637	0
5785	1,0003	1,6682	1
5786	1,0000	0,1633	0
5787	1,0000	0,4451	4
5788	1,0000	0,1886	1
5789	1,0000	0,0000	0
5790	1,0035	2,8886	1
5791	1,0001	0,7032	1
5797	1,0000	0,0000	0
5804	1,0001	1,9026	0
5854	1,0023	4,1599	0
6188	1,0061	7,6713	0
6212	1,0013	4,9452	0
6217	1,0017	2,8728	0
6281	1,0000	0,0207	1
6282	1,0064	9,6785	0
6285	1,1411	33,5774	0
6355	1,0000	0,0053	0
6357	1,0027	4,7556	1
6360	1,0092	6,5720	3
6406	1,0009	4,6259	0
6471	1,0065	3,3029	1
6472	1,0429	6,4629	1
6723	1,0334	13,7016	0
7003	1,0000	0,3138	3
7004	1,0000	0,1203	1
7264	1,3993	103,4245	1
7345	1,0182	8,3881	0
7346	1,0000	0,0000	0
7565	1,0000	0,2965	2
8633	1,0000	0,0285	0
8634	1,0025	2,7304	2
8635	1,0001	1,0698	0
8636	1,0000	1,0823	1
8637	1,0001	0,6812	0
8644	1,0058	4,9333	2
8666	1,0036	13,3391	0
8702	1,0001	0,8641	1
8707	1,0003	2,8746	0
8708	1,0006	2,1631	0
8709	1,0000	0,0000	0
8777	1,0000	0,4070	0
8801	1,0000	0,7030	2
8872	1,0000	0,0000	0
8877	1,0019	4,6189	1
8878	1,0000	0,0111	0
8964	1,0051	7,6090	1
9015	1,0008	2,6922	0
9016	1,0008	1,5624	2
9017	1,0011	1,5619	0
9018	1,0000	0,4952	0
9019	1,0000	0,6202	0
9020	1,0000	1,1327	0
9021	1,0015	3,1857	0
9022	1,0000	0,0000	0
9034	1,0000	0,1248	1
9035	1,0000	0,0000	0
9036	1,0038	3,7226	2
9037	1,0008	5,0861	1
9042	1,2275	22,8429	0
9052	1,0130	6,9518	2
9164	1,0013	1,6469	3
9165	1,0000	0,0000	0
9166	1,0002	1,8547	1
9167	1,0003	1,0290	1
9168	1,0002	1,2884	1
9170	1,0033	5,1611	0
9171	1,0140	9,0547	0
9172	1,0168	7,8805	0
9173	1,0000	0,0000	0
9174	1,0000	0,9469	1
9221	1,0000	0,1277	0
9223	1,0001	0,8181	0
9224	1,0000	0,0000	0
9226	1,0000	0,7266	0
9228	1,0000	1,0506	0
9232	1,0000	0,1466	0
9235	1,0000	0,0000	0
9237	1,0000	0,6357	0
9240	1,0000	0,6291	0
9249	1,0000	0,1719	0
9261	1,0000	0,6636	0
9290	1,0875	16,0776	1
9296	0,0000	18,9298	0
9403	1,0031	9,9388	0

9407	1,0196	8,2778	1
9456	1,0012	3,4611	0
9636	1,0009	3,7909	1
9640	1,0770	11,7506	0
9685	1,0000	0,7651	0
9690	1,0012	3,7764	0
9691	1,0078	7,2386	1
9816	1,0000	0,0104	0
9863	1,0038	11,0433	1
9866	1,0000	0,0000	0
10088	1,0471	12,5573	0
10126	1,0000	0,0000	0
10183	1,0000	0,3301	0
10185	1,0001	0,8510	1
10188	1,0000	0,9598	1
10266	1,0863	14,1468	0
10283	1,0000	0,1154	0
10288	1,2321	14,0861	0
10289	1,0046	3,5503	0
10293	1,0000	0,0218	2
10294	1,0000	0,0000	0
10296	1,0000	0,2669	0
10297	1,0000	1,0234	0
10381	1,1883	19,6215	0
10387	1,0611	24,1385	0
10415	1,0018	3,6449	1
10427	1,0000	0,1891	0
10429	1,0000	0,0140	0
10436	1,0000	0,5576	1
10437	1,0000	0,0222	0
10441	1,0000	0,0146	0
10556	1,0007	2,9449	0
10557	1,0005	4,5432	0
10692	1,0004	3,3009	0
10694	1,0000	0,0000	0
10695	1,0000	0,0000	0
10696	1,0000	0,0000	0
10698	1,1720	15,7328	1
10733	1,0233	14,6471	0
10735	1,0401	14,6856	1
10778	1,0001	1,7930	0
10781	1,0610	7,4721	0
10782	1,0000	0,0000	0
10783	1,0000	0,0000	0
10784	1,0002	2,9191	0
10785	1,0000	0,0792	0
10792	1,0000	0,5647	0
10794	1,0092	6,0468	1
10798	1,0001	1,6904	0
10799	1,0000	0,8384	0
10801	1,0000	0,0000	0
10802	1,0003	2,4765	0
10846	1,0000	0,0873	2
10847	1,0000	0,0241	3
10895	1,0070	3,9594	0
10898	1,0000	0,0557	0
10934	1,0302	7,1990	1
11015	1,2923	26,9024	0
11140	1,0005	2,4987	1
11148	1,0400	8,9423	0
11149	1,0078	8,4554	0
11151	1,0049	13,3123	0
11152	1,0149	12,6424	0
11213	1,0109	9,9179	1
11214	1,0005	4,5407	0
11215	1,0056	5,0441	1
11216	1,0039	5,4576	0
11217	1,0028	4,8768	0
11218	1,0032	4,1114	0
11219	1,0000	1,0524	0
11220	1,0003	2,1027	0
11221	1,0021	8,8043	0
11257	1,0001	0,7589	1
11258	1,0000	0,1626	1
11259	1,0002	1,6891	0
11282	1,0000	0,4912	0
11393	1,0093	10,7121	0
11483	1,0021	5,3151	0
11494	1,0007	3,0300	0
11497	1,0099	9,8617	0
11540	1,0017	5,1389	1
11586	1,0000	0,0104	0
11640	1,0000	0,0000	0
11647	1,0000	0,0000	0
11654	1,0001	1,7814	0
11655	1,0000	0,2904	2

11656	1,0000	0,0941	0
11657	1,0010	3,2629	1
11717	1,0000	0,0000	0
11753	1,0007	3,4106	1
11848	1,0000	0,0210	1
11849	1,0000	0,0000	0
11872	1,0160	3,7265	0
11873	1,0049	5,8295	1
11875	1,0000	0,0000	0
11882	1,0009	4,7834	0
11883	1,0000	0,0000	0
11884	1,0005	3,9216	1
11889	1,0002	1,5382	0
11890	1,0001	1,3551	0
11891	1,0000	0,3885	0
11892	1,0000	0,0465	0
11893	1,0000	0,0025	0
11894	1,0002	1,8237	0
11895	1,0004	1,3786	1
11896	1,0001	1,6824	0
11897	1,0000	0,5441	0
11931	1,0000	0,0000	0
11935	1,0002	1,3496	0
11936	1,0003	1,1800	0
11937	1,0002	1,8183	0
11938	1,0001	1,7725	0
11939	1,0003	1,9160	0
12010	1,0000	0,0000	0
12047	1,1217	7,8468	0
12059	1,0087	12,0365	0
12060	1,0440	21,1073	0
12063	1,3855	20,7086	0
12098	1,0000	0,0000	0
12099	1,0000	0,6160	0
12107	1,0000	0,0000	0
12108	1,0000	0,8674	0
12159	1,0002	1,5099	1
12160	1,0006	2,2077	0
12166	1,0365	12,5182	0
12167	1,0000	0,0000	0
12181	1,0001	0,9999	1
12185	1,0001	0,7682	1
12186	1,1258	15,7378	0
12188	1,0115	7,6927	1
12189	1,0018	4,2812	1
12194	1,0000	0,0000	0
12195	1,0000	0,0000	0
12198	1,0002	2,7077	0
12201	1,0022	7,6173	0
12204	1,0043	10,2502	1
12205	1,0000	0,0000	0
12206	1,0022	3,8133	0
12214	1,0000	0,8526	0
12215	1,0001	1,8349	0
12216	1,0000	1,3466	0
12217	1,0007	4,7936	0
12218	1,0000	0,0000	0
12219	1,0038	4,5686	0
12222	1,0049	5,0336	0
12223	1,0000	1,2086	0
12224	1,0000	0,2943	0
12246	1,0140	19,0604	0
12265	1,0001	1,3636	1
12266	1,0014	6,4519	0
12390	1,0000	0,0000	0
12420	1,0000	0,0103	1
12421	1,0000	0,0741	0
12422	1,0000	0,0915	1
12424	1,0000	0,0000	0
12429	1,0001	0,4726	2
12431	1,0006	1,6864	0
12432	1,0004	1,1845	2
12433	1,0000	0,0000	0
12434	1,0000	0,2254	0
12443	1,0000	0,2176	1
12446	1,0001	1,6312	0
12447	1,0001	0,9793	1
12448	1,0019	4,5562	0
12450	1,0001	1,0551	1
12451	1,0004	1,7839	0
12461	1,0000	0,0000	0
12462	1,0000	0,0319	1
12516	1,0000	0,0050	0
12518	1,0000	0,0000	0
12566	1,4100	16,9090	0
12630	1,3344	14,3506	0

12631	1,0191	13,2270	0
12762	1,0005	4,6663	1
12763	1,0000	0,0000	0
12839	1,1608	20,9898	0
12840	1,0032	5,5578	0
12841	1,0000	0,0000	0
12842	1,0000	0,0000	0
12858	1,0420	11,2112	0
12930	1,0000	0,0068	1
12959	1,0000	0,0000	0
12960	1,0001	2,1010	0
12973	1,0000	0,0000	0
12978	1,0000	0,0000	0
12979	1,0000	0,0000	0
12980	1,0008	4,5734	0
12982	1,0000	0,5115	0
12984	1,0000	0,0000	0
12985	1,0155	11,4472	1
12986	1,0004	2,2066	0
13105	1,0153	19,9224	0
13124	1,0003	1,5323	1
13141	1,0000	0,0000	0
13142	1,0000	0,0000	0
13150	1,0144	12,2310	1
13233	1,0026	5,7138	0
13337	1,0000	0,3498	0
13338	1,0000	0,2029	0
13339	1,0001	1,2886	0
13340	1,0000	0,0048	0
13418	1,0001	0,7372	1
13420	1,1565	27,2491	0
13493	1,0000	0,6642	0
13514	1,2333	49,0298	0
13603	1,0000	0,0000	0
13604	1,0000	0,1008	1
13605	1,0015	2,8323	2
13607	1,0000	0,0000	0
13608	1,0005	3,6918	0
13613	1,0000	0,0000	0
13643	1,0002	2,6473	0
13660	1,0005	1,6762	0
13672	1,0000	0,4080	1
13674	1,0000	0,0000	0
13675	1,0000	0,4392	0
13676	1,0000	0,0000	0
13679	1,0012	2,2781	0
13680	1,0009	3,8818	0
13684	1,0008	2,6922	0
13734	1,0207	15,8413	1
13736	1,0304	28,7233	0
13784	1,0000	0,0000	0
13787	1,0000	0,8454	1
13885	1,0000	0,1876	1
13886	1,0000	0,6859	1
13887	1,0000	0,2847	1
14004	1,0000	0,0000	0
14097	1,0000	0,0000	0
14120	1,0001	1,7068	0
14129	1,0078	5,6846	0
14130	1,0005	3,0358	0
14136	1,0025	5,0119	0
14138	1,0067	13,5575	0
14143	1,0002	2,6035	0
14155	1,0397	21,1008	1
14241	1,0000	0,0000	0
14250	1,0670	21,6862	1
14315	1,0000	0,4565	0
14317	1,0000	0,3939	1
14318	1,0000	1,0248	0
14320	1,0001	1,8164	0
14321	1,0000	0,2938	0
14322	1,0001	1,6205	0
14324	1,0001	1,0706	2
14325	1,0002	2,1078	0
14327	1,0000	0,3968	0
14328	1,0000	0,3536	0
14366	1,0000	0,0716	0
14375	1,0004	2,0772	0
14376	1,0001	1,5182	0
14377	1,0000	0,0000	0
14461	1,0168	9,2472	0
14693	1,0000	0,6528	0
14813	1,0127	4,0579	3
14892	1,0000	0,0038	0
14893	1,0000	0,0193	0
14894	1,0000	0,0000	0

14898	1,0000	0,0872	0
14899	1,0003	2,0950	0
14901	1,0000	0,0000	0
14902	1,0005	2,4325	0
14903	1,0000	0,8463	0
14904	1,0000	0,6496	1
14905	1,0000	0,7334	1
14906	1,0001	1,3475	0
14907	1,0001	1,7155	0
14908	1,0000	0,0242	0
15084	1,0001	1,6868	0
15091	1,0037	5,1281	1
15116	1,0003	1,7232	1
15126	1,0000	0,0000	0
15130	1,0000	0,0000	0
15132	1,0000	0,0000	0
15134	1,0003	1,8602	0
15139	1,0004	1,4321	0
15140	1,0002	1,9088	0
15141	1,0000	0,4539	0
15143	1,0000	1,0406	0
15521	1,0000	0,0000	0
15522	1,0000	0,9660	0
15724	1,0271	6,2157	0
15725	1,1156	9,1666	0
15726	1,1062	10,9267	1
16184	1,0000	0,0000	0
16185	1,0000	0,0000	0
16186	1,0031	5,0554	1
16191	1,0001	1,4608	0
16326	1,0158	6,1321	0
16327	1,0008	3,1487	0
16328	1,0037	10,0366	0
16481	1,0000	0,7762	1
16482	1,0000	0,0000	0
16483	1,0000	0,0000	0
16484	1,0000	0,4051	0
16485	1,0002	1,3581	0
16627	1,0000	0,0000	0
16636	1,0000	0,0000	0
16637	1,0000	0,0000	0
16660	1,0536	16,3071	0
16661	1,0209	14,2706	0
16664	1,0236	11,1493	0
16666	1,0002	2,2354	1
16667	1,0002	2,6325	0
16688	1,0003	1,9286	0
16695	1,0000	0,0000	0
16696	1,0000	0,3045	0
16714	1,0007	4,4681	0
16715	1,0001	1,4353	0
16719	1,0000	0,0689	0
16751	1,0000	0,6580	0
16777	1,0004	4,3812	1
16782	1,0000	0,0000	0
16808	1,0030	7,2362	1
17011	1,0001	1,5721	0
17087	1,0000	0,0000	0
17088	1,0003	2,4540	1
17089	1,0000	0,0000	0
17090	1,0001	1,9861	0
17125	1,0172	34,1164	1
17228	1,0004	3,0869	0
17251	1,0006	2,6018	2
17252	1,0032	9,1563	0
17261	1,0000	0,0000	0
17263	1,0000	0,0000	0
17264	1,0000	0,0000	0
17266	1,0000	0,0113	0
17267	1,0000	0,1735	0
17268	1,0000	0,0000	0
17270	1,0000	0,0000	0
17271	1,0000	0,0000	0
17272	1,0000	0,0000	0
17273	1,0000	0,0000	0
17280	1,0002	1,4862	0
17281	1,0000	0,0000	0
17309	1,0000	0,0000	0
17310	1,0000	0,0000	0
17312	1,0000	0,0000	0
17315	1,0000	0,0000	0
17320	1,0002	2,7014	0
17321	1,0000	0,0000	0
17325	1,0000	0,0000	0
17326	1,0000	0,0000	0
17327	1,0000	0,2457	0

17328	1,0000	0,0743	0
17329	1,0000	0,0000	0
17330	1,0000	0,0000	0
17331	1,0002	1,2493	2
17332	1,0005	2,9011	0
17521	1,0241	24,9524	0
17524	1,0105	16,5514	0
17645	1,0594	17,4876	0
17647	1,0198	22,6880	0
17648	1,0981	21,7022	0
17654	1,0744	19,3084	0
17657	1,0000	0,0311	0
17658	1,0008	3,2614	1
17662	1,0000	0,0000	0
17663	1,0000	0,0000	0
17668	1,0000	0,0000	0
17698	1,0001	1,7063	0
17719	1,0002	2,4859	1
17775	0,0000	13,1283	0
17778	0,0000	18,5166	0
17779	0,0000	19,2258	0
17840	1,5434	9,3199	0
17980	0,0000	18,5027	0
17982	1,0007	1,8016	0
17983	1,0102	6,5320	0
18232	1,0148	3,7085	0
18233	1,0003	1,5123	1
18425	1,0109	5,9621	0
19067	1,0000	0,2570	2
19068	1,0000	0,0104	1
19069	1,0000	0,0000	0
19165	1,0000	0,0000	0
19459	1,2841	36,0422	0
19506	1,0000	0,0000	0
19560	1,1015	12,4564	0
19610	1,0000	0,0000	0
19724	1,0000	0,0000	0
19726	1,0000	0,0000	0
19740	1,0003	2,4018	0
19744	1,0007	1,8013	0
19745	1,0003	2,8230	0
19746	1,0000	0,0000	0
19747	1,0000	0,2529	0
19749	1,0002	1,5335	0
19751	1,0000	0,0000	0
19753	1,0000	0,0000	0
19755	1,0000	0,0053	0
19756	1,0000	0,0000	0
19757	1,0000	0,0000	0
19759	1,0004	1,6458	0
19761	1,0250	5,2584	0
19762	1,0000	0,0000	0
19808	1,2123	17,0562	0
19869	1,0024	7,9260	0
19979	1,0002	2,0429	0
20065	1,0003	3,0381	0
20423	1,0000	0,4238	1
20432	1,0371	13,9878	0
20434	1,1119	23,0652	0
23972	1,0651	10,6077	0
23973	1,0035	5,5350	0
23974	1,2842	12,0126	0
23975	1,8259	10,3729	0
24059	1,0015	9,8111	0
24088	1,0000	0,2328	1
24089	1,0000	0,1948	0
24090	1,0000	0,0000	0
24091	1,0000	0,0392	0
24092	1,0000	0,0000	0
24093	1,0004	1,4017	0
24094	1,0000	0,0000	0
24095	1,0000	0,0000	0
24132	1,0000	0,0000	0
24254	1,1125	15,3845	1
24256	1,0002	2,8664	0
24257	1,0137	15,5691	2
24289	1,0091	16,9158	0
24292	1,0000	0,0000	0
24293	1,0030	15,3516	0
24294	1,0000	0,0000	0
24296	1,1844	13,3106	1
24297	1,2494	15,1342	0
24299	1,0005	2,8364	0
24501	1,0002	2,6169	0
24530	1,0000	0,0000	0
24531	1,0001	1,5136	0

24533	1,0000	0,0000	0
24534	1,0000	0,0000	0
24610	1,0000	0,0000	0
24612	1,0000	0,1242	0
24613	1,0000	0,0000	0
24629	1,0003	2,5859	0
24636	1,0000	0,0000	0
24638	1,0000	0,0000	0
24639	1,0000	0,0931	0
24641	1,0007	4,4061	0
24642	1,0001	3,1528	0
24643	1,0000	0,0000	0
24644	1,0006	4,5044	0
24647	1,0000	0,2993	0
24648	1,0000	0,0000	0
24649	1,0000	0,0000	0
24650	1,0000	0,0000	0
24684	1,5380	22,1795	0
24685	1,3908	25,1771	0
24987	1,0000	0,0000	0
25016	1,0003	2,0255	0
25017	1,0005	2,3976	0
25018	1,0004	2,3230	0
25019	1,0007	2,8689	0
25020	1,0004	2,2753	0
25023	1,0010	3,2509	0
25024	1,0012	3,8767	0
25025	1,0010	3,3031	0
25029	1,0002	1,1447	4
25034	1,0000	0,0000	0
25039	1,0000	0,0000	0
25041	1,0000	0,0000	0
25046	1,0000	0,0000	0
25053	1,0000	0,1562	0
25055	1,0000	0,0313	0
25056	1,0000	0,0000	0
25059	1,0000	0,4059	0
25063	1,0001	1,6640	0
25064	1,0000	0,7970	0
25066	1,0000	0,9085	0
25068	1,0000	0,3983	0
25069	1,0000	0,7135	0
25071	1,0000	0,0000	0
25073	1,0000	0,1413	0
25156	1,0002	2,1992	0
25187	1,0000	0,6609	0
25190	1,0000	0,5020	0
25196	1,0000	0,2716	0
25202	1,0000	0,0000	0
25204	1,0000	0,0576	0
25207	1,0000	0,0801	0
25209	1,0000	0,0809	0
25215	1,0000	0,0950	0
25216	1,0000	0,0000	0
25227	1,0001	0,4586	2
25236	1,0004	2,0338	0
25240	1,0002	1,9022	0
25263	1,0067	8,1070	0
25270	1,0000	0,0000	0
25272	1,0000	0,0000	0
25273	1,0000	0,0000	0
25476	1,0277	12,5268	3
25502	1,0000	0,0000	0
25511	1,0030	9,3217	0
25868	1,0000	0,0643	0
25869	1,0000	0,0000	0
25870	1,0000	0,0000	0
26176	1,0000	0,0000	0
26178	1,0000	0,1434	0
26179	1,0000	0,0000	0
26596	1,0000	0,0000	0
26598	1,0000	0,0000	0
26603	1,0000	0,0559	0
26605	1,0000	0,0000	0
26609	1,0000	0,0995	0
26610	1,0000	0,0000	0
26613	1,0000	0,2361	0
26614	1,0000	0,0000	0
26616	1,0001	1,2182	0
26618	1,0000	0,0606	0
26619	1,0000	0,0214	0
26621	1,0000	0,0167	0
26623	1,0000	0,0000	0
26767	1,2261	25,9738	4
26823	1,0014	3,7576	0
26825	1,1991	33,3468	2

31041	1,0000	0,0292	0
32710	1,0000	1,1274	0
46156	1,0003	4,3959	0
46157	1,0009	6,4668	0
46158	1,0000	0,0000	0
46159	1,0002	2,3347	0
46160	1,0000	0,0000	0
46161	1,0000	0,0000	0
46167	1,0078	7,5925	1
46174	1,1267	18,7536	2
46181	1,4588	16,6156	0
46189	1,0336	9,2398	0
46191	1,3214	18,1924	0
46192	1,0087	15,6260	0
46198	1,1058	12,2844	0
46199	1,0016	6,7891	0
46200	1,1625	14,7352	0
46201	1,2356	17,6183	0
46206	1,0121	17,7507	0
46209	1,0216	23,7448	0
46263	1,0001	0,9220	0
46264	1,0002	2,2900	0
46265	1,0002	0,7959	0
46266	1,0001	0,7270	1
46267	1,0001	0,9716	0
46269	1,0000	1,2721	0
46270	1,0000	0,7635	0
46271	1,0000	1,2712	0
46272	1,0000	0,1998	0
46273	1,0000	0,0000	0
46274	1,0000	0,1804	0
46275	1,0000	0,0000	0
46276	1,0000	0,0000	0
46278	1,0000	0,0099	0
46279	1,0000	0,3954	0
46280	1,0000	0,9118	0
46281	1,0006	1,9879	2
46282	1,0094	5,1834	0
46283	1,0067	4,8399	0
46284	1,0002	1,4625	1
46285	1,0000	0,0000	0
46286	1,0009	4,7804	0
46287	1,0003	0,8173	1
46288	1,0000	0,0024	0
46289	1,0000	0,7109	1
46290	1,0000	0,0000	0
46291	1,0000	0,3179	0
46292	1,0000	0,0000	0
46293	1,0000	0,9938	0
46294	1,0017	4,4195	0
46295	1,0012	3,5343	0
46296	1,0004	3,9987	0
46297	1,0014	4,3184	0
46298	1,0005	2,5627	0
46299	1,0001	1,3577	0
46300	1,0072	6,1968	0
46301	1,0133	8,4493	0
46302	1,0129	9,8780	0
46303	1,0000	0,2605	0
46304	1,0000	0,0000	0
46305	1,0000	0,0000	0
46306	1,0000	0,0000	0
46331	1,0091	16,2185	0
46332	1,0129	11,4389	0
46333	1,0001	0,9515	1
46334	1,0000	0,3125	0
46336	1,0039	4,3388	0
46337	1,0099	11,1491	0
46338	1,0191	9,7768	0
46340	1,2599	14,5500	0
46346	1,0000	0,0000	0
46347	1,2509	15,0450	0
46348	1,2735	15,6606	0
46562	1,0019	3,3675	0
46564	1,0000	0,1711	1
46565	1,0000	0,0000	0
46566	1,0000	0,2783	0
46567	1,0000	0,7781	0
46568	1,0002	1,2835	0
46569	1,0000	0,4671	0
46570	1,0000	0,0526	1
46571	1,0000	0,0000	0
46572	1,0000	0,1032	0
46575	1,2745	13,1028	0
46578	1,0005	3,5102	0
46579	1,0157	6,7931	0

46581	1,0036	5,3008	0
46591	1,0036	4,7144	1
46601	1,0374	9,4350	1
46641	1,0545	17,1216	0
46649	1,0000	0,0000	0
46650	1,0000	0,0000	0
46651	1,0000	0,0000	0
46652	1,0000	0,0000	0
46653	1,0000	0,0012	0
46654	1,0000	0,0011	0
46655	1,0000	0,0000	0
46656	1,0000	0,0000	0
46657	1,0000	0,0775	0
46658	1,0000	0,0000	0
46659	1,0000	0,0000	0
46660	1,0000	0,0000	0
46661	1,0000	0,0000	0
46795	1,0000	0,4837	1
46990	1,0389	13,1291	0
47339	1,0383	15,6909	1
47424	1,0125	7,7322	4
47425	1,0008	3,2397	1
47467	1,0000	0,0000	0
47546	2,6054	17,4973	0
47582	1,0130	5,9045	1
47583	1,0000	0,8040	0
47587	1,0010	3,1604	1
47588	1,0000	0,2761	0
47590	1,0000	0,0000	0
47767	1,0002	2,1505	0
47768	1,0000	0,0000	0
47770	1,0052	11,6885	0
47771	1,0000	0,0000	0
47772	1,0000	0,0000	0
47773	1,0000	0,0000	0
47774	1,0000	0,0000	0
47775	1,0007	2,8046	0
47777	1,0000	0,0000	0
47792	1,0003	3,2714	0
47796	1,0000	0,0486	0
47797	1,0000	0,0000	0
47798	1,0000	0,2682	0
47799	1,0000	0,0362	0
47801	1,0003	3,0553	0
47802	1,0008	3,5001	0
47803	1,0003	2,9921	0
47806	1,0000	0,0000	0
47807	1,0000	0,0000	0
47809	1,0000	0,0000	0
47810	1,0000	0,3871	0
47812	1,0000	0,0000	0
47817	1,0000	0,0000	0
47836	1,0001	1,0521	0
47837	1,0010	2,2238	0
47838	1,0025	5,8423	0
47857	1,0000	0,9597	1
47859	1,0001	1,2523	0
47861	1,0004	2,1255	0
47867	1,0019	3,7142	0
47868	1,0004	3,6018	0
47869	1,0002	2,5936	0
47870	1,0004	2,3328	0
47871	1,0004	1,7054	0
47872	1,0000	0,0000	0
47873	1,0000	0,0000	0
48397	1,0029	6,2192	1
48398	1,0015	4,0222	0
48399	1,0010	4,3559	0
48401	1,0018	5,0393	0
48402	1,0009	3,5999	1
48996	1,0001	1,3308	0
49403	1,0000	0,1608	0
49407	1,0000	0,6267	0
49408	1,0000	1,3361	1
49409	1,0000	0,0000	0
49410	1,0000	0,1560	0
49411	1,0000	0,0000	0
49412	1,0000	0,0000	0
49413	1,0041	5,6181	0
49414	1,0000	0,6943	0
49415	1,0000	0,0000	0
49416	1,0000	0,7796	0
49417	1,0000	1,7138	0
49418	1,0000	0,0000	0
49419	1,0000	0,5348	0
49465	1,0000	0,7505	0

49625	1,0000	0,0000	0
49626	1,0000	0,0000	0
49628	1,0000	0,3869	0
49629	1,0002	2,5192	0
49631	1,0000	0,0000	0
49632	1,0000	0,0000	0
49634	1,0090	14,7350	1
49635	1,0054	5,8597	0
49636	1,0133	18,5149	0
49640	1,0050	7,4061	0
49647	1,0296	9,5938	1
49648	1,0418	13,6544	0
49878	1,0000	0,0000	0
49879	1,0000	0,1681	0
49881	1,0000	0,0000	0
49882	1,0000	0,8177	0
49884	1,0065	4,9294	2
49889	1,0184	13,2021	0
49917	1,0000	0,8545	0
50159	1,0000	0,0728	1
50163	1,0000	1,3953	0
50165	1,0000	0,2136	0
50166	1,0000	0,8963	0
50171	1,0090	6,0145	2
50172	1,0002	1,7517	0
50173	1,0083	8,1341	1
50188	1,0000	0,0000	0
50189	1,0000	0,0000	0
50190	1,0000	0,0000	0
50191	1,0001	1,6910	0
50355	1,0072	6,0285	0
50361	1,1151	11,7960	0
50362	1,0007	1,6193	0
50363	1,0004	2,4037	0
50364	1,0013	4,0881	0
50369	1,0043	4,4932	1
50471	1,0000	0,0000	0
50651	1,0008	5,2070	0
50652	1,0005	1,2627	0
50757	1,2505	23,0114	0
50758	1,0000	0,0000	0
50869	1,0003	1,3559	1
50872	1,0049	6,5493	0

50948	1,0000	0,5080	0
50949	1,0000	1,0549	0
50950	1,0000	0,0000	0
50951	1,0000	0,0000	0
50952	1,0000	0,0000	0
50953	1,0000	0,0000	0
50954	1,0000	0,3450	0
50955	1,0000	0,0000	0
50956	1,0000	0,9497	1
50957	1,0001	0,8584	0
50958	1,0000	0,0000	0
50959	1,0000	0,0000	0
50960	1,0000	0,0000	0
50961	1,0001	1,3233	0
50962	1,0000	0,0000	0
50964	4,4891	34,2597	2
52115	1,0000	0,5834	0
52120	1,0052	11,3984	1
52126	1,0083	6,2973	0
52134	1,0001	1,7973	0
52492	1,0218	4,1655	2
52636	1,0000	0,0554	1
52639	1,0000	0,7041	0
53115	2,4902	15,8092	0
53116	1,5374	20,0336	0
53121	1,0000	0,0000	0
53122	1,0000	0,0000	0
53123	1,0000	0,0000	0
53124	1,0000	0,0000	0
53125	1,0000	0,0000	0
53126	1,0013	2,3341	0
53127	1,0001	1,3555	0
53414	1,0000	0,0000	0
53415	1,0000	0,0000	0
53416	1,0000	0,0000	0
53737	1,0000	0,0000	0
53742	1,0000	0,0000	0
53743	1,0000	0,0000	0
53757	1,0000	0,0000	0
53758	1,0000	0,0000	0
53764	1,0000	0,0000	0
53765	1,0000	0,0000	0
53766	1,0000	0,0000	0

53767	1,0000	0,0509	0
53772	1,0140	11,2606	0
53773	1,0038	6,0596	0
73086	1,0031	3,0938	1
73087	1,0379	6,5151	0
73196	1,0656	11,1679	3
73197	1,0031	10,0326	0
73488	1,0000	0,0000	0
73493	1,0001	2,0314	0
73784	1,0000	0,0000	0
73785	1,0000	0,0000	0
73786	1,0000	0,0000	0
73796	1,0000	0,0080	1
73977	1,0000	0,0000	0
74036	1,0002	3,2949	0
74434	1,0016	2,0946	2
74435	1,0001	2,2180	0
74467	1,0000	1,7389	0
74468	1,0001	2,0605	0
74469	1,0001	1,3714	1
74503	1,0000	0,0000	0
74565	1,0000	0,0069	0
74566	1,0000	0,0025	0
74611	1,0003	3,7007	0
74746	2,6256	10,7828	0
74773	1,0000	0,0625	0
74774	1,0000	0,0000	0
74776	5,8619	18,0839	0
74778	1,0000	0,0000	0
74779	1,0007	3,4268	0
74786	1,0000	0,0000	0
74787	1,0000	0,0000	0
74816	1,0008	4,6609	0
74964	1,0006	3,5512	1
75074	1,4187	89,9999	0
75082	1,0023	8,0741	1
75083	1,0000	0,0000	0
75104	1,0157	9,6798	2
75131	1,0012	5,7804	0
75132	1,0000	0,0000	0
75134	1,3852	15,6783	0
75135	1,0000	0,0000	0
75159	0,0000	15,1804	0
75165	1,0003	6,3474	0
75166	1,0000	0,9276	0
75167	1,0007	5,4394	1
75168	1,0018	5,1502	0
75169	1,0003	1,5436	0
75170	1,0008	3,2671	1
75171	1,0021	4,8932	0
75179	1,0025	3,8693	0
75185	1,0000	0,7144	0
75186	1,0000	0,0000	0
75202	1,0019	5,6362	0
75203	1,0000	0,6076	0
75207	0,0000	16,7716	0
75209	1,0078	14,8071	0
75228	1,0233	14,5063	0
75245	1,0000	0,0000	0
75247	1,0083	15,9772	0
75249	1,0037	3,4114	1
75262	1,0000	1,1790	0
75266	1,0013	6,5397	0
75282	1,0001	1,2036	0
75283	1,0036	5,7941	0
75312	1,0002	2,7882	0
75353	1,0084	18,6439	0
75355	1,0293	17,3084	0
75409	1,0385	8,2376	0
75410	1,0124	12,0920	1
75412	1,0001	1,1969	0
75651	1,0069	6,2874	0
75790	1,0000	0,0013	0
75793	1,0000	0,9290	0
75795	1,0001	2,1096	0
75797	1,0001	1,5411	0
75803	1,0000	0,7249	0
75876	1,0000	0,0000	0
98166	1,0000	0,0000	0
98704	1,0000	0,0000	0
104096	1,4225	16,4259	0
104097	2,1620	17,9136	1
104098	1,5522	16,0299	0
104121	1,0091	4,6764	0
104122	1,0029	4,0203	2
104123	1,0013	5,8422	0

104251	1,0508	15,7129	0
104254	1,0003	2,4103	2
104255	1,0002	2,7707	2
104256	1,0002	1,9508	2
104257	1,0107	5,5346	0
104258	1,0007	11,9713	0
104264	1,0147	6,5946	0
104270	1,0134	11,3633	0
104273	1,0000	0,9323	0
104274	1,0000	0,0000	0
104275	1,0000	0,0000	0
104276	1,0000	0,0704	0
104277	1,0052	5,7404	0
104279	1,0020	6,3038	1
104280	1,0000	0,0000	0
104281	1,0000	0,7621	0
104282	1,0000	0,0000	0
104283	1,0000	0,0000	0
104284	1,0000	0,0000	0
104285	1,0000	0,1388	0
104286	1,0105	9,1572	0
104287	1,0226	4,6616	2
104288	1,0000	0,0000	0
104289	1,0000	0,0000	0
104290	1,0000	0,5850	0
104291	1,0003	3,2544	0
104297	1,0127	10,3935	0
104305	1,0134	6,1880	0
104315	1,0003	1,6435	0
104323	0,0000	13,2616	0
104331	1,0000	0,8312	1
104338	1,0040	3,3043	0
104339	1,0002	1,3428	1
104340	1,0024	7,4067	1
104341	1,0000	0,0000	0
104364	1,1627	20,4211	1
104367	1,0033	5,7120	0
104419	1,0482	18,5981	0
104488	1,0364	20,5222	1
104507	1,0403	29,0955	0
104519	1,0000	0,0000	0
104800	1,0424	14,1823	0
104806	1,0913	21,2859	0

104817	1,0000	0,0000	0
105945	1,0009	2,7117	1
108283	1,0036	12,8132	0
108284	1,0386	9,8847	0
108286	1,0793	13,2859	0
108643	1,0119	5,4519	0
108923	1,0000	1,5165	0
113312	1,0000	0,2702	0
124202	1,0000	0,0000	0
124204	1,0000	0,1990	0
128000	1,0000	0,0000	0
128382	1,0121	2,8570	0
128383	1,0017	2,6698	1
128384	1,0023	3,1348	0
128385	1,0000	0,0000	0
128386	1,0000	0,2108	0
128387	1,0000	0,3506	0
128388	1,0000	0,0000	0
128389	1,0000	0,2696	0
128390	1,0000	0,0000	0
128391	1,0000	0,4183	0
128392	1,0006	4,6353	0
128393	1,0026	4,8959	0
128394	1,0000	0,0000	0
128395	1,0019	7,4192	0
128400	2,2247	10,3787	0
128401	1,0954	8,7447	0
128404	4,1155	43,0515	1
129522	1,0000	0,0000	0
137892	1,0000	0,0000	0
137894	1,6652	16,0898	2
137922	1,0000	0,0000	0
137925	1,0013	9,9458	0
137927	1,0000	0,0000	0
137929	1,1109	9,3501	2
137930	1,0146	8,0113	0
137937	1,0908	10,4686	0
137938	1,0000	0,0000	0
137941	1,0000	0,0000	0
137947	1,1412	11,7280	0
137951	1,0220	9,9706	0
137952	1,0814	14,9638	0
137961	1,1102	9,6009	0

137962	1,0000	0,0000	0
138361	1,0000	0,0000	0
138376	1,0000	0,0000	0
138378	1,0001	1,9409	0
138380	1,0000	2,9906	0
138381	1,0000	0,0021	0
138382	1,0000	0,0000	0
138384	1,0000	0,0295	1
138388	1,0000	0,0000	0
138389	1,0000	0,0000	0
138390	1,0012	5,6122	0
138391	1,0002	1,3868	0
138392	1,0022	2,8087	0
138393	1,0001	2,1494	0
138505	1,2584	57,8818	1
138629	1,1350	35,1678	0
138640	1,0000	0,0000	0
138664	1,0104	23,6641	1
138665	1,0611	27,1925	2
138666	1,0247	34,4152	0
138978	1,0137	10,9965	1
139254	1,5240	98,5372	0
139255	1,0000	0,5848	1
139256	1,0214	13,5340	0
139354	2,7591	14,2764	0
139355	1,0897	11,3591	0
139356	1,0193	5,2192	2
139357	1,0000	0,0000	0
139359	1,0000	0,0000	0
139360	1,0000	0,2862	0
139361	1,0000	0,0000	0
139362	1,0000	0,0000	0
139363	1,0000	0,5597	0
139365	1,0000	0,0000	0
139366	1,0000	0,0000	0
139376	1,0142	8,4652	1
139377	1,0059	8,7730	0
139382	1,0168	6,9406	3
139557	1,0444	10,8764	0
139560	1,2193	13,7240	0
139561	1,0053	6,6688	1
139567	1,0002	1,4655	0
139568	1,0006	4,2544	0
139571	1,0011	3,4565	0
139671	1,0000	0,0000	0
141214	1,0023	4,7184	0
141215	0,0000	12,4574	0
141216	1,0000	0,6396	0
141217	1,0000	0,4587	1
141218	1,0000	0,0000	0
141219	1,0000	0,0000	0
141220	1,0029	5,3672	0
141222	1,0036	5,9617	0
141223	1,0013	3,6167	0
141224	1,0087	6,5314	0
141233	1,0000	0,4280	0
141234	1,0000	0,0443	0
141235	1,0000	0,1030	0
141236	1,0000	0,5588	0
141237	1,0000	0,5685	2
141238	1,0000	0,0000	0
141240	1,0209	4,5817	3
141241	1,0000	0,0012	0
141242	1,0000	0,2302	0
141243	1,0000	0,0061	0
141244	1,0139	7,1180	0
141245	1,0031	4,2358	2
141246	1,0320	10,8306	3
141247	1,0288	9,6839	0
141248	4,3624	10,7971	0
141249	1,0631	11,8976	0
141250	1,0000	0,0000	0
141251	8,5717	14,1155	0
141252	1,0136	8,9403	0
141253	1,0450	9,4997	2
141254	1,0000	0,0065	0
141255	1,0091	4,6680	2
141256	1,0001	1,5733	3
141257	1,0000	0,4625	0
141258	1,0000	0,4043	1
141259	1,0000	0,0000	0
141261	1,0061	5,5964	0
141262	1,0094	7,0137	0
141263	1,0000	0,0000	0
141265	1,0350	10,5549	0
141266	1,0000	0,5536	0

141267	1,0044	6,6236	2
141270	1,0109	9,1394	1
141303	1,0004	2,3882	1
141304	1,0000	0,0000	0
141308	1,0016	6,0321	2
141309	1,0407	8,0952	0
141310	1,0228	15,0508	0
141323	1,0000	0,0000	0
141324	1,0000	0,1911	0
141325	1,0315	5,8010	4
141326	1,0145	6,7144	2
141327	1,0000	0,0000	0
141340	1,0000	0,0000	0
141342	1,0008	2,9413	1
141367	1,0183	5,3145	1
141379	1,0241	15,2196	0
141380	1,0028	5,1991	0
141386	1,0608	14,9991	0
141413	1,0051	7,3882	0
141416	1,0102	4,6463	1
141419	1,0334	6,0448	1
141421	1,0005	3,1791	1
141422	1,0000	0,0000	0
141423	1,0041	5,2534	0
141424	1,0001	1,2498	0
141425	1,0000	1,7526	2
141426	1,0000	1,0961	0
141462	1,0004	3,9136	2
141476	1,0046	5,9395	5
141477	1,0001	1,9034	1
141478	1,0580	11,4479	0
141479	1,0000	0,2656	3
141480	1,0012	1,8351	4
141481	1,0035	4,4263	1
141482	1,0038	5,1026	0
141493	1,0005	1,3823	0
141494	1,0000	0,0000	0
141495	1,0000	0,0000	0
141498	1,0030	6,0800	0
141499	1,0249	10,5107	1
141500	0,0000	13,7240	0
141501	0,0000	16,3814	0
141502	1,0024	7,3996	1
141512	1,0038	3,7700	3
141513	1,0006	2,7053	1
141518	1,1831	14,9105	3
141528	1,0004	2,0564	0
141539	1,0000	0,0000	0
141547	1,0137	8,8227	1
141559	1,0116	7,2631	1
141564	1,0003	3,4457	0
141569	1,0000	0,0163	0
141570	1,0000	0,3556	3
141572	1,0045	3,2842	0
141573	1,0047	3,8399	0
141574	1,0007	1,8871	0
141586	1,0118	11,4978	0
141587	1,0049	5,4120	1
141588	1,0033	5,9266	1
141589	1,0004	2,6484	2
141590	1,0000	0,7076	0
141591	1,0169	16,3043	1
141595	1,0123	4,3557	0
141597	1,0082	14,8616	0
141598	1,0000	0,8056	2
141599	1,0010	6,5789	1
141600	1,0002	0,7821	0
141636	1,0000	0,0000	0
141647	1,0011	3,1820	0
141648	0,0000	16,5262	0
141649	1,0001	0,4668	3
141650	1,0000	0,7911	3
141651	1,0000	0,2280	1
141652	1,0000	0,0271	2
141653	1,0000	0,0944	0
141654	1,0002	1,4114	3
141655	1,0019	4,2086	1
141656	1,0000	0,0681	0
141684	1,0036	5,8404	0
141687	1,0187	9,2650	1
141688	1,0081	17,6631	0
141696	1,0046	9,0863	1
141697	1,0000	0,0000	0
141703	1,0015	6,5164	0
141731	1,0028	3,1988	3
141732	1,0008	3,1541	0

141734	1,0017	1,5071	0
141735	1,0000	0,0000	0
141780	1,0042	6,4464	0
141781	1,0061	7,7120	0
141819	1,0061	18,0230	0
141820	1,0017	4,0385	0
141823	1,0000	0,0000	0
141824	1,0002	1,6498	0
141825	1,0005	1,6195	0
141826	1,0061	2,3598	0
141833	1,0011	3,5583	0
141881	1,0224	5,3262	0
141882	1,0141	4,1501	1
141947	1,3692	18,5466	0
141949	1,0158	21,0123	0
141950	1,0797	18,8946	0
141953	1,0000	0,0000	0
141975	1,0101	12,2659	1
141976	1,0007	1,6680	1
141982	1,0746	15,0955	1
142002	1,0072	20,7638	0
142007	1,0000	0,0000	0
142008	1,0273	2,8306	0
142009	1,0013	1,9101	0
142010	1,0002	0,9152	0
142011	1,0038	2,9205	0
142027	1,0209	9,9771	0
142043	1,0087	3,5846	0
142046	1,0021	18,5996	1
142051	1,0007	2,1706	0
142052	1,0009	2,9455	1
142055	1,2078	16,3110	0
142061	1,0000	0,4938	0
142062	1,0003	3,0560	0
142069	1,0486	19,7470	1
142073	1,0456	13,9873	2
142083	1,1463	24,4088	1
142093	1,0016	2,3281	1
142094	0,0000	24,6986	1
142100	1,0000	0,0000	0
142101	1,0000	0,0000	0
142102	1,0001	1,5232	0
142103	1,0458	13,0321	1
142104	1,0807	13,6578	1
142105	1,0262	10,4898	1
142107	1,0151	8,7987	0
142108	1,0021	2,2825	1
142109	1,0052	3,2126	0
142110	1,0014	3,1474	0
142117	1,0074	10,9549	1
142119	1,0062	8,0312	2
142120	1,0027	2,3677	1
142121	1,3919	24,8614	0
142122	1,0000	0,0000	0
142123	1,0000	0,0000	0
142125	1,0597	17,3592	0
142135	1,0000	0,0000	0
142136	1,0041	6,2310	0
142137	1,0049	7,8074	0
142146	1,0010	2,0028	1
142179	1,0038	10,8659	0
142246	1,0917	28,9755	1
142247	1,0001	0,5080	1
142248	1,0054	3,0336	3
142249	1,4927	15,8857	2
142250	1,0411	11,9179	1
142261	1,0478	7,4658	2
142262	1,0582	8,9466	0
142263	1,0004	2,6782	1
142264	1,0004	3,1917	0
142265	1,0150	7,8340	0
142267	1,0187	4,7286	2
142268	1,0179	5,0326	5
142269	1,0248	7,3093	3
142270	1,0262	4,6325	2
142271	1,0059	2,2683	2
142272	1,0000	0,0000	0
142273	1,0045	3,6802	0
142274	1,0001	0,9722	2
142275	1,0035	3,0287	2
142276	1,0028	4,1844	2
142277	1,0011	2,3636	0
142320	1,0128	12,6268	0
142322	1,0047	11,3054	0
142329	1,0051	2,8115	2
142330	1,0016	2,2734	0

142331	1,0082	1,7238	0
142345	1,0257	14,8631	0
142379	1,0150	8,8478	1
142383	1,0102	23,5212	0
142392	1,2622	45,8585	1
142565	1,0232	10,8901	0
142566	1,0179	7,5792	0
142567	1,0062	5,5623	1
142568	1,0216	11,6577	1
142569	1,0005	3,6902	0
142570	1,0000	1,1464	0
142660	1,0000	0,0000	0
142661	1,0047	5,3554	0
142662	1,0225	14,2633	0
142732	1,0443	13,3846	0
142751	1,0000	0,0000	0
142752	1,0000	0,0000	0
142753	0,0000	15,8324	0
142754	1,0041	6,4003	0
142755	1,0051	6,9927	1
142756	1,0013	3,4994	2
142757	1,0240	9,9971	0
142760	1,0007	2,4904	0
142761	1,0066	5,4319	1
142764	1,0060	5,1023	0
142792	1,0099	7,2429	2
142960	1,0000	0,0000	0
142961	1,0282	20,0734	0
143110	1,0000	0,0000	0
143111	1,0000	0,0000	0
143113	1,0563	20,3970	0
143141	1,0133	7,9354	2
143147	1,3900	28,0866	2
143148	1,0686	22,6862	0
143167	1,0048	5,6708	0
143168	1,0000	0,0000	0
143169	1,0002	2,2274	0
143170	1,0001	0,8915	1
143172	1,3344	18,4369	0
143809	1,0000	0,0000	0
143931	0,0000	20,7008	2
143932	1,0020	9,8245	0
143935	1,0008	4,5614	0

150269	1,0000	0,0000	0
150357	1,0440	17,9430	1
150375	1,0019	5,1425	0
150561	1,2287	39,3411	0
151919	1,1634	48,3548	0
151920	1,0227	15,8516	0
153201	1,1114	41,3918	0
153202	1,0175	11,0674	0
153666	1,0000	0,0000	0
154289	1,0009	3,1370	0
154290	1,0003	1,8409	0
154291	1,0005	2,2974	0
154292	1,0003	1,2353	0
154293	1,0000	0,3261	0
154294	1,0000	0,0000	0
154295	1,0000	0,0000	0
154296	1,0000	0,0000	0
154297	1,0000	0,0000	0
154299	1,0000	0,0000	0
154300	1,0000	0,1759	0
154301	1,0001	1,4298	0
154302	1,0009	2,3723	0
154303	1,0016	2,8628	0
154304	1,0037	5,2259	0
154305	1,0004	4,4428	0
154332	1,0148	11,3096	0
154424	1,0000	0,0000	0
154425	1,0448	59,1741	1
154457	1,0000	0,0000	0
154508	1,0026	12,1190	0
154509	1,0015	10,0479	0
154511	1,1886	12,5959	2
154606	1,0179	13,1444	0
154607	3,0244	12,6818	0
154609	1,0000	1,1897	0
154610	1,0000	0,0000	0
154611	1,0000	0,0000	0
154614	1,0000	0,0000	0
154618	1,0000	0,0000	0
154622	1,0010	2,9395	0
154626	1,0051	6,6657	0
154627	1,0112	10,9910	1
154628	2,9956	12,6891	0

154629	1,0986	13,7990	0
154630	1,0000	0,0000	0
154631	1,0012	5,8602	0
154632	1,0005	2,0757	0
154633	1,0003	2,7718	0
156696	8,5941	39,7933	1
157772	1,1796	34,2106	2
158218	1,2742	27,4324	0
158482	1,0000	0,0000	0
158505	1,0404	24,3539	1
158507	1,0331	28,8631	1
158508	1,0000	0,0000	0
158509	1,0000	0,0000	0
159063	1,0074	7,6448	0
164959	0,0000	17,2093	4
165127	1,0000	0,8428	0
165131	1,0001	0,6738	1
165133	1,0007	2,2580	1
165134	1,0161	11,0097	0
165136	1,0001	1,7736	0
165138	1,0029	8,7959	0
165139	1,0000	0,0000	0
166560	1,0009	4,7536	0
166590	1,0007	4,6545	0
166595	1,0011	2,9887	1
166596	1,0001	0,4377	3
166598	1,0021	3,5687	1
166600	1,0001	1,6480	0
166608	1,0002	2,4000	1
166609	1,0000	1,2049	0
166611	1,0017	4,6799	0
166866	1,0000	0,0000	0
166873	1,0000	0,0000	0
166875	1,0000	0,4843	0
166876	1,0003	2,3459	3
166903	1,5445	13,6272	0
166909	1,0064	4,8645	0
167718	1,0229	7,2321	1
168140	1,0060	3,8900	1
168407	1,0000	0,0000	0
168441	1,0095	3,7616	0
168494	1,0122	20,7893	0
168506	1,0657	6,6522	1
168556	1,0000	0,0000	0
168559	1,0000	0,0000	0
168757	1,3912	11,0473	0
168783	1,0000	0,0000	0
168784	1,0000	0,0000	0
177933	1,0008	5,3780	0
188544	1,0000	0,0000	0
188776	1,3434	24,1239	0
188777	1,0000	0,0000	0
188810	1,0088	49,1901	0
188811	1,3663	24,2018	1
188947	1,0000	0,0000	0

Table 24 – Dataset of sub-indices

segment_id	S_long	S_trans	S_dep_set	S_poth_rough	S_bumps	S_min_dep
1223	0,0000	0,0000	0,0000	0,7986	0,0000	0,6750
1224	0,0000	0,7219	0,1000	0,1000	0,6750	0,0000
1245	0,6948	0,0000	0,0000	0,0000	0,0000	0,6750
1367	0,5485	0,6257	0,6873	0,0000	0,0000	0,9000
1523	0,0000	0,6497	0,0000	0,0000	0,0000	0,0000
1593	0,0000	0,7161	0,0500	0,0000	0,0000	0,4500
1594	0,0000	0,9385	0,0000	0,0000	0,6750	0,0000
1614	0,0000	0,5920	0,0000	0,0000	0,4500	0,0000
2957	0,5485	0,0000	0,0500	0,0000	0,0000	0,0000
2960	0,7720	0,0000	0,0000	0,0000	0,0000	0,0000
2964	0,8313	0,0000	0,7570	0,1000	0,0000	0,6750
2969	0,7964	0,0000	0,0000	0,0000	0,0000	0,0000
2973	0,9240	0,0000	0,0000	0,0500	0,0000	0,0000
2984	0,6635	0,0000	0,1000	0,0000	0,4500	0,0000
3010	0,0000	0,3850	0,0000	0,6628	0,0000	0,0000
3011	0,2926	0,0000	0,0000	0,0500	0,6750	0,0000
3013	0,5242	0,0000	0,0000	0,1000	0,0000	0,0000
3016	0,5144	0,0000	0,0000	0,0000	0,0000	0,0000
3020	0,5181	0,5342	0,3728	0,0000	0,2250	0,0000
3021	0,0000	0,0000	0,4335	0,0000	0,0000	0,0000
3022	0,0000	0,0000	0,6861	0,0000	0,0000	0,0000
3023	0,2682	0,0000	0,0000	0,0000	0,0000	0,9000
3121	0,0000	0,3898	0,4302	0,4213	0,2250	0,0000
3161	0,4754	0,5198	0,7380	0,0000	0,0000	0,0000
3164	0,3007	0,0000	0,1000	0,6731	0,0000	0,0000
3165	0,2682	0,3321	0,0500	0,0000	0,0000	0,0000
3180	0,5729	0,0000	0,0000	0,0000	0,0000	0,9000
3181	0,6339	0,0000	0,0000	0,5219	0,0000	0,0000
3182	0,3047	0,6100	0,5241	0,8344	0,0000	0,0000
3186	0,3291	0,5111	0,5057	0,1000	0,0000	0,0000
3187	0,4851	0,5775	0,4085	0,7533	0,2250	0,0000
3190	0,3535	0,5005	0,4854	0,2713	0,0000	0,0000
3202	0,3169	0,8085	0,3633	0,1000	0,6750	0,0000
3214	0,5760	0,6642	0,0000	0,7433	0,0000	0,2250
3215	0,0000	0,6353	0,1000	0,7131	0,0000	0,4500
3273	0,9020	0,0000	0,1000	0,0000	0,0000	0,0000
3279	0,4876	0,0000	0,0000	0,7838	0,4500	0,0000
3333	0,0000	0,8952	0,1000	0,0500	0,0000	0,0000
3335	0,0000	0,7508	0,0000	0,0000	0,0000	0,0000
3337	0,0000	0,0000	0,0000	0,8338	0,0000	0,0000
3338	0,6339	0,6136	0,0000	0,8187	0,0000	0,2250
3348	0,0000	0,5342	0,0000	0,0000	0,6750	0,2250
3352	0,4673	0,0000	0,3728	0,0500	0,4500	0,0000
3356	0,2743	0,0000	0,1513	0,2506	0,0000	0,2250
3417	0,0000	0,0000	0,0000	0,4219	0,0000	0,6750
3418	0,3657	0,0000	0,6475	0,0000	0,0000	0,0000
3431	0,7253	0,0000	0,3234	0,1000	0,0000	0,2250

3468	0,4266	0,0000	0,0500	0,0000	0,4500	0,0000
3478	0,7679	0,0000	0,1000	0,0000	0,0000	0,0000
3479	0,2804	0,3032	0,5129	0,7137	0,0000	0,0000
3495	0,0000	0,0000	0,8127	0,8246	0,0000	0,0000
3496	0,0000	0,0000	0,6266	0,0000	0,0000	0,0000
3520	0,4876	0,0000	0,0000	0,0000	0,0000	0,0000
3605	0,6278	0,0000	0,0000	0,6500	0,2250	0,0000
3606	0,8228	0,0000	0,0000	0,0000	0,0000	0,0000
3608	0,0000	0,0000	0,5956	0,0000	0,0000	0,0000
3614	0,5302	0,0000	0,0500	0,0000	0,0000	0,0000
3615	0,9142	0,0000	0,0000	0,0000	0,0000	0,0000
3616	0,6460	0,0000	0,1000	0,0500	0,0000	0,0000
3666	0,9264	0,0000	0,0000	0,7058	0,0000	0,0000
3667	0,6064	0,0000	0,0000	0,8439	0,6750	0,9000
3709	0,4876	0,0000	0,5652	0,0000	0,4500	0,0000
3710	0,7029	0,0000	0,0000	0,7838	0,0000	0,0000
3712	0,3352	0,0000	0,4956	0,1000	0,0000	0,0000
3713	0,3169	0,0000	0,3987	0,4571	0,2250	0,0000
3714	0,6460	0,0000	0,1000	0,5924	0,0000	0,6750
3721	0,3291	0,0000	0,0000	0,1000	0,2250	0,9000
3724	0,0000	0,0000	0,4228	0,4817	0,9000	0,0000
3727	0,3535	0,3754	0,3538	0,7030	0,0000	0,4500
3728	0,4413	0,0000	0,1000	0,4770	0,0000	0,2250
3729	0,2926	0,0000	0,0000	0,0000	0,0000	0,0000
3730	0,2682	0,0000	0,1000	0,0000	0,0000	0,0000
3885	0,3866	0,5198	0,5241	0,5904	0,0000	0,0000
3899	0,4036	0,3826	0,6266	0,2814	0,0000	0,9000

3900	0,0000	0,0000	0,0000	0,8948	0,0000	0,6750
3901	0,0000	0,4332	0,4228	0,6728	0,0000	0,9000
3902	0,0000	0,0000	0,1000	0,4216	0,0000	0,0000
3936	0,2804	0,0000	0,4430	0,0500	0,0000	0,2250
3955	0,6582	0,0000	0,6456	0,0000	0,0000	0,0000
3972	0,8463	0,7219	0,0000	0,7714	0,0000	0,4500
3973	0,6643	0,7941	0,6867	0,7198	0,0000	0,0000
3974	0,0000	0,0000	0,0500	0,8140	0,6750	0,0000
3975	0,7005	0,0000	0,8127	0,6030	0,0000	0,4500
3976	0,7537	0,6738	0,1000	0,7285	0,2250	0,0000
4032	0,8533	0,0000	0,0000	0,0000	0,4500	0,9000
4033	0,6826	0,0000	0,1000	0,0000	0,0000	0,2250
4041	0,8837	0,0000	0,0000	0,5225	0,0000	0,2250
4066	0,9142	0,0000	0,1000	0,0000	0,0000	0,0000
4072	0,5394	0,0000	0,0000	0,0000	0,0000	0,4500
4073	0,8914	0,0000	0,0500	0,0000	0,0000	0,0000
4074	0,8086	0,0000	0,0000	0,0000	0,2250	0,2250
4075	0,6278	0,0000	0,0000	0,3314	0,0000	0,0000
4076	0,6034	1,0000	0,1000	0,3216	0,4500	0,9000
4077	0,0000	0,0000	0,6165	0,9146	0,6750	0,0000
4078	0,7436	0,0000	0,0000	0,0000	0,4500	0,6750
4080	0,5485	0,3032	0,0000	0,0000	0,4500	0,0000
4081	0,5363	0,0000	0,1000	0,0000	0,0000	0,0000
4082	0,5363	0,0000	0,0000	0,0000	0,0000	0,0000
4087	0,5120	0,7219	0,1000	0,0000	0,0000	0,0000
4088	0,7192	0,0000	0,0000	0,0500	0,0000	0,9000
4089	0,4957	0,0000	0,0000	0,4015	0,9000	0,0000

4113	0,2621	0,0000	0,3504	0,0000	0,0000	0,6750
4115	0,3962	0,4187	0,3722	0,0000	0,6750	0,2250
4116	0,5964	0,3112	0,2677	0,3210	0,4500	0,6750
4117	0,2451	0,0000	0,5348	0,0000	0,0000	0,0000
4121	0,0000	0,0000	0,1000	0,3613	0,0000	0,0000
4125	0,4541	0,0000	0,1000	0,1000	0,6750	0,9000
4137	0,5729	0,0000	0,0000	0,5829	0,0000	0,0000
4138	0,6963	0,0000	0,1000	0,0000	0,2250	0,0000
4139	0,8533	0,7797	0,6563	0,0000	0,0000	0,0000
4255	0,4754	0,0000	0,3133	0,3867	0,0000	0,6750
4256	0,4510	0,4620	0,5747	0,5242	0,6750	0,0000
4257	0,3007	0,0000	0,5646	0,6835	0,0000	0,0000
4297	0,2438	0,5631	0,0500	0,4921	0,0000	0,0000
4360	0,3291	0,0000	0,0500	0,0000	0,0000	0,2250
4579	0,5607	0,3321	0,4382	0,7039	0,6750	0,0000
4580	0,4023	0,0000	0,0500	0,0000	0,0000	0,0000
4591	0,7000	0,0000	0,0000	0,5994	0,0000	0,0000
4625	0,7247	0,6786	0,0000	0,7734	0,0000	0,0000
4656	0,5587	0,6136	0,4470	0,0000	0,0000	0,2250
4657	0,4510	0,4620	0,0000	0,0500	0,0000	0,0000
4658	0,5201	0,4909	0,7886	0,6433	0,0000	0,0000
4660	0,5026	0,3634	0,0000	0,1000	0,0000	0,0000
4661	0,4693	0,4187	0,7994	0,0000	0,0000	0,0000
4663	0,5729	0,4548	0,5219	0,0000	0,0000	0,0000
4664	0,3291	0,0000	0,0000	0,0000	0,4500	0,0000
4701	0,6308	0,0000	0,1000	0,0000	0,0000	0,2250
4702	0,5953	0,0000	0,0000	0,0000	0,0000	0,0000
4703	0,7338	0,0000	0,7930	0,8240	0,0000	0,9000
4785	0,0000	0,8519	0,0000	0,5320	0,2250	0,0000
4786	0,2986	0,0000	0,0000	0,1000	0,6750	0,0000
4794	0,5866	0,0000	0,0500	0,3710	0,9000	0,0000
4845	0,4339	0,3176	0,0000	0,1000	0,0000	0,2250
4846	0,3596	0,0000	0,0000	0,0000	0,0000	0,0000
4847	0,4063	0,3610	0,0000	0,5430	0,0000	0,0000
4858	0,6034	0,0000	0,0000	0,6829	0,2250	0,0000
4861	0,6460	0,0000	0,0000	0,8640	0,2250	0,0000
4974	0,8175	0,8085	0,0500	0,8237	0,6750	0,0000
4995	1,0000	0,8085	0,6103	0,5731	0,0000	0,0000
4996	1,0000	0,9770	0,5057	0,6099	0,0000	0,2250
4997	0,8898	0,3610	0,4335	0,5286	0,0000	0,0000
4998	0,7619	1,0000	0,0000	0,3982	0,0000	0,9000
4999	1,0000	0,6208	0,0500	0,1000	0,0000	0,0000
5060	0,5892	0,0000	0,0000	0,1000	0,0000	0,0000
5062	0,4548	0,3032	0,1000	0,0000	0,4500	0,0000
5063	0,3698	0,0000	0,1000	0,4719	0,4500	0,0000
5064	0,4327	0,1444	0,0000	0,0000	0,2250	0,0000
5065	0,0000	0,3898	0,0000	0,6436	0,0000	0,0000
5066	0,4327	0,0000	0,0000	0,1000	0,4500	0,0000
5067	0,0000	0,3393	0,0000	0,3610	0,0000	0,2250
5070	0,8655	0,0000	0,0000	0,0000	0,0000	0,0000
5080	0,0000	0,3032	0,0000	0,3418	0,0000	0,0000
5081	0,4754	0,4187	0,7306	0,6885	0,0000	0,0000
5205	0,3901	0,0000	0,0000	0,0000	0,2250	0,0000
5210	0,3291	0,0000	0,4703	0,0000	0,0000	0,0000

5296	0,6948	0,0000	0,0000	0,1000	0,6750	0,0000
5317	0,2926	0,0000	0,0000	0,0000	0,0000	0,0000
5320	0,4364	0,0000	0,0000	0,0000	0,0000	0,0000
5321	0,6095	0,0000	0,0000	0,0000	0,0000	0,0000
5322	0,8898	0,0000	0,1000	0,0000	0,9000	0,0000
5323	0,7094	0,0000	0,0000	0,0000	0,0000	0,0000
5598	0,0000	0,0000	0,0500	0,2512	0,2250	0,2250
5724	0,0000	0,0000	0,8892	0,3713	0,0000	0,0000
5725	0,4963	0,5053	0,3734	0,6866	0,9000	0,0000
5727	0,2560	0,0000	0,0000	0,1000	0,4500	0,0000
5732	0,3901	0,0000	0,0000	0,0000	0,0000	0,0000
5747	0,5607	0,0000	0,0000	0,0000	0,0000	0,0000
5748	0,4686	0,0000	0,4633	0,8643	0,6750	0,0000
5749	0,2926	0,4524	0,6019	0,0000	0,2250	0,4500
5785	0,4876	0,3898	0,7753	0,0000	0,6750	0,9000
5786	0,5900	0,0000	0,7003	0,6614	0,6750	0,0000
5787	0,0000	0,0000	0,0000	0,4817	0,0000	0,0000
5788	0,5022	0,4235	0,6534	0,5901	0,0000	0,0000
5789	0,5607	0,0000	0,0000	0,4927	0,0000	0,0000
5790	0,6777	0,6714	0,6468	0,7734	0,0000	0,0000
5791	0,4351	0,0000	0,6032	0,5311	0,0000	0,6750
5797	0,0000	0,0000	0,0000	0,9000	0,0000	0,0000
5804	0,4236	0,0000	0,3633	0,4616	0,0000	0,0000
5854	0,5760	0,3754	0,6086	0,4113	0,2250	0,0000
6188	0,4876	0,0000	0,0500	0,0000	0,9000	0,9000
6212	0,8777	0,0000	0,0000	0,6329	0,9000	0,0000
6217	0,7344	0,0000	0,0000	0,4625	0,0000	0,0000

6281	0,3718	0,0000	0,5949	0,3317	0,0000	0,0000
6282	0,5404	0,0000	0,0000	0,0000	0,2250	0,9000
6285	0,5973	0,0000	0,0000	0,0000	0,4500	0,0000
6355	0,0000	0,0000	0,0000	0,6580	0,0000	0,0000
6357	0,0000	0,0000	0,5462	0,1000	0,6750	0,2250
6360	1,0000	0,0000	0,1000	0,0000	0,0000	0,0000
6406	0,0000	0,0000	0,0000	0,3518	0,2250	0,2250
6471	0,8821	0,8374	0,0500	0,6737	0,0000	0,0000
6472	0,8115	0,6353	0,1000	0,1000	0,0000	0,0000
6723	0,0000	0,0000	0,0500	0,7945	0,4500	0,0000
7003	0,0000	0,0000	0,8892	0,1000	0,0000	0,0000
7004	0,0000	0,0000	0,0000	0,7338	0,0000	0,0000
7264	0,5729	0,0000	0,0000	0,1000	0,2250	0,0000
7345	0,5621	0,3610	0,0000	0,1000	0,0000	0,0000
7346	0,0000	0,0000	0,0000	1,0000	0,0000	0,0000
7565	0,5485	0,0000	0,0000	0,1000	0,0000	0,0000
8633	0,0000	0,0000	0,0000	0,8240	0,0000	0,0000
8634	0,0000	0,0000	0,4038	0,3716	0,0000	0,0000
8635	0,4510	0,0000	0,0000	0,5225	0,2250	0,0000
8636	0,0000	0,0000	0,5139	0,3971	0,4500	0,4500
8637	0,2438	0,0000	0,0000	0,0000	0,4500	0,0000
8644	0,3779	0,0000	0,0500	0,0000	0,0000	0,0000
8666	0,2011	0,4428	0,5956	0,0000	0,0000	0,4500
8702	0,3230	0,0000	0,0500	0,0000	0,0000	0,2250
8707	0,4663	0,3754	0,4228	0,0000	0,0000	0,6750
8708	0,6073	0,5703	0,3892	0,0000	0,0000	0,0000
8709	0,4851	0,5414	0,4842	0,5829	0,0000	0,0000

8777	0,5688	0,0000	0,4835	0,0000	0,4500	0,0000
8801	0,2986	0,0000	0,5051	0,0000	0,0000	0,0000
8872	0,5120	0,0000	0,0000	0,5116	0,2250	0,0000
8877	0,3352	0,3321	0,4139	0,0000	0,4500	0,0000
8878	0,3809	0,0000	0,0000	0,0000	0,0000	0,0000
8964	0,0000	0,0000	0,0000	0,5256	0,0000	0,0000
9015	0,7236	0,5920	0,1000	0,7640	0,0000	0,6750
9016	0,7342	0,0000	0,0000	0,7916	0,0000	0,0000
9017	0,7241	0,0000	0,0500	0,0500	0,0000	0,0000
9018	0,6548	0,7652	0,0000	0,0000	0,0000	0,0000
9019	0,6400	0,0000	0,0000	0,6301	0,0000	0,6750
9020	0,0000	0,0000	0,0000	0,8246	0,2250	0,0000
9021	0,5607	0,0000	0,0000	0,0000	0,9000	0,0000
9022	0,6948	0,0000	0,1000	0,0000	0,4500	0,9000
9034	0,3413	0,0000	0,0000	0,5628	0,6750	0,6750
9035	0,2560	0,0000	0,1000	0,0000	0,6750	0,0000
9036	0,4144	0,3321	0,0000	0,6329	0,0000	0,0000
9037	0,0000	0,5342	0,0000	0,3012	0,0000	0,0000
9042	0,5485	0,0000	0,4127	0,3820	0,4500	0,0000
9052	0,0000	0,0000	0,0000	0,3012	0,2250	0,0000
9164	0,4114	0,3682	0,0000	0,0500	0,0000	0,9000
9165	0,4559	0,5602	0,5274	0,0000	0,0000	0,0000
9166	0,3413	0,0000	0,0500	0,1000	0,0000	0,6750
9167	0,0000	0,0000	0,0000	0,8992	0,2250	0,2250
9168	0,0000	0,0000	0,0500	0,5776	0,0000	0,0000
9170	0,3596	0,4332	0,5968	0,5933	0,0000	0,2250
9171	0,3047	0,0000	0,0000	0,5430	0,0000	0,6750

9172	0,4053	0,0000	0,4741	0,0000	0,0000	0,6750
9173	0,4419	0,2888	0,6226	0,0000	0,9000	0,0000
9174	0,2682	0,0000	0,6304	0,6181	0,0000	0,0000
9221	0,6603	0,0000	0,0000	0,1000	0,4500	0,0000
9223	0,4998	0,0000	0,4551	0,0000	0,0000	0,0000
9224	0,8391	0,0000	0,0500	0,0000	0,0000	0,0000
9226	0,6217	0,0000	0,0000	0,0500	0,6750	0,0000
9228	1,0000	0,7219	0,0000	0,0500	0,0000	0,2250
9232	0,7801	0,0000	0,0000	0,0000	0,0000	0,0000
9235	0,6857	0,0000	0,5652	0,1000	0,0000	0,0000
9237	0,7923	0,0000	0,0500	0,0500	0,0000	0,0000
9240	0,5973	0,0000	0,0000	0,0000	0,0000	0,0000
9249	0,0000	0,0000	0,5652	0,9500	0,4500	0,0000
9261	0,2048	0,0000	0,0000	0,1000	0,0000	0,0000
9290	0,3931	0,0000	0,3032	0,5133	0,0000	0,4500
9296	0,7428	0,0000	0,7589	0,7160	0,0000	0,4500
9403	0,4632	0,3321	0,7677	0,6536	0,0000	0,0000
9407	0,6339	0,5077	0,5038	0,5504	0,0000	0,0000
9456	0,7594	0,0000	0,7589	0,0000	0,0000	0,0000
9636	0,5424	0,0000	0,1000	0,0000	0,6750	0,0000
9640	0,8373	0,7869	0,0000	0,5832	0,9000	0,0000
9685	0,3169	0,5727	0,3487	0,0000	0,0000	0,0000
9690	0,7679	0,3898	0,6266	0,0000	0,0000	0,0000
9691	0,6826	0,5342	0,0000	0,1000	0,0000	0,4500
9816	0,2682	0,0000	0,0000	0,0000	0,4500	0,0000
9863	0,8411	0,6353	0,0000	0,0500	0,9000	0,0000
9866	0,6918	0,0000	0,0000	0,7536	0,0000	0,0000

10088	0,0000	1,0000	0,0000	0,2881	0,0000	0,6750
10126	0,0000	0,0000	0,0000	0,5731	0,0000	0,0000
10183	0,4104	0,3898	0,0000	0,1000	0,0000	0,0000
10185	0,3291	0,0000	0,0000	0,0000	0,0000	0,0000
10188	0,0000	0,2888	0,1000	0,0500	0,0000	0,0000
10266	0,5242	0,3465	0,8430	0,3116	0,6750	0,2250
10283	0,0000	0,6930	0,8285	0,0000	0,0000	0,2250
10288	0,4870	0,0000	0,1000	0,0000	0,0000	0,0000
10289	0,2560	0,0000	0,0000	0,9000	0,0000	0,9000
10293	0,4510	0,0000	0,0500	0,0000	0,4500	0,0000
10294	0,3535	0,5775	0,0000	0,0000	0,0000	0,0000
10296	0,0000	0,0000	0,0500	0,9143	0,0000	0,0000
10297	0,3291	0,0000	0,0000	0,0000	0,6750	0,9000
10381	0,6659	0,0000	0,0000	0,0000	0,0000	0,0000
10387	0,8045	0,7075	0,0000	0,7684	0,0000	0,0000
10415	0,2804	0,0000	0,6310	0,5320	0,9000	0,0000
10427	0,0000	0,0000	0,6057	0,0000	0,2250	0,0000
10429	0,4480	0,4981	0,0000	0,0000	0,0000	0,0000
10436	0,5059	0,4043	0,7671	0,4256	0,0000	0,0000
10437	0,0000	0,0000	0,6151	0,4705	0,0000	0,0000
10441	0,3291	0,0000	0,1000	0,1000	0,0000	0,0000
10556	0,4266	0,0000	0,0000	0,0000	0,0000	0,0000
10557	0,9508	0,0000	0,4652	0,3012	0,0000	0,0000
10692	0,7314	0,0000	0,0000	0,1000	0,9000	0,0000
10694	0,6034	0,0000	0,0000	0,0000	0,0000	0,0000
10695	0,6826	0,0000	0,6259	0,0000	0,0000	0,0000
10696	0,4043	0,0000	0,0000	0,0000	0,0000	0,0000
10698	0,4632	0,0000	0,5443	0,1000	0,0000	0,0000
10733	0,4475	0,4043	0,7481	0,6326	0,0000	0,9000
10735	0,7177	0,0000	0,6253	0,8908	0,2250	0,0000
10778	0,0000	0,0000	0,0000	0,3616	0,0000	0,0000
10781	0,2438	0,0000	0,0500	0,0000	0,0000	0,2250
10782	0,4693	0,0000	0,0000	0,0000	0,0000	0,0000
10783	0,3474	0,0000	0,0000	0,0500	0,0000	0,0000
10784	0,4483	0,0000	0,0000	0,0000	0,0000	0,0000
10785	0,5051	0,5102	0,0500	0,0000	0,0000	0,0000
10792	0,5485	0,1877	0,0000	0,0000	0,4500	0,0000
10794	0,4815	0,0000	0,0000	0,5524	0,4500	0,9000
10798	0,3854	0,0000	0,1000	0,6326	0,0000	0,0000
10799	0,3494	0,3152	0,1000	0,5424	0,0000	0,0000
10801	0,5729	0,0000	0,0000	0,5933	0,9000	0,0000
10802	0,7352	0,0000	0,7481	0,0000	0,4500	0,0000
10846	0,3779	0,0000	0,0000	0,3414	0,0000	0,0000
10847	0,7273	0,8952	0,0000	0,5387	0,9000	0,4500
10895	0,6972	0,6786	0,0000	0,0000	0,0000	0,0000
10898	0,9813	0,0000	0,8190	0,0000	0,0000	0,0000
10934	0,8124	0,0000	0,5854	0,0000	0,0000	0,0000
11015	0,2560	0,0000	0,0000	0,0000	0,0000	0,0000
11140	0,6956	0,7739	0,8791	0,7785	0,0000	0,0000
11148	0,6494	0,6208	0,0000	0,0000	0,4500	0,0000
11149	0,6339	0,0000	0,6576	0,0500	0,4500	0,0000
11151	0,5594	0,0000	0,0000	0,1000	0,6750	0,0000
11152	0,4998	0,0000	0,7589	0,0000	0,2250	0,6750
11213	0,0000	0,3898	0,0000	0,0000	0,2250	0,0000

11214	0,4343	0,6305	0,9595	0,8240	0,0000	0,0000
11215	0,5255	0,7941	0,1000	0,0000	0,0000	0,0000
11216	0,6921	0,3465	0,3842	0,0000	0,9000	0,0000
11217	0,7558	0,0000	0,0000	0,1000	0,0000	0,0000
11218	0,6893	0,7219	0,9500	0,1000	0,0000	0,0000
11219	0,5028	0,0000	0,0000	0,0000	0,0000	0,9000
11220	0,3291	0,0000	0,3943	0,3317	0,0000	0,9000
11221	0,4023	0,0000	0,0000	0,7888	0,0000	0,0000
11257	0,0000	0,0000	0,0000	0,6033	0,0000	0,0000
11258	0,0000	0,0000	0,6051	0,5561	0,0000	0,0000
11259	0,4977	0,0000	0,4443	0,5625	0,0000	0,0000
11282	0,5973	0,4043	0,7232	0,4169	0,0000	0,0000
11393	0,0000	0,0000	0,4430	0,0000	0,0000	0,0000
11483	0,6582	0,0000	0,6715	0,1000	0,4500	0,0000
11494	0,3494	0,0000	0,0500	0,1000	0,6750	0,0000
11497	0,4865	0,3589	0,3120	0,1607	0,0000	0,0000
11540	0,3169	0,0000	0,0000	0,0000	0,0000	0,0000
11586	0,3559	0,4187	0,6810	0,0000	0,0000	0,0000
11640	0,0000	0,4187	0,4146	0,3183	0,4500	0,4500
11647	0,0000	0,0000	0,0000	1,0000	0,4500	0,0000
11654	0,4470	0,0000	0,0500	0,6591	0,0000	0,4500
11655	0,0000	0,0000	0,0000	0,7159	0,0000	0,0000
11656	0,2682	0,0000	0,1000	0,7140	0,0000	0,2250
11657	0,0000	0,0000	0,4167	0,6276	0,0000	0,0000
11717	0,4530	0,3032	0,0000	0,0000	0,9000	0,4500
11753	0,5089	0,0000	0,7174	0,1000	0,0000	0,0000
11848	0,4510	0,0000	0,0500	0,0000	0,0000	0,0000
11849	0,0000	0,0000	0,0500	0,4018	0,0000	0,0000
11872	0,3616	0,0000	0,0000	0,1000	0,6750	0,0000
11873	0,5729	0,0000	0,0000	0,0500	0,0000	0,2250
11875	0,9264	0,0000	0,0000	0,0000	0,0000	0,2250
11882	0,8594	0,0000	0,1000	0,0000	0,0000	0,4500
11883	0,0000	0,0000	0,7975	0,0000	0,0000	0,9000
11884	0,4730	0,3610	0,7002	0,3418	0,0000	0,0000
11889	0,4554	0,0000	0,0500	0,6024	0,6750	0,0000
11890	0,4388	0,0000	0,0000	0,3414	0,0000	0,2250
11891	0,5150	0,2695	0,0000	0,0000	0,2250	0,0000
11892	0,5242	0,0000	0,1000	0,0000	0,0000	0,0000
11893	0,5120	0,0000	0,0000	0,0000	0,9000	0,6750
11894	0,1585	0,0000	0,0500	0,1000	0,0000	0,0000
11895	0,3274	0,0000	0,1000	0,3216	0,0000	0,0000
11896	0,4348	0,0000	0,0000	0,0000	0,0000	0,0000
11897	0,2072	0,0000	0,0000	0,0000	0,2250	0,4500
11931	0,4998	0,0000	0,1000	0,1000	0,0000	0,9000
11935	0,7789	0,6208	0,0000	0,5628	0,2250	0,0000
11936	0,7314	0,0000	0,6171	0,0000	0,0000	0,6750
11937	0,8807	0,6368	0,9466	0,1000	0,0000	0,0000
11938	0,7893	0,0000	0,8658	0,0000	0,0000	0,0000
11939	0,6807	0,6930	0,5608	0,5128	0,6750	0,0000
12010	0,4023	0,8519	0,1000	0,0500	0,0000	0,0000
12047	0,7923	0,0000	1,0000	0,4113	0,6750	0,0000
12059	0,8167	0,0000	0,1000	0,0000	0,0000	0,0000
12060	0,0000	0,0000	0,0000	0,6125	0,0000	0,0000
12063	0,1493	0,0000	0,1000	0,5427	0,0000	0,2250

12098	0,6521	0,2021	0,1000	0,0000	0,0000	0,0000
12099	0,3535	0,0000	0,0000	0,3918	0,2250	0,0000
12107	0,0000	0,0000	0,5797	0,0000	0,0000	0,0000
12108	0,3779	0,0000	0,0000	0,0500	0,0000	0,2250
12159	0,4266	0,6401	0,4601	0,6471	0,0000	0,0000
12160	0,6060	0,0000	0,0500	0,0000	0,0000	0,0000
12166	0,6265	0,0000	0,0000	0,8448	0,0000	0,0000
12167	0,7964	0,0000	0,0000	0,5725	0,0000	0,2250
12181	0,0000	0,3754	0,4044	0,0000	0,0000	0,0000
12185	0,7192	0,0000	0,0000	0,0000	0,0000	0,0000
12186	0,9752	0,2743	0,0000	0,0500	0,0000	0,0000
12188	0,4477	0,4112	0,2880	0,3418	0,0000	0,2250
12189	0,4747	0,3486	0,3519	0,0000	0,0000	0,0000
12194	0,6704	0,0000	0,0000	0,1000	0,0000	0,2250
12195	0,6095	0,0000	0,1000	0,0500	0,0000	0,0000
12198	0,7619	0,0000	0,1000	0,0000	0,0000	0,0000
12201	0,8472	0,0000	0,1000	0,6930	0,4500	0,0000
12204	0,3557	0,1588	0,0000	0,0000	0,2250	0,0000
12205	0,5924	0,0000	0,0000	0,0500	0,0000	0,4500
12206	0,6704	0,8663	0,1000	0,5933	0,0000	0,9000
12214	0,5051	0,9818	0,0000	0,1908	0,0000	0,0000
12215	0,6972	0,6930	0,0000	0,0500	0,0000	0,2250
12216	0,8059	0,0000	0,6557	0,1000	0,0000	0,0000
12217	0,4242	0,1444	0,0000	0,2107	0,0000	0,2250
12218	0,4144	0,0000	0,0000	0,2808	0,0000	0,0000
12219	0,3880	0,3032	0,0000	0,0000	0,0000	0,0000
12222	0,6907	0,0000	0,6975	0,0000	0,0000	0,0000
12223	0,7598	0,7267	0,0500	0,0500	0,0000	0,2250
12224	0,6948	0,6930	0,7367	0,1000	0,0000	0,2250
12246	0,0000	0,0000	0,0000	0,8942	0,0000	0,0000
12265	0,4449	0,3465	0,0000	0,4625	0,2250	0,0000
12266	0,4510	0,0000	0,0000	0,0000	0,0000	0,0000
12390	0,2438	0,0000	0,1000	0,0000	0,6750	0,9000
12420	0,0000	0,0000	0,9899	0,0000	0,4500	0,0000
12421	0,4998	0,0000	0,4892	0,4488	0,2250	0,0000
12422	0,4876	0,0000	0,5759	0,4725	0,0000	0,0000
12424	0,3901	0,0000	0,1000	0,0000	0,0000	0,6750
12429	0,3169	0,0000	0,1000	0,0000	0,0000	0,0000
12431	0,0000	0,0000	0,5646	0,0000	0,0000	0,2250
12432	0,2682	0,0000	0,1000	0,8439	0,0000	0,0000
12433	0,3901	0,0000	0,6158	0,0000	0,2250	0,9000
12434	0,4551	0,0000	0,0000	0,0000	0,0000	0,0000
12443	0,6582	0,0000	0,0000	0,0500	0,0000	0,6750
12446	0,0000	0,4620	0,0000	0,0500	0,9000	0,4500
12447	0,3413	0,0000	0,0000	0,0000	0,0000	0,6750
12448	0,2682	0,0000	0,3329	0,1000	0,0000	0,0000
12450	0,2682	0,0000	0,0000	0,0000	0,0000	0,4500
12451	0,0000	0,0000	0,4329	0,0000	0,0000	0,9000
12461	0,0000	0,6208	0,1000	0,0000	0,2250	0,4500
12462	0,0000	0,0000	0,7987	0,0000	0,2250	0,0000
12516	0,5089	0,0000	0,4158	0,5580	0,9000	0,4500
12518	0,5363	0,5487	0,5652	0,0000	0,2250	0,0000
12566	0,4815	0,4120	0,4159	0,4043	0,0000	0,2250
12630	0,3550	0,2888	0,2816	0,2210	0,4500	0,0000

12631	0,4002	0,0000	0,0000	0,0000	0,0000	0,0000
12762	0,5363	0,6353	0,0000	0,0500	0,0000	0,0000
12763	0,2804	0,3032	0,0000	0,0000	0,0000	0,0000
12839	0,0000	0,0000	0,9500	0,0000	0,0000	0,0000
12840	0,5363	0,0000	0,4234	0,0000	0,6750	0,0000
12841	0,3535	0,5848	0,3842	0,3982	0,0000	0,0000
12842	0,4493	0,0000	0,5968	0,5521	0,2250	0,0000
12858	0,7436	0,0000	0,0500	0,7785	0,0000	0,0000
12930	0,8881	0,3393	0,5342	0,4021	0,0000	0,0000
12959	0,4226	0,0000	0,0000	0,0000	0,0000	0,0000
12960	0,0000	0,5198	0,0000	0,0500	0,4500	0,0000
12973	0,2468	0,0000	0,0000	0,0000	0,0000	0,0000
12978	0,5729	0,0000	0,0500	0,1000	0,4500	0,0000
12979	0,2844	0,0000	0,1614	0,0000	0,0000	0,2250
12980	0,5217	0,1877	0,0000	0,0000	0,9000	0,0000
12982	0,3828	0,0000	0,0000	0,0000	0,0000	0,6750
12984	0,4862	0,0000	0,1000	0,0500	0,0000	0,6750
12985	0,4632	0,0000	0,0000	0,0500	0,0000	0,4500
12986	0,6247	0,0000	0,1000	0,0000	0,6750	0,6750
13105	0,0000	0,0000	0,0000	0,6936	0,0000	0,0000
13124	0,3291	0,0000	0,5888	0,3867	0,0000	0,0000
13141	0,2560	0,0000	0,0000	0,3314	0,0000	0,0000
13142	0,7453	0,8374	0,0000	0,6737	0,0000	0,0000
13150	0,0000	0,0000	0,0000	0,3979	0,0000	0,0000
13233	0,3108	0,0000	0,0500	0,0000	0,9000	0,0000
13337	0,4815	0,4375	0,4267	0,4988	0,0000	0,0000
13338	0,6765	0,4668	0,3930	0,0000	0,0000	0,6750
13339	0,4377	0,4043	0,5423	0,4491	0,0000	0,0000
13340	0,0000	0,8158	0,0000	0,5430	0,0000	0,0000
13418	0,5363	0,0000	0,0000	0,0000	0,0000	0,9000
13420	0,7801	0,3465	0,0000	0,0000	0,0000	0,0000
13493	0,5120	0,0000	0,5899	0,0500	0,0000	0,0000
13514	0,0000	0,5342	0,4430	0,0500	0,0000	0,0000
13603	0,0000	0,0000	0,9000	0,6838	0,6750	0,0000
13604	0,9654	0,0000	0,0000	0,1000	0,0000	0,0000
13605	0,6704	0,0000	0,0000	0,1000	0,0000	0,2250
13607	0,4925	0,3610	0,5449	0,0000	0,0000	0,0000
13608	0,4829	0,0000	0,1000	0,0000	0,0000	0,2250
13613	0,0000	0,7075	0,0000	0,8970	0,0000	0,0000
13643	0,2682	0,0000	0,3639	0,0000	0,0000	0,2250
13660	0,0000	0,0000	0,0000	0,6961	0,0000	0,0000
13672	0,5607	0,0000	0,0500	0,0000	0,0000	0,0000
13674	0,6491	0,6353	0,0000	0,0000	0,6750	0,0000
13675	0,5120	0,0000	0,1000	0,0000	0,0000	0,0000
13676	0,2560	0,0000	0,1000	0,1000	0,0000	0,2250
13679	0,7395	0,0000	0,0000	0,0500	0,0000	0,0000
13680	0,8208	0,0000	0,0000	0,1000	0,9000	0,9000
13684	0,6643	0,0000	0,0000	0,0000	0,0000	0,0000
13734	0,8045	0,0000	0,0000	0,4524	0,0000	0,0000
13736	0,6460	0,0000	0,0000	0,7391	0,0000	0,0000
13784	0,9047	0,0000	0,9500	0,0000	0,9000	0,0000
13787	0,4591	0,0000	0,0000	0,4722	0,0000	0,0000
13885	0,6948	0,0000	0,0000	0,6986	0,0000	0,9000
13886	0,0000	0,0000	0,0000	0,6930	0,0000	0,2250

13887	0,6034	0,0000	0,1000	0,0000	0,0000	0,0000
14004	0,5729	0,0000	0,0000	0,1000	0,4500	0,0000
14097	0,0000	0,0000	0,1000	0,5625	0,0000	0,9000
14120	0,5071	0,0000	0,0000	0,5222	0,0000	0,0000
14129	0,5363	0,0000	0,0000	0,0000	0,0000	0,0000
14130	0,5973	0,0000	0,1000	0,0000	0,0000	0,9000
14136	0,0000	0,0000	0,0000	0,6637	0,9000	0,4500
14138	0,0000	0,0000	0,0000	0,6430	0,0000	0,0000
14143	0,4632	0,0000	0,4443	0,3451	0,9000	0,2250
14155	0,0000	0,3321	0,0000	0,4725	0,9000	0,0000
14241	0,8167	0,0000	0,0500	0,0000	0,0000	0,0000
14250	0,0000	0,0000	0,0000	0,3116	0,0000	0,0000
14315	0,8289	0,0000	0,0000	0,0000	0,0000	0,0000
14317	0,7192	0,0000	0,0000	0,0000	0,6750	0,6750
14318	0,7070	0,0000	0,0000	0,0000	0,9000	0,0000
14320	1,0000	0,0000	0,0000	0,0000	0,0000	0,2250
14321	0,0000	0,0000	0,0000	0,3713	0,0000	0,0000
14322	0,0000	0,0000	0,0000	0,7436	0,0000	0,0000
14324	0,5892	0,0000	0,6361	0,0000	0,0000	0,0000
14325	0,8248	0,0000	0,6677	0,0000	0,0000	0,0000
14327	0,0000	0,8591	0,0000	0,0000	0,4500	0,0000
14328	0,0000	0,9674	0,0000	0,1000	0,0000	0,0000
14366	0,4815	0,0000	0,0000	0,1000	0,0000	0,9000
14375	0,4370	0,0000	0,1000	0,0000	0,4500	0,6750
14376	0,5668	0,3321	0,0500	0,1000	0,0000	0,4500
14377	0,2621	0,0000	0,1000	0,0000	0,0000	0,0000
14461	0,5323	0,0000	0,0000	0,0000	0,0000	0,0000

14693	0,4185	0,0000	0,0000	0,0500	0,0000	0,0000
14813	0,2986	0,0000	0,4139	0,0500	0,6750	0,0000
14892	0,5120	0,0000	0,0000	0,0000	0,0000	0,6750
14893	0,4803	0,0000	0,0500	0,0000	0,0000	0,0000
14894	0,1585	0,0000	0,1000	0,0500	0,0000	0,6750
14898	0,3291	0,0000	0,0000	0,0500	0,0000	0,0000
14899	0,4774	0,0000	0,0000	0,0000	0,0000	0,0000
14901	0,0000	0,0000	0,3418	0,0000	0,0000	0,0000
14902	0,3718	0,0000	0,0000	0,5370	0,0000	0,0000
14903	0,7070	0,0000	0,5125	0,0000	0,6750	0,0000
14904	0,4495	0,3946	0,0000	0,3029	0,0000	0,4500
14905	0,4406	0,0000	0,1000	0,3820	0,4500	0,0000
14906	0,4297	0,0000	0,0000	0,2908	0,6750	0,0000
14907	0,3698	0,0000	0,0500	0,0000	0,0000	0,2250
14908	0,0000	0,0000	0,0000	0,3817	0,0000	0,0000
15084	0,4282	0,0000	0,0000	0,0500	0,0000	0,0000
15091	0,1524	0,0000	0,0000	0,0000	0,9000	0,0000
15116	0,9691	0,0000	0,0000	0,1000	0,0000	0,0000
15126	0,8118	0,0000	0,0000	0,4524	0,4500	0,0000
15130	0,5363	0,8952	0,0000	0,0000	0,9000	0,0000
15132	0,9752	0,6930	0,0500	0,6930	0,4500	0,0000
15134	0,7639	0,0000	0,6880	0,5826	0,0000	0,6750
15139	0,8380	0,7075	0,0000	0,0500	0,4500	0,0000
15140	0,7842	0,0000	0,0500	0,0000	0,0000	0,0000
15141	0,7598	0,0000	0,8785	0,6939	0,0000	0,0000
15143	0,6521	0,8302	0,0500	0,0500	0,0000	0,4500
15521	0,4754	0,0000	0,0000	0,1000	0,9000	0,2250

15522	0,5729	0,0000	0,0000	0,0000	0,0000	0,0000
15724	0,4478	0,0000	0,0000	0,3911	0,0000	0,0000
15725	0,7029	0,0000	0,0000	0,2808	0,0000	0,0000
15726	0,2950	0,0000	0,4392	0,2878	0,0000	0,4500
16184	0,7740	0,0000	0,0000	0,5725	0,6750	0,0000
16185	0,4998	0,0000	0,5057	0,5119	0,0000	0,0000
16186	0,7923	0,6064	0,7245	0,8042	0,2250	0,0000
16191	0,9666	0,0000	0,0000	0,1000	0,6750	0,0000
16326	0,8411	0,0000	0,0000	0,6737	0,2250	0,0000
16327	0,8685	0,5775	0,0000	0,8542	0,6750	0,9000
16328	0,7606	0,0000	0,6361	0,0000	0,0000	0,0000
16481	0,3718	0,0000	0,0000	0,0000	0,0000	0,0000
16482	0,4023	0,0000	0,0000	0,1000	0,0000	0,2250
16483	0,7131	0,0000	0,3275	0,3216	0,0000	0,0000
16484	0,6704	0,3465	0,6051	0,4418	0,4500	0,9000
16485	0,4480	0,0000	0,5646	0,4122	0,0000	0,0000
16627	0,0000	0,0000	0,0000	0,1808	0,0000	0,0000
16636	0,7923	0,0000	0,8218	0,6628	0,9000	0,6750
16637	0,7070	0,0000	0,1000	0,6832	0,0000	0,0000
16660	0,7253	0,0000	0,0500	0,0000	0,0000	0,0000
16661	0,0000	0,6136	0,0000	0,0000	0,2250	0,0000
16664	0,1463	0,0000	0,4443	0,0500	0,0000	0,0000
16666	0,4754	0,4620	0,6006	0,5567	0,0000	0,6750
16667	0,5694	0,4813	0,5777	0,6678	0,0000	0,0000
16688	0,0000	0,0000	0,0000	0,3341	0,0000	0,2250
16695	0,7679	0,0000	0,7857	0,1000	0,4500	0,0000
16696	0,5668	0,0000	0,6373	0,0000	0,0000	0,0000

16714	0,0000	0,0000	0,0000	0,6829	0,0000	0,0000
16715	0,5323	0,0000	0,0000	0,1000	0,0000	0,0000
16719	0,7436	0,0000	0,0000	0,7637	0,0000	0,0000
16751	0,3169	0,0000	0,0500	0,7634	0,6750	0,4500
16777	0,6826	0,5920	0,0000	0,0000	0,0000	0,0000
16782	0,8655	0,0000	0,0000	0,0000	0,0000	0,0000
16808	0,4179	0,2852	0,0000	0,1000	0,4500	0,0000
17011	0,4815	0,0000	0,0500	0,0000	0,0000	0,0000
17087	0,7791	0,7364	0,7582	0,0000	0,0000	0,0000
17088	0,6777	0,6353	0,8563	0,6194	0,9000	0,0000
17089	0,7923	0,6690	0,8656	0,8108	0,9000	0,2250
17090	0,7490	0,6353	0,6931	0,8967	0,0000	0,0000
17125	0,0000	0,0000	0,0500	0,6363	0,9000	0,0000
17228	0,6716	0,0000	0,0000	0,1000	0,6750	0,9000
17251	0,3535	0,4765	0,3728	0,0500	0,6750	0,4500
17252	0,7314	0,0000	0,4228	0,1000	0,0000	0,0000
17261	0,2357	0,0000	0,0000	0,0000	0,4500	0,0000
17263	0,8655	0,0000	0,0500	0,0000	0,0000	0,0000
17264	0,5242	0,2166	0,0000	0,0500	0,0000	0,9000
17266	0,3088	0,1733	0,0500	0,0500	0,6750	0,0000
17267	0,4998	0,0000	0,0000	0,0000	0,0000	0,6750
17268	0,1707	0,0000	0,0000	0,3216	0,0000	0,0000
17270	0,2194	0,0000	0,1000	0,3914	0,0000	0,9000
17271	0,4632	0,0000	0,0000	0,1000	0,9000	0,0000
17272	0,4023	0,0000	0,0000	0,0000	0,0000	0,6750
17273	0,4023	0,0000	0,1000	0,1000	0,0000	0,6750
17280	0,4050	0,0000	0,0000	0,2308	0,0000	0,0000

17281	0,3169	0,0000	0,0000	0,0500	0,0000	0,0000
17309	0,7253	0,0000	0,0000	0,0000	0,0000	0,0000
17310	0,3657	0,2599	0,5259	0,0000	0,0000	0,0000
17312	0,4876	0,0000	0,0000	0,1000	0,0000	0,0000
17315	0,0000	0,0000	0,0500	0,2311	0,2250	0,6750
17320	0,1666	0,0000	0,0000	0,3518	0,2250	0,0000
17321	0,2267	0,0000	0,1000	0,2613	0,0000	0,2250
17325	0,1950	0,0000	0,0000	0,3015	0,0000	0,0000
17326	0,0000	0,0000	0,0000	0,3408	0,0000	0,0000
17327	0,3962	0,0000	0,0000	0,3814	0,0000	0,0000
17328	0,3505	0,1444	0,0000	0,2761	0,0000	0,0000
17329	0,6948	0,0000	0,1000	0,0000	0,0000	0,6750
17330	0,3779	0,0000	0,0000	0,1000	0,0000	0,4500
17331	0,4617	0,0000	0,0000	0,2761	0,4500	0,0000
17332	0,4283	0,2743	0,0000	0,3440	0,0000	0,6750
17521	0,3901	0,0000	0,3639	0,1000	0,6750	0,0000
17524	0,0000	0,0000	0,2728	0,0000	0,0000	0,4500
17645	0,0000	0,0000	0,5766	0,0000	0,0000	0,0000
17647	0,0000	0,5775	0,0000	0,3613	0,6750	0,0000
17648	0,0000	0,0000	0,0000	0,3116	0,9000	0,0000
17654	0,5302	0,0000	0,4646	0,0000	0,6750	0,0000
17657	0,0000	0,0000	0,0000	0,3860	0,0000	0,0000
17658	0,3047	0,0000	0,0000	0,1000	0,0000	0,0000
17662	0,4998	0,0000	0,0500	0,0000	0,0000	0,0000
17663	0,4470	0,0000	0,3127	0,0000	0,0000	0,0000
17668	0,7265	0,7219	0,7975	0,8137	0,0000	0,0000
17698	0,2926	0,0000	0,1000	0,0000	0,0000	0,2250
17719	0,0000	0,0000	0,0500	0,8439	0,0000	0,6750
17775	0,3364	0,0000	0,0000	0,0000	0,0000	0,0000
17778	0,0000	0,7941	0,0000	0,0500	0,0000	0,0000
17779	0,5485	0,0000	0,0000	0,0000	0,9000	0,0000
17840	0,8228	0,0000	0,0000	0,0000	0,9000	0,0000
17980	0,4764	0,4909	0,6266	0,5424	0,0000	0,0000
17982	0,5942	0,9529	0,0000	0,1000	0,0000	0,0000
17983	0,0000	0,0000	0,7165	0,0000	0,0000	0,0000
18232	0,5485	0,9096	0,0000	0,7170	0,0000	0,6750
18233	0,8594	0,0000	0,1000	0,6211	0,2250	0,0000
18425	0,6765	0,0000	0,1000	0,6930	0,2250	0,0000
19067	0,4541	0,4187	0,0000	0,0000	0,0000	0,0000
19068	0,3007	0,0000	0,0500	0,4438	0,0000	0,0000
19069	0,0000	0,4476	0,2525	0,6077	0,0000	0,0000
19165	0,5912	0,0000	0,0000	0,4927	0,0000	0,0000
19459	0,3657	0,0000	0,0000	0,0500	0,0000	0,9000
19506	0,2621	0,0000	0,0000	0,0000	0,0000	0,0000
19560	0,7874	0,0000	0,0500	0,7684	0,0000	0,9000
19610	0,2560	0,0000	0,8582	0,0000	0,2250	0,0000
19724	0,5607	0,0000	0,0000	0,0000	0,0000	0,0000
19726	0,5628	0,0000	0,1000	0,0500	0,0000	0,4500
19740	0,7585	0,6353	0,5608	0,6329	0,0000	0,0000
19744	0,6687	0,0000	0,0000	0,6634	0,9000	0,0000
19745	0,7177	0,0000	0,0000	0,0500	0,2250	0,0000
19746	0,7046	0,0000	0,0000	0,0000	0,2250	0,0000
19747	0,8028	0,9024	0,1000	0,0000	0,0000	0,0000
19749	0,6979	0,7460	0,0500	0,6234	0,0000	0,0000

19751	0,7679	0,6979	0,0000	0,7640	0,0000	0,0000
19753	0,6777	0,0000	0,0500	0,7033	0,2250	0,0000
19755	0,9995	0,5775	0,0000	0,0000	0,9000	0,4500
19756	0,7558	0,7652	0,0000	0,8500	0,9000	0,4500
19757	0,6582	0,9385	0,0500	0,8542	0,0000	0,0000
19759	0,5120	0,8013	0,9399	0,7335	0,0000	0,4500
19761	0,5900	0,6930	0,6266	0,9000	0,2250	0,9000
19762	0,7883	0,0000	0,0000	0,0000	0,0000	0,2250
19808	0,5760	0,0000	0,0000	0,1908	0,0000	0,0000
19869	0,5363	0,3610	0,3633	0,1000	0,4500	0,0000
19979	0,3901	0,0000	0,1000	0,1000	0,0000	0,0000
20065	0,3413	0,0000	0,0500	0,0000	0,0000	0,4500
20423	0,4532	0,4139	0,5629	0,6909	0,0000	0,2250
20432	0,6623	0,0000	0,0000	0,0000	0,6750	0,0000
20434	0,7314	0,0000	0,0000	0,0500	0,0000	0,0000
23972	0,5242	0,0000	0,0000	0,0000	0,0000	0,0000
23973	0,5688	0,6786	0,6456	0,0000	0,0000	0,0000
23974	0,5973	0,6353	0,0000	0,0000	0,6750	0,0000
23975	0,6979	0,7556	0,5766	0,0500	0,0000	0,4500
24059	0,7314	0,0000	0,0000	0,1000	0,0000	0,2250
24088	0,5621	0,6714	0,7304	0,6396	0,0000	0,6750
24089	0,6790	0,0000	0,7633	0,7643	0,2250	0,0000
24090	0,8045	0,0000	0,7025	0,7697	0,0000	0,0000
24091	0,6387	0,6979	0,7184	0,7746	0,0000	0,0000
24092	0,7460	0,0000	0,6924	0,5430	0,0000	0,0000
24093	0,6826	0,6208	0,7195	0,7084	0,0000	0,2250
24094	0,5705	0,5848	0,7454	0,5393	0,0000	0,9000
24095	0,6613	0,0000	0,7441	0,7936	0,0000	0,0000
24132	0,6826	0,5920	0,6354	0,1000	0,0000	0,0000
24254	0,6674	0,0000	0,7215	0,4826	0,0000	0,0000
24256	0,5790	0,0000	0,0000	0,5125	0,0000	0,2250
24257	0,5607	0,0000	0,1000	0,0000	0,4500	0,0000
24289	0,5973	0,7075	0,0500	0,0000	0,0000	0,6750
24292	0,7131	0,0000	0,0000	0,0000	0,6750	0,0000
24293	0,6003	0,0000	0,0000	0,0000	0,2250	0,0000
24294	0,7131	0,0000	0,0000	0,0000	0,0000	0,4500
24296	0,7476	0,0000	0,0000	0,5326	0,4500	0,0000
24297	0,6635	0,0000	0,6063	0,7439	0,0000	0,9000
24299	0,7331	0,0000	0,6184	0,0500	0,0000	0,0000
24501	0,7264	0,0000	0,7823	0,5128	0,0000	0,0000
24530	0,6861	0,0000	0,0500	0,0000	0,0000	0,6750
24531	0,0000	0,0000	0,5152	0,6930	0,0000	0,0000
24533	0,8005	0,0000	0,0000	0,0500	0,2250	0,9000
24534	0,6729	0,0000	0,0000	0,6731	0,0000	0,0000
24610	0,8045	0,7364	0,1000	0,1000	0,0000	0,0000
24612	0,6095	0,0000	0,0000	0,0000	0,2250	0,0000
24613	0,7131	0,0000	0,1000	0,0000	0,2250	0,0000
24629	0,7695	0,0000	0,0500	0,8500	0,0000	0,0000
24636	0,6081	0,0000	0,1000	0,8146	0,0000	0,4500
24638	0,7815	0,0000	0,7070	0,6125	0,0000	0,0000
24639	0,7436	0,5775	0,0500	0,0000	0,0000	0,9000
24641	0,6918	0,5920	0,0500	0,1000	0,0000	0,4500
24642	0,6186	0,0000	0,1000	0,0000	0,2250	0,0000
24643	0,5997	0,0000	0,0500	0,6832	0,2250	0,0000

24644	0,5912	0,0000	0,7671	0,5463	0,0000	0,0000
24647	0,6339	0,0000	0,0000	0,0500	0,0000	0,0000
24648	0,6704	0,0000	0,0000	0,1000	0,0000	0,6750
24649	0,7819	0,6064	0,7285	0,5882	0,0000	0,2250
24650	0,6046	0,0000	0,0000	0,0000	0,0000	0,0000
24684	0,7126	0,7315	0,7704	0,8106	0,0000	0,0000
24685	0,7679	0,6353	0,8266	0,0000	0,0000	0,0000
24987	0,7558	0,0000	0,6962	0,0000	0,0000	0,0000
25016	0,9045	0,0000	0,0000	0,7391	0,0000	0,6750
25017	0,8005	0,6786	0,6975	0,0000	0,0000	0,0000
25018	0,8028	0,0000	0,0000	0,1000	0,0000	0,2250
25019	0,0000	0,9674	0,6968	0,0000	0,0000	0,4500
25020	0,0000	0,6930	0,1000	0,0500	0,0000	0,0000
25023	0,7497	0,0000	0,5652	0,0000	0,2250	0,2250
25024	0,0000	0,0000	0,0000	0,6637	0,0000	0,0000
25025	0,5242	0,0000	0,0000	0,0500	0,0000	0,0000
25029	0,7679	0,0000	0,0000	0,0000	0,2250	0,0000
25034	0,0000	0,0000	0,0500	0,6664	0,0000	0,0000
25039	0,6217	0,0000	0,0000	0,7234	0,0000	0,0000
25041	0,5567	0,0000	0,0000	0,7382	0,0000	0,0000
25046	0,6887	0,0000	0,0000	0,5427	0,0000	0,6750
25053	0,6948	0,0000	0,0000	0,7838	0,4500	0,9000
25055	0,7977	0,0000	0,0000	0,8014	0,0000	0,0000
25056	0,6205	0,0000	0,0000	0,6835	0,0000	0,0000
25059	0,5120	0,0000	0,0000	0,7539	0,0000	0,4500
25063	0,7021	0,0000	0,0500	0,7662	0,2250	0,0000
25064	0,6867	0,0000	0,0000	0,7187	0,6750	0,0000

25066	0,8330	0,5920	0,0500	0,7212	0,0000	0,0000
25068	0,6070	0,0000	0,1000	0,7005	0,0000	0,0000
25069	0,5302	0,0000	0,0000	0,6711	0,0000	0,6750
25071	0,6278	0,0000	0,0000	0,7212	0,0000	0,0000
25073	0,9630	0,0000	0,0000	0,7734	0,4500	0,0000
25156	0,7793	0,0000	0,0000	0,6829	0,0000	0,0000
25187	0,9240	0,0000	0,0000	0,6687	0,0000	0,0000
25190	0,0000	0,6208	0,1000	0,7039	0,0000	0,9000
25196	0,5607	0,0000	0,1000	0,7536	0,2250	0,0000
25202	0,0000	0,0000	0,0000	0,4927	0,0000	0,0000
25204	0,0000	0,0000	0,0000	0,6564	0,0000	0,0000
25207	0,6247	0,0000	0,0000	0,7080	0,0000	0,0000
25209	0,6613	0,0000	0,0000	0,6282	0,0000	0,4500
25215	0,0000	0,0000	0,1000	0,5580	0,0000	0,0000
25216	0,0000	0,0000	0,0000	0,5480	0,0000	0,0000
25227	0,7704	0,0000	0,5861	0,0000	0,0000	0,9000
25236	0,7314	0,0000	0,0500	0,0000	0,0000	0,4500
25240	0,7883	0,7508	0,1000	0,6234	0,0000	0,0000
25263	0,9447	0,0000	0,0000	0,0000	0,0000	0,0000
25270	0,8219	0,0000	0,0000	0,5524	0,4500	0,0000
25272	0,5932	0,0000	0,1000	0,0000	0,0000	0,0000
25273	0,7774	0,0000	0,8285	0,0000	0,0000	0,0000
25476	0,8898	0,0000	0,0000	0,0000	0,0000	0,0000
25502	0,7566	0,6497	0,7848	0,6631	0,9000	0,0000
25511	0,7902	0,6930	0,8019	0,0000	0,0000	0,0000
25868	0,7697	0,7652	0,8095	0,0000	0,0000	0,0000
25869	0,7301	0,5920	0,7209	0,1000	0,9000	0,4500

25870	0,7131	0,0000	0,0000	0,0000	0,2250	0,0000
26176	0,0000	0,5920	0,1000	0,7436	0,2250	0,0000
26178	0,6704	0,6064	0,0000	0,6631	0,9000	0,0000
26179	0,7649	0,0000	0,0000	0,6869	0,9000	0,0000
26596	0,6369	0,0000	0,0000	0,0000	0,0000	0,0000
26598	0,6659	0,0000	0,0000	0,1000	0,0000	0,0000
26603	0,6643	0,7075	0,0000	0,7533	0,0000	0,0000
26605	0,6948	0,0000	0,1000	0,0500	0,6750	0,0000
26609	0,6305	0,0000	0,1000	0,0000	0,0000	0,2250
26610	0,7700	0,0000	0,1000	0,0000	0,0000	0,4500
26613	0,6135	0,0000	0,0000	0,1000	0,0000	0,0000
26614	0,6308	0,0000	0,0000	0,0000	0,4500	0,0000
26616	0,7314	0,0000	0,0000	0,0000	0,0000	0,0000
26618	0,8472	0,0000	0,1000	0,0000	0,9000	0,0000
26619	0,6286	0,0000	0,0000	0,0000	0,9000	0,0000
26621	0,6135	0,0000	0,4551	0,0000	0,0000	0,9000
26623	0,8045	0,0000	0,0000	0,0000	0,0000	0,0000
26767	0,7172	0,0000	0,0000	0,0000	0,6750	0,4500
26823	0,6643	0,0000	0,7063	0,0000	0,0000	0,9000
26825	0,6704	0,0000	0,4551	0,0000	0,6750	0,0000
31041	0,6556	0,7783	0,6854	0,5668	0,0000	0,4944
32710	0,2560	0,0000	0,0500	0,0000	0,0000	0,0000
46156	0,5120	0,0000	0,8835	0,9646	0,9000	0,0000
46157	0,5607	0,0000	0,8791	0,8261	0,0000	0,0000
46158	0,6257	0,0000	0,0000	0,7489	0,9000	0,0000
46159	0,5973	0,0000	0,6367	0,8519	0,0000	0,4500
46160	0,6400	0,0000	0,6158	0,0500	0,0000	0,6750

46161	0,0000	0,5992	0,0000	0,0500	0,9000	0,0000
46167	0,8411	0,0000	0,0000	0,0000	0,0000	0,6750
46174	0,0000	0,7797	0,0000	0,0000	0,0000	0,4500
46181	0,6826	0,0000	0,6215	0,8215	0,0000	0,0000
46189	0,8167	0,0000	0,9044	0,0500	0,0000	0,0000
46191	0,6765	0,0000	0,0000	0,0000	0,0000	0,0000
46192	0,2804	0,0000	0,0500	0,0000	0,0000	0,2250
46198	0,3494	0,0000	0,0000	0,0000	0,0000	0,6750
46199	0,0000	0,0000	0,5456	0,0000	0,2250	0,0000
46200	0,5668	0,0000	0,0000	0,0000	0,0000	0,0000
46201	0,4998	0,0000	0,0000	0,0000	0,0000	0,0000
46206	0,5851	0,0000	0,0000	0,7137	0,2250	0,0000
46209	0,5546	0,5342	0,0000	0,0000	0,0000	0,0000
46263	0,6811	0,0000	0,0000	0,6231	0,0000	0,9000
46264	0,6369	0,0000	0,8785	0,0000	0,0000	0,0000
46265	0,7720	0,0000	0,8110	0,4625	0,0000	0,0000
46266	0,8045	0,0000	0,0000	0,0000	0,0000	0,2250
46267	0,6217	0,0000	0,8089	0,5524	0,0000	0,0000
46269	0,0000	0,0000	0,7842	0,1000	0,2250	0,0000
46270	0,4937	0,0000	0,8454	0,5927	0,0000	0,2250
46271	0,8533	0,0000	0,7622	0,0000	0,0000	0,0000
46272	0,6141	0,0000	0,0000	0,0000	0,4500	0,0000
46273	0,0000	0,0000	0,5158	0,6433	0,0000	0,9000
46274	0,7558	0,0000	0,5395	0,7131	0,0000	0,0000
46275	0,5607	0,0000	0,0000	0,4960	0,6750	0,0000
46276	0,0000	0,0000	0,6124	0,6470	0,0000	0,4500
46278	0,6460	0,0000	0,6259	0,1000	0,0000	0,9000

46279	0,0000	0,6714	0,6354	0,0000	0,0000	0,0000
46280	0,7588	0,0000	0,6051	0,6285	0,9000	0,0000
46281	0,6935	0,5920	0,6759	0,7439	0,0000	0,9000
46282	0,6253	0,0000	0,6158	0,0000	0,0000	0,4500
46283	0,7679	0,0000	0,7042	0,6329	0,0000	0,0000
46284	0,7138	0,0000	0,6399	0,7972	0,0000	0,0000
46285	0,7964	0,0000	0,6158	0,5480	0,9000	0,9000
46286	0,7876	0,0000	0,8859	0,8341	0,6750	0,0000
46287	0,6034	0,0000	0,7205	0,6167	0,6750	0,0000
46288	0,6339	0,0000	0,0500	0,0000	0,0000	0,2250
46289	0,8167	0,0000	0,8042	0,8170	0,0000	0,6750
46290	0,9630	0,0000	0,7380	0,8378	0,0000	0,0000
46291	0,6972	0,6497	0,7521	0,8076	0,4500	0,0000
46292	0,5120	0,0000	0,0000	0,0500	0,9000	0,0000
46293	0,7413	0,0000	0,8177	0,6737	0,0000	0,9000
46294	0,7107	0,0000	0,7947	0,7388	0,9000	0,6750
46295	0,8306	0,7291	0,5867	0,6933	0,2250	0,0000
46296	0,7175	0,6425	0,7899	0,7134	0,0000	0,0000
46297	0,6554	0,6930	0,6171	0,5942	0,0000	0,9000
46298	0,6247	0,0000	0,5665	0,7308	0,0000	0,0000
46299	0,6918	0,7797	0,5968	0,0000	0,0000	0,0000
46300	0,7967	0,0000	0,6848	0,0000	0,0000	0,4500
46301	0,6196	0,0000	0,5928	0,0000	0,4500	0,0000
46302	0,7517	0,7075	0,8011	0,7486	0,0000	0,2250
46303	0,7461	0,8591	0,6731	0,7718	0,6750	0,0000
46304	0,7212	0,8374	0,7353	0,5125	0,0000	0,6750
46305	0,6617	0,6786	0,7956	0,7881	0,2250	0,2250
46306	0,8045	0,6642	0,8656	0,8151	0,0000	0,0000
46331	0,0000	0,0000	0,8285	0,0000	0,4500	0,2250
46332	0,7593	0,6642	0,6411	0,7237	0,0000	0,0000
46333	0,5607	0,0000	0,6300	0,5927	0,9000	0,0000
46334	0,6420	0,0000	0,0000	0,6436	0,0000	0,2250
46336	0,6758	0,0000	0,6741	0,4725	0,0000	0,2250
46337	0,6314	0,0000	0,8937	0,0000	0,0000	0,9000
46338	0,7002	0,0000	0,8025	0,5228	0,0000	0,6750
46340	0,6595	0,6497	0,6753	0,6737	0,0000	0,0000
46346	0,6095	0,6930	0,0000	0,0500	0,0000	0,4500
46347	0,7558	0,0000	0,5911	0,0000	0,0000	0,0000
46348	0,6786	0,7027	0,1000	0,0000	0,0000	0,0000
46562	0,6460	0,7580	0,0000	0,0000	0,4500	0,6750
46564	0,4937	0,5602	0,0500	0,1000	0,4500	0,0000
46565	0,6643	0,4332	0,6557	0,0000	0,0000	0,0000
46566	0,0000	0,6930	0,0000	0,0000	0,0000	0,0000
46567	0,4693	0,0000	0,0000	0,0000	0,0000	0,2250
46568	0,4307	0,5660	0,4380	0,0000	0,0000	0,0000
46569	0,4185	0,0000	0,5797	0,0000	0,0000	0,6750
46570	0,5912	0,6389	0,0500	0,4424	0,0000	0,9000
46571	0,2804	0,5270	0,7671	0,0000	0,0000	0,0000
46572	0,4480	0,3971	0,5108	0,4924	0,0000	0,0000
46575	0,0000	0,6533	0,7677	0,3616	0,0000	0,0000
46578	0,0000	0,6642	0,1000	0,0500	0,0000	0,0000
46579	0,4510	0,0000	0,0000	0,0500	0,0000	0,0000
46581	0,5753	0,6353	0,5187	0,0000	0,2250	0,0000
46591	0,4388	0,0000	0,0000	0,0000	0,0000	0,0000

46601	0,5851	0,6353	0,6367	0,0000	0,9000	0,0000
46641	0,0000	0,3610	0,5652	0,4414	0,2250	0,0000
46649	0,7029	0,7364	0,8994	0,0000	0,2250	0,0000
46650	0,8343	0,7219	0,7258	0,0000	0,0000	0,0000
46651	0,8248	0,0000	0,5854	0,0000	0,0000	0,0000
46652	0,6321	0,0000	0,7327	0,6427	0,0000	0,0000
46653	0,6485	0,6786	0,8859	0,5966	0,0000	0,2250
46654	0,7906	0,0000	0,8615	0,1000	0,0000	0,0000
46655	0,7891	0,6305	0,6003	0,6922	0,0000	0,0000
46656	0,8716	0,0000	0,8070	0,0000	0,0000	0,9000
46657	0,7850	0,7436	0,9353	0,6486	0,2250	0,0000
46658	0,6041	0,7845	0,8123	0,8036	0,0000	0,0000
46659	0,7070	0,0000	0,7004	0,0000	0,0000	0,0000
46660	0,7360	0,6266	0,7227	0,6936	0,6750	0,0000
46661	0,7436	0,0000	0,9063	0,0500	0,6750	0,4500
46795	0,5193	0,0000	0,0000	0,0000	0,6750	0,0000
46990	0,6156	0,6930	0,1000	0,0000	0,0000	0,0000
47339	0,0000	0,0000	0,8500	0,0000	0,0000	0,0000
47424	0,0000	0,8122	0,0500	0,0000	0,2250	0,0000
47425	0,0000	0,0000	0,0000	0,7237	0,9000	0,0000
47467	0,0000	0,7797	0,6812	0,6292	0,0000	0,0000
47546	0,4388	0,0000	0,7278	0,6637	0,0000	0,0000
47582	0,8056	0,6642	0,6576	0,0000	0,2250	0,0000
47583	0,6757	0,4837	0,6886	0,0500	0,9000	0,4500
47587	0,6613	0,6738	0,7650	0,0000	0,0000	0,0000
47588	0,8228	0,7147	0,4905	0,1000	0,4500	0,0000
47590	0,8801	0,7219	0,6171	0,1000	0,0000	0,9000

47767	0,8411	0,0000	0,3930	0,0000	0,2250	0,0000
47768	0,0000	0,0000	0,1000	0,4323	0,2250	0,6750
47770	0,5921	0,0000	0,4430	0,0500	0,0000	0,0000
47771	0,5973	0,0000	0,0500	0,1000	0,4500	0,0000
47772	0,5028	0,0000	0,3228	0,0000	0,0000	0,0000
47773	0,7436	0,0000	0,0000	0,0000	0,0000	0,0000
47774	0,5485	0,0000	0,0000	0,0000	0,0000	0,0000
47775	0,4266	0,0000	0,0000	0,0000	0,0000	0,0000
47777	0,3901	0,0000	0,0000	0,3719	0,0000	0,0000
47792	0,7253	0,0000	0,6525	0,0500	0,0000	0,2250
47796	0,6796	0,0000	0,0000	0,1000	0,0000	0,0000
47797	0,7923	0,0000	0,4956	0,8847	0,9000	0,6750
47798	0,6460	0,0000	0,7424	0,0000	0,9000	0,0000
47799	0,0000	0,7508	0,0500	0,5829	0,2250	0,2250
47801	0,6339	0,7436	0,0000	0,5625	0,0000	0,0000
47802	0,6217	0,8085	0,7741	0,0000	0,0000	0,0000
47803	0,8289	0,5775	0,0000	0,0000	0,0000	0,0000
47806	0,5729	0,7797	0,6405	0,0000	0,0000	0,9000
47807	0,0000	0,6822	0,0000	0,6734	0,0000	0,2250
47809	0,9508	0,0000	0,1000	0,0500	0,0000	0,0000
47810	0,5485	0,7364	0,5354	0,0000	0,0000	0,0000
47812	0,7944	0,6786	0,7063	0,0000	0,0000	0,6750
47817	0,6745	0,7400	0,6513	0,0000	0,0000	0,6750
47836	0,3779	0,0000	0,5044	0,0000	0,0000	0,0000
47837	0,6765	0,0000	0,0000	0,0500	0,0000	0,0000
47838	0,8265	0,2888	0,0000	0,1000	0,6750	0,0000
47857	1,0000	0,0000	0,1000	0,0000	0,6750	0,0000

47859	0,6339	0,0000	0,5481	0,0000	0,0000	0,0000
47861	0,8289	0,0000	0,5354	0,0000	0,0000	0,6750
47867	0,5485	0,0000	0,0000	0,0000	0,0000	0,0000
47868	0,5242	0,0000	0,6677	0,0500	0,0000	0,0000
47869	0,0000	0,6497	0,6519	0,0000	0,0000	0,0000
47870	0,7314	0,0000	0,7222	0,0000	0,0000	0,0000
47871	0,5973	0,0000	0,5759	0,0000	0,9000	0,4500
47872	0,8167	0,5920	0,0000	0,9500	0,0000	0,0000
47873	0,6826	0,0000	0,0000	0,5326	0,0000	0,0000
48397	0,5485	0,0000	0,0000	0,0000	0,0000	0,0000
48398	0,3982	0,0000	0,0000	0,0000	0,6750	0,0000
48399	0,0000	0,5920	0,0000	0,1000	0,6750	0,0000
48401	0,7679	0,0000	0,0500	0,1000	0,0000	0,0000
48402	0,8777	0,6786	0,0500	0,0000	0,0000	0,0000
48996	0,6582	0,7364	0,9000	0,1000	0,0000	0,0000
49403	0,4510	0,0000	0,0000	0,8140	0,0000	0,0000
49407	0,7558	0,0000	0,0000	0,0000	0,0000	0,0000
49408	0,6686	0,3465	0,0000	0,0000	0,0000	0,4500
49409	0,6217	0,0000	0,0000	0,0000	0,0000	0,9000
49410	0,6777	0,0000	0,0000	0,0000	0,0000	0,0000
49411	0,5785	0,0000	0,0000	0,0000	0,0000	0,0000
49412	0,8777	0,0000	0,0500	0,0000	0,0000	0,0000
49413	0,5900	0,0000	0,1000	0,0000	0,6750	0,0000
49414	0,5208	0,6353	0,0000	0,6527	0,2250	0,6750
49415	0,4364	0,0000	0,0000	0,4918	0,0000	0,0000
49416	0,6400	0,0000	0,0000	0,0000	0,0000	0,0000
49417	0,6192	0,4620	0,1000	0,0000	0,2250	0,9000

49418	0,2804	0,0000	0,0000	0,0500	0,0000	0,0000
49419	0,5120	0,0000	0,0000	0,0000	0,0000	0,0000
49465	0,2560	0,0000	0,0000	0,0000	0,0000	0,0000
49625	0,0000	0,6401	0,0000	0,0000	0,0000	0,0000
49626	0,5363	0,0000	0,0000	0,0000	0,4500	0,0000
49628	0,7923	0,8230	0,6778	0,0000	0,0000	0,0000
49629	0,5821	0,0000	0,4633	0,4219	0,0000	0,0000
49631	0,6095	0,5487	0,0500	0,1000	0,0000	0,4500
49632	0,0000	0,5487	0,0000	0,1000	0,0000	0,0000
49634	0,6887	0,7508	0,6323	0,0000	0,0000	0,0000
49635	0,3657	0,0000	0,0500	0,0500	0,0000	0,2250
49636	0,8553	0,6930	0,7576	0,5128	0,0000	0,0000
49640	0,7558	0,0000	0,0000	0,0000	0,0000	0,0000
49647	0,5851	0,4043	0,4835	0,5161	0,6750	0,9000
49648	0,3535	0,0000	0,0000	0,0000	0,0000	0,0000
49878	0,5607	0,6353	0,0000	0,0000	0,4500	0,4500
49879	0,7236	0,6401	0,0000	0,8187	0,4500	0,0000
49881	0,4876	0,0000	0,0000	0,0000	0,0000	0,0000
49882	0,6826	0,0000	0,0000	0,0000	0,0000	0,0000
49884	0,0000	0,0000	0,0000	0,6363	0,0000	0,4500
49889	0,6729	0,6545	0,0500	0,6033	0,0000	0,2250
49917	0,7558	0,6930	0,0000	0,0000	0,0000	0,2250
50159	0,0000	0,0000	0,1000	0,6430	0,0000	0,0000
50163	0,5485	0,0000	0,0500	0,0000	0,0000	0,0000
50165	0,6217	0,0000	0,1000	0,0000	0,6750	0,0000
50166	0,0000	0,6786	0,0000	0,0000	0,9000	0,0000
50171	0,7009	0,0000	0,0000	0,6279	0,6750	0,0000

50172	0,8045	0,0000	0,7671	0,8640	0,0000	0,0000
50173	0,5242	0,0000	0,9399	0,7030	0,0000	0,0000
50188	0,7009	0,0000	0,0000	0,0000	0,0000	0,0000
50189	0,5868	0,0000	0,0000	0,1000	0,4500	0,0000
50190	0,4754	0,0000	0,0000	0,0000	0,0000	0,6750
50191	0,6582	0,0000	0,1000	0,1000	0,0000	0,0000
50355	0,0000	0,5920	0,1000	0,0000	0,0000	0,0000
50361	0,3291	0,0000	0,0000	0,0000	0,2250	0,0000
50362	0,4998	0,4909	0,0000	0,5071	0,0000	0,6750
50363	0,5760	0,0000	0,5089	0,0000	0,0000	0,0000
50364	0,5924	0,0000	0,6192	0,0500	0,0000	0,6750
50369	0,0000	0,0000	0,7373	0,0500	0,9000	0,0000
50471	0,7395	0,7869	0,0500	0,1000	0,6750	0,9000
50651	0,5607	0,0000	0,6652	0,8942	0,0000	0,0000
50652	0,0000	0,0000	0,8741	0,5276	0,0000	0,0000
50757	0,7070	0,0000	0,0000	0,0000	0,0000	0,0000
50758	0,0000	0,0000	0,0000	0,6326	0,0000	0,0000
50869	0,6491	0,7941	0,0000	0,6943	0,0000	0,0000
50872	0,7131	0,0000	0,8177	0,0000	0,0000	0,0000
50948	0,4251	0,0000	0,0000	0,4786	0,0000	0,2250
50949	0,5033	0,0000	0,5816	0,6731	0,0000	0,0000
50950	0,5719	0,3754	0,0000	0,0500	0,6750	0,0000
50951	0,4591	0,3465	0,5051	0,3820	0,9000	0,0000
50952	0,5485	0,0000	0,0000	0,5192	0,0000	0,9000
50953	0,6542	0,0000	0,0000	0,0000	0,6750	0,6750
50954	0,5567	0,0000	0,0000	0,7053	0,0000	0,9000
50955	0,3047	0,0000	0,0000	0,0000	0,9000	0,0000
50956	0,0000	0,0000	0,0000	0,3451	0,0000	0,0000
50957	0,3474	0,0000	0,1000	0,6577	0,0000	0,9000
50958	0,4510	0,0000	0,0000	0,0000	0,4500	0,2250
50959	0,5120	0,0000	0,0000	0,1000	0,0000	0,0000
50960	0,6704	0,0000	0,0000	0,1000	0,0000	0,0000
50961	0,7466	0,0000	0,0000	0,3512	0,0000	0,0000
50962	0,5851	0,0000	0,0500	0,0000	0,0000	0,2250
50964	0,7070	0,0000	0,0000	0,0000	0,4500	0,0000
52115	0,0000	0,0000	0,8886	0,0500	0,0000	0,0000
52120	0,0000	0,0000	0,5759	0,0000	0,6750	0,0000
52126	0,5851	0,3249	0,9089	0,6527	0,0000	0,4500
52134	0,0000	0,0000	0,4437	0,8308	0,4500	0,0000
52492	0,0000	0,0000	0,7806	0,1000	0,0000	0,2250
52636	0,3779	0,0000	0,7430	0,0000	0,0000	0,0000
52639	0,5363	0,0000	0,0000	0,0000	0,0000	0,0000
53115	0,6424	0,6064	0,8816	0,8643	0,0000	0,0000
53116	0,8126	0,0000	0,0000	0,0000	0,2250	0,0000
53121	0,0000	0,6281	0,8993	0,6631	0,2250	0,4500
53122	0,5790	0,0000	0,8348	0,6033	0,0000	0,6750
53123	0,7588	0,6382	0,6036	0,9000	0,0000	0,0000
53124	0,4876	0,6930	0,8589	0,0000	0,0000	0,0000
53125	0,6948	0,6064	0,0000	0,0000	0,4500	0,0000
53126	0,7558	0,6208	0,0500	0,1000	0,4500	0,9000
53127	0,8167	0,5920	0,6610	0,1000	0,0000	0,0000
53414	0,7124	0,0000	0,6089	0,4625	0,0000	0,0000
53415	0,6907	0,0000	0,8690	0,0000	0,0000	0,0000
53416	0,8594	0,0000	0,0000	0,0000	0,4500	0,0000

53737	0,9181	0,0000	0,8484	0,7039	0,0000	0,9000
53742	0,7161	0,7219	0,9899	0,0000	0,0000	0,0000
53743	0,0000	0,0000	0,7032	0,6360	0,0000	0,0000
53757	0,7424	0,0000	0,4659	0,0000	0,9000	0,0000
53758	0,5607	0,5920	0,7886	0,7311	0,2250	0,0000
53764	0,0000	0,0000	0,7099	0,0000	0,0000	0,4500
53765	0,8248	0,0000	0,7127	0,8338	0,0000	0,0000
53766	0,7466	0,0000	0,7975	0,7737	0,0000	0,0000
53767	0,7436	0,0000	0,0000	0,0000	0,0000	0,6750
53772	0,6786	0,6786	0,4652	0,0000	0,0000	0,4500
53773	0,6628	0,0000	0,6165	0,8240	0,0000	0,0000
73086	0,4676	0,1877	0,6975	0,0000	0,2250	0,2250
73087	0,3502	0,3834	0,6171	0,3452	0,0000	0,6750
73196	0,4023	0,5920	0,1000	0,0500	0,0000	0,0000
73197	0,2560	0,0000	0,1000	0,0000	0,2250	0,0000
73488	0,2926	0,0000	0,0000	0,1808	0,0000	0,0000
73493	0,2316	0,0000	0,0000	0,3710	0,0000	0,6750
73784	0,3007	0,0000	0,0000	0,0000	0,0000	0,0000
73785	0,3657	0,2455	0,0000	0,0000	0,9000	0,0000
73786	0,2194	0,0000	0,0000	0,0000	0,0000	0,0000
73796	0,6339	0,0000	0,0500	0,0000	0,0000	0,0000
73977	0,0000	0,0000	0,0000	0,8240	0,6750	0,2250
74036	0,2397	0,8085	0,0000	0,1000	0,4500	0,0000
74434	0,0000	0,0000	0,0000	0,2009	0,0000	0,0000
74435	0,4876	0,0000	0,0000	0,0000	0,6750	0,9000
74467	0,3860	0,0000	0,0000	0,0000	0,6750	0,4500
74468	0,2699	0,0000	0,0000	0,3619	0,0000	0,6750

74469	0,0000	0,0000	0,0000	0,2509	0,2250	0,2250
74503	0,0000	0,0000	0,0000	0,3213	0,6750	0,0000
74565	0,2438	0,0000	0,0000	0,1000	0,9000	0,9000
74566	0,5546	0,0000	0,0000	0,0000	0,0000	0,0000
74611	0,3251	0,0000	0,0000	0,0000	0,4500	0,4500
74746	0,4790	0,4700	0,5794	0,5161	0,0000	0,0000
74773	0,6369	0,5872	0,7627	0,4817	0,0000	0,0000
74774	0,0000	0,4971	0,0000	0,0000	0,0000	0,0000
74776	0,5810	0,3754	0,0000	0,4770	0,0000	0,2250
74778	0,5892	0,0000	0,0000	0,0000	0,0000	0,0000
74779	0,8086	0,7508	0,1000	0,0000	0,0000	0,2250
74786	0,6722	0,4259	0,8791	0,6430	0,0000	0,0000
74787	0,2804	0,0000	0,0000	0,0000	0,0000	0,9000
74816	0,7753	0,0000	0,0000	0,1000	0,0000	0,2250
74964	0,6217	0,0000	0,5152	0,0000	0,6750	0,0000
75074	0,8868	0,6786	0,8076	0,0000	0,0000	0,4500
75082	0,7883	0,6237	0,8230	0,9000	0,0000	0,0000
75083	0,8386	0,6642	0,7570	0,0000	0,0000	0,4500
75104	0,0000	0,5949	0,0000	0,0000	0,0000	0,2250
75131	0,4930	0,3658	0,0000	0,0500	0,0000	0,0000
75132	0,6704	0,7039	0,0500	0,0000	0,0000	0,6750
75134	0,5461	0,6353	0,4399	0,3116	0,0000	0,0000
75135	0,6217	0,0000	0,1000	0,6024	0,0000	0,0000
75159	0,0000	0,0000	1,0000	0,9243	0,0000	0,0000
75165	0,7558	0,0000	0,6620	0,7030	0,0000	0,0000
75166	0,7476	0,0000	0,7677	0,0500	0,0000	0,0000
75167	0,8005	0,7652	0,9392	0,1000	0,0000	0,0000

75168	0,0000	0,0000	0,9578	0,0000	0,0000	0,9000
75169	0,9188	0,0000	0,8751	0,0000	0,0000	0,9000
75170	0,5729	0,0000	0,8447	0,0000	0,0000	0,0000
75171	0,8130	0,6064	0,9095	0,0000	0,0000	0,0000
75179	0,2966	0,6786	0,0000	0,1000	0,4500	0,0000
75185	0,5455	0,3176	0,6725	0,5999	0,0000	0,0000
75186	0,3698	0,4380	0,6076	0,0000	0,6750	0,4500
75202	0,6436	0,6642	0,6468	0,6734	0,0000	0,9000
75203	0,6156	0,0000	0,0500	0,0500	0,0000	0,0000
75207	0,0000	0,0000	0,7367	0,0000	0,2250	0,6750
75209	0,7761	0,0000	0,0500	0,6728	0,0000	0,0000
75228	0,6509	0,7364	0,7772	0,0000	0,4500	0,2250
75245	0,4480	0,4548	0,7329	0,1000	0,9000	0,0000
75247	0,7151	0,8158	0,5006	0,3166	0,0000	0,0000
75249	0,4632	0,5198	0,4500	0,0000	0,6750	0,0000
75262	0,6582	0,3610	0,0500	0,0000	0,0000	0,0000
75266	0,7029	0,4043	0,6192	0,5421	0,0000	0,2250
75282	0,7381	0,0000	0,0000	0,1000	0,6750	0,2250
75283	0,8370	0,7652	0,6772	0,0000	0,0000	0,2250
75312	0,8045	0,5848	0,7042	0,5125	0,0000	0,0000
75353	0,9020	0,7291	0,7475	0,0500	0,0000	0,0000
75355	0,4998	0,0000	0,0000	0,0000	0,6750	0,0000
75409	0,6623	0,0000	0,0000	0,0000	0,9000	0,0000
75410	0,6826	0,0000	0,0500	0,0000	0,0000	0,4500
75412	0,7344	0,6497	0,6772	0,0000	0,0000	0,0000
75651	1,0000	0,0000	0,0000	0,6536	0,0000	0,0000
75790	0,0000	0,0000	0,1000	0,7835	0,9000	0,0000
75793	0,5973	0,0000	0,1000	0,5832	0,0000	0,0000
75795	0,7167	0,0000	0,0000	0,5997	0,0000	0,0000
75797	0,5729	0,0000	0,0500	0,7838	0,0000	0,9000
75803	0,6460	0,0000	0,1000	0,0000	0,0000	0,0000
75876	0,4998	0,0000	0,0000	0,0500	0,0000	0,4500
98166	0,7222	0,7374	0,7828	0,6301	0,0000	0,4514
98704	0,7135	0,7364	0,6007	0,6249	0,4500	0,2250
104096	0,6460	0,0000	0,5395	0,6681	0,0000	0,2250
104097	0,5339	0,6518	0,5190	0,8133	0,0000	0,4500
104098	0,7517	0,5631	0,0000	0,0000	0,2250	0,0000
104121	0,5973	0,4524	0,5332	0,0000	0,0000	0,6750
104122	0,4778	0,4524	0,7133	0,0000	0,0000	0,0000
104123	0,3535	0,5775	0,8443	0,0000	0,4500	0,9000
104251	0,4144	0,5505	0,0000	0,0500	0,0000	0,0000
104254	0,5282	0,5174	0,4666	0,5779	0,4500	0,0000
104255	0,9090	0,4043	0,0000	0,4414	0,0000	0,0000
104256	0,4023	0,4079	0,5361	0,6829	0,0000	0,0000
104257	0,9318	0,0000	0,0000	0,0000	0,0000	0,2250
104258	0,0000	0,9048	0,0000	0,0000	0,2250	0,6750
104264	0,8837	0,3610	0,4284	0,0500	0,0000	0,0000
104270	0,0000	0,0000	0,0000	0,4015	0,0000	0,0000
104273	0,0000	0,0000	0,0000	0,6369	0,9000	0,0000
104274	0,0000	0,3537	0,8500	0,7603	0,0000	0,0000
104275	0,0000	0,4476	0,5753	0,7131	0,0000	0,0000
104276	0,3515	0,5699	0,6057	0,5438	0,0000	0,0000
104277	0,4480	0,3465	0,3627	0,6125	0,2250	0,0000
104279	0,4144	0,3104	0,6318	0,7137	0,6750	0,9000

104280	0,8045	0,0000	0,8689	0,0500	0,0000	0,0000
104281	0,4545	0,3658	0,6232	0,3616	0,0000	0,4500
104282	0,4591	0,4765	0,5517	0,0000	0,0000	0,0000
104283	0,4713	0,0000	0,0000	0,0000	0,0000	0,6750
104284	0,0000	0,6208	0,0000	0,0000	0,0000	0,9000
104285	0,6501	0,9096	0,0000	0,0000	0,0000	0,0000
104286	0,0000	0,5053	0,8146	0,7298	0,9000	0,0000
104287	0,0000	0,5053	0,8500	0,5018	0,0000	0,9000
104288	0,0000	0,6160	0,0000	0,0000	0,0000	0,0000
104289	0,0000	0,0000	0,0000	0,7841	0,0000	0,0000
104290	0,0000	0,0000	0,0000	0,4722	0,0000	0,0000
104291	0,3383	0,5270	1,0000	0,0000	0,0000	0,4500
104297	0,4266	0,0000	0,7217	0,0000	0,0000	0,0000
104305	0,5729	0,4115	0,6226	0,6628	0,9000	0,0000
104315	0,5038	0,0000	0,6435	0,4021	0,0000	0,0000
104323	0,0000	0,0000	0,0500	0,6335	0,6750	0,6750
104331	0,0000	0,3682	0,8319	0,5488	0,6750	0,0000
104338	0,4144	0,0000	0,0500	0,7090	0,0000	0,0000
104339	0,0000	0,0000	0,0000	0,3216	0,2250	0,0000
104340	0,6144	0,0000	0,3690	0,4116	0,0000	0,9000
104341	0,8106	0,0000	0,7987	0,0500	0,9000	0,6750
104364	0,5485	0,0000	0,8392	0,5924	0,2250	0,0000
104367	0,5038	0,0000	0,0000	0,1000	0,0000	0,9000
104419	0,4205	0,0000	0,7285	0,0000	0,9000	0,9000
104488	0,2682	0,0000	0,7272	0,5524	0,0000	0,0000
104507	0,4632	0,5342	0,0000	0,1000	0,0000	0,9000
104519	0,2560	0,0000	0,9000	0,3814	0,0000	0,4500

104800	0,5201	0,7075	0,6051	0,6731	0,0000	0,2250
104806	0,8289	0,4765	0,0000	0,1000	0,0000	0,0000
104817	0,6582	0,0000	0,1000	0,0000	0,0000	0,0000
105945	0,5760	0,0000	0,5658	0,7936	0,0000	0,2250
108283	0,7366	0,4043	0,5146	0,0000	0,2250	0,0000
108284	0,0000	0,0000	0,2930	0,0000	0,0000	0,4500
108286	0,5851	0,0000	0,0500	0,0000	0,6750	0,0000
108643	0,4023	0,0000	0,3430	0,5172	0,0000	0,0000
108923	0,3779	0,0000	0,0000	0,0500	0,0000	0,0000
113312	0,4876	0,0000	0,0000	0,0500	0,0000	0,0000
124202	0,4876	0,5920	0,0000	0,8891	0,0000	0,0000
124204	0,8655	0,0000	0,0500	0,6433	0,6750	0,0000
128000	0,8898	0,0000	0,4753	0,0000	0,0000	0,0000
128382	0,6314	0,6930	0,5867	0,0000	0,0000	0,9000
128383	0,6108	0,0000	0,5361	0,7039	0,0000	0,9000
128384	0,5875	0,7472	0,0000	0,6798	0,0000	0,9000
128385	0,6826	0,0000	0,1000	0,6125	0,9000	0,2250
128386	0,5120	0,6497	0,8785	0,7268	0,0000	0,0000
128387	0,6907	0,8374	0,6854	0,7436	0,0000	0,0000
128388	0,0000	0,6208	0,6496	0,7506	0,0000	0,0000
128389	0,6826	0,6425	0,7772	0,0000	0,0000	0,2250
128390	0,6689	0,7833	0,6344	0,6080	0,2250	0,0000
128391	0,7497	0,0000	0,6253	0,7533	0,0000	0,0000
128392	0,7828	0,7652	0,1000	0,6427	0,0000	0,0000
128393	0,6826	0,8663	0,6057	0,7131	0,6750	0,0000
128394	0,5242	0,6064	0,7778	0,0000	0,0000	0,0000
128395	0,6217	0,8663	0,7907	0,0000	0,0000	0,0000

128400	0,0000	0,7364	0,0000	0,7643	0,0000	0,0000
128401	0,0000	0,5920	0,0000	0,0000	0,2250	0,6750
128404	0,7131	0,0000	0,7652	0,7335	0,0000	0,0000
129522	0,5810	0,6208	0,0500	0,5930	0,0000	0,0000
137892	0,0000	0,0000	0,0000	0,4314	0,9000	0,0000
137894	0,0000	0,5775	0,0000	0,1000	0,0000	0,0000
137922	0,6080	0,2888	0,0000	0,0000	0,0000	0,0000
137925	0,4946	0,0000	0,0000	0,0500	0,0000	0,2250
137927	0,5062	0,0000	0,8987	0,0500	0,2250	0,0000
137929	0,4785	0,3934	0,0000	0,0500	0,0000	0,0000
137930	0,6095	0,5920	0,0000	0,0000	0,0000	0,0000
137937	0,4729	0,0000	0,3430	0,1000	0,0000	0,0000
137938	0,7558	0,0000	0,0000	0,0500	0,0000	0,0000
137941	0,5339	0,5198	0,0500	0,3317	0,0000	0,0000
137947	0,5607	0,3802	0,0000	0,0500	0,0000	0,6750
137951	0,3169	0,0000	0,0000	0,0000	0,2250	0,0000
137952	0,0000	0,3032	0,0000	0,0000	0,0000	0,0000
137961	0,0000	0,0000	0,0000	0,4424	0,4500	0,0000
137962	0,0000	0,7219	0,0000	0,0000	0,0000	0,0000
138361	0,0000	0,6497	0,0500	0,0000	0,2250	0,4500
138376	0,5426	0,0000	0,6557	0,0000	0,0000	0,0000
138378	0,0000	0,6353	0,3127	0,5379	0,0000	0,0000
138380	0,5222	0,7508	0,0500	0,0000	0,0000	0,0000
138381	0,6190	0,6208	0,3627	0,5675	0,0000	0,0000
138382	0,7070	0,4909	0,0000	0,0000	0,6750	0,0000
138384	0,0000	0,0000	0,0000	0,4807	0,0000	0,0000
138388	0,4297	0,0000	0,6597	0,0000	0,0000	0,9000

138389	0,7801	0,0000	0,3930	0,0000	0,0000	0,0000
138390	0,6114	0,5053	0,0000	0,0000	0,6750	0,0000
138391	0,4632	0,3176	0,0500	0,1000	0,0000	0,0000
138392	0,3853	0,0000	0,5241	0,4994	0,9000	0,0000
138393	0,6424	0,0000	0,4544	0,5524	0,0000	0,0000
138505	0,5729	0,0000	0,0000	0,0000	0,0000	0,0000
138629	0,6643	0,0000	0,5557	0,5122	0,4500	0,0000
138640	0,2804	0,0000	0,0000	0,4119	0,2250	0,0000
138664	0,0000	0,0000	0,1000	0,6190	0,9000	0,0000
138665	0,5120	0,0000	0,0000	0,0000	0,0000	0,0000
138666	0,7631	0,0000	0,4528	0,5950	0,0000	0,6750
138978	0,0000	0,0000	0,0000	0,4817	0,2250	0,0000
139254	0,2934	0,5487	0,1000	0,0000	0,9000	0,4500
139255	0,4041	0,0000	0,0000	0,1000	0,6750	0,4500
139256	0,4632	0,0000	0,0000	0,0000	0,4500	0,0000
139354	0,4068	0,0000	0,5071	0,0000	0,0000	0,0000
139355	0,5690	0,4043	0,0000	0,0000	0,0000	0,0000
139356	0,5111	0,5404	0,4451	0,5631	0,6750	0,9000
139357	0,7405	0,0000	0,0000	0,0500	0,0000	0,9000
139359	0,6467	0,0000	0,0000	0,0500	0,0000	0,9000
139360	0,5242	0,0000	0,0000	0,5564	0,4500	0,0000
139361	0,3951	0,4765	0,7228	0,5597	0,0000	0,0000
139362	0,6826	0,0000	0,0000	0,0500	0,9000	0,0000
139363	0,6034	0,0000	0,0000	0,6763	0,0000	0,6750
139365	0,4904	0,6376	0,4937	0,4239	0,6750	0,9000
139366	0,4205	0,0000	0,0000	0,0500	0,0000	0,0000
139376	0,6619	0,0000	0,0000	0,0500	0,0000	0,0000

139377	0,5607	0,0000	0,0000	0,4924	0,0000	0,2250
139382	0,6156	0,0000	0,0000	0,0000	0,0000	0,0000
139557	0,6765	0,3321	0,5854	0,0000	0,6750	0,0000
139560	0,3779	0,0000	0,0000	0,0000	0,0000	0,0000
139561	0,6521	0,0000	0,0000	0,2613	0,9000	0,0000
139567	0,4364	0,0000	0,5787	0,2874	0,0000	0,0000
139568	0,2926	0,0000	0,7171	0,0000	0,0000	0,0000
139571	0,4754	0,0000	0,0000	0,0000	0,9000	0,0000
139671	0,0000	0,0000	0,4105	0,0000	0,6750	0,0000
141214	0,6960	0,9204	0,6823	0,6628	0,0000	0,4500
141215	0,7192	0,7335	0,7634	0,8108	0,1219	0,3658
141216	0,7586	0,8066	0,7712	0,7312	0,0000	0,0000
141217	0,7405	0,7089	0,7266	0,5846	0,3386	0,0000
141218	0,8058	0,8007	0,7710	0,8200	0,0000	0,0000
141219	0,9020	1,0000	0,0000	0,6084	0,0000	0,0000
141220	0,7429	0,7508	0,6468	0,5625	0,0000	0,0000
141222	0,6278	0,0000	0,5962	0,0000	0,0000	0,0000
141223	0,6750	0,6208	0,9190	0,0000	0,9000	0,0000
141224	0,6929	0,7674	0,6758	0,5225	0,3938	0,2626
141233	0,7458	0,7291	0,7025	0,5762	0,0000	0,0000
141234	0,7410	0,7445	0,5824	0,7054	0,2827	0,1414
141235	0,8257	0,7588	0,8023	0,7755	0,0000	0,0000
141236	0,8437	0,9006	0,6306	0,8302	0,1285	0,0000
141237	0,8584	0,6325	0,6051	0,6885	0,0000	0,0000
141238	0,8756	0,6257	0,0000	0,6634	0,0000	0,0000
141240	0,8088	0,7412	0,7965	0,7436	0,0000	0,0000
141241	0,9291	0,8576	0,7823	0,6436	0,0000	0,0000
141242	0,9171	1,0000	0,8785	0,8422	0,0000	0,0000
141243	0,7707	0,5583	0,7778	0,6436	0,0000	0,4514
141244	0,7862	0,6190	0,6044	0,7251	0,0000	0,0000
141245	0,8059	1,0000	0,0500	0,5889	0,4514	0,0000
141246	0,0000	1,0000	0,1000	0,6077	0,0000	0,0000
141247	0,8362	0,8663	0,0000	0,5980	0,2250	0,0000
141248	1,0000	0,0000	0,0500	0,0000	0,0000	0,0000
141249	0,4266	0,0000	0,6051	0,8500	0,0000	0,0000
141250	0,7558	0,9674	0,0000	0,0000	0,2250	0,0000
141251	0,6796	0,6869	0,5051	0,7539	0,9000	0,0000
141252	0,4632	1,0000	0,0000	0,0000	0,0000	0,1129
141253	0,6793	0,8013	0,7985	0,8255	0,0000	0,0000
141254	0,7056	0,7797	0,8196	0,6860	0,0000	0,9000
141255	0,7766	0,8418	0,7959	0,4927	0,3716	0,0000
141256	0,7222	0,7163	0,6627	0,7320	0,0000	0,0000
141257	0,7090	0,6208	0,7745	0,7596	0,0000	0,1129
141258	0,6980	0,6808	0,9132	0,6257	0,0000	0,0000
141259	0,7896	0,7976	0,8047	0,6728	0,0000	0,0000
141261	0,4754	0,0000	0,0000	0,0000	0,0000	0,2250
141262	0,5242	0,0000	0,0000	0,6734	0,9000	0,6750
141263	0,0000	0,0000	0,9426	0,7788	0,0000	0,0000
141265	0,6904	0,6353	0,8967	0,7442	0,0000	0,0000
141266	0,8703	0,6064	0,0000	0,6074	0,0000	0,0000
141267	0,5242	0,7219	0,6981	0,5725	0,0000	0,0000
141270	0,0000	0,6497	0,9399	0,7131	0,0000	0,0000
141303	0,6298	0,0000	0,8285	0,4625	0,0000	0,0000
141304	0,6509	0,6245	0,8690	0,7895	0,0000	0,0000

141308	0,5892	0,0000	0,9797	0,5933	0,0000	0,1129
141309	0,7972	0,6930	0,8619	0,6758	0,0000	0,4514
141310	0,7558	0,6449	0,0000	0,5980	0,0000	0,1129
141323	0,7172	0,9890	0,7323	0,6125	0,0000	0,0000
141324	0,7679	0,6353	0,0000	0,7591	0,0000	0,0000
141325	0,7541	0,7068	0,7212	0,6536	0,0000	0,0000
141326	0,8031	0,8271	0,9293	0,7765	0,0000	0,0000
141327	0,9427	0,0000	0,8500	0,9448	0,0000	0,0000
141340	0,0000	0,0000	0,7880	0,5430	0,4514	0,0000
141342	0,8045	0,0000	0,0000	0,6231	0,0000	0,9000
141367	0,7273	0,6497	0,6867	0,0000	0,0000	0,0000
141379	0,7558	0,0000	0,7975	0,6027	0,0000	0,0000
141380	0,7850	0,8422	0,1000	0,1000	0,0000	0,2250
141386	0,8258	0,9818	0,9500	0,6228	0,0000	0,0000
141413	0,7154	0,6642	0,4909	0,6832	0,0000	0,0000
141416	0,5363	0,0000	0,8447	0,0000	0,0000	0,2250
141419	0,6836	0,0000	0,8582	0,5849	0,0000	0,0000
141421	0,8350	0,6305	0,6996	0,6789	0,0000	0,0000
141422	0,6433	0,5920	0,6863	0,7416	0,2257	0,4514
141423	0,7611	0,6353	0,7684	0,7332	0,0000	0,0000
141424	0,7131	0,0000	0,9399	0,7423	0,0000	0,1129
141425	0,6664	0,8898	0,7442	0,7489	0,0000	0,0000
141426	0,8455	0,3898	0,5158	0,6533	0,4500	0,0000
141462	0,0000	0,0000	0,0000	0,7282	0,2640	0,0000
141476	0,7032	0,7508	0,5940	0,7015	0,0000	0,0000
141477	0,7054	0,7786	0,6873	0,5720	0,0000	0,0000
141478	0,7298	0,7211	0,6091	0,6300	0,3498	0,0000

141479	0,6760	0,7241	0,7770	0,6253	0,0000	0,0000
141480	0,6711	0,7540	0,7893	0,7489	0,0000	0,0000
141481	0,7189	0,7470	0,6935	0,7838	0,0000	0,4514
141482	0,8581	0,8003	0,7171	0,8750	0,3386	0,3386
141493	0,6972	0,7405	0,0000	0,6771	0,0000	0,0000
141494	0,8777	1,0000	0,0000	0,0000	0,0000	0,2257
141495	0,6887	0,0000	0,6827	0,6315	0,0000	0,0000
141498	0,0000	0,0000	0,7063	0,8945	0,0000	0,0000
141499	0,7070	0,0000	0,1000	0,6430	0,0000	0,0000
141500	0,7338	0,0000	0,9797	0,6519	0,0000	0,0000
141501	0,6966	0,7101	0,7880	0,7603	0,0000	0,0000
141502	0,7484	0,0000	0,8892	0,7945	0,0000	0,2250
141512	0,7035	0,0000	0,0000	0,8137	0,0000	0,0000
141513	0,7356	0,8771	0,9000	0,6628	0,4981	0,0000
141518	0,5973	0,0000	0,0000	0,0000	0,0000	0,9000
141528	0,0000	0,0000	0,0000	0,7936	0,4514	0,0000
141539	0,9874	0,0000	0,5665	0,1000	0,0000	0,0000
141547	0,5607	0,0000	0,0000	0,7835	0,0000	0,0000
141559	0,6420	0,0000	0,9443	0,6480	0,0000	0,2250
141564	0,7314	0,0000	0,0000	0,0000	0,0000	0,0000
141569	0,0000	0,0000	0,0000	0,6430	0,0000	0,0000
141570	0,0000	0,0000	0,0000	0,6326	0,0000	0,0000
141572	0,5778	0,0000	0,0000	0,0000	0,0000	0,4500
141573	0,6278	0,0000	0,0000	0,8646	0,4500	0,0000
141574	0,6704	0,0000	0,0000	0,9445	0,0000	0,0000
141586	0,9874	0,7797	0,7407	0,6838	0,0000	0,0000
141587	0,8451	0,0000	0,0000	0,5631	0,0000	0,6750

141588	0,7408	0,7436	0,4666	0,7533	0,3386	0,0000
141589	0,8624	1,0000	0,0000	0,9344	0,2257	0,1129
141590	0,7162	0,4620	0,8042	0,6237	0,0000	0,3386
141591	0,7436	0,6064	0,6152	0,8094	0,1129	0,0000
141595	0,6704	0,0000	0,0500	0,0000	0,0000	0,0000
141597	0,7874	0,8085	0,4424	0,6930	0,0000	0,0000
141598	0,8280	0,8711	0,5703	0,7039	0,4781	0,3586
141599	0,7698	1,0000	0,4639	0,7181	0,0000	0,4615
141600	0,8014	0,5920	0,6456	0,6386	0,2398	0,0000
141636	0,7871	0,7797	0,9021	0,7332	0,0000	0,6750
141647	0,9386	0,0000	0,1000	0,0000	0,2250	0,6750
141648	0,7815	0,8653	0,6057	0,7493	0,0000	0,5745
141649	0,7404	0,8663	0,4146	0,7554	0,0000	0,0000
141650	0,8459	0,6930	0,1000	0,7727	0,0000	0,0000
141651	0,8299	0,6401	0,1000	0,7729	0,0000	0,0000
141652	0,7246	0,6112	0,0500	0,7211	0,0000	0,4514
141653	0,8167	0,7364	0,0500	0,7087	0,0000	0,0000
141654	0,5877	0,7219	0,0000	0,7338	0,0000	0,1129
141655	0,6867	0,8779	0,7880	0,8042	0,0000	0,1173
141656	0,5485	0,9962	0,5962	0,6634	0,3386	0,1129
141684	1,0000	0,0000	0,1000	0,7643	0,0000	0,0000
141687	0,0000	0,0000	0,1000	0,6228	0,0000	0,0000
141688	0,7631	0,0000	0,0000	0,6530	0,0000	0,4500
141696	0,7253	0,0000	0,0000	0,8137	0,2250	0,0000
141697	0,7216	0,0000	0,0000	0,7755	0,0000	0,0000
141703	0,6339	0,6786	0,6791	0,6933	0,6750	0,0000
141731	0,8302	0,7532	0,7084	0,6878	0,2257	0,0000
141732	0,8620	1,0000	0,8015	0,6430	0,0000	0,0000
141734	0,7619	0,0000	0,0000	0,7382	0,0000	0,0000
141735	0,5242	0,7219	0,6867	0,1000	0,9000	0,0000
141780	0,0000	0,0000	0,1000	0,0000	0,0000	0,3386
141781	0,8858	0,0000	0,7671	0,0000	0,6750	0,0000
141819	0,6521	0,6497	0,5259	0,6880	0,0000	0,0000
141820	1,0000	0,6930	0,7034	0,6939	0,0000	0,0000
141823	0,7639	0,0000	0,0000	0,0500	0,0000	0,0000
141824	0,7893	0,0000	0,7880	0,0000	0,0000	0,0000
141825	0,7584	0,5775	0,6171	0,7187	0,0000	0,2250
141826	0,7322	0,7364	0,7272	0,9017	0,0000	0,0000
141833	0,9752	0,0000	0,0000	0,0000	0,0000	0,0000
141881	0,7385	0,0000	0,4652	0,7788	0,0000	0,0000
141882	0,7445	0,6690	0,0000	0,4675	0,2250	0,2250
141947	0,7996	0,0000	0,6215	0,8341	0,4514	0,0000
141949	0,5120	0,0000	0,0000	0,5430	0,0000	0,0000
141950	0,7781	0,0000	0,0000	0,7838	0,4725	0,0000
141953	0,0000	0,6642	0,8184	0,5631	0,0000	0,0000
141975	0,8263	0,7487	0,7836	0,6664	0,0000	0,0000
141976	0,9017	1,0000	0,5911	0,6228	0,2257	0,0000
141982	0,8258	0,0000	0,0000	0,0000	0,4500	0,2250
142002	0,6887	0,0000	0,0000	0,7606	0,0000	0,0000
142007	0,9914	0,8230	0,7184	0,1000	0,0000	0,0000
142008	0,7438	0,8410	0,7876	0,8288	0,6750	0,2250
142009	0,6761	0,7291	0,8089	0,7050	0,0000	0,4500
142010	0,7137	0,7003	0,0000	0,6634	0,0000	0,2250
142011	0,7407	0,6979	0,8582	0,5530	0,4500	0,0000

142027	0,7862	0,0000	0,0500	0,7332	0,0000	0,0000
142043	0,8749	0,8355	0,6333	0,6933	0,0000	0,0000
142046	0,7509	0,5342	0,9089	0,0500	0,0000	0,0000
142051	0,7445	0,7681	0,3532	0,6444	0,4514	0,2257
142052	0,7809	0,7718	0,0000	0,5301	0,5105	0,0000
142055	0,9630	0,0000	0,0000	0,0500	0,6750	0,0000
142061	0,7862	0,7956	0,4646	0,7538	0,1129	0,3386
142062	0,8086	0,9168	0,6956	0,5993	0,0000	0,0000
142069	0,4998	0,0000	0,1000	1,0000	0,0000	0,1129
142073	0,0000	0,0000	0,0000	1,0000	0,2250	0,2250
142083	0,6217	0,0000	0,6057	0,7401	0,0000	0,0000
142093	0,6192	0,0000	0,6778	0,6030	0,0000	0,6750
142094	0,7601	0,7251	0,6458	0,6945	0,0000	0,0000
142100	0,7514	0,9529	0,5937	0,7761	0,0000	0,0000
142101	0,5509	1,0000	0,5661	0,7872	0,0000	0,0000
142102	0,7517	0,5775	0,7373	0,0000	0,0000	0,0000
142103	0,6958	0,5378	0,8616	0,5329	0,0000	0,3444
142104	0,5824	0,6180	0,9120	0,6194	0,0000	0,0000
142105	0,6487	0,6419	0,7349	0,5487	0,2257	0,2257
142107	0,8289	0,9587	0,7408	0,4725	0,0000	0,0000
142108	0,6509	0,6497	0,0500	0,7206	0,2257	0,4514
142109	0,7986	0,7838	0,0500	0,6483	0,1129	0,0000
142110	0,7314	0,5342	0,7420	0,8137	0,2257	0,2257
142117	0,6887	0,0000	0,8656	0,7533	0,0000	0,2250
142119	0,6830	0,6411	0,6754	0,7517	0,4500	0,0000
142120	0,7716	0,7161	0,6616	0,6199	0,3430	0,1143
142121	0,7548	0,7392	0,7215	0,6796	0,5466	0,0000

142122	0,7720	0,0000	0,0000	0,0500	0,2250	0,0000
142123	0,8211	1,0000	0,0500	0,4216	0,0000	0,0000
142125	1,0000	0,7508	0,0000	0,0000	0,0000	0,4514
142135	0,7740	0,0000	0,1000	0,1000	0,4500	0,0000
142136	0,8006	0,7544	0,6462	0,7479	0,0000	0,0000
142137	0,8021	0,7668	0,0000	0,8061	0,0000	0,0000
142146	0,8167	0,0000	0,6456	0,6033	0,0000	0,4500
142179	0,7801	0,8085	0,5158	0,6731	0,0000	0,0000
142246	0,6509	0,0000	0,6671	0,7615	0,0000	0,0000
142247	0,7862	0,0000	0,0000	0,7979	0,0000	0,0000
142248	0,6664	0,7508	0,5614	0,7030	0,0000	0,2250
142249	0,6753	0,8326	0,6747	0,7151	0,0000	0,2250
142250	0,8072	0,8158	0,6266	0,7076	0,0000	0,0000
142261	0,6876	0,7797	0,5595	0,7231	0,4626	0,0000
142262	0,0000	0,0000	0,5057	0,8146	0,2257	0,0000
142263	1,0000	0,0000	0,0000	0,7714	0,5775	0,0000
142264	0,8898	0,0000	0,1000	0,0000	0,2464	0,0000
142265	0,6835	0,0000	0,8500	0,6310	0,0000	0,0000
142267	0,6777	0,0000	0,5854	0,5829	0,9000	0,0000
142268	0,6623	0,0000	0,8730	0,7838	0,0000	0,0000
142269	0,6329	0,7941	0,6171	0,6033	0,9000	0,6750
142270	0,7954	0,8085	0,8230	0,6933	0,0000	0,0000
142271	0,6115	0,6208	0,0000	0,5927	0,0000	0,0000
142272	0,6674	0,7436	0,6711	0,7913	0,6750	0,9000
142273	0,7575	0,0000	0,6861	0,6634	0,0000	0,0000
142274	0,6826	0,8807	0,8190	0,6067	0,0000	0,0000
142275	0,7714	0,8230	0,0500	0,7687	0,0000	0,2250

142276	0,6826	0,5775	0,4753	0,6798	0,0000	0,0000
142277	0,6867	0,7652	0,0000	0,7964	0,0000	0,0000
142320	0,9386	0,0000	0,5361	0,0000	0,0000	0,0000
142322	1,0000	0,8952	0,1000	0,6869	0,6750	0,0000
142329	0,7503	0,6160	0,7873	0,5977	0,0000	0,0000
142330	0,8010	1,0000	0,7684	0,0000	0,0000	0,0000
142331	0,7747	0,7725	0,6981	0,0000	0,4500	0,2250
142345	0,5973	0,0000	0,0000	0,0000	0,6750	0,0000
142379	0,6095	0,6786	0,6658	0,6530	0,2250	0,0000
142383	0,6257	0,0000	0,0000	0,0000	0,2250	0,0000
142392	0,5485	0,6786	0,7892	0,0000	0,0000	0,0000
142565	0,7958	0,8085	0,0500	0,0000	0,2250	0,2250
142566	0,0000	0,0000	0,0000	0,6879	0,4514	0,0000
142567	0,6050	0,6642	0,5759	0,0000	0,0000	0,0000
142568	0,8227	0,5390	0,7481	0,7458	0,0000	0,0000
142569	0,8289	0,0000	0,0500	0,5933	0,0000	0,0000
142570	1,0000	0,0000	0,0000	0,0000	0,0000	0,0000
142660	0,6745	0,0000	0,0000	0,0000	0,0000	0,1129
142661	0,6989	0,8548	0,1000	0,8427	0,0000	0,0000
142662	0,5892	0,6208	0,0000	0,9746	0,0000	0,1129
142732	0,7366	0,6699	0,8184	0,9000	0,0000	0,0000
142751	0,9183	0,0000	0,0000	0,7835	0,0000	0,0000
142752	0,4226	0,4837	0,0000	0,0000	0,0000	0,0000
142753	0,6521	0,8302	0,5696	0,6084	0,5129	0,5129
142754	0,8533	0,3898	0,0500	0,8500	0,0000	0,0000
142755	0,6460	0,6786	1,0000	0,7863	0,0000	0,0000
142756	0,6664	0,6064	0,7266	0,8841	0,0000	0,9000

142757	0,7070	0,7941	0,0000	0,1000	0,0000	0,0000
142760	0,5607	0,0000	0,5354	0,6480	0,0000	0,6750
142761	0,0000	0,8807	0,0000	0,5329	0,0000	0,0000
142764	0,7375	0,0000	0,0000	0,6939	0,0000	0,0000
142792	0,6034	0,8230	0,0000	0,7231	0,0000	0,0000
142960	0,0000	0,0000	0,0000	0,8036	0,0000	0,0000
142961	0,0000	0,0000	0,0000	0,5527	0,0000	0,0000
143110	0,6921	0,6208	0,7086	0,6533	0,4695	0,1174
143111	0,6680	0,8904	0,9000	0,6637	0,0000	0,0000
143113	0,7436	0,8013	0,7734	0,0000	0,0000	0,9000
143141	0,8216	0,6064	0,9000	0,6728	0,0000	0,0000
143147	0,7850	0,0000	0,7424	0,5044	0,4514	0,0000
143148	0,4815	0,0000	0,1000	0,4719	0,0000	0,0000
143167	0,7009	0,6642	0,5361	0,6731	0,0000	0,0000
143168	0,0000	0,0000	0,6981	0,0000	0,0000	0,0000
143169	0,7151	0,0000	0,6542	0,5786	0,3389	0,2259
143170	0,0000	0,0000	0,6816	0,6563	0,0000	0,0000
143172	0,7964	0,5920	0,7468	0,8225	0,4514	0,0000
143809	0,4998	0,0000	0,7266	0,6385	0,6750	0,0000
143931	0,6440	0,8807	0,0000	0,7835	0,4514	0,0000
143932	0,0000	0,0000	0,1000	0,0000	0,0000	0,0000
143935	0,9995	0,0000	0,0000	0,1000	0,0000	0,2250
150269	0,5457	0,5550	0,6058	0,5815	0,3457	0,3457
150357	0,5177	0,6006	0,7092	0,6904	0,0000	0,0000
150375	0,4806	0,0000	0,4633	0,0000	0,0000	0,0000
150561	0,0000	0,0000	0,6759	0,0000	0,9000	0,2250
151919	0,5688	0,6714	0,6358	0,5731	0,0000	0,0000

151920	0,0000	0,0000	0,0000	0,9347	0,0000	0,0000
153201	0,7265	0,7362	0,7648	0,7315	0,0000	0,3386
153202	0,6788	0,0000	0,5989	0,0000	0,9000	0,2250
153666	0,7340	0,7420	0,7456	0,7889	0,4514	0,0000
154289	0,5272	0,0000	0,3937	0,6027	0,0000	0,0000
154290	0,6169	0,3862	0,0500	0,0000	0,0000	0,2250
154291	0,5482	0,0000	0,0000	0,0000	0,4500	0,0000
154292	0,5115	0,4332	0,1000	0,0000	0,0000	0,0000
154293	0,5123	0,3850	0,6278	0,1000	0,2250	0,0000
154294	0,4963	0,0000	0,5776	0,0000	0,0000	0,0000
154295	0,5025	0,8374	0,5213	0,0000	0,0000	0,2250
154296	0,6141	0,0000	0,2627	0,4012	0,0000	0,0000
154297	0,3169	0,3176	0,0000	0,1000	0,0000	0,9000
154299	0,0000	0,0000	0,0000	0,3883	0,2250	0,9000
154300	0,3047	0,0000	0,0000	0,3113	0,0000	0,0000
154301	0,5242	0,0000	0,0000	0,0000	0,2250	0,0000
154302	0,5099	0,6305	0,0000	0,0000	0,0000	0,0000
154303	0,5782	0,5487	0,6395	0,0000	0,0000	0,0000
154304	0,5438	0,6172	0,6563	0,0000	0,0000	0,0000
154305	0,5523	0,0000	0,6252	0,1000	0,0000	0,6750
154332	0,4492	0,6064	0,8076	0,0000	0,0000	0,0000
154424	0,5798	0,6208	0,0000	0,0000	0,0000	0,0000
154425	0,7984	0,0000	0,0000	0,0000	0,0000	0,0000
154457	0,6054	0,4476	0,6620	0,4918	0,6750	0,0000
154508	0,5821	0,0000	0,8709	0,1000	0,2250	0,0000
154509	0,5242	0,0000	0,6044	0,3914	0,2250	0,0000
154511	0,5369	0,0000	0,4833	0,0000	0,0000	0,4500
154606	0,5298	0,4813	0,0500	0,0000	0,0000	0,9000
154607	0,3901	0,0000	0,1000	0,0000	0,0000	0,9000
154609	0,3383	0,0000	0,0000	0,4018	0,0000	0,0000
154610	0,0000	0,0000	0,0000	0,5320	0,0000	0,9000
154611	0,0000	0,0000	0,0000	0,3216	0,4500	0,0000
154614	0,0000	0,0000	0,0000	0,5823	0,0000	0,0000
154618	0,3941	0,0000	0,0000	0,0000	0,0000	0,0000
154622	0,4937	0,0000	0,0000	0,0000	0,4500	0,0000
154626	0,6181	0,5053	0,0000	0,1000	0,0000	0,2250
154627	0,6887	0,0000	0,0000	0,0000	0,9000	0,9000
154628	0,6339	0,0000	0,0000	0,1000	0,0000	0,6750
154629	0,4876	0,0000	0,0000	0,1000	0,2250	0,0000
154630	0,6084	0,4043	0,0000	0,0000	0,9000	0,0000
154631	0,6471	0,6642	0,1000	0,0000	0,0000	0,9000
154632	0,6308	0,4909	0,0000	0,0500	0,0000	0,0000
154633	0,4144	0,5775	0,0500	0,1000	0,0000	0,4500
156696	0,4725	0,0000	0,3741	0,0000	0,0000	0,0000
157772	0,7353	0,7269	0,8403	0,6226	0,2257	0,4514
158218	0,6848	0,7244	0,7567	0,7808	0,0000	0,0000
158482	0,7281	0,6944	0,8250	0,7977	0,0000	0,0000
158505	0,7221	0,7496	0,6491	0,6976	0,0000	0,4500
158507	0,7580	0,0000	0,7069	0,7237	0,6750	0,0000
158508	0,7517	0,0000	0,6165	0,1000	0,0000	0,0000
158509	0,7278	0,7134	0,6587	0,7944	0,0000	0,6750
159063	0,0000	0,1660	0,7147	0,7740	0,0000	0,0000
164959	0,0000	0,0000	0,0000	0,6737	0,0000	0,6750
165127	0,0000	0,0000	0,1000	0,5725	0,6750	0,0000

165131	0,0000	0,0000	0,0000	0,8344	0,9000	0,6750
165133	0,5729	0,0000	0,0000	0,5728	0,0000	0,0000
165134	0,0000	0,0000	0,0000	0,6829	0,9000	0,0000
165136	0,0000	0,0000	0,0500	0,6731	0,0000	0,0000
165138	0,0000	0,7652	0,0000	0,6134	0,0000	0,0000
165139	0,7192	0,5920	0,0000	0,6567	0,9000	0,2250
166560	0,5302	0,0000	0,1000	0,9448	0,6750	0,0000
166590	0,0000	0,7219	0,0000	0,7131	0,0000	0,0000
166595	0,0000	0,0000	0,0500	0,6930	0,0000	0,0000
166596	0,0000	0,0000	0,0000	0,5927	0,0000	0,0000
166598	0,0000	0,0000	0,1000	0,6412	0,9000	0,0000
166600	0,0000	0,0000	0,1000	0,5524	0,0000	0,0000
166608	0,7436	0,7364	0,0000	0,5748	0,0000	0,0000
166609	0,9508	0,0000	0,0000	0,0000	0,0000	0,0000
166611	0,0000	0,0000	0,0500	0,5427	0,0000	0,0000
166866	0,7679	0,0000	0,0000	0,0000	0,9000	0,0000
166873	0,0000	0,7364	0,1000	0,0000	0,0000	0,0000
166875	0,0000	0,5920	0,0500	0,0000	0,0000	0,0000
166876	0,0000	0,6642	0,0500	0,0500	0,0000	0,9000
166903	0,0000	0,0000	0,0500	0,8338	0,0000	0,0000
166909	0,0000	0,0000	0,0000	0,6276	0,0000	0,0000
167718	1,0000	0,0000	0,0000	0,0000	0,0000	0,0000
168140	0,6704	0,0000	0,1000	0,0500	0,0000	0,0000
168407	0,8289	0,0000	0,1000	0,0000	0,0000	0,0000
168441	0,8045	0,0000	0,0000	0,0000	0,2250	0,9000
168494	0,0000	0,0000	0,0000	0,7936	0,4500	0,0000
168506	0,6704	0,0000	0,0000	0,0000	0,0000	0,6750
168556	0,0000	0,6642	0,0000	0,0000	0,0000	0,9000
168559	0,0000	0,6930	0,0000	0,0000	0,0000	0,9000
168757	0,7923	0,9096	0,1000	0,0500	0,0000	0,0000
168783	0,8167	0,0000	0,0000	0,0000	0,0000	0,0000
168784	0,0000	0,7075	0,0000	0,0000	0,6750	0,0000
177933	0,6836	0,6991	0,7850	0,7331	0,4500	0,0000
188544	0,6142	0,6981	0,6553	0,6993	0,0000	0,9000
188776	0,0000	0,0000	0,6867	0,0000	0,0000	0,0000
188777	0,6935	0,6958	0,7264	0,6292	0,0000	0,2250
188810	0,7111	0,6882	0,7752	0,0000	0,0000	0,0000
188811	0,6582	0,7219	0,0000	0,0000	0,0000	0,6750
188947	0,0000	0,6714	0,1000	0,0500	0,0000	0,0000